FRONTIERS IN CHEMISTRY - RISING STARS: ASIA

EDITED BY: Jyotirmayee Mohanty, Hongyan Sun, Taner Yonar,
Tsuyoshi Minami, Jafar Soleymani, Basem Moosa, Lei Guo,
Qianxiong Zhou and Wukun Liu

frontiers Research Topics

About Frontiers

Frontiers is more than just an open-access publisher of scholarly articles: it is a pioneering approach to the world of academia, radically improving the way scholarly research is managed. The grand vision of Frontiers is a world where all people have an equal opportunity to seek, share and generate knowledge. Frontiers provides immediate and permanent online open access to all its publications, but this alone is not enough to realize our grand goals.

Frontiers Journal Series

The Frontiers Journal Series is a multi-tier and interdisciplinary set of open-access, online journals, promising a paradigm shift from the current review, selection and dissemination processes in academic publishing. All Frontiers journals are driven by researchers for researchers; therefore, they constitute a service to the scholarly community. At the same time, the Frontiers Journal Series operates on a revolutionary invention, the tiered publishing system, initially addressing specific communities of scholars, and gradually climbing up to broader public understanding, thus serving the interests of the lay society, too.

Dedication to Quality

Each Frontiers article is a landmark of the highest quality, thanks to genuinely collaborative interactions between authors and review editors, who include some of the world's best academicians. Research must be certified by peers before entering a stream of knowledge that may eventually reach the public - and shape society; therefore, Frontiers only applies the most rigorous and unbiased reviews.

Frontiers revolutionizes research publishing by freely delivering the most outstanding research, evaluated with no bias from both the academic and social point of view. By applying the most advanced information technologies, Frontiers is catapulting scholarly publishing into a new generation.

What are Frontiers Research Topics?

Frontiers Research Topics are very popular trademarks of the Frontiers Journals Series: they are collections of at least ten articles, all centered on a particular subject. With their unique mix of varied contributions from Original Research to Review Articles, Frontiers Research Topics unify the most influential researchers, the latest key findings and historical advances in a hot research area! Find out more on how to host your own Frontiers Research Topic or contribute to one as an author by contacting the Frontiers Editorial Office: frontiersin.org/about/contact

FRONTIERS IN CHEMISTRY - RISING STARS: ASIA

Topic Editors:
Jyotirmayee Mohanty, Bhabha Atomic Research Centre (BARC), India
Hongyan Sun, City University of Hong Kong, Hong Kong, SAR China
Taner Yonar, Uludağ University, Turkey
Tsuyoshi Minami, University of Tokyo, Japan
Jafar Soleymani, Tabriz University of Medical Sciences, Iran
Basem Moosa, King Abdullah University of Science and Technology, Saudi Arabia
Lei Guo, Tongren Universityen, China
Qianxiong Zhou, Technical Institute of Physics and Chemistry (CAS), China
Wukun Liu, Nanjing University of Chinese Medicine, China

Table of Contents

Editorial: Frontiers in Chemistry-Rising Stars: Asia

Lei Guo[1], Jyotirmayee Mohanty[2]*, Wukun Liu[3], Taner Yonar[4], Hongyan Sun[5], Tsuyoshi Minami[6], Jafar Soleymani[7], Basem Moosa[8] and Qianxiong Zhou[9]

[1]School of Material and Chemical Engineering, Tongren University, Tongren, China, [2]Radiation and Photochemistry Division, Bhabha Atomic Research Centre, Mumbai, India, [3]Jiangsu Collaborative Innovation Center of Chinese Medicinal Resources Industrialization, Nanjing University of Chinese Medicine, Nanjing, China, [4]Environmental Engineering Department, Engineering Faculty, Bursa Uludag University, Bursa, Turkey, [5]Department of Chemistry and Center of Super-Diamond and Advanced Films (COSDAF), City University of Hong Kong, Hong Kong SAR, China, [6]Institute of Industrial Science, The University of Tokyo, Tokyo, Japan, [7]Pharmaceutical Analysis Research Center, Tabriz University of Medical Sciences, Tabriz, Iran, [8]Physical Science and Engineering Division, King Abdullah University of Science and Technology, Thuwal, Saudi Arabia, [9]Key Laboratory of Photochemical Conversion and Optoelectronic Materials, Technical Institute of Physics and Chemistry, Chinese Academy of Sciences, Beijing, China

Editorial on the Research Topic

Frontiers in Chemistry-Rising Stars: Asia

Rising Stars: Asia is dedicated to collecting the high-quality work of outstanding researchers in the early stages of their independent careers, working across the Asian continent including the countries like China, India, Saudi Arabia, South Korea, Jordan, and Pakistan in the field of chemistry. This collection aims to showcase research from all fields of chemistry, *i.e.*, nanoscience, inorganic chemistry, green sustainable chemistry, medicinal and pharmaceutical chemistry, analytical chemistry, computational chemistry and more prominently, the chemical biology. This collection also presents advances in theory, and methodology, along with applications to fascinating problems.

Chemical biology mainly deals with the application of chemical techniques/methods, analysis, and chemicals produced through synthetic chemistry, to the study and manipulation of biological processes. Chemicals including natural and unnatural small molecules and drugs are used to address biological problems at a mechanistic level. These studies are encouraging and have inspired outstanding Asian researchers to design new compounds and more advanced analytical techniques to maximize the chemical results of their research. The primary objective of this research topic is to explore the latest developments in the field, focusing on design and synthesis of novel compounds, and/or their computational optimization as well as their biological applications.

Bharti et al. successfully demonstrated the green synthesis of crystalline gold-zinc oxide nanocomposites under organic solvent-free conditions at room temperature. They have achieved stable Au-ZnO/Zn(OH)$_2$ nanocomposites by varying the reaction time and reagent concentrations. The *in situ* embedded gold nanoparticles enhance the luminescent properties of the nanocomposite materials which have been explored as bioimaging materials in human cells and applied for visible light–induced photodegradation of rhodamine-B dye. The study can be utilized to design and develop luminescent nanocomposite materials for bioimaging and dye degradation applications.

Sharfalddin et al. synthesized five transition metal complexes of sulfaclozine with Cu(II), Co(II), Ni(II), Zn(II), and Fe(II), and characterized their structural properties through various measurements. The conclusions drawn by theoretical calculations are consistent with the experimental results, indicating that copper and nickel in the metal complex have good coordination stability. DNA binding titration and molecular docking simulation have been utilized to evaluate the bio-activities of the characterized complexes. These results were supported by *in vitro* cytotoxicity assays showing that the Cu(II) and Ni(II) complexes display promising antitumor activity against colon and breast cancer cell lines.

Chen et al. synthesized seventeen kinds of glycosides of 1,3,4-thiadiazole derivatives and studied their antifungal activities. According to the structure-activity relationship analysis, the type and position of the substituents of the benzene ring in the derivatives play an important role in antifungal activity. The *in vitro* antibacterial activity experiments show that the derivatives have good antibacterial activity when the para-substituent is a fluorine atom or a nitro group.

Tian et al. investigated the chemical, phytochemical, toxicological and pharmacological properties of *Vaccaria segetalis* in the past 40 years. They summarized a large number of literatures, and mainly introduced the research progress of *Vaccaria segetalis* in detail from the aspects of its composition, clinical application, and biological activity.

Malik et al. synthesized eight new pyran-linked phthalazinone pyrazole hybrid compounds and evaluated their cytotoxicity in lung cancer and cervical cancer cells, respectively. The results show that the hybrid compound of methyl substitution on pyrazole and two cyano groups on pyran has a good inhibitory response to both types of cells. In addition, molecular modeling studies have shown that the two kinds of hybrid compounds have higher binding affinity to proteins and show excellent drug likelihood.

Zhu et al. introduced the development of isocyanide in biomolecular labeling from three strategies: two-component bio-orthogonal reaction, multi-component reaction, and metal chelate reaction. Among them, isocyanide-tetrazine reaction is a well-studied biomolecular labeling technology which enriches the potency of isocyanide as a bio-orthogonal handle. In addition, the methods of introducing isocyano groups into biomacromolecules are discussed in detail to facilitate the development of biomolecular markers in the future.

Choe et al. have described about the biodegradable plastics and the factors affecting the biodegradation of these plastics. The biodegradation levels reported by various groups or studies in different environments vary to a great extent. This article clarifies the common misconceptions and truths about biodegradation by bridging the three gaps in biodegradable plastics. These enable readers to accurately understand the current status and future development direction of real biodegradable plastics.

Xiao et al. established a high-throughput ICP-MS method for the detection of 62 elemental impurities in high-matrix calcium carbonate. The impurity content in calcium carbonate preparation from 9 manufacturers and two types of raw materials (light calcium carbonate and ground calcium carbonate) was examined, which showed that ground calcium carbonate was more suitable for the pediatric supplements.

Wang et al. discussed the structure and physiological functions of mitochondria and mitochondria dysfunction related diseases. Moreover, the research progress of mitochondria-targeting agents based on small molecules, biomolecules, and nanomaterial and their potential in targeted drug delivery,

novel biological applications and therapeutic strategies is comprehensively described. Therefore, this study will greatly promote the design and exploration of mitochondrial targeting molecules and their targeting mechanisms.

Fasfous et al. prepared Fe/Ti-oxide modified carbon nanotube nanocomposites and analyzed its ability to adsorb Co ions in a simulated solution. The presence of CNTs hampers the growth of Fe_3O_4 and TiO_2 particles and forming smaller nano-particles leading to better Co removal from solution. Better Co retention was observed at higher Ti/Fe loads and lower mass of CNTs. The results show that the combination of Fe/Ti oxide and CNTs has a synergistic effect on the retention of cobalt ions.

Yasmeen et al. were inspired by the use of graphics to manipulate chemical structures and nanostructures and studied the largest-edge Mostar invariant of an n-vertex cactus graph with a fixed number of cycles. Some lemmas have been proved by using graph transformations and calculations.

Wu et al. designed and synthesized a series of pyrimidine derivatives containing amide groups. These synthetic pyrimidine derivatives were verified for their biological activity through *in vitro* antifungal experiments. The results show that 5-Bromo-2-fluoro-N-(3-((2-methyl-6-(trifluoromethyl)Pyrimidin-4-yl)oxy)phenyl)benzamide has excellent antifungal activity, which also shows that the compound has the potential to be developed as a pesticide.

We have presented here some snippets of different research activities in the field of chemical biology. We expect that this will be a handy reference tool for students and researchers working in different areas of chemistry to carry out biological studies of some novel systems having potential applications.

AUTHOR CONTRIBUTIONS

LG and JM wrote the first draft. WL, TY, HS, TM, JS, BM, and QZ provided critical comments and editorial suggestions for revisions. All the authors agreed on the submitted version.

Synthesis and Bioactivities of Novel 1,3,4-Thiadiazole Derivatives of Glucosides

Meihang Chen[1]*, Xun Zhang[1], Daowang Lu[1], Hairong Luo[1], Zengyan Zhou[1], Xufeng Qin[1], Wenneng Wu[2]* and Guoping Zhang[3]

[1]Colleges of Material and Chemistry Engineering, Tongren University, Tongren, China, [2]Colleges of Food and Pharmaceutical Engineering, Guiyang University, Guiyang, China, [3]Colleges of Chemistry and Material Science, Huaibei Normal University, Huaibei, China

A series of novel 1,3,4-thiadiazole derivatives of glucosides were synthesized by the starting materials D-glucose and 5-amino-1,3,4-thiadiazole-2-thiol in good yields with employing a convergent synthetic route. The results of bioactivities showed that some of the target compounds exhibited good antifungal activities. Especially, compounds **4i** showed higher bioactivities against *Phytophthora infestans* (*P. infestans*), with the EC_{50} values of 3.43, than that of Dimethomorph (5.52 μg/ml). In addition, the target compounds exhibited moderate to poor antibacterial activities against *Xanthomonas oryzae p*v. *oryzae* (*Xoo*), *Xanthomonas campestris p*v. *citri* (*Xcc*).

Keywords: thiadiazole, amide, glucoside, synthesis, bioactivity

INTRODUCTION

Crop disease, caused by fungi, bacteria, viruses, and nematodes and parasitic seed plants, can effect on the biological or non-biological factors of plants causing the phenomenon of a series of morphological, physiological and biochemical pathologic changes, further blocking the normal growth and the development process and the human economic benefits (Zhan et al., 2015). Nowadays, some of the traditional fungicides and bactericides, such as Carbendazim, Kresoxim-methyl, Streptomycin sulfate, Bismerthiazol, etc., have been widely used to prevent and control plant fungal and bacterial diseases. However, long-term using these pesticides could lead to drug resistance, serious ecological, and environmental problem (Aktar et al., 2009). Therefore, development of novel and promising fungicides and bactericides is still an urgent task.

1,3,4-Thiadiazole derivatives have shown extensive biological activities, such as anti-inflammatory (Maddila et al., 2016), anticancer (Yang et al., 2012; Sridhar et al., 2020), antifungal (Alwan et al., 2015; Bhinge et al., 2015; Chudzik et al., 2019), antibacterial (Aggarwal et al., 2012; Taflan et al., 2019; Zhang et al., 2019), and plant growth regulator (Knyazyan et al., 2012) activities. Since 1,3,4-thiadiazole compounds with antibacterial activity was synthesized by Masaki in the 1950s, 1,3,4-thiadiazole pesticides, such as Bismerthiazol and Thiodiazole-copper, have been developed and widely used in agriculture. Recent years, a variety of studies found that amide derivatives containing 1,3,4-thiadiazole thioether moiety showed good antifungal activities against *Fusarium oxysporum* (*F. oxysporum*), *Cytospora mandshurica* (*C. mandshurica*), and *Gibberella zeae* (*G. zeae*) at 50 mg/L (Xie et al., 2016) and exhibited exciting antibacterial activities against *Xanthomonas oryzae p*v. *oryzae* (*Xoo*), *Xanthomonas campestris p*v. *citri* (*Xcc*), and *Ralstonia solanacearum* (*Rs*) (Chen J. et al., 2019).
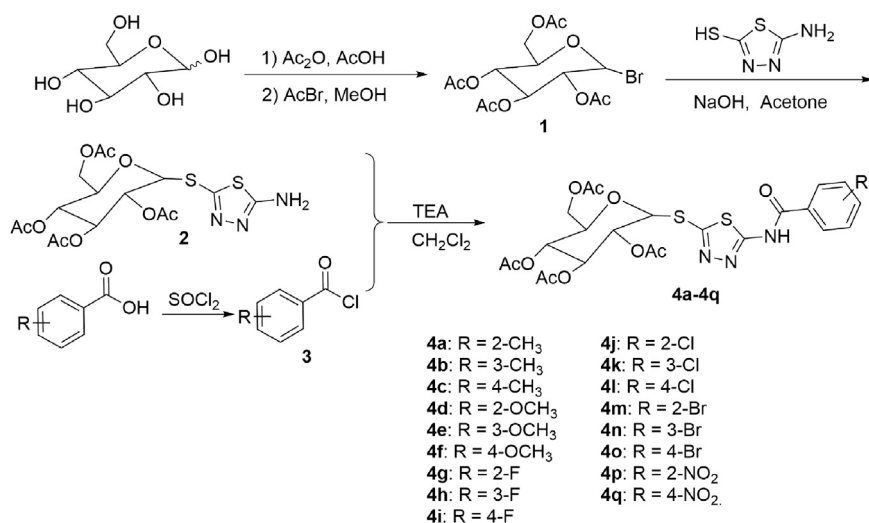
FIGURE 1 | Synthetic route of the target compounds **4a–4q**.

Glycosides are secondary metabolites that widely exist in all organs of plants, such as flowers, fruits, leaves, skins, and roots, etc (Gruner et al., 2002), and previous studies found that glycosides had a wide range of pharmacological activities, such as antiviral (Chen W. et al., 2019; Khodair et al., 2019), antibacterial (Mohammed et al., 2019), anticancer (Gurung et al., 2018; Rahim et al., 2020), antioxidant (Jiang et al., 2018; Hawas et al., 2019), and anti-HIV (He et al., 2019) activities. Meanwhile, studies also found that glycoside derivatives showed exceeding inhibitory activities against plant pathogens. For example, Ningnanmycin, an important glycoside biological pesticide, is mainly used in rice seedling blight, soybean root rot, rice stripe disease, apple spot deciduous leaf disease and cucumber powdery mildew (Hu et al., 1997). In addition, it was also found that glycosylation is one of the effective ways to improve the functional activity of active lead compounds and develop new drugs. (Gurung et al., 2018; Wu et al., 2014).

In order to develop new lead compounds with highly bioactivity, in this study, we aimed to introduce a 1,3,4-thiadiazole group into glucosides moiety to design a series of novel 1,3,4-thiadiazole derivatives of glucosides and then evaluate for their antifungal and antibacterial activities. Results indicated that some of the target compounds exhibited good antifungal activities. Especially, the compounds **4i** showed higher bioactivities against *Phytophthora infestans* (*P. infestans*), with the EC_{50} values of 3.43 μg/ml, respectively, than that of Dimethomorph (5.52 μg/ml). In addition, the target compounds showed moderate to poor antibacterial activities against *Xoo* and *Xcc*. As far as we know, this is the first report on the antifungal and antibacterial activities of 1,3,4-thiadiazole derivatives of glucosides.

MATERIALS AND METHODS

Materials and Instruments

Melting points were determined on an XT-4 melting apparatus (Beijing Tech Instrument Co., China). ^{1}H NMR and ^{13}C NMR spectra were measured on a Bruker AVANCE III TM 400 and HD 600 MHz Digital NMR Spectrometer (Bruker Company, Billerica, MA, US.) in CDCl$_3$ as solvent and recorded in relative to internal standard tetramethylsilane. High-resolution mass spectrometry (HRMS) was carried out on an Agilent Technologies 6540 UHD Accurate-Mass Q-TOF LC/MS (Agilent Technologies, Palo Alto, CA, United States). The course of the reactions was monitored by thin-layer chromatography (TLC) analysis on silica gel GF254. All reagents and solvents meet the standards of analytical reagent before use.

Chemistry

Preparation of 2,3,4,6-tetra-*O*-acetyl-α-*D*-glucopyranosyl bromide (**1**). As shown in **Figure 1**, acetic anhydride (88 ml, 0.9 mol) was added to a solution of *D*-glucose (29.75 g, 0.15 mol) in glacial acetic acid (300 ml) and stirred at room temperature for 20 min. Then, perchloric acid (0.3 ml) was added to the above reaction mixture at room temperature. After TLC analysis showed complete disappearance of *D*-glucose, a solution of acetyl bromide (34 ml, 0.45 mol) in 50 ml CH$_2$Cl$_2$ was added to the resultant reaction mixture and stirred at room temperature. After the completion of the reaction, the reaction mixture was poured into water and extracted with CH$_2$Cl$_2$. The organic layer was dried, filtered, and evaporated in vacuo to remove CH$_2$Cl$_2$. The crude product was recrystallized by a mixture of petroleum ether and diethyl ether (volume ratio 1:2) to afford intermediate **1**. (Scattolin et al., 2020). ^{1}H NMR spectral data for intermediate **1** are listed in the Supplementary Material.

Preparation of (2*R*,3*R*,4*S*,5*R*,6*R*)-2-(acetoxymethyl)-6-((5-amino-1,3,4-thiadiazol-2-yl)thio)tetra hydro-2*H*-pyran-3,4,5-triyltriacetate (**2**). A mixture of 2-amino-5-mercapto-1,3,4-thiadiazole (1.33 g, 10.0 mmol), acetone (50 ml), NaOH (0.4 g, 10.0 mmol), and water (10 ml) was stirred for 30 min at room temperature. Then, a solution of intermediate **1** (0.98 g, 10.0 mmol) in 5 ml acetone was added dropwise and continuously stirred at room temperature. After the reaction

completed (monitored by TLC), acetone was evaporated in vacuo, the residues were diluted with water, extracted with CH_2Cl_2. The combined CH_2Cl_2 extract was dried over anhydrous sodium sulfate, evaporated in vacuo and separated by silica gel column chromatography to afford intermediate **2** (Kamat et al., 2007). ^{1}H NMR spectral data for intermediate **2** are listed in the Supplementary Material.

General procedure for preparation of the target compounds **4a–4q**. Substituted benzoic acid (1.2 mmol) was added in 2 ml $SOCl_2$ and refluxed for about 2 h $SOCl_2$ was distilled off in vacuo to obtain intermediates **3**. And then, a solution of intermediate **3** in 2 ml CH_2Cl_2 was added dropwise to a mixture of the intermediate **2** (1.0 mmol) and triethylamine (TEA, 1.2 mmol) in 10 ml CH_2Cl_2. After the reaction was completed (monitored by TLC), the mixture was diluted with water, the organic layer was dried over anhydrous sodium sulfate, filtered and distilled off in vacuo, and the crude products were recrystallized with isopropanol to afford title compounds **4a–4q**.

(2R,3R,4S,5R,6R)-2-(acetoxymethyl)-6-((5-(2-methylbenzamido)-1,3,4-thiadiazol-2-yl)thio)tetrahy dro-2H-pyran-3,4,5-triyltriacetate (**4a**). White solid; yield 67.1%; m. p. 160–162°C; R_f = 0.67 (ethyl acetate: petroleum ether, 1:2); IR (KBr, cm^{-1}) v: 3,433 (NH), 1747 (COO), 1,678 (CON); ^{1}H NMR (400 MHz, CDCl$_3$, ppm) δ: 7.66 (d, J = 8.3 Hz, 1H, Ar-H), 7.49 (d, J = 7.6 Hz, 1H, Ar-H), 7.42–7.30 (m, 2H, Ar-H), 5.29 (t, J = 10.0 Hz, 1H, H-3′), 5.21–5.06 (m, 3H, H-1′, H-2′, H-4′), 4.34–4.16 (m, 2H, H-5′, H-6′), 3.84–3.80 (m, 1H, H-6′′), 2.55 (s, 3H, CH$_3$), 2.15 (s, 3H, CH$_3$), 2.10 (s, 3H, CH$_3$), 2.04 (s, 3H, CH$_3$), 2.02 (s, 3H, CH$_3$); ^{13}C NMR (150 MHz, CDCl$_3$, ppm) δ: 170.66 (COCH$_3$), 170.17 (COCH$_3$), 169.45 (COCH$_3$), 169.34 (CONH), 169.28 (thiadiazole-C), 158.58 (thiadiazole-C), 157.90 (Ar-C), 137.27 (Ar-C), 132.05 (Ar-C), 131.56 (Ar-C), 130.75 (Ar-C), 129.18 (Ar-C), 82.52 (C-1′), 75.97 (C-5′), 73.89 (C-3′), 69.28 (C-2′), 67.87 (C-4′), 61.62 (C-6′), 20.74 (CH$_3$), 20.61 (CH$_3$), 20.59 (CH$_3$), 20.02 (CH$_3$); HRMS [M + H]$^+$ calculated for $C_{24}H_{27}N_3O_{10}S_2$: m/z 582.1230, found 582.1209.

(2R,3R,4S,5R,6R)-2-(acetoxymethyl)-6-((5-(3-methylbenzamido)-1,3,4-thiadiazol-2-yl)thio)tetra hydro-2H-pyran-3,4,5-triyltriacetate (**4b**). White solid; yield 65.3%; m. p. 163–165°C; R_f = 0.45 (ethyl acetate: petroleum ether, 1:2); IR (KBr, cm^{-1}) v: 3,468 (NH), 1749 (COO), 1,666 (CON); ^{1}H NMR (400 MHz, CDCl$_3$, ppm) δ: 7.99 (s, 1H, Ar-H), 7.94 (d, J = 7.5 Hz, 1H, Ar-H), 7.51–7.43 (m, 2H, Ar-H), 5.28 (t, J = 9.0 Hz, 1H, H-3′), 5.21–4.98 (m, 3H, H-1′, H-2′, H-3′), 4.40–4.05 (m, 2H, H-5′, H-6′), 3.74–3.70 (m, 1H, H-6′′), 2.48 (s, 3H, CH$_3$), 2.14 (s, 3H, CH$_3$), 2.09 (s, 3H, CH$_3$), 2.05 (s, 3H, CH$_3$), 2.02 (s, 3H, CH$_3$); ^{13}C NMR (150 MHz, CDCl$_3$, ppm) δ: 171.01 (COCH$_3$), 170.16 (COCH$_3$), 169.41 (COCH$_3$), 165.24 (CONH), 162.64 (thiadiazole-C), 155.20 (thiadiazole-C), 139.01 (Ar-C), 134.34 (Ar-C), 130.86 (Ar-C), 128.75 (Ar-C), 125.40 (Ar-C), 84.07 (C-1′), 76.31 (C-5′), 73.58 (C-3′), 69.67 (C-2′), 67.79 (C-4′), 61.77 (C-6′), 21.35 (CH$_3$), 20.72 (CH$_3$), 20.64 (CH$_3$), 20.58 (CH$_3$); HRMS [M + H]$^+$ calculated for $C_{24}H_{27}N_3O_{10}S_2$: m/z 582.1230, found 582.1208.

(2R,3R,4S,5R,6R)-2-(acetoxymethyl)-6-((5-(4-methylbenzamido)-1,3,4-thiadiazol-2-yl)thio)tetra hydro-2H-pyran-3,4,5-triyltriacetate (**4c**). White solid; yield 75.1%; m. p. 159–161°C; R_f = 0.63 (ethyl acetate: petroleum ether, 1:2); IR (KBr, cm^{-1}) v: 3,433 (NH), 1747 (COO), 1,666 (CON); ^{1}H NMR (400 MHz, CDCl$_3$, ppm) δ: 11.76 (s, 1 H, NH), 8.05 (d, J = 8.1 Hz, 2 H, Ar-H), 7.36 (d, J = 8.0 Hz, 2H, Ar-

H), 5.49 (d, J = 3.2 Hz, 1H, H-1′), 5.38 (t, J = 10.0 Hz, 1H, H-3′), 5.11 (dd, J = 9.9, 3.3 Hz, 1H, H-2′), 5.05 (d, J = 10.1 Hz, 1H, H-4′), 4.21 (d, J = 6.1 Hz, 2H, H-5′, H-6′′), 4.05–4.01 (m, 1H, H-6′), 2.47 (s, 3H, CH$_3$), 2.19 (s, 3H, CH$_3$), 2.12 (s, 3H, CH$_3$), 2.09 (s, 3H, CH$_3$), 2.00 (s, 3H, CH$_3$); ^{13}C NMR (150 MHz, CDCl$_3$, ppm) δ: 170.93 (COCH$_3$), 170.10 (COCH$_3$), 169.35 (COCH$_3$), 164.84 (CONH), 162.72 (thiadiazole-C), 155.32 (thiadiazole-C), 144.59 (Ar-C), 129.77 (Ar-C), 128.41 (Ar-C), 84.08 (C-1′), 76.36 (C-5′), 73.60 (C-3′), 69.71 (C-2′), 67.79 (C-4′), 61.76 (C-6′), 21.77 (CH$_3$), 20.72 (CH$_3$), 20.68 (CH$_3$), 20.60 (CH$_3$); HRMS [M + H]$^+$ calculated for $C_{24}H_{27}N_3O_{10}S_2$: m/z 582.1230, found 582.1209.

(2R,3R,4S,5R,6R)-2-(acetoxymethyl)-6-((5-(2-methoxybenzamido)-1,3,4-thiadiazol-2yL)thio)tetra hydro-2H-pyran-3,4,5-triyltriacetate (**4d**). White solid; yield 68.7%; m. p. 168–170°C; R_f = 0.33 (ethyl acetate: petroleum ether, 1:2); IR (KBr, cm^{-1}) v: 3,433 (NH), 1749 (COO), 1,687 (CON); ^{1}H NMR (400 MHz, CDCl$_3$, ppm) δ: 12.13 (s, 1H, NH), 8.25 (d, J = 9.6 Hz, 1H, Ar-H), 7.61 (t, J = 8.8 Hz, 1H, Ar-H), 7.19 (t, J = 7.6 Hz, 1H, Ar-H), 7.10 (d, J = 8.4 Hz, 1H, Ar-H), 5.30 (t, J = 9.2 Hz, 1H, H-3′), 5.18–5.08 (m, 3H, H-1′, H-2′, H-4′), 4.32–4.22 (m, 2H, H-5′, H-6′), 4.12 (s, 3H, OCH$_3$), 3.86–3.82 (m, 1H, H-6′′), 2.16 (s, 3H, CH$_3$), 2.10 (s, 3H, CH$_3$), 2.04 (s, 3H, CH$_3$), 2.01 (s, 3H, CH$_3$); ^{13}C NMR (150 MHz, CDCl$_3$, ppm) δ: 171.01 (COCH$_3$), 170.13 (COCH$_3$), 169.40 (COCH$_3$), 169.38 (COCH$_3$), 162.61 (CONH), 161.06 (thiadiazole-C), 158.08 (thiadiazole-C), 155.19 (Ar-C), 135.32 (Ar-C), 132.83 (Ar-C), 121.94 (Ar-C), 118.07 (Ar-C), 111.82 (Ar-C), 84.17 (C-1′), 76.32 (C-5′), 73.63 (C-3′), 69.67 (C-2′), 67.85 (C-4′), 61.83 (C-6′), 56.48 (OCH$_3$), 21.77 (CH$_3$), 20.72 (CH$_3$), 20.68(CH$_3$), 20.60 (CH$_3$); HRMS [M + H]$^+$ calculated for $C_{24}H_{27}N_3O_{11}S_2$: m/z 598.1142, found 598.1161.

(2R,3R,4S,5R,6R)-2-(acetoxymethyl)-6-((5-(3-methoxybenzamido)-1,3,4-thiadiazol-2-yl)thio)tetra hydro-2H-pyran-3,4,5-triyltriacetate (**4e**). White solid; yield 73.2%; m. p. 169–171°C; R_f = 0.41 (ethyl acetate: petroleum ether, 1:2); IR (KBr, cm^{-1}) v: 3,450 (NH), 1749 (COO), 1,666 (CON); ^{1}H NMR (400 MHz, CDCl$_3$, ppm) δ: 11.40 (s, 1H, NH), 7.67 (d, J = 7.7 Hz, 1H, Ar-H), 7.58 (s, 1H, Ar-H), 7.48 (t, J = 8.0 Hz, 1H, Ar-H), 7.23 (d, J = 10.7 Hz, 1H, Ar-H), 5.29 (t, J = 9.2 Hz, 1H, H-3′), 5.21–5.04 (m, 3H, H-1′, H-2′, H-4′), 4.34–4.11 (m, 2H, H-5′, H-6′), 3.90 (s, 3H, OCH$_3$), 3.75–3.71 (m, 1H, H-6′′), 2.13 (s, 3H, CH$_3$), 2.10 (s, 3H, CH$_3$), 2.05 (s, 3H, CH$_3$), 2.02 (s, 3H, CH$_3$); ^{13}C NMR (150 MHz, CDCl$_3$, ppm) δ: 170.54 (COCH$_3$), 170.23 (COCH$_3$), 169.95 (COCH$_3$), 169.50 (CONH), 165.04 (thiadiazole-C), 160.01(thiadiazole-C), 132.19 (Ar-C), 130.08 (Ar-C), 120.61 (Ar-C), 120.05 (Ar-C), 113.18 (Ar-C), 84.44 (C-1′), 75.17 (C-5′), 71.62 (C-3′), 67.16 (C-2′), 66.98 (C-4′), 61.56 (C-6′), 55.60 (OCH$_3$), 20.74 (CH$_3$), 20.66 (CH$_3$), 20.65 (CH$_3$), 20.56 (CH$_3$); HRMS [M + H]$^+$ calculated for $C_{24}H_{27}N_3O_{11}S_2$: m/z 598.1142, found 598.1162.

(2R,3R,4S,5R,6R)-2-(acetoxymethyl)-6-((5-(4-methoxybenzamido)-1,3,4-thiadiazol-2-yl)thio)tetra hydro-2H-pyran-3,4,5-triyltriacetate (**4f**). White solid; yield 75.0%; m. p. 166–168°C; R_f = 0.52 (ethyl acetate: petroleum ether, 1:2); IR (KBr, cm^{-1}) v: 3,462 (NH), 1747 (COO), 1,664 (CON); ^{1}H NMR (400 MHz, CDCl$_3$, ppm) δ: 8.04 (d, J = 8.9 Hz, 2H, Ar-H), 7.04 (d, J = 8.9 Hz, 2H, Ar-H), 5.28 (t, J = 9.2 Hz, 1H, H-3′), 5.20–5.04 (m, 3H, H-1′, H-2′, H-4′), 4.32–4.17 (m, 2H, H-5′, H-6′), 3.92 (s, 3H, OCH$_3$), 3.83–3.77 (m, 1H, H-6′′), 2.15 (s, 3H, CH$_3$), 2.10 (s, 3H, CH$_3$), 2.04 (s, 3H, CH$_3$), 2.01 (s, 3H, CH$_3$); ^{13}C NMR (150 MHz, CDCl$_3$, ppm) δ: 170.58 (COCH$_3$),

170.44 (COCH$_3$), 169.87(CONH), 169.79(thiadiazole-C), 163.63 (thiadiazole-C), 155.45 (Ar-C), 131.02 (Ar-C), 123.57 (Ar-C), 114.53 (Ar-C), 83.14 (C-1′), 74.69 (C-5′), 71.15 (C-3′), 68.07 (C-2′), 67.31 (C-4′), 62.42 (C-6′), 56.07 (OCH$_3$), 20.91 (CH$_3$), 20.88 (CH$_3$), 20.79 (CH$_3$), 20.76 (CH$_3$); HRMS [M + H]$^+$ calculated for C$_{24}$H$_{27}$N$_3$O$_{11}$S$_2$: m/z 598.1142, found 598.1162.

(2R,3R,4S,5R,6R)-2-(acetoxymethyl)-6-((5-(2-fluorobenzamido)-1,3,4-thiadiazol-2-yl)thio)tetrahy dro-2H-pyran-3,4,5-triyltriacetate (**4g**). White solid; yield 55.4%; m. p. 173–175°C; R_f = 0.61 (ethyl acetate: petroleum ether, 1:2); IR (KBr, cm^{-1}) v: 3,421 (NH), 1749 (COO), 1,676 (CON); ^{1}H NMR (400 MHz, CDCl$_3$, ppm) δ: 10.29 (s, 1H, NH), 8.17 (t, J = 7.8 Hz, 1H, Ar-H), 7.66 (d, J = 7.4 Hz, 1H, Ar-H), 7.38 (t, J = 8.0 Hz, 1H, Ar-H), 7.31–7.23 (m, 1H, Ar-H), 5.35–5.23 (m, 1H, H-3′), 5.19–5.08 (m, 3H, H-1′, H-2′, H-4′), 4.31 (dd, J = 12.5, 5.0 Hz, 1H, H-5′), 4.21 (dd, J = 12.5, 2.0 Hz, 1H, H-6′), 3.85–3.83 (m, 1H, H-6′′), 2.16 (s, 3H, CH$_3$), 2.10 (s, 3H, CH$_3$), 2.04 (s, 3H, CH$_3$), 2.01 (s, 3H, CH$_3$); ^{13}C NMR (150 MHz, CDCl$_3$, ppm) δ: 170.93 (COCH$_3$), 170.07 (COCH$_3$), 169.34 (COCH$_3$), 169.29 (COCH$_3$), 164.45 (CONH), 163.34 (thiadiazole-C), 155.18 (thiadiazole-C), 132.36 (Ar-C), 130.21 (Ar-C), 129.51 (Ar-C), 128.78 (Ar-C), 83.81 (C-1′), 76.48 (C-5′), 73.57 (C-3′), 69.68 (C-2′), 67.69 (C-4′), 61.69 (C-6′), 20.73 (CH$_3$), 20.60 (CH$_3$); HRMS [M + H]$^+$ calculated for C$_{23}$H$_{24}$FN$_3$O$_{10}$S$_2$: m/z 586.0932, found 586.0964.

(2R,3R,4S,5R, 6R)-2-(acetoxymethyl)-6-((5-(3-fluorobenzamido)-1,3,4-thiadiazol-2-yl)thio)tetra hydro-2H-pyran-3,4,5-triyltriacetate (**4h**). White solid; yield 70.2%; m. p. 174–176°C; R_f = 0.63 (ethyl acetate: petroleum ether, 1:2); IR (KBr, cm^{-1}) v: 3,435 (NH), 1749 (COO), 1,670 (CON); ^{1}H NMR (400 MHz, CDCl$_3$, ppm) δ: 12.30 (s, 1H, NH), 8.29 (s, 1H, Ar-H), 17–8.02 (M, 1H, Ar-H), 7.81 (d, J = 8.7 Hz, 1H, Ar-H), 7.46 (t, J = 7.9 Hz, 1H, Ar-H), 5.32–5.28 (m, 1H, H-3′), 5.20–5.05 (m, 3H, H-1′, H-2′, H-4′), 4.28 (dd, J = 12.5, 5.0 Hz, 1H, H-5′), 4.24–4.11 (m, 1H, H-6′), 3.78–3.73 (m, 1H, H-6′′), 2.14 (s, 3H, CH$_3$), 2.09 (s, 3H, CH$_3$), 2.05 (s, 3H, CH$_3$), 2.02 (s, 3H, CH$_3$); ^{13}C NMR (150 MHz, CDCl$_3$, ppm) δ: 170.93 (COCH$_3$), 170.07 (COCH$_3$), 169.34 (COCH$_3$), 169.29 (COCH$_3$), 164.45 (CONH), 163.34 (thiadiazole-C), 155.18 (thiadiazole-C), 132.36 (Ar-C), 130.21 (Ar-C), 129.51 (Ar-C), 128.78 (Ar-C), 83.81(C-1′), 76.48 (C-5′), 73.57 (C-3′), 69.68 (C-2′), 67.69 (C-4′), 61.69 (C-6′), 20.73 (CH$_3$), 20.60 (CH$_3$); HRMS [M + H]$^+$ calculated for C$_{23}$H$_{24}$FN$_3$O$_{10}$S$_2$: m/z 586.0932, found 586.0963.

(2R,3R,4S,5R,6R)-2-(acetoxymethyl)-6-((5-(4-fluorobenzamido)-1,3,4-thiadiazol-2-yl)thio)tetra hydro-2H-pyran-3,4,5-triyltriacetate (**4i**). White solid; yield 65.8%; m. p. 170–172°C; R_f = 0.64 (ethyl acetate: petroleum ether, 1:2); IR (KBr, cm^{-1}) v: 3,475 (NH), 1751 (COO), 1,676 (CON); ^{1}H NMR (400 MHz, CDCl$_3$, ppm) δ: 12.54 (s, 1H, NH), 8.36 (d, J = 8.2 Hz, 2H, Ar-H), 7.85 (d, J = 8.3 Hz, 2H, Ar-H), 5.28 (t, J = 9.3 Hz, 1H, H-3′), 5.18–5.09 (m, 2H H-1′, H-2′), 5.00 (d, J = 10.0 Hz, 1H, H-4′), 4.33 (dd, J = 12.5, 4.8 Hz, 1H, H-5′), 4.23 (dd, J = 12.5, 2.0 Hz, 1H, H-6′), 3.86–3.82 (m, 1H, H-6′′), 2.17 (s, 3H, CH$_3$), 2.09 (s, 3H, CH$_3$), 2.04 (s, 3H, CH$_3$), 2.01 (s, 3H, CH$_3$); ^{13}C NMR (150 MHz, CDCl$_3$, ppm) δ: 170.31 (COCH$_3$), 170.21 (COCH$_3$), 170.00 (COCH$_3$), 169.58 (COCH$_3$), 166.22 (CONH), 159.08 (thiadiazole-C), 158.51 (thiadiazole-C), 134.35 (Ar-C), 134.29 (Ar-C), 115.52 (Ar-C), 115.38 (Ar-C), 83.14 (C-1′),

74.72(C-5′), 71.83(C-3′), 67.12(C-2′), 66.83(C-4′), 61.34 (C-6′), 20.73 (CH$_3$), 20.67 (CH$_3$), 20.65 (CH$_3$), 20.59 (CH$_3$); HRMS [M + H]$^+$ calculated for C$_{23}$H$_{24}$FN$_3$O$_{10}$S$_2$: m/z 586.0932, found 586.0962.

(2R,3R,4S,5R,6R)-2-(acetoxymethyl)-6-((5-(2-chlorobenzamido)-1,3,4-thiadiazol-2-yl)thio)tetra hydro-2H-pyran-3,4,5-triyltriacetate (**4j**). White solid; yield 70.1%; m. p. 178–180°C; R_f = 0.55 (ethyl acetate: petroleum ether, 1:2); IR (KBr, cm^{-1}) v: 3,441 (NH), 1747 (COO), 1,668 (CON); ^{1}H NMR (400 MHz, CDCl$_3$, ppm) δ: 10.48 (s, 1H, NH), 7.90 (d, J = 8.4 Hz, 1H, Ar-H), 7.57–7.41 (m, 3H, Ar-H), 5.31–5.11 (m, 4H, H-3′, H-1′, H-2′, H-4′), 4.32–4.19 (m, 2H, H-5′, H-6′), 3.86–3.81 (m, 1H, H-6′′), 2.15 (s, 3H, CH$_3$), 2.10 (s, 3H, CH$_3$), 2.04 (s, 3H, CH$_3$), 2.01 (s, 3H, CH$_3$); ^{13}C NMR (150 MHz, CDCl$_3$, ppm) δ: 170.93 (COCH$_3$), 170.12 (COCH$_3$), 169.37 (COCH$_3$), 169.33 (COCH$_3$), 163.64 (CONH), 160.98 (thiadiazole-C), 155.66 (thiadiazole-C), 133.34 (Ar-C), 131.70 (Ar-C), 131.24 (Ar-C), 131.19 (Ar-C), 131.02 (Ar-C), 127.60 (Ar-C), 84.00 (C-1′), 76.39 (C-5′), 73.57 (C-3′), 69.65 (C-2′), 67.80 (C-4′), 61.75 (C-6′), 20.78 (CH$_3$), 20.68 (CH$_3$), 20.60 (CH$_3$); HRMS [M + H]$^+$ calculated for C$_{23}$H$_{24}$ClN$_3$O$_{10}$S$_2$: m/z 602.0641, found 602.0663.

(2R,3R,4S,5R,6R)-2-(acetoxymethyl)-6-((5-(3-chlorobenzamido)-1,3,4-thiadiazol-2-yl)thio)tetra hydro-2H-pyran-3,4,5-triyltriacetate (**4k**). White solid; yield 65.3%; m. p. 179–180°C; R_f = 0.66 (ethyl acetate: petroleum ether, 1:2); IR (KBr, cm^{-1}) v: 3,442 (NH), 1749 (COO), 1,674 (CON); ^{1}H NMR (400 MHz, CDCl$_3$, ppm) δ: 12.34 (s, 1H, NH), 8.16 (s, 1H, Ar-H), 8.08 (d, J = 7.8 Hz, 1H, Ar-H), 7.66 (d, J = 8.0 Hz, 1H, Ar-H), 7.52 (t, J = 7.9 Hz, 1H, Ar-H), 5.29 (t, J = 9.2 Hz, 1H, H-3′), 5.22–5.06 (m, 3H, H-1′, H-2′, H-4′), 4.37–4.10 (m, 2H, H-5′, H-6′), 3.84–3.81 (m, 1H, H-6′′), 2.14 (s, 3H, CH$_3$), 2.09 (s, 3H, CH$_3$), 2.05 (s, 3H, CH$_3$), 2.02 (s, 3H, CH$_3$); ^{13}C NMR (150 MHz, CDCl$_3$, ppm) δ: 170.89 (COCH$_3$), 170.12 (COCH$_3$), 169.35 (COCH$_3$), 169.33 (COCH$_3$), 164.26 (CONH), 163.15 (thiadiazole-C), 155.75 (thiadiazole-C), 135.22 (Ar-C), 133.60 (Ar-C), 132.57 (Ar-C), 130.32 (Ar-C), 128.74 (Ar-C), 126.94 (Ar-C), 83.98 (C-1′), 76.37 (C-5′), 73.52 (C-3′), 69.64 (C-2′), 67.79 (C-4′), 61.75 (C-6′), 20.74 (CH$_3$), 20.66 (CH$_3$), 20.60 (CH$_3$); HRMS [M + H]$^+$ calculated for C$_{23}$H$_{24}$ClN$_3$O$_{10}$S$_2$: m/z 602.0641, found 602.0661.

(2R,3R,4S,5R,6R)-2-(acetoxymethyl)-6-((5-(4-chlorobenzamido)-1,3,4-thiadiazol-2-yl)thio)tetra hydro-2H-pyran-3,4,5-triyltriacetate (**4l**). White solid; yield 78.5%; m. p. 178–180°C; R_f = 0.48 (ethyl acetate: petroleum ether, 1:2); IR (KBr, cm^{-1}) v: 3,450 (NH), 1751 (COO), 1,672 (CON); ^{1}H NMR (400 MHz, CDCl$_3$, ppm) δ: 11.88 (s, 1H, NH), 8.13 (d, J = 8.6 Hz, 2H, Ar-H), 7.55 (d, J = 8.6 Hz, 2H, Ar-H), 5.29 (t, J = 9.2 Hz, 1H, H-3′), 5.21–5.00 (m, 3H, H-1′, H-2′, H-4′), 4.36–4.25 (m, 1H, H-5′), 4.20 (dd, J = 12.5, 2.0 Hz, 1H, H-6′), 3.84–3.81 (m, 1H, H-6′′), 2.15 (s, 3H, CH$_3$), 2.11 (s, 3H, CH$_3$), 2.04 (s, 3H, CH$_3$), 2.01 (s, 3H, CH$_3$); ^{13}C NMR (150 MHz, CDCl$_3$, ppm) δ: 170.59 (COCH$_3$), 170.26 (COCH$_3$), 169.92 (COCH$_3$), 169.48 (COCH$_3$), 164.45 (CONH), 163.56 (thiadiazole-C), 155.49 (thiadiazole-C), 139.98 (Ar-C), 130.24 (Ar-C), 129.32 (Ar-C), 129.06 (Ar-C), 84.26 (C-1′), 75.32 (C-5′), 71.62 (C-3′), 67.09 (C-2′), 66.90 (C-4′), 61.66 (C-6′), 20.79 (CH$_3$), 20.70 (CH$_3$), 20.68 (CH$_3$),

20.58 (CH$_3$); HRMS [M + H]$^+$ calculated for C$_{23}$H$_{24}$ClN$_3$O$_{10}$S$_2$: m/z 602.0641, found 602.0664.

(2R,3R,4S,5R,6R)-2-(acetoxymethyl)-6-((5-(2-bromobenzamido)-1,3,4-thiadiazol-2-yl)thio)tetra hydro-2H-pyran-3,4,5-triyltriacetate (**4m**). White solid; yield 69.4%; m. p. 190–192°C; R_f = 0.65 (ethyl acetate: petroleum ether, 1:2); IR (KBr, cm^{-1}) v: 3,473 (NH), 1745 (COO), 1,689 (CON); ^{1}H NMR (400 MHz, CDCl$_3$, ppm) δ: 11.35 (s, 1H, NH), 7.76 (d, J = 7.2 Hz, 1H, Ar-H), 7.72 (d, J = 7.4 Hz, 1H, Ar-H), 7.51–7.44 (m, 2H, Ar-H), 5.29 (t, J = 9.2, 1H, H-3´), 5.16–5.08 (m, 3H, H-1´, H-2´, H-4´), 4.29 (dd, J = 12.5, 5.0 Hz, 1H, H-5´), 4.18 (dd, J = 12.5, 2.0 Hz, 1H, H-6´), 3.82–3.78 (m, 1H, H-6´´), 2.14 (s, 3H, CH$_3$), 2.10 (s, 3H, CH$_3$), 2.05 (s, 3H, CH$_3$), 2.02 (s, 3H, CH$_3$); ^{13}C NMR (150 MHz, CDCl$_3$, ppm) δ: 170.62 (COCH$_3$), 170.25 (COCH$_3$), 169.99 (COCH$_3$), 169.49 (COCH$_3$), 164.27 (CONH), 163.20 (thiadiazole-C), 155.98 (thiadiazole-C), 135.18 (Ar-C), 133.49 (Ar-C), 132.58 (Ar-C), 130.28 (Ar-C), 128.69 (Ar-C), 126.99 (Ar-C), 84.45 (C-1´), 75.22 (C-5´), 71.60 (C-3´), 67.17 (C-2´), 66.96 (C-4´), 61.64 (C-6´), 20.73 (CH$_3$), 20.67 (CH$_3$), 20.57 (CH$_3$); HRMS [M + H]$^+$ calculated for C$_{23}$H$_{24}$BrN$_3$O$_{10}$S$_2$: m/z 646.0171, found 646.0161.

(2R,3R,4S,5R,6R)-2-(acetoxymethyl)-6-((5-(3-bromobenzamido)-1,3,4-thiadiazol-2-yl)thio)tetrahy dro-2H-pyran-3,4,5-triyltriacetate (**4n**). White solid; yield 60.2%; m. p. 191–193°C; R_f = 0.70 (ethyl acetate: petroleum ether, 1:2); IR (KBr, cm^{-1}) v: 3,475 (NH), 1753 (COO), 1,676 (CON); ^{1}H NMR (400 MHz, CDCl$_3$, ppm) δ: 12.30 (s, 1H, NH), 8.29 (s, 1H, Ar-H), 8.11 (d, J = 9.2 Hz, Ar-H), 7.81 (d, J = 8.7 Hz, 1H, Ar-H), 7.46 (t, J = 7.9 Hz, 1H, Ar-H), 5.29 (t, J = 9.3 Hz, 1H, H-3´), 5.17–5.12 (m, 3H, H-1´, H-2´, H-4´), 4.28 (dd, J = 12.5, 5.0 Hz, 1H, H-5´), 4.19–4.16 (m, 1H, H-6´), 3.78–3.73 (m, 1H, H-6´´), 2.14 (s, 3H, CH$_3$), 2.09 (s, 3H, CH$_3$), 2.05 (s, 3H, CH$_3$), 2.02 (s, 3H, CH$_3$); ^{13}C NMR (150 MHz, CDCl$_3$, ppm) δ: 170.87 (COCH$_3$), 170.11 (COCH$_3$), 169.34 (COCH$_3$), 169.32 (COCH$_3$), 164.09 (CONH), 163.06 (thiadiazole-C), 155.82 (thiadiazole-C), 136.53 (Ar-C), 132.78 (Ar-C), 131.53 (Ar-C), 130.56 (Ar-C), 127.36 (Ar-C), 123.19 (Ar-C), 84.00 (C-1´), 76.39 (C-5´), 73.52 (C-3´), 69.67 (C-2´), 67.80 (C-4´), 61.76 (C-6´), 20.74 (CH$_3$), 20.68 (CH$_3$), 20.60(CH$_3$); HRMS [M + H]$^+$ calculated for C$_{23}$H$_{24}$BrN$_3$O$_{10}$S$_2$: m/z 646.0171, found 646.0162.

(2R,3R,4S,5R,6R)-2-(acetoxymethyl)-6-((5-(4-bromobenzamido)-1,3,4-thiadiazol-2-yl)thio)tetra dro-2H-pyran-3,4,5-triyltriacetate (**4o**). White solid; yield 70.3%; m. p. 188–190°C; R_f = 0.75 (ethyl acetate: petroleum ether, 1:2); IR (KBr, cm^{-1}) v: 3,435 (NH), 1751 (COO), 1,674 (CON); ^{1}H NMR (400 MHz, CDCl$_3$, ppm) δ: 12.45 (s, 1H, NH), 8.11 (d, J = 8.5 Hz, 2H, Ar-H), 7.72 (d, J = 8.5 Hz, 2H, Ar-H), 5.30 (t, J = 9.2 Hz, 1H, H-3´), 5.18–5.02 (m, 3H, H-1´, H-2´, H-4´), 4.32 (dd, J = 12.6, 4.8 Hz, 1H, H-5´), 4.20 (d, J = 12.3 Hz, 1H, H-6´), 3.82–3.79 (m, 1H, H-6´´), 2.16 (s, 3H, CH$_3$), 2.13 (s, 3H, CH$_3$), 2.04 (s, 3H, CH$_3$), 2.01 (s, 3H, CH$_3$); ^{13}C NMR (150 MHz, CDCl$_3$, ppm) δ: 170.93 (COCH$_3$), 170.07 (COCH$_3$), 169.34 (COCH$_3$), 169.29 (COCH$_3$), 164.45 (CONH), 163.34 (thiadiazole-C), 155.18 (thiadiazole-C), 132.36 (Ar-C), 130.21 (Ar-C), 129.51 (Ar-C), 128.78 (Ar-C), 83.81 (C-1´), 76.48(C-5´), 73.57 (C-3´), 69.68 (C-2´), 67.69 (C-4´), 61.69 (C-6´), 20.73 (CH$_3$), 20.60 (CH$_3$); HRMS [M + H]$^+$ calculated for C$_{23}$H$_{24}$BrN$_3$O$_{10}$S$_2$: m/z 646.0171, found 646.0161.

(2R,3R,4S,5R,6R)-2-(acetoxymethyl)-6-((5-(2-nitrobenzamido)-1,3,4-thiadiazol-2-yl)thio)tetrahy dro-2H-pyran-3,4,5-triyltriacetate (**4p**). Yellow solid; yield 53.4%; m. p. 188–190°C; R_f = 0.42 (ethyl acetate: petroleum ether, 1:2); IR (KBr, cm^{-1}) v: 3,458 (NH), 1751 (COO), 1,689 (CON); ^{1}H NMR (400 MHz, CDCl$_3$, ppm) δ: 13.02 (s, 1H, NH), 8.22 (d, J = 7.9 Hz, 1H, Ar-H), 7.85–7.75 (m, 3H, Ar-H), 5.32 (t, J = 9.0 Hz, 1H, H-3´), 5.15–5.03 (m, 3H, H-1´, H-2´, H-4´), 4.28 (dd, J = 12.5, 5.1 Hz, 1H, H-5´), 4.18 (dd, J = 12.5, 2.0 Hz, 1H, H-6´), 3.86–3.81 (m, 1H, H-6´´), 2.29 (s, 3H, CH$_3$), 2.12 (s, 3H, CH$_3$), 2.05 (s, 3H, CH$_3$), 2.04 (s, 3H, CH$_3$); ^{13}C NMR (150 MHz, CDCl, ppm) δ: 170.97 (COCH$_3$), 170.14 (COCH$_3$), 169.38 (COCH$_3$), 169.27 (COCH$_3$), 164.63 (CONH), 162.12 (thiadiazole-C), 134.30 (thiadiazole-C), 131.80 (Ar-C), 129.81 (Ar-C), 129.50 (Ar-C), 124.88 (Ar-C), 84.14 (C-1´), 76.38 (C-5´), 73.47 (C-3´), 69.76 (C-2´), 67.73 (C-4´), 61.71 (C-6´), 20.72 (CH$_3$), 20.67 (CH$_3$), 20.60 (CH$_3$); HRMS [M + H]$^+$ calculated for C$_{23}$H$_{24}$N$_4$O$_{12}$S$_2$: m/z 613.0915, found 613.0908.

(2R,3R,4S,5R,6R)-2-(acetoxymethyl)-6-((5-(4-nitrobenzamido)-1,3,4-thiadiazol-2-yl)thio)tetrahy dro-2H-pyran-3,4,5-triyltriacetate (**4q**). Yellow solid; yield 55.8%; m. p. 189–191°C; R_f = 0.67 (ethyl acetate: petroleum ether, 1:2); IR (KBr, cm^{-1}) v: 3,437 (NH), 1751 (COO), 1,678 (CON); ^{1}H NMR (400 MHz, CDCl$_3$, ppm) δ: 13.02 (s, 1H, NH), 8.48–8.42 (m, 4H, Ar-H), 5.29 (t, J = 9.3 Hz, 1H, H-3´), 5.19–5.12 (m, 2H, H-1´, H-2´), 4.97 (d, J = 10.0 Hz, 1H, H-4´), 4.35 (dd, J = 12.6, 4.6 Hz, 1H, H-5´), 4.26–4.22 (m, 1H, H-6´), 3.88–3.84 (m, 1H, H-6´´), 2.19 (s, 3H, CH$_3$), 2.15 (s, 3H, CH$_3$), 2.05 (s, 3H, CH$_3$), 2.01 (s, 3H, CH$_3$); ^{13}C NMR (150 MHz, CDCl$_3$, ppm) δ: 170.93 (COCH$_3$), 170.03 (COCH$_3$), 169.34 (COCH$_3$), 169.31 (COCH$_3$), 163.85 (CONH), 163.78 (thiadiazole-C), 155.13 (thiadiazole-C), 150.75 (Ar-C), 135.98 (Ar-C), 130.16 (Ar-C), 124.19 (Ar-C), 83.33 (C-1´), 76.66 (C-5´), 73.49 (C-3´), 69.98 (C-2´), 67.59 (C-4´), 61.62 (C-6´), 20.72 (CH$_3$), 20.69 (CH$_3$), 20.60 (CH$_3$), 20.58 (CH$_3$), 20.57 (CH$_3$); HRMS [M + H]$^+$ calculated for C$_{23}$H$_{24}$N$_4$O$_{12}$S$_2$: m/z 613.0915, found 613.0906.

Antifungal Activity *In Vitro*

The *in vitro* antifungal activities of the target compounds against *G. zeae, Botryosphaeria dothidea* (*B. dothidea*), *Phomopsis* sp., *P. infestans,* and *Thanatephorus cucumeris* (*T. cucumeris*) are evaluated by using the poison plate technique. All of the target compounds **4a–4q** were dissolved in 1 ml DMSO before mixing with 90 ml potato dextrose agar (PDA) to prepare concentration of 50 μg/ml. Then, mycelia dishes of approximately 4 mm diameter were cut from the culture medium. A mycelium is obtained using a germ-free inoculation needle and inoculated in the middle of the PDA plate aseptically. The inoculated plates are incubated at 27 ± 1°C for 5 days. DMSO in sterile distilled water served as the negative control and Dimethomorph served as the positive control. Each treatment condition consisted of three replicates (Maddila et al., 2016). The relative inhibition rates *I* (%) were calculated as follows equation, where *C* was the diameter of fungal growth on untreated PDA, *T* was the diameter of fungi on treated PDA.

$$I\ (\%)\ =\ [(C - T)/(C - 0.4)]\ \times\ 100\%$$

Antibacterial Activity *In Vitro*

The *in vitro* antibacterial activities of the target compounds **4a–4q** against *Xoo* and *Xcc* were evaluated by using the turbidimeter test, the commercial agricultural antibacterial Thiodiazole-copper used as control. The test compounds were dissolved in 150 μL of dimethylformamide (DMF) and diluted with 0.1% (v/v) Tween-20 to prepare two concentrations of 200 and 100 μg/ml. One milliliter of the liquid sample was added to the 40 ml non-toxic nutrient broth medium (NB: 1.5 g of beef extract, 2.5 g of peptone, 0.5 g of yeast powder, 5.0 g of glucose, and 500 ml of distilled water, pH 7.0–7.2). Then, 40 μL of NB medium containing *Xoo* or *Xcc* was added to 5 ml of solvent NB containing the test compounds or Thiodiazole–copper. The inoculated test tubes were incubated at 30 ± 1°C under continuous shaking at 180 rpm for 48 h. The culture growth was monitored spectrophotometrically by measuring the optical density at 600 nm (OD_{600}) and expressed as corrected turbidity (Dalgaard et al., 1994). The relative inhibition rates I (%) were calculated as follows equation, where C_{tur} was the corrected turbidity value of bacterial growth on untreated NB, T_{tur} was the corrected turbidity value of bacterial growth on treated NB.

$$I\ (\%)\ =\ (C_{tur} - T_{tur})/C_{tur}\ \times\ 100\%$$

RESULTS AND DISCUSSION

In this study, the target compounds **4a–4q** were synthesized in five steps, including acetylation, bromination, thioetherification, chlorination, and condensation. Among of them, it was found that 2,3,4,6-tetra-*O*-acetyl-α-*D*-gluco-pyranosyl bromide **1**) reacted with 2-amino-5-mercapto-1,3,4-thiadiazole to obtain (2*R*,3*R*,4*S*,5*R*,6*R*)-2-(acetoxymethyl)-6-((5-amino-1,3,4-thiadiazol-2-yl)thio)-tetrahydro-2*H*-pyran-3,4,5-triyltriacetate **2**) of β-configuration with high stereo selectivity in acetone solution of NaOH at room temperature, which indicated that the reaction process was S_N2 and configuration transformation occurred in the reaction process.

All the synthesized compounds were characterized by ^{1}H NMR, ^{13}C NMR, and HRMS. In the ^{1}H NMR spectra of the obtained amide, pyran and acetyl proton signals should be distinguished. For example, for compound **4i**, the proton signals of NH group was observed as a singlet at 12.54 ppm, signals of benzene ring protons were registered at 8.36 and 7.85 ppm, respectively, and the proton signal of pyran was registered in the range of 5.18–3.82 ppm. Moreover, four singlets at 2.17, 2.09, 2.04, and 2.01 ppm indicated to CH_3 protons of acetyl.

The *in vitro* antifungal activities of the target compounds were evaluated against five different fungus including *P. infestans, G.*

TABLE 1 | The *in vitro* antifungal activities of the target compounds **4a–4q** at 50 μg/ml.

Compounds	Inhibition rate (%)				
	G. zeae	*B. dothidea*	*P. infestans*	*Phomopsis* sp	*T. cucumeris*
4a	58.6 ± 2.2	58.1 ± 1.6	44.4 ± 1.5	21.0 ± 2.4	17.1 ± 1.2
4b	62.2 ± 1.4	54.8 ± 0.7	28.5 ± 2.0	38.7 ± 1.3	29.0 ± 1.2
4c	65.7 ± 1.3	60.1 ± 1.1	19.8 ± 0.6	43.0 ± 2.9	56.9 ± 2.4
4days	58.9 ± 1.1	52.0 ± 1.2	40.9 ± 1.4	50.0 ± 1.3	44.5 ± 1.5
4e	53.6 ± 0.7	40.7 ± 1.1	29.4 ± 0.7	26.7 ± 0.4	32.0 ± 1.4
4f	51.7 ± 1.1	43.3 ± 0.1	35.0 ± 1.9	30.8 ± 2.3	42.2 ± 2.0
4g	58.4 ± 1.2	60.7 ± 1.2	77.3 ± 2.1	56.7 ± 2.1	62.0 ± 1.0
4h	35.6 ± 0.6	33.5 ± 0.8	73.0 ± 1.0	30.8 ± 1.0	22.2 ± 2.2
4i	48.9 ± 1.7	58.1 ± 1.5	83.5 ± 0.6	55.2 ± 2.1	64.3 ± 1.5
4j	58.3 ± 1.6	51.1 ± 0.9	30.1 ± 2.6	58.4 ± 1.7	44.7 ± 1.6
4k	55.2 ± 2.2	55.2 ± 1.2	61.9 ± 2.0	43.7 ± 2.0	37.0 ± 1.8
4L	58.0 ± 2.3	49.2 ± 1.3	70.0 ± 1.2	31.5 ± 0.9	59.8 ± 0.9
4m	73.1 ± 1.0	41.0 ± 1.6	63.6 ± 1.3	48.4 ± 1.1	44.3 ± 1.6
4n	70.3 ± 1.1	45.6 ± 1.1	73.1 ± 1.8	33.7 ± 0.8	58.5 ± 1.8
4o	45.0 ± 2.2	22.1 ± 0.9	75.9 ± 1.2	40.0 ± 2.3	54.3 ± 1.7
4p	53.4 ± 1.9	61.3 ± 1.1	79.0 ± 1.1	64.0 ± 1.3	62.8 ± 0.7
4q	56.8 ± 1.5	62.0 ± 2.0	81.1 ± 0.3	63.1 ± 1.2	65.1 ± 1.3
Dimethomorph	74.3 ± 2.0	72.3 ± 1.6	78.2 ± 1.1	69.3 ± 1.6	68.3 ± 1.6

TABLE 2 | The EC_{50} values of compounds **4i**, **4p,** and **4q** against *P. infestans*.

Compds	Toxic regression equation	*r*	EC_{50} (μg/ml)
4i	y = 0.85x + 4.53	0.98	3.43 ± 1.5
4p	y = 0.98x + 4.22	0.98	6.15 ± 2.1
4q	y = 1.13x + 4.20	0.97	5.02 ± 1.8
Dimethomorph	y = 0.94x + 4.30	0.99	5.52 ± 1.2

zeae, B. dothidea, Phomopsis sp., and *T. cucumeris*. Bioassay results, as shown in **Table 1**, revealed that the target compounds exhibited moderate to good antifungal activities against *P. infestans*, **G**. *zeae*, *B. dothidea, Phomopsis* sp., and *T. cucumeris*, with the inhibitory rates range of 19.8–83.5%, 35.6–73.1%, 22.1–62.0%, 21.0–64.0%, and 17.1–65.1%, respectively. Meanwhile, it was found that the inhibitory rates of the target compounds against *G. zeae* in the range of 35.6–73.1% at the 50 μg/ml, which was higher than the previously reported

TABLE 3 | The *in vitro* antibacterial activities of the target compounds **4a–4q**.

Compds	*Xoo*		*Xcc*	
	200 μg/ml	100 μg/ml	200 μg/ml	100 μg/ml
4a	60.1 ± 1.1	38.1 ± 2.1	64.9 ± 1.2	31.7 ± 2.2
4b	63.5 ± 1.5	37.3 ± 1.3	60.1 ± 2.2	39.2 ± 1.4
4c	54.2 ± 2.0	38.5 ± 1.0	55.4 ± 1.9	34.8 ± 2.1
4days	58.6 ± 1.8	42.3 ± 1.3	66.8 ± 2.1	36.3 ± 2.8
4e	44.0 ± 2.1	35.2 ± 1.5	51.4 ± 1.5	34.9 ± 2.2
4f	43.6 ± 1.9	32.6 ± 1.6	47.3 ± 1.5	25.8 ± 1.7
4g	49.0 ± 1.5	31.7 ± 2.3	33.2 ± 1.9	16.6 ± 1.5
4h	45.2 ± 1.5	33.4 ± 2.1	67.2 ± 2.0	43.3 ± 2.6
4i	59.4 ± 2.2	34.4 ± 1.7	68.6 ± 1.0	39.6 ± 1.4
4j	53.5 ± 1.6	32.8 ± 1.3	61.9 ± 1.3	45.5 ± 2.1
4k	51.0 ± 1.6	31.6 ± 1.1	26.5 ± 1.8	15.6 ± 1.7
4L	71.2 ± 0.9	42.6 ± 1.0	77.5 ± 1.4	45.3 ± 2.6
4m	74.4 ± 1.2	44.8 ± 1.5	77.5 ± 1.6	42.3 ± 1.6
4n	68.4 ± 2.1	42.6 ± 1.1	79.0 ± 2.0	47.2 ± 1.8
4o	74.6 ± 1.6	43.8 ± 1.3	75.8 ± 2.8	45.1 ± 1.3
4p	70.1 ± 2.5	43.1 ± 1.4	76.2 ± 2.0	43.1 ± 1.2
4q	69.7 ± 1.2	42.3 ± 1.4	80.8 ± 2.5	45.0 ± 1.3
Thiodiazole-copper	76.2 ± 1.3	45.2 ± 1.3	86.2 ± 2.1	44.5 ± 1.7

inhibitory activity of *N*-(2-chloro-4-phenyl-5-(trifluoromethyl) cyclopenta-1,4-dien-1-yl)-5-((4-nitrobenzyl)thio)-1,3,4-thiadiazol-2-amine against *G. zeae* (23.9%) at the 50 μg/ml (Xie et al., 2016). Especially, compound **4i** and **4q** showed higher antifungal activity against *P. infestans,* with the inhibition rates of 83.5%, 81.1%, respectively, than that of Dimethomorph (78.2%). Based on the preliminary antifungal bioassays, the EC_{50} values of partial compounds against *P. infestans* were also tested and presented in **Table 2**. **Table 2** showed that compounds **4i** exhibited good bioactivities against *P. infestans*, with EC_{50} values of 3.43 μg/ml, which were higher than that of Dimethomorph (5.52 μg/ml). While, the target compounds showed lower antibacterial activities (**Table 3**) against *Xoo* and *Xcc* at 200 and 100 μg/ml than those of Thiodiazole-copper as well as the amide derivatives containing 1,3,4-thiadiazole of the previously reported by Chen (Chen J. et al., 2019).

From the structure-activity relationships (SAR) analysis, it was found that there was clear SAR against *P. infestans*. Inspection of the chemical structures of the target compounds suggests that the group R in the target compounds significantly influence the antifungal activity against *P. infestans*. With a fluorinated or nitrificated substituent (4-F and 4-NO_2) on the phenyl ring, the compounds exhibited enhanced bioactivity against *P. infestans* (**4i** and **4q**). Further, the position of substituent groups in the phenyl ring also plays an important role in the antifungal activity against *P. infestans*, with a four substituent (4-F or 4-NO_2) in the

phenyl ring exhibited higher antifungal activity than other positions.

CONCLUSION

A series of novel 1,3,4-thiadiazole derivatives of glucosides were prepared via acetylation, bromination, thioetherification, chlorination, and condensation. Bioassay results showed that some of the target compounds revealed better inhibitory activity against *P. infestans*. In addition, SAR analysis found that the type and position of substituent groups in the phenyl ring of the target compounds plays an important role in increasing the antifungal activity against *P. infestans*.

DATA AVAILABILITY STATEMENT

The original contributions presented in the study are included in the article/**Supplementary Material**; further inquiries can be directed to the corresponding author/s.

AUTHOR CONTRIBUTIONS

MC and WW contributed to the synthesis, purification, characterization of all compounds, and prepared the original manuscript. XZ and DL performed the biological activity research. HL and ZZ analyzed the experimental results. GZ and XQ drafted the first and second version of the manuscript. All authors discussed, edited, and approved the final version.

FUNDING

SUPPLEMENTARY MATERIAL

The Supplementary Material for this article can be found online at: https://www.frontiersin.org/articles/10.3389/fchem.2021.645876/full#supplementary-material.

REFERENCES

Aggarwal, N., Kumar, R., Dureja, P., and Khurana, J. M. (2012). Synthesis of novel nalidixic acid-based 1,3,4-thiadiazole and 1,3,4-oxadiazole derivatives as potent antibacterial agents. *Chem. Biol. Drug Des.* 79, 384–397. doi:10.1111/j.1747-0285.2011.01316.x

Aktar, M. W., Sengupta, D., and Chowdhury, A. (2009). Impact of pesticides use in agriculture: their benefits and hazards. *Interdiscipl. Toxicol.* 2, 1–12. doi:10.2478/v10102-009-0001-7

Alwan, W. S., Karpoormath, R., Palkar, M. B., Patel, H. M., Rane, R. A., Shaikh, M. S., et al. (2015). Novel imidazo[2,1-*b*]-1,3,4-thiadiazole as promising antifungal agents against clinical isolate of *Cryptococcus neoformans*. *Eur. J. Med. Chem.* 95, 514–525. doi:10.1016/j.ejmech.2015.03.02110.1016/j.ejmech.2015.03.021

Bhinge, S. D., Chature, V., and Sonawane, L. V. (2015). Synthesis of some novel 1,3,4-thiadiazole derivatives and biological screening for anti-microbial, antifungal and anthelmintic activity. *Pharm. Chem. J.* 49, 1–6. doi:10.1007/s11094-015-1287-8

Chen, J., Yi, C., Wang, S., Wu, S., Li, S., Hu, D., et al. (2019). Novel amide derivatives containing 1,3,4-thiadiazole moiety: design, synthesis, nematocidal and antibacterial activities. *Bioorg. Med. Chem. Lett.* 29, 1203–1210. doi:10.1016/j.bmcl.2019.03.01710.1016/j.bmcl.2019.03.017

Chen, W., Zhang, H., Wang, J., and Hu, X. (2019). Flavonoid glycosides from the bulbs of *lilium speciosum* var. *gloriosoides* and their potential antiviral activity against. *RSV. Chem. Nat. Compd.* 55, 461–464. doi:10.1007/s10600-019-02714-7

Chudzik, B., Bonio, K., Dabrowski, W., Pietrzak, D., Niewiadomy, A., Olender, A., et al. (2019). Synergistic antifungal interactions of amphotericin B with 4-(5-methyl-1,3,4-thiadiazole-2-yl) benzene-1,3-diol. *Sci. Rep.* 9, 12945–12959. doi:10.1038/s41598-019-49425-1

Dalgaard, P., Ross, T., Kamperman, L., Neumeyer, K., and Mcmeekin, T. A. (1994). Estimation of bacterial growth rates from turbidimetric and viable count data. *Int. J. Food Microbiol.* 23, 391–404. doi:10.1016/0168-1605(94)90165-1

Gruner, S. A. W., Locardi, E., Lohof, E., and Kessler, H. (2009). Carbohydrate-based mimetics in drug design: sugar amino acids and carbohydrate scaffolds. *Chem. Rev.* 102, 491–456. doi:10.1021/cr0004409

Gurung, R. B., Gong, S. Y., Dhakal, D., Le, T. T., Jung, N. R., Hye, j. j, et al. (2018). Synthesis of curcumin glycosides with enhanced anticancer properties using one-pot multienzyme glycosylation technique. *J. Microbiol. Biotechnol.* 27, 1639–1648. doi:10.4014/jmb.1701.01054

Hawas, U. W., El-Kassem, L. T. A., Shaher, F., and Al-Farawati, R. (2019). *In vitro* inhibition of hepatitis c virus protease and antioxidant by flavonoid glycosides from the saudi costal plant *sarcocornia fruticosa*. *Nat. Prod. Lett.* 33, 3364–3371. doi:10.1080/14786419.2018.1477153

He, X., Wang, Y., Luo, R. H., Yang, L. M., and Wang, L.,Dale, G., et al. (2019). Dimeric pyranonaphthoquinone glycosides with anti-HIV and cytotoxic activities from a*soil-derived streptomyces*. *J. Nat. Prod.* 82, 1813–1819. doi:10.1021/acs.jnatprod.9b00022

Hu, H. Z., Xiang, G. X., Chen, J. X., Chen, W., Wu, l., and Xu, S. (1997). *An antibiotic pesticide-Ningnanmycin, CN1036307C.*

Jiang, X. L., Wang, L., Wang, E. J., Zhang, G. L., Chen, B., Wang, M. K., et al. (2018). Flavonoid glycosides and alkaloids from the embryos of *nelumbo nucifera* seeds and their antioxidant activity. *Fitoterapia.* 125, 184–190. doi:10.1016/j.fitote.2018.01.009

Kamat, M. N., Rath, N. P., and Demchenko, A. V. (2007). Versatile synthesis and mechanism of activation of s-benzoxazolyl glycosides. *J. Org. Chem.* 72 (18), 6938–6946. doi:10.1021/jo071184410.1021/jo0711844

Khodair, A. I., Attia, A. M., Gendy, E. A., Elshaier, Y. A. M. M., and MohammedEl-Magd, A. M. A. (2019). Discovery of new S-glycosides and N-glycosides of pyridine-biphenyl system with antiviral activity and induction of apoptosis in MCF7 cells. *J. Heterocycl. Chem.* 56, 1733–1746. doi:10.1002/jhet.3527

Knyazyan, A., Eliazyan, K., Pivazyan, V., Ghazaryan, E., Harutyunyan, S., and Yengoyan, A. (2012). Synthesis and growth regulatory activity of novel 5-(3-alkyl-4-methyl-2-thioxo-2,3-dihydro-thiazol-5-yl)-3H-[1,3,4]thiadiazole(oxadiazole)-2-thiones and their derivatives. *Heterocycl. Commun.* 18, 103–108. doi:10.1515/hc-2012-0040

Maddila, S., Gorle, S., Sampath, C., and Lavanya, P. (2016). Synthesis and anti-inflammatory activity of some new 1,3,4-thiadiazole containing pyrazole and pyrrole nucleus. *J. Saudi Chem. Soc.* 20, 306–312. doi:10.1016/j.jscs.2012.11.007

Mohammed, H. S., Abdel-Aziz, M. M., Abu-Baker, M. S., Saad, A. M., Mohamed, M. A., and Ghareeb, M. A. (2019). Antibacterial and potential antidiabetic activities of flavone C-glycosides isolated from *Beta vulgaris* subspecies cicla. var. flavescens (Amaranthaceae) cultivated in Egypt. *Curr. Pharmaceut. Biotechnol.* 20, 595–604. doi:10.2174/1389201020666190613161212

Rahim, A., Mostofa, M. G., Sadik, M. G., Rahman, M. A. A., and Alam, A. K. (2020). The anticancer activity of two glycosides from the leaves of *Leea aequata* L. *Nat. Prod. Res.* (27). 1–5. doi:10.1080/14786419.2020.1798661

Scattolin, T., Bortolamiol, E., Rizzolio, F., Demitri, N., and Visentin, F. (2020). Allyl palladium complexes bearing carbohydrate-based n-heterocyclic carbenes: anticancer agents for selective and potent *in vitro* cytotoxicity. *Appl. Organomet. Chem.* 34, e5876. doi:10.1002/aoc.5876

Sridhar, G., Palle, S., Vantikommu, J., and Gangarapu, K. (2020). Design, synthesis, and biological evaluation of amide derivatives of imidazo[2,1-b][1,3,4]thiadiazole as anticancer agents. *Synth. Commun.* 50, 3221–3233. doi:10.1080/00397911.2020.1797814

Taflan, E., Bayrak, H., Er, M., Alpay Karaoğlu, Ş., and Bozdeveci, A. (2019). Novel imidazo[2,1-b][1,3,4]thiadiazole (ITD) hybrid compounds: design, synthesis, efficient antibacterial activity and antioxidant effects. *Bioorg. Chem.* 89, 102998. doi:10.1016/j.bioorg.2019.102998

Wu, M., Han, G., Meng, C., Wang, Z., Liu, Y., and Wang, Q. (2014). Design, synthesis, and anti-tobacco mosaic virus (TMV) activity of glycoconjugates of phenanthroindolizidines alkaloids. *Mol. Divers.* 18, 25–37. doi:10.1007/s11030-013-9484-4

Xie, Y., Gong, H., Wang, X., Ruan, X., Zhang, J., Li, Q., et al. (2016). Synthesis and biological activity of novel pyrazole amide derivatives containing 1,3,4-thiadiazole thioether moiety. *Agrochemicals.* 55, 872–876.

Yang, X. H., Xiang, L., Li, X., Zhao, T. T., Zhang, H., Zhou, W. P., et al. (2012). Synthesis, biological evaluation, and molecular docking studies of 1,3,4-thiadiazol-2-amide derivatives as novel anticancer agents. *Bioorg. Med. Chem.* 20, 2789–2795. doi:10.1016/j.bmc.2012.03.040

Zhan, J., Thrall, P. H., Papaïx, J., Xie, L., and Burdon, J. J. (2015). Playing on a pathogen's weakness: using evolution to guide sustainable plant disease control strategies. *Annu. Rev. Phytopathol.* 53, 19–43. doi:10.1146/annurev-phyto-080614-120040

Zhang, M., Xu, W., Wei, K., Liu, H., and Xue, W. (2019). Synthesis and evaluation of 1,3,4-thiadiazole derivatives containing cyclopentylpropionamide as potential antibacterial agent. *J. Heterocycl. Chem.* 56, 1966–1977. doi:10.1002/jhet.3576

Green Synthesis of Luminescent Gold-Zinc Oxide Nanocomposites: Cell Imaging and Visible Light–Induced Dye Degradation

Kanika Bharti[1], Shahbaz Ahmad Lone[1], Ankita Singh[1], Sandip Nathani[2], Partha Roy[2] and Kalyan K. Sadhu[1]*

[1]Department of Chemistry, Indian Institution of Technology Roorkee, Roorkee, India, [2]Department of Biotechnology, Indian Institution of Technology Roorkee, Roorkee, India

Green synthesis of gold-zinc oxide (Au-ZnO) nanocomposite was successfully attempted under organic solvent–free conditions at room temperature. Prolonged stirring of the reaction mixture introduced crystallinity in the ZnO phase of Au-ZnO nanocomposites. Luminescence properties were observed in these crystalline Au-ZnO nanocomposites due to *in situ* embedding of gold nanoparticles (AuNP) of 5–6 nm diameter on the surface. This efficient strategy involved the reduction of Au(III) by Zn(0) powder in aqueous medium, where sodium citrate (NaCt) was the stabilizing agent. Reaction time and variation of reagent concentrations were investigated to control the Au:Zn ratio within the nanocomposites. The reaction with the least amount of NaCt for a long duration resulted in Au-ZnO/Zn(OH)$_2$ nanocomposite. X-ray photoelectron spectroscopy (XPS) confirmed the formation of Zn(OH)$_2$ and ZnO in the same nanocomposite. These nanocomposites were reconnoitered as bioimaging materials in human cells and applied for visible light–induced photodegradation of rhodamine-B dye.

Keywords: nanocomposites, green synthesis, luminescence, photodegradation, redox chemistry

INTRODUCTION

The development of luminescent AuNP has been an active area of material research over the past decade due to its potential applications from bench to clinical settings (Liu et al., 2013; Yu et al., 2019). Luminescent AuNP with 3 nm diameter showed a pH-dependent membrane adsorption property (Yu et al., 2011). Gold nanoclusters with small diameters and aggregated AuNP have also found to be luminescent in nature (Gan et al., 2016; Goswami et al., 2016; Saini et al., 2017; J. Wang et al., 2018a; Y. Wang et al., 2018b; Wu et al., 2019). In addition to imaging applications, deposition of gold nanoclusters or nanoparticles was successfully attempted on Ag@SiO$_2$ or covalent organic framework for important functional activities such as circulating miRNA in human serum (Zhang Q. et al., 2019) or surface-enhanced Raman scattering (He et al., 2017), respectively. Building upon this past research, the present study developed a method to deposit luminescent AuNP with 5–6 nm diameter on the surface of Au-ZnO nanocomposites.

Au-metal oxide nanocomposites are known not only for their high surface-area-to-volume ratio but also for enhanced stability during their catalytic activity (Li et al., 2011; Ray and Pal, 2017; Wei et al., 2017; Cyganowski et al., 2019; Kauffman et al., 2019; Mageed et al., 2019). These hybrid nanomaterials possess unique optical, electronic, and magnetic properties, which are governed by
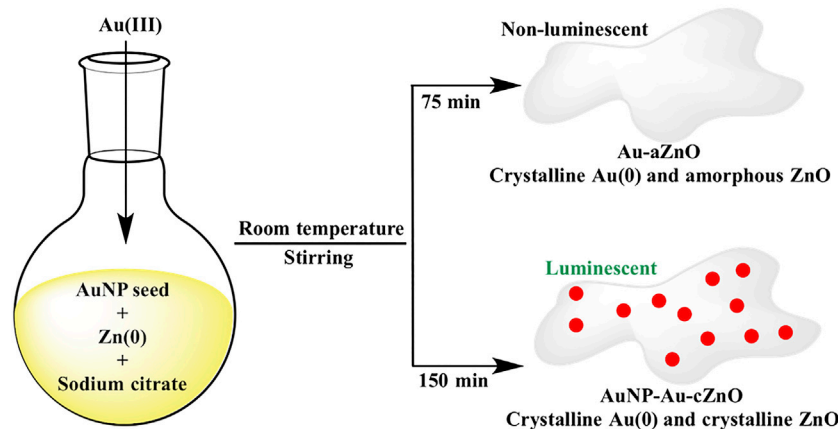
SCHEME 1 | Synthetic route of Au-aZnO (**aZn1**-**aZn8**) and AuNP-Au-cZnO (**cZn1**-**cZn4**) nanocomposites in aqueous medium.

their structural features, size, and compositional heterogeneities (Zu et al., 2015; Chamorro et al., 2016; Dutta Chowdhury et al., 2017; Lee et al., 2017; Song et al., 2017; Hu et al., 2018; Liu F. et al., 2019). A handful of synthetic methods of Au-metal oxide nanocomposites such as chemical vapor deposition, physical vapor deposition, hydrothermal method, spray pyrolysis, electrophoretic deposition, microwave-assisted thermal decomposition, magnetron sputtering, and spin coating are described in the literature (He et al., 2010; Shingange et al., 2016; Klug et al., 2017; Y. Wang et al., 2017a).

Considering the growing demand for Au-metal oxide–based nanocomposites for industrial and biomedical applications (Chen D. et al., 2015; Chen et al., 2017; Liu et al., 2018; Zhou et al., 2018; Gao et al., 2019; Jia et al., 2019; Zhang M. et al., 2019), there is a critical need to design a more facile and well-regulated synthetic route. Synthesis of metal-based nanocomposites by organic solvent–free conditions has drawn a lot of attention in the current decade (Li et al., 2013; Yao et al., 2013; Zhang et al., 2016; Qi et al., 2019; Ritchie et al., 2019). Au-ZnO nanocomposites, which are well known for a variety of applications, have been synthesized at high temperature in the presence of organic solvent (Yao et al., 2011; Tahir et al., 2013; Hang et al., 2016; Chang et al., 2017; Lupan et al., 2019). There are two reports, where AuNP was decorated on the crystalline ZnO nanorod surface at high temperature (Unlu et al., 2015; Ning et al., 2019). However, there is a lacuna of AuNP on the surface of Au-ZnO nanocomposites due to the synthetic challenges involving the two gold nanostructures simultaneously on the same material. In our synthetic methodology, the occlusion of AuNP of 5–6 nm diameter was successful for the first time on the surface of Au-ZnO nanocomposites in aqueous medium and at room temperature by the reduction of Au(III) salt with Zn(0) powder in the presence of AuNP as seed and NaCt as the stabilizing agent.

Au-ZnO nanocomposites with different Au:Zn compositions were prepared by varying the amount of AuNP seed, NaCt, and Zn metal powder. The reaction mixture in solution or the isolated nanocomposite materials in solid state were characterized by electronic absorption, XPS, FE-SEM (field

emission scanning electron microscopy), energy dispersive X-ray (EDX), TEM (transmission electron microscopy), PXRD (powder X-ray diffraction), and surface charge analysis. All these characterizations of nanocomposites confirmed the key roles of AuNP seed, NaCt, and Zn metal in controlling Au:Zn ratio.

The redox reaction between Au(III) and Zn(0) was initially performed for 75 min, and this led to development of Au-ZnO nanocomposites (Au-aZnO, **aZn1**-**aZn8**) with ZnO in the amorphous phase (Scheme 1). However, when the same reaction was continued for 150 min, both Au and ZnO were found to be in crystalline phase without much variation in Au:Zn ratio. Interestingly, AuNP of 5–6 nm diameter was occluded on the surface of crystalline Au-ZnO nanocomposites (AuNP-Au-cZnO, **cZn1**-**cZn4**) during 150 min stirring of the reaction mixture (Scheme 1). Introduction of AuNP in AuNP-Au-cZnO showed a luminescent property with maximum emission at 496 nm after excitation of the samples at 436 nm. In comparison, Au-aZnO did not show any luminescence properties. This method opens up new avenues for fabricating Au-ZnO nanocomposites with different compositions under mild conditions. The excitation wavelength of the luminescent AuNP-Au-cZnO nanocomposites helped in the photodegradation of rhodamine-B in the presence of 455 nm light.

MATERIALS AND METHODS

Materials. The chemicals gold (III) chloride trihydrate and rhodamine-B were purchased from Sigma-Aldrich, and trisodium citrate dihydrate was purchased from Merck chemicals. Zinc powder was purchased from SISCO Research Laboratory. All glassware and stirrer bars were washed with freshly prepared aqua regia (mixture of 1:3 volume ratio of nitric acid:hydrochloric acid) and then with Millipore water and dried in an oven before use.

Synthesis of gold nanoparticle seed. AuNP seed (average size 19 ± 3 nm) solution with surface plasmon resonance (SPR) peak

at 524 nm was prepared by the NaCt-based reduction method (Wuithschick et al., 2015). The concentration in terms of nanoparticle per ml was calculated as per methods given in the literature (Johonston, 2002; Lewis et al., 2006).

Preparation of seed stock. Seed solution was prepared by taking 200 µL as-synthesized gold nanoparticle and adding to it 19.8 ml of 1% (w/v) trisodium citrate dihydrate solution to make final volume to 20 ml.

Synthetic schemes and brief characteristics of all nanocomposites have been summarized in **Supplementary Schemes S1, S2**.

Syntheses of the nanocomposites aZn1 to aZn5. For zinc-gold nanocomposites, five different solutions were prepared. Each solution contained 20 mg (0.05 mmol) $HAuCl_4$ in 200 ml of Millipore water. To these solutions, five different nanoparticles per mL (22.4×10^4, 45×10^4, 90×10^4, 180×10^4, and 900×10^4) as seed were added, respectively, to produce **aZn1** to **aZn5**. In each of these five solutions, additional 2 ml 1% (w/v) solution of trisodium citrate dihydrate (0.07 mmol) and 20 mg zinc powder (0.3 mmol) were added. All these reaction mixtures were stirred for 75 min at room temperature followed by filtration.

Syntheses of nanocomposites aZn6 and aZn7. Two solutions contained 20 mg (0.05 mmol) $HAuCl_4$ in 200 ml of Millipore water. In both the solutions, 2 ml 1% (w/v) solution of trisodium citrate dihydrate (0.07 mmol) and 200 mg (3 mmol) of zinc were added. Two different seeds, 900×10^4/ml and 22.4×10^4/ml (nanoparticle/ml), were added to produce **aZn6** and **aZn7**, respectively. The reaction mixtures were stirred at room temperature for 75 min and filtered.

Syntheses of gold-zinc nanocomposites using variable citrate concentration. Five different solutions were prepared. Each solution contained 20 mg (0.05 mmol) $HAuCl_4$ in 200 ml of Millipore water. The addition of seed (nanoparticle/ml) was restricted to 22.4×10^4/ml in each solution, and the reaction was stirred for 75 min. Five different amounts (0.2, 0.4, 0.6, 0.8, and 1.0 ml) of 1% (w/v) solution of trisodium citrate dihydrate were added followed by addition of 20 mg zinc powder (0.3 mmol). The reaction mixtures were stirred for 75 min and filtered. The filtered solutions were characterized by UV-visible spectroscopy.

Synthesis of nanocomposite aZn8. One solution contained 20 mg (0.05 mmol) $HAuCl_4$ in 200 ml of Millipore water. To this were added seed (nanoparticle/ml) of 900×10^4/ml and 0.021 mmol of trisodium citrate dihydrate followed by addition of zinc (3.0 mmol) powder to obtain **aZn8**. The reaction mixture was stirred at room temperature for 75 min and filtered.

Synthesis of cZn1. 20 mg (0.05 mmol) $HAuCl_4$ was added to 200 ml of Millipore water. To the solution, seed of 900×10^4/ml (nanoparticle/ml) was added during stirring followed by 2 ml 1% (w/v) solution of trisodium citrate dihydrate (0.07 mmol) and 20 mg zinc powder (0.3 mmol) to obtain **cZn1**. Reaction mixture was stirred for 150 min at room temperature followed by filtration.

Synthesis of cZn2. 20 mg (0.05 mmol) $HAuCl_4$ was added to 200 ml of Millipore water. Then, during stirring, seed of $900 \times$ 10^4/ml (nanoparticle/ml) was added followed by 2 ml 1% (w/v) solution of trisodium citrate dihydrate (0.07 mmol) and 200 mg (3 mmol) of zinc metal powder to obtain **cZn2**. The reaction mixtures were stirred at room temperature for 150 min and filtered.

Synthesis of cZn3. 20 mg (0.05 mmol) $HAuCl_4$ was added to 200 ml of Millipore water. Then, during stirring, seed of $22.4 \times$ 10^4/ml (nanoparticle/ml) was added followed by 2 ml 1% (w/v) solution of trisodium citrate dihydrate (0.07 mmol) and 200 mg (3 mmol) of zinc metal powder to obtain **cZn3**. The reaction mixtures were stirred at room temperature for 150 min and filtered.

Synthesis of cZn4. 20 mg (0.05 mmol) $HAuCl_4$ was added to 200 ml of Millipore water. Then, during stirring, seed of $900 \times$ 10^4/ml (nanoparticle/ml) was added followed by 600 µL 1% (w/v) solution of trisodium citrate dihydrate (0.021 mmol) and 200 mg (3 mmol) of zinc metal powder to obtain **cZn4**. The reaction mixtures were stirred at room temperature for 150 min and filtered.

Yield of cZn1 to cZn4. The bulk scale reactions were carried out with 100 mg (0.25 mmol) $HAuCl_4$ in one batch. The other reagents were taken in the same ratio mentioned in the syntheses. After the filtration process, the filtrate was centrifuged and finally dried under vacuum to isolate the solid **cZn1** to **cZn4**. The yields of **cZn1**, **cZn2**, **cZn3**, and **cZn4** were 45, 57, 54, and 43 mg, respectively. These solids were stored at room temperature in dark for further application and characterization.

Synthesis of ZnO. ZnO was prepared by the reported method of (Pourrahimi et al., 2014). 250 ml of 0.1 M zinc sulfate salt was stirred for 15 min at 60°C. After 15 min, 250 ml 0.25 M NaOH solution was heated separately at 60°C and added to the zinc sulfate solution during stirring. The reaction was continued with stirring for 60 min. The white precipitate obtained was kept for calcination at 400°C for 3 h in a muffle furnace.

METHODS

Absorption spectroscopy. Nanocomposite solutions were characterized using a UV-Vis spectrometer (UV-1601, Shimadzu). Absorbance measurement was taken over 400–800 nm wavelength range.

Transmission electron microscopy (TEM). The TEM images of nanocomposites and SAED patterns were obtained using FEI, Technai G2 20 S-TWIN. Image J software was used to analyze the average diameter of GNPs.

Field emission scanning electron microscopy (FE-SEM). The FE-SEM (Carl ZEISS Ultra plus Gemini, Germany) images were employed to analyze the morphological features. Energy-dispersive X-ray (EDX) and EDX-mapping of the nanocomposites were performed to find the composition.

X-ray photoelectron spectroscopy (XPS). XPS experiments were performed with PHI 5000 Versa Prob II, FEI Inc., and a C60 sputter gun has been used for characterization. The chemical states of the gold nanoparticles were characterized by XPS with monochromatized Al K(α) excitation (h = 1486.6 eV). The C 1s (284.8 eV) was used as a reference to calibrate the peak X-ray

photoelectron spectroscopy (XPS) with Auger electron spectroscopy (AES) module positions of the elements.

Powder X-ray diffraction (PXRD). PXRD was performed using Bruker-D8 advance with an X-ray source, a 2.2 kW Cu anode, and an accelerating voltage of 40 kV.

Luminescence measurement. Luminescence of nanocomposites **cZn1**, **cZn2**, **cZn3**, and **cZn4** was measured using a Synergy microplate reader (Biotek United States) instrument, within the range of 470–700 nm with λ_{ex} = 436 nm. The relative quantum yield was calculated with respect to fluorescein in 0.1 M NaOH (Q.Y. = 0.95) as reference (Brouwer, 2011) for comparison. The excitation spectra were measured using the same instrument within the range of 380–460 nm with λ_{em} = 496 nm.

Surface charge measurement. Surface charge measurements were obtained using a Zetasizer Nano ZS90 (Malvern Instruments). DTS applications 7.03 software was used to analyze the data.

Time-resolved fluorescence measurement. Fluorescence decay of fluorescein was estimated using the TCSPC system from Horiba Jobin Yvon FluoroHub Instrument, with λ_{ex} = 435 nm and λ_{em} = 496 nm. Data analysis was performed with DAS6 software. The decay time data were analyzed using exponential sum, employing a nonlinear least squares reconvolution analysis. Average fluorescence lifetimes were calculated as $\Sigma\alpha_i\tau_i^2/\Sigma\alpha_i\tau_i$ with normalized α_I (Lakowicz, 2006).

Photocatalytic degradation of rhodamine-B using 455 nm LED or 254 nm UV light. Nanocomposites **cZn1**, **cZn2**, **cZn3**, and **cZn4** (10 mg) were dispersed in 18 ml deionized water, separately sonicating them for 10 min. To these, 2.0 ml of 1.0 $\times 10^{-4}$ M rhodamine-B stock solution was added and stirred in dark for 30 min before irradiation in 455 nm LED light or 254 nm UV light. The samples were then kept under light; absorption spectra were recorded at regular intervals of time. The photocatalysis experiments were carried out at pH 7 and at room temperature. A decrease in absorption maximum at 556 nm was observed with photocatalytic degradation of the rhodamine-B dye.

Cell viability assay. To determine the cytotoxic effect of the test materials, MTT (3-(4,5-dimethylthiazol-2-yl)-2,S-diphenyltetrazolium bromide) assay was carried out according to the protocol reported elsewhere. In brief, the cells (5000 cells/200 μL/well) were seeded in a 96-well plate. Nanocomposite suspension at 50 μg/ml concentrations was added to the monolayer in triplicate and incubated for 2, 4, 8, 12, and 24 h. Then, after the addition of 20 μL of 5 mg/ml MTT (Sigma-Aldrich, MO, United States) reagent, the cells were allowed to incubate for another 4 h at 37°C. The formazan crystals formed inside the cells were then solubilized by adding 200 μL of DMSO (HiMedia, Mumbai, India) to each well. The viable cells that showed the formation of violet crystals were quantified at 570 nm using a microplate reader (Omega fluostar, BMG Labtech Ltd., Germany). The cell cytotoxicity was expressed as percentage cell viability in comparison to the control group.

Fluorescence microscopy. The internalization of nanocomposites was monitored at 2 h, and the images were captured using a fluorescence microscope (Evos Floid cell imaging station, Invitrogen, United States) under ×200 magnification. In brief, HEK293 cells (5000 cells/200 μL/well) were seeded in a 96-well plate and allowed to adhere for 24 h. Then, nanocomposites (50 μg/ml) were incubated with the cells for 2 h, and the images were captured after washing with PBS.

RESULTS AND DISCUSSION

Synthesis of optimized materials of amorphous and crystalline Au-ZnO nanocomposites (Au-aZnO, **aZn5-aZn8,** and AuNP-Au-cZnO, **cZn1-cZn4**). Two different types of nanocomposites on the basis of Zn powder as reducing agent were synthesized from aqueous solution of HAuCl₄ by variation of AuNP seed, Zn powder, and NaCt as stabilizing agents as mentioned in **Table 1**. In order to develop the crystalline nature in the ZnO part of the newly synthesized nanocomposites (**cZn1-cZn4**) by maintaining green synthetic methodology (Ning et al., 2019), we focused on the reaction time duration instead of introducing organic solvent or high temperature. The crystallinity in the nanocomposites was obtained by increasing the reaction time twice to that of the initial reactions. During all the syntheses, a reducing agent was added at last. The pH of the solution before the addition of Zn powder varied within the range of 6.8–7.0, while the pH of the solution increased within the range of 7.3–7.8 after stirring for either 75 min or 150 min. This pH range helped in the stabilization of the basic Au-ZnO nanocomposite in the aqueous medium. The procedure was adapted on the basis of redox reaction between Au(III) and Zn(0), which does not require a basic or acidic medium. As ZnO is amphoteric in nature, there is a chance that zinc salt will form at a pH that is too low and that zinc hydroxide will form at a high pH (Degen and Kosec, 2000).

The concentration of seed was varied within the range of 22.4 $\times 10^4$ per ml to 900 $\times 10^4$ per ml. There is a blueshift in the absorbance (marked with an arrow in **Supplementary Figure S1**) from **aZn1** to **aZn5**. However, all these redshifted absorbance peaks with respect to seed are either due to the growth of seed **aZn1** or due to the incorporation of ZnO layer in the Au-ZnO composite **aZn5** (Viter et al., 2015). We performed a series of experiments (**Supplementary Figure S1**) to generate the SPR peaks for gold nanomaterials by varying the zinc amount. We have noticed that a minimum of 6 equivalents of zinc is required to produce stable SPR peak and the peak intensity gets saturated in presence of 60 equivalents. The presence of 60 equivalents of reducing agent with respect to HAuCl₄ did not show much difference in Zn amount among the synthesized nanocomposites (**aZn6**, **aZn7**, **cZn2**, and **cZn3**). Lowering down the concentration of reducing agent from 60 equivalents to 6 equivalents drastically decreased the incorporated Zn amount (*vide infra*) within the nanocomposites **aZn5** or **cZn1**. The treatment of 30% stabilizing agent with respect to the synthesis of **aZn6** or **cZn2** showed a 50% decrease in the incorporated Zn amount in the nanocomposites **aZn8** or **cZn4**.

Synthesis of remaining Au-ZnO nanocomposites (Au-aZnO, aZn1-aZn4) and characterization of aZn1-aZn8. Room temperature reaction in aqueous medium with variable AuNP seed concentration in the presence of NaCt (0.07 mmol) as

TABLE 1 | Summary of Au-ZnO nanocomposites based on EDX analysis from FE-SEM.

Au(III) (mmol)	Sodium citrate (mmol)	Zn (mmol)	Seed concentration (×10⁴ per ml)	Zn:Au in nanocomposite	
				Reaction time 75 min	Reaction time 150 min
0.05	0.07	0.3	900	0.1:1 (**aZn5**)	0.1:1 (**cZn1**)
0.05	0.07	3	900	1.0:1 (**aZn6**)	1.1:1 (**cZn2**)
0.05	0.07	3	22.5	0.9:1 (**aZn7**)	1.1:1 (**cZn3**)
0.05	0.021	3	900	0.5:1 (**aZn8**)	0.5:1 (**cZn4**)

stabilizing agent and Zn (0.3 mmol) as reducing agent for HAuCl$_4$ (0.05 mmol) produced a violet color in different solutions (**Supplementary Figure S1**) within 75 min. The redshift observed in the SPR band of **aZn1** (λ_{max} = 575 nm) formed using 22.5 × 10⁴ particles/ml in comparison to seed is due to formation of ZnO. This type of shift due to the formation of the ZnO layer on Au-film was reported in the literature (Viter et al., 2015). Reaction with 900 × 10⁴/ml seed concentration showed **aZn5** with enhanced coloration with blueshift (λ_{max} = 555 nm) compared to **aZn1**. However, this absorption exhibited clear redshift with respect to seed particle (Yu et al., 2005). In absence of AuNP seed, there was no SPR absorbance in the reaction mixture even after 3 h of reactions between HAuCl$_4$ and Zn powder in the presence of NaCt.

The formations of Au-ZnO nanocomposites were confirmed with TEM, FE-SEM images, and EDX analysis of **aZn1** to **aZn5** (**Supplementary Figures S2, S3**). In the synthesis process, the metal powder was engaged in redox reaction between Au(III)/Au(0) and Zn(II)/Zn(0) couple, in addition to playing the role of simple metal source, thereby leading to the formation of Au-ZnO nanocomposites. Although the incorporation of Zn in the respective nanocomposite **aZn1** was sparse, we were successful in increasing the Au:Zn ratio up to 1:0.1 (weight percentage) in **aZn5**.

An increase in the concentration of Zn (3 mmol) led to rapid (~1 min) appearance of violet color in the reaction mixture for **aZn6** (**Supplementary Figure S4**). In PXRD (**Supplementary Figure S5**), only the characteristic peaks of Au(0) were observed for **aZn6**, suggesting the amorphous (X. Wang et al., 2017b) nature of ZnO in Au-aZnO nanocomposites. An enhancement of approximately 10 times the Zn content in **aZn6** (Au:Zn = 1:1) was confirmed by FE-SEM and EDX analysis (**Supplementary Figure S6**). No visible color generation in the absence of Zn powder (**Supplementary Figure S4**) affirmed the role of the metal powder in the redox process. The variation of seed concentration involving higher amount of Zn powder did not show any appreciable shift in the plasmonic bands (**Supplementary Figure S4**). Nanocomposite **aZn7** synthesized using 3 mmol Zn powder with 22.4 × 10⁴/ml seed concentration resulted in Au:Zn = 1:0.9 (**Supplementary Figure S7**).

In order to rule out the competitive reduction of Au(III) by NaCt, the amount of the same was decreased from 0.035 to 0.007 mmol for Au-aZnO nanocomposites preparation at a constant seed concentration of 22.4 × 10⁴/ml and Zn powder of 0.3 mmol (**Supplementary Figure S8**). We performed the synthesis of nanocomposites with different concentrations of

sodium citrate. We observed that a stable SPR peak was generated in the presence of 0.021 mmol of sodium citrate. This result suggested that a threshold amount of NaCt (0.021 mmol) was essential as the stabilizing agent in the reduction process to synthesize the Au-aZnO nanocomposites. Lowering the NaCt concentration from 0.07 to 0.021 mmol with 900 × 10⁴/ml led to the lowering of Zn incorporation in Au-ZnO nanocomposites, Au:Zn = 1:0.5 in **aZn8** (**Supplementary Figures S9, S10**). The chemical compositions of the Au-aZnO nanocomposites obtained from EDX analysis were further confirmed by XPS analysis. This also reveals the oxidation states of different elemental species present in Au-aZnO nanocomposites (**Supplementary Figure S11**). Binding energy studies confirmed the peaks of Au 4f$_{7/2}$ (Fuggle et al., 1977), Zn 2p$_{3/2}$ (Strohmeier and Hercules, 1984), and O 1s (Tan et al., 1990) at 83.0, 1021.4, and 530 eV, respectively, in these nanocomposites. These Au-aZnO nanocomposites were found to be nonluminescent in nature unlike the previously reported emissive ZnO nanoparticles (Tang et al., 2010; Jangir et al., 2017; Raji and Gopchandran, 2017).

Characterization of crystalline Au-ZnO nanocomposites (AuNP-Au-cZnO, **cZn1**-**cZn4**). EDX analyses of the samples after the reaction with a longer duration resulted in a similar amount of ZnO incorporation in the nanocomposites (**Supplementary Figures S12–S15**). However, crystallinity was introduced (**Figure 1A**; **Supplementary Figure S16**) in both the Au and ZnO components of the **cZn2**, **cZn3**, and **cZn4** nanocomposites. In the case of **cZn1**, the amount of ZnO was very less, which restricted visualization of the crystallinity of ZnO in this sample by PXRD. The distinct difference in the PXRD data for the samples **cZn2** to **cZn4** confirmed the additional peaks due to crystalline ZnO in these nanocomposites. XRD peak positions (in degrees) and their corresponding FWHM values (in degrees) are shown in **Supplementary Table S1**. In XRD patterns (**Figure 1**; **Supplementary Figure S16**), there is a small redshift as compared to ZnO (JCPDS no. 00-021-1486 and Caglar et al., 2009) due to the inclusion of gold in nanocomposites. This interaction of gold and zinc oxide in our nanocomposites has been further supported with more FWHM values compared to bare ZnO.

In the case of absorption studies, the nanocomposites **cZn1** to **cZn4** showed redshift in SPR peak (λ_{max} at ~565 nm, **Supplementary Figure S17**) with respect to AuNP seed solution. The absorption peak at 565 nm was observed in the case of **cZn1**. However, in the case of **cZn4**, a broad flat peak was observed around a wide range of 500–700 nm. The changes in absorbance spectra with respect to **cZn2** are due to variation of
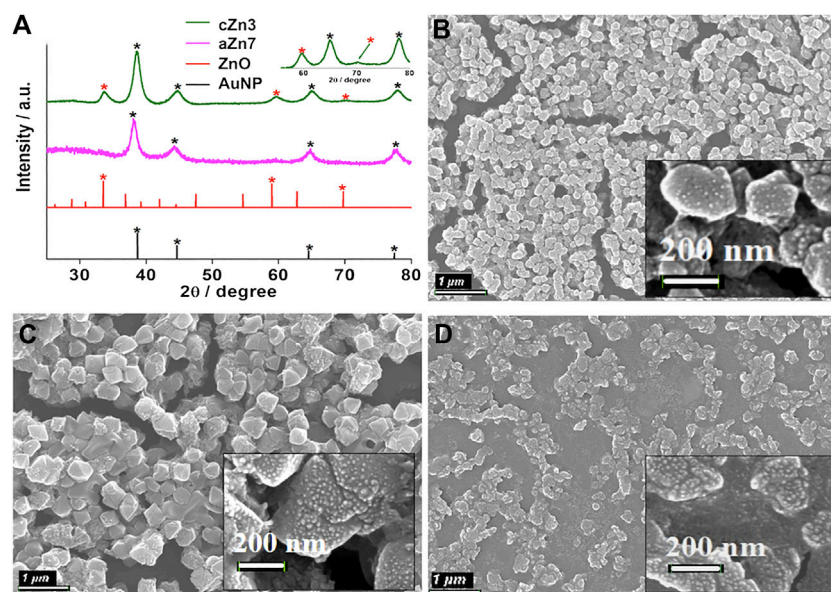
FIGURE 1 | (A) XRD of **aZn7** and **cZn3** compared with the AuNP (JCPDS no. 00–004–0784) and ZnO (JCPDS no. 00–021–1486); FE-SEM images of AuNP-Au-cZnO nanocomposites: **(B) cZn2**, **(C) cZn3**, and **(D) cZn4**. The scale bar for B–D: 1 μM and the scale bar for inset images: 200 nm.

seed nanoparticle/ml (**cZn3**), reducing agent (**cZn1**), and stabilizing agent (**cZn4**). These variations in the experimental conditions result in the different compositions of zinc to gold ratio in **cZn1** to **cZn4** (**Table 1**). There is strong interface damping of the surface plasmon due to the interaction with ZnO. The broadening and decrease of the peak intensity of the plasmonic band from **cZn1** to **cZn2** are due to an increase in ZnO layers as compared to gold seed. It indicates a strong charge carrier interaction at the interface between Au and ZnO (Gogurla et al., 2020). The slight variation in the absorbance in **cZn2** and **cZn3** is due to difference in the seed nanoparticle/ml for these syntheses. The broad and low intense SPR peak in **cZn4** is due to the less amount of stabilizing agent, which is essential to stabilize the AuNP and its SPR absorbance. The FE-SEM image of **cZn1** exhibited octahedral shape nanostructure (**Supplementary Figure S18**). The other FE-SEM images (**Figures 1B–D**) demonstrated that structure and shape morphologies were tuned in all four cases **cZn1** to **cZn4** with respect to **aZn5**, **aZn6**, **aZn7**, and **aZn8**. Interesting surface morphologies with clear appearances of dots were observed in FE-SEM images for the nanocomposites **cZn2** to **cZn4**. These dots were further clarified in the focused surfaces (**Figures 1B–D** insets) of the nanocomposites. The overall particle size of the AuNP-cZnO composite was increased up to 200 nm (**Figure 1B**) and to 400 nm (**Figure 1D**) due to the growth reaction between HAuCl$_4$ and Zn powder at the edge of the AuNP seed as support and NaCt as a stabilizing agent.

In order to clarify the crystalline nature of both Au and ZnO in the nanocomposites, selected area electron diffraction (SAED) pattern was recorded. In the case of **cZn4**, the SAED patterns confirmed the presence of crystalline Au and ZnO in the same
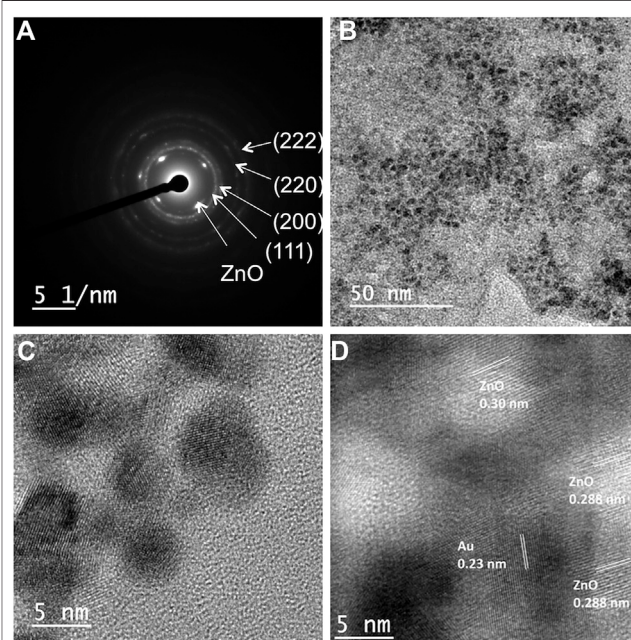
FIGURE 2 | (A) SAED image of **cZn4**; (B) TEM image and (C) HR-TEM showing 5–6 nm AuNPs on nanocomposite **cZn4**, (D) HR-TEM image showing fringe lines corresponding to both Au and ZnO in **cZn4**.

sample (**Figure 2A**). The diffraction patterns for Au planes were similar in **cZn1** to **cZn4**. The difference in the diffraction pattern is due to ZnO. The calculated distances between ZnO planes from diffraction SAED pattern are 0.29, 0.34, 0.30, and 0.28 nm for **cZn1**, **cZn2**, **cZn3**, and **cZn4**, respectively. This change in the
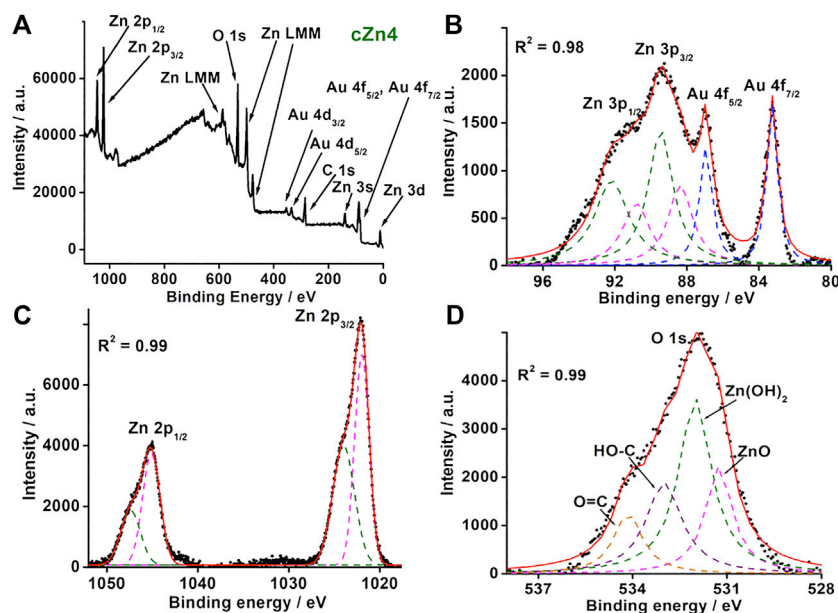
FIGURE 3 | (A) Survey XPS spectrum and **(B–D)** high-resolution XPS spectra for Au 4f, Zn 3p, Zn 2p, and O 1s of nanocomposite **cZn4**.

ZnO plane from **cZn2** to **cZn4** is due to the additional incorporation of gold nanoparticles in these nanocomposites. Furthermore, the TEM image of **cZn4** (**Figure 2B**) corroborated the formation of small size AuNPs on the surface of AuNP-Au-cZnO nanocomposites. The aforementioned result confirmed the generation of AuNP on the nanocomposite surface via the reduction of Au(III) by Zn(0) powder. The high-resolution TEM (HR-TEM) image of the surface confirmed the occlusion of AuNP of 5–6 nm diameter (**Figure 2C**) on the **cZn4** nanocomposite surface. This type of Au-ZnO nanocomposite surfaces (**Supplementary Figure S19**) was also observed for **cZn1-cZn3**. From Williamson Hall plot (**Supplementary Figure S20**) analysis, lattice strains are calculated, and values are 0.00253, 0.00224, 0.00418, and 0.00808 for **cZn1, cZn2, cZn3**, and **cZn4**, respectively. This trend in lattice strain is due to the change in crystal packing (confirmed from HR-TEM and SAED patterns) associated with the degree of disorders (Gogurla et al., 2018).

During the synthesis of nanocomposites, 19 nm AuNP seeds did not convert to 5–6 nm AuNP, which was occluded *in situ* on the Au-ZnO surface. These 5–6 nm Au nanoparticles were obtained directly during the reduction of $HAuCl_4$ by Zn powder in the synthetic process. This generation of 5–6 nm AuNP was not even due to Ostwald ripening as this type of ripening process was involved in the postsynthetic step (Jang et al., 2012). Moreover, Ostwald ripening showed very less enhancement with higher particle size such as 15 nm AuNP (Pattadar and Zamborini, 2019).

Another HR-TEM image of the **cZn4** surface, on which AuNP occlusion was observed, confirmed lattice fringes corresponding to both Au and ZnO. The d-spacing of 0.23 and 0.20 nm (**Figure 2D**; **Supplementary Figure S21**) revealed the presence

of Au (111) and Au (200) planes (Guo et al., 2017). The interplanar spacings of 0.288 and 0.30 nm were found consistent with ZnO, which is in agreement with the XRD spectral peaks according to Joint Committee on Powder Diffraction and Standards (JCPDS no. 00-021-1486; Pradhan and Leung, 2008). Lattice mismatches between Au and ZnO were also observed in this HR-TEM image.

In order to find the detailed composition of **cZn1-cZn4**, the XPS survey scans for all the samples were performed (**Figure 3A**; **Supplementary Figures S22–S24**). These survey scans indicated the presence of Au, C, O, and Zn in the nanocomposites. For nanocomposite **cZn1** (**Supplementary Figure S22**), carbon 1s spectra showed two peaks at 284.8 and 288.7 eV due to aliphatic carbon of –COO group (Di Mauro et al., 2017). The high-resolution scan XPS spectra of Zn illustrated Zn $2p_{3/2}$ and Zn $2p_{1/2}$ peak at 1021 and 1044.8 eV, which were reported for the ZnO system. The O 1s spectrum shows a peak at 531.68 eV due to O^{2-} species present in oxygen deficient regions of ZnO and 531.68 eV for C=O bond. Deconvulating high-resolution XPS spectra of Au showed a peak at 83.2, 86.9, 88.8, and 91.67 eV, which corresponded to Au $4f_{7/2}$, Au $4f_{5/2}$, Zn $3p_{3/2}$, and Zn $3p_{1/2}$, respectively. The binding energies for Au $4f_{7/2}$ and Au $4f_{5/2}$ were shifted slightly in comparison to Au(0) at 84 and 88 eV due to electron transfer from ZnO to Au (Gogurla et al., 2014). The XPS analyses for **cZn2** and **cZn3** (**Supplementary Figures S23, S24**) showed similar characteristics.

For nanocomposite **cZn4** (**Supplementary Figure S25**), carbon 1s spectra showed a similar trend to that of **cZn1**. The high-resolution XPS spectrum of Au (**Figure 3B**) was resolved into six peaks and out of these two corresponded to Au $4f_{7/2}$ (83.19 eV) and Au $4f_{5/2}$ (86.98 eV). The other four peaks at 88.35, 89.40, 90.80, and 92.18 eV were due to Zn $3p_{3/2}$ and $3p_{1/2}$ from

ZnO and Zn(OH)$_2$. High-resolution XPS spectrum for Zn (**Figure 3C**) was resolved into four peaks at Zn 2p$_{3/2}$ (1022.9 eV) and Zn 2p$_{1/2}$ (1045.12 eV) which correspond to ZnO and XPS peak at Zn 2p$_{3/2}$ (1023.9 eV) and Zn 2p$_{1/2}$ (1047.44 eV) contributing to Zn(OH)$_2$ (Klug et al., 2017). The O 1s spectrum (**Figure 3D**) showed four peaks at 531.2, 532.0, 533.0, and 534.14 eV due to oxygen vacancies in ZnO and Zn(OH)$_2$ and the oxygen atom of C-O, C=O bonds (Geng et al., 2018). The band gap due to zinc hydroxide compares to the band gap of ZnO (Karakawa et al., 2018). The ratio of two XPS peak areas of bare ZnO (**Supplementary Figure S26**) with nanocomposites suggests the maximum interaction between Au and ZnO in **cZn2** and **cZn4** (**Supplementary Table S2**).

FE-SEM, HR-TEM, and XPS together confirmed the occlusion of AuNP on the surface of Au-ZnO nanocomposites in the cases of **cZn2** and **cZn3**. In the case of **cZn4**, synthesized with the threshold amount of NaCt, AuNP occlusion took place on the surface of Au-ZnO/Zn(OH)$_2$. The surface charges of **cZn1** and **cZn2** were found to be −3.78 and −0.33 mV (**SupplementaryTable S3**). These differences were due to the variation of electron transfer from ZnO to Au (Gogurla et al., 2014). In the case of **cZn3**, highly negative charge surface (-24.4 mV) was obtained due to the presence of less amount of seeds (nanoparticle/ml) in comparison to **cZn2**. For **cZn4**, the electron transfer from ZnO to Au was less due to the presence of Zn(OH)$_2$ in the nanocomposite. This reflected in the slightly positive surface of **cZn4** (0.36 mV) nanocomposites.

Luminescent properties of crystalline Au-ZnO nanocomposites (cZn1-cZn4) and their applications. The absorbance spectra of these nanocomposites showed peaks at 358 nm (**Supplementary Figure S17**). The excitation of sample **cZn2** at 350 nm produced dual emission peaks at 398 and 448 nm (**Supplementary Figure S27A**) with a broad tail up to 700 nm. The excitation spectra for 398 and 448 nm showed a peak at 358 nm (**Supplementary Figure S27B**), which was similar to the absorption peak. In order to find out the origin of the broadening, the deconvolution of the emission spectra was performed. This resulted in the emission of three additional peaks at 496, 547, and 590 nm. The emission around 398 nm was due to band-to-band transition of ZnO nanomaterial (Kuiri and Pramanik 2018). The excitation spectrum (**Supplementary Figure S27B**) for the emission at 448 nm showed a peak at 358 nm, which was due to the presence of ZnO in the nanocomposite (Liu et al., 2019). The last two emissions at 547 and 590 nm were due to oxygen vacancies in the ZnO nanocomposites. Reported ZnO nanostructures exhibited visible emissions within 420–569 nm by exciting at 370 nm (Khokhra et al., 2017) due to the zinc defects such as interstitials, natural and singly and doubly ionized interstitials. The emission peaks at 448, 547, and 590 nm by exciting the sample at 358 nm in our case are due to the point defect of ZnO. The remaining emission at 496 nm by excitation at 436 nm is due to the formation of 5–6 nm AuNP. The time-resolved fluorescence study (**Supplementary Figure S28**) in our case showed the similar trend of three decay components, which were similar to the previously reported emission from gold nanoclusters (Chattoraj and Bhattacharyya 2014). The quantum yields at 398, 448, 496, 547, and 590 nm wavelengths

for **cZn2** were found to be 4.23, 3.48, 2.00, 0.81, and 0.56%, respectively. The excitation spectra for the other three emission peaks showed a peak at 436 nm (**Figure 4A**). The origin of this excitation peak at 436 nm was probably due to the energy transfer from the initial dual emission for *in situ* stabilized AuNP on Au-ZnO nanocomposites. The maximum emission from **cZn2** was observed at 496 nm by exciting the aqueous suspension at 436 nm (**Figure 4B**). In order to avoid excitation in the UV region at 358 nm, we chose 436 nm as excitation wavelength for our further studies. We checked the luminescence property of **cZn1** to **cZn4** by measuring the emission and excitation spectra (**Figures 4A,B**) in aqueous suspension. The quantum yields of these broad emissions for **cZn1**, **cZn3**, and **cZn4** were found to be 0.27, 0.67, and 0.95%, respectively. The poor quantum yield was due to the mixing of emission from ZnO nanocomponent with the excitation peak due to 5–6 nm AuNP on the AuNP-cZnO surface. The difference in emission behavior is mostly due to the formation of small size AuNP and this type of emission is highly dependent on the size and shape of gold nanoparticles (Chen et al., 2015). The emission maxima vary with Zn powder, AuNP seed, and NaCt concentration as reflected by **cZn1**, **cZn3**, and **cZn4**, respectively for **cZn2**.

We tested the fluorescence imaging of **cZn1-cZn4** nanocomposites in HEK293 cells. The cells were treated with **cZn1-cZn4** (50 μg/ml) for 2 h (at a cell viability of almost 85%) and fixed on a glass slide with paraformaldehyde reagent. The HEK293 cell nuclei and cytoplasm showed bright emission (**Figures 4C–E**; **Supplementary Figures S29, S30**, blue color for visualization) for **cZn2-cZn4**. **cZn1** did not show any prominent luminescent image due to poor quantum yield. The MTT assays were performed with **cZn1-cZn4** on the test cell line after incubation for up to 24 h and found to be nontoxic up to 2 h at a concentration of 50 μg/ml ($p < 0.5$, **Supplementary Figure S31**).

These excitation spectra in the visible region for the nanocomposites triggered the photodegradation of rhodamine-B in presence of visible light (**Figure 4F**; **Supplementary Figure S32**) unlike the recent report with 254 nm light for Au-ZnO nanocomposites. We carried out the photodegradation of rhodamine-B in presence of 455 nm LED. This wavelength was close to the excitation spectrum (**Supplementary Figure S27B**) from 5–6 nm AuNP in the AuNP-cZnO nanocomposites. This emission at 496 nm was stable even after 455 nm LED light illumination for 1 h. **cZn4** showed the best degradation performance with the rate constant 0.25 h^{-1} (**Table 2**). The nonradiative decay rate constants (**Supplementary Figure S28**) were in a similar range for all the four samples. However, the radiative decay rate constant for **cZn4** was maximum and at least two times compared to the nearest radiative decay rate constant for **cZn3**. The photodegradation studies with visible 455 nm light were dependent on the emission properties originating from 5–6 nm AuNP. The control experiments with **aZn5-aZn8** nanocomposites without 5–6 nm AuNP showed no photodegradation of the dye in the presence of 455 nm light. The dye degradation rate constants (**Table 2**) in the presence of 254 nm light were much less in comparison to 455 nm LED
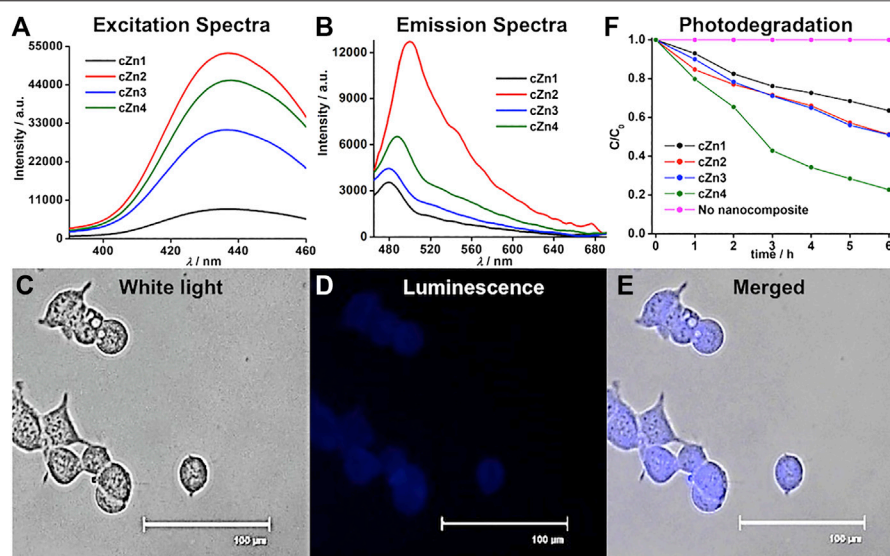
FIGURE 4 | (A) Excitation, **(B)** emission spectra of nanocomposites **cZn1**-**cZn4**, **(C–E)** imaging of **cZn2** in HEK293 cells, where cells were excited at 390/40 nm and emissions were monitored with 446/33 blue filter for luminescence image, scale bar: 100 μm, **(F)** photodegradation of rhodamine-B in presence of nanocomposites **cZn1**-**cZn4**.

TABLE 2 | Rate constants for photodegradation of rhodamine-B.

Nanocomposite	Rate constant (h^{-1})	
	λ = 455 nm	λ = 254 nm
cZn1	0.08	0.04
cZn2	0.11	0.07
cZn3	0.11	0.05
cZn4	0.25	0.11
ZnO	0.02	0.04

probably due to the inherent excitation maxima at 436 nm in these nanocomposites. ZnO-based rate constants (**Supplementary Figure S32**; **Table 2**) for rhodamine dye degradation are 0.02 h^{-1} and 0.04 h^{-1} by irradiation at 455 and 254 nm light, respectively. These rate constants were less in comparison to the rate constants with Au-ZnO nanocomposites.

CONCLUSION

In conclusion, we demonstrated facile room temperature synthesis of crystalline Au-ZnO nanocomposites by metal mediated redox reaction using water as a solvent. The synthetic modification successfully helped in the development of luminescent properties via the occlusion of AuNP on the crystalline Au-ZnO/Zn(OH)$_2$ nanocomposite surface. These luminescent nanocomposites were successfully applied in the visible light–induced photodegradation of rhodamine-B dye.

Currently, we are working on the occlusion of other luminescent materials on the nanocomposite surface.

DATA AVAILABILITY STATEMENT

The original contributions presented in the study are included in the article/**Supplementary Material**; further inquiries can be directed to the corresponding author.

AUTHOR CONTRIBUTIONS

KB synthesized **cZn1–cZn4** in bulk scale, characterized the materials, and performed dye degradation experiments. SL synthesized **aZn1–aZn8** and characterized the materials. AS synthesized **cZn1** and differentiated it from **aZn1**. SN and PR undertook cell culture studies and analysis of the imaging data. KS conceived the idea, participated in data analysis, and wrote the manuscript.

FUNDING

SUPPLEMENTARY MATERIAL

The Supplementary Material for this article can be found online at: https://www.frontiersin.org/articles/10.3389/fchem.2021.639090/full#supplementary-material.

REFERENCES

Brouwer, A. M. (2011). Standards for photoluminescence quantum yield measurements in solution (IUPAC Technical Report). *Pure Appl. Chem.* 83, 2213–2228. doi:10.1351/pac-rep-10-09-31

Caglar, Y., Ilican, S., Caglar, M., Yakuphanoglu, F., Wu, J., Gao, K., et al. (2009). Influence of heat treatment on the nanocrystalline structure of ZnO film deposited on p-Si. *J. Alloys Compd.* 481, 885–889. doi:10.1016/j.jallcom.2009.03.140

Chamorro, W., Ghanbaja, J., Battie, Y., Naciri, A. E., Soldera, F., Mücklich, F., et al. (2016). Local structure-driven localized surface plasmon absorption and enhanced photoluminescence in ZnO-Au thin films. *J. Phys. Chem. C* 120, 29405–29413. doi:10.1021/acs.jpcc.6b09974

Chang, Y. M., Lin, M. L., Lai, T. Y., Chen, C. H., Lee, H. Y., Lin, C. M., et al. (2017). Broadband omnidirectional light trapping in gold-decorated ZnO nanopillar arrays. *ACS Appl. Mater. Interfaces* 9, 11985–11992. doi:10.1021/acsami.6b16412

Chattoraj, S., and Bhattacharyya, K. (2014). Fluorescent gold nanocluster inside a live breast cell: etching and higher uptake in cancer cell. *J. Phys. Chem. C* 118, 22339–22346. doi:10.1021/jp506745p

Chen, D., Zhang, X., and Lee, A. F. (2015). Synthetic strategies to nanostructured photocatalysts for CO$_2$ reduction to solar fuels and chemicals. *J. Mater. Chem. A* 3, 14487–14516. doi:10.1039/c5ta01592h

Chen, J., Chen, Q., Liang, C., Yang, Z., Zhang, L., Yi, X., et al. (2017). Albumin-templated biomineralizing growth of composite nanoparticles as smart nano-theranostics for enhanced radiotherapy of tumors. *Nanoscale* 9, 14826–14835. doi:10.1039/c7nr05316a

Chen, L. Y., Wang, C. W., Yuan, Z., and Chang, H. T. (2015). Fluorescent gold nanoclusters: recent advances in sensing and imaging. *Anal. Chem.* 87, 216–229. doi:10.1021/ac503636j

Cyganowski, P., Lesniewicz, A., Dzimitrowicz, A., Wolska, J., Pohl, P., and Jermakowicz-Bartkowiak, D. (2019). Molecular reactors for synthesis of polymeric nanocomposites with noble metal nanoparticles for catalytic decomposition of 4-nitrophenol. *J. Colloid Interface Sci.* 541, 226–233. doi:10.1016/j.jcis.2019.01.097

Degen, A., and Kosec, M. (2000). Effect of pH and impurities on the surface charge of zinc oxide in aqueous solution. *J. Eur. Ceram. Soc.* 20, 667–673. doi:10.1016/s0955-2219(99)00203-4

Di Mauro, A., Cantarella, M., Nicotra, G., Pellegrino, G., Gulino, A., Brundo, M. V., et al. (2017). Novel synthesis of ZnO/PMMA nanocomposites for photocatalytic applications. *Sci. Rep.* 7, 40895. doi:10.1038/srep40895

Dutta Chowdhury, A., Agnihotri, N., Doong, R. A., and De, A. (2017). Label-free and nondestructive separation technique for isolation of targeted DNA from DNA-protein mixture using magnetic Au-Fe$_3$O$_4$ nanoprobes. *Anal. Chem.* 89, 12244–12251. doi:10.1021/acs.analchem.7b03095

Fuggle, J. C., Källne, E., Watson, L. M., and Fabian, D. J. (1977). Electronic structure of aluminum and aluminum-noble-metal alloys studied by soft-x-ray and x-ray photoelectron spectroscopies. *Phys. Rev. B* 16, 750–761. doi:10.1103/physrevb.16.750

Gan, Z., Lin, Y., Luo, L., Han, G., Liu, W., Liu, Z., et al. (2016). Fluorescent gold nanoclusters with interlocked staples and a fully thiolate-bound kernel. *Angew. Chem. Int. Ed.* 55, 11567–11571. doi:10.1002/anie.201606661

Gao, Z., Li, Y., Zhang, C., Zhang, S., Jia, Y., Li, F., et al. (2019). AuCu$_x$O-embedded mesoporous CeO$_2$ nanocomposites as a signal probe for electrochemical sensitive detection of amyloid-beta protein. *ACS Appl. Mater. Interfaces* 11, 12335–12341. doi:10.1021/acsami.9b01445

Geng, Z., Kong, X., Chen, W., Su, H., Liu, Y., Cai, F., et al. (2018). Oxygen vacancies in ZnO nanosheets enhance CO$_2$ electrochemical reduction to CO. *Angew. Chem. Int. Ed.* 57, 6054–6059. doi:10.1002/anie.201711255

Gogurla, N., Bayan, S., Chakrabarty, P., and Ray, S. K. (2018). Plasmon mediated enhancement of visible light emission of Au-ZnO nanocomposites. *J. Lumin.* 194, 15–21. doi:10.1016/j.jlumin.2017.09.044

Gogurla, N., Chowdhury, R. K., Battacharya, S., Datta, P. K., and Ray, S. K. (2020). Plasmon charge transfer dynamics in layered Au–ZnO nanocomposites. *J. Appl. Phys.* 127, 053105. doi:10.1063/1.5134892

Gogurla, N., Sinha, A. K., Santra, S., Manna, S., and Ray, S. K. (2014). Multifunctional Au-ZnO plasmonic nanostructures for enhanced UV photodetector and room temperature NO sensing devices. *Sci. Rep.* 4, 6483. doi:10.1038/srep06483

Goswami, N., Lin, F., Liu, Y., Leong, D. T., and Xie, J. (2016). Highly luminescent thiolated gold nanoclusters impregnated in nanogel. *Chem. Mater.* 28, 4009–4016. doi:10.1021/acs.chemmater.6b01431

Guo, J., Zhang, Y., Shi, L., Zhu, Y., Mideksa, M. F., Hou, K., et al. (2017). Boosting hot electrons in hetero-superstructures for plasmon-enhanced catalysis. *J. Am. Chem. Soc.* 139, 17964–17972. doi:10.1021/jacs.7b08903

Hang, D. R., Islam, S. E., Chen, C. H., and Sharma, K. H. (2016). Full solution-processed synthesis and mechanisms of a recyclable and bifunctional Au/ZnO plasmonic platform for enhanced UV/vis photocatalysis and optical properties. *Chemistry* 22, 14950–14961. doi:10.1002/chem.201602578

He, H., Cai, W., Lin, Y., and Chen, B. (2010). Surface decoration of ZnO nanorod arrays by electrophoresis in the Au colloidal solution prepared by laser ablation in water. *Langmuir* 26 (11), 8925–8932. doi:10.1021/la904723a

He, J., Xu, F., Chen, Z., Hou, X., Liu, Q., and Long, Z. (2017). AuNPs/COFs as a new type of SERS substrate for sensitive recognition of polyaromatic hydrocarbons. *Chem. Commun.* 53, 11044–11047. doi:10.1039/c7cc06440c

Hu, Y., Liu, Y., Xie, X., Bao, W., and Hao, J. (2018). Surfactant-regulated fabrication of gold nanostars in magnetic core/shell hybrid nanoparticles for controlled release of drug. *J. Colloid Interface Sci.* 529, 547–555. doi:10.1016/j.jcis.2018.06.027

Jang, E., Lim, E.-K., Choi, J., Park, J., Huh, Y.-J., Suh, J.-S., et al. (2012). Br-assisted Ostwald ripening of Au nanoparticles under H$_2$O$_2$ redox. *Cryst. Growth Des.* 12, 37–39. doi:10.1021/cg201243n

Jangir, L. K., Kumari, Y., Kumar, A., Kumar, M., and Awasthi, K. (2017). Investigation of luminescence and structural properties of ZnO nanoparticles, synthesized with different precursors. *Mater. Chem. Front.* 1, 1413–1421. doi:10.1039/C7QM00058H

Jia, H., Du, A., Zhang, H., Yang, J., Jiang, R., Wang, J., et al. (2019). Site-selective growth of crystalline ceria with oxygen vacancies on gold nanocrystals for near-infrared nitrogen photofixation. *J. Am. Chem. Soc.* 141, 5083–5086. doi:10.1021/jacs.8b13062

Johnston, R. L. (2002). *Atomic and molecular clusters*. London, United Kingdom: Taylor & Francis.

Karakawa, M., Sugahara, T., Hirose, Y., Suganuma, K., and Aso, Y. (2018). Thin film of amorphous zinc hydroxide semiconductor for optical devices with an energy-efficient beneficial coating by metal organic decomposition process. *Sci. Rep.* 8, 10839. doi:10.1038/s41598-018-27953-6

Kauffman, D. R., Deng, X., Sorescu, D. C., Nguyen-Phan, T.-D., Wang, C., Marin, C. M., et al. (2019). Edge-enhanced oxygen evolution reactivity at ultrathin, Au-supported Fe$_2$O$_3$ electrocatalysts. *ACS Catal.* 9, 5375–5382. doi:10.1021/acscatal.9b01093

Khokhra, R., Bharti, B., Lee, H. N., and Kumar, R. (2017). Visible and UV photo-detection in ZnO nanostructured thin films via simple tuning of solution method. *Sci. Rep.* 7, 15032. doi:10.1038/s41598-017-15125-x

Klug, M. T., Dorval Courchesne, N.-M., Lee, Y. E., Yun, D. S., Qi, J., Heldman, N. C., et al. (2017). Mediated growth of zinc chalcogen shells on gold nanoparticles by free-base amino acids. *Chem. Mater.* 29, 6993–7001. doi:10.1021/acs.chemmater.7b02571

Kuiri, P. K., and Pramanik, S. (2018). Large enhancement of UV luminescence emission of ZnO nanoparticles by coupling excitons with Ag surface plasmons. *J. Appl. Phys.* 123, 54302. doi:10.1063/1.5021387

Lakowicz, J. R. (2006). *Principles of fluorescence spectroscopy*. 3rd Edn. Berlin, Germany: Springer Science + Business Media, LLC..

Lee, D. K., Song, Y., Tran, V. T., Kim, J., Park, E. Y., and Lee, J. (2017). Preparation of concave magnetoplasmonic core-shell supraparticles of gold-coated iron oxide via ion-reducible layer-by-layer method for surface enhanced Raman scattering. *J. Colloid Interface Sci.* 499, 54–61. doi:10.1016/j.jcis.2017.03.098

Lewis, D. J., Day, T. M., Macpherson, J. V., and Pikramenou, Z. (2006). Luminescent nanobeads: attachment of surface reactive Eu(III) complexes to gold nanoparticles. *Chem. Commun.*, 1433–1435. doi:10.1039/b518091k

Li, C., Bolisetty, S., and Mezzenga, R. (2013). Hybrid nanocomposites of gold single-crystal platelets and amyloid fibrils with tunable fluorescence, conductivity, and sensing properties. *Adv. Mater.* 25, 3694–3700. doi:10.1002/adma.201300904

Li, P., Wei, Z., Wu, T., Peng, Q., and Li, Y. (2011). Au-ZnO hybrid nanopyramids and their photocatalytic properties. *J. Am. Chem. Soc.* 133, 5660–5663. doi:10.1021/ja111102u

Liu, F., Goyal, S., Forrester, M., Ma, T., Miller, K., Mansoorieh, Y., et al. (2019). Self-assembly of Janus dumbbell nanocrystals and their enhanced surface plasmon resonance. *Nano Lett.* 19, 1587–1594. doi:10.1021/acs.nanolett.8b04464

Liu, J., Li, J., Wei, F., Zhao, X., Su, Y., and Han, X. (2019). Ag-ZnO submicrometer rod arrays for high-efficiency photocatalytic degradation of congo red and disinfection. *ACS Sustainable Chem. Eng.* 7, 11258–11266. doi:10.1021/acssuschemeng.9b00610

Liu, J., Yu, M., Zhou, C., Yang, S., Ning, X., and Zheng, J. (2013). Passive tumor targeting of renal-clearable luminescent gold nanoparticles: long tumor retention and fast normal tissue clearance. *J. Am. Chem. Soc.* 135, 4978–4981. doi:10.1021/ja401612x

Liu, Y., Lv, X., Liu, H., Zhou, Z., Huang, J., Lei, S., et al. (2018). Porous gold nanocluster-decorated manganese monoxide nanocomposites for microenvironment-activatable MR/photoacoustic/CT tumor imaging. *Nanoscale* 10, 3631–3638. doi:10.1039/c7nr08535d

Lupan, O., Postica, V., Wolff, N., Su, J., Labat, F., Ciofini, I., et al. (2019). Low-temperature solution synthesis of Au-modified ZnO nanowires for highly efficient hydrogen nanosensors. *ACS Appl. Mater. Interfaces* 11, 32115–32126. doi:10.1021/acsami.9b08598

Mageed, A. M., Klyushin, A., Rezvani, A., Gericke, A. K., Schlogl, R., and Behm, R. J. (2019). Negative charging of Au nanoparticles during methanol synthesis from CO_2/H_2 on a Au/ZnO catalyst: insights from operando IR and near-ambient-pressure XPS and XAS measurements. *Angew. Chem. Int. Ed.* 58, 10325–10329. doi:10.1002/anie.201900150

Ning, Y., Fielding, L. A., Nutter, J., Kulak, A. N., Meldrum, F. C., and Armes, S. P. (2019). Spatially controlled occlusion of polymer-stabilized gold nanoparticles within ZnO. *Angew. Chem. Int. Ed.* 58, 4302–4307. doi:10.1002/anie.201814492

Pattadar, D. K., and Zamborini, F. P. (2019). Effect of size, coverage, and dispersity on the potential-controlled Ostwald ripening of metal nanoparticles. *Langmuir* 35, 16416–16426. doi:10.1021/acs.langmuir.9b02421

Pourrahimi, A. M., Liu, D., Pallon, L. K. H., Andersson, R. L., Martínez Abad, A., Lagarón, J.-M., et al. (2014). Water-based synthesis and cleaning methods for high purity ZnO nanoparticles—comparing acetate, chloride, sulphate and nitrate zinc salt precursors. *RSC Adv.* 4, 35568–35577. doi:10.1039/c4ra06651k

Pradhan, D., and Leung, K. T. (2008). Vertical growth of two-dimensional zinc oxide nanostructures on ITO-coated glass: effects of deposition temperature and deposition time. *J. Phys. Chem. C* 112, 1357–1364. doi:10.1021/jp076890n

Qi, C., Musetti, S., Fu, L. H., Zhu, Y. J., and Huang, L. (2019). Biomolecule-assisted green synthesis of nanostructured calcium phosphates and their biomedical applications. *Chem. Soc. Rev.* 48, 2698–2737. doi:10.1039/c8cs00489g

Raji, R., and Gopchandran, K. G. (2017). ZnO nanostructures with tunable visible luminescence: effects of kinetics of chemical reduction and annealing. *J. Sci. Adv. Mater. Devices* 2, 51–58. doi:10.1016/j.jsamd.2017.02.002

Ray, C., and Pal, T. (2017). Retracted Article: recent advances of metal-metal oxide nanocomposites and their tailored nanostructures in numerous catalytic applications. *J. Mater. Chem. A* 5, 9465–9487. doi:10.1039/c7ta02116j

Ritchie, C., Chesman, A. S. R., Jasieniak, J., and Mulvaney, P. (2019). Aqueous synthesis of $Cu_2ZnSnSe_4$ nanocrystals. *Chem. Mater.* 31, 2138–2150. doi:10.1021/acs.chemmater.9b00100

Saini, M., Masirkar, Y., Varshney, R., Roy, P., and Sadhu, K. K. (2017). Fluorogen-free aggregation induced NIR emission from gold nanoparticles. *Chem. Commun.* 53, 6199–6202. doi:10.1039/c7cc00641a

Shingange, K., Tshabalala, Z. P., Ntwaeaborwa, O. M., Motaung, D. E., and Mhlongo, G. H. (2016). Highly selective NH_3 gas sensor based on Au loaded ZnO nanostructures prepared using microwave-assisted method. *J. Colloid Interface Sci.* 479, 127–138. doi:10.1016/j.jcis.2016.06.046

Song, J., Wu, B., Zhou, Z., Zhu, G., Liu, Y., Yang, Z., et al. (2017). Double-layered plasmonic-magnetic vesicles by self-assembly of Janus amphiphilic gold-iron(II,III) oxide nanoparticles. *Angew. Chem. Int. Ed.* 56, 8110–8114. doi:10.1002/anie.201702572

Strohmeier, B. R, and Hercules, D. M. (1984). Surface spectroscopic characterization of the interaction between zinc ions and γ-alumina. *J. Catal.* 86, 266–279. doi:10.1016/0021-9517(84)90372-5

Tahir, M. N., Natalio, F., Cambaz, M. A., Panthöfer, M., Branscheid, R., Kolb, U., et al. (2013). Controlled synthesis of linear and branched Au@ZnO hybrid nanocrystals and their photocatalytic properties. *Nanoscale* 5, 9944–9949. doi:10.1039/c3nr02817h

Tan, B. J., Klabunde, K. J., and Sherwood, P. M. A. (1990). X-ray photoelectron spectroscopy studies of solvated metal atom dispersed catalysts, monometallic iron and bimetallic iron-cobalt particles on alumina. *Chem. Mater.* 2, 186–191. doi:10.1021/cm00008a021

Tang, X., Choo, E. S. G., Li, L., Ding, J., and Xue, J. (2010). Synthesis of ZnO nanoparticles with tunable emission colors and their cell labeling applications. *Chem. Mater.* 22, 3383–3388. doi:10.1021/cm903869r

Unlu, I., Soares, J. W., Steeves, D. M., and Whitten, J. E. (2015). Photocatalytic activity and fluorescence of gold/zinc oxide nanoparticles formed by dithiol linking. *Langmuir* 31, 8718–8725. doi:10.1021/acs.langmuir.5b01632

Viter, R., Balevicius, Z., Abou Chaaya, A., Baleviciute, I., Tumenas, S., Mikoliunaite, L., et al. (2015). The influence of localized plasmons on the optical properties of Au/ZnO nanostructures. *J. Mater. Chem. C* 3, 6815–6821. doi:10.1039/c5tc00964b

Wang, J., Ma, S., Ren, J., Yang, J., Qu, Y., Ding, D., et al. (2018). Fluorescence enhancement of cysteine-rich protein-templated gold nanoclusters using silver(I) ions and its sensing application for mercury(II). *Sens. Actuators B* 267, 342–350. doi:10.1016/j.snb.2018.04.034

Wang, X., Shi, W., Jin, Z., Huang, W., Lin, J., Ma, G., et al. (2017b). Remarkable SERS activity observed from amorphous ZnO nanocages. *Angew. Chem. Int. Ed.* 56, 9851–9855. doi:10.1002/anie.201705187

Wang, Y., Guo, H., Zhang, Y., Tai, F., Wang, Y., Dong, Q., et al. (2018b). Achieving highly water-soluble and luminescent gold nanoclusters modified by β-cyclodextrin as multifunctional nanoprobe for biological applications. *Dyes Pigm.* 157, 359–368. doi:10.1016/j.dyepig.2018.05.015

Wang, Y., Wang, S. S., Lu, Y., Jiang, J., Yang, S. A., Cui, Y., et al. (2017). Strain-induced isostructural and magnetic phase transitions in monolayer MoN2. *Nano Lett.* 16, 4576–4582. doi:10.1021/acs.nanolett.6b01841

Wei, R.-B., Kuang, P.-Y., Cheng, H., Chen, Y.-B., Long, J.-Y., Zhang, M.-Y., et al. (2017). Plasmon-enhanced photoelectrochemical water splitting on gold nanoparticle decorated ZnO/CdS nanotube arrays. *ACS Sustainable Chem. Eng.* 5, 4249–4257. doi:10.1021/acssuschemeng.7b00242

Wu, Z., Du, Y., Liu, J., Yao, Q., Chen, T., Cao, Y., et al. (2019). Aurophilic interactions in the self-assembly of gold nanoclusters into nanoribbons with enhanced luminescence. *Angew. Chem. Int. Ed.* 58, 8139–8144. doi:10.1002/anie.201903584

Wuithschick, M., Birnbaum, A., Witte, S., Sztucki, M., Vainio, U., Pinna, N., et al. (2015). Turkevich in new robes: key questions answered for the most common gold nanoparticle synthesis. *ACS Nano* 9, 7052–7071. doi:10.1021/acsnano.5b01579

Yao, K. X., Liu, X., Zhao, L., Zeng, H. C., and Han, Y. (2011). Site-specific growth of Au particles on ZnO nanopyramids under ultraviolet illumination. *Nanoscale* 3, 4195–4200. doi:10.1039/c1nr10685f

Yao, Y., Xue, M., Zhang, Z., Zhang, M., Wang, Y., and Huang, F. (2013). Gold nanoparticles stabilized by an amphiphilic pillar[5]arene: preparation, self-assembly into composite microtubes in water and application in green catalysis. *Chem. Sci.* 4, 3667–3672. doi:10.1039/c3sc51547f

Yu, H., Chen, M., Rice, P. M., Wang, S. X., White, R. L., and Sun, S. (2005). Dumbbell-like bifunctional Au−Fe3O4 nanoparticles. *Nano Lett.* 5, 379–382. doi:10.1021/nl047955q

Yu, M., Xu, J., and Zheng, J. (2019). Renal clearable luminescent gold nanoparticles: from the bench to the clinic. *Angew. Chem. Int. Ed.* 58, 4112–4128. doi:10.1002/anie.201807847

Yu, M., Zhou, C., Liu, J., Hankins, J. D., and Zheng, J. (2011). Luminescent gold nanoparticles with pH-dependent membrane adsorption. *J. Am. Chem. Soc.* 133, 11014–11017. doi:10.1021/ja201930p

Zhang, L., Rajagopalan, R., Guo, H., Hu, X., Dou, S., and Liu, H. (2016). A green and facile way to prepare granadilla-like silicon-based anode materials for Li-ion batteries. *Adv. Funct. Mater.* 26, 440–446. doi:10.1002/adfm.201503777

Zhang, M., Wu, F., Wang, W., Shen, J., Zhou, N., and Wu, C. (2019). Multifunctional nanocomposites for targeted, photothermal, and chemotherapy. *Chem. Mater.* 31, 1847–1859. doi:10.1021/acs.chemmater.8b00934

Zhang, Q., Liu, J., Dong, Y., Li, W., Xing, R., Ma, Y., et al. (2019). Gold nanoparticle-decorated Ag@SiO2 nanocomposite-based plasmonic affinity

sandwich assay of circulating microRNAs in human serum. *ACS Appl. Nano Mater.* 2, 3960–3970. doi:10.1021/acsanm.9b00855

Zhou, X., Zhao, G., Chen, M., Gao, W., Zhou, X., Xie, X., et al. (2018). Facile and green approach to prepare nanostructured Au@MnO$_2$ and its applications for catalysis and fluorescence sensing of glutathione in human blood. *ACS Sustainable Chem. Eng.* 6, 3948–3956. doi:10.1021/acssuschemeng.7b04313

Zu, L., Qin, Y., and Yang, J. (2015). *In situ* synergistic crystallization-induced synthesis of novel Au nanostar-encrusted ZnO mesocrystals with high-quality heterojunctions for high-performance gas sensors. *J. Mater. Chem. A* 3, 10209–10218. doi:10.1039/c5ta02182k

Isocyanides: Promising Functionalities in Bioorthogonal Labeling of Biomolecules

Yuchen Zhu[1], Jia-Yu Liao[1,2]* and Linghui Qian[1,2,3,4]*

[1]College of Pharmaceutical Sciences, Zhejiang University, Hangzhou, China, [2]Hangzhou Institute of Innovative Medicine, Zhejiang University, Hangzhou, China, [3]Cancer Center, Zhejiang University, Hangzhou, China, [4]Zhejiang Province Key Laboratory of Anti-Cancer Drug Research, College of Pharmaceutical Sciences, Zhejiang University, Hangzhou, China

Isocyanides have drawn increasing attention in biological applications due to their attractive properties and unique reactivities, which can undergo various reactions, such as multicomponent reactions, α-addition reactions, [4 + 1] cycloaddition reactions, and the reaction scope keeps expanding. In addition to acting as reactants for the preparation of structurally interesting and diverse N-heterocycles or peptidomimetics, this type of functionality may be a good choice in the labeling and modulation of biomolecules due to the high biocompatibility and small size to minimize modifications on the parent molecule. It has been demonstrated that isocyanides can participate in biomolecule labeling through three strategies, including the two-component bioorthogonal reaction, multicomponent reaction, and metal chelation. Among them, the isocyanide-tetrazine reaction has been better studied recently, augmenting the potency of isocyanide as a bioorthogonal handle. This review will focus on the recent progress in isocyanide chemistry for labeling of biomolecules. Meanwhile, methods to introduce isocyano groups into biomacromolecules are also described to facilitate wider applications of this unique functionality.

Keywords: bioorthogonal chemistry, biomolecule labeling, isocyanide, ligation, cleavage

INTRODUCTION

Isocyanides are a class of highly versatile and irreplaceable reagents as the isocyano group may serve as both nucleophile and electrophile in chemical reactions (Nenajdenko, 2012). Over the past several decades, isocyanide chemistry has drawn much attention and found wide applications in synthetic organic and medicinal chemistry for the construction of structurally interesting and diverse N-heterocycles or peptidomimetics. The classical reactions involving isocyanides include but not limited to multicomponent reactions (MCRs), such as the well-known Passerini and Ugi reaction, α-addition reactions with electrophilic substrates, as well as [4 + 1] cycloaddition reactions. Since many of the above reactions could take place smoothly in aqueous media, and isocyanides are stable at biologically relevant pH [stable at pH 4–9 (Goldstein and Niv, 1993)] without obvious biotoxicity (Deb and Franzini, 2020), isocyanide chemistry has been successfully employed to realize the labeling of biomacromolecules, including proteins and polysaccharides. More intriguing, the isocyano group with a bond length of only 1.17 Å is known to date as the smallest bioorthogonal functionality suitable for living systems (**Figure 1**; though terminal alkyne is a bit smaller in size, it cannot be readily used in living systems through Cu-catalyzed azide-alkyne cycloaddition), allowing to modify the target biomolecule with minimum interference in the structure and function, thus may be
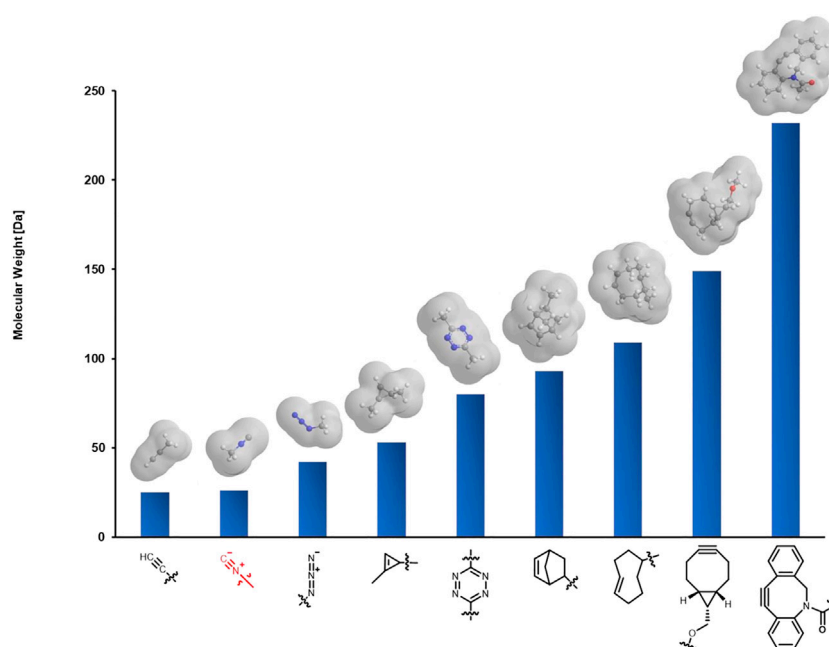
FIGURE 1 | Comparison of the size of isocyano group with other commonly used bioorthogonal functionalities. Molecules are shown with the corresponding methyl derivatives.

suitable for cellular, subcellular, and even *in vivo* imaging. Other than bioimaging, it is also expected to achieve the activation of specific proteases and targeted drug release when used in combination with other strategies (Zhang et al., 2020). To facilitate wider applications of isocyanides in biological labeling, three strategies developed recently will be systematically described here.

STRATEGY 1: ISOCYANIDE AS A BIOORTHOGONAL HANDLE

Bioorthogonal reactions are chemical reactions that neither interact nor interfere with a biological system. They have the following properties: 1) rapid reaction rate at low concentrations; 2) chemical selectivity, free from the influence of electrophilic and nucleophilic residues in biomolecules; 3) both reactants and products are stable under physiological conditions; 4) the products are small and chemically inert to avoid interfering with the activity of the target biomolecule (Kenry and Liu, 2019). Traditionally, bioorthogonal chemistry has largely been viewed as two-component "ligation" reactions since Bertozzi et al. proposed the term of bioorthogonal reaction in 2003 (Lemieux et al., 2003; Prescher and Bertozzi, 2005) to describe the biocompatible Staudinger ligation between an azido-containing unnatural sugar displayed on the living cell surface and a modified triphenylphosphine-fluorophore conjugate. To date, there are many bioorthogonal reactions

available, such as Cu-catalyzed azide-alkyne cycloaddition (CuAAC), strain-promoted (Cu-free) azide-alkyne cycloaddition (SPAAC), inverse electron demand Diels-Alder (IEDDA) reactions including the tetrazine ligation and the isocyanide-based click reaction (Patterson et al., 2014; Smeenk et al., 2021). These reactions have been widely used in the labeling of biomolecules. In 2013, Robillard et al. reported the "click to release" reaction between tetrazine and *trans*-cyclooctene (TCO, with a carbamate group next to the double bond), initiating the release of drugs from the TCO (Versteegen et al., 2013). Such bioorthogonal bond cleavage reactions were thoroughly reviewed by Chen's group in 2016, highlighting their applications in regulating cellular proteins or manipulating biological functions (Li and Chen, 2016; Zhang et al., 2016). Both the bioorthogonal ligation and cleavage reactions have expanded the chemical toolkit for biological discovery, and functionalities such as isocyanides that can undergo either ligation or cleavage controlled by their substituents will be particularly useful.

Isocyanide-Tetrazine Chemistry

As early as 1982, Seitz et al. reported the first example of [4 + 1] cycloaddition reaction of benzyl isocyanides with tetrazines to prepare pharmacologically interesting amino-pyrazoles (Imming et al., 1982). The first step of this transformation is the formation of tetraazanorbornadienimine derivatives **1** through [4 + 1] cycloaddition. This type of intermediate was unstable and
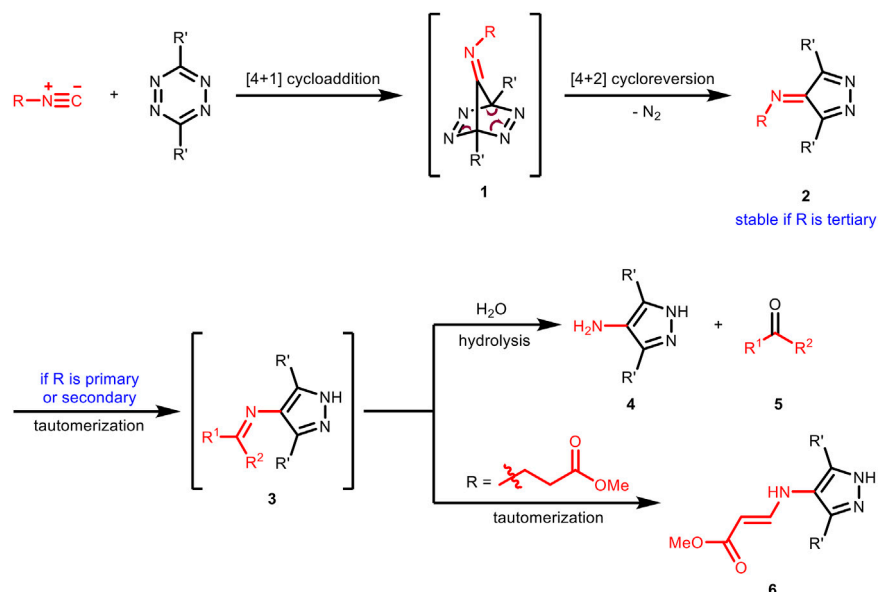
FIGURE 2 | Mechanism of the reaction between isocyanides and tetrazines.
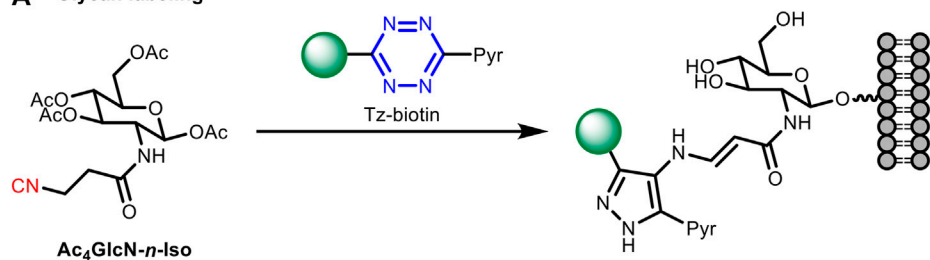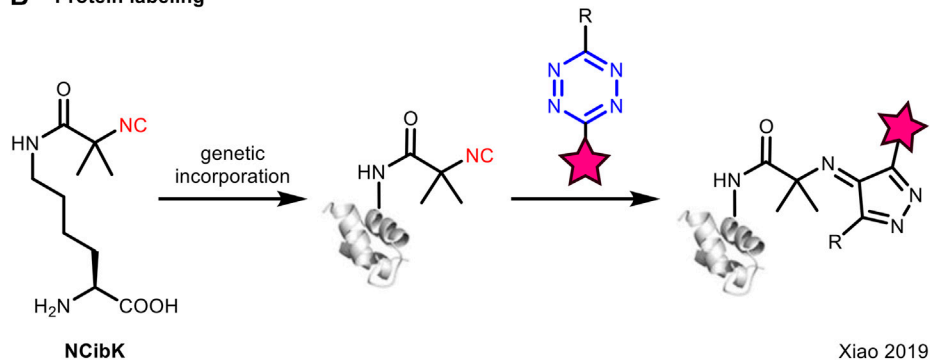
FIGURE 3 | Application of isocyanide-tetrazine chemistry for bioorthogonal ligation with **(A)** glycans or **(B)** proteins.

would spontaneously undergo [4 + 2] cycloreversion with the release of N_2 to result in imine derivatives **2**, which would further tautomerize to the aromatic pyrazoles **3** and then hydrolyze to amino-pyrazoles **4** and carbonyls **5** (**Figure 2**). Because of the stability issue of **2**, this [4 + 1] cycloaddition reaction could not be used directly for chemical ligation

reactions in aqueous media. In 2011, Leeper et al. investigated this chemistry systematically with different types of isocyanides (Stöckmann et al., 2011). They found that for primary and secondary isocyanides, the imines **2** could not be isolated and the corresponding amino-pyrazoles and aldehydes/ketones were obtained as the final products in

FIGURE 4 | Application of isocyanide-tetrazine chemistry for bioorthogonal cleavage in **(A)** single release of small molecules, **(B)** single release of proteins, or **(C)** dual release of fluorophores.
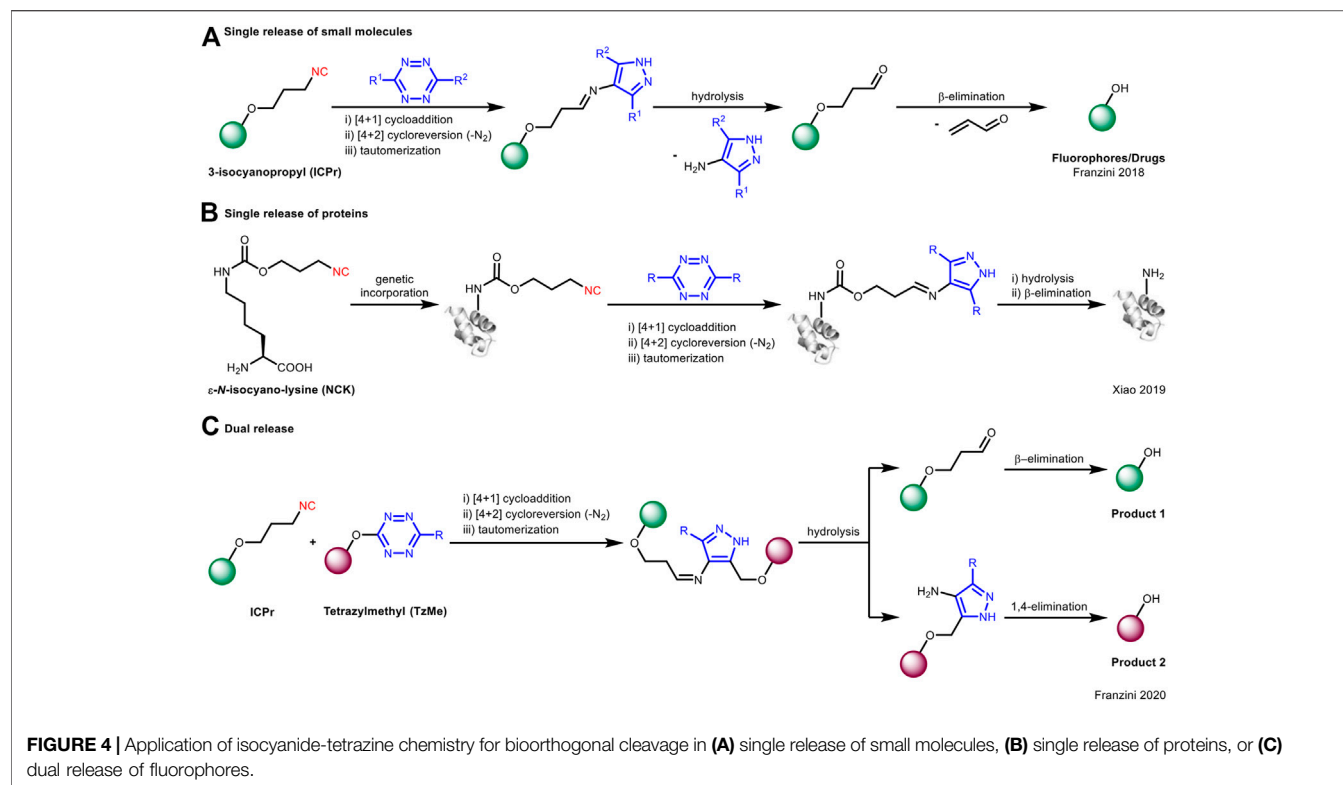
the same manner with Seitz's report. In contrast, the imine products **2** from the reaction of tertiary isocyanides was found to be stable as the tautomerization process (from **2** to **3**) was prohibited. Besides, imines **3** formed from propanoate-derived isocyanides did not hydrolyze either, but instead tautomerized again to give the vinylogous urethane derivatives **6** (**Figure 2**).

It is noteworthy that the isocyanide-tetrazine [4 + 1] cycloaddition is much slower than the conventional counterpart of tetrazine such as TCO, and this may limit its application in biomolecule labeling (Stairs et al., 2013). To compensate for the low reaction rate, Leeper et al. employed a high concentration of Tz-biotin (non-fluorogenic) for conjugation to primary 3-isocyanopropanamide-derived glycans (**Ac₄GlcN-*n*-Iso**) on the cell surface (**Figure 3A**). However, this method did not essentially solve the kinetic problem between isocyanides and tetrazines. Later, Xiao et al. (Chen et al., 2019) designed a *tert*-butyl isocyano group conjugated lysine (**NCibK**) for protein labeling via [4 + 1] cycloaddition reaction with tetrazine probes (**Figure 3B**). The unnatural amino acid **NCibK** was introduced into proteins via genetic code expansion technology. This was the first example to use isocyanide-tetrazine ligation to achieve protein labeling, though the reaction rate is not high.

On the contrary, Franzini et al. took advantage of the spontaneous hydrolysis of the cycloaddition product from primary isocyanide and tetrazine for "click to release" (Tu et al., 2018). In this case, they used 3-isocyanopropyl (**ICPr**) substituents as masking groups which can be effectively removed upon reacting with tetrazines to liberate phenol-containing active

molecules under physiological conditions (**Figure 4A**). This concept could be extended to the release of proteins (**Figure 4B**; Chen et al., 2019). Furthermore, by the use of both primary isocyanide and tetrazine as "protecting groups," the caged fluorophores would undergo bioorthogonal bond cleavage to liberate dual fluorophores through a single reaction (**Figure 4C**; Tu et al., 2020).

Meanwhile, Franzini's group thoroughly explored the structure-activity relationship of the reaction between isocyanides and tetrazines (**Table 1**), and found that tetrazines with bulky substituents could form stable adducts with primary isocyanides, thus obviating the need for engineering the isocyanide moiety (e.g., tertiary isocyanides) (Tu et al., 2019; Xu et al., 2019). What's more interesting is that stable asymmetric tetrazines with bulky and electron-withdrawing substituents (**Tz-4**) can react with isocyanides rapidly under high-water conditions (**Table 1**, Entries 12–13). Computational analysis showed that dispersion forces between the isocyano group and the bulky tetrazine substituents in the transition state contribute to the acceleration. The use of sterically hindered tetrazine allows the rapid conjugation with primary/secondary isocyanides, thus promoting isocyanides to be among the most promising bioorthogonal reporters.

Isocyanide-Chlorooxime Chemistry

Other than tetrazines, Helma et al. successfully applied the classical reaction of isocyanides with chlorooximes (**Figure 5A**) for bioorthogonal ligation (**Figure 5B**; Schäfer et al., 2019). It showed a modest reaction rate ($k_2 \approx 1 \text{ M}^{-1} \text{ s}^{-1}$)

Entry	Tetrazine	Counterpart	k_2 [M^{-1}S^{-1}]	Condition
1	Tz-1	t-OcNC	1.48 ± 0.03	DMSO/H$_2$O = 4:1, T = 37°C
2	Tz-1	Cp	0.563 ± 0.025	DMSO/H$_2$O = 4:1, T = 37°C
3	Tz-1	Nb	0.827 ± 0.042	DMSO/H$_2$O = 4:1, T = 37°C
4	Tz-1	TCO	>100	DMSO/H$_2$O = 4:1, T = 37°C
5	Tz-2	PhEtNC	1.15 ± 0.20	DMSO/H$_2$O = 4:1, T = 37°C
6	Tz-3	PhEtNC	1.53 ± 0.01	DMSO/H$_2$O = 4:1, T = 37°C
7	Tz-4	PhEtNC	2.42 ± 0.10	DMSO/H$_2$O = 4:1, T = 37°C
8	Tz-4	t-OcNC	6.27 ± 0.05	DMSO/H$_2$O = 4:1, T = 37°C
9	Tz-4	Cp	0.588 ± 0.055	DMSO/H$_2$O = 4:1, T = 37°C
10	Tz-4	Nb	0.013 ± 0.005	DMSO/H$_2$O = 4:1, T = 37°C
11	Tz-4	TCO	0.234 ± 0.002	DMSO/H$_2$O = 4:1, T = 37 °C
12	Tz-4	PhEtNC	29.4 ± 0.8	DMSO/H$_2$O = 1:4, T = 37°C
13	Tz-4	t-OcNC	57 ± 5	DMSO/H$_2$O = 1:4, T = 37°C

Data sources: Tu et al., 2019.
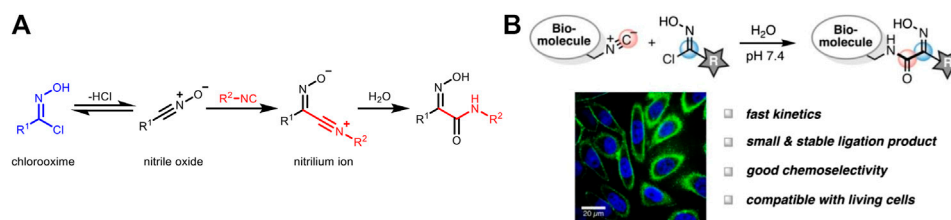
FIGURE 5 | **(A)** Mechanism of the reaction between isocyanides and chlorooximes. **(B)** Isocyanide-chlorooxime ligation for the labeling of biomolecules in live cells. Re-printed with permission from American Chemistry Society Publications 2019 (Schäfer et al., 2019).
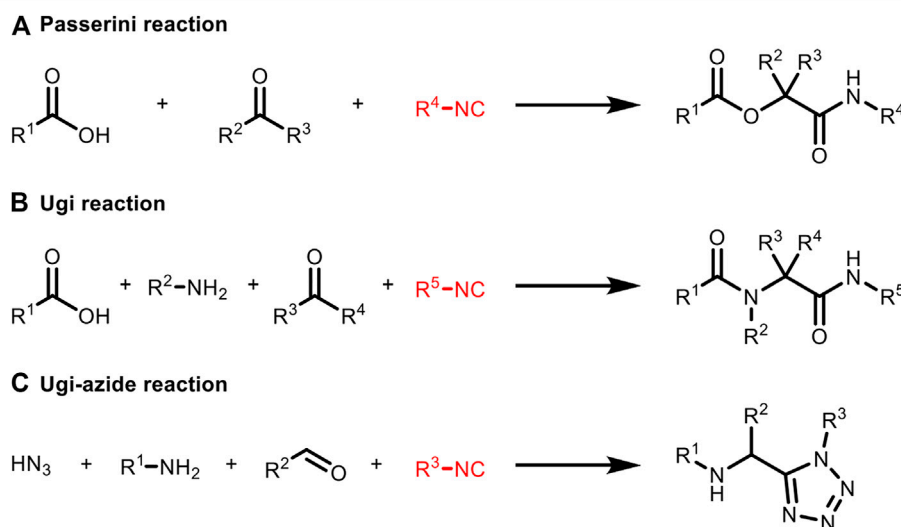
FIGURE 6 | Isocyanide-based MCRs applied to bioconjugation include **(A)** Passerini reaction, **(B)** Ugi reaction and **(C)** Ugi-azide reaction. All the substituents (R^1–R^5) can be biomolecular fragments.

with conversion greater than 95%. Moreover, this reaction is highly selective, thus compatible with other bioorthogonal reactions when used in combination. In this study, isocyanide-modified N-acetylmannosamine derivatives

(carbohydrate metabolism precursor) was incubated with live cells, and then a biotin probe containing a chlorooxime group was added. There was a significantly enhanced fluorescence signal after incubation, highlighting

FIGURE 7 | (A) Ugi reaction for the conjugation of single residue of native proteins. **(B)** Ugi reaction for the conjugation of two neighboring residues of native proteins.

FIGURE 8 | (A) 10 valence-electron CO and [NC]⁻ that function as terminal ligands to transition metals. **(B)** Isocyano-containing biomolecules can be labelled via metal chelation. M = transition metal.
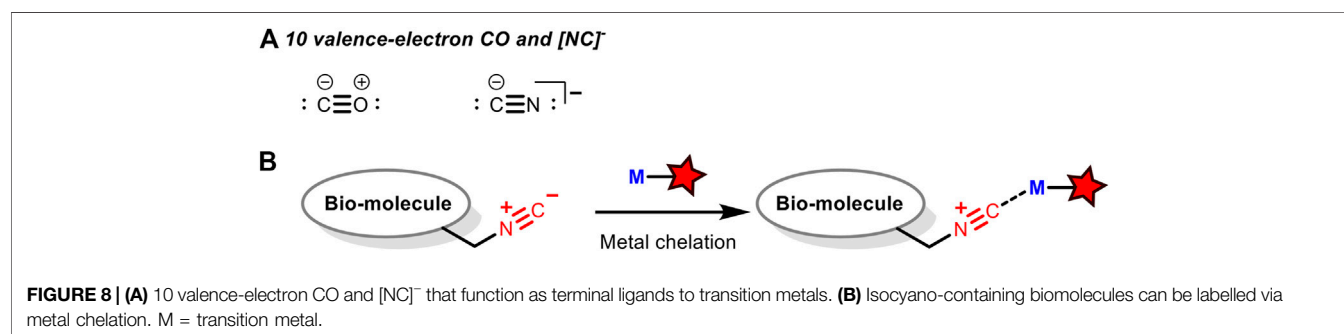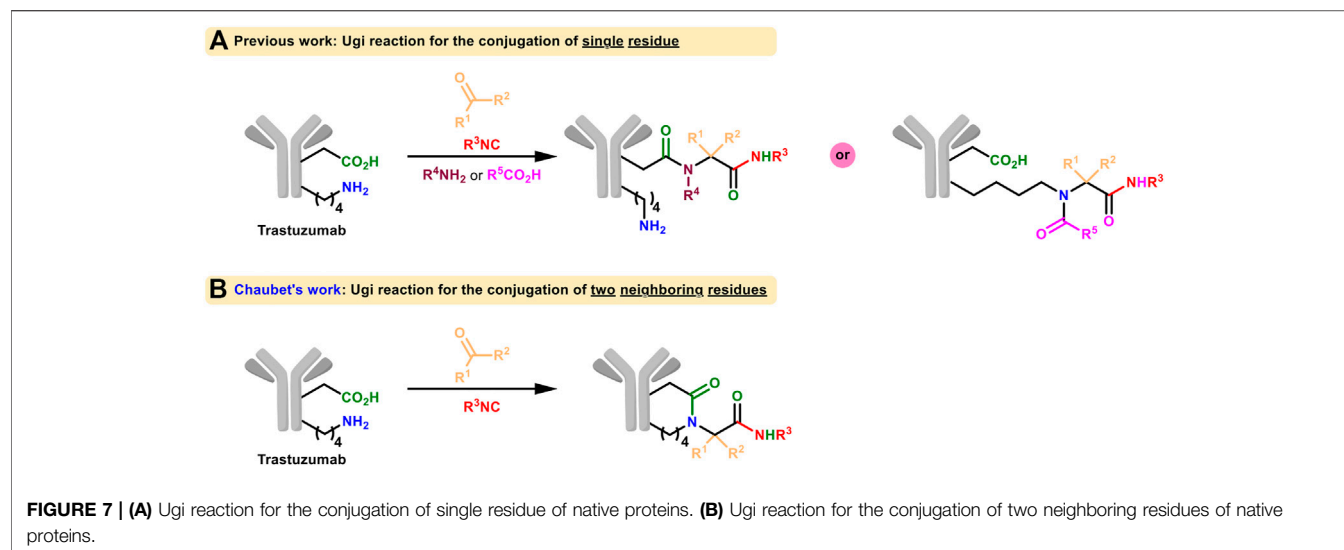
the capability of isocyanide-chlorooxime ligation for live-cell labeling.

STRATEGY 2: ISOCYANIDE-BASED MCR

In 1983, Vodrážka et al. applied Ugi reaction to immobilize glucose oxidase on a polymer carrier which was the earliest report of protein bioconjugation based on MCR (Marek et al., 1983). In 2000, Lang et al. reported that the Ugi reaction was used to achieve the binding of bovine serum albumin (BSA) with isocyano-modified β-D-glucosyl groups (Ziegler et al., 2000). This is the first proof that isocyanide can undergo a Ugi reaction under physiological conditions. Recently, Rivera et al. gave a detailed description of the multicomponent coupling of various biomacromolecules, including those employing isocyanides (**Figure 6**; Reguera et al., 2018).

More examples using isocyanide as one of the MCR components for protein labeling were presented afterwards (**Figure 7A**). Very recently, the side-chain amine and carboxylic groups of two neighboring lysines and aspartate/glutamate on trastuzumab were conjugated in the presence of isocyanide and aldehyde through Ugi reaction by

Chaubet et al. to achieve site-selective modification (**Figure 7B**; Sornay et al., 2020). This method can be used to obtain antibody conjugates with different payloads as well as to label native proteins in a site-specific manner. But due to the requirement of multicomponent coordination, it is not practical for living systems yet.

STRATEGY 3: ISOCYANIDE AS A COORDINATION LIGAND FOR TRANSITION METALS

Akin to carbon monoxide as a strong σ-donor and a good π-acceptor, isocyanides could coordinate with transition metals. Therefore, it is possible to design transition metal-based fluorescent probes to recognize biological macromolecules tagged with isocyanides through their coordination. Although there is no report on such applications yet, there are many related researches to detect carbon monoxides with transition metal-derived fluorescent probes (Alcarazo et al., 2009; Yuan et al., 2013; Kos and Plenio, 2015; Alday et al., 2020). As isoelectronic with carbon monoxide (**Figure 8A**),

FIGURE 9 | Preparation of isocyanides by **(A)** the reaction of silver cyanide with alkyl iodide, **(B)** Hoffman carbylamine reaction with phase transfer catalysis, **(C)** ring-opening reaction of oxazole, **(D)** one-pot reaction using trimethylsilyl cyanide (TMSCN) and benzylic/tertiary alcohol, or **(E)** dehydration of formamide.
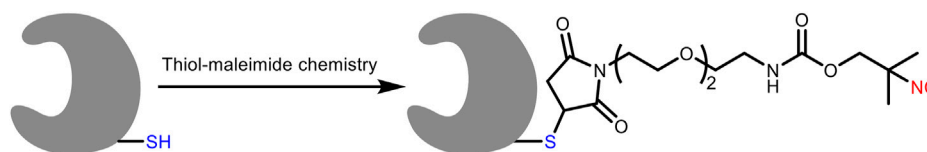
FIGURE 10 | An isocyano-containing linker tagged to the protein through cysteine ligation.

isocyanide may also be used as a ligand which can be recognized by such fluorescent probes to achieve the non-covalent fluorescent labeling of biomacromolecules (**Figure 8B**).

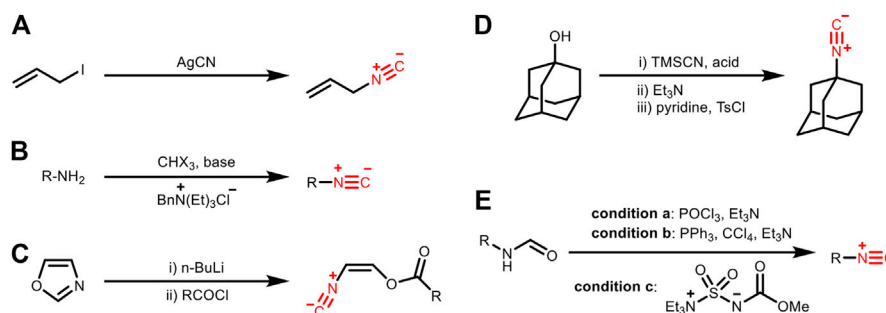## METHODS TO INTRODUCE THE ISOCYANO GROUP INTO BIOMACROMOLECULES

There are many methods for introducing the isocyano group into small molecules, among which five of them are classic (**Figure 9**): A) by the reaction of silver cyanide with alkyl iodide; B) Hoffman carbylamine reaction with phase transfer catalysis; C) ring-opening reaction of oxazole to prepare unsaturated isocyanides; D) one-pot reaction using trimethylsilyl cyanide (TMSCN) and benzylic or tertiary alcohol; E) dehydration of formamide (Bode et al., 2016). Among these methods, the dehydration of formamide is the most popular one. In contrast, how to introduce the isocyano group into biomacromolecules like proteins and carbohydrates for subsequent bioorthogonal modification (i.e., labeling or modulation through bond cleavage) has been less addressed.

Introducing the Isocyano Group Into Proteins
With Bifunctional Linkers
In 2011, Leeper et al. labeled the cysteine residues on the protein with the isocyano group via an isocyano-maleimide bifunctional linker (**Figure 10**; Stöckmann et al., 2011).

However, a problem with this strategy is that the C-S bond is not stable under physiological conditions, and reverse Michael addition may cause cleavage of the isocyanide side chain. With efforts made in recent years to improve the stability of the Michael addition adduct, this problem can be properly addressed (Huang et al., 2019).

By Site-Directed Insertion of Unnatural Amino Acids
This strategy is among the mainstream for protein modification. The unnatural amino acid containing an isocyano group can be inserted into the protein by two methods, namely the selective pressure incorporation (SPI) and the stop codon suppression (SCS) (Drienovská and Roelfes, 2020). The SPI method is based on that some tRNAs can recognize and bind those unnatural amino acids with structures similar to natural amino acids. When there are not enough natural amino acids in the biological system (auxotrophic), the insertion of unnatural amino acids can be realized. However, this method highly relies on the structure of unnatural amino acids and may randomly insert unnatural amino acids into different sites of the protein, which may affect its structure and function. The SCS method is more widely used, which introduces an exogenous translation system (including tRNA and aminoacyl tRNA synthetase) that does not recognize endogenous amino acids but can specifically recognize unnatural amino acids (Fu et al., 2018). At present, more than 200 unnatural amino acids can be inserted into protein in this way, including the isocyanide derivatives.

Introducing the Isocyano Group Into Carbohydrates
Traditional glycan analysis methods include chemical derivatization (e.g., film method, dinitrosalicylic acid method), pre-column derivatization (e.g., sugar chains with fluorescent

FIGURE 11 | (A) Metabolic oligosaccharide engineering. **(B)** Chemoenzymatic glycan labeling.
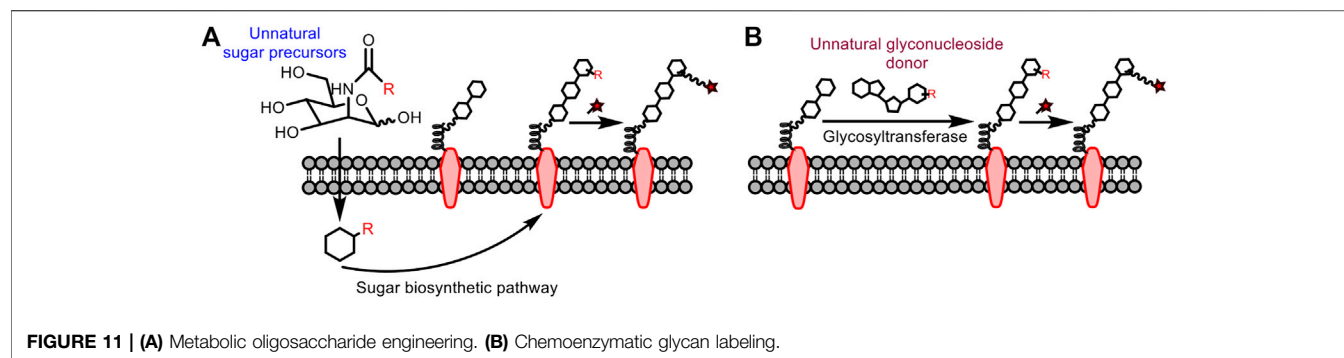
groups to be analyzed by HPLC, etc.,), and biological macromolecule recognition (such as antibodies and clusterins) (Ghazarian et al., 2011). However, the chemical derivatization is not selective; the pre-column derivatization is destructive to sugars and not practical for *in vivo* applications; the biological macromolecule recognition is faced with the problem of low affinity for sugar. To this end, methods suitable for analyzing polysaccharides in living systems are in high demand. To insert the bioorthogonal handle into the sugar for subsequent fluorescent modification, there are mainly two strategies (**Figure 11**), metabolic oligosaccharide engineering (Dube and Bertozzi, 2003) and chemoenzymatic glycan labeling (Lopez Aguilar et al., 2017).

Metabolic Oligosaccharide Engineering

This strategy was first proposed by Reutter's group (Kayser et al., 1992). They found that unnatural analogues of mannosamine carrying a functional reporter can be used as metabolic precursors to participate in the biosynthetic pathway of sialic acid *in vivo*, after which the mannosamine can be visualized following conjugation with the fluorophore. In addition, isocyanide-based bioorthogonal reactions can be carried out smoothly even with the endogenous glycans in low abundance. However, the reporter must be small enough to be tolerated by the sugar biosynthetic system. In 2013, Leeper et al. tried to label glycans through sugar metabolism of *N*-acetyl-glucosamine and mannosamine derivatives containing isocyano groups, and then to use fluorophores with tetrazine for conjugation (Stairs et al., 2013). In 2019, Wennemers et al. also used this idea to incubate isocyano-modified *N*-acetylmannosamines with cells followed by the addition of biotin probes containing chlorooxime (Schäfer et al., 2019). Both studies demonstrate the potential of isocyanide as a bioorthogonal reporter for glycan labeling. However, it still has limitations: the sugar precursor may participate in multiple metabolic pathways after entering the cell to form various tagged sugars, thus not applicable for specific labeling.

Chemoenzymatic Method

As mentioned above, metabolic engineering through monosaccharide cannot meet the requirement to label more complex sugar chains. The chemoenzymatic method transfers monosaccharide analogues in the form of nucleotide sugar

donors to specific glycan acceptors through glycosyltransferase, so that the glycan acceptors are equipped with the functional tag from the donor. This method was first reported by Hill et al. (Paulson et al., 1979) and the bioorthogonal reaction involving isocyanides is expected to be compatible with more complicated sugars in addition to monosaccharides. To be noted, this chemoenzymatic method highly relies on the development of glycosyltransferases that are tolerable to unnatural sugar donors and specific to the glycan acceptor.

Introducing the Isocyano Group Into DNA

Other than the important biological roles, DNA can also work as versatile tags for organic compounds. As early as 1992, Brenner and Lerner proposed the concept of adding a DNA barcode to chemically synthesized molecules to form DNA-encoded libraries (Brenner and Lerner, 1992). MCRs proved to be compatible with solid-phase synthesis and can be effective for creating scaffold diversity with a low synthetic cost (Rivera et al., 2021). In 2019, Brunschweiger's team reported isocyanide-involved MCRs for DNA-encoded combinatorial synthesis (Kunig et al., 2019). This concept has great potential to be applied for fluorescence labeling or other derivatizations of DNA with isocyanides as well as to introduce an isocyano group into DNA.

PERSPECTIVES

The isocyano functionality has many advantages such as small size, unique reactivity, as well as good biocompatibility, thus are considered as promising bioorthogonal handles. To undergo a bioorthogonal reaction, there should be a suitable counterpart allowing good reaction kinetics and ideal products. Therefore, the application of isocyanides in biological systems increased rapidly after the finding that large sterically hindered tetrazines can form stable products rapidly after conjugation with primary isocyanides. Very recently, chlorooxime is found to be another complementary counterpart for bioorthogonal ligation with isocyanides, further expanding the bioorthogonal chemistry repertoire involving isocyanides.

Previously, Shasqi et al. employed the tetrazine-TCO reaction to achieve the enrichment of TCO-doxorubicin at the tumor site

after injection with tetrazine-modified sodium hyaluronate biopolymer, thereby exerting anti-cancer effects with low side effects. This is the first bioorthogonal reaction applied to patients (Wu et al., 2021). If the TCO is replaced with an isocyano group, the water solubility of the drug can be improved and the impact on the structure of the drug could be minimized due to its small size. More interestingly, such a functional pair is attractive in the labeling of proteins and carbohydrates. Certain strategies such as genetic incorporation and metabolic engineering have been developed to insert the isocyano group into these biomolecules, allowing direct imaging or modulation of these "recombinant" targets. While multicomponent reactions involving isocyanides and side chains of the target protein have been proposed to modify native proteins, it is not practical for living systems due to the requirement of multicomponent coordination. In addition to explore the reactivity of isocyanides in bioorthogonal chemistry, we are also looking forward to methods that can tag the endogenous targets in living systems with isocyano groups, to promote their wide applications.

AUTHOR CONTRIBUTIONS

All authors listed have made a substantial, direct, and intellectual contribution to the work and approved it for publication.

FUNDING

SUPPLEMENTARY MATERIAL

The Supplementary Material for this article can be found online at: https://www.frontiersin.org/articles/10.3389/fchem.2021.670751/full#supplementary-material

REFERENCES

Alcarazo, M., Lehmann, C. W., Anoop, A., Thiel, W., and Fürstner, A. (2009). Coordination Chemistry at Carbon. *Nat. Chem* 1, 295–301. doi:10.1038/nchem.248

Alday, J., Mazzeo, A., and Suarez, S. (2020). Selective Detection of Gasotransmitters Using Fluorescent Probes Based on Transition Metal Complexes. *Inorg. Chim. Acta* 510, 119696. doi:10.1016/j.ica.2020.119696

Bode, M. L., Gravestock, D., and Rousseau, A. L. (2016). Synthesis, Reactions and Uses of Isocyanides in Organic Synthesis. An Update. *Org. Preparations Procedures Int.* 48, 89–221. doi:10.1080/00304948.2016.1138072

Brenner, S., and Lerner, R. A. (1992). Encoded Combinatorial Chemistry. *Proc. Natl. Acad. Sci.* 89, 5381–5383. doi:10.1073/pnas.89.12.5381

Chen, Y., Wu, K.-L., Tang, J., Loredo, A., Clements, J., Pei, J., et al. (2019). Addition of Isocyanide-Containing Amino Acids to the Genetic Code for Protein Labeling and Activation. *ACS Chem. Biol.* 14, 2793–2799. doi:10.1021/acschembio.9b00678

Deb, T., and Franzini, R. M. (2020). The Unique Bioorthogonal Chemistry of Isonitriles. *Synlett* 31, 938–944. doi:10.1055/s-0039-1690849

Drienovská, I., and Roelfes, G. (2020). Expanding the Enzyme Universe with Genetically Encoded Unnatural Amino Acids. *Nat. Catal.* 3, 193–202. doi:10.1038/s41929-019-0410-8

Dube, D., and Bertozzi, C. R. (2003). Metabolic Oligosaccharide Engineering as a Tool for Glycobiology. *Curr. Opin. Chem. Biol.* 7, 616–625. doi:10.1016/j.cbpa.2003.08.006

Fu, C., Kobayashi, T., Wang, N., Hoppmann, C., Yang, B., Irannejad, R., et al. (2018). Genetically Encoding Quinoline Reverses Chromophore Charge and Enables Fluorescent Protein Brightening in Acidic Vesicles. *J. Am. Chem. Soc.* 140, 11058–11066. doi:10.1021/jacs.8b05814

Ghazarian, H., Idoni, B., and Oppenheimer, S. B. (2011). A Glycobiology Review: Carbohydrates, Lectins and Implications in Cancer Therapeutics. *Acta Histochem.* 113, 236–247. doi:10.1016/j.acthis.2010.02.004

Goldstein, L., and Niv, A. (1993). Isonitrile Derivatives of Polyacrylamide as Supports for the Immobilization of Biomolecules. *Appl. Biochem. Biotechnol.* 42, 19–35. doi:10.1007/BF02788899

Huang, W., Wu, X., Gao, X., Yu, Y., Lei, H., Zhu, Z., et al. (2019). Maleimide-thiol Adducts Stabilized through Stretching. *Nat. Chem.* 11, 310–319. doi:10.1038/s41557-018-0209-2

Imming, P., Mohr, R., Müller, E., Overheu, W., and Seitz, G. (1982). [4 + 1] Cycloaddition of Isocyanides to 1,2,4,5-Tetrazines: A Novel Synthesis of Pyrazole. *Angew. Chem. Int. Ed. Engl.* 21, 284. doi:10.1002/anie.198202841

Kayser, H., Zeitler, R., Kannicht, C., Grunow, D., Nuck, R., and Reutter, W. (1992). Biosynthesis of a Nonphysiological Sialic Acid in Different Rat Organs, Using *N*-Propanoyl-D-Hexosamines as Precursors. *J. Biol. Chem.* 267, 16934–16938. doi:10.1016/S0021-9258(18)41874-1

Kenry, and Liu, B. (2019). Bio-orthogonal Click Chemistry for In Vivo Bioimaging. *Trends Chem.* 1, 763–778. doi:10.1016/j.trechm.2019.08.003

Kos, P., and Plenio, H. (2015). Metal Complexes of a Boron-Dipyrromethene (BODIPY)-tagged *N*-Heterocyclic Carbene (NHC) as Luminescent Carbon Monoxide Chemodosimeters. *Chem. Eur. J.* 21, 1088–1095. doi:10.1002/chem.201405316

Kunig, V. B. K., Ehrt, C., Dömling, A., and Brunschweiger, A. (2019). Isocyanide Multicomponent Reactions on Solid-Phase-Coupled DNA Oligonucleotides for Encoded Library Synthesis. *Org. Lett.* 21, 7238–7243. doi:10.1021/acs.orglett.9b02448

Lemieux, G. A., de Graffenried, C. L., and Bertozzi, C. R. (2003). A Fluorogenic Dye Activated by the Staudinger Ligation. *J. Am. Chem. Soc.* 125, 4708–4709. doi:10.1021/ja029013y

Li, J., and Chen, P. R. (2016). Development and Application of Bond Cleavage Reactions in Bioorthogonal Chemistry. *Nat. Chem. Biol.* 12, 129–137. doi:10.1038/nchembio.2024

Lopez Aguilar, A., Briard, J. G., Yang, L., Ovryn, B., Macauley, M. S., and Wu, P. (2017). Tools for Studying Glycans: Recent Advances in Chemoenzymatic Glycan Labeling. *ACS Chem. Biol.* 12, 611–621. doi:10.1021/acschembio.6b01089

Marek, M., Jarý, J., Valentová, O., and Vodrážka, Z. (1983). Immobilization of Glycoenzymes by Means of Their Glycosidic Components. *Biotechnol. Lett.* 5, 653–658. doi:10.1007/BF01386357

Nenajdenko, V. G. (2012). *Isocyanide Chemistry: Applications in Synthesis and Material Science*. Weinheim: Wiley VCH.

Patterson, D. M., Nazarova, L. A., and Prescher, J. A. (2014). Finding the Right (Bioorthogonal) Chemistry. *ACS Chem. Biol.* 9, 592–605. doi:10.1021/cb400828a

Paulson, J. C., Sadler, J. E., and Hill, R. L. (1979). Restoration of Specific Myxovirus Receptors to Asialoerythrocytes by Incorporation of Sialic Acid with Pure Sialyltransferases. *J. Biol. Chem.* 254, 2120–2124. doi:10.1016/S0021-9258(17)37774-8

Prescher, J. A., and Bertozzi, C. R. (2005). Chemistry in Living Systems. *Nat. Chem. Biol.* 1, 13–21. doi:10.1038/nchembio0605-13

Reguera, L., Méndez, Y., Humpierre, A. R., Valdés, O., and Rivera, D. G. (2018). Multicomponent Reactions in Ligation and Bioconjugation Chemistry. *Acc. Chem. Res.* 51, 1475–1486. doi:10.1021/acs.accounts.8b00126

Rivera, D. G., Ricardo, M. G., Vasco, A. V., Wessjohann, L. A., and Van der Eycken, E. V. (2021). On-resin Multicomponent Protocols for Biopolymer

Assembly and Derivatization. *Nat. Protoc.* 16, 561–578. doi:10.1038/s41596-020-00445-6

Schäfer, R. J. B., Monaco, M. R., Li, M., Tirla, A., Rivera-Fuentes, P., and Wennemers, H. (2019). The Bioorthogonal Isonitrile-Chlorooxime Ligation. *J. Am. Chem. Soc.* 141, 18644–18648. doi:10.1021/jacs.9b07632

Smeenk, M. L. W. J., Agramunt, J., and Bonger, K. M. (2021). Recent Developments in Bioorthogonal Chemistry and the Orthogonality within. *Curr. Opin. Chem. Biol.* 60, 79–88. doi:10.1016/j.cbpa.2020.09.002

Sornay, C., Hessmann, S., Erb, S., Dovgan, I., Ehkirch, A., Botzanowski, T., et al. (2020). Investigating Ugi/Passerini Multicomponent Reactions for the Site-Selective Conjugation of Native Trastuzumab*. *Chem. Eur. J.* 26, 13797–13805. doi:10.1002/chem.202002432

Stairs, S., Neves, A. A., Stöckmann, H., Wainman, Y. A., Ireland-Zecchini, H., Brindle, K. M., et al. (2013). Metabolic Glycan Imaging by Isonitrile-Tetrazine Click Chemistry. *ChemBioChem* 14, 1063–1067. doi:10.1002/cbic.201300130

Stöckmann, H., Neves, A. A., Stairs, S., Brindle, K. M., and Leeper, F. J. (2011). Exploring Isonitrile-Based Click Chemistry for Ligation with Biomolecules. *Org. Biomol. Chem.* 9, 7303–7305. doi:10.1039/c1ob06424j

Tu, J., Svatunek, D., Parvez, S., Eckvahl, H. J., Xu, M., Peterson, R. T., et al. (2020). Isonitrile-responsive and Bioorthogonally Removable Tetrazine Protecting Groups. *Chem. Sci.* 11, 169–179. doi:10.1039/c9sc04649f

Tu, J., Svatunek, D., Parvez, S., Liu, A. C., Levandowski, B. J., Eckvahl, H. J., et al. (2019). Stable, Reactive, and Orthogonal Tetrazines: Dispersion Forces Promote the Cycloaddition with Isonitriles. *Angew. Chem. Int. Ed.* 58, 9043–9048. doi:10.1002/anie.201903877

Tu, J., Xu, M., Parvez, S., Peterson, R. T., and Franzini, R. M. (2018). Bioorthogonal Removal of 3-isocyanopropyl Groups Enables the Controlled Release of Fluorophores and Drugs In Vivo. *J. Am. Chem. Soc.* 140, 8410–8414. doi:10.1021/jacs.8b05093

Versteegen, R. M., Rossin, R., ten Hoeve, W., Janssen, H. M., and Robillard, M. S. (2013). Click to Release: Instantaneous Doxorubicin Elimination upon Tetrazine Ligation. *Angew. Chem. Int. Ed.* 52, 14112–14116. doi:10.1002/anie.201305969

Wu, K., Yee, N. A., Srinivasan, S., Mahmoodi, A., Zakharian, M., Mejia Oneto, J. M., et al. (2021). Click Activated Protodrugs against Cancer Increase the Therapeutic Potential of Chemotherapy through Local Capture and Activation. *Chem. Sci.* 12, 1259–1271. doi:10.1039/d0sc06099b

Xu, M., Deb, T., Tu, J., and Franzini, R. M. (2019). Tuning Isonitrile/tetrazine Chemistry for Accelerated Deprotection and Formation of Stable Conjugates. *J. Org. Chem.* 84, 15520–15529. doi:10.1021/acs.joc.9b02522

Yuan, L., Lin, W., Tan, L., Zheng, K., and Huang, W. (2013). Lighting up Carbon Monoxide: Fluorescent Probes for Monitoring CO in Living Cells. *Angew. Chem. Int. Ed.* 52, 1628–1630. doi:10.1002/anie.201208346

Zhang, G., Li, J., Xie, R., Fan, X., Liu, Y., Zheng, S., et al. (2016). Bioorthogonal Chemical Activation of Kinases in Living Systems. *ACS Cent. Sci.* 2, 325–331. doi:10.1021/acscentsci.6b00024

Zhang, X., Luo, H., Fan, X., and Chen, P. R. (2020). Development and Applications of Inverse-Electron-Demand Diels-Alder Reaction in Bioorthogonal Chemistry. *Sci. Sin. Chim.* 50, 1280–1295. doi:10.1360/SSC-2020-0110

Ziegler, T., Gerling, S., and Lang, M. (2000). Preparation of Bioconjugates through an Ugi Reaction. *Angew. Chem. Int. Ed.* 39, 2109–2112. doi:10.1002/1521-3773(20000616)39:12<2109::AID-ANIE2109>3.0.CO;2-9

![frontiers in Chemistry]

Vaccaria segetalis: A Review of Ethnomedicinal, Phytochemical, Pharmacological, and Toxicological Findings

Meng Tian, Yuwen Huang, Xin Wang, Maosheng Cao, Zijiao Zhao, Tong Chen, Chenfeng Yuan, Nan Wang, Boqi Zhang, Chunjin Li* and Xu Zhou*

College of Animal Sciences, Jilin University, Changchun, China

Vaccaria segetalis is a dry mature seed of Vaccaria hispanica (Mill.) Rauschert, which belongs to the genus *V. segetalis* (Neck.) Garcke. There are multiple medicinal parts of *V. segetalis*, according to the records, including roots, stems, leaves, flowers, and seeds, which should be used together. Currently, *V. segetalis* is most frequently used in the treatment of menstruation, dysmenorrhea, breast milk stoppages, and chylorrhea. Numerous studies present historical evidence of the use of *V. segetalis* to treat several diseases and describe its beneficial effects including prolactin- (PRL-) like, estrogen-like, antitumor, antiangiogenesis, and antioxidant activity. We summarized the period from January 1980 to December 2019 regarding *V. segetalis*. This review paper indicates that *V. segetalis* has promising clinical applications. The main active ingredients of the plant have been elucidated in recent years. We summarized the previously and newly discovered pharmacological effects of *V. segetalis* in addition to its active ingredients, ethnopharmacological uses, and toxicological properties, and provided a focus for future research.

Keywords: *Vaccaria segetalis*, prolactin activity, estrogen-like activity, anti-tumor activity, anti-oxidant activation

INTRODUCTION

Vaccaria segetalis (Neck.) Garcke is an annual herb and is widely distributed worldwide throughout the cold temperature zone. The seeds of *V. segetalis*, which are known as Wang Bu Liu Xing, have been used in traditional Chinese medicine (TCM) to treat amenorrhea, dysmenorrhea, lactation failures, and carbuncles (Sang et al., 2003). *V. segetalis* has been used in China for 2000 years as documented in the oldest materia medica *Shen Nong Ben Cao Jing*. In recent years, being its clinical application more extensive, and many new clinical applications, such as the treatment of shingles (Min-ying, 2005), gallstones (Zhi-hong and Cai-ying, 1989), hypertension (Liu, 2018), and rhinitis (Liang and Xiu-jun, 2013), have been identified. *V. segetalis* is composed of several chemical components. Saponins (Ma et al., 2008), flavonoids (Wang et al., 2011), polysaccharides (Qing et al., 2014), and cyclic peptides (Sang et al., 2002) are believed to be the principal active constituents of *V. segetalis*. The seeds also contain components such as coumarins, lipids, fatty acids, and metallic elements (Jin-Ling et al., 2014). Recently, an increasing number of studies have suggested that *V. segetalis* extract has various bioactivities, such as prolactin- (PRL-) like, estrogen-like, antitumor, antiangiogenesis, and antioxidant activity, and it is also shown to dilate blood vessels and relieve osteoporosis (Li-Fan and Liang, 2007). This article also summarizes toxicological research regarding *V. segetalis*.

Complementary/alternative medicine has developed rapidly in recent years, and its use has gradually expanded globally. The use of Chinese herbal medicine as a part of complementary/alternative medicine has been the focus of many scholars. Although a few literature studies have described *V. segetalis* to date, no article has systematically summarized and evaluated the research results. We conducted this review to summarize the existing literature studies and to focus on analyses of the chemical constituents and pharmacological activities of *V. segetalis*. Our goal is to permit other researchers to more easily review existing research and provide new directions for future research.

ETHNOPHARMACOLOGICAL USES

Preparation of *V. segetalis*

Dry mature seeds from *V. segetalis* were prepared by using a multistep process. *V. segetalis* has different traits in different preparation stages (Tian-Yi, 2011). A specific preparation method is described below. In the first stage, after the fruits mature in summer, the plants are cut and dried. Then, the seeds are beat and dried. During this time, the seed is a black sphere with a diameter of approximately 2 mm. In the second stage, the seeds are fried until most seeds burst into white flowers. In the final stage, the seeds that burst into white flowers are ground into powder.

Methods of Administration

There are three administration methods for different preparation stages of *V. segetalis* because of its different traits. In the first type, seeds can be applied directly by pressing acupoints. In the second type, the seeds are fried until the white flowers burst, and the seeds are decocted in water. In the third type, the ground powder is applied directly to the affected area.

Indication

The seeds of *V. segetalis* are often used as black spheres in acupressure methods. Based on the TCM theory, acupoints are the specifically chosen sites for physical stimulation (Rong et al., 2011). A few studies have revealed that stimulating different acupoints on the body surface could provide various therapeutic benefits (Li et al., 2015). Previous research illustrated that pressing acupoints with seeds can improve hypertension. In one study, Liu (2018) selected the auricular points that were related to blood pressure, pressed one seed at each acupoint, and kneaded each acupoint for 3–5 min. This treatment was

Abbreviations: PRL, Prolactin; LPS, Lipopolysaccharide; ERK, Extracellular signal-regulated kinases; JNK, C-Jun N-terminal kinase; CPID, Chronic pelvic inflammatory disease; MPF, Man-Pen-Fang; IL-6, Interleukin-6; TNF-α, Tumor necrosis factor-α; TGF-β, Transforming growth factor-β; COX-2; VNE, Cyclooxygenase-2; Vaccaria n-butanol extract; PECAM-1, Platelet-endothelial cell adhesion molecule-1; A549, Human; lung carcinoma; Panc-1, Human pancreatic carcinoma; MCF-7, Human breast adenocarcinoma; PC-3, Human prostate adenocarcinoma; LNCaP, Human prostate carcinoma; HMECs, Human mammary epithelial cells; CAM, The chick chorioallantoic membrane; bFGF, basic fibroblast growth factor; VEGF, Vascular endothelial growth factor; HepG2, Human hepatoma cells; ROS, Reactive oxygen species; DBP, Dibutyl phthalate; GH, Growth hormone; IGF, Insulin-like growth factor.

performed thrice a day, and the contralateral acupoints were alternatively pressed every 3 days. After 2 weeks of treatment, the hypertension symptoms of a patient had resolved (Liu, 2018). Gallstones can also be treated in this manner. In another study, the researchers used the seeds of *V. segetalis* to press the gallbladder, liver, duodenum, and sympathetic points on both sides of the ears of patients dozens of times and found that the gallbladder contracted significantly. Consequently, small stones and silt-like stones in the gallbladder were discharged into the intestinal lumen with bile, and then excreted from the body (Zhi-hong and Cai-ying, 1989). In addition, this method was used to treat rhinitis. A research team also used the seeds to press the ear points that were related to the nose 3–5 times a day, for 1–3 min each time. Ear points were changed every 3 days, switching between the two ears, and the course of treatment was 10 days (Liang and Xiu-jun, 2013). *V. segetalis* as a white flower after frying is often used in water decoctions. *V. segetalis* has also been used in combination with other Chinese herbal medicine to treat gonorrhea and promote the milk production. According to *The Precious Mirror of Hygiene* (AD 1343), ancient Chinese herbalists used *V. segetalis* to boost the milk production and milk lactation. The traditional Chinese herbal medicine prescription consists of equal amount of the spike of *Dianthus superbus* L., *Ophiopogon japonicas* (L.f.) Ker-Gawl (inner column removal), *V. segetalis*, fossil fragments (ancient mammals such as elephants, rhinos, three-toed horses, cattle, and deer), and the scale of *Manis pentadactyla* Linnaeus to the total of 50 g. The components are mixed and ground into a powder. In total, 5 g of the mixture are consumed with hot wine thrice a day. Then, 5 g of the mixture are added to a soup consisting of pork knuckle and *Akebia quinata* (Houtt.) Decne. and consumed thrice a day. Finally, the remaining mixture is rubbed on the left and right breasts 30 times with a wooden comb after consuming the aforementioned soup thrice a day (Tian-Yi, 2011). In recent years, a new application method has been to grind the white flower into a powder for an external application on the affected area. This was proven to be effective for treating shingles (Min-ying, 2005).

In summary, the applications of *V. segetalis* have been gradually expanded and improved with the accumulated research data. *V. segetalis* can be used externally or internally. It has been used for a long time based on the physical properties of the seeds to stimulate acupuncture points to treat diseases and their mixing in water decoctions with the other Chinese herbs. The newest application method is a direct application of the powder to the wound surface to treat shingles. We speculate that these activities are related to the active ingredients in seeds. We believe that the in-depth studies of *V. segetalis* will increase its clinical applications.

PRIMARY ACTIVE INGREDIENTS IN *V. SEGETALIS*

Vaccaria segetalis is mainly composed of saponins, cyclic peptides, flavonoids, and polysaccharides, and the other components include volatile oils, coumarins, lipids, and

fatty acids. Several studies have investigated these active substance constituents.

Saponins

Several types of saponins are present in the seeds of *V. segetalis*. These saponins primarily include quillaic acid compounds, which account for ∼65% of the total (**Table 1**). The other saponins include gypsogenin bisdesmosides (∼15%), gypsogenic acid monodesmosides (∼10%), and vaccaric acid bisdesmosides (∼10%). The structures of the known saponins are summarized in **Table 1**. Triterpenoid saponins are the main components of *V. segetalis*. They are oleanol-type pentacyclic triterpenoids, which are also known as β-aromatic alkanes. These compounds are widely distributed in the plant kingdom. Triterpenoid saponins mostly have antioxidant (Guan et al., 2013), antitumor (Bozak et al., 1990; Haralampidis et al., 2002; Choi et al., 2005), and anti-inflammatory effects (Bernard et al., 2001; Banno et al., 2005; Guan et al., 2013). They also protect the cardiovascular system through their antihypertensive, anti-atherosclerotic, and vasodilatory effects (Rosalía et al., 2004). The main pharmacological activities of *Panax ginseng* C. A. Meyer, *Glycyrrhiza uralensis* Fisch., and *Bupleurum L*, which are widely used in daily life, are derived from their saponin components.

Cyclic Peptides

Cyclic peptides have been found in several medicinal species such as *Pseudostellaria heterophylla* Miq., *Lycium chinense* Mill., and *Psammosilene tunicoides*, and exhibit a wide range of structure-dependent bioactivities (Tan and Zhou, 2006). Cyclic peptides are important components of *V. segetalis* (Dahiya and Dahiya, 2021). With the development and integration of modern medicine and traditional complementary medicine, the roles of cyclic peptides have been further confirmed. To date, eight cyclic peptides have been isolated from the seeds of *V. segetalis* (**Table 2**). Cyclic peptide molecules have antitumor activity (Feng et al., 2012), and they regulate uterine contraction, which implies estrogen-like activity for segetalins A, B, G, and H (Itokawa et al., 1995; Yun et al., 1997). In addition, a few studies illustrated that segetalins A, D, F, and G have vasodilatory activity against norepinephrine-induced aortic contraction in rats (Morita et al., 1997a). The pharmacological effects of cyclic peptides provide new options for the treatment of diseases.

Flavonoids

Flavonoids comprise a broad class of ketone containing compounds that exist widely in nature. Flavonoids are widely distributed in plants in the form of glycosides, which are called flavonoid glycosides. In particular, *Sophora japonica*, *Scutellaria baicalensis*, *Pueraria lobata*, and *Ginkgo biloba* are rich in flavonoids. The structure of vaccarin, a flavone isolated from the seeds of *V. segetalis*, is presented in **Figure 1** (Sang et al., 2000c). Flavonoids have many effects, such as protective effects on endothelial cells (Kozlowska and Szostak-Wegierek, 2014), hypoglycemic effects (Chen et al., 2017), antiviral effects (Zakaryan et al., 2017), and the ability to enhance lactation capacity (Tong et al., 2013).

Polysaccharides

Polysaccharides are formed by the polymerization of more than 10 monosaccharide molecules *via* glycosidic bonds. They have high molecular weights, and they usually consist of several hundreds to thousands of monosaccharide molecules. Polysaccharides and their derivatives, such as lentinan, *Astragalus* polysaccharide, *Polyporus* polysaccharide, *Lycium barbarum* polysaccharide, and *Ganoderma lucidum* polysaccharide, are bioactive substances in TCM. They have antitumor (Mao et al., 2016; Tang et al., 2016), antioxidant (Hui et al., 2019), and anti-inflammatory effects (Wang et al., 2019), and promote cell proliferation (Zheng et al., 2014). Polysaccharides have been isolated from the seeds of *V. segetalis* in recent years (Zhou et al., 2015).Various active ingredients in *V. segetalis* provide a theoretical and realistic basis for the study of its pharmacological effects.

Other Components of *V. segetalis*

V. segetalis also contains coumarins, lipids, fatty acids, and other ingredients, along with adenosine and adenine. The main components of *V. segetalis* volatile oils are oleic acid amide, n-octadecane, myristylamide, and n-pentadecane (Yun et al., 1998). In addition to the currently known major active ingredients, several unknown ingredients of the plant require further investigation to be identified.
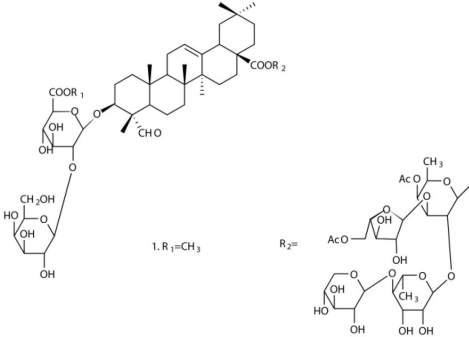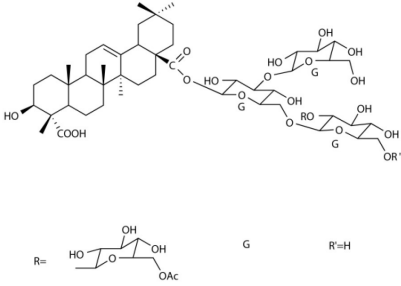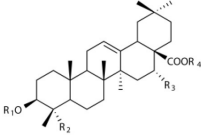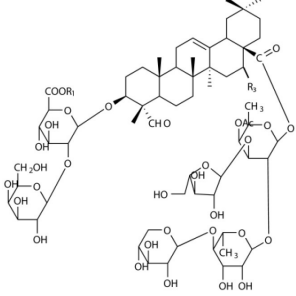
PHARMACOLOGICAL ACTIVITY OF *V. SEGETALIS*

Recently, *V. segetalis* has mainly been used in folk medicine based on its anti-inflammatory, antioxidant, anti-angiogenic, and antitumor effects, in addition to its ability to promote vasodilation, muscle contraction, and lactation. The active ingredients responsible for these effects are polysaccharides, saponins, flavonoids, and cyclic peptides (Peng et al., 2014). We will now specifically introduce its pharmacological activities.

Anti-inflammatory Activity
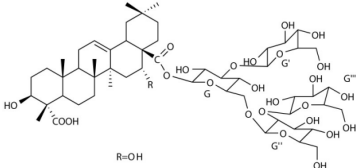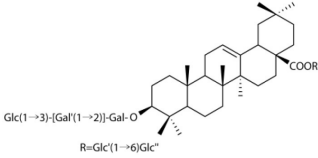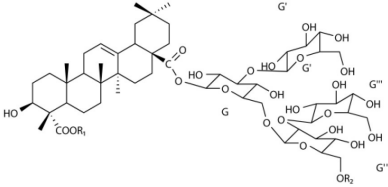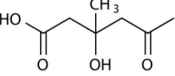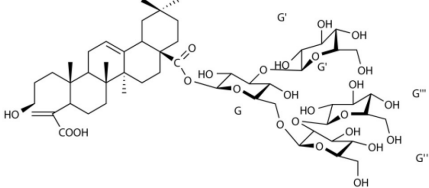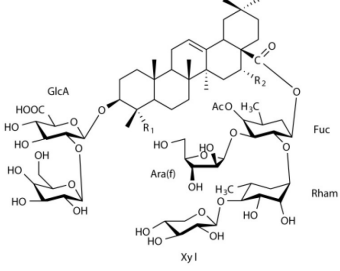
According to *Shen Nong Ben Cao Jing*, *V. segetalis* has been used to treat urinary symptoms such as blood strangury for 2000 years. Gonorrhea in Chinese medicine refers to diseases such as urinary tract infection, prostatitis, and seminal vesicle inflammation. The traditional Chinese herbal medicine prescription is as follows: 30 g of the seeds of *V. segetalis* and 6 g each of the roots of *Angelica sinensis* Diels, *Chinese teasel*, *Paeonia lactiflora* Pall., and *Salvia miltiorrhiza* are orally administered as two doses *via* decoction (Zhu-mo, 2005). Based on an extensive application of *V. segetalis* in the treatment of inflammatory diseases, we searched and collated the articles published in the past 30 years to explore the intrinsic mechanism of *V. segetalis* in the treatment of inflammatory diseases.

Hypaphorine from the different sources exhibits anti-inflammatory properties (Silva et al., 2012). *V. segetalis* extract, along with its hypaphorine, displayed anti-inflammatory activity both *in vitro* and *in vivo* (Aswad et al., 2018). In this study, mice were intraperitoneally injected with 200 mg/kg of the 6.019% of *Vaccaria* hydroalcoholic extract, and the results suggested that it

TABLE 1 | Saponins present in the seeds of *Vaccaria segetalis*.

Saponins	Formulae	Structure	Pharmacological activities	References
Segetosides				
Segetoside B	$C_{69}H_{106}O_{33}$		Inhibition of luteal cell	Sang et al., 2002
Segetoside C	$C_{56}H_{88}O_{32}$		Unknown	Sang et al., 1999
Segetoside(D–E)	Common structure			
Segetoside D	$C_{69}H_{106}O_{34}$	R_1 = GlcA(Bu ester)^2 ← Gal; R_2 = CHO; R_3 = OH; R_4 = X_1	Anti-cancer	Güçlü-Ustündag and Mazza, 2007
Segetoside E	$C_{72}H_{112}O_{34}$	R_1 = GlcA(Me ester)^2 ← Gal; R_2 = CHO; R_3 = H; R_4 = X_3	Unknown	Sang et al., 1999
Segetoside(F–I)	Common structure			
Segetoside F	$C_{67}H_{104}O_{32}$	R_1=CH_3 R_2=H R_3=H	Inhibition of luteal cell	Sang et al., 2000d
Segetoside G	$C_{70}H_{110}O_{32}$	R_1=$CH_3CH_2CH_2CH_2$ R_2=H R_3=H	Unknown	Sang et al., 2000a
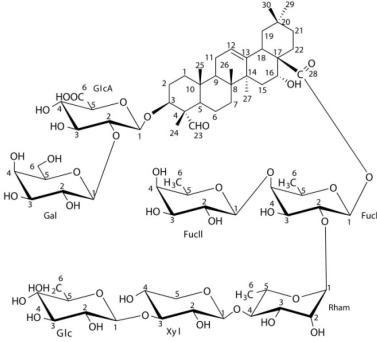
(Continued)

TABLE 1 | Continued

Saponins	Formulae	Structure	Pharmacological activities	References
Segetoside H	$C_{68}H_{104}O_{33}$	R_1=H R_2=Ac R_3=H	Unknown	Sang et al., 2000a
Segetoside I	$C_{68}H_{104}O_{34}$	R_1=H R_2=Ac R_3=OH	Anti-tumor activity; Activation of apoptotic	Sang et al., 2000b
Segetoside K	$C_{54}H_{86}O_{26}$	R=OH	Unknown	Sang et al., 2000a
Segetoside L	$C_{60}H_{98}O_{28}$	Glc(1→3)-[Gal'(1→2)]-Gal-O R=Glc'(1→6)Glc''	Unknown	Minliangzou and Ainalao, 1999
Vaccarosides				
Vaccaroside (A–C)	Common structure			
Vaccaroside A	$C_{54}H_{86}O_{25}$	R_1=H R_2=H	Unknown	Sang et al., 1999
Vaccaroside B	$C_{60}H_{94}O_{29}$	R_1 = H R_2=	Unknown	Ma et al., 2008
Vaccaroside C	$C_{54}H_{86}O_{25}$	R_1 = glc R_2=H	Unknown	Koike et al., 1998
Vaccaroside D	$C_{54}H_{86}O_{25}$		Unknown	Koike et al., 1998
Vaccaroside (E–H)	Common structure			

(Continued)

TABLE 1 | Continued

Saponins	Formulae	Structure		Pharmacological activities	References
Vaccaroside E	$C_{66}H_{102}O_{33}$	R_1 CHO	R_2 OH	Unknown	Jia et al., 1998
Vaccaroside F	$C_{65}H_{102}O_{33}$	R_1 OH	R_2 OH	Unknown	Jia et al., 1998
Vaccaroside G	$C_{66}H_{102}O_{32}$	R_1 CHO	R_2 H	Unknown	Jia et al., 1998
Vaccaroside H	$C_{65}H_{102}O_{32}$	R_1 OH	R_2 H	Unknown	Jia et al., 1998
Vaccaroside I	$C_{71}H_{112}O_{37}$			Unknown	Ma et al., 2008

could significantly inhibit xylene-induced ear edema and reduce peritoneal capillary permeability and leukocyte infiltration induced by an intraperitoneal injection of acetic acid (Wang et al., 2015). Similar results were obtained in cells. For example, Sun et al. (2017) found that the *Vaccaria* hypaphorine concentration dependently downregulated the expression of inflammatory cytokine and inflammatory enzyme, and then counteracted the increased phosphorylation of nucleus transfer-related proteins that were induced by inflammation, thereby inhibiting a nuclear factor- (NF-) κB signaling pathway to exert its anti-inflammatory effect in lipopolysaccharide- (LPS-) stimulated Raw 264.7 cells. Osteoclasts are the only cells in the human body that undergo the bone resorption. Inhibiting the differentiation and formation of osteoclasts can effectively inhibit bone loss and osteolysis (Wei et al., 2018). A previous study suggested that *Vaccaria* hypaphorine inhibits the formation, differentiation, and resorption of osteoclast to attenuate inflammatory bone loss in LPS-treated mice by inhibiting an extracellular signal-regulated kinase (ERK), p38, a c-Jun N-terminal kinase (JNK), and an NF-κB p65 phosphorylation (Chen et al., 2018). However, Liu et al. (2019) demonstrated that *Vaccaria* inhibits formation and function of osteoclast *in vivo* and *in vitro*, as well as Ti particle-induced osteolysis. Chronic pelvic inflammatory disease (CPID) refers to chronic inflammation of the female internal organs, surrounding connective tissue, and pelvic peritoneum (Chen, 2012; Bu et al., 2015). Man Pen Fang (MPF), a Chinese herbal compound consisting of the whole plants of *Thlaspi arvense* L. (Cruciferae), *Gleditsia sinensis* Lam. (Fabaceae), *Smilax china* L. (Liliaceae), *Euonymus alatus* (Thunb.) Sieb. (Celastraceae), and the seeds of *V. segetalis* (Neck; Caryophyllaceae), was proven to be effective for treating CPID in the previous studies (Kim et al.,

2015; Li et al., 2016). In this formulation, *V. segetalis* (Neck) plays an important role because it has analgesic and anti-inflammatory properties, and activates blood circulation by dissipating blood stasis. In previous studies, Zhang et al. (2017) constructed a CPID mouse model (Tuffrey et al., 1992; Chen et al., 2008) and treated the animals with MPF. They revealed that MPF has a significant dose-dependent anti-inflammatory effect during the CPID treatment, and it also plays a positive role by decreasing the serum levels of inflammatory cytokines such as interleukin- (IL-) 6, IL-10, tumor necrosis factor (TNF)-α, and transforming growth factor (TGF)-β (Zhang et al., 2017). Zhang et al. (2017) conducted mechanistic research on TCMs and provided a theoretical support for the use of MPF to treat CPID. Trichinosis is an infectious disease caused by parasites, and it poses a serious hazard to the pork industry and human health (Rostami et al., 2017). In the host, *Trichinella* activates inflammatory cells to overexpress cyclooxygenase-2 (COX-2; Othman et al., 2016) and other inflammatory factors. Xu et al. (2019) demonstrated that *Vaccaria* n-butanol extract (VNE) from the seeds of *V. segetalis* can significantly relieve the symptoms of *Trichinella spiralis* infection. However, VNE from the seeds of *V. segetalis* did not significantly and directly affect the viability of *T. spiralis* muscle larvae. The study suggested that the survival rate of *T. spiralis* muscle larvae did not differ between the control and VNE treatment. Moreover, VNE exerted anti-inflammatory effects by repressing the IL-1β, IL-6, TNF-α, and COX-2 expression in mice. Therefore, it was speculated that VNE is likely to exert its anti-inflammatory effect by reducing the inflammatory response in infected mice and exhibiting similar insecticidal effects to *T. spiralis* (Xu et al., 2019). Albendazole is commonly used to treat human trichinellosis. However, because of its clinical side effects,

TABLE 2 | Cyclic peptides present in the seeds of *V. segetalis*.

Cyclic peptide	Formulae	Structure	Pharmacological activities	References
Segetalins A	$C_{31}H_{43}N_7O_6$	cyclo[Ala-Gly-Val-Pro-Val-Trp]	Vasorelaxant activity; Estrogen-like activity	Morita et al., 2006
Segetalins B	$C_{24}H_{32}N_6O_5$	cyclo[Ala-Gly-Val-Ala-Trp]	Estrogen-like activity	Morita et al., 1997b
Segetalins C	$C_{40}H_{51}N_9O_7$	cyclo[Ala-Phe-Pro-Gly-Leu-His-Phe]	Antimicrobial activity	Dahiya and Kaur, 2008
Segetalins D	$C_{37}H_{49}N_7O_8$	cyclo[Ala-Phe-Pro-Gly-Leu-Ser-Phe]	Estrogen-like activity	Morita et al., 1997a
Segetalins E	$C_{43}H_{56}N_8O_8$	cyclo[Gly-Tyr-Val-Pro-Leu-Trp-Pro]	Unknown	Sang et al., 2000d
Segetalins F	$C_{44}H_{62}N_{10}O_{14}$	cyclo[Ala-Ser-Tyr-Ser-Ser-Lys-Pro-Phe-Ser]	Vasorelaxant activity	Morita et al., 2006
Segetalins G	$C_{25}H_{38}N_6O_6$	cyclo[Ala-Gly-Val-Lys-Tyr]	Estrogen-like activity; Diastolic activity	Yun et al., 1997
Segetalins H	$C_{29}H_{38}N_8O_8$	cyclo[Arg-Phe-Ser-Gly-Tyr]	Estrogen-like activity; Vasodilatory activity	Yun et al., 1997
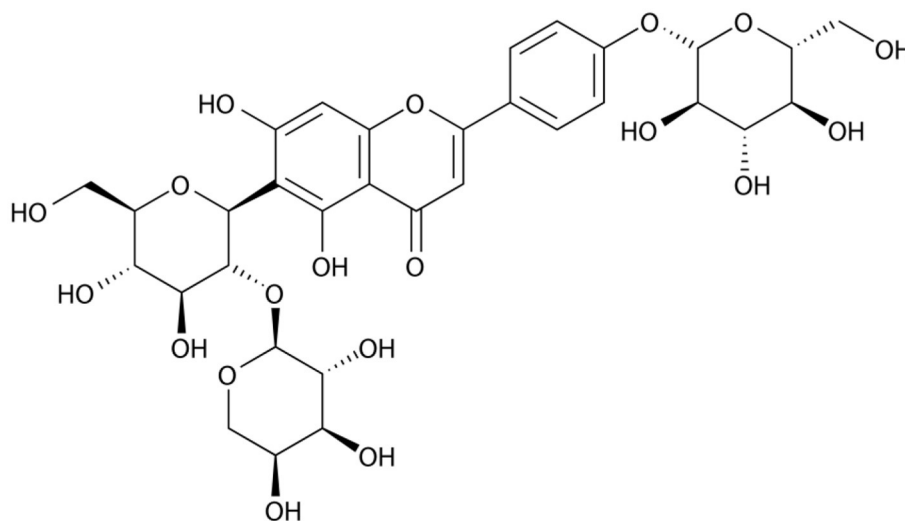
FIGURE 1 | Structure of vaccarin.

VNE may be an adjuvant to the existing drug. A recent study provided insights into the mechanism of the anti-inflammatory effects of *V. segetalis*. Mao found that crude polysaccharides from the seeds of *V. segetalis* (SVCP) can effectively prevent the urinary tract infections that are induced by uropathogenic Escherichia coli (UPEC) in 2020. SVCP-induced upregulation of IL-6 and IL-8 helps to eliminate bacteria in the urine, and does not cause tissue damage and acute pyelonephritis *via* the upregulation of pro-inflammatory cytokines. In addition, the authors found that the application of SVCP could upregulate the PIGR expression in rat kidneys, which was significantly suppressed by UPEC (Mao et al., 2020). This suggests that SVCP can prevent the infection caused by UPEC by stimulating an innate immunity of the kidneys. In addition, (Mao et al., 2021) explored the potential mechanism of SVCP in the treatment of kidney infections in a recent research study. The administration of SVCP upregulated the low expression of Cathelicidin family (LL-37 and CRAMP) in the UPEC-induced kidney infection model, and upregulated the expression of Toll-like receptors (TLRs). TLR agonists can stimulate the expression of cathelicidin (Liu et al., 2006; Vandamme et al., 2012). In summary, SVCP may increase the expression of cathelicidin by activating TLRS to protect the kidney from infection. This enriches the mechanism of action of SVCP.

Currently, antibiotics are the most widely used drugs to treat inflammation-related diseases. However, the long-term use of antibiotics in large quantities will lead to drug resistance and cause serious side effects in some patients, leading to treatment failures. The anti-inflammatory effect of *V. segetalis* provides new avenues for the treatment of inflammatory diseases.

Anticancer Activity

In 1971, Folkman (1971) first proposed the theory of tumor angiogenesis. Through an in-depth study of malignancies, the researchers found that angiogenesis is an important process in tumorigenesis and tumor development. Angiogenesis can be activated at different stages of tumor development. Currently, anti-angiogenic drugs represent a leading field in the development of new antitumor drugs (Viallard and Larrivee, 2017). The inhibition of angiogenesis has become a necessary strategy for antitumor therapy (D'Amato and Adamis, 1995; Folkman, 1995; Tímár et al., 2001). Continuous proliferation and migration of vascular endothelial cells are the primary steps in angiogenesis. During the neovascularization, endothelial cells first establish a cell-to-cell contact and then proliferate and migrate to a perivascular matrix where cellular connections are re-established and new vessels are formed (Carmeliet and Jain, 2000). Vascular endothelial cells can also secrete vascular growth factors to promote the proliferation of vascular endothelial cells and tumor cells. The inhibition of vascular endothelial cells can inhibit the proliferation of tumor cells and increase apoptosis in metastatic tumor cells. Therefore, anti-angiogenic therapy targeting vascular endothelial cells involved in the proliferation and migration can be an effective antitumor strategy.

Platelet-endothelial cell adhesion molecule-1 (PECAM-1), which is also known as CD31, is a key molecule of cell adhesion. In the process of neovascularization, CD31 is closely related to the movement of endothelial cells, and it may be involved in the signal transduction that is responsible for cell adhesion (Sun et al., 2000). CD31-blocking antibodies inhibit angiogenesis that is induced by cytokines and tumors in different animal models (Lertkiatmongkol et al., 2016).

Many studies have suggested that *V. segetalis* has anticancer and anti-angiogenic effects. We have summarized the pharmacological data and the effects of an herb (**Table 3**). The results illustrated that *V. segetalis* extract has anticancer effects in various cancer cells. *V. segetalis* extract reduced the expression of CD31 in peripheral endothelial cells and reduced the microvessel density in surrounding tissues. Further research revealed that *V. segetalis* water extract significantly inhibits the

TABLE 3 | Anticancer activity of *V. segetalis*.

	Model used	Plant part used	Extract type	Admin	Dosage/duration	Control	Results	References
Anti-angiogenesis and anticancer	*In vivo*. Mice, injection of Lewis lung cancer cells	Seeds, *Vaccaria segetalis*	Seeds, decocted twice, filtered, decompressed and condensed into concretes, and freeze-dried to powder	Per oral	Mice were fed with the solution (100 μg/mL) prepared with dry powder after the fourth day of inoculation	Baseline control/Negative control	*Vaccaria segetalis* extract (40 μg) reduced tumors by 58.3%, reduced CD31 expression in peripheral endothelial cells, and reduced the microvessel density in surrounding tissues. It indicated that the extract prevented progress of established tumors and reduced angiogenesis	Feng et al., 2012
	In vitro. MTT assay	Seeds, *Vaccaria segetalis*	Seeds, decocted twice, filtered, decompressed and condensed into concretes, and freeze-dried to powder	*In vitro*	Different concentrations (μg/ml)	Negative control	$IC_{50} = 50$ μg/mL *Vaccaria segetalis* extract inhibited the migration of HMECs in a dose-dependent manner. It suggested that the extract can inhibit the migration of vascular endothelial cells	Feng et al., 2012
	In vivo. CAM assay; *In vivo*. Mice, injection of Matrigels.	Seeds, *Vaccaria segetalis*	Seeds, decocted twice, filtered, decompressed and condensed into concretes, and freeze-dried to powder	Injection; Matrigels mixed drugs	Prepare the extract as (100 μg / ml) and treat with 10 μL; 100 μL 100 μg/mL Vaccaria segetalis extract	Negative control; Baseline control/Positive control/negative control	The new blood vessel formation in the extract group was significantly reduced The extract significantly reduced the number of invasive endothelial cells in the Matrigel plug and inhibited microvessel formation	Feng et al., 2012
Anti-angiogenesis and Anticancer	*In vivo*. Mice, subcutaneous injection of H22 cells for solid carcinoma model	Seeds, *Vaccaria segetalis*	Vaccaria segetalis 70% ethanol extract, purified by D-101 resin column.	Intragastric administrate	Treatment group (1, 2.5, and 5 mg/kg)	Negative control/three treatment groups	The results suggested that mouse body weight increased, CD31 expression in tumor vessels decreased, and the apoptosis in tumor cells and vascular endothelial cells was induced. It implied that the use of *Vaccaria segetalis* improved the health of mice, and had the effect of inhibiting tumor growth and anti-angiogenesis	Gao Y. Y. et al., 2010
Anticancer	*In vitro*. Cancer cell line (A549, MCF-7, PC-3, LNCaP) Normal human mammary epithelial cells (HMECs); Antiproliferative assay	Seeds, *Vaccaria segetalis*	*Vaccaria segetalis* water extract	*In vitro*.	Different concentration (μg/ml)	Treatment groups	The result suggested that *Vaccaria segetalis* had anticancer effects *in vitro* and these effects are markedly greater in various cancer cells This experiment indicated that *Vaccaria segetalis* water extract can inhibit proliferation of cancer cell lines	Mark et al., 2005
Anti-angiogenesis	*In vivo*. Mice, injection of Matrigels.	Seeds, *Vaccaria segetalis*	Seeds, decocted twice, filtered, decompressed and condensed into concretes, and freeze-dried to powder	Matrigels mixed drugs	0.1 g extract	Negative control/Positive control	Reduction of endothelial cells and decrease of the formation of abundant microvessels induced by basic fibroblast growth factor (bFGF)	Passaniti et al., 1992
Anticancer by promoting apoptosis of cancer cells	*In vitro*. MTT assay/DNA fragmentation; *In vivo*. Mice, HepG2 xenograft Kunming	Seeds, *Vaccaria segetalis*	Segetoside I, standardized by crude ethanol extract, CH2Cl2/MeOH mixture, MeOH–H2O (RP-8 and RP-18 columns) gradient elution	*In vitro*; Intraperitoneal injection	Different concentration of segetoside I; Segetoside I (1.25, 2.5, 5 mg/kg)	Negative control/Positive control	$IC_{50} = 8.62$ μM; Dose-dependent DNA fragmentation and increase Bax/Bcl-2 expressions by Segetoside I (0.82, 8.2, 82 μM); Dose-dependent inhibition of tumor growth with segetoside I	Firempong et al., 2016

proliferation and migration of human mammary epithelial cells (HMECs) in a concentration-dependent manner. This indicates that the main function of *V. segetalis* extract is to block the proliferation and migration of endothelial cells. *V. segetalis* has anticancer effects *in vitro*, and these effects are markedly enhanced in select cancer cells. Other studies demonstrated that *V. segetalis* extract can decrease the formation of abundant microvessels, which was induced by a basic fibroblast growth factor (bFGF). bFGF is found in almost all mesoderm-derived and neuroectoderm-derived tissues as well as the tumors derived from these tissues. bFGF has been shown to have a mitogenic, chemotactic, and angiogenic activity, which promotes cell growth, differentiation, and motility (Finzel et al., 1984). By analyzing a few literature studies, we determined that *V. segetalis* extract can reduce the formation and expansion of tumors by suppressing the formation of abundant microvessels and preventing the proliferation and migration of epithelial cells. Additionally, *V. segetalis* extract will likely to inhibit angiogenesis that is induced by cytokines and tumors by reducing the expression of CD31. Inhibiting angiogenesis was also shown, which often leads to the reduction of tumors; thus, angiogenesis is a critical prerequisite for the tumor formation, and the anti-angiogenic effect of *V. segetalis* provides a new strategy for treating tumors. Anti-angiogenic drugs that are commonly used in clinical practice include vascular endothelial growth factor (VEGF) monoclonal antibodies (Cao et al., 2015), thalidomide (Bladé et al., 2001), and vandetanib (Vitagliano et al., 2010), but these drugs can cause serious side effects and increase medical costs. The discovery and study of anti-angiogenic effects of *V. segetalis* have provided new directions for the development of anticancer drugs in the future.

Tumors are caused by the acceleration of cell proliferation and suppression of apoptosis. Tumor treatment can also be accomplished by inducing apoptosis in tumor cells. Many studies support the apoptotic effect of *V. segetalis* in cancer cells. The results identified the *V. segetalis* compounds that have significant antitumor effects, and these are triterpenoid saponins (segetoside H and segetoside I) and some unknown compounds (Gao Y. Y. et al., 2010; Balsevich et al., 2012). Segetosides H and I, which are isolated from *V. segetalis*, have significant anticancer effects (**Table 3**; Yun et al., 1998). Previous studies demonstrated that segetoside I can induce DNA fragmentation and the upregulation of apoptosis-related genes, suggesting that the activation of apoptotic signaling events may have been initiated. Segetoside I also suppressed hepatic tumor growth in mice with virtually no cytotoxicity, and prolonged animal survival (Firempong et al., 2016), and thus, it may be an effective candidate for treating tumors. These results suggest that segetosides H and I can induce cancer cell apoptosis by activating apoptotic pathways to prevent the development of cancer, which may make them valuable antitumor chemotherapeutics.

In summary, we propose that *V. segetalis* extract can exert its anticancer effects in two ways. First, the extract can inhibit the tumor growth and angiogenesis around the tumor and second, it can activate apoptosis pathways in cancer cells. To study the mechanism of the anticancer action of *V. segetalis* in the future, we should focus on angiogenesis-related and

apoptosis-related pathways. Although *V. segetalis* has been used as traditional Chinese herbal medicine for more than 2000 years, its anticancer effect has been newly proposed in recent years and the current experiments remain in the preclinical stage, including cell and animal models. Deeper mechanism studies and more expansive clinical data are needed to prove and support medication methods, dosages, and other variables. Thus, much work remains before *V. segetalis* or its extracts can be used to treat patients with cancer.

Inhibition of Apoptosis

Apoptosis is also known as a programmed cell death. Despite its ability to induce apoptosis in tumor cells as mentioned previously, *V. segetalis* can inhibit apoptosis that is caused by apoptotic factors in normal cells. Vaccarin was shown to exert a potential protective effect in H_2O_2-injured human EA.hy926 endothelial cells by inhibiting the Notch signaling pathway and downregulating caspase-3, which has a dominant role in the execution of the apoptotic process. Caspase-3 activation is a central link in apoptosis (Xie et al., 2015). H_2O_2 is often used to develop a validation model, and it stimulates cells to produce reactive oxygen species (ROS) (Schieber and Chandel, 2014). Previous studies revealed that the ROS production and apoptosis can occur simultaneously (Corbacho et al., 2002). Further studies illustrated that vaccarin can suppress a high glucose-induced damage in EA.hy926 cells, which was shown by improved cell viability and migratory ability, and this treatment effectively suppressed the caspase-3 overexpression (Qiu et al., 2016).

The abovementioned studies demonstrated that vaccarin, which is an active ingredient of *V. segetalis*, can downregulate the apoptotic gene expression that is induced by apoptotic factors, thereby inhibiting apoptosis. We can imagine a clinical role for vaccarin as an antioxidant based on its ability to prevent H_2O_2-induced apoptosis, specifically as a daily supplement.

Dilation of Blood Vessels

Vasodilators can be used to treat hypertension, coronary atherosclerotic heart disease, angina pectoris, and cerebrovascular sclerosis. *V. segetalis* is often used to treat headache, hypertension, asthmatic pneumonia, and other diseases. Because of its vasodilatory effects, *V. segetalis* (Neck) Garcke decoction had a significant concentration-dependent relaxing effect on the norepinephrine-induced precontraction of the rabbit aortic smooth muscle. After removing endothelial cells, the relaxation effect of *V. segetalis* (Neck) Garcke on noradrenaline-precontracted arterial rings was significantly decreased (Hua'e et al., 2007). Morita et al. (1997a) found that segetalins A, D, F, G, and H exhibited vasodilatory activity against norepinephrine-induced aortic contraction in rats, and among these, segetalins G and H had the strongest diastolic activity. In addition, a study by Jing et al. (2007) reported the same relaxation in aortic ring samples that lacked an endothelium. The volatile oil in *V. segetalis* may be responsible for this function (Shiva Kumar et al., 2017). The specific mechanisms of segetalin action on vasodilation and contractile activity require further investigation. Previously, we explained that TCM often uses the seeds of *V. segetalis* to mechanically stimulate auricular points

to assist in the treatment of hypertension. In addition to the unique characteristics of its seeds, we speculate that it is also possible that the volatile oil of *V. segetalis* could enter the body through the skin at the ear point. (Morita et al., 2006) found that the segetalins in *V. segetalis* extract have a vasodilatory activity. Although the vasodilatory activity of segetalins has been reported in animal models, there are no clinical data to date. However, the evidence points to a new strategy for the treatment of vasoconstriction-related diseases.

Promotion of Lactation

A recent study indicated that the use of *V. segetalis* during breastfeeding to promote breast milk is common in Macau (Zheng et al., 2020). Many studies have revealed that *V. segetalis*, *Leonurus*, and *Astragalus* can significantly promote lactation in female rats (Baoming and Anshan, 2007). Although this treatment remains in use, the mechanism by which *V. segetalis* induces lactation is unclear.

One of the primary ingredients in *V. segetalis* is vaccarin (Jia et al., 1998), which promotes the proliferation of mammary epithelial cells and enhances their secretory function (Leonoudakis et al., 2010). Mammary epithelial cells are the breast biological generators that synthesize and secrete milk. The number and activity of mammary epithelial cells are closely related to the lactation performance of livestock (Planas-Silva et al., 2006). The latest research has enriched the lactation mechanism of Vaccarin. Vaccarin and PRL have similar effects in stimulating the proliferation of breast epithelial cells and enhancing their secretory function, the expression of Cylin D1, the phosphorylation of mechanistic target of rapamycin (mTOR), and the regulation of the expression of a sterol regulatory element binding protein 1c (SREBP-1c). In addition, Vaccarin can promote the expression of PRL receptors. In summary, Vaccarin can promote the breast epithelial cell proliferation and enhance its secretion ability *via* the PRL receptor-PI3K-Cyclin D1/SREBP-1c/mTOR signaling pathways (Yu et al., 2020). JAK2 is important for the PRL signal transduction and normal breast tissue development, and STAT5a is necessary for the breast development (Gass et al., 2003). β-casein is an important milk protein, and its secretion level reflects the lactation ability of breast epithelial cells to a certain extent. Gao X. J. et al. (2010) found that the dibutyl phthalate (DBP) injection can increase the milk production in cows. Liu et al. (2010) found that DBP could significantly increase the proliferation and viability of mammary epithelial cells in dairy cows. It was also found that DBP could increase the β-casein expression and lactose secretion in breast epithelial cells (Tong et al., 2013). In addition, Tong et al. found that DBP from *V. segetalis* can promote lactation and the proliferation of breast epithelial cells and activate a JAK-STAT5-signaling pathway by increasing the STAT5 phosphorylation levels (Tong et al., 2011). These studies demonstrated that DBP has estrogenic activity, and that it can activate a lactation-signaling pathway and promote lactation by regulating the milk protein, lactose, and milk fat synthesis. However, as a highly toxic substance, the dosage and application of DBP require more theoretical research and experimental support.

The low postpartum lactation ability of mammals is mainly attributable to the insufficient activation of the relevant endocrine system in the body, preventing mammary glands from producing milk normally and hindering milk excretion. Chinese herbal medicine can promote lactation by regulating the metabolism of postpartum mammals and increasing endocrine levels *in vivo*. Kleinberg and Ruan (2008) found that *V. segetalis* increased the content of growth hormones (GHs) and PRL in serum from dairy cows, which in turn promoted the breast development and improved the lactation performance. Jun-Xian et al. (2013) used *V. segetalis* water extract, which had a similar effect to estrogen and PRL, and its components could bind to an estrogen receptor to activate a STAT5-signaling pathway, thereby promoting the P-STAT5 expression and milk protein synthesis. Bryant (2009) found that the PRL promoter transcription and PRL synthesis can be induced by stimulating the estrogen receptor system and pituitary transcription factor Pit-1. PRL controls the regulation of milk protein at the translational level, thereby promoting the synthesis of milk proteins. Another study reported similar results and suggested that *V. segetalis* has a specific estrogen-like effect; specifically, its components can bind to an estrogen receptor, and thereby promoting the synthesis of PRL (Itokawa et al., 1995).

Based on these findings, we concluded that the stimulatory effects of *V. segetalis* on the production of milk occur through DBP and that DBP has PRL-like effects. In addition, a few studies have found that the other substances in *V. segetalis* have estrogen-like effects, and estrogen-like active ingredients can bind with estrogen receptors to promote the synthesis of PRL. This implies a synergy between the actions of various substances in *V. segetalis*. These results provide new ideas for future studies on *V. segetalis*.

Estrogen-Like Action

Many studies have revealed the estrogen-like effect *of V. segetalis*. Pakoussi et al. (2018) found that phytoestrogens enhance uterine contractions. Morita et al. (1997c) discovered vaccaroid A in *V. segetalis* and found that it has a role in promoting uterine contractions. Moreover, the research has illustrated that segetalins A, B, G, and H are cyclic hexapeptides and pentapeptides with estrogenic activity in ovariectomized rats (Morita et al., 1993, 1995; Yun et al., 1997). Segetalins are the only natural cyclic peptides that were reported to have estrogenic activity. When they are digested into acyclic segetalins by enzymes, they lose their activity, indicating that their conformation plays an important role in their function (Morita et al., 1997a). A study found that segetalins G and H at a dose of 2.5 mg/kg significantly increased uterine weight vs. the control ($p < 0.01$) in ovariectomized rats that did not receive the estrogen supplementation for 2 weeks (Yun et al., 1997). Itokawa et al. (1995) applied segetalins A and B to ovariectomized rats for 14 consecutive days and observed similar effects to those of segetalins G and H, verifying that segetalins A, B, G, and H have estrogen-like effects. Ovariectomy-induced bone loss in rats and postmenopausal bone loss in women share many similar features, and the clinical symptoms are often treated by 17β-estradiol supplementation (Kalu, 1991). To study the estrogen-like activity of *V. segetalis* and facilitate its future clinical applications, Shih et al. (2009) constructed an ovariectomized

TABLE 4 | Cytotoxic activity (IC50, mM) of compounds 1–6.

Cell lines	1	2	3	4	5	6	*Topotecan*	*Docetaxel*
LNcap	3.6	3.4	2.5	4.2	12.9	1.2	0.053	
A-549	1.0	3.0	11.0	1.0	7.2	0.4		<0.01
P-388	0.8	9.4	0.7	3.7	1.6	0.1		<0.01

Compound 1, vaccaroside I; Compound 2, vaccaroside E; Compound 3, vaccaroside G; Compound 4, vaccaroside B; Compound 5, segetoside H; Compound 6, segetoside I.
LNCaP, human prostate cancer cell line; A549, human lung cancer cell line; P388, mouse leukemia cell line.
Topotecan and docetaxel were used as positive controls.

rat model to simulate postmenopausal bone loss in women. In the ovariectomized group, the calcium content of the femur and the fourth lumbar vertebra was significantly reduced, whereas these effects were alleviated by the supplementation with 17β-estradiol or *V. segetalis* extract. *V. segetalis* extract does not cause side effects such as uterine or vaginal hypertrophy. This provides a new direction for the treatment of osteoporosis. Moreover, because of its estrogen-like activity, *V. segetalis* can be used as an alternative to estrogen for people with allergies to synthetic estrogens. In addition, *V. segetalis* can avoid the side effects of estrogen supplementation.

TOXICOLOGY RESEARCH

Several toxicological studies related to *V. segetalis* have been conducted. In one study, *V. segetalis* extract obtained *via* a reflux with 75% ethanol was used to treat mice. The minimum toxic amount of *V. segetalis* extract in mice was 100 mg/kg, and the minimum lethal dose was 1,500 mg/kg. *V. segetalis* extract was more toxic to the heart and kidneys of mice at 1,000 mg/kg (approximately lethal dose) than lung, and there was no serious functional damage in mice treated with 200 mg/kg of *V. segetalis* extract. Therefore, *V. segetalis* shows a good safety profile, and it could be a promising therapeutic modality (Gao et al., 2013).

Segetoside I is an extract of *V. segetalis*, and it has been a focus of research. One study showed that intraperitoneal segetoside I in mice had an LD50 (median lethal dose) of 14.5 mg/kg (Firempong et al., 2016). The mice were treated with segetoside I at different concentrations and sacrificed after 14 days, and their respective organ coefficients were determined. The tissue coefficients of the heart, liver, and kidney did not change significantly, whereas the tissue coefficient of the spleen increased with increasing doses of segetoside I. The spleen coefficient was significantly improved by segetoside I at the concentration of 1.25, 2.5, and 5 mg/kg. This demonstrated that segetoside I did not significantly affect the body weight of mice, but that it damaged the spleen at doses exceeding 5 mg/kg. In addition, the studies have explored the cytotoxic effects of different extracts of *V. segetalis* in different cells, and IC50 was obtained (**Table 4**; Ma et al., 2008).

In a previous study, it was mentioned that *V. segetalis* has an anti-inflammatory effect, but at the same time it has an estrogen-like effect, which also leads to certain side effects. Overdose of estrogen by men who have not entered puberty will cause the secondary sex characteristics of men to not appear but the second

sex characteristics of women; excessive estrogen in puberty men will cause a gradual decline of the second sex characteristics of men, in addition to causing endocrine disorders, obesity, and even affect fertility (Kabir et al., 2015). This has led to a clinical application of Wang Buliuxing more oriented to females, and whether Wang Buliuxing can be used for the treatment of males and the applied dosage need more literature support. In addition, the anti-inflammatory effect of Wang Buliu Xing may hide an inflammatory process caused by the microorganism infection, which may lead to an aggravation of the infection, and thus may not fundamentally solve the problem.

Taken together, the toxicological information on *V. segetalis* remains extremely limited, and further research is required to determine the extraction, purification, and application of the active ingredients of *V. segetalis*.

CONCLUSION

V. segetalis is a plant used in traditional Chinese herbal medicine that occupies an extremely important position in the Chinese medicine theory. With an increasing amount of research on the active ingredients of *V. segetalis*, *V. segetalis* could be used with modern medicine to treat blood strangury, lactation deficiencies, and chylorrhea. *V. segetalis* can also be used to treat hypertension, headache, and gallstones through its unique ability to physically stimulate the corresponding acupuncture points on the ear or body. This article has provided in detail the chemical and pharmacological properties of *V. segetalis* and summarized the recent literature studies. The main ingredients in *V. segetalis* include flavonoids, cyclic peptides, saponins, and polysaccharides, but several active substances have not been identified, indicating the need for a more systematic phytochemical research. In terms of its pharmacological effects, *V. segetalis* has anti-inflammatory, anti-angiogenic, anticancer, anti-apoptosis, and estrogenic effects, dilates blood vessels, and promotes lactation. Many diseases are treated poorly using modern medicine, and traditional and complementary medicine can provide new treatment modalities for these diseases.

Although substantial research has been conducted on *V. segetalis*, many unknown elements in *V. segetalis* remain. In addition, some studies used hydroalcoholic crude extracts instead of the pure active ingredients of *V. segetalis* as the experimental objects. We speculate that hydroalcoholic crude extracts are used because the extraction process for the active ingredients of *V. segetalis* is more complicated. In addition, we found that *V.*

segetalis crude extracts and some effective active ingredients also have anticancer effects that have not been mentioned in clinical applications, thereby further enhancing the significance of *V. segetalis* in modern research and providing new directions of future research.

Future research on *V. segetalis* should specifically focus on the four issues that are described below. First, we should continue to explore the unknown elements in *V. segetalis*. Second, the processes for extracting the effective active substances of *V. segetalis* should be further improved. Third, the mechanisms of the anti-inflammatory, anticancer, and anti-apoptotic effects of *V. segetalis* should be further elucidated. Finally, more research on the pharmacology and toxicology is needed to provide additional evidence for clinical applications.

AUTHOR CONTRIBUTIONS

CL, XZ, and MT conceptualized the study. MT, YH, XW, TC, CY, NW, ZZ, and BZ investigated the study. MT wrote original draft preparation. CL and XZ helped in writing and editing the review. All authors contributed to the article and approved the submitted version.

FUNDING

ACKNOWLEDGMENTS

REFERENCES

Aswad, M., Rayan, M., Abu-Lafi, S., Falah, M., Raiyn, J., Abdallah, Z., et al. (2018). Nature is the best source of anti-inflammatory drugs: indexing natural products for their anti-inflammatory bioactivity. *Inflamm. Res.* 67, 67–75. doi: 10.1007/s00011-017-1096-5

Balsevich, J. J., Ramirez-Erosa, I., Hickie, R. A., Dunlop, D. M., Bishop, G. G., and Deibert, L. K. (2012). Antiproliferative activity of *Saponaria vaccaria* constituents and related compounds. *Fitoterapia* 83, 170–181. doi: 10.1016/j.fitote.2011.10.010

Banno, N., Akihisa, T., Tokuda, H., Yasukawa, K., Taguchi, Y., Akazawa, H., et al. (2005). Anti-inflammatory and antitumor-promoting effects of the triterpene acids from the leaves of *Eriobotrya japonica*. *Biol. Pharm. Bull.* 28, 1995–1999. doi: 10.1248/bpb.28.1995

Baoming, S., and Anshan, S. (2007). Effects of Chinese herbs on lactation of rat and performance of offspring. *J. North. Agric. Univer.* 14, 22–26. doi: CNKI:SUN:DBYN.0.2007-01-006

Bernard, P., Scior, T., Didier, B., Hibert, M., and Berthon, J. Y. (2001). Ethnopharmacology and bioinformatic combination for leads discovery: application to phospholipase A(2) inhibitors. *Phytochemistry* 58, 865–874. doi: 10.1016/S0031-9422(01)00312-0

Bladé, J., Esteve, J., Rosi?ol, L., Perales, M., Montoto, S., Tuset, M., et al. (2001). Thalidomide in refractory and relapsing multiple myeloma. *Semin. Oncol.* 28, 588–592. doi: 10.1016/S0093-7754(01)90029-6

Bozak, K. R., Yu, H., Sirevg, R., and Christoffersen, R. E. (1990). Sequence analysis of ripening-related cytochrome P-450 cDNAs from avocado fruit. *Proc. Natl. Acad. Sci. U.S.A.* 87, 3904–3908. doi: 10.1073/pnas.87.10.3904

Bryant, W. (2009). Environmental estrogens stimulate gene transcription in the prolactin promoter. *Int. J. Biol.* 2, 35–43. doi: 10.5539/ijb.v2n1p35

Bu, X., Liu, Y., Lu, Q., and Jin, Z. (2015). Effects of "danzhi decoction" on chronic pelvic pain, hemodynamics, and proinflammatory factors in the murine model of sequelae of pelvic inflammatory disease. *Evid. Based Complement. Alternat. Med.* 2015:547251. doi: 10.1155/2015/547251

Cao, R., Zhang, S., Ma, D., and Hu, L. (2015). A multi-center randomized phase II clinical study of bevacizumab plus irinotecan, 5-fluorouracil, and leucovorin (FOLFIRI) compared with FOLFIRI alone as second-line treatment for Chinese patients with metastatic colorectal cancer. *Med. Oncol.* 32:325. doi: 10.1007/s12032-014-0325-9

Carmeliet, P., and Jain, R. K. (2000). Angiogenesis in cancer and other diseases. *Nature* 407, 249–257. doi: 10.1038/35025220

Chen, H., Guo, T., Wang, D., and Qin, R. (2018). Vaccaria hypaphorine impairs RANKL-induced osteoclastogenesis by inhibition of ERK, p38, JNK and NF-κB pathway and prevents inflammatory bone loss in mice. *Biomed. Pharmacother.* 97, 1155–1163. doi: 10.1016/j.biopha.2017.11.044

Chen, K. J. (2012). Blood stasis syndrome and its treatment with activating blood circulation to remove blood stasis therapy. *Chin. J. Integrat. Med.* 18, 891–896. doi: 10.1007/s11655-012-1291-5

Chen, Y., Liu, Q., Chen, Y., Huang, W., Jin, B., Ding, Z., et al. (2017). Study on hypoglycemic effects of total flavonoid aglycon from leaves of *Carya cathayensis*. *Chin. Arch. Tradit. Chin. Med.* 35, 2033–2035. doi: CNKI:SUN:ZYHS.0.2017-08-028

Chen, Y., Tian, L., Wang, X., and Wang, C. X. (2008). Drug particles of FUYANNING to chronic pelvic inflammatory disease model of the impact of rats' IL-2 IL-6. *Chin. Arch. Tradit. Chin. Med.*

Choi, D. W., Jung, J. D., Ha, Y. I., Park, H. W., Dong, S. I., Chung, H. J., et al. (2005). Analysis of transcripts in methyl jasmonate-treated ginseng hairy roots to identify genes involved in the biosynthesis of ginsenosides and other secondary metabolites. *Plant Cell Rep.* 23, 557–566. doi: 10.1007/s00299-004-0845-4

Corbacho, A. M., Martinez De La Escalera, G., and Clapp, C. (2002). Roles of prolactin and related members of the prolactin/growth hormone/placental lactogen family in angiogenesis. *J. Endocrinol.* 173, 219–238. doi: 10.1677/joe.0.1730219

Dahiya, R., and Dahiya, S. (2021). Natural cyclic polypeptides as vital phytochemical constituents from seeds of selected medicinal plants. *Arch. Pharm. Chem. Life Sci.* 354:e2000446. doi: 10.1002/ardp.2020 00446

Dahiya, R., and Kaur, K. (2008). Synthesis and pharmacological investigation of segetalin C as a novel antifungal and cytotoxic agent. *Arzneimittelforschung* 58, 29–34. doi: 10.1055/s-0031-1296463

D'Amato, R. J., and Adamis, A. P. (1995). Angiogenesis inhibition in age-related macular degeneration. *Ophthalmology* 102, 1261–1262. doi: 10.1016/S0161-6420(95)30876-7

Feng, L., Zhang, X., Hua, H., Qiu, L., Zhang, L., and Lv, Z. (2012). *Vaccaria segetalis* extract can inhibit angiogenesis. *Asian Biomed.* 6, 683–692. doi: 10.5372/1905-7415.0605.108

Finzel, B. C., Poulos, T. L., and Kraut, J. (1984). Crystal structure of yeast cytochrome c peroxidase refined at 1.7-A resolution. *J. Biol. Chem.* 259, 13027–13036. doi: 10.1016/S0021-9258(18)90651-4

Firempong, C. K., Zhang, H. Y., Wang, Y., Chen, J., Cao, X., Deng, W., et al. (2016). Segetoside I, a plant-derived bisdesmosidic saponin, induces apoptosis in human hepatoma cells *in vitro* and inhibits tumor growth *in vivo*. *Pharmacol. Res.* 110, 101–110. doi: 10.1016/j.phrs.2016.04.032

Folkman, J. (1971). Tumor angiogenesis: therapeutic implications. *N. Engl. J. Med.* 285, 1182–1186. doi: 10.1056/NEJM197111182852108

Folkman, J. (1995). Angiogenesis in cancer, vascular, rheumatoid and other disease. *Nat. Med.* 1, 27–31. doi: 10.1038/nm0195-27

Gao, X. J., Tong, H. L., Li-Min, L. U., and Qing-Zhang, L. I. (2010). Preparation of dibutyl phthalate isomer from Semen Vaccariae and its influence on milk production and milk quality of dairy cow. *China Dairy Indust.* 2010, 36–37. doi: 10.3969/j.issn.1001-2230.2010.04.011

Gao, Y. Y., Feng, L., and Qiu, L. Y. (2013). Research on acute toxicology of *Vaccaria segetalis* extract. *Guangzhou Chem. Indust.* 41, 17–21. doi: 10.3969/j.issn.1001-9677.2013.19.003

Gao, Y. Y., Qiu, L. Y., Kang, X. X., Wang, H., and Jin, J. (2010). "AntiTumor effect and its mechanism of vaccaria segetalis on mouse inoculated H22 solid carcinoma," in *International Conference on Bioinformatics & Biomedical Engineering* WuXi. doi: 10.1109/ICBBE.2010.5517710

Gass, S., Harris, J., Ormandy, C., and Brisken, C. (2003). Using gene expression arrays to elucidate transcriptional profiles underlying prolactin function. *J. Mammary Gland Biol. Neoplasia* 8, 269–285. doi: 10.1023/B:JOMG.0000010029.85796.63

Guan, F. Q., Liu, M., Yu, S., Chen, Y., Zhao, Y. Y., Wang, M., et al. (2013). The antioxidant activity evaluations of the triterpene saponins from *Lonicera macranthoides in vitro*. *Lishizh. Med. Mater. Med. Res.* 24, 1315–1317. doi: 10.3969/j.issn.1008-0805.2013.06.013

Güçlü-Üstündag, O., and Mazza, G. (2007). Saponins: properties, applications and processing. *Crit. Rev. Food Sci. Nutr.* 47, 231–258. doi: 10.1080/10408390600698197

Haralampidis, K., Trojanowska, M., and Osbourn, A. E. (2002). Biosynthesis of triterpenoid saponins in plants. *Adv. Biochem. Eng. Biotechnol.* 75, 31–49. doi: 10.1007/3-540-44604-4_2

Hua'e, J., Caiqin, N., Jianmin, H., and Tuanxiao, Z. (2007). Vasodilatation effects of the water decoction of vaccaria segetalis(neck)garche on rabbit aorta *in vitro*. *J. Sichu. Tradit. Chin. Med.* 25, 13–15.

Hui, Y., Jun-Li, H., and Chuang, W. (2019). Anti-oxidation and anti-aging activity of polysaccharide from *Malus micromalus* makino fruit wine. *Int. J. Biol. Macromol.* 121, 1203–1212. doi: 10.1016/j.ijbiomac.2018.10.096

Itokawa, H., Yun, Y., Morita, H., Takeya, K., and Yamada, K. (1995). Estrogen-like activity of cyclic peptides from *Vaccaria segetalis* extracts. *Planta Med.* 61, 561–562. doi: 10.1055/s-2006-959373

Jia, Z., Koike, K., Kudo, M., Li, H., and Nikaido, T. (1998). *Triterpenoid saponins* and sapogenins from *Vaccaria segetalis*. *Phytochemistry* 48, 529–536. doi: 10.1016/S0031-9422(97)01128-X

Jing, H., Of, D., Medicine, W., and First, T. (2007). Vasodilatation effects of the water decoction of *Vaccaria segetalis*(neck) garche on rabbit aorta *in vitro*. *J. Sichu. Tradit. Chin. Med.* 25, 13–15. doi: 10.3969/j.issn.1000-3649.2007.08.008

Jin-Ling, H. U., Hong, H. U., and Yang, L. (2014). Studies on the chemical constituents from the seeds of *Vaccaria segetalis*. *J. Pharmaceut. Res.* 33, 71–72.

Jun-Xian, L. U., Gao, Y. S., Tang, M. J., Jun-Hua, P. U., Zhang, X. Y., and Qing-Lian, G. E. (2013). Effects of free gossypol on immunity of the HISEX young hens. *China Anim. Husb. Vet. Med.* 40, 118–121. doi: 10.3969/j.issn.1671-7236.2013.04.026

Kabir, E. R., Rahman, M. S., and Rahman, I. (2015). A review on endocrine disruptors and their possible impacts on human health. *Environ. Toxicol. Pharmacol.* 40, 241–258. doi: 10.1016/j.etap.2015.06.009

Kalu, D. N. (1991). The ovariectomized rat model of postmenopausal bone loss. *Bone Miner.* 15, 175–191. doi: 10.1016/0169-6009(91)90124-I

Kim, Y., Koh, J. H., Ahn, Y. J., Oh, S., and Kim, S. H. (2015). The Synergic anti-inflammatory impact of *Gleditsia sinensis* Lam. and *Lactobacillus brevis* KY21 on intestinal epithelial cells in a DSS-induced colitis model. *Korean J. Food Sci. Anim. Resourc.* 35, 604–610. doi: 10.5851/kosfa.2015.35.5.604

Kleinberg, D. L., and Ruan, W. (2008). IGF-I, GH, and sex steroid effects in normal mammary gland development. *J. Mammary Gland Biol. Neoplas.* 13, 353–360. doi: 10.1007/s10911-008-9103-7

Koike, K., Jia, Z., and Nikaido, T. (1998). Triterpenoid saponins from *Vaccaria segetalis*. *Phytochemistry* 47, 1343–1349. doi: 10.1016/S0031-9422(97)00707-3

Kozlowska, A., and Szostak-Wegierek, D. (2014). Flavonoids–food sources and health benefits. *Rocz. Panstw. Zakl. Hig.* 65, 79–85.

Leonoudakis, D., Singh, M., Mohajer, R., Mohajer, P., Fata, J. E., Campbell, K. P., et al. (2010). Dystroglycan controls signaling of multiple hormones

through modulation of STAT5 activity. *J. Cell Sci.* 123, 3683–3692. doi: 10.1242/jcs.070680

Lertkiatmongkol, P., Liao, D., Mei, H., Hu, Y., and Newman, P. J. (2016). Endothelial functions of platelet/endothelial cell adhesion molecule-1 (CD31). *Curr. Opin. Hematol.* 23, 253–259. doi: 10.1097/MOH.0000000000000239

Li, F., He, T., Xu, Q., Lin, L. T., Li, H., Liu, Y., et al. (2015). What is the acupoint? A preliminary review of acupoints. *Pain Med.* 16, 1905–1915. doi: 10.1111/pme.12761

Li, K. K., Zhou, X., Wong, H. L., Ng, C. F., Fu, W. M., Leung, P. C., et al. (2016). *In vivo* and *in vitro* anti-inflammatory effects of Zao-Jiao-Ci (the spine of Gleditsia sinensis Lam.) aqueous extract and its mechanisms of action. *J. Ethnopharmacol.* 192, 192–200. doi: 10.1016/j.jep.2016.07.020

Liang, X., and Xiu-jun, J. (2013). Observation on the therapeutic effect of auricular point pressing bean on 30 cases of allergic rhinitis. *J. N. Chin. Med.* 45, 181–182. doi: CNKI:SUN:REND.0.2013-11-092

Li-Fan, and Liang, J. Y. (2007). Research progress of *Vaccaria segetalis*. *Strait Pharm. J.* 19, 1–1.

Liu, J., Limin, L., Xiaofei, L., and Qingzhang, L. (2010). Effects on the proliferation and lactation ability of dairy cow mammary gland epithelial cells by semen vaccariae active isomer. *Key Lab. Dairy Sci. Educ.* 33, 66–68.

Liu, P. T., Stenger, S., Li, H., Wenzel, L., Tan, B. H., Krutzik, S. R., et al. (2006). Toll-like receptor triggering of a vitamin D-mediated human antimicrobial response. *Science* 311, 1770–1773. doi: 10.1126/science.1123933

Liu, Y. (2018). Auricular pressing therapy in the treatment of hypertension for 30 cases. *Chin. Med. Mod. Dist. Educ. China.* 16:127–128

Liu, Y., Song, F. M., Ma, S. T., Moro, A., and Feng, W. Y. (2019). Vaccarin prevents titanium particle-induced osteolysis and inhibits RANKL-induced osteoclastogenesis by blocking NF-kappaB and MAPK signaling pathways. *J. Cell Physiol.* 234, 13832–13842. doi: 10.1002/jcp.28063

Ma, C. H., Fan, M. S., Lin, L. P., Tang, W. D., Lou, L. G., Ding, J., et al. (2008). Cytotoxic triterpenoid saponins from *Vaccaria segetalis*. *J. Asian Nat. Prod. Res.* 10, 177–184. doi: 10.1080/10286020701394381

Mao, G. H., Ren, Y., Li, Q., Wu, H. Y., Jin, D., Zhao, T., et al. (2016). Anti-tumor and immunomodulatory activity of selenium (Se)-polysaccharide from Se-enriched *Grifola frondosa*. *Int. J. Biol. Macromol.* 82, 607–613. doi: 10.1016/j.ijbiomac.2015.10.083

Mao, X., Guo, H., Yao, R., Bao, L., Sun, J., Bao, Y., et al. (2020). Crude polysaccharides from the seeds of Vaccaria segetalis prevent the urinary tract infection through the stimulation of kidney innate immunity. *J. Ethnopharmacol.* 260:112578. doi: 10.1016/j.jep.2020.112578

Mao, X., Yao, R., Guo, H., Bao, L., Bao, Y., Xu, Y., et al. (2021). Polysaccharides extract from Vaccaria segetalis seeds inhibits kidney infection by regulating cathelicidin expression. *J. Ethnopharmacol.* 267:113505. doi: 10.1016/j.jep.2020.113505

Mark, Shoemaker, M., Hamilton, B., Dairkee, S. H., Cohen, I., and Campbell, M. J. (2005). In vitro anticancer activity of twelve Chinese medicinal herbs. *Phytother. Res.* 19:649–51. doi: 10.1002/ptr.1702

Minliangzou, Z., and Ainalao, S. (1999). Segetoside L, a new triterpenoid saponin from *Vaccaria segetalis*. ??????(???)15, 55–57.

Min-ying, T. (2005). 59 cases of herpes zoster treated with *Vaccaria segetalis*. *Chin. J. Rural Med. Pharm.* 13, 51–51. doi: CNKI:SUN:XCYY.0.2006-06-053

Morita, H., Eda, M., Iizuka, T., Hirasawa, Y., Sekiguchi, M., Yun, Y. S., et al. (2006). Structure of a new cyclic nonapeptide, segetalin F, and vasorelaxant activity of segetalins from *Vaccaria segetalis*. *Bioorgan. Med. Chem. Lett.* 16, 4458–4461. doi: 10.1016/j.bmcl.2006.06.083

Morita, H., Nagashima, S., Takeya, K., and Itokawa, H. (1993). Astins A and B, antitumor cyclic pentapeptides from *Aster tataricus*. *Chem. Pharm. Bull.* 41, 992–993. doi: 10.1248/cpb.41.992

Morita, H., Yun, Y. S., Takeya, K., and Itokawa, H. (1997a). Conformational preference for segetalins G and H, cyclic peptides with estrogen-like activity from seeds of *Vaccaria segetalis*. *Bioorgan. Med. Chem.* 5, 2063–2067. doi: 10.1016/S0968-0896(97)00135-1

Morita, H., Yun, Y. S., Takeya, K., Itokawa, H., and Shiro, M. (1995). Conformational analysis of a cyclic hexapeptide, segetalin A from *Vaccaria segetalis*.? *Tetrahedron* 51, 5987–6002. doi: 10.1016/0040-4020(95)00277-F

Morita, H., Yun, Y. S., Takeya, K., Itokawa, H., and Shirota, O. (1997b). Thionation of segetalins A and B, cyclic peptides with estrogen-like activity from seeds of *Vaccaria segetalis*. *Bioorgan. Med. Chem.* 5, 631–636. doi: 10.1016/S0968-0896(97)00001-1

Morita, H., Yun, Y. S., Takeya, K., Itokawa, H., Yamada, K., Shirota, O., et al. (1997c). A new triterpenoid saponin with contractility of rat uterine from Vaccaria segetalis. *Bioorg. Med. Chem. Lett.* 7, 1095–1096. doi: 10.1016/S0960-894X(97)00168-6

Othman, A. A., Abou Rayia, D. M., Ashour, D. S., Saied, E. M., Zineldeen, D. H., and El-Ebiary, A. A. (2016). Atorvastatin and metformin administration modulates experimental *Trichinella spiralis* infection. *Parasitol. Int.* 65, 105–112. doi: 10.1016/j.parint.2015.11.001

Pakoussi, T., Mouzou, A. P., Metowogo, K., Aklikokou, K. A., and Gbeassor, M. (2018). How do *Spondias mombin* L (*Anacardiaceae*) leaves extract increase uterine smooth muscle contractions to facilitate child birth in parturient women? *Afr. Health Sci.* 18, 235–243. doi: 10.4314/ahs.v18i2.6

Passaniti, A., Taylor, R. M., Pili, R., Guo, Y., Long, P. V., Haney, J. A., et al. (1992). A simple, quantitative method for assessing angiogenesis and antiangiogenic agents using reconstituted basement membrane, heparin, and fibroblast growth factor. *Lab Invest.* 67, 519–528.

Peng, Q., Feng, Z., Rui, X., Zhixiong, L., Mingcang, C., Zhaolin, S., et al. (2014). Identification of multiple constituents from seed of *Vaccaria segetalis* with an adsorbent-separation strategy based on liquid chromatography coupled to quadrupole time-of-flight mass spectrometry. *Rapid Commun. Mass Spectrom.* 28, 1243–1257. doi: 10.1002/rcm.6893

Planas-Silva, M. D., Waltz, P. K., and Kilker, R. L. (2006). Estrogen induces death of tamoxifen-resistant MCF-7 cells: contrasting effect of the estrogen receptor downregulator fulvestrant. *J. Steroid Biochem. Mol. Biol.* 98, 193–198. doi: 10.1016/j.jsbmb.2005.10.003

Qing, L. I., Pan, Z. L., Jie, W. U., and Zhang, H. J. (2014). Study on extraction process and content determination of polysaccharides from *Semen vaccaria*. *Sci. Technol. Food Indust.* 35:299–299.

Qiu, Y., Du, B., Xie, F., Cai, W., Liu, Y., Li, Y., et al. (2016). Vaccarin attenuates high glucose-induced human EAâ? chy926 endothelial cell injury through inhibition of notch signaling. *Mol. Med. Rep.* 13, 2143–2150. doi: 10.3892/mmr.2016.4801

Rong, P., Zhu, B., Li, Y., Gao, X., Ben, H., Li, Y., et al. (2011). Mechanism of acupuncture regulating visceral sensation and mobility. *Front. Med.* 5, 151–156. doi: 10.1007/s11684-011-0129-7

Rosalía, R. R., María Dolores, H., Perona, J. S., and Valentina, R. G. (2004). Potential vasorelaxant effects of oleanolic acid and erythrodiol, two triterpenoids contained in 'orujo' olive oil, on rat aorta. *Br. J. Nutr.* 92, 635–642. doi: 10.1079/BJN20041231

Rostami, A., Gamble, H. R., Dupouy-Camet, J., Khazan, H., and Bruschi, F. (2017). Meat sources of infection for outbreaks of human trichinellosis. *Food Microbiol.* 64, 65–71. doi: 10.1016/j.fm.2016.12.012

Sang, S., Lao, A., Chen, Z., Uzawa, J., and And, Y. F. (2003). "Chemistry and bioactivity of the seeds of *Vaccaria segetalis*," in *ACS Symposium Series* Shanghai. doi: 10.1021/bk-2003-0859.ch021

Sang, S., Lao, A., Wang, H., Chen, Z., Uzawa, J., and Fujimoto, Y. (1999). Triterpenoid saponins from *Vaccaria segetalis*. *J. Asian Nat. Prod. Res.* 1, 199–205. doi: 10.1080/10286029908039865

Sang, S. M., Lao, A., Leng, Y., Gu, Z., Chen, Z., Uzawa, J., et al. (2000d). Segetoside F a new triterpenoid saponin with inhibition of luteal cell from the seeds of *Vaccaria segetalis*. *Tetrahed. Lett.* 41, 9205–9207. doi: 10.1016/S0040-4039(00)01710-X

Sang, S. M., Lao, A. N., Chen, Z. L., Uzawa, J., and Fujimoto, Y. (2000b). Three new triterpenoid saponins from the seeds of *Vaccaria segetalis*. *J. Asian Nat. Prod. Res.* 2, 187–193. doi: 10.1080/10286020008039910

Sang, S. M., Lao, A. N., Leng, Y., Cao, L., Chen, Z. L., Uzawa, J., et al. (2002). A new triterpenoid saponin with inhibition of luteal cell from the seeds of *Vaccaria segetalis*. *J. Asian Nat. Prod. Res.* 4, 297–301. doi: 10.1080/1028602021000049096

Sang, S. M., Xia, Z. H., Mao, S. L., Lao, A., and Chen, Z. L. (2000c). [Studies on the flavonol glycosides from the seeds of *Vaccaria segetalis*]. *Zhongguo Zhong Yao Za Zhi* 25, 221–222.

Sang, S. M., Zou, M. L., Lao, A. N., Liang, Z., and Fujimoto, Y. (2000a). A new triterpenoid saponin from the seeds of *Vaccaria segetalis*. ??????(???)11, 49–52. doi: 10.1021/cm990982a

Schieber, M., and Chandel, N. S. (2014). ROS function in redox signaling and oxidative stress. *Curr. Biol.* 24, R453–462. doi: 10.1016/j.cub.2014.03.034

Shih, C. C., Lin, C. H., and Lin, W. L. (2009). Ameliorative effects of *Vaccaria segetalis* extract on osteopenia in ovariectomized rats. *J. Nat. Med.* 63, 386–392. doi: 10.1007/s11418-009-0341-9

Shiva Kumar, A., Jeyaprakash, K., Chellappan, D. R., and Murugan, R. (2017). Vasorelaxant and cardiovascular properties of the essential oil of *Pogostemon elsholtzioides*. *J. Ethnopharmacol.* 199, 86–90. doi: 10.1016/j.jep.2017.01.036

Silva, B., Guedes, J. M., Arêde, A., and Costa, A. (2012). Synthesis and bioactivity of secondary metabolites from marine sponges containing dibrominated indolic systems. *Cheminform* 17:6083. doi: 10.3390/molecules17056083

Sun, H., Cai, W., Wang, X., Liu, Y., Hou, B., Zhu, X., et al. (2017). Vaccaria hypaphorine alleviates lipopolysaccharide-induced inflammation via inactivation of NFkappaB and ERK pathways in Raw 264.7 cells. *BMC Complement. Alternat. Med.* 17:120. doi: 10.1186/s12906-017-1635-1

Sun, J., Paddock, C., Shubert, J., Zhang, H. B., Amin, K., Newman, P. J., et al. (2000). Contributions of the extracellular and cytoplasmic domains of platelet-endothelial cell adhesion molecule-1 (PECAM-1/CD31) in regulating cell-cell localization. *J. Cell Sci.* 113 (Pt. 8), 1459–1469. doi: 10.1023/A:1005568132027

Tan, N. H., and Zhou, J. (2006). Plant cyclopeptides. *Chem. Rev.* 106, 840–895. doi: 10.1021/cr040699h

Tang, X., Huang, J., Xiong, H., Zhang, K., Chen, C., Wei, X., et al. (2016). Anti-Tumor Effects of the polysaccharide isolated from tarphochlamys affinis in H22 tumor-bearing mice. *Cell. Physiol. Biochem.* 39, 1040–1050. doi: 10.1159/000447811

Tian-Yi, L. (2011). *Precious Mirror of Health*. Shijiazhuang: China Medical Science Technology Press.

Tímár, J., Döme, B., Fazekas, K., Janovics, A., and Paku, S. (2001). Angiogenesis-dependent diseases and angiogenesis therapy. *Pathol. Oncol. Res.* 7, 85–94. doi: 10.1007/BF03032573

Tong, H., Gao, X., Li, Q., Liu, J., Li, N., and Wan, Z. (2011). Metabolic regulation of mammary gland epithelial cells of dairy cow by galactopoietic compound isolated from Vaccariae segetalis. *Agric. Sci. China* 10, 1106–1116. doi: 10.1016/S1671-2927(11)60100-4

Tong, H., Gao, X., Sheng, Z., Li, Q., Li, S., Li, N., et al. (2013). Galactopoietic activity of dibutyl phthalate isolated from Vaccaria segetalis. *J. Northeast Agric. Univ.*, 20, 28–33. doi: 10.1016/S1006-8104(14)60043-X

Tuffrey, M., Alexander, F., Woods, C., and Taylor-Robinson, D. (1992). Genetic susceptibility to chlamydial salpingitis and subsequent infertility in mice. *J. Reprod. Fertil.* 95, 31–38. doi: 10.1530/jrf.0.0950031

Vandamme, D., Landuyt, B., Luyten, W., and Schoofs, L. (2012). A comprehensive summary of LL-37, the factotum human cathelicidin peptide. *Cell. Immunol.* 280, 22–35. doi: 10.1016/j.cellimm.2012.11.009

Viallard, C., and Larrivee, B. (2017). Tumor angiogenesis and vascular normalization: alternative therapeutic targets. *Angiogenesis* 20, 409–426. doi: 10.1007/s10456-017-9562-9

Vitagliano, D., De Falco, V., Tamburrino, A., Coluzzi, S., Troncone, G., Chiappetta, G., et al. (2010). The tyrosine kinase inhibitor ZD6474 blocks proliferation of RET mutant medullary thyroid carcinoma cells. *Endocr. Relat. Cancer* 18, 1–11. doi: 10.1677/ERC-09-0292

Wang, F., Chen, S., Deng, L., Chen, L., Huang, Y., Tian, M., et al. (2019). Protective effects of astragaloside IV against LPS-induced endometritis in mice through inhibiting activation of the NF-kappaB, p38 and JNK signaling pathways. *Molecules* 24:373. doi: 10.3390/molecules24020373

Wang, L., Cui, D., Wang, X., Zhang, J., Yang, Z., Qin, Z., et al. (2015). Analgesic and anti-inflammatory effects of hydroalcoholic extract isolated from Semen vaccariae. *Pak. J. Pharm. Sci.* 28(3 Suppl), 1043–1048

Wang, X., Dong, H., Liu, Y., Yang, B., Wang, X., and Huang, L. (2011). Application of high-speed counter-current chromatography for preparative separation of cyclic peptides from *Vaccaria segetalis*. *J. Chromatogr. B* 879, 811–814. doi: 10.1016/j.jchromb.2011.02.001

Wei, C. M., Su, Y. J., Qin, X., Ding, J. X., Liu, Q., Song, F. M., et al. (2018). Monocrotaline suppresses RANKL-induced osteoclastogenesis *in vitro* and prevents LPS-induced bone loss *in vivo*. *Cell. Physiol. Biochem.* 48, 644–656. doi: 10.1159/000491892

Xie, F., Cai, W., Liu, Y., Li, Y., Du, B., Feng, L., et al. (2015). Vaccarin attenuates the human EA.hy926 endothelial cell oxidative stress injury through inhibition of notch signaling. *Int. J. Mol. Med.* 35, 135–142. doi: 10.3892/ijmm.2014. 1977

Xu, F., Hou, B., Zhu, X., Liu, Y., Shi, X., Li, S., et al. (2019). Vaccaria n-butanol extract lower the production of proinflammatory cytokines and the infection risk of *T. spiralis* *in vivo*. *Acta Parasitol.* 64, 520–527. doi: 10.2478/s11686-019-00064-6

Yu, Y., Yuan, X., Li, P., Wang, Y., Yu, M., and Gao, X. (2020). Vaccarin promotes proliferation of and milk synthesis in bovine mammary epithelial cells through the Prl receptor-PI3K signaling pathway. *Eur. J. Pharmacol.* 880:173190. doi: 10.1016/j.ejphar.2020.173190

Yun, Y. S., Morita, H., Takeya, K., and Itokawa, H. (1997). Cyclic peptides from higher plants. 34. Segetalins G and H, structures and estrogen-like activity of cyclic pentapeptides from *Vaccaria segetalis*. *J. Nat. Prod.* 60, 216–218. doi: 10.1021/np960617n

Yun, Y. S., Shimizu, K., Morita, H., Takeya, K., Itokawa, H., and Shirota, O. (1998). Triterpenoid saponin from *Vaccaria segetalis*. *Phytochemistry* 47, 143–144. doi: 10.1016/S0031-9422(97)00496-2

Zakaryan, H., Arabyan, E., Oo, A., and Zandi, K. (2017). Flavonoids: promising natural compounds against viral infections. *Arch. Virol.* 162, 2539–2551. doi: 10.1007/s00705-017-3417-y

Zhang, L. J., Zhu, J. Y., Sun, M. Y., Song, Y. N., Rahman, K., Peng, C., et al. (2017). Anti-inflammatory effect of Man-Pen-Fang, a Chinese herbal compound, on chronic pelvic inflammation in rats. *J. Ethnopharmacol.* 208, 57–65. doi: 10.1016/j.jep.2017.06.034

Zheng, J., Ma, L. T., Ren, Q. Y., Li, L., Zhang, Y., Shi, H. J., et al. (2014). The influence of astragalus polysaccharide and beta-elemene on LX-2 cell growth, apoptosis and activation. *BMC Gastroenterol.* 14:224. doi: 10.1186/s12876-014-0224-8

Zheng, T., Chen, W., Hu, H., Wang, Y., Harnett, J. E., and Ung, C. O. L. (2020). The prevalence, perceptions and behaviors associated with traditional/complementary medicine use by breastfeeding women living in Macau: a cross-sectional survey study. *BMC Complement. Med. Ther.* 20:122. doi: 10.1186/s12906-020-02921-8

Zhi-hong, Y., and Cai-ying, S. (1989). The effect of auricular plaster on gallbladder contraction. *J. Gansu Coll. Trad. Chin. Med.* 1, 31–32.

Zhou, G., Tang, L., Wang, T., Zhou, X., and Wang, Z. (2015). Phytochemistry and pharmacological activities of *Vaccaria hispanica* (miller) rauschert: a review. *Phytochem. Rev.* 15, 813–827. doi: 10.1007/s11101-015-9425-1

Zhu-mo, N. (2005). *Materia Medica (Selected Chinese Ancient Books)*. Shanghai: Shanghai Science and Technology Press.

Recent Advances in Chemical Biology of Mitochondria Targeting

Haiwei Wang[1†], Bin Fang[1,2†], Bo Peng[1,3,4*†], Limin Wang[1], Yufei Xue[3,4], Hua Bai[1], Shenci Lu[1], Nicolas H. Voelcker[1,3,4,5,6*], Lin Li[1*], Li Fu[2] and Wei Huang[1,7]

[1]Frontiers Science Center for Flexible Electronics, Xi'an Institute of Flexible Electronics (IFE) and Xi'an Institute of Biomedical Materials & Engineering, Northwestern Polytechnical University, Xi'an, China, [2]School of Materials Science and Engineering, Northwestern Polytechnical University, Xi'an, China, [3]Commonwealth Scientific and Industrial Research Organisation (CSIRO), Clayton, VIC, Australia, [4]Drug Delivery, Disposition and Dynamics, Monash Institute of Pharmaceutical Sciences, Monash University, Parkville, VIC, Australia, [5]Melbourne Centre for Nanofabrication, Victorian Node of the Australian National Fabrication Facility, Clayton, VIC, Australia, [6]Department of Materials Science & Engineering, Monash University, Clayton, VIC, Australia, [7]Key Laboratory of Flexible Electronics (KLOFE) & Institute of Advanced Materials (IAM), Nanjing Tech University (NanjingTech), Nanjing, China

Mitochondria are vital subcellular organelles that generate most cellular chemical energy, regulate cell metabolism and maintain cell function. Mitochondrial dysfunction is directly linked to numerous diseases including neurodegenerative disorders, diabetes, thyroid squamous disease, cancer and septicemia. Thus, the design of specific mitochondria-targeting molecules and the realization of real-time acquisition of mitochondrial activity are powerful tools in the study and treatment of mitochondria dysfunction in related diseases. Recent advances in mitochondria-targeting agents have led to several important mitochondria chemical probes that offer the opportunity for selective targeting molecules, novel biological applications and therapeutic strategies. This review details the structural and physiological functional characteristics of mitochondria, and comprehensively summarizes and classifies mitochondria-targeting agents. In addition, their pros and cons and their related chemical biological applications are discussed. Finally, the potential biomedical applications of these agents are briefly prospected.

Keywords: mitochondrial, mitochondrial dysfunction, mitochondrial-targeting molecules, chemical biology, chemical probe, nanomedicine

INTRODUCTION

Mitochondria are one of the most important organelles in cells, playing a key role in cell survival. On the one hand, mitochondria synthesize adenosine triphosphate (ATP), the energy required to maintain cell viability by mitochondrial oxidative phosphorylation (OXPHOS); on the other hand, damaged mitochondria produce reactive oxygen species (ROS), cytochrome c and other signals, which initiate apoptosis by activating caspase family proteins (Chan, 2006). Mitochondrial dysfunction is usually characterized as the loss of efficiency of ATP production, which is a characteristic of aging and most all chronic diseases, such as neurodegenerative disorders, cancers and diabetes (Nicolson, 2014). Therefore, mitochondrial targeting therapies might be the key to solving intractable diseases and hold great potential in the treatment of various diseases (Murphy and Hartley, 2018).

A comprehensive analysis of the activity, expression and migration of mitochondrial biomarkers in the process of disease occurrence and development will provide important information for a better understanding of the diseases. Therefore, current attention focuses on the development of sensitive
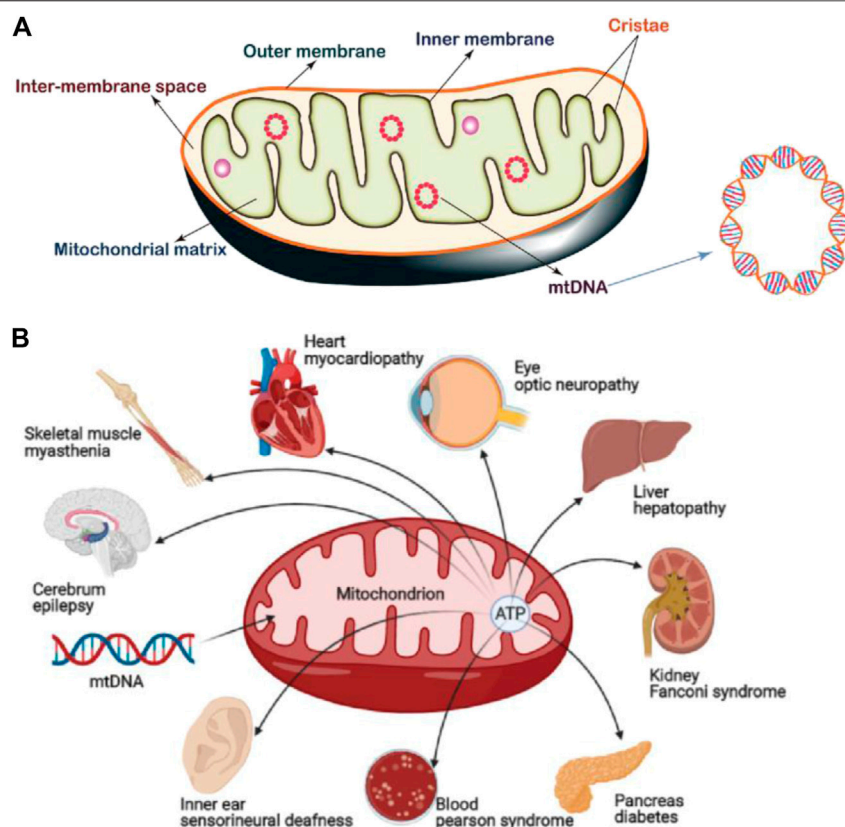
FIGURE 1 | (A) Mitochondrial structure, which can be divided by four functional areas: 1) outer mitochondrial membrane (OMM), 2) mitochondrial membrane space (IMS), 3) inner mitochondrial membrane (IMM), and 4) mitochondrial matrix (MM). Mitochondria also possess their own gene information (mtDNA). Image reproduced with permission, from Ref. Samanta et al. (2019). (B) Common mitochondrial diseases. 1B was created with BioRender.com.

technologies/systems that can identify and monitor mitochondrial functions. In this review, the structure, function and related disease characteristics of mitochondria are introduced. Mitochondrial targeting methods are summarized and classified, such as mitochondria-targeting small molecules, biomolecules and nanomaterials. Moreover, an analysis and discussion of the characteristics of these mitochondria-targeting motifs and related biological applications is provided to the reader. We believe that this review will arouse widespread interest among scientists working on mitochondria and provide chemical biologists with valuable information to further address the challenges.

THE STRUCTURE, FUNCTION AND RELATED DISEASES OF MITOCHONDRIA

The structure of mitochondria is very different from other subcellular organelles in the cell. The basic structure of mitochondria can be divided into four functional areas: 1) outer mitochondrial membrane (OMM), 2) mitochondrial membrane space (IMS), 3) inner mitochondrial membrane (IMM), and 4) mitochondrial matrix (MM) (Mannella, 2000). The OMM has a smooth surface morphology and functions as the

cell organelle boundary membrane. The specific receptors on the OMM are termed mitochondrial outer membrane complex which selectively recognize and uptake certain substances into the mitochondria. The IMM folds inward to form mitochondrial cristae which results in larger surface area, therefore it is able to carry more biochemical reactions per time unit (**Figure 1A**). These two membranes define the borders of the extramitochondrial region, inter-membrane space and matrix (Osellame et al., 2012). In addition, the morphology and position of mitochondria in the cell are very important and are strictly regulated by the processes of mitosis, biogenesis and autophagy to ensure the relative stability of the mitochondrial population.

Upon mitochondrial damage, events such as the changes of morphology, membrane potential and permeability to Ca^{2+}, reduction of membrane phosphate esters, and oxidative phosphorylation coupling, affect the normal function of the entire cell and lead to the occurrence of diseases. For example, mitochondrial myopathy, cerebral myopathy, Leber's hereditary optic neuropathy etc. are caused by pathological changes after mitochondrial damage (Claudia et al., 2019; Fogle et al., 2019; Winkler et al., 2019).

In addition, a damaged mitochondrial structure and mitochondrial metabolic abnormalities also play important

roles in the occurrence and development of many diseases (Viscomi and Zeviani, 2020), (**Figure 1B**). For example, as a common neurodegenerative disorder, the pathogenesis of Parkinson's disease (PD) has been strongly linked with mitochondrial dysfunction (Chen et al., 2020). Studies proved that mitochondrial respiratory defects may result in chronic ROS production that leads to the death of dopaminergic neurons. Moreover, disruption of mitochondrial kinetics due to toxic damage or other conditions may also lead to neurodegeneration. In some cases, mitochondrial dysfunction caused by gene mutation is the fundamental cause for the pathogenesis and inheritance of PD (Dauer and Przedborski, 2003; Thomas and Beal, 2007; Bose and Beal, 2016). Therefore, diseases where the progression can be correlated with or compensated for mitochondrial function are collectively referred as mitochondrial diseases. At present, in addition to neurodegenerative disorders (Baldassarro et al., 2019), there are numerous diseases related to abnormal mitochondrial structure and function, including mental diseases (Ashwini et al., 2015), tumor (Schubert et al., 2020), aging (Bornstein et al., 2020), cardiovascular disease (Veloso et al., 2019), diabetes (Szendroedi et al., 2012), etc. Therapeutics which target mitochondria also result in positive responses in some cases (Jeena et al., 2019). Although these diseases appear in different tissue sites and show different symptoms, mitochondrial dysfunction is the common feature, mainly manifested as insufficient production capacity due to impaired oxidative phosphorylation, increased ROS, and abnormal apoptosis signals (Lesnefsky and Hoppel, 2006).

In recent years, research on rectifying the structure and function of mitochondria has been carried out rapidly. For example, fixing mitochondrial DNA mutations through genome editing technology was reported to have a certain curative effect on angiocardiopathy (Gammage et al., 2018). In addition, diagnostic and therapeutic agents targeting mitochondria, such as a substance called Gboxin, an inhibitor of oxidative phosphorylation, can produce specific inhibition of diabetes or glioma (Shi et al., 2019). Although great efforts have been put into the treatment of mitochondria-related diseases (Slone and Huang, 2020), in most cases, the structure and function of mitochondria have been irreversibly damaged which result in limited therapeutic effects. Alternatively, a newly emerged approach, mitochondrial replacement therapy (MRT), which supplements the cells with healthy mitochondria is a promising approach to fundamentally treat mitochondria-related diseases (Schumacker et al., 2014) (Mccully et al., 2016). In addition, combination therapies such as phototherapy and small molecule anticancer drugs have been developed as alternatives to synergistic treatment (Xie et al., 2020).

MITOCHONDRIA-TARGETING AGENTS

For mitochondria therapies and biological studies, the selectivity or even specificity of agents targeting the mitochondrial structures is essential to the design of corresponding

FIGURE 2 | Summary of mitochondria-targeting small molecules.
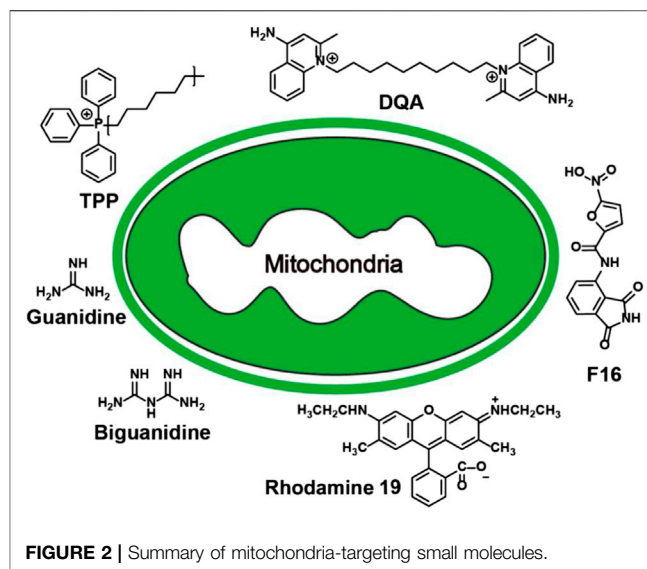
therapeutics and probes. This selectivity will result in less off-target toxicity and also lower the effective concentration of drugs/probes, therefore enhancing the corresponding bioavailability (Jhaveri and Torchilin, 2016; Yao et al., 2021). Substantial progress in the understanding of mitochondria provides critical information that paves the way for the design of mitochondrial targeting methods and agents.

Mitochondria-Targeting Small Molecules

Due to the presence of a proton pump (PP) in the IMM, the protons in the MM are pumped into the IMS, resulting in positive charges in the IMS. MM carries negative charges, which form the transmembrane potential (MTP) across the IMM, which is also known as mitochondrial membrane potential (Zorova et al., 2018). There is usually a negative potential difference (~180–200 mV) on both sides of the IMM, which is the mitochondrial membrane potential ($\Delta\Psi$m) (Smith et al., 2012). Changes in mitochondrial membrane potential or even minor changes will greatly affect the function of mitochondria.

Existing mitochondria-targeting small molecules include triphenylphosphonium, dequalinium, (E)-4-(1H-Indol-3-ylvinyl)-N-methylpyridineiodide, tetramethylrhodamine ethyl ester (TMRE), guanidine salt, tetramethylrhodamine methyl ester (TMRM), rhodamine 19, rhodamine 123 and tetrachlorotetraethyl benzimidazole carbocyanine iodine Compounds (5,5′,6,6′-tetrachloro-1,1′,3,3′-tetraethyl-imidacarbocyanine, JC-1) (Chazotte, 2011; Perelman et al., 2012; Cunha-Oliveira et al., 2018) (**Figure 2**). Most of them are delocalization lipophilic cations (DLCs). The lipid solubility of these molecules enables them to cross the cell membrane and mitochondrial membrane, and the positive charge enables them to enter MM under the action of the mitochondrial membrane potential, endowing them with mitochondrial targeting ability (Murphy, 2008). In addition, because the MTP of normal cell is lower than that of cancer cells and transformed cells, DLCs can preferentially concentrate in the pathological cells (Kalyanaraman et al., 2018). Most of these small molecules were discovered decades
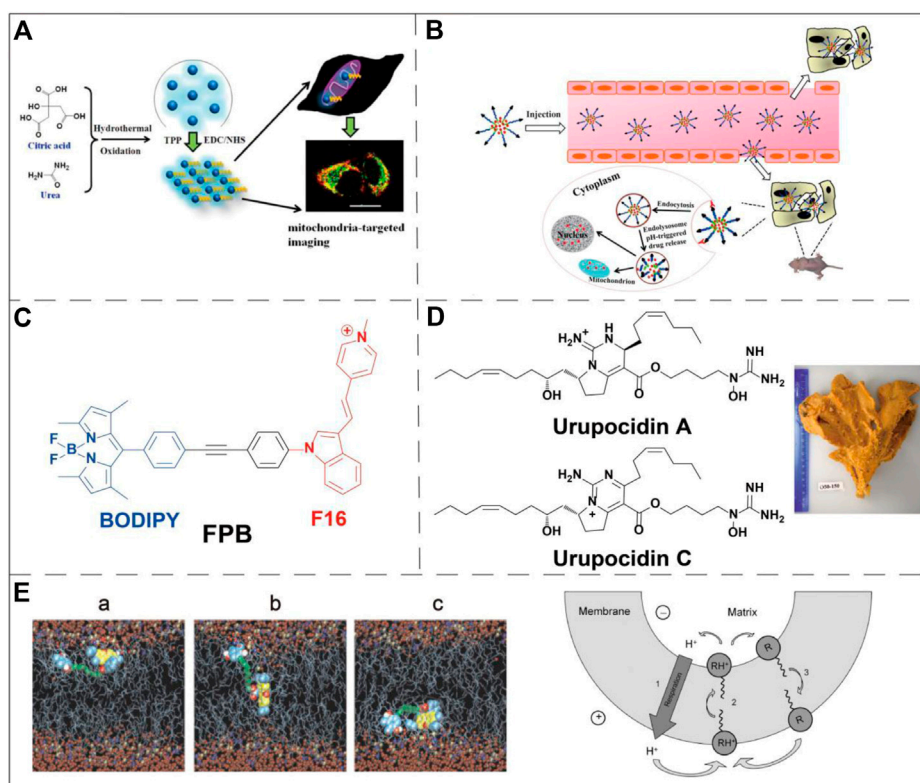
FIGURE 3 | Examples of mitochondria-targeting small molecules applications. **(A)** TPP$^+$ was conjugated to fluorescent carbon dots to selectively monitor mitochondria via one- or two-phono live cell image. Image reproduced with permission, from Wang et al. (2014). **(B)** Schematic diagram for the doxorubicin delivery in breast cancer cells using a pH-responsive DQA-Dox micelle system. Image reproduced with permission, from Ref Song et al. (2015). **(C)** Chemical structure of a conjugate molecule of F16 and BODIPY, F16 was used as a guiding ligand for mitochondria. He et al. (2015). **(D)** Marine alkaloid sourced and guanidine-containing complex capable of targeting mitochondria. Image reproduced with permission, from Ref Dyshlovoy et al. (2020). **(E)** Snapshot of the permeation of Rh 19 derivative through bilayer lipid membrane (left panel) and schematic diagram of its mechanism (right panel, where R stands for a deprotonated neutral form, and RH$^+$ stands for a singly protonated cationic form). Image reproduced with permission, from Ref Antonenko et al. (2011).

ago. Therefore, the use of small molecule-based mitochondria-targeting molecules for various biological applications is relatively mature.

Triphenylphosphonium (TPP$^+$)

The most successful case of using lipophilic cations for mitochondrial targeting is the discovery of triphenylphosphonium (TPP$^+$) (Liberman et al., 1969; Wang et al., 2020). The review written by Kalyanaraman et al. comprehensively summarizes the structures and synthesis of TPP$^+$-based compounds and their applications in biology (Zielonka et al., 2017). Here we will briefly highlight several biological applications using TPP$^+$ for mitochondrial targeting. TPP$^+$ contains three benzene rings that enable incorporation into many functional molecules and form a delocalized positive charge that can pass through the mitochondrial double-layer hydrophobic membrane. Many biologically active molecules have been conjugated to TPP$^+$ to realize mitochondrial targeting. For example, the antioxidant vitamin E linked to TPP$^+$ can more effectively protect mitochondria from oxidation. Chemically linking doxorubicin (Dox) and TPP$^+$ showed a good mitochondria-targeting effect, and induced

tumor cell apoptosis through the mitochondrial pathway, overcoming tumor cell drug resistance (Kalinovich et al., 2016). The chemical combination of TPP$^+$ with nano-formulations also has the effect of mitochondrial targeting. For example, paclitaxel-loaded liposomes prepared using TPP$^+$-modified polyethylene glycol-phosphatidylethanolamine (PEG-PE) have shown to be effective in targeting mitochondria in cancer cells (Biswas et al., 2012a). Similar designs include TPP$^+$-modified polyamidoamine (PAMAM), coumarin-iron oxide (CIO), gold nanoparticles (AuNPs) and polyglycolic acid-polyethylene glycol (PLGA-PEG) nanoparticles, etc (Biswas et al., 2012b; Jung et al., 2015; Marrache and Dhar, 2015; Pathak et al., 2015; Agrawal et al., 2017; Wang et al., 2017). All these TPP$^+$-modified nanovehicles exhibit mitochondrial targeting ability and excellent anti-tumor effect *in vivo* and *in vitro*. In addition, TPP$^+$ has been widely used in the design of fluorogenic probes for the detection of mitochondrial biomarkers (Wang et al., 2014; Fu et al., 2021) (**Figure 3A**). By conjugating TPP$^+$, a NIR reporter, and a sulfenic acid-reactive group, Gao et al. synthesized a novel NIR probe DATC, which is able to visualize endogenous protein sulfenic acids expressed in the mitochondria (Gao et al., 2020).

Dequalinium (DQA)

Dequalinium (DQA) is a lipophilic compound discovered by Weiss et al. (1987). DQA consists of two cationic quinoline groups connected by a 10-carbon alkyl chain. It is a delocalized lipophilic cationic molecule with a mitochondrial targeting effect. Weiss et al. found that this compound inhibited the proliferation of multiple cancer cell lines both *in vitro* and *in vivo*. Studies have shown that DQA can induce ROS production by inhibiting ATP synthesis, which further leads to the expression of cytochrome c and the decline of mitochondrial membrane potential. This pathway finally activates the caspase-3/9 dependent endogenous apoptosis pathway (Sancho et al., 2007). Therefore, the cytotoxicity of DQA limits its application in many biological studies, such as fluorescent probes or cell biology research. However, the cytotoxicity also makes DQA an excellent drug delivery ligand in the field of anti-cancer therapy. Studies have conjugated DQA chloride with Dox (DQA-Dox) to achieve targeted delivery of Dox to mitochondria. The drug conjugate DQA-Dox was found mainly accumulating in the mitochondria of MCF-7/ADR cells, and exhibited high cancer cell cytotoxicity (Song et al., 2015) (**Figure 3B**).

(E)-4-(1H-Indol-3-ylvinyl)-N-Methylpyridineiodide (F16)

As a delocalized lipophilic cationic molecule, (E)-4-(1H-Indol-3-ylvinyl)-N-methylpyridineiodide (F16) exhibits a mitochondrial targeting effect. It was initially discovered via cell-based high-throughput screening. This small molecule can selectively inhibit the proliferation of a variety of cancer cell lines (Rathinavelu et al., 2017). Similar to DQA, F16 itself is cytotoxic, its accumulation in mitochondria can cause the depolarization of mitochondrial membranes, destroy the mitochondrial structure, leading to the opening of the mitochondrial permeability transformation channel. The opening of the pores subsequently causes the production of cytochrome c and promotes cell apoptosis (Spivak et al., 2021). By combining F16 with the widely used boron-dipyrromethene (BODIPY) fluorescent dye through a phenylethynyl linker, a dual-functional mitochondria-targeting molecule was prepared (**Figure 3C**). This conjugate possesses anti-cancer activity, optical properties suitable for bioimaging and cancer cell specificity. Cell-based viability assays showed that the conjugate's IC_{50} against SGC-7901 cells is very close to that of its BODIPY-free precursor, F16. This result suggests that the installation of BODIPY (without obvious toxicity in free form) does not interfere the cytotoxicity of the original drug F16 (He et al., 2015).

Guanidine/Biguanidine

Both guanidine and biguanide are delocalized lipophilic cationic molecules, which have a delocalized positive charge and therefore exhibit stronger lipophilicity than groups with a localized charge. Some studies have found that a new marine guarantin alkaloid can selectively kill prostate cancer cells and that the cytotoxic effect is related to mitochondrial targeting (Dyshlovoy et al., 2020) (**Figure 3D**). This study confirmed for the first time that mitochondrial targeting is the central mechanism of the anti-cancer effect of these molecules and their derivatives. At the same time, it was proposed that isolated alkaloids could be used to treat mitochondrial membrane infiltration, and then release cytotoxic mitochondrial proteins into cell cytoplasm, upregulate ROS, and finally promote apoptosis of prostate cancer cells. Similar to DQA and F16, the cytotoxicity of guanidine and biguanide limit their applications in certain types of biological studies.

Rhodamine

Rhodamine 123 (Rh123) is the most common member of the rhodamine-based targeting agents. Johnson and his colleagues verified the localization of Rh123 in the mitochondria of living cells in 1980 (Johnson et al., 1980). Due to the lipophilic and cationic properties, Rh123 is able to penetrate the IMM driven by the mitochondrial membrane potential and accumulate in the MM. As a fluorescent dye, Rh123 has been widely used to measure the mitochondrial membrane potential (Pan et al., 2020). Notably, Rh 123 exhibits selective anticancer activity in *in vivo* tumor models. The combination of 2-deoxyglucose or methylglyoxal bisamidinylhydrazone with Rh123 may also further enhance this selective cytotoxicity (Kageyama et al., 2005). However, in relevant clinical experiments, the maximum tolerated dose of Rh123 is low, and excessive Rh123 exhibited severe cytotoxicity (Jones et al., 2005). Rhodamine 19 (Rh19), the successor of Rh123, exhibits considerable mitochondrial targeting activity, and more recently has replaced TPP$^+$ for the design of drug conjugate showing excellent mitochondrial targeting ability and anti-cancer activity (Antonenko et al., 2011) (**Figure 3E**). Compared with TPP$^+$, intrinsic fluorescence of Rh19 enables live-time monitoring mitochondrial via confocal microscopy. Rh19 has also been utilized to study the expression behavior of related active substances in mitochondria by means of super-resolution micro-imaging (Miljanic et al., 2002; Khailova et al., 2014); In addition, Rh19 is less cytotoxic than TPP$^+$ which further extend its applications in various biological research (Rogov et al., 2016).

Transition Metal Complex Targeting

The use of metal complexes in biological applications has seen remarkable advances in recent decades (Allardyce et al., 2005; Coogan and Fernández-Moreira, 2014). These modularly prepared metal complexes usually contain easily modified organic ligands (Lo and Kam-Wing, 2015; Wang et al., 2016). In recent years, metal complexes that specifically target organelles have been conjugated to anticancer drugs in order to improve the therapeutic effect of the drugs (Ma et al., 2014).

Zhou et al. designed a copper complex CTB ([Cu(ttpy-tpp)Br$_2$]Br (ttpy-tpp = 4′-*p*-Tolyl-(2,2′:6′,2″-terpyridyl) triphenylphosphonium bromide) which could target mitochondria in drug-resistant tumor cells and overcome the resistance to cisplatin (Zhou et al., 2014) (**Figure 4A**). Hu et al. demonstrated that gold (III) meso-tetraphenylporphyrin (gold-1a) had excellent mitochondrial targeting ability and potential anticancer activity via targeting heat-shock protein 60 (Hsp60) (Hu et al., 2016) (**Figure 4B**). Sun et al. found that a metal complex named BODIPY-pt which was composed by the combination of the fluorescent dye BODIPY and platinum
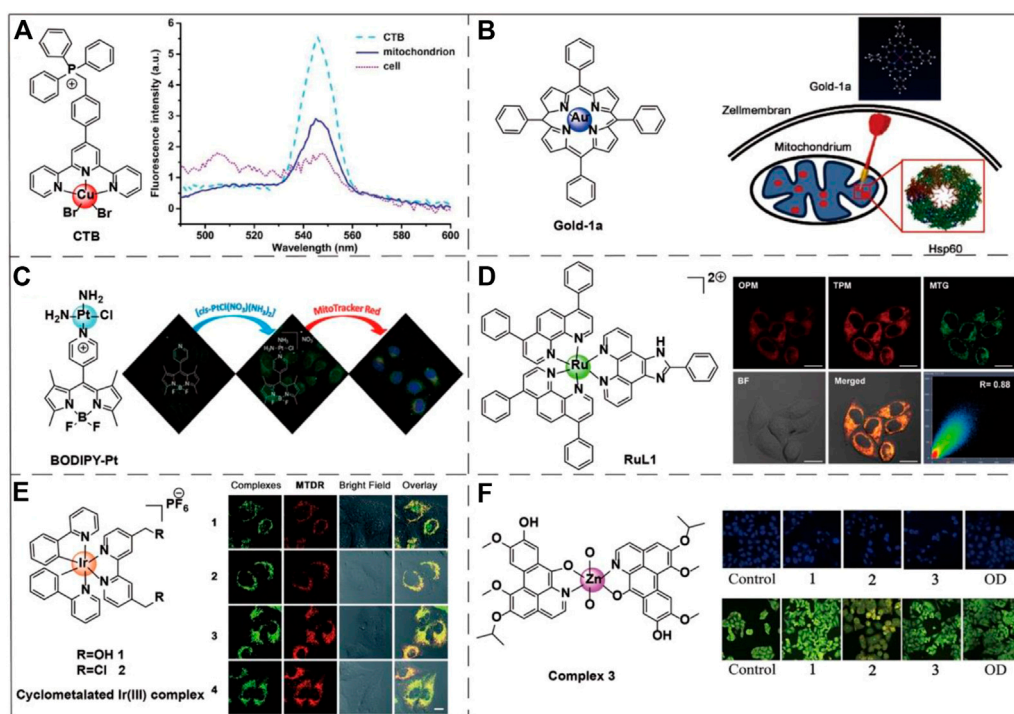
FIGURE 4 | Chemical structures of six transition metal complexes and the corresponding applications. **(A)** The chemical structure of CTB and its fluorescence spectra in different biological environments. Image reproduced with permission, from Zhou et al. (2014). **(B)** The chemical structure of gold-1a and its effective targeting to the mitochondrial chaperone Hsp60. Image reproduced with permission, from Ref Hu et al. (2016). **(C)** The chemical structure of BODIPY-Pt is also sensitive to mitochondrial membrane potential. On the right side of the figure is the fluorescence diagram of BODIPY-Pt under MitoTracker™ Red. Image reproduced with permission, from Ref Sun et al. (2015). **(D)** RuL1 is a Ru(II) polyamide complex-based photodynamic anticancer drug that targets mitochondria. On the right side of the figure are the one-photon (OPM) and two-photon (TPM) fluorescence imaging of the Ru(II) metal complex colocalized with the MitoTracker™ Green (MTG) in HeLa cells. Image reproduced with permission, from Ref Liu et al. (2015). **(E)** An example of Ir(III) transition metal complex structure capable of accumulating within mitochondria. The right-hand side of the figure shows the fluorescence of the Ir(III) metal complex in A549 cells nicely colocalized with the MitoTracker™ Deep Red staining. Image reproduced with permission, from Ref Cao et al. (2017). **(F)** An example of a Zn(II) transition metal complex structure capable of inducing mitochondrial apoptosis. The right side of the figure shows the DAPI nuclei staining (blue color) and AO/EB viability staining (green color) of HepG2 cells apoptosis caused by three transition metal complexes via a caspase-dependent mitochondrion pathway. 1, 2, and 3, respectively, represent Co(II), Ni(II), and Zn(II) complexes. The oxoaporphine derivative (OD) has good anti-tumor activity and was used as the positive control. Image reproduced with permission, from Qin et al. (2017).

(PtIV) could be selectively ingested by mitochondria. BODIPY-pt also exhibited excellent anti-proliferative activities against human cervical cancer (HeLa) and breast cancer (MCF-7) cell-lines (Sun et al., 2015) (**Figure 4C**). Recent studies have shown that ruthenium (RuII) (**Figure 4D**) and iridium (IrIII) (**Figure 4E**) complexes can target mitochondria (Liu et al., 2015; Cao et al., 2017; Yao et al., 2021). Especially in the treatment of cancer by photothermal therapy (PTT), the complexes with these two transition metals as the metal center can effectively target the mitochondria of cancer cells and enhance the therapeutic effect (Liu et al., 2015). Qin et al. designed three transition metal complexes with cobalt, nickel, and zinc as metal centers to conduct a comparative anti-cancer activity test. The experiments showed that all three transition metal complexes exhibited excellent anti-tumor activity and have great potential as anti-cancer drugs (Qin et al., 2017) (**Figure 4F**).

Mitochondria-Targeting Bioactive Molecule

Peptides have been widely used in the biological field due to their excellent selectivity, high activity and the mature solid-phase peptide synthesis (Boyle and Woolfson, 2011). For mitochondria-targeting peptides, various short peptides and polypeptides have been discovered which are proposed as an alternative to lipophilic cations for mitochondria-targeting molecules. These peptides usually carry hydrophobic (such as phenylalanine, tyrosine, isoleucine) and positively charged (such as arginine, lysine) amino acids. The corresponding mechanism for mitochondrial targeting is mainly based the targeting of mitochondrial membrane potential or the mitochondrial transmembrane proteins. Although there are numerous studies on mitochondria-targeting peptides, there is still plenty of scope for this approach and potential to be further explored.

Mitochondria-Penetrating Peptides (MPPs)

Mitochondria-penetrating peptides (MPPs) are a type of widely utilized mitochondria-targeting molecules that have been discovered in 2008. Horton et al. gave a comprehensive introduction to the discovery process and the synthetic methods of MPPs (Horton et al., 2008). Wu et al. summarized recent advances in the applications of MPPs in cancer therapy via
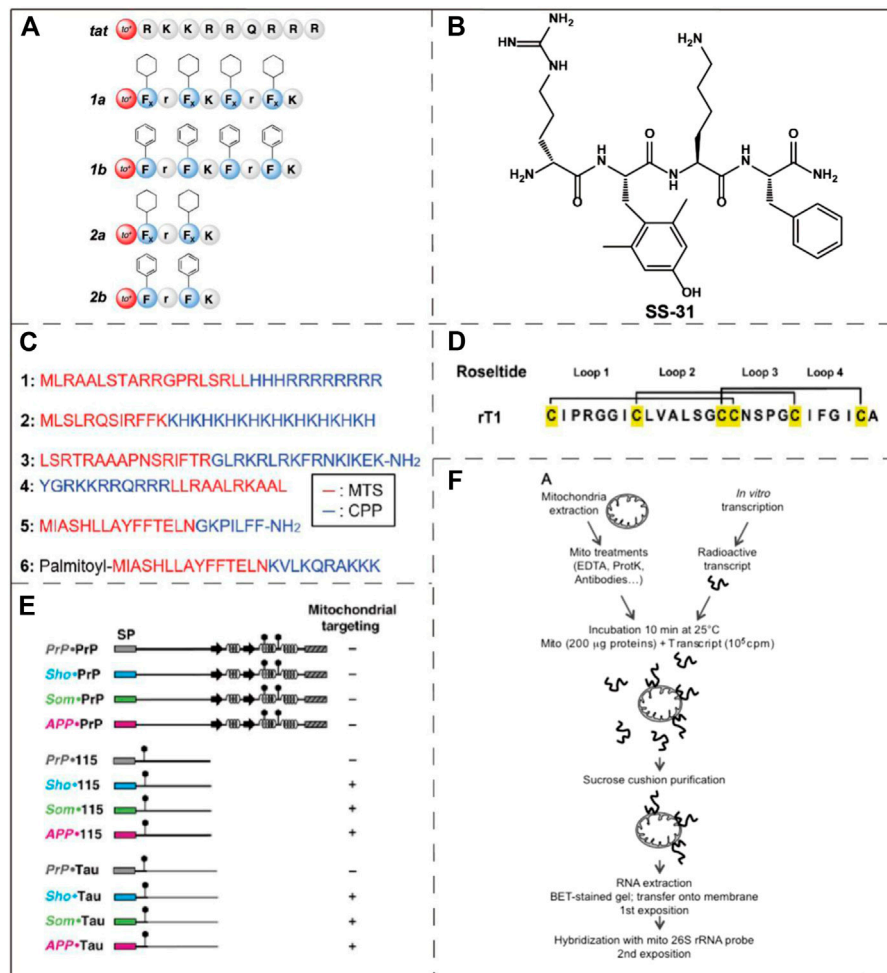
FIGURE 5 | Examples of mitochondria-targeting bioactive peptides and nucleic acids. **(A)** The structure of an array of MPPs which were designed by Yousif et al. Image reproduced with permission, from Ref Yousif et al. (2010). **(B)** The chemical structure of SS-31. Image reproduced with permission, from Ref Birk et al. (2013). **(C)** Amino acid sequences of six MTSs. Image reproduced with permission, from Ref Kim et al. (2020). **(D)** The structure of roseltide rT1. Image reproduced with permission, from Ref Kam et al. (2019). **(E)** Identification of mitochondrial targeting states by different ER signal peptides. Image reproduced with permission, from Ref Pfeiffer et al. (2013). **(F)** Naked mRNA can bind to isolated mitochondria. Reproduced, with permission, from Ref Michaud et al. (2014).

mitochondrial targeting (Wu et al., 2018). MPPs have excellent cell permeability and mitochondrial targeting because they have alternating cationic and hydrophobic residues. At the same time, Horton et al. consider that the uptake of MPPs by cells seems to be independent of the endocytosis pathway, excluding endosome/lysosome isolation, which also increases the chance of MPP reaching mitochondria. Yousif et al. designed an array of MPPs (**Figure 5A**), which is a short peptide library that can penetrate both cell membranes and mitochondrial membranes (Yousif et al., 2010). Chuah et al. used lysine-histidine (KH) peptide as a cell-penetrating peptide (CPP). KH peptide was coupled to two different mitochondria-targeting signals molecules (a 12-mer peptide from cytochrome c oxidase and a 32-mer peptide from ornithine transaminase). The resulting molecule encapsulated plasmid DNA by self-assembly and successfully realized mitochondrial transfection (Chuah et al., 2016). However, the use of mitochondrial membrane potentials

to target mitochondria has not been fully explored yet (Wu et al., 2018).

Szeto-Schiller (SS) Peptide

Szeto-Schiller (SS) peptides named for the researchers who discovered them (Zhao et al., 2004) constitute another type of mitochondria-targeting peptide. These peptides were initially developed as antioxidants, but significant accumulation in the IMM was observed. SS peptides have antioxidant activity due to its 2,4-dimethyltyrosine (Dmt) residues. In addition to reducing mitochondrial ROS, they also inhibit the production of cytochrome c. With the continuous optimizations on SS peptides, several prominent derivatives, for instance SS-31, have been reported. As one of the most potent SS-peptides, SS-31 has been widely explored in many disease models such as neurodegenerative disorders, heart failure and ischemia-reperfusion injury (Szeto and Schiller, 2011). SS-31 is currently

in phase II clinical trials, as a treatment for ischemia-reperfusion and microvascular injury (Wang et al., 2017). Although it has been proved that SS-31 is selectively localized to the IMM by interacting with cardiolipin, the exact mechanism of its mitochondrial targeting ability is still unclear (Birk et al., 2013) (**Figure 5B**).

Mitochondria-Targeting Sequences (MTSs)

Mitochondria-targeting sequences (MTSs) are usually composed of 20–40 amino acids, which usually bind to specific receptors on mitochondrial membrane (Neupert, 2015) (**Figure 5C**). The specific receptors commonly include a translation enzyme of the OMM (e.g. translocator of the OMM) and translation of inner membrane complex (e.g. translocator of the IMM). They play a role in the introduction of MTSs into the mitochondria, mainly powered by ATP or mitochondrial transmembrane potential. MTSs have some disadvantages which are its large structure, low solubility and insufficient permeability across the cell membrane (Yousif et al., 2009). Despite these shortcomings, the excellent selectivity and low toxicity of MTSs make them an appropriate choice in certain biological applications. Mossalam et al. fused tumor suppressor p53 to several MTSs to promote mitochondrial-induced rapid apoptosis (Mossalam et al., 2012). These MTSs are derived from Bcl-XL, the adventitia translocation enzyme (TOM 20), cytochrome C oxidase subunit VIII, and ornithine transcarbamylase, respectively. The MTSs applied that study target either the OMM or IMM by specifically recognizing and binding to the corresponding proteins. The result demonstrated that the interactions between p53 and mitochondria membrane proteins allows tuning of the apoptosis induction efficiency. The assisted p53-Bcl-XL interaction induced the greatest increase in programmed cell death. In the genetic study of Drosophila, Li et al. revealed the important role played by the mitochondrial protease YME1L in the clearance of poly (GR), and also found that poly (GR) could be potentially used as a mitochondria-targeting sequence (Li et al., 2020).

Cysteine-Rich Peptides (CRPs)

Cysteine-rich peptides (CRPs) are natural peptides that can be extracted from plants and have broad development opportunities (Kim et al., 2020). CRPs contain multiple cysteine residues and form special disulfide bonds, the excellent rigidity and tightness of which provide metabolic stability under physiological conditions (**Figure 5D**). Tam et al. confirmed a novel class of CRPs, roseltides (rT1-rT8), are human neutrophil elastase inhibitors (Loo et al., 2016). Among them, roseltide rT1 was originally developed as an inhibitor of a protease in humans, but it was found to have structural features that target mitochondria. Roseltide rT1 contains a positively charged loop1 and a hydrophobic loop2, which can be specifically recognized by translocator of the OMM and transport roseltide rT1 to the MM (Kam et al., 2019). The sequences of roseltide rT1 and MTSs have the common feature of amphiphilic helix structure. Roseltide rT1 has several advantages, such as resistance to proteolysis and rapid mitochondrial localization.

Endoplasmic Reticulum (ER) Signal Peptide

In eukaryotic cells, protein transport and targeting specific organelles is critically important to cell function and homeostasis. The ability to mobilize proteins to the endoplasmic reticulum (ER) and mitochondria mainly depends on the structure of the N-terminal signal peptides of the proteins. Pfeiffer et al. conducted a study and unexpectedly found that ER signal peptides from three special proteins can specifically target mitochondria (Pfeiffer et al., 2013) (**Figure 5E**). ER targeting occurs during protein co-translation, and mitochondrial targeting occurs after protein translation. The ER signal peptides can mediate ER co-translation and introduction. Therefore, when the ER signal peptides are fused with the N-terminal of the foreign polypeptides, the ER signal peptides have the ability to shuttle the foreign polypeptide into the ER. However, when the attached polypeptides are intrinsically disordered domain, the ER signaling peptide will introduce them into the mitochondria. Meanwhile, experimental studies have shown that the greater the effect of ER signal peptides on mitochondrial membrane potential, the lower its efficiency of introducing into ER. It is thus concluded that the targeting of ER signal peptides to mitochondria is inversely proportional to the ER targeting efficiency of heterologous polypeptide. At the same time, results also indicated that ER signal peptides can be used to target the MM and can affect the function of mitochondria. However, the exact mechanism of these ER signal peptides targeting mitochondria has not been fully illustrated.

mRNA

Among the proteins in the mitochondria, only a small fraction of the proteins produced are encoded by the mitochondrial genome, most of them are encoded by the nucleus and then imported into the mitochondria. These foreign proteins are translated by the free cytoplasmic multimers and finally transported to the mitochondria. It has also been verified that a large number of cytoplasmic genes encoding mitochondrial proteins are found on the surface of mitochondria in both plants and animals (Marc et al., 2002; Michaud et al., 2010; Matsumoto et al., 2012). Michaud et al. conducted an *in vitro* binding assay using isolated plant mitochondria to naked mRNA, and the results showed that naked mRNA can specifically bind to isolated mitochondria *in vitro*, but required the participation of the mitochondrial outer membrane complex (Michaud et al., 2014) (**Figure 5F**). Therefore, some mRNAs may allow specific targeting of mitochondria, but there is no clarity in relation to the relevant mechanisms.

Mitochondria-Targeting Nanomaterials

Mitochondria-targeting molecule-drug conjugates usually have disadvantages such as poor water solubility and cytotoxicity which limit their further applications in the clinic. One solution is to deliver therapeutic reagents to the tumor mitochondria using a nanoscale drug delivery system (DSS). Mitochondria-targeting nanomaterials generally have two ways to achieve mitochondrial targeting: 1) mitochondrial targeting is achieved by linking with targeted cationic molecules or biophilic
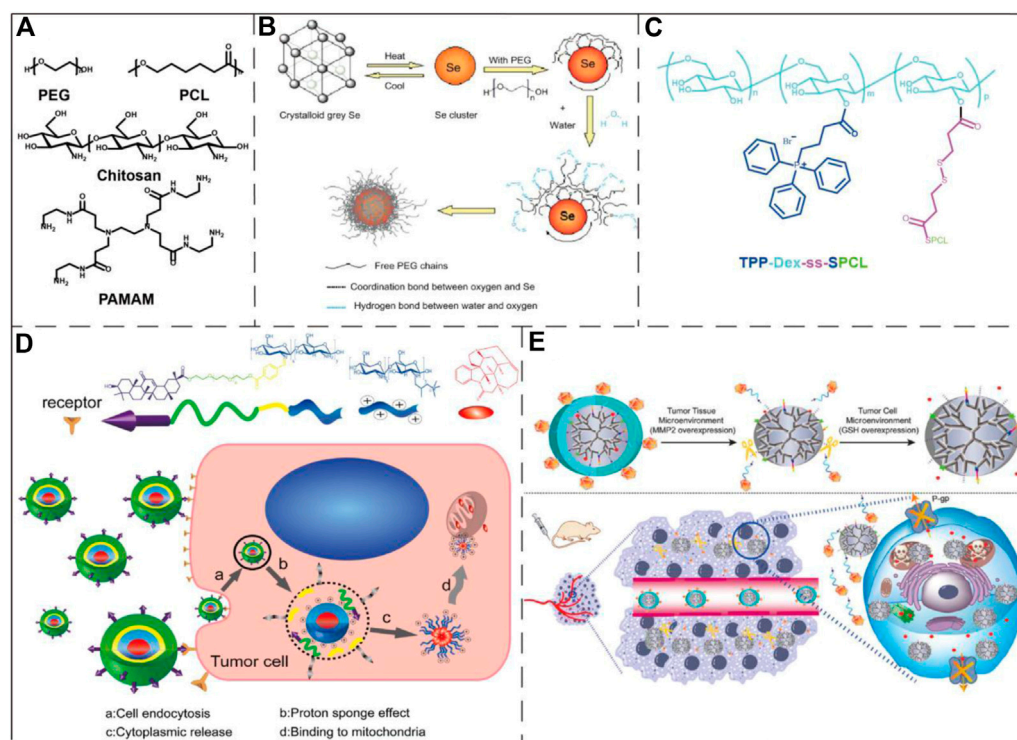
FIGURE 6 | Examples of polymeric/polymer-coated nanoparticles and micelles in the application of drug delivery to mitochondria. **(A)** The chemical structures of PEG, PCL, chitosan, and PAMAM. **(B)** Schematic diagram of a PEG-coated selenium cluster. Image reproduced with permission, from Ref Zheng et al. (2012). **(C)** The chemical structure of a mitochondria-targeting co-polymer with TPP$^+$ side chains. Image reproduced with permission, from Ref Tan et al. (2019). **(D)** Schematic illustration of the chitosan nanoparticle mitochondrial targeting process. The nanoparticles were first internalized (a) and then escaped from the endosome into the cytosol (b–c). Lastly, the nanoparticles reached to mitochondria via the positively charged quaternary amine groups and induced cell apoptosis. Image reproduced with permission, from Chen et al. (2015). **(E)** The upper part of the figure represented that the conjugate consisting of PAMAM and enzymatic detachable glucose-PEG was first exfoliated by the outer PEG layer after the action of matrix metalloproteinase 2, and then glutathione stimulated the release of PTX. The lower part of the figure shows the action process of the conjugate in the tumor-bearing mouse model. Image reproduced with permission, from Ref Ma et al. (2018).

peptide molecules, 2) a small number of nanomaterials of which the intrinsic physiochemical properties enable mitochondrial targeting. Commonly used mitochondria-targeting nanomaterials include liposomes, micelles, dendrimers, carbon nanoparticles, and metal nanoparticles or nanoclusters. Our recent review comprehensively summarized the bio-applications of the mitochondria-targeting DDSs (Yao et al., 2021).

Polymeric/Polymer-Coated Nanoparticles and Micelles

Polymer nanoparticles are assembled from amphiphilic polymers which have the advantages of high biocompatibility, low toxicity, high drug loading capacity, small size, easy modification and good aqueous solubility (Mahapatro and Singh, 2011). Some polymeric nanoparticles and micelles have been used in mitochondrial targeting, including polyethylene glycol (PEG), chitosan, dendrimers, polycaprolactone (PCL), hyaluronic acid and some micelles formed by small amphiphilic molecules, etc (**Figure 6A**). Zheng et al. reported the preparation of ultrasmall selenium nanoclusters with PEG (PEG-SeNCs) (**Figure 6B**). PEG-SeNCs exhibited stronger growth inhibition

and induced concentration-dependent apoptosis to the drug-resistant hepatocellular carcinoma (R-HepG2) cells. Further molecular investigation revealed that the anti-cancer effect was due to the depletion of mitochondrial membrane potential and generation of superoxide anions (Zheng et al., 2012). Tan et al. created a PCL-based mitochondria-targeting DDS, by using TPP$^+$ as mitochondria-targeting molecule. The resulting nanoparticle was applied in the treatment of metastatic breast cancer (Tan et al., 2019) (**Figure 6C**). Chen et al. designed a multifunctional chitosan nanoparticle which was able to achieve efficient intracellular transport and mitochondrial positioning and improve the anti-tumor efficacy (**Figure 6D**). The mitochondrial targeting was realized through the interaction of the positively charged nanoparticles and cancer cell mitochondria with the higher negative potential (Chen et al., 2015). Ma et al. constructed a mitochondria-targeting conjugate consisting of PAMAM and enzymatic detachable glucose-PEG that transported paclitaxel (PTX) into the mitochondria (**Figure 6E**). Their research results show that this conjugate can well target mitochondria and act on tumor cells, and can be used to make up for the multi-drug resistance problem of PTX (Ma et al., 2018).
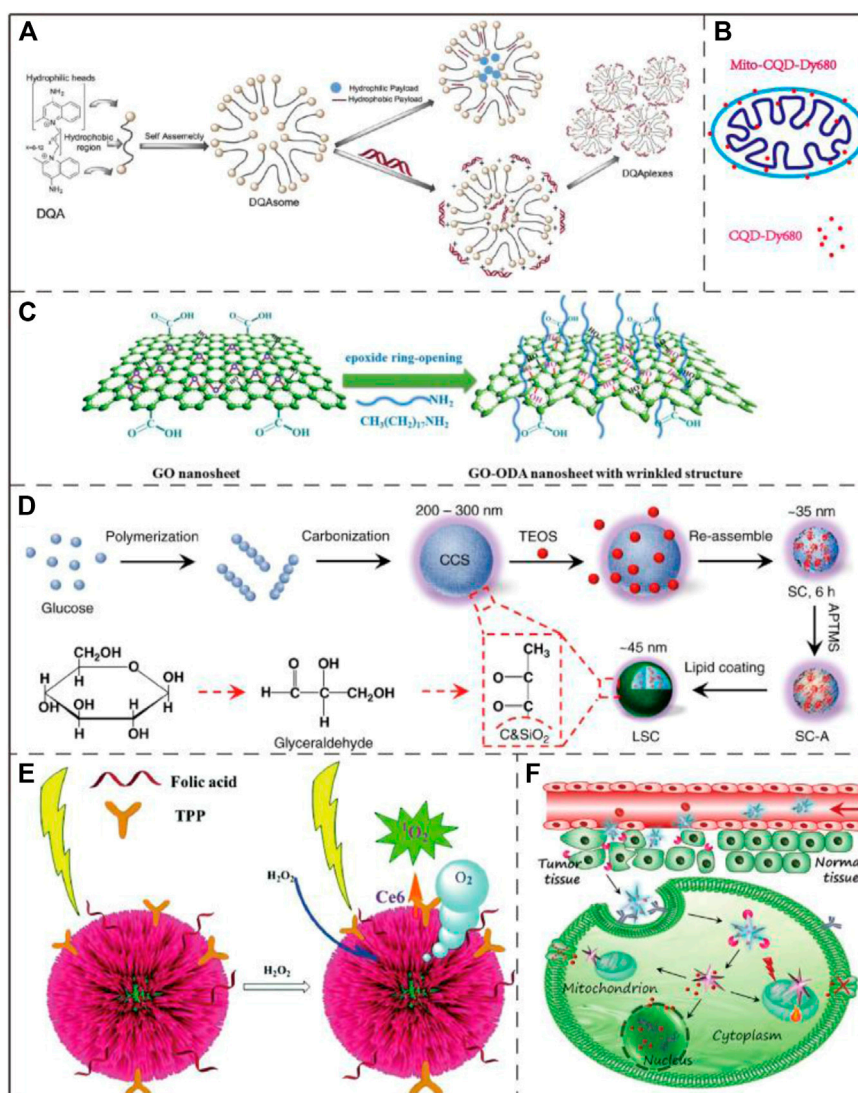
FIGURE 7 | Application examples of DQAsomes and four different types of inorganic nanoparticles. **(A)** Chemical structure of DQA and its self-assembly into liposome-like vesicles. Image reproduced with permission, from Ref Pathak et al. (2015). **(B)** A mitochondrial transport system based on CQDs. Image reproduced with permission, from Ref Zheng et al. (2018). **(C)** Schematic diagram of GO functionalization process. Image reproduced with permission, from Ref Zhang et al. (2020). **(D)** Schematic diagram of LSC-based nanoparticle fabrication. CCS, colloidal carbon sphere; TEOS, tetraethyl orthosilicate; SC, silica-carbon; APTMS (3-Aminopropyl) trimethoxysilane. Image reproduced with permission, from Ref Wang et al. (2018). **(E)** Schematic diagram of three-dimensional structure of Au@Pt nanoparticles and ROS generation process upon NIR light irradiation. Image reproduced with permission, from Ref Yang et al. (2017). **(F)** Schematic diagram of the process that AuNS nano-platform carries Dox enters into tumor cells by endocytosis and targets mitochondria to combine chemotherapy and PTT. Image reproduced with permission, from Ref Chen et al. (2017).

DQAsomes and DQA-Liposomes

As one of the most widely studied mitochondria-targeting small molecules (*Dequalinium (DQA)*), DQA forms vesicle-like aggregates with a diameter of 70–700 nm in an aqueous solution due to the molecule's amphiphilic nature. The resulting nanoparticles are termed DQAsomes. DQAsomes are widely used as carriers to deliver nucleic acids and cytotoxic drugs to mitochondria (**Figure 7A**). As a mitochondria-targeting molecule, DQA has certain selective cytotoxicity to cancer cells due to its activity of interrupting mitochondrial membrane potential, inducing ROS production and inhibiting ATP

synthesis (Galeano et al., 2005). Due to the low endosomal escape ability and transfection efficiency, the potential of DQAsomes in transfection and mitochondria-targeting drug delivery is limited (Weissig et al., 1998). However, more mitochondria-targeting nanomaterials based on DQA-liposomes have recently been identified (D'Souza et al., 2003). DQAsomes may be described as the prototype of mitochondria-targeting nanocarrier systems. Since the first biological application in 1998, DQAsomes have realized the transfer of small molecule drugs and nucleic acids to mitochondria in living cells (Volkmar, 2015).
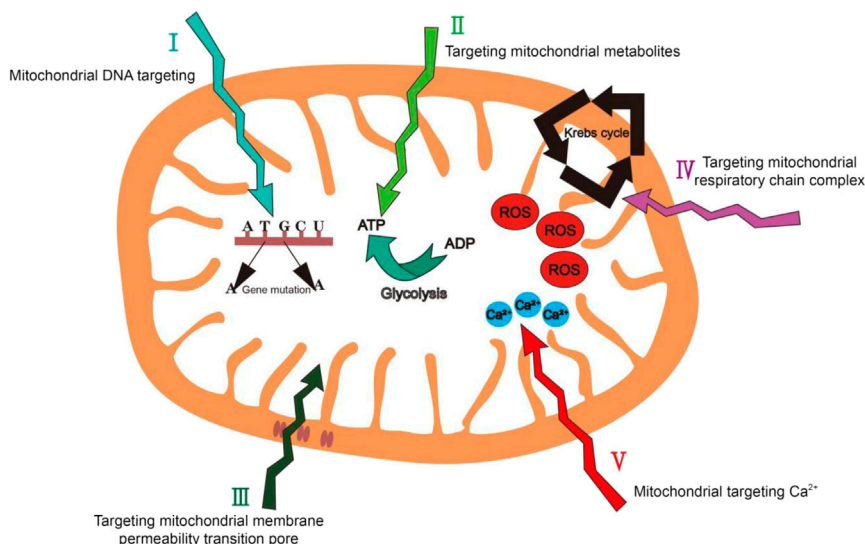
FIGURE 8 | Summary of mitochondrial targeting strategies we have proposed in this review.

Inorganic Nanoparticles

With the gradual deepening of scientific research, inorganic nanomaterials have become more and more extensive in the field of biomedicine no matter from the initial chiral inorganic nanoparticles or later enriching their properties with polymer modification or self-assembly (Cumbal et al., 2003; Nie et al., 2010; Xia et al., 2011). The use of inorganic nanoparticle materials for therapeutic purposes, imaging and drug delivery have been widely reported. Compared with organic nanoparticle materials, inorganic nanoparticle materials have the advantages of hydrophilicity, low toxicity and outstanding metabolic stability (Xu et al., 2019). Recently developed mitochondria-targeting inorganic nanomaterials include graphene oxide (GO), carbon quantum dots (CQDs), lipid membrane-coated silica-carbon (LSC) and metal nanoparticles.

Carbon Quantum Dot (CQDs)

Due to the stable fluorescence and extremely low cytotoxicity, carbon quantum dots (CQDs) have been used as fluorescent probes in the fields of bioimaging, biomarking and biosensing (Zheng et al., 2018) (**Figure 7B**). Hua et al. prepared a novel fluorescent CQD with an intrinsic mitochondrial targeting capacity through one-step hydrothermal treatment without further addition of other mitochondrial ligands. The as-synthesized CQD were employed for both mitochondrial imaging and mitochondria-targeting photodynamic cancer treatment (Hua et al., 2017).

Graphene Oxide (GO)

Graphene oxide (GO) features high stability and large specific surface area and can bind to mitochondrial therapeutic drugs through π-π accumulation and hydrophobic interaction (**Figure 7C**). It has been reported that single-walled carbon nanotubes (SWNTs) can selectively target mitochondria after functionalization due to mitochondrial transmembrane potential (Zhou et al., 2010). Similar to SWNTs, GO can also target

mitochondria based-on the same mechanism. Due to this intrinsic property, Wei et al. developed a photodynamic therapy (PDT) system that uses GO as a carrier to achieve drug delivery and on/off phototoxicity with mitochondrial targeting and attacking ability (Wei et al., 2016).

Lipid Membrane-Coated Silica-Carbon (LSC)

Wang et al. reported that the lipid membrane-coated silica-carbon (LSC) hybrid nanoparticle with the pyruvate groups can target mitochondria. This LSC nanoparticles had good bioavailability, strong optical absorption in the NIR region, good photodynamic ability and excellent PTT effect. Upon near-infrared (NIR) laser treatment, the LSC nanoparticles are able to promote mitochondrial ROS production. Experimental results further demonstrated that this novel LSC nanoparticles effectively inhibited the growth of multi-drug-resistant tumors without significant systemic toxicity (Wang et al., 2018) (**Figure 7D**).

Metal Nanoparticles

Among the metal nanoparticles, gold nanoparticles (AuNPs) are the most widely used metal nanoparticle in mitochondrial research (Costa et al., 2010; Giljohann et al., 2010; Ngwa et al., 2011). Marrache et al. co-conjugated AuNPs with TPP$^+$ and the energy blocker 3-bromopyruate (3-BP) to enhance its ability to target mitochondria and inhibit the metabolic ability of cancer cells at the same time (Marrache and Dhar, 2015). Lin et al. designed a metal nanoparticle Au@Pt where Pt formed a shell over the Au core, the nanoparticle was further functionalized with folic acid, TPP$^+$ and a photosensitizer, which exhibited enhanced PDT and PTT efficacy in cancer treatment (Yang et al., 2017) (**Figure 7E**). Chen et al. designed a nano-platform named AuNS-pep/Dox@HA based gold nanostar (AuNS), the mitochondrial targeting was achieved by the conjugation of cationic peptide R$_8$ and mitochondria-targeting peptide TPP-KLA to the AuNS

TABLE 1 | Summary of different types of mitochondria-targeting molecule and the corresponding targeting mechanisms and biological applications.

Targeted molecular types		Targeting mechanism		Ref.
Small molecules	TPP+	Mitochondrial membrane potential	Detection of mitochondria with fluorescent carbon dot	Wang et al. (2014)
	DQA	Mitochondrial membrane potential	Delivering drugs to breast cancer cells	Song et al. (2015)
	F16	Mitochondrial membrane potential	Treatment of cancer in combination with BODIPY	He et al. (2015)
	Guanidine/Biguanidine	Mitochondrial membrane potential	Can selectively kill prostate cancer cells	Dyshlovoy et al. (2020)
	Rhodamine	Mitochondrial membrane potential	Has good anticancer activity	Antonenko et al. (2011)
Transition metal complex	CTB	Link targeted small molecule TPP$^+$	Can target mitochondria in drug-resistant tumor cells and overcome resistance to cisplatin	Zhou et al. (2014)
	Gold-1a	Can specifically target Hsp60 targets on mitochondria	Has good anticancer activity	Hu et al. (2016)
	BODIPY-Pt	Mitochondrial membrane potential	Can inhibit the proliferation of human cervical cancer and human breast cancer cells	Sun et al. (2015)
	RuL1	Mitochondrial membrane potential	Two-photon photodynamic anticancer drug for mitochondrial target	Liu et al. (2015)
	Cyolometalated Ir(III) complex	Mitochondrial membrane potential	As anticancer drug by targeting mitochondria	Cao et al. (2017)
	Complex 3	Mitochondrial membrane potential	Has good anticancer activity	Qin et al. (2017)
Bioactive molecule	MPPs	Mitochondrial membrane potential and lipotropism	Mitochondrial transport vector	Yousif et al. (2010)
	SS peptides	Unclear	Used to protect mitochondrial crista	Birk et al. (2013)
	MTSs	Recognizing specific receptors on mitochondria	Carrying medicine for treating tumor	Mossalam et al. (2012)
	CRPs	Recognizing specific receptors on mitochondria	Promote ATP production	Kam et al. (2019)
	ER signal peptide	Unclear	Temporary non-biological application	Pfeiffer et al. (2013)
	mRNA	Unclear	Temporary non-biological application	Michaud et al. (2014)
Nanomaterials	Polymeric/polymer-coated nanoparticles and micelles	Binding to molecules with targeting capability	Can deliver drug, treat cancer and tumor	Zheng et al. (2012); Chen et al. (2015); Ma et al. (2018)
	DQAsomes and DQA-liposomes	Mitochondrial membrane potential and lipotropism	Transfer of small molecule drugs and nucleic acids to the mitochondria of living cells	Volkmar (2015)
	Inorganic nanoparticles	Binding to molecules with targeting capability	For mitochondrial image and mitochondrial targeted photodynamic cancer treatment	Hua et al. (2017)

surface. This nano-platform combined chemotherapy (Dox) and PTT, and exhibited strong tumor growth inhibition both *in vitro* and *in vivo* (Chen et al., 2017) (**Figure 7F**). By using the specific reaction between 1,3-cyclohexanedione (CHD) and the sulfenic acids from oxidized proteins in tumor mitochondria, Ding et al. successfully enhanced the tumor accumulation and retention of AuNPs in cancer cells, greatly improving the sensitivity of X-ray computed tomography (CT) imaging and the radiotherapy effect of live mouse tumors. (Ding et al., 2020).

MITOCHONDRIAL TARGETING STRATEGIES

Based on the structure and functional characteristics of mitochondria, in addition to the well-developed targeting strategies (i.e. targeting mitochondrial membrane potential and mitochondrial membrane proteins), here we propose five promising mitochondrial biomarkers which have not been fully explored yet: 1) mitochondrial genetic information; 2)

mitochondrial metabolites; 3) the mitochondrial membrane permeability transition pore 4) the mitochondrial respiratory-chain complex and 5) mitochondrial Ca^{2+} (**Figure 8**).

Mitochondrial DNA

Mitochondrial DNA (mtDNA) has 16.5 kb base pairs and encodes 13 complexes. There is only one type of mtDNA in an organism. However, mtDNA lacks the protection of histidine protein, has weak repairability and is vulnerable to damage. In tumor cells, there are a large number of mtDNA mutations (Fliss et al., 2000). The base T to A or G to A is the most mutation type, and the induction of ROS may also be related to this mutation. The accumulation of mitochondrial DNA mutations leads to serious, currently incurable diseases. Therefore, it can be used as a mitochondrial biomarker in tumor cells (Gao et al., 2019).

Mitochondrial Metabolites

Mitochondria use glycolysis to maintain cell proliferation and ATP level (Jr and Thompson, 2010). The level of cellular ATP is highly sensitive to external environmental stimuli, including hypoxia,

hormones, nutrients and cytotoxic agents (Ashcroft and Gribble, 1998). In normal cells, OXPHOS is the main source of ATP. Nicotinamide adenine dinucleotide (NADH) pyruvate that is produced by oxidative glycolysis increases ATP production along the electron transfer chain through the IMM. However, during the process of tumor cell formation, glycolysis and ATP production as well as the activity of certain enzymes has changed, making tumor cells rely more on glycolysis to meet their energy needs. The changes in tumor cell metabolism provide opportunities targeting tumor cell mitochondria (Tragni et al., 2021).

Mitochondrial Membrane Permeability Transition Pore (MPTP)

The mitochondrial membrane permeability transition pore (MPTP) a protein which is the structural basis of mitochondrial permeability transformation function. MPTP is very sensitive to the changes of the concentrations of multiple cellular ions, especially for the intracellular signal transduction system. Excessive influx of Ca^{2+} ions, oxidation of mitochondrial glutathione and increased levels of ROS will cause the continuous opening of membrane channel pores, resulting in the production of cytochrome c and the attenuation of mitochondrial membrane potential (Saotome et al., 2005). Therefore, MPTP has a very important effect in cell survival and apoptosis. The turning on of MPTP can cause mitochondria to depolarize, and abnormal MPTP turning on will result in significant change of the mitochondrial membrane potential, causing mitochondria to secrete apoptosis factors into the cytoplasm leading to cell death. The difference in MPTP between tumor cells and normal cells makes MPTP become an effective therapeutic target for the treatment of cancers (Berridge et al., 2009).

Mitochondrial Respiratory Chain Complex

The mitochondrial respiratory chain is composed of five complexes and is located on the IMM (Rustin et al., 1997). In tumor cells, the electron transport chain activity is 20–30% lower than in normal cells (Galli et al., 2003). This is because the activity of superoxide dismutase 1 will decrease with the gradual development of tumor, while the activity of nitric oxide synthase will increase significantly, which further result in disordered level of OXPHOS in tumor cells (Sanchez-Pino et al., 2007). Therefore, the lower electron transport chain activity is usually considered as a biomarker of tumors. The mitochondria-targeting groups that are designed based on the disordered level of mitochondrial respiratory chain complex will also have an excellent targeting ability for tumor cell mitochondria.

Mitochondrial Ca^{2+}

Mitochondria play an important regulatory role in Ca^{2+} ion signals and Ca^{2+} ions have key physiological effects in the process of cell energy metabolism and signal transmission. Its overload can lead to a variety of pathological conditions, including neuronal apoptosis and death in nervous system diseases (Li et al., 2014). Therefore, targeting Ca^{2+} inside mitochondria to treat related diseases, most of which are nervous system diseases, has emerged as a promising mitochondrial targeting strategy (Waldeck-Weiermair et al., 2019).

SUMMARY AND OUTLOOK

In this review, we summarize and highlight the current advances in mitochondria-targeting molecules and materials (**Table 1**). With the discovery of more and more mitochondrial-related diseases, disease treatments that target mitochondria have received increasing attentions, which also indicates the urgency and broad prospect of the research and development of mitochondria-targeting agents. Different diseases and cellular environments have specific requirements for mitochondria-targeting agents. To be more specific, for the treatment of mitochondrial disease, the toxicity of the targeting agents needs to be reduced as much as possible. On the other hand, in order to kill harmful cells such as tumor cells, the cytotoxicity of these molecules may have a beneficial effect. In addition, mitochondria-targeting agents have also been widely used in mitochondrial imaging and monitoring, which will facilitate the physiological studies of mitochondria and generate novel mitochondrial theragnostic methods. Therefore, a variety of targeting agents is needed to meet the requirements of different situations. However, based on the current research progress of mitochondria-targeting agents, this goal has not been fully achieved.

Mitochondria-targeting small molecules are widely used in various applications. Most of these mitochondria-targeting molecules can be directly conjugated with drugs, which have the advantage of enabling relatively accurate targeted delivery of drugs to the mitochondria. Among all the mitochondria-targeting molecules, TPP[+] is the most commonly used molecule due to the high efficiency, flexible conjugation strategy and low cost. While Rh19, as the successor, holds several advantages over TPP[+], although the applications of Rh19 in biological studies still need to be further explored. However, the conjugation of such mitochondria-targeting molecules and drugs generally has the disadvantage of poor water solubility, and some mitochondria-targeting ligands have significant cytotoxicity. Notably, due to the bulky size of those molecules, direct conjugation of them to drugs may affect the activity and therapeutic effects of the conjugated drugs. Therefore, mitochondria-targeting small molecules that have low cytotoxicity, high water solubility and relatively small size should be the future development direction.

Mitochondria-targeting biomolecules are a kind of targeting groups with good development prospects at present. Most of these mitochondria-targeting macromolecules are amino acid-based polypeptides. Compared with the mitochondria-targeting small molecules, biomolecules have excellent specificity against mitochondria to a great extent without causing adverse effects on other organelles or cells. This kind of targeting agent has little or even negligible toxicity to cells. However, the exact targeting mechanism of many mitochondria-targeting biomolecules that have been identified and applied is still unclear. Thus, the development direction of such mitochondria-targeting groups is not only to find new substances that can target mitochondria, but also to explore their targeting mechanism. We believe that the discovery of the targeting mechanism of these targeting groups will greatly promote their development and clinical applications.

Mitochondria-targeting nanomaterials can be used as a platform or carrier to shuttle a drug payload to the organelle,

so they should be considered the most urgently needed targeting group for development in clinical application. However, due to the uncertainty of their *in vivo* distribution, immunogenicity and excretion, the clinical application of these nanomedicines is still lagging behind. Mitochondria-targeting nanomaterials should continue to develop toward multi-function, improve the efficiency of treatment. However, many of them are currently only limited to laboratories or research institutes. Future development, such as the enhancement of their blood-brain barrier permeability will hold great potential in the treatment of neurodegenerative diseases which are widely linked with mitochondrial dysfunction.

In summary, research on mitochondria-targeting moieties still has a long way to go. It not only needs to meet the requirements of scientific research, but more importantly, it needs to be applied clinically to meet various requirements for the treatment of mitochondrial diseases and solve more mitochondrial medical problems.

AUTHOR CONTRIBUTIONS

HW Wrote draft of article; BF Wrote draft of article; BP Proposed the review topic, revised draft of article; LW Revised draft of article; YX Revised draft of article; HB Revised draft of article; SL Revised draft of article; NV Outlined review structure, revised draft of article. LL Outlined review structure, revised draft of article; LF Revised draft of article; WH Revised draft of article.

FUNDING

REFERENCES

Agrawal, P., Singh, R. P., Sonali, L., Kumari, G., Koch, B., Rajesh, C. V., et al. (2017). TPGS-chitosan Cross-Linked Targeted Nanoparticles for Effective Brain Cancer Therapy. *Mater. Sci. Eng. C.* 74, 167–176. doi:10.1016/j.msec.2017.02.008

Allardyce, C. S., Dorcier, A., Scolaro, C., and Dyson, P. J. (2005). Development of Organometallic (Organo-transition Metal) Pharmaceuticals. *Appl. Organometal. Chem.* 19 (1), 1–10. doi:10.1002/aoc.725

Antonenko, Y. N., Avetisyan, A. V., Cherepanov, D. A., Knorre, D. A., Korshunova, G. A., Markova, O. V., et al. (2011). Derivatives of Rhodamine 19 as Mild Mitochondria-Targeted Cationic Uncouplers. *J. Biol. Chem.* 286 (20), 17831–17840. doi:10.1074/jbc.M110.212837

Ashcroft, F. M., and Gribble, F. M. (1998). Correlating Structure and Function in ATP-Sensitive K+ Channels. *Trends Neurosciences* 21 (7), 288–294. doi:10.1016/s0166-2236(98)01225-9

Ashwini, R., Ganesan, V., Michael, B., and Monojit, D. (2015). Mitochondrial Dysfunction in Schizophrenia: Pathways, Mechanisms and Implications. *Neurosci. Biobehav Rev.* 48, 10–21. doi:10.1016/j.neubiorev.2014.11.005

Baldassarro, V. A., Krężel, W., Fernández, M., Schuhbaur, B., Giardino, L., and Calzà, L. (2019). Neural Stem Cells of Parkinson's Disease Patients Exhibit Aberrant Mitochondrial Morphology and Functionality. *Stem Cel Rep.* 37, 878–889. doi:10.1016/j.stemcr.2019.03.00410.1016/j.scr.2019.101443

Berridge, M. V., Herst, P. M., and Lawen, A. (2009). Targeting Mitochondrial Permeability in Cancer Drug Development. *Mol. Nutr. Food Res.* 53 (1), 76–86. doi:10.1002/mnfr.200700493

Birk, A. V., Liu, S., Soong, Y., Mills, W., Singh, P., Warren, J. D., et al. (2013). The Mitochondrial-Targeted Compound SS-31 Re-energizes Ischemic Mitochondria by Interacting with Cardiolipin. *Jasn* 24 (8), 1250–1261. doi:10.1681/ASN.2012121216

Biswas, S., Dodwadkar, N. S., Deshpande, P. P., and Torchilin, V. P. (2012a). Liposomes Loaded with Paclitaxel and Modified with Novel Triphenylphosphonium-PEG-PE Conjugate Possess Low Toxicity, Target Mitochondria and Demonstrate Enhanced Antitumor Effects In Vitro and In Vivo. *J. Controlled Release* 159 (3), 393–402. doi:10.1016/j.jconrel.2012.01.009

Biswas, S., Dodwadkar, N. S., Piroyan, A., and Torchilin, V. P. (2012b). Surface Conjugation of Triphenylphosphonium to Target Poly(amidoamine) Dendrimers to Mitochondria. *Biomaterials* 33 (18), 4773–4782. doi:10.1016/j.biomaterials.2012.03.032

Bornstein, R., Gonzalez, B., and Johnson, S. C. (2020). Mitochondrial Pathways in Human Health and Aging. *Mitochondrion* 54, 72–84. doi:10.1016/j.mito.2020.07.007

Bose, A., and Beal, M. F. (2016). Mitochondrial Dysfunction in Parkinson's Disease. *J. Neurochem.* 139 (Suppl. 1), 216–231. doi:10.1111/jnc.13731

Boyle, A. L., and Woolfson, D. N. (2011). De Novo designed Peptides for Biological Applications. *Chem. Soc. Rev.* 40 (8), 4295–4306. doi:10.1039/c0cs00152j

Cao, J.-J., Tan, C.-P., Chen, M.-H., Wu, N., Yao, D.-Y., Liu, X.-G., et al. (2017). Targeting Cancer Cell Metabolism with Mitochondria-Immobilized Phosphorescent Cyclometalated Iridium(iii) Complexes. *Chem. Sci.* 8, 631–640. doi:10.1039/C6SC02901A

Chan, D. C. (2006). Mitochondria: Dynamic Organelles in Disease, Aging, and Development. *Cell* 125 (7), 1241–1252. doi:10.1016/j.cell.2006.06.010

Chazotte, B. (2011). Labeling Mitochondria with TMRM or TMRE. *Cold Spring Harbor Protoc.* 2011 (7), prot5641–pdb. doi:10.1101/pdb.prot5641

Chen, S., Lei, Q., Qiu, W.-X., Liu, L.-H., Zheng, D.-W., Fan, J.-X., et al. (2017). Mitochondria-targeting "Nanoheater" for Enhanced Photothermal/chemo-Therapy. *Biomaterials* 117, 92–104. doi:10.1016/j.biomaterials.2016.11.056

Chen, Z., Li, G., and Liu, J. (2020). Autonomic Dysfunction in Parkinson's Disease: Implications for Pathophysiology, Diagnosis, and Treatment. *Neurobiol. Dis.* 134, 104700. doi:10.1016/j.nbd.2019.104700

Chen, Z., Zhang, L., Song, Y., He, J., Wu, L., Zhao, C., et al. (2015). Hierarchical Targeted Hepatocyte Mitochondrial Multifunctional Chitosan Nanoparticles for Anticancer Drug Delivery. *Biomaterials* 52, 240–250. doi:10.1016/j.biomaterials.2015.02.001

Chuah, J.-A., Matsugami, A., Hayashi, F., and Numata, K. (2016). Self-Assembled Peptide-Based System for Mitochondrial-Targeted Gene Delivery: Functional and Structural Insights. *Biomacromolecules* 17 (11), 3547–3557. doi:10.1021/acs.biomac.6b01056

Claudia, P., Thomas, K., Günter, R., and Siegfried, G. P. (2019). [Leber's Hereditary Optic Neuropathy]. *Klin Monbl Augenheilkd* 236 (11), 1271–1282. doi:10.1055/a-0972-1552

Coogan, M. P., and Fernández-Moreira, V. (2014). Progress with, and Prospects for, Metal Complexes in Cell Imaging. *Chem. Commun.* 50 (4), 384–399. doi:10.1039/c3cc45229h

Costa, C. S., Ronconi, J. V. V., Daufenbach, J. F., Gonçalves, C. L., Rezin, G. T., Streck, E. L., et al. (2010). *In vitro* effects of Silver Nanoparticles on the Mitochondrial Respiratory Chain. *Mol. Cel Biochem.* 342 (1-2), 51–56. doi:10.1007/s11010-010-0467-9

Cumbal, L., Greenleaf, J., Leun, D., and SenGupta, A. K. (2003). Polymer Supported Inorganic Nanoparticles: Characterization and Environmental Applications. *Reactive Funct. Polym.* 54 (1), 167–180. doi:10.1016/S1381-5148(02)00192-X

Cunha-Oliveira, T., Rego, A. C., Cardoso, S. M., Borges, F., Swerdlow, R. H., Macedo, T., et al. (2006). Mitochondrial Dysfunction and Caspase Activation in Rat Cortical Neurons Treated with Cocaine or Amphetamine. *Brain Res.* 1089 (1), 44–54. doi:10.1016/j.brainres.2006.03.061

D'Souza, G. G. M., Rammohan, R., Cheng, S. M., Torchilin, V. P., and Weissig, V. (2003). DQAsome-mediated Delivery of Plasmid DNA toward Mitochondria in Living Cells. *J. Control. Release* 92 (1-2), 189–197. doi:10.1016/s0168-3659(03)00297-9

Dauer, W., and Przedborski, S. (2003). Parkinson's Disease. *Neuron* 39 (6), 889–909. doi:10.1016/s0896-6273(03)00568-3

Ding, J., Mao, Q., Zhao, M., Gao, Y., Wang, A., Ye, S., et al. (2020). Protein Sulfenic Acid-Mediated Anchoring of Gold Nanoparticles for Enhanced CT Imaging and Radiotherapy of Tumors In Vivo. *Nanoscale* 12 (45), 22963–22969. doi:10.1039/d0nr06440h

Dyshlovoy, S. A., Kudryashova, E. K., Kaune, M., Makarieva, T. N., Shubina, L. K., Busenbender, T., et al. (2020). Urupocidin C: a New Marine Guanidine Alkaloid Which Selectively Kills Prostate Cancer Cells via Mitochondria Targeting. *Sci. Rep.* 10 (1), 9764. doi:10.1038/s41598-020-66428-5

Fliss, M. S., Usadel, H., Caballero, O. L., Wu, L., Buta, M. R., Eleff, S. M., et al. (2000). Facile Detection of Mitochondrial DNA Mutations in Tumors and Bodily Fluids. *Science* 287 (5460), 2017–2019. doi:10.1126/science.287.5460.2017

Fogle, K. J., Mobini, C. L., Paseos, A. S., and Palladino, M. J. (2019). Sleep and Circadian Defects in a Drosophila Model of Mitochondrial Encephalomyopathy. *Neurobiol. Sleep Circadian Rhythms* 6, 44–52. doi:10.1016/j.nbscr.2019.01.003

Fu, G., Yin, G., Niu, T., Wu, W., Han, H., Chen, H., et al. (2021). A Novel Ratiometric Fluorescent Probe for the Detection of Mitochondrial pH Dynamics during Cell Damage. *Analyst* 146 (2), 620–627. doi:10.1039/d0an01240h

Galeano, E., Nieto, E., García-Pérez, A. I., Delgado, M. D., Pinilla, M., and Sancho, P. (2005). Effects of the Antitumoural Dequalinium on NB4 and K562 Human Leukemia Cell Lines. *Leuk. Res.* 29 (10), 1201–1211. doi:10.1016/j.leukres.2005.03.014

Galli, S., Labato, M. I. s., Joffe´, E. B. d. K., Carreras, M. ı. C., and Poderoso, J. J. (2003). Decreased Mitochondrial Nitric Oxide Synthase Activity and Hydrogen Peroxide Relate Persistent Tumoral Proliferation to Embryonic Behavior. *Cancer Res.* 63 (19), 6370–6377. doi:10.1097/00002820-200310000-00012

Gammage, P. A., Viscomi, C., Simard, M.-L., Costa, A. S. H., Gaude, E., Powell, C. A., et al. (2018). Genome Editing in Mitochondria Corrects a Pathogenic mtDNA Mutation In Vivo. *Nat. Med.* 24 (11), 1691–1695. doi:10.1038/s41591-018-0165-9

Gao, F., Li, L., Fan, J., Cao, J., Li, Y., Chen, L., et al. (2019). An Off-On Two-Photon Carbazole-Based Fluorescent Probe: Highly Targeting and Super-resolution Imaging of mtDNA. *Anal. Chem.* 91 (5), 3336–3341. doi:10.1021/acs.analchem.8b04418

Gao, Y., Sun, R., Zhao, M., Ding, J., Wang, A., Ye, S., et al. (2020). Sulfenic Acid-Mediated On-site-specific Immobilization of Mitochondrial-Targeted NIR Fluorescent Probe for Prolonged Tumor Imaging. *Anal. Chem.* 92 (10), 6977–6983. doi:10.1021/acs.analchem.9b05855

Giljohann, D. A., Seferos, D. S., Daniel, W. L., Massich, M. D., Patel, P. C., and Mirkin, C. A. (2010). Gold Nanoparticles for Biology and Medicine. *Angew. Chem. Int. Edition* 49 (19), 3280–3294. doi:10.1002/anie.200904359

He, H., Li, D.-W., Yang, L.-Y., Fu, L., Zhu, X.-J., Wong, W.-K., et al. (2015). A Novel Bifunctional Mitochondria-Targeted Anticancer Agent with High Selectivity for Cancer Cells. *Sci. Rep.* 5 (1), 1–10. doi:10.1038/srep13543

Horton, K. L., Stewart, K. M., Fonseca, S. B., Guo, Q., and Kelley, S. O. (2008). Mitochondria-penetrating Peptides. *Chem. Biol.* 15 (4), 375–382. doi:10.1016/j.chembiol.2008.03.015

Hu, D., Liu, Y., Lai, Y.-T., Tong, K.-C., Fung, Y.-M., Lok, C.-N., et al. (2016). Anticancer Gold(III) Porphyrins Target Mitochondrial Chaperone Hsp60. *Angew. Chem. Int. Ed.* 55 (4), 1387–1391. doi:10.1002/anie.201509612

Hua, X.-W., Bao, Y.-W., Chen, Z., and Wu, F.-G. (2017). Carbon Quantum Dots with Intrinsic Mitochondrial Targeting Ability for Mitochondria-Based Theranostics. *Nanoscale* 9 (30), 10948–10960. doi:10.1039/c7nr03658b

Jeena, M. T., Kim, S., Jin, S., and Ryu, J.-H. (2019). Recent Progress in Mitochondria-Targeted Drug and Drug-free Agents for Cancer Therapy. *Cancers* 12 (1), 4. doi:10.3390/cancers12010004

Jhaveri, A., and Torchilin, V. (2016). Intracellular Delivery of Nanocarriers and Targeting to Subcellular Organelles. *Expert Opin. Drug Deliv.* 13 (1), 49–70. doi:10.1517/17425247.2015.1086745

Johnson, L. V., Walsh, M. L., and Chen, L. B. (1980). Localization of Mitochondria in Living Cells with Rhodamine 123. *Proc. Natl. Acad. Sci.* 77 (2), 990–994. doi:10.1073/pnas.77.2.990

Jones, L. W., Narayan, K. S., Shapiro, C. E., and Sweatman, T. W. (2005). Rhodamine-123: Therapy for Hormone Refractory Prostate Cancer, a Phase I Clinical Trial. *J. Chemother.* 17 (4), 435–440. doi:10.1179/joc.2005.17.4.435

Jr, W. G. K., and Thompson, C. B. (2010). Q&A: Cancer: Clues from Cell Metabolism. *Nature* 465 (7298), 562–564. doi:10.1038/465562a

Jung, H. S., Han, J., Lee, J.-H., Lee, J. H., Choi, J.-M., Kweon, H.-S., et al. (2015). Enhanced NIR Radiation-Triggered Hyperthermia by Mitochondrial Targeting. *J. Am. Chem. Soc.* 137 (8), 3017–3023. doi:10.1021/ja5122809

Kageyama, M., Namiki, H., Fukushima, H., Ito, Y., Shibata, N., and Takada, K. (2005). *In vivo* effects of Cyclosporin A and Ketoconazole on the Pharmacokinetics of Representative Substrates for P-Glycoprotein and Cytochrome P450 (CYP) 3A in Rats. *Biol. Pharm. Bull.* 28 (2), 316–322. doi:10.1248/bpb.28.316

Kalinovich, A. V., Mattsson, C. L., Youssef, M. R., Petrovic, N., Ost, M., Skulachev, V. P., et al. (2016). Mitochondria-targeted Dodecyltriphenylphosphonium (C12TPP) Combats High-Fat-Diet-Induced Obesity in Mice. *Int. J. Obes.* 40, 1864–1874. doi:10.1038/ijo.2016.146

Kalyanaraman, B., Cheng, G., Hardy, M., Ouari, O., Lopez, M., Joseph, J., et al. (2018). A Review of the Basics of Mitochondrial Bioenergetics, Metabolism, and Related Signaling Pathways in Cancer Cells: Therapeutic Targeting of Tumor Mitochondria with Lipophilic Cationic Compounds. *Redox Biol.* 14, 316–327. doi:10.1016/j.redox.2017.09.020

Kam, A., Loo, S., Dutta, B., Sze, S. K., and Tam, J. P. (2019). Plant-derived Mitochondria-Targeting Cysteine-Rich Peptide Modulates Cellular Bioenergetics. *J. Biol. Chem.* 294 (11), 4000–4011. doi:10.1074/jbc.RA118.006693

Khailova, L. S., Silachev, D. N., Rokitskaya, T. I., Avetisyan, A. V., Lyamsaev, K. G., Severina, II, et al. (2014). A Short-Chain Alkyl Derivative of Rhodamine 19 Acts as a Mild Uncoupler of Mitochondria and a Neuroprotector. *Biochim. Biophys. Acta (Bba) - Bioenerg.* 1837 (10), 1739–1747. doi:10.1016/j.bbabio.2014.07.006

Kim, S., Nam, H. Y., Lee, J., and Seo, J. (2020). Mitochondrion-Targeting Peptides and Peptidomimetics: Recent Progress and Design Principles. *Biochemistry* 59 (3), 270–284. doi:10.1021/acs.biochem.9b00857

Lesnefsky, E. J., and Hoppel, C. L. (2006). Oxidative Phosphorylation and Aging. *Ageing Res. Rev.* 5 (4), 402–433. doi:10.1016/j.arr.2006.04.001

Li, H., Wang, X., Zhang, N., Gottipati, M. K., Parpura, V., and Ding, S. (2014). Imaging of Mitochondrial Ca2+ Dynamics in Astrocytes Using Cell-specific Mitochondria-Targeted GCaMP5G/6s: Mitochondrial Ca2+ Uptake and Cytosolic Ca2+ Availability via the Endoplasmic Reticulum Store. *Cell Calcium* 56, 457–466. doi:10.1016/j.ceca.2014.09.008

Li, S., Wu, Z., Tantray, I., Li, Y., Chen, S., Dong, J., et al. (2020). Quality-control Mechanisms Targeting Translationally Stalled and C-Terminally Extended Poly(GR) Associated with ALS/FTD. *Proc. Natl. Acad. Sci. USA* 117 (40), 25104–25115. doi:10.1073/pnas.2005506117

Liberman, E. A., Topaly, V. P., Tsofina, L. M., Jasaitis, A. A., and Skulachev, V. P. (1969). Mechanism of Coupling of Oxidative Phosphorylation and the Membrane Potential of Mitochondria. *Nature* 222 (5198), 1076–1078. doi:10.1038/2221076a0

Liew, S. S., Qin, X., Zhou, J., Li, L., Huang, W., and Yao, S. Q. (2021). Smart Design of Nanomaterials for Mitochondria-Targeted Nanotherapeutics. *Angew. Chem. Int. Ed. Engl.* 60, 2232–2256. doi:10.1002/anie.201915826

Liu, J., Chen, Y., Li, G., Zhang, P., Jin, C., Zeng, L., et al. (2015). Ruthenium(II) Polypyridyl Complexes as Mitochondria-Targeted Two-Photon Photodynamic

Anticancer Agents. *Biomaterials* 56, 140–153. doi:10.1016/j.biomaterials.2015.04.002

Lo, K. K.-W., and Kam-Wing, K. (2015). Luminescent Rhenium(I) and Iridium(III) Polypyridine Complexes as Biological Probes, Imaging Reagents, and Photocytotoxic Agents. *Acc. Chem. Res.* 48 (12), 2985–2995. doi:10.1021/acs.accounts.5b00211

Loo, S., Kam, A., Xiao, T., Nguyen, G. K. T., Liu, C. F., and Tam, J. P. (2016). Identification and Characterization of Roseltide, a Knottin-type Neutrophil Elastase Inhibitor Derived from Hibiscus sabdariffa. *Sci. Rep.* 6 (1), 39401. doi:10.1038/srep39401

Ma, D.-L., He, H.-Z., Leung, K.-H., Chan, D. S.-H., and Leung, C.-H. (2013). Bioactive Luminescent Transition-Metal Complexes for Biomedical Applications. *Angew. Chem. Int. Ed.* 52 (30), 7666–7682. doi:10.1002/anie.201208414

Ma, P., Chen, J., Bi, X., Li, Z., Gao, X., Li, H., et al. (2018). Overcoming Multidrug Resistance through the GLUT1-Mediated and Enzyme-Triggered Mitochondrial Targeting Conjugate with Redox-Sensitive Paclitaxel Release. *ACS Appl. Mater. Inter.* 10 (15), 12351–12363. doi:10.1021/acsami.7b18437

Mahapatro, A., and Singh, D. K. (2011). Biodegradable Nanoparticles Are Excellent Vehicle for Site Directed In-Vivo Delivery of Drugs and Vaccines. *J. Nanobiotechnology* 9 (1), 55–11. doi:10.1186/1477-3155-9-55

Mannella, T. G. F. C. A. (2000). The Internal Structure of Mitochondria. *Trends Biochem. Sci.* 25 (7), 319–324. doi:10.1016/S0968-00040001609-1

Marc, P., Margeot, A., Devaux, F., Blugeon, C., Corral-Debrinski, M., and Jacq, C. (2002). Genome-wide Analysis of mRNAs Targeted to Yeast Mitochondria. *EMBO Rep.* 3 (2), 159–164. doi:10.1093/embo-reports/kvf025

Marrache, S., and Dhar, S. (2015). The Energy Blocker inside the Power House: Mitochondria Targeted Delivery of 3-bromopyruvate. *Chem. Sci.* 6 (3), 1832–1845. doi:10.1039/c4sc01963f

Matsumoto, S., Uchiumi, T., Saito, T., Yagi, M., Takazaki, S., Kanki, T., et al. (2012). Localization of mRNAs Encoding Human Mitochondrial Oxidative Phosphorylation Proteins. *Mitochondrion* 12 (3), 391–398. doi:10.1016/j.mito.2012.02.004

Mccully, J. D., Levitsky, S., Nido, P. J., and Cowan, D. B. (2016). Mitochondrial Transplantation for Therapeutic Use. *Clin. Translational Med.* 5 (1), 16. doi:10.1186/s40169-016-0095-4

Michaud, M., Maréchal-Drouard, L., and Duchêne, A.-M. (2010). RNA Trafficking in Plant Cells: Targeting of Cytosolic mRNAs to the Mitochondrial Surface. *Plant Mol. Biol.* 73 (6), 697–704. doi:10.1007/s11103-010-9650-3

Michaud, M., Maréchal-Drouard, L., and Duchêne, A.-M. (2014). Targeting of Cytosolic mRNA to Mitochondria: Naked RNA Can Bind to the Mitochondrial Surface. *Biochimie* 100, 159–166. doi:10.1016/j.biochi.2013.11.007

Miljanic, S., Cimerman, Z., Frkanec, L., and Zinic, M. (2002). Lipophilic Derivative of Rhodamine 19: Characterization and Spectroscopic Properties. *Analytica Chim. Acta* 468 (1), 13–25. doi:10.1016/S0003-2670(02)00627-X

Mossalam, M., Matissek, K. J., Okal, A., Constance, J. E., and Lim, C. S. (2012). Direct Induction of Apoptosis Using an Optimal Mitochondrially Targeted P53. *Mol. Pharmaceutics* 9 (5), 1449–1458. doi:10.1021/mp3000259

Murphy, M. P., and Hartley, R. C. (2018). Mitochondria as a Therapeutic Target for Common Pathologies. *Nat. Rev. Drug Discov.* 17, 865–886. doi:10.1038/nrd.2018.174

Murphy, M. P. (2008). Targeting Lipophilic Cations to Mitochondria. *Biochim. Biophys. Acta (Bba) - Bioenerg.* 1777 (7-8), 1028–1031. doi:10.1016/j.bbabio.2008.03.029

Neupert, W. (2015). A Perspective on Transport of Proteins into Mitochondria: a Myriad of Open Questions. *J. Mol. Biol.* 427 (6 Pt A), 1135–1158. doi:10.1016/j.jmb.2015.02.001

Ngwa, H. A., Kanthasamy, A., Gu, Y., Ning, F., Anantharam, V., and Kanthasamy, A. G. (2011). Manganese Nanoparticle Activates Mitochondrial Dependent Apoptotic Signaling and Autophagy in Dopaminergic Neuronal Cells. *Toxicol. Appl. Pharmacol.* 256 (3), 227–240. doi:10.1016/j.taap.2011.07.018

Nicolson, G. L. (2014). Mitochondrial Dysfunction and Chronic Disease: Treatment with Natural Supplements. *Altern. Ther. Health Med.* 20 Suppl 1 (4), 18–25.

Nie, Z., Petukhova, A., and Kumacheva, E. (2010). Properties and Emerging Applications of Self-Assembled Structures Made from Inorganic Nanoparticles. *Nat. Nanotech* 5 (1), 15–25. doi:10.1038/nnano.2009.453

Osellame, L. D., Blacker, T. S., and Duchen, M. R. (2012). Cellular and Molecular Mechanisms of Mitochondrial Function. *Best Pract. Res. Clin. Endocrinol. Metab.* 26 (6), 711–723. doi:10.1016/j.beem.2012.05.003

Pan, R. L., Hu, W. Q., Pan, J., Huang, L., and Shen, H. M. (2020). Achyranthes Bidentata Polypeptides Prevent Apoptosis by Inhibiting the Glutamate Current in Cultured Hippocampal Neurons. *Neural Regen. Res.* 15 (6), 1086–1093. doi:10.4103/1673-5374.270317

Pathak, R. K., Kolishetti, N., and Dhar, S. (2015). Targeted Nanoparticles in Mitochondrial Medicine. *Wiley Interdiscip. Rev. Nanomed Nanobiotechnol* 7 (3), 315–329. doi:10.1002/wnan.1305

Perelman, A., Wachtel, C., Cohen, M., Haupt, S., Shapiro, H., and Tzur, A. (2012). JC-1: Alternative Excitation Wavelengths Facilitate Mitochondrial Membrane Potential Cytometry. *Cell Death Dis.* 3, e430. doi:10.1038/cddis.2012.171

Pfeiffer, N. V., Dirndorfer, D., Lang, S., Resenberger, U. K., Restelli, L. M., Hemion, C., et al. (2013). Structural Features within the Nascent Chain Regulate Alternative Targeting of Secretory Proteins to Mitochondria. *EMBO J.* 32, 1036–1051. doi:10.1038/emboj.2013.46

Qin, J.-L., Shen, W.-Y., Chen, Z.-F., Zhao, L.-F., Qin, Q.-P., Yu, Y.-C., et al. (2017). Oxoaporphine Metal Complexes (CoII, NiII, ZnII) with High Antitumor Activity by Inducing Mitochondria-Mediated Apoptosis and S-phase Arrest in HepG2. *Sci. Rep.* 7 (1), 1–18. doi:10.1038/srep46056

Rathinavelu, A., Alhazzani, K., Dhandayuthapani, S., and Kanagasabai, T. (2017). Anti-cancer Effects of F16: A Novel Vascular Endothelial Growth Factor Receptor-specific Inhibitor. *Tumour Biol.* 39 (11), 101042831772684. doi:10.1177/1010428317726841

Rogov, A. G., Trendeleva, T. A., Aliverdieva, D. A., and Zvyagilskaya, R. A. (2016). More about Interactions of Rhodamine 19 Butyl Ester with Rat Liver Mitochondria. *Biochem. Mosc.* 81 (4), 432–438. doi:10.1134/s0006297916040155

Rustin, P., Bourgeron, T., Parfait, B., Chretien, D., Munnich, A., and Rötig, A. (1997). Inborn Errors of the Krebs Cycle: a Group of Unusual Mitochondrial Diseases in Human. *Biochim. Biophys. Acta (Bba) - Mol. Basis Dis.* 1361 (2), 185–197. doi:10.1016/S0925-4439(97)00035-5

Samanta, S., He, Y., Sharma, A., Kim, J., Pan, W., Yang, Z., et al. (2019). Fluorescent Probes for Nanoscopic Imaging of Mitochondria. *Chem.* 5 (7), 1697–1726. doi:10.1016/j.chempr.2019.03.011

Sanchez-Pino, M.-J., Moreno, P., and Navarro, A. (2007). Mitocondrial Dysfunction in Human Colorectal Cancer Progression. *Front. Biosci.* 12, 1190–1199. doi:10.2741/2137

Sancho, P., Galeano, E., Nieto, E., Delgado, M. D., and García-Pérez, A. I. (2007). Dequalinium Induces Cell Death in Human Leukemia Cells by Early Mitochondrial Alterations Which Enhance ROS Production. *Leuk. Res.* 31 (7), 969–978. doi:10.1016/j.leukres.2006.11.018

Saotome, M., Katoh, H., Satoh, H., Nagasaka, S., Yoshihara, S., Terada, H., et al. (2005). Mitochondrial Membrane Potential Modulates Regulation of Mitochondrial Ca2+ in Rat Ventricular Myocytes. *Am. J. Physiology-Heart Circulatory Physiol.* 288 (4), H1820–H1828. doi:10.1152/ajpheart.00589.2004

Schubert, A. D., Broner, E. C., Agrawal, N., London, N., Pearson, A., Gupta, A., et al. (2020). Somatic Mitochondrial Mutation Discovery Using Ultra-deep Sequencing of the Mitochondrial Genome Reveals Spatial Tumor Heterogeneity in Head and Neck Squamous Cell Carcinoma. *Cancer Lett.* 471, 49–60. doi:10.1016/j.canlet.2019.12.006

Schumacker, P. T., Gillespie, M. N., Nakahira, K., Choi, A. M. K., Crouser, E. D., Piantadosi, C. A., et al. (2014). Mitochondria in Lung Biology and Pathology: More Than Just a Powerhouse. *Am. J. Physiology-Lung Cell Mol. Physiol.* 306 (11), L962–L974. doi:10.1152/ajplung.00073.2014

Shi, Y., Lim, S. K., Liang, Q., Iyer, S. V., Wang, H.-Y., Wang, Z., et al. (2019). Gboxin Is an Oxidative Phosphorylation Inhibitor that Targets Glioblastoma. *Nature* 567 (7748), 341–346. doi:10.1038/s41586-019-0993-x

Slone, J., and Huang, T. (2020). The Special Considerations of Gene Therapy for Mitochondrial Diseases. *Npj Genom. Med.* 5 (1), 1–7. doi:10.1038/s41525-020-0116-5

Smith, R. A. J., Hartley, R. C., Cochemé, H. M., and Murphy, M. P. (2012). Mitochondrial Pharmacology. *Trends Pharmacol. Sci.* 33 (6), 341–352. doi:10.1016/j.tips.2012.03.010

Song, Y.-f., Liu, D.-z., Cheng, Y., Liu, M., Ye, W.-l., Zhang, B.-l., et al. (2015). Dual Subcellular Compartment Delivery of Doxorubicin to Overcome Drug Resistant and Enhance Antitumor Activity. *Sci. Rep.* 5, 16125. doi:10.1038/srep16125

Spivak, A. Y., Nedopekina, D. A., Gubaidullin, R. R., Davletshin, E. V., Tukhbatullin, A. A., D'yakonov, V. A., et al. (2021). Pentacyclic Triterpene

Acid Conjugated with Mitochondria-Targeting Cation F16: Synthesis and Evaluation of Cytotoxic Activities. *Med. Chem. Res.* 30, 940–951. doi:10.1007/s00044-021-02702-z

Sun, T., Guan, X., Zheng, M., Jing, X., and Xie, Z. (2015). Mitochondria-localized Fluorescent BODIPY-Platinum Conjugate. *ACS Med. Chem. Lett.* 6 (4), 430–433. doi:10.1021/acsmedchemlett.5b00041

Szendroedi, J., Phielix, E., and Roden, M. (2012). The Role of Mitochondria in Insulin Resistance and Type 2 Diabetes Mellitus. *Nat. Rev. Endocrinol.* 8 (2), 92–103. doi:10.1038/nrendo.2011.138

Szeto, H. H., and Schiller, P. W. (2011). Novel Therapies Targeting Inner Mitochondrial Membrane-From Discovery to Clinical Development. *Pharm. Res.* 28 (11), 2669–2679. doi:10.1007/s11095-011-0476-8

Tan, X., Zhou, Y., Shen, L., Jia, H., and Tan, X. (2019). A Mitochondria-Targeted Delivery System of Doxorubicin and Evodiamine for the Treatment of Metastatic Breast Cancer. *RSC Adv.* 9 (63), 37067–37078. doi:10.1039/C9RA07096F

Thomas, B., and Beal, M. F. (2007). Parkinson's Disease. *Hum. Mol. Genet.* 16, R183–R194. doi:10.1093/hmg/ddm159

Tragni, V., Cotugno, P., De Grassi, A., Massari, F., Di Ronzo, F., Aresta, A. M., et al. (2021). Targeting Mitochondrial Metabolite Transporters in Penicillium expansum for Reducing Patulin Production. *Plant Physiol. Biochem.* 158, 158–181. doi:10.1016/j.plaphy.2020.07.027

Veloso, C. D., Belew, G. D., Ferreira, L. L., Grilo, L. F., Jones, J. G., Portincasa, P., et al. (2019). A Mitochondrial Approach to Cardiovascular Risk and Disease. *Cpd* 25, 3175–3194. doi:10.2174/1389203720666190830163735

Viscomi, C., and Zeviani, M. (2020). Strategies for Fighting Mitochondrial Diseases. *J. Intern. Med.* 287 (6), 665–684. doi:10.1111/joim.13046

Volkmar, F. R. (2015). US and Autism. *Methods Mol. Biol.* 1265, 1–5. doi:10.1007/978-1-4939-2288-8_110.1007/978-1-4614-6435-8_102039-1

Waldeck-Weiermair, M., Gottschalk, B., Madreiter-Sokolowski, C. T., Ramadani-Muja, J., Ziomek, G., Klec, C., et al. (2019). Development and Application of Sub-mitochondrial Targeted $Ca2 +$ Biosensors. *Front. Cel. Neurosci.* 13, 449. doi:10.3389/fncel.2019.00449

Wang, B., Wang, Y., Wu, H., Song, X., Guo, X., Zhang, D., et al. (2014). A Mitochondria-Targeted Fluorescent Probe Based on TPP-Conjugated Carbon Dots for Both One- and Two-Photon Fluorescence Cell Imaging. *RSC Adv.* 4 (91), 49960–49963. doi:10.1039/c4ra07467j

Wang, D.-L., Liu, M., Miao, C., Kang, X., and Leung, T.-S. (2016). Metal Complexes for the Detection of Disease-Related Protein Biomarkers. *Coord. Chem. Rev.* 324, 90–105. doi:10.1016/j.ccr.2016.07.010

Wang, H., Gao, Z., Liu, X., Agarwal, P., Zhao, S., Conroy, D. W., et al. (2018). Targeted Production of Reactive Oxygen Species in Mitochondria to Overcome Cancer Drug Resistance. *Nat. Commun.* 9 (1), 562. doi:10.1038/s41467-018-02915-8

Wang, J. Y., Li, J. Q., Xiao, Y. M., Fu, B., and Qin, Z. H. (2020). Triphenylphosphonium (TPP)-Based Antioxidants: A New Perspective on Antioxidant Design. *ChemMedChem* 15 (5), 404–410. doi:10.1002/cmdc.201900695

Wang, Z., Guo, W., Kuang, X., Hou, S., and Liu, H. (2017). Nanopreparations for Mitochondria Targeting Drug Delivery System: Current Strategies and Future Prospective. *Asian J. Pharm. Sci.* 12 (6), 498–508. doi:10.1016/j.ajps.2017.05.006

Wei, Y., Zhou, F., Zhang, D., Chen, Q., and Xing, D. (2016). A Graphene Oxide Based Smart Drug Delivery System for Tumor Mitochondria-Targeting Photodynamic Therapy. *Nanoscale* 8 (6), 3530–3538. doi:10.1039/c5nr07785k

Weiss, M. J., Wong, J. R., Ha, C. S., Bleday, R., Salem, R. R., Steele, G. D., Jr., et al. (1987). Dequalinium, a Topical Antimicrobial Agent, Displays Anticarcinoma Activity Based on Selective Mitochondrial Accumulation. *Proc. Natl. Acad. Sci.* 84 (15), 5444–5448. doi:10.1073/pnas.84.15.5444

Weissig, V., Lasch, J., Erdos, G., Meyer, H. W., Rowe, T. C., and Hughes, J. (1998). DQAsomes: A Novel Potential Drug and Gene Delivery System Made from Dequalinium (TM). *Pharm. Res.* 15 (2), 334–337. doi:10.1023/A:1011991307631

Winkler, K., Kuznetsov, A. V., Lins, H., Kirches, E., Bossanyi, P. V., Dietzmann, K., et al. (2019). Laser-excited Fluorescence Studies of Mitochondrial Function in Saponin-Skinned Skeletal Muscle Fibers of Patients with Chronic Progressive External Ophthalmoplegia. *Biochim. Biophys. Acta* 1272 (3), 181–184. doi:10.1016/0925-4439(95)00085-2

Wu, J., Li, J., Wang, H., and Liu, C.-B. (2018). Mitochondrial-targeted Penetrating Peptide Delivery for Cancer Therapy. *Expert Opin. Drug Deliv.* 15 (10), 951–964. doi:10.1080/17425247.2018.1517750

Xia, Y., Zhou, Y., and Tang, Z. (2011). Chiral Inorganic Nanoparticles: Origin, Optical Properties and Bioapplications. *Nanoscale* 3 (4), 1374–1382. doi:10.1039/c0nr00903b

Xie, Z., Fan, T., An, J., Choi, W., Duo, Y., Ge, Y., et al. (2020). Emerging Combination Strategies with Phototherapy in Cancer Nanomedicine. *Chem. Soc. Rev.* 49 (22), 8065–8087. doi:10.1039/d0cs00215a

Xu, Z., Chen, X., Sun, Z., Li, C., and Jiang, B. (2019). Recent Progress on Mitochondrial Targeted Cancer Therapy Based on Inorganic Nanomaterials. *Mater. Today Chem.* 12 (C), 240–260. doi:10.1016/j.mtchem.2019.02.004

Yang, S., Shi, Q., Zhu, C., Luo, Y., Qian, L., He, L., et al. (2017). Mitochondrial-targeted Multifunctional Mesoporous Au@Pt Nanoparticles for Dual-Mode Photodynamic and Photothermal Therapy of Cancers. *Nanoscale* 9 (41), 15813–15824. doi:10.1039/c7nr04881e

Yousif, L. F., Stewart, K. M., Horton, K. L., and Kelley, S. O. (2009). Mitochondria-Penetrating Peptides: Sequence Effects and Model Cargo Transport. *ChembioChem* 10 (12), 2081–2088. doi:10.1002/cbic.200900017

Yousif, L. F., Stewart, K. M., and Kelley, S. O. (2009). Targeting Mitochondria with Organelle-specific Compounds: Strategies and Applications. *Chembiochem* 10 (12), 1939–1950. doi:10.1002/cbic.200900185

Zhang, L., Ma, J., Lyu, B., Zhang, Y., Gao, D., Liu, C., et al. (2020). Mitochondrial Structure-Inspired High Specific Surface Area Polymer Microspheres by Encapsulating Modified Graphene Oxide Nanosheets. *Eur. Polym. J.* 130, 109682. doi:10.1016/j.eurpolymj.2020.109682

Zhao, K., Zhao, G.-M., Wu, D., Soong, Y., Birk, A. V., Schiller, P. W., et al. (2004). Cell-permeable Peptide Antioxidants Targeted to Inner Mitochondrial Membrane Inhibit Mitochondrial Swelling, Oxidative Cell Death, and Reperfusion Injury. *J. Biol. Chem.* 279, 34682–34690. doi:10.1074/jbc.M402999200

Zheng, S., Li, X., Zhang, Y., Xie, Q., Wong, Y. S., Zheng, W., et al. (2012). PEG-nanolized Ultrasmall Selenium Nanoparticles Overcome Drug Resistance in Hepatocellular Carcinoma HepG2 Cells through Induction of Mitochondria Dysfunction. *Int. J. Nanomedicine* 7 (default), 3939–3949. doi:10.2147/IJN.S30940

Zheng, S. Y., Li, W., Wang, Z., Hao, S., Sun, L., Nisic, M., et al. (2018). Mitochondria-based Aircraft Carrier Enhances In Vivo Imaging of Carbon Quantum Dots and Delivery of Anticancer Drug. *Nanoscale* 10, 3744–3752. doi:10.1039.C7NR08816G10.1039/c8nr02643b

Zhou, F., Xing, D., Wu, B., Wu, S., Ou, Z., and Chen, W. R. (2010). New Insights of Transmembranal Mechanism and Subcellular Localization of Noncovalently Modified Single-Walled Carbon Nanotubes. *Nano Lett.* 10 (5), 1677–1681. doi:10.1021/nl100004m

Zhou, W., Wang, X., Hu, M., Zhu, C., and Guo, Z. (2014). A Mitochondrion-Targeting Copper Complex Exhibits Potent Cytotoxicity against Cisplatin-Resistant Tumor Cells through Multiple Mechanisms of Action. *Chem. Sci.* 5 (7), 2761–2770. doi:10.1039/c4sc00384e

Zielonka, J., Joseph, J., Sikora, A., Hardy, M., Ouari, O., Vasquez-Vivar, J., et al. (2017). Mitochondria-targeted Triphenylphosphonium-Based Compounds: Syntheses, Mechanisms of Action, and Therapeutic and Diagnostic Applications. *Chem. Rev.* 117 (15), 10043–10120. doi:10.1021/acs.chemrev.7b00042

Zorova, L. D., Popkov, V. A., Plotnikov, E. Y., Silachev, D. N., Pevzner, I. B., Jankauskas, S. S., et al. (2018). Mitochondrial Membrane Potential. *Anal. Biochem.* 552, 50–59. doi:10.1016/j.ab.2017.07.009

Bridging Three Gaps in Biodegradable Plastics: Misconceptions and Truths About Biodegradation

Shinhyeong Choe[1], Yujin Kim[1], Yejin Won[2] and Jaewook Myung[1]*

[1]Department of Civil and Environmental Engineering, KAIST, Daejeon, South Korea, [2]Department of Systems Biotechnology, Chung-Ang University, Seoul, South Korea

In the wake of plastic pollution increasing around the world, biodegradable plastics are one of the fastest-growing segments within the global plastics market. The biodegradation of these plastics depends on diverse factors including, but not limited to, the physicochemical structure of the materials, environmental conditions, and the microbial populations involved in the biodegradation. Although laboratory-based biodegradation tests simulate natural processes, they cannot precisely mimic the natural biodegradation of biodegradable plastics due to the disparity of several factors. In addition, the biodegradation levels claimed and/or reported by individuals and studies in different environments vary to a great extent. Biodegradable plastics are considered a sustainable alternative to non-biodegradable conventional plastics and are being promoted as an eco-friendlier choice for consumers. However, biodegradable plastics might not be as biodegradable as commonly believed, particularly in natural environments. This mini-review aims to bridge the following three gaps in biodegradable plastics by elucidating the common misconceptions and truths about biodegradation: i) the gaps among reported biodegradation level of biodegradable plastics; ii) the gaps between the biodegradation conditions in the controlled laboratory system and in the natural environment; and iii) the gaps between public perception and the actual environmental fate of biodegradable products. These gaps are critically reviewed with feasible solutions. This work will ease the assessment of biodegradable plastics and provide sound communication on corresponding claims–a prerequisite for successful market performance.

Keywords: bioplastics, biodegradable plastics, biodegradable products, misconception, sustainability, biopolymer, biodegradation

INTRODUCTION

The massive accumulation of plastics in the natural environment is threatening the sustainability of our planet (Jambeck et al., 2015; UN Environment, 2018). As of 2014, over 250,000 tons of plastics were estimated to be floating in the sea (Eriksen et al., 2014). It is predicted that by 2030, 90 Mt/year of plastics will enter the aquatic ecosystem under the scenario where the current plastic production trend continues without improvements in the waste management system (Borrelle et al., 2020). Bioplastics refer to synthetic polymers that are biodegradable [e.g., poly(lactic acid) (PLA)] and/or are derived from bio-based materials [e.g., bio-based poly(ethylene) (bio-PE)]. Biodegradable plastics are one of the fastest-growing segments within the global plastics market. The global production

capacity for biodegradable plastics was 1.2 Mt/year in 2020 and is expected to grow rapidly (European Bioplastics, 2020).

Numerous standards have paved the way for evaluating the biodegradability of plastic by simulating various environments, including natural conditions such as soil and aquatic environments, and systemically controlled conditions such as industrial composting and anaerobic digestion. Studies on the biodegradability of biodegradable plastics have been conducted according to the most prominent standards such as International Organization for Standardization (ISO), American Society for Testing and Material (ASTM), and European Norm (EN) (Eubeler et al., 2009). Although laboratory-based biodegradation tests simulate natural processes, they cannot precisely mimic the natural biodegradation of biodegradable plastics due to the disparity of several factors. In addition, the biodegradation levels claimed and/or reported by individuals and studies in different environments vary to a great extent.

Despite of legislative efforts for the standardization and specification of biodegradable plastics, the complicated descriptions and coverage of bioplastics and biodegradable plastics (e.g., bio-based, biodegradable, compostable, oxo-biodegradable plastic, etc.) are confusing to the public. The word "bioplastic" is commonly perceived as a synonym for "biodegradable plastic" (Dilkes-Hoffman et al., 2019). In addition, a common perception of biodegradable plastics is that the materials will biodegrade in natural environments. The reality is that many "so-called" biodegradable plastics are not biodegradable in the aqueous environments (Bagheri et al., 2017; Emadian et al., 2017).

Most countries label the products decomposed under controlled composting test within the designated period. Some examples of these test standards are ASTM D5338 in the United States, EN 13432 in European Union, KS M ISO14855 in Korea, and JIS K 6953 in Japan. The test-passed products are labeled as "compostable" in many countries, whereas "eco-labeled" and "biodegradable" labels are inappropriately applied in Korea and Japan (**Supplementary Table S1**). This can lead to overestimation of biodegradability of the labeled products.

This mini-review aims to bridge the following three gaps in biodegradable plastics by elucidating the common misconceptions and truths about biodegradation: i) the gaps among reported biodegradation level of biodegradable plastics; ii) the gaps between the biodegradation conditions in the controlled laboratory system and in the natural environment; and iii) the gaps between public perception and the actual environmental fate of biodegradable products. These gaps are critically reviewed with feasible solutions. This work will ease the assessment of biodegradable plastics and provide sound communication on corresponding claims–a prerequisite for successful market performance.

PRINCIPLE OF THE BIODEGRADATION PROCESS

The first step to bridge the gaps is to understand the biodegradation of biodegradable plastics–How then do these materials decompose in the natural environments? Biodegradation is a biological process, whereby polymers are partially or completely converted into the end products by the action of microorganisms (Song et al., 2009; Luckachan and Pillai, 2011; Soroudi and Jakubowicz, 2013). Biodegradable plastics are decomposed via four stages: biodeterioration, depolymerization, assimilation, and mineralization (Harrison et al., 2018). First, the microbial biofilms are formed on the surface of the materials, and decomposers and/or abiotic factors fragment them into tiny fractions, while polymers lose their initial physicochemical properties. Second, from the biofilm, the extracellular enzymes are excreted. Numerous enzymes specifically depolymerize polymers into smaller units such as oligomers, dimers, and monomers, reducing the molecular weight. Third, these molecules are metabolically assimilated in the cytoplasm, producing new biomass and energy as well as primary and secondary metabolites. Eventually, these metabolites are mineralized into the end products such as carbon dioxide, methane, water, and mineral salts (Lucas et al., 2008).

The biodegradation of biodegradable plastics depends on diverse factors including, but not limited to, the physicochemical structure of the materials, environmental conditions, and the microbial populations involved in the biodegradation (Massardier-Nageotte et al., 2006). In the natural ecosystem, biotic and abiotic factors synergistically decompose biodegradable plastics. Biotic factors are plastic-decomposing microorganisms such as bacteria, fungi, archaea, and algae (Lee et al., 2005; Kyrikou and Briassoulis, 2007; Gonzalez-Fernandez et al., 2015). Some examples of abiotic factors include temperature, sunlight, mechanical impact (weathering), oxygen, humidity, and acidity (Song et al., 2009; Thakur et al., 2018). Abiotic hydrolysis is the main degradation step, as humidity and temperature enable cleavage of the ester linkage (Karamanlioglu et al., 2017). The rate of hydrolysis and biodeterioration increases when the temperature exceeds the glass temperature of the polymer (Henton et al., 2005). The presence of oxygen determines the type of decomposers and biological reaction. When oxygen is available, aerobic organisms utilize the polymers as carbon and energy sources (Sudesh and Iwata, 2008). In anaerobic conditions, anaerobic organisms decompose polymers and generate biogas, mainly in the form of methane (Tokiwa et al., 2009; Mekonnen et al., 2013; Bátori et al., 2018).

It should be underlined that degradation and biodegradation are different (Shah et al., 2008; Luckachan and Pillai, 2011). Degradation of non-biodegradable plastics terminates at the fragmentation stage, generating even more persistent microplastics (Wagner et al., 2014; Auta et al., 2017; Mason et al., 2018). In contrast, biodegradation involves further biological steps, ultimately mineralizing the polymers. We suggest that the definition of biodegradable plastics be established based on their capacity to be mineralized into gaseous end products when the surrounding condition meets biodegradability requirements such as temperature, moisture, and microbial populations.

THE FIRST GAP: DIFFERENCES IN REPORTED BIODEGRADATION OF BIODEGRADABLE PLASTICS

We collected the results of studies that quantitatively measured biodegradation level via weight loss and/or
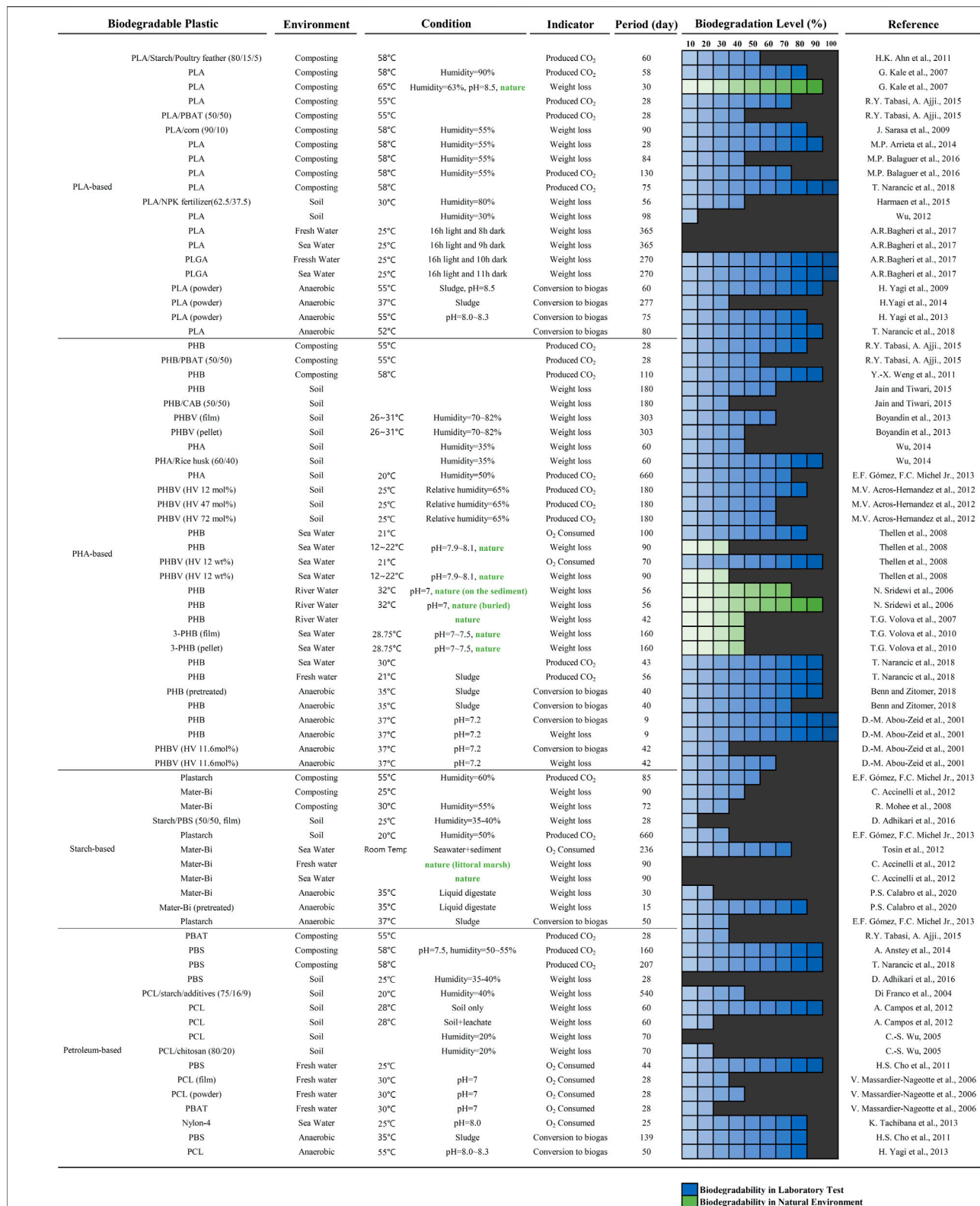
FIGURE 1 | Biodegradation study results of biodegradable plastics in the laboratory (blue) and in the natural environments (green), selected by the authors. The comprehensive biodegradation data are available in the supplementary material (**Supplementary Table S2**). Note that the analytical analysis (averaging) was conducted based on the supplementary data set.

produced gaseous end products (**Figure 1**). Despite some variations among studies, we analyzed the biodegradation data to obtain critical insights into biodegradable plastics.

The bio-based and biodegradable poly(hydroxyalkanoates) (PHA) and PLA are most widely studied. PHA-based bioplastics are biodegradable in all indicated environments (Volova et al., 2007; Woolnough et al., 2008; Yagi et al., 2014). PLA-based bioplastics, on the other hand, are well biodegradable under industrial composting and anaerobic digesting conditions, but are hardly biodegradable in soil and aquatic environments (Pranamuda et al., 1997; Itävaara et al., 2002; Tsuji and Suzuyoshi, 2002a; Tsuji and Suzuyoshi, 2002b; Shogren et al., 2003; Martin et al., 2014). PLA requires specific high-temperature conditions and degrades through abiotic hydrolysis (Elsawy et al., 2017; Gorrasi and Pantani, 2017). On the contrary, poly(lactide-co-glycolide) (PLGA), a PLA-based copolymer, was completely biodegraded in seawater and freshwater within 270 days (Bagheri et al., 2017).

The type of environment is a significant determinant of biodegradation. Each environment has different conditions such as temperature, humidity, and microbial populations (Kale et al., 2007; Tokiwa et al., 2009). Based on comprehensive data analysis (**Supplementary Table S2**), we show the manifest difference in biodegradation in various environments. The average biodegradation level can be arranged in descending order as follows: industrial composting (72.3% over 75 days), anaerobic digestion (64.6% over 88 days), marine (47.1% over 155 days), soil (39.7% over 159 days), and aerobic aqueous (31.7 over 113 days) environments. Industrial composting is a highly optimized system for the biodegradation by thermophilic microorganisms (Gómez and Michel, 2013; Arrieta et al., 2014). Due to the high temperature (typically 55–60°C, Mathur, 1998) and proper water content (50–60% is appropriate for most materials, Mathur, 1998), the highest biodegradation level and shortest period are achieved under industrial composting conditions.

The microbial populations and the fraction of decomposers in the microbial community significantly differ depending on the environment. Microorganisms generally thrive where the environmental conditions suffice. Industrial composting and soil environments contain more microbes per unit than aquatic environments (Watson et al., 1977; Flemming and Wuertz, 2019; Wang et al., 2020). Even if the same material is tested under the same type of environment, the biodegradation level can vary to a great extent. For example, in one study (Boyandin et al., 2013), the weight of poly(3-hydroxybutyrate) (PHB) films buried in natural soil was reduced by 98 and 47% near Hanoi and Nha Trang, Vietnam, respectively. The higher biodegradation in the Hanoi area was attributed to richer PHA degrading microbial populations in the soil.

Although biodegradation cannot be measured via weight loss, it is widely applied in degradation tests (Shah et al., 2008). Weight loss can incorporate the influence of biodegradation, abiotic hydrolysis, and production of water-soluble products (e.g., plasticizers). In one study (Abou-Zeid et al., 2001), the weight of poly(3-hydroxybutyrate-co-3-hydroxyvalerate) (PHBV) was reduced by 60%, but only 29% of the theoretical biogas was formed. Measuring the gaseous end product by a respirometry system determines the biodegradation level precisely, although some carbons are assimilated into the new biomass (Shah et al., 2008). The biomass should be accounted for in the carbon balance during

biodegradation. However, no analytical methods are available until now (Degli Innocenti and Breton, 2020). Therefore, weight loss should be applied as a biodegradation indicator only when the condition meets biodegradability requirements.

In sum, due to numerous biotic and abiotic factors being complicatedly involved in the biodegradation process, discrepancies among reported biodegradation level are inevitably present, and are difficult to standardize.

THE SECOND GAP: DISPARITY IN BIODEGRADATION CONDITIONS IN THE LABORATORY AND IN THE NATURAL ENVIRONMENTS

Biodegradability studies have been mainly conducted under laboratory systems based on test standards by simulating various biodegradation environments. However, biodegradation is highly accelerated in designed laboratory systems where the condition meets all biodegradability requirements. It is important to understand that there is a discrepancy between biodegradation conditions in the laboratory and in the natural environments (**Figure 2A**).

Temperature is a significant abiotic factor that influences microbial activity (Shen and Burgess, 2012; Pischedda et al., 2019), thermal degradation, and aging (Deroiné et al., 2014). Biodegradable plastics experience fluctuating temperature in nature, whereas they remain under stable temperature in a laboratory system (Rudnik and Briassoulis, 2011). For instance, in temperate regions, seasonal temperature fluctuation accelerates or delays biodegradation. Biodegradation research conducted under both conditions showed such disparity: 30°C in laboratory incubation (ASTM D6691) compared to 12–22°C in aquarium incubation subjected to continuously flowing seawater (Thellen et al., 2008).

Access to sunlight accelerates the decomposition of polymers (photodegradation). Most plastics tend to absorb high-energy radiation in the ultraviolet (UV) portion of the spectrum, which can activate their electrons to higher reactivity and cause oxidation, cleavage, and other degradation (Shah et al., 2008; Sadi et al., 2010). UV radiation can disrupt polymeric chains and embrittle the polymers by being absorbed in oxygen-containing components (Lucas et al., 2008; Rujnić-Sokele and Pilipović, 2017). Several ISO standards suggest that the samples be located under a dark or diffused light incubator. However, artificial light (i.e., a light bulb) in a laboratory system generally does not generate UV radiation. This contrasts with the conditions in a natural environment with intermittent (e.g., floating and sinking in the ocean) or long-term exposure to sunlight.

Mechanical stress is a significant abiotic parameter that affects the degradation of plastics. Weathering degradation of plastics results in their surface embrittlement and microcracking (Andrady, 2011). The free surface energy increased after weathering of PLA-lignin bioplastics (Spiridon et al., 2015). In addition, continuously pumped seawater may increase the time for microorganisms to colonize surfaces (Deroiné et al., 2014; Wright et al., 2020). Laboratory systems mimic these natural mechanical stresses by agitating incubators. However, agitation during the laboratory experiment showed little influence on biodegradation level (Briese et al., 1994).

FIGURE 2 | (A) Disparity in biodegradation conditions in the laboratory and in the natural environments. **(B)** The discrepancy between public perception and the actual biodegradability of labeled products. An industrial composting test is commonly applied for the certification, but the conditions in industrial composting facilities hardly exist in natural environments.

The shape of materials considerably affects biodegradation rate (Volova et al., 2010; Boyandin et al., 2013). In the laboratory test, the samples are generally prepared in powder, film, or pellet forms for the assessment of their biodegradability. This maximizes surface area and facilitates the biodeterioration stage by providing more surface area for microorganisms to colonize, and therefore accelerates biodegradation rate

(Andrady, 1994; Chinaglia et al., 2018). However, in most cases, littered products are decomposed from their original shapes, and disintegration occurs via multiple factors like weathering, UV radiation, microbial activity.

The presence of co-substrates such as food or beverage residue influences microbial activity (Andrady, 1994), as much of the plastic waste found in the environment consists of food-related packaging (Marsh and Bugusu, 2007; Heidbreder et al., 2019). These substrates shorten the lag phase of biodegradation by accelerating biofilm formation. However, in laboratory experiments, pure polymers are commonly tested. In this context, blending organic materials with biodegradable plastics influences the biodegradation rate. Biodegradation was accelerated when biodegradable plastics were blended with various materials, such as corn (Sarasa et al., 2009), poultry feather fibers (Ahn et al., 2011), rice husk (Wu, 2014), potato peel waste (Wei et al., 2015), and empty fruit bunch fiber (Wei et al., 2015).

The microbial populations differ depending on the environment. The heterogeneity of environmental microorganisms (inoculum) leads to inconsistent biodegradability test results (Haider et al., 2019). The laboratory settings are designed to highly condense or isolate decomposers since they utilize polymers as the sole carbon and energy sources (Dussud et al., 2018), thereby accelerating biodegradation. In the natural environment, however, competition within the environmental microbiome takes place due to the presence of various carbon sources and the heterogeneity of the microbial populations (Andrady, 1994).

In sum, due to the disparity of key factors, biodegradation tests under laboratory systems do not sufficiently reflect natural conditions and this can lead to overestimation of the biodegradation level of biodegradable plastics in the event of littering. Therefore, biodegradation test standards should clearly indicate the limit of representativeness and/or new specific standards should provide more options to minimize the gaps to transfer natural biodegradation to the laboratory. For instance, the temperature range should be altered depending on the geographical region. Access to sunlight and water should also be considered to imitate synergistic reactions of biotic and abiotic factors.

THE THIRD GAP: MISCONCEPTIONS AND TRUTHS ON THE ENVIRONMENTAL FATE OF BIODEGRADABLE PRODUCTS

The general knowledge of bioplastics is low, but perception, particularly of biodegradable plastics, is positive (Lynch et al., 2017; Dilkes-Hoffman et al., 2019). Choosing biodegradable products could be adopted as a possible solution to plastic pollution rather than reducing plastic consumption (Klein et al., 2019). Marketers are keen to tout the biodegradability of materials. However, a biodegradable label on products often leads to littering wastes with the belief that biodegradable plastics will decompose naturally (Klöckner, 2013; UNEP, 2015). The truth is that they might not be as biodegradable as commonly believed (**Figure 2B**).

The overestimation of the biodegradability of biodegradable plastics derives from three factors: i) reported biodegradability resulted from an optimized laboratory system; ii) the overlapping term between biodegradable and compostable plastics; and iii) a lack of discrete recycling codes and treatment systems.

First, biodegradability has been tested under laboratory systems and the results are valid. However, as examined earlier, biodegradation occurs only when surrounding condition suffices biodegradability requirements. In other words, a biodegradable plastic under laboratory test may not biodegrade in natural condition. Second, many countries clearly distinguish between compostable and biodegradable products via labeling system (**Supplementary Table S1**). However, as compostable plastics are often coined as biodegradable polymers (Haider et al., 2019), the public easily misunderstand the biodegradability of compostable products. In addition, few are aware that compostable and biodegradable plastics are different, and the conditions in industrial composting facilities hardly exist in natural environments. Finally, recycling code (resin identification code, in some countries) on biodegradable plastics is "7", which indicates "other polymers". As a result, they are hardly recycled, and in turn are incinerated, landfilled or littered (Pathak et al., 2014). Incinerating is not a desirable mode for fossil-based biodegradable plastics, as it consumes a high amount of energy and emits greenhouse gases (Razza et al., 2015; Folino et al., 2020a). Also, some biodegradable products may not have completed their life cycle when landfilled (Shin et al., 1997; Quecholac-Piña et al., 2020).

PLA provides a good illustration to explain these misconceptions. PLA is derived from bio-based resources and is applied to daily commodities such as disposable packaging and cups (Karamanlioglu et al., 2017). As PLA is promoted as an eco-friendly material, the public may assume that it is naturally decomposed in the ocean. However, PLA is well biodegradable only under industrial composting and anaerobic digesting conditions (**Supplementary Table S2**). Even if products are labeled compostable (as in most Western countries), many people might be confused between compostable and biodegradable plastics. Furthermore, the recycling code on PLA products is generally "7", which may lead most littered PLA products to not being properly treated.

Therefore, we suggest that a separate recycling code for compostable plastics be established to ensure that these plastics end up their life cycle in an industrial composting facility, and littering should be the last resort. Furthermore, following the growing production trend of biodegradable plastics, separate collection systems and treatment facilities should be built, making so-called biodegradable products genuinely biodegradable. Education on biodegradable plastics should be provided so that the public can make informed decisions (UNEP, 2015). For instance, it should be understood that industrial composting test does not necessarily guarantee biodegradation in natural conditions, especially in aquatic environments. The labeling on compostable products should clearly indicate that they are only biodegradable in an industrial composting facility. Society should have access to reliable, authoritative, and clear guidance on what terms such as "compostable" or "biodegradable" actually mean. The national legalization on the i) definition, ii) classification, iii) labeling, iv) collection system, and v) treatment guideline will enhance public awareness of biodegradable plastics and eliminate misconceptions.

DISCUSSION AND OUTLOOK

Biodegradable polymers are only beneficial when they can actually biodegrade (Gross and Kalra, 2002). Bridging the aforementioned three gaps will enhance sound communication on biodegradable plastics, eliminating confusion and misconceptions. Understanding the truths about biodegradable plastics will provide support for the progressive substitution of conventional plastics with biodegradable plastics. There are also other anticipated outcomes: i) Products with high biodegradability will be promoted in the market. ii) Policies on eco-friendlier and sound design will be established as well as financial incentives. iii) The development of biodegradation accelerating technology will be triggered. iv) Waste littering based on the false belief in the biodegradability of biodegradable plastics will be minimized. v) Bridging the gaps in biodegradable plastics will open up a sustainable future.

AUTHOR CONTRIBUTIONS

FUNDING

SUPPLEMENTARY MATERIAL

The Supplementary Material for this article can be found online at: https://www.frontiersin.org/articles/10.3389/fchem.2021.671750/full#supplementary-material

REFERENCES

Abou-Zeid, D.-M., Müller, R.-J., and Deckwer, W.-D. (2001). Degradation of Natural and Synthetic Polyesters under Anaerobic Conditions. *J. Biotechnol.* 86 (2), 113–126. doi:10.1016/s0168-1656(00)00406-5

Ahn, H. K., Huda, M. S., Smith, M. C., Mulbry, W., Schmidt, W. F., and Reeves, J. B., III (2011). Biodegradability of Injection Molded Bioplastic Pots Containing Polylactic Acid and Poultry Feather Fiber. *Bioresour. Tech.* 102 (7), 4930–4933. doi:10.1016/j.biortech.2011.01.042

Andrady, A. L. (1994). Assessment of Environmental Biodegradation of Synthetic Polymers. *J. Macromolecular Sci. C: Polym. Rev.* 34 (1), 25–76. doi:10.1080/15321799408009632

Andrady, A. L. (2011). Microplastics in the Marine Environment. *Mar. Pollut. Bull.* 62 (8), 1596–1605. doi:10.1016/j.marpolbul.2011.05.030

Arrieta, M. P., López, J., Rayón, E., and Jiménez, A. (2014). Disintegrability under Composting Conditions of Plasticized PLA-PHB Blends. *Polym. Degrad. Stab.* 108, 307–318. doi:10.1016/j.polymdegradstab.2014.01.034

Auta, H. S., Emenike, C. U., and Fauziah, S. H. (2017). Distribution and Importance of Microplastics in the Marine Environment: a Review of the Sources, Fate, Effects, and Potential Solutions. *Environ. Int.* 102, 165–176. doi:10.1016/j.envint.2017.02.013

Bagheri, A. R., Laforsch, C., Greiner, A., and Agarwal, S. (2017). Fate of So-Called Biodegradable Polymers in Seawater and Freshwater. *Glob. Challenges* 1 (4), 1700048. doi:10.1002/gch2.201700048

Bátori, V., Åkesson, D., Zamani, A., Taherzadeh, M. J., and Sárvári Horváth, I. (2018). Anaerobic Degradation of Bioplastics: A Review. *Waste Manage.* 80, 406–413. doi:10.1016/j.wasman.2018.09.040

Borrelle, S. B., Ringma, J., Law, K. L., Monnahan, C. C., Lebreton, L., McGivern, A., et al. (2020). Predicted Growth in Plastic Waste Exceeds Efforts to Mitigate Plastic Pollution. *Science* 369 (6510), 1515–1518. doi:10.1126/science.aba3656

Boyandin, A. N., Prudnikova, S. V., Karpov, V. A., Ivonin, V. N., Đỗ, N. L., Nguyễn, T. H., et al. (2013). Microbial Degradation of Polyhydroxyalkanoates in Tropical Soils. *Int. Biodeterioration Biodegradation* 83, 77–84. doi:10.1016/j.ibiod.2013.04.014

Briese, B. H., Jendrossek, D., and Schlegel, H. G. (1994). Degradation of Poly(3-Hydroxybutyrate-Co-3-Hydroxyvalerate) by Aerobic Sewage Sludge. *FEMS Microbiol. Lett.* 117 (1), 107–111. doi:10.1111/j.1574-6968.1994.tb06750.x

Chinaglia, S., Tosin, M., and Degli-Innocenti, F. (2018). Biodegradation Rate of Biodegradable Plastics at Molecular Level. *Polym Degrad and Stabil* 147, 237–244.

Folino, A., Calabro', P. S., Fazzino, F., and Komilis, D. (2020a). Preliminary Evaluation of the Anaerobic Biodegradability of Three Biobased Materials Used for the Production of Disposable Plastics. *J. Hazard. Mater.* 390, 121653. doi:10.1016/j.jhazmat.2019.121653

Degli Innocenti, F., and Breton, T. (2020). Intrinsic Biodegradability of Plastics and Ecological Risk in the Case of Leakage. *ACS Sustain. Chem. Eng.* 8 (25), 9239–9249. doi:10.1021/acssuschemeng.0c01230

Deroiné, M., Le Duigou, A., Corre, Y.-M., Le Gac, P.-Y., Davies, P., César, G., et al. (2014). Seawater Accelerated Ageing of Poly(3-Hydroxybutyrate-Co-3-Hydroxyvalerate). *Polym. Degrad. Stab.* 105, 237–247. doi:10.1016/j.polymdegradstab.2014.04.026

Dilkes-Hoffman, L., Ashworth, P., Laycock, B., Pratt, S., and Lant, P. (2019). Public Attitudes towards Bioplastics - Knowledge, Perception and End-Of-Life Management. *Resour. Conservation Recycling* 151, 104479. doi:10.1016/j.resconrec.2019.104479

Dussud, C., Hudec, C., George, M., Fabre, P., Higgs, P., Bruzaud, S., et al. (2018). Colonization of Non-biodegradable and Biodegradable Plastics by Marine Microorganisms. *Front. Microbiol.* 9, 1571. doi:10.3389/fmicb.2018.01571

Elsawy, M. A., Kim, K.-H., Park, J.-W., and Deep, A. (2017). Hydrolytic Degradation of Polylactic Acid (PLA) and its Composites. *Renew. Sustain. Energ. Rev.* 79, 1346–1352. doi:10.1016/j.rser.2017.05.143

Emadian, S. M., Onay, T. T., and Demirel, B. (2017). Biodegradation of Bioplastics in Natural Environments. *Waste Manage.* 59, 526–536. doi:10.1016/j.wasman.2016.10.006

Eriksen, M., Lebreton, L. C., Carson, H. S., Thiel, M., Moore, C. J., Borerro, J. C., et al. (2014). Plastic Pollution in the World's Oceans: More Than 5 Trillion Plastic Pieces Weighing over 250,000 Tons Afloat at Sea. *PLOS one* 9 (12), e111913. doi:10.1371/journal.pone.0111913

Eubeler, J. P., Zok, S., Bernhard, M., and Knepper, T. P. (2009). Environmental Biodegradation of Synthetic Polymers I. Test Methodologies and Procedures. *Trac Trends Anal. Chem.* 28 (9), 1057–1072. doi:10.1016/j.trac.2009.06.007

European Bioplastics (2020). *Bioplastics Market Development Update 2020*. Berlin: European Bioplastics.

Flemming, H.-C., and Wuertz, S. (2019). Bacteria and Archaea on Earth and Their Abundance in Biofilms. *Nat. Rev. Microbiol.* 17 (4), 247–260. doi:10.1038/s41579-019-0158-9

Gómez, E. F., and Michel, F. C., Jr (2013). Biodegradability of Conventional and Bio-Based Plastics and Natural Fiber Composites during Composting, Anaerobic Digestion and Long-Term Soil Incubation. *Polym. Degrad. Stab.* 98 (12), 2583–2591. doi:10.1016/j.polymdegradstab.2013.09.018

Gonzalez-Fernandez, C., Sialve, B., and Molinuevo-Salces, B. (2015). Anaerobic Digestion of Microalgal Biomass: Challenges, Opportunities and Research Needs. *Bioresour. Tech.* 198, 896–906. doi:10.1016/j.biortech.2015.09.095

Gorrasi, G., and Pantani, R. (2017). *Hydrolysis and Biodegradation of Poly (Lactic Acid).* Synthesis, Structure and Properties of Poly (Lactic Acid). (Boston, MA: Springer), 119–151. doi:10.1007/12_2016_12

Gross, R. A., and Kalra, B. (2002). Biodegradable Polymers for the Environment. *Science* 297 (5582), 803–807. doi:10.1126/science.297.5582.803

Haider, T. P., Völker, C., Kramm, J., Landfester, K., and Wurm, F. R. (2019). Plastics of the Future? the Impact of Biodegradable Polymers on the Environment and on Society. *Angew. Chem. Int. Ed.* 58 (1), 50–62. doi:10.1002/anie.201805766

Harrison, J. P., Boardman, C., O'Callaghan, K., Delort, A.-M., and Song, J. (2018). Biodegradability Standards for Carrier Bags and Plastic Films in Aquatic Environments: a Critical Review. *R. Soc. Open Sci.* 5 (5), 171792, 2018 . Royal Society Open Science. doi:10.1098/rsos.171792

Heidbreder, L. M., Bablok, I., Drews, S., and Menzel, C. (2019). Tackling the Plastic Problem: A Review on Perceptions, Behaviors, and Interventions. *Sci. Total Environ.* 668, 1077–1093. doi:10.1016/j.scitotenv.2019.02.437

Henton, D. E., Gruber, P., Lunt, J., and Randall, J. (2005). Polylactic Acid Technology. *Nat. Fibers, Biopolymers, Biocomposites* 16, 527–577. doi:10.1002/1521-4095(200012)12:23<1841::AID-ADMA1841>3.0.CO;2-E

Itävaara, M., Karjomaa, S., and Selin, J.-F. (2002). Biodegradation of Polylactide in Aerobic and Anaerobic Thermophilic Conditions. *Chemosphere* 46 (6), 879–885. doi:10.1016/s0045-6535(01)00163-1

Jambeck, J. R., Geyer, R., Wilcox, C., Siegler, T. R., Perryman, M., Andrady, A., et al. (2015). Plastic Waste Inputs from Land into the Ocean. *Science* 347 (6223), 768–771. doi:10.1126/science.1260352

Kale, G., Kijchavengkul, T., Auras, R., Rubino, M., Selke, S. E., and Singh, S. P. (2007). Compostability of Bioplastic Packaging Materials: an Overview. *Macromol. Biosci.* 7 (3), 255–277. doi:10.1002/mabi.200600168

Karamanlioglu, M., Preziosi, R., and Robson, G. D. (2017). Abiotic and Biotic Environmental Degradation of the Bioplastic Polymer Poly(lactic Acid): A Review. *Polym. Degrad. Stab.* 137, 122–130. doi:10.1016/j.polymdegradstab.2017.01.009

Klein, F., Emberger-Klein, A., Menrad, K., Möhring, W., and Blesin, J.-M. (2019). Influencing Factors for the Purchase Intention of Consumers Choosing Bioplastic Products in Germany. *Sustainable Prod. Consumption* 19, 33–43. doi:10.1016/j.spc.2019.01.004

Klöckner, C. A. (2013). A Comprehensive Model of the Psychology of Environmental Behaviour-A Meta-Analysis. *Glob. Environ. Change* 23 (5), 1028–1038. doi:10.1016/j.gloenvcha.2013.05.014

Kyrikou, I., and Briassoulis, D. (2007). Biodegradation of Agricultural Plastic Films: a Critical Review. *J. Polym. Environ.* 15 (2), 125–150. doi:10.1007/s10924-007-0053-8

Lee, K.-M., Gimore, D. F., and Huss, M. J. (2005). Fungal Degradation of the Bioplastic PHB (Poly-3-Hydroxy- Butyric Acid). *J. Polym. Environ.* 13 (3), 213–219. doi:10.1007/s10924-005-4756-4

Lucas, N., Bienaime, C., Belloy, C., Queneudec, M., Silvestre, F., and Nava-Saucedo, J.-E. (2008). Polymer Biodegradation: Mechanisms and Estimation Techniques - A Review. *Chemosphere* 73 (4), 429–442. doi:10.1016/j.chemosphere.2008.06.064

Luckachan, G. E., and Pillai, C. K. S. (2011). Biodegradable Polymers- A Review on Recent Trends and Emerging Perspectives. *J. Polym. Environ.* 19 (3), 637–676. doi:10.1007/s10924-011-0317-1

Lynch, D. H. J., Klaassen, P., and Broerse, J. E. W. (2017). Unraveling Dutch Citizens' Perceptions on the Bio-Based Economy: The Case of Bioplastics, Bio-

Jetfuels and Small-Scale Bio-Refineries. *Ind. Crops Prod.* 106, 130–137. doi:10.1016/j.indcrop.2016.10.035

Marsh, K., and Bugusu, B. (2007). Food Packaging?Roles, Materials, and Environmental Issues. *J. Food Sci.* 72 (3), R39–R55. doi:10.1111/j.1750-3841.2007.00301.x

Martin, R. T., Camargo, L. P., and Miller, S. A. (2014). Marine-degradable Polylactic Acid. *Green. Chem.* 16 (4), 1768–1773. doi:10.1039/c3gc42604a

Mason, S. A., Welch, V. G., and Neratko, J. (2018). Synthetic Polymer Contamination in Bottled Water. *Front. Chem.* 6, 407. doi:10.3389/fchem.2018.00407

Massardier-Nageotte, V., Pestre, C., Cruard-Pradet, T., and Bayard, R. (2006). Aerobic and Anaerobic Biodegradability of Polymer Films and Physico-Chemical Characterization. *Polym. Degrad. Stab.* 91 (3), 620–627. doi:10.1016/j.polymdegradstab.2005.02.029

Mathur, S. P. (1998). "Composting Processes," in *Bioconversion of Waste Materials to Industrial Products* (Boston, MA: Springer), 154–193. doi:10.1007/978-1-4615-5821-7_4

Mekonnen, T., Mussone, P., Khalil, H., and Bressler, D. (2013). Progress in Bio-Based Plastics and Plasticizing Modifications. *J. Mater. Chem. A.* 1 (43), 13379–13398. doi:10.1039/c3ta12555f

Pathak, S., Sneha, C., and Mathew, B. B. (2014). Bioplastics: its Timeline Based Scenario & Challenges. *J. Polym. Biopolymer Phys. Chem.* 2 (4), 84–90.

Pischedda, A., Tosin, M., and Degli-Innocenti, F. (2019). Biodegradation of Plastics in Soil: The Effect of Temperature. *Polym. Degrad. Stab.* 170, 109017. doi:10.1016/j.polymdegradstab.2019.109017

Pranamuda, H., Tokiwa, Y., and Tanaka, H. (1997). Polylactide Degradation by an Amycolatopsis Sp. *Appl. Environ. Microbiol.* 63 (4), 1637–1640. doi:10.1128/aem.63.4.1637-1640.1997

Quecholac-Piña, X., Hernández-Berriel, M. d. C., Mañón-Salas, M. d. C., Espinosa-Valdemar, R. M., and Vázquez-Morillas, A. (2020). Degradation of Plastics under Anaerobic Conditions: a Short Review. *Polymers* 12 (1), 109. doi:10.3390/polym12010109

Razza, F., Degli Innocenti, F., Dobon, A., Aliaga, C., Sanchez, C., and Hortal, M. (2015). Environmental Profile of a Bio-Based and Biodegradable Foamed Packaging Prototype in Comparison with the Current Benchmark. *J. Clean. Prod.* 102, 493–500. doi:10.1016/j.jclepro.2015.04.033

Rudnik, E., and Briassoulis, D. (2011). Degradation Behaviour of Poly(lactic Acid) Films and Fibres in Soil under Mediterranean Field Conditions and Laboratory Simulations Testing. *Ind. Crops Prod.* 33 (3), 648–658. doi:10.1016/j.indcrop.2010.12.031

Rujnić-Sokele, M., and Pilipović, A. (2017). Challenges and Opportunities of Biodegradable Plastics: A Mini Review. *Waste Manage. Res.* 35 (2), 132–140.

Sadi, R. K., Fechine, G. J. M., and Demarquette, N. R. (2010). Photodegradation of Poly(3-Hydroxybutyrate). *Polym. Degrad. Stab.* 95 (12), 2318–2327. doi:10.1016/j.polymdegradstab.2010.09.003

Sarasa, J., Gracia, J. M., and Javierre, C. (2009). Study of the Biodisintegration of a Bioplastic Material Waste. *Bioresour. Tech.* 100 (15), 3764–3768. doi:10.1016/j.biortech.2008.11.049

Shah, A. A., Hasan, F., Hameed, A., and Ahmed, S. (2008). Biological Degradation of Plastics: a Comprehensive Review. *Biotechnol. Adv.* 26 (3), 246–265. doi:10.1016/j.biotechadv.2007.12.005

Shen, J., and Burgess, D. J. (2012). Accelerated In-Vitro Release Testing Methods for Extended-Release Parenteral Dosage Forms. *J. Pharm. Pharmacol.* 64 (7), 986–996. doi:10.1111/j.2042-7158.2012.01482.x

Shin, P. K., Kim, M. H., and Kim, J. M. (1997). Biodegradability of Degradable Plastics Exposed to Anaerobic Digested Sludge and Simulated Landfill Conditions. *J. Environ. Polym. Degrad.* 5 (1), 33–39.

Shogren, R. L., Doane, W. M., Garlotta, D., Lawton, J. W., and Willett, J. L. (2003). Biodegradation of Starch/polylactic Acid/poly(hydroxyester-Ether) Composite Bars in Soil. *Polym. Degrad. Stab.* 79 (3), 405–411. doi:10.1016/s0141-3910(02)00356-7

Song, J. H., Murphy, R. J., Narayan, R., and Davies, G. B. H. (2009). Biodegradable and Compostable Alternatives to Conventional Plastics. *Phil. Trans. R. Soc. B* 364 (1526), 2127–2139. doi:10.1098/rstb.2008.0289

Soroudi, A., and Jakubowicz, I. (2013). Recycling of Bioplastics, Their Blends and Biocomposites: A Review. *Eur. Polym. J.* 49 (10), 2839–2858. doi:10.1016/j.eurpolymj.2013.07.025

Spiridon, I., Leluk, K., Resmerita, A. M., and Darie, R. N. (2015). Evaluation of PLA-Lignin Bioplastics Properties before and after Accelerated Weathering. *Composites B: Eng.* 69, 342–349. doi:10.1016/j.compositesb.2014.10.006

Sudesh, K., and Iwata, T. (2008). Sustainability of Biobased and Biodegradable Plastics. *Clean. Soil Air Water* 36 (5-6), 433–442. doi:10.1002/clen.200700183

Thakur, S., Chaudhary, J., Sharma, B., Verma, A., Tamulevicius, S., and Thakur, V. K. (2018). Sustainability of Bioplastics: Opportunities and Challenges. *Curr. Opin. Green Sustain. Chem.* 13, 68–75. doi:10.1016/j.cogsc.2018.04.013

Thellen, C., Coyne, M., Froio, D., Auerbach, M., Wirsen, C., and Ratto, J. A. (2008). A Processing, Characterization and Marine Biodegradation Study of Melt-Extruded Polyhydroxyalkanoate (PHA) Films. *J. Polym. Environ.* 16 (1), 1–11. doi:10.1007/s10924-008-0079-6

Tokiwa, Y., Calabia, B., Ugwu, C., and Aiba, S. (2009). Biodegradability of Plastics. *Ijms* 10 (9), 3722–3742. doi:10.3390/ijms10093722

Tsuji, H., and Suzuyoshi, K. (2002a). Environmental Degradation of Biodegradable Polyesters 1. Poly(ε-Caprolactone), poly[(R)-3-hydroxybutyrate], and poly(L-Lactide) Films in Controlled Static Seawater. *Polym. Degrad. Stab.* 75 (2), 347–355. doi:10.1016/s0141-3910(01)00240-3

Tsuji, H., and Suzuyoshi, K. (2002b). Environmental Degradation of Biodegradable Polyesters 2. Poly(ε-Caprolactone), poly[(R)-3-hydroxybutyrate], and poly(L-Lactide) Films in Natural Dynamic Seawater. *Polym. Degrad. Stab.* 75 (2), 357–365. doi:10.1016/s0141-3910(01)00239-7

UN Environment (2018). *SINGLE-USE PLASTICS: A Roadmap for Sustainability.* Nairobi: United Nations Environment Programme.

UNEP (2015). *Biodegradable Plastics and Marine Litter. Misconceptions, Concerns and Impacts on Marine Envionments.* Nairobi: United Nations Environment Programme.

Volova, T. G., Boyandin, A. N., Vasiliev, A. D., Karpov, V. A., Prudnikova, S. V., Mishukova, O. V., et al. (2010). Biodegradation of Polyhydroxyalkanoates (PHAs) in Tropical Coastal Waters and Identification of PHA-Degrading Bacteria. *Polym. Degrad. Stab.* 95 (12), 2350–2359. doi:10.1016/j.polymdegradstab.2010.08.023

Volova, T. G., Gladyshev, M. I., Trusova, M. Y., and Zhila, N. O. (2007). Degradation of Polyhydroxyalkanoates in Eutrophic Reservoir. *Polym. Degrad. Stab.* 92 (4), 580–586. doi:10.1016/j.polymdegradstab.2007.01.011

Wagner, M., Scherer, C., Alvarez-Muñoz, D., Brennholt, N., Bourrain, X., Buchinger, S., et al. (2014). Microplastics in Freshwater Ecosystems: what We Know and what We Need to Know. *Environ. Sci. Europe* 26 (1), 1–9. doi:10.1186/s12302-014-0012-7

Wang, G. X., Huang, D., Ji, J. H., Völker, C., and Wurm, F. R. (2020). Seawater-Degradable Polymers—Fighting the Marine Plastic Pollution. *Adv. Sci*, 2001121. doi:10.1002/advs.202001121

Watson, S. W., Novitsky, T. J., Quinby, H. L., and Valois, F. W. (1977). Determination of Bacterial Number and Biomass in the Marine Environment. *Appl. Environ. Microbiol.* 33 (4), 940–946. doi:10.1128/aem.33.4.940-946.1977

Wei, L., Liang, S., and McDonald, A. G. (2015). Thermophysical Properties and Biodegradation Behavior of Green Composites Made from Polyhydroxybutyrate and Potato Peel Waste Fermentation Residue. *Ind. Crops Prod.* 69, 91–103. doi:10.1016/j.indcrop.2015.02.011

Woolnough, C. A., Charlton, T., Yee, L. H., Sarris, M., and Foster, L. J. R. (2008). Surface Changes in Polyhydroxyalkanoate Films during Biodegradation and Biofouling. *Polym. Int.* 57 (9), 1042–1051. doi:10.1002/pi.2444

Wright, R. J., Erni-Cassola, G., Zadjelovic, V., Latva, M., and Christie-Oleza, J. A. (2020). Marine Plastic Debris: A New Surface for Microbial Colonization. *Environ. Sci. Technol.* 54 (19), 11657–11672. doi:10.1021/acs.est.0c02305

Wu, C.-S. (2014). Preparation and Characterization of Polyhydroxyalkanoate Bioplastic-Based Green Renewable Composites from Rice Husk. *J. Polym. Environ.* 22 (3), 384–392. doi:10.1007/s10924-014-0662-y

Yagi, H., Ninomiya, F., Funabashi, M., and Kunioka, M. (2014). Mesophilic Anaerobic Biodegradation Test and Analysis of Eubacteria and Archaea Involved in Anaerobic Biodegradation of Four Specified Biodegradable Polyesters. *Polym. Degrad. Stab.* 110, 278–283. doi:10.1016/j.polymdegradstab.2014.08.031

Elemental Impurities in Pediatric Calcium Carbonate Preparations-High Throughput Quantification and Risk Assessment

Chaoqiang Xiao[1,3†], Li Zhu[2†], Xia Zhang[2], Rumeng Gao[3], Shuwang He[3], Zhihua Lv[1*] and Changqin Hu[2*]

[1]Key Laboratory of Marine Drugs, Chinese Ministry of Education, School of Medicine and Pharmacy, Ocean University of China, Qingdao, China, [2]Key Laboratory for Quality Research and Evaluation of Chemical Drugs, National Institutes for Food and drug Control, Beijing, China, [3]Dyne High-Tech Pediatric Pharmaceutical R&D Institute, Beijing, China

Calcium carbonate which is extracted from the Earth in combination with other mineral impurities, is largely used in preparations for pediatric supplements. Elemental impurities in drug products pose toxicological concerns without therapeutic benefits. Thus, it is very urgent to assess the safety of chronic exposure to elements that may be present in trace amounts. In the present study, we developed high throughput ICP-MS method for the quantitative determination of 62 elemental impurities in high matric calcium carbonate samples and validated according to USP 233. Calcium carbonate preparations which state clearly used for child (including neonates, infants, toddlers and children) from 9 manufactures and two types of raw materials (light calcium carbonate and ground calcium carbonate) were investigated in terms of the content and variability of 62 elemental impurities. According to the results, ground calcium carbonate was more suitable to be used in pediatric preparations concerning elemental impurities. Parts of elemental impurities in $CaCO_3$ preparations which are derived from the raw materials and the preparation process, may cause potential risks for children. These results indicate that it is necessary to establish a modern instrumental analysis method to evaluate and control elemental impurities in $CaCO_3$ raw materials and preparations.

Keywords: calcium carbonate, pediatric drugs, element impurities, risk assessment, ICP-MS

INTRODUCTION

For children, toddlers, and infants, calcium in food often does not meet the needs of the body in this stage of rapid growth and development; since insufficient calcium intake will affect growth and development, potentially leading to diseases such as osteomalacia and rickets (Baker et al., 1999; Lee and Jiang, 2008; Pu et al., 2016), calcium supplement preparations are suggested to meet the body's demand.

Because of its high calcium content and low price, calcium carbonate is currently recognized as the main calcium source with the highest performance-price ratio in China and other countries, and is thus the preferred raw material for calcium supplement preparations. Calcium carbonate is extracted from the Earth in combination with other minerals, and can be divided into light and ground calcium carbonate according to the production method (Wang et al., 2007). Light calcium carbonate is produced by a chemical processing method, and generally uses limestone and shells as raw materials,

whereas ground calcium carbonate is produced by crushing natural calcite directly by a mechanical method.

However, the natural sources of calcium carbonate may contain various elemental impurities such as lead, arsenic, and mercury that are introduced from raw materials or during the production of preparations. Children may be particularly sensitive to the toxic effects of these metals because they tend to absorb a relatively higher fraction of an oral dose than adults. These harmful consequences for children include developmental delays, neurocognitive disorders, behavioral disorders, respiratory problems, cancer, and cardiovascular diseases (Olympio et al., 2009; Brandão and Gontijo, 2012; Al Osman et al., 2019; Jurowski et al., 2019).

In particular, pediatric patients show high sensitivity to lead, which causes irreversible damage to the nervous system that can directly affect intelligence, behavior, and normal development (Measuring Lead Exposure in Infants, Children, and Other Sensitive Populations, 1993; Levin et al., 2008). In adult rats, the absorption of radioactive cerium salts from the gastrointestinal tract ranges from 0.05% to less than 0.1% of the administered dose, whereas suckling rats absorb 40–98% of the administered dose, with the youngest rats retaining the largest percentage of the dose (Kutty et al., 1996). Analysis of the geographic distribution of endemic endomyocardial fibrosis in India suggested a link to high cerium soil concentrations (IRIS Toxicological Review of Cerium Oxide and Cerium Compounds (Interagency Science Discussion Draft), 2009). Metals, especially chromium, cobalt, and nickel, are the most common contact allergens in children (Brandão and Gontijo, 2012), among which cobalt has been regarded as possibly carcinogenic to humans (Colognato et al., 2008). Other elements such as magnesium, manganese, nickel, copper, zinc, and selenium have both nutritional and toxic effects to human health depending on dose (Linshaw et al., 1998; Avula et al., 2010; Singh et al., 2011).

As elemental impurities in drug products pose toxicological concerns without a therapeutic benefit, their levels should be controlled within acceptable limits (Q3D Elemental impurities-guidance for industry, 2020). January 1, 2008, The Guideline for Elemental Impurities (Q3D) of the ICH represents a new paradigm in the control of elemental impurities in pharmaceuticals. The ICH Q3D covers 24 elements, providing permitted daily exposure (PDE) information, which further changed the approach toward control of elemental impurities from the traditional "heavy metals test" to a scientific-based risk assessment using modern analytical instrumentation (Guideline for elemental impurities, 2019). The ICH Q3D is currently the most important guiding principle in the study of elemental impurities, which involves risk assessment for control, and suggests that the inherent characteristics of raw and auxiliary materials from natural sources should be considered in this assessment. The acceptable limits of elemental impurities in drugs as specified by the ICH Q3D are generally set according to the PDE calculated from the no-observed-adverse-effect level or lowest-observed-adverse-effect level in the most relevant animal studies. However, children are not simply a miniature version of adults but rather have different physiological characteristics. Therefore, the limit requirements of the ICH

Q3D for elemental impurities in therapeutic drugs may not be completely applicable to pediatric drugs. Thus, the National Food Safety Standard Infant Formula and other guidelines (National Health Commission of the People's Republic of China, 2010; Standard for Infant Formula and Formulations for Special Medical Purposes Intended for Infants, 2007) should be used as a supplement to assess the risk of some elemental impurities for drugs that are commonly taken by young children to best ensure the safety of pediatric medication.

Toward this goal, the aims of this study were to compare the elemental impurity content and variability characteristics of light and ground calcium carbonate to provide guidance for the appropriate selection of calcium carbonate raw materials and to assess the risk of chronic exposure to elements that may be present in trace amounts in supplement preparations for children.

At present, the United States Pharmacopeia (USP), European Pharmacopeia (EP), and Pharmacopeia of the People's Republic of China (ChP) control elemental impurities of calcium carbonate raw materials mainly through inspection of barium, iron, mercury, and heavy metals (colorimetry), however, the limit of other potential elemental impurities has not been reported. As we known, the colorimetry is not adequate for the purpose of controlling low levels of potentially elemental impurities in drug, and consequently needs to be replaced by highly sensitive instrumental methods such as atomic absorption spectrometry (AAS) (Sheth and Patel, 2020), X-ray fluorescence spectrometry (XRF) (Chowdhury et al., 2020; Sauer et al., 2020), instrumental neutron activation analysis (INAA) (Kamath et al., 2014), inductively coupled plasma-optical emission spectrometry (ICP-OES) (Merusomayajula et al., 2021) and ICP-MS (Chawla et al., 2020). AAS techniques are often restricted by poorer sensitivity and not being multi-element analytical techniques. There are several studies on the application of XRF techniques in pharmaceutical industry, because of the higher detection limits, they are not very popular for quantitative determinations of metal impurities in pharmaceutical samples. INAA is time-consuming, not independent, requires a reactor nearby and involves longer cooling times for detecting certain elements. ICP-OES and ICP-MS, which was recommended in the USP <233> chapter, can be used for simultaneous determination of several elements. However, both of the two methods suffer from matrix and spectral interference. By contrast, the ICP-MS method has advantages of high sensitivity and specificity (Barin et al., 2016; Janchevska et al., 2020).

Therefore, we developed high throughput ICP-MS method for the quantitative determination of 62 elemental impurities in high matric calcium carbonate samples and validated according to USP 233. The limit of each element here was determined by referring to the daily environmental intake levels (Snyder, 1974), PDE values of related elements in the ICH Q3D and the content range in the products. This method was used to evaluate calcium carbonate preparations which state clearly used for child (including neonates, infants, toddlers, children, and adolescents) and two types of raw materials (light and ground

calcium carbonate), providing the first comprehensive risk assessment of elemental impurities with limit requirements.

MATERIAL AND METHODS

Sample

Two types of calcium carbonate Active Pharmaceutical Ingredient were provided by seven manufacturers. Calcium carbonate preparations, which state clearly used for children (including neonates, infants, toddlers and children), including compound calcium carbonate (effervescent) granules, calcium carbonate D3 (tablets/granules), calcium carbonate, and calcium and zinc gluconate (oral liquid), were available from the Chinese market.

All calcium carbonate preparations have already been tested and they all meet the requirements of the quality standards of ChP 2020.

Sample Preparation

Calcium Carbonate Samples

Two sample processing methods were adopted. In the first method, samples were prepared by dissolving approximately 100 mg of calcium carbonate preparations and calcium carbonate API in a 25 ml volumetric flask with 1.25 ml of concentrated nitric acid and shaking several times to accelerate the dissolution, and then reconstituting with ultrapure water (Milli-Q water purification system) after the reaction is performed about 1 h in room temperature (about 25°C). In the second method, samples were prepared by dissolving approximately 100 mg of calcium carbonate preparations and calcium carbonate API in a 25 ml volumetric flask with 1 ml of concentrated nitric acid and 0.25 ml of hydrochloric acid (CNW Technologies GmbH) with shaking several times to accelerate the dissolution, and then reconstituting with ultrapure water containing 0.1% hydrofluoric acid (HF) after the reaction is performed about 1 h in room temperature (about 25°C). Liquid preparations were tested as a whole vial (5 ml). The test solution was properly diluted as necessary before sample loading. In addition, a blank sample solution was prepared in parallel.

Internal Standard

A 500 ng/ml mixture of iridium and ruthenium (Guobiao (Beijing) Testing & Certification Co., Ltd.) was used as the internal standard, which was introduced online into the spray chamber using a peristaltic pump.

Calibration Standards

The elemental impurities were divided into two groups. The first group included 42 elements (Li, B, Na, Sc, Ti, V, Fe, Co, Cu, Zn, Ge, As, Se, Br, Rb, Zr, Mo, Ag, Cd, In, Te, Ba, Pr, Ce, Nd, Sm, Tb, Dy, Er, Tm, Yb, Lu, Pb, Bi, Th, U, Mg, Al, Mn, Sr, La, and Os) with 5% nitric acid used as the solvent to prepare a multi-element standard stock solution (S1). The second group included 20 elements (Be, Cr, Ni, Ga, Y, Nb, Rh, Pd, Sn, Sb, Cs, Gd, Ho, Hf, Ta, W, Pt, Au, Hg, Tl) with an acid mixture (HNO_3:HCl:H_2O:

HF = 4:1:95:0.1) used as the solvent to prepare a multi-element standard stock solution (S2). The single-element standard solutions were obtained from Guobiao (Beijing) Testing & Certification Co., Ltd. except for Os, which was obtained from Aladdin.

The S1 and S2 stock solutions were prepared as a series of standard solutions of 0, 0.5, 1.0, 1.5, and 10 J, respectively, in which J is the limit for each elemental impurity in the final analysis solution.

Spiked Samples

Spiked samples were prepared at 50% (0.5J), 100% (1.0J), and 150% (1.5J) of the target limit by spiking 100 mg of the calcium carbonate preparations with 250, 500, and 750 µL of the spiking solution, and diluent filled to a total volume of 25 ml. Six preparations at the 100% spiking level were prepared, and three preparations at the 50 and 150% spiking levels were respectively prepared.

Instrumentation

All element determinations were performed on an Agilent 7900 ICP-MS system equipped with standard nickel sampling and skimmer cones, a glass concentric nebulizer, quartz spray chamber, and quartz torch with a 2.5 mm internal diameter injector. The instrument also features a collision/reaction cell including a standard helium (He)-mode cell gas line, which provides effective removal of most common polyatomic interferents. The He gas used in collision cells was of high purity (99.999%). Argon gas was used for plasma and dilution at the recommended purity (99.999%). The instrumental experimental parameters for ICP-MS are listed in **Table 1**. An Agilent SPS-4 Auto-sampler was used to deliver the samples.

Li, Be, and B were measured using No Gas mode; He gas mode was used for other elements, and the stable time was set to 10 s. The integration time was 0.3 s. Ru (mass number 101) was selected as the internal standard for elements with a mass number below 150, and Ir (mass number 193) was used as the internal standard for elements with a mass number above 150. **Table 2** lists the measured mass number of each element. The instruments were tuned systematically. The resolution/mass axis and sensitivity met the measurement requirements of the instruments. Instrument tuning and P/A factor tuning were conducted before batch operation to achieve the best experimental conditions.

RESULTS AND DISCUSSION

Development and Validation of the ICP-MS Method

To achieve a comprehensive assessment of potential elemental impurities in calcium carbonate, there are 62 kinds of target elemental impurities in the study, including most of the elements other than synthetic, radioactive, inert gases and major components of air. The majority of elemental impurity content is in ppb-ppt level. However, ICP-OES is not sensitive enough. The addition of the sample may lead to higher matrix effect and

Parameter	Setting	Parameter	Setting
Plasma power	1550 W	Sample lifting rate	0.1 rps
Sampling depth	10.0 mm	Spray chamber temperature	2°C
Nebuliser	MicroMist nebulizer	Acquisition mode	Mass spectrum
He gas flow	4.3 ml/min	Peak type	3 points
Carrier gas flow	1.01 L/min	Number of replicates	3

there are too many kinds of impurity and serious line interference. Therefore, ICP-MS method with higher sensitivity is selected in this study. To avoid interactions between elemental impurities, elemental impurities had been properly grouped. A high-throughput method was established for the analysis of 62 elemental impurities in calcium carbonate preparations using different digestion methods. The instrument was equipped with a collision reaction cell. Multiatomic mass spectral interference was eliminated by collision mode of He. As the mass number of Li, Be and B elements is close to that of He, the collision between He and collision reaction cell may lead to undetectable or extremely low response. Therefore, to gain higher sensitivity, No Gas mode was chosen. The dilution of the sample should be considered in combination with the LOD and LOQ of each elemental impurity and matrix interference. Insufficient dilution could cause strong matrix interference. At the same time, it could cause rapid changes in the instrument state. For example, the taper hole accumulation of Ca may lead to the high matrix of the Ca element and poor recovery of elements. On the other hand, over dilution may make higher demands on the LOD of the element. Strongly memory effect of Nb, Ta, and Hf cause LOQ close to their proposed J value under 5% nitric acid matrix. So it's difficult to meet the detection requirements. Therefore, 0.1% hydrofluoric acid was used to reduce or eliminate the memory effect. With these optimizations, Nb, Ta, and Hf were ultimately detected with excellent limits of quantification (<4 ppb) in He mode. High temperature digestion could cause low recovery of Os and other elements. Hg and other elements need appropriate amount of HCl as a stabilizer (Barin et al., 2016). HCl contains a large amount of Br element, and Ag element reacts with Cl ion to affect the quantity of Ag. This study selected Room temperature digestion. Compared the effects of nitric acid and a mixture of 80:20 nitric acid-hydrochloric acid, simple dissolution in 5% HNO_3 and HNO_3/HCl、2% HNO_3 and HNO_3/HCl which were selected as appropriate for the detection of different elemental impurities. Results indicated simple dissolution needs more time for the reaction. However, the sample contained a large amount of Ca. To further reduce the influence of matrix effect on the results, the standard curve method of internal standard correction was selected. According to the results of the pre-experiment, Ir and Ru were not detected in the samples. Therefore, these two elements were selected as internal standard in this study.

Except for related elements in the ICH Q3D, the PDE values of other elements was also determined by referring to the daily environmental intake levels and the content range in the

products. According to USP<233>, the method validation was based on the J, which was calculated depending on the PDE.

The ICP-MS method was successfully validated in terms of linearity, limit of quantification, accuracy, precision, intermediate precision, specificity, and range to fulfill the requirements for the validation of alternative procedures stated in USP chapter 233. The correlation coefficients for each element were all ≥0.99. The limits of quantitation and range for all elements met the accuracy requirement. The spike recoveries of elements from calcium carbonate preparations are listed in **Table 2**. Except for the recovery rate of 68% for Br and U at 0.5 J, which was slightly lower than the limit requirement of 70%, all of the other elements met the accuracy requirement of 70–150%. A second analyst prepared and analyzed six preparations of the approximately 100% target limit spiked samples (J) with freshly prepared spiking solutions on a different day. The samples were quantified against fresh calibration standards. Ruggedness was established as operator/day to operator/day precision change in the mean. The results determined for ruggedness are summarized in **Table 2**. The RSD% for all preparations ($n = 12$) for each target element was ≤25%. All acceptance criteria described in USP chapters 233/232 for ruggedness were met.

Risk Assessment and Control of Impurity Elements in Calcium Carbonate API Samples

Calcium carbonate is found throughout nature, including in the form of limestone, marble, calcite, and coral. The majority of industrial products containing calcium carbonate are powder materials that are produced through processing the calcium carbonate ore by a mechanical method (i.e., ground calcium carbonate) or a chemical method (i.e., light calcium carbonate). In this study, we assessed light calcium carbonate from four different manufacturers (including seven batches from manufacturer I and one batch each from the other manufacturers) and assessed ground calcium carbonate from three different manufacturers (including four batches from manufacturer V and one batch each from the other manufacturers).

Comparing the test results of light calcium carbonate from manufacturer I and ground calcium carbonate from manufacturer V (Table S1), 15 elemental impurities were not detected in the light calcium carbonate, 23 elemental impurities were not detected in the ground calcium carbonate, and 13 elemental impurities were not detected in either type of calcium carbonate. Taking elemental impurity content within

TABLE 2 | Accuracy (mean spike recovery%), repeatability, and intermediate precision (as RSD%).
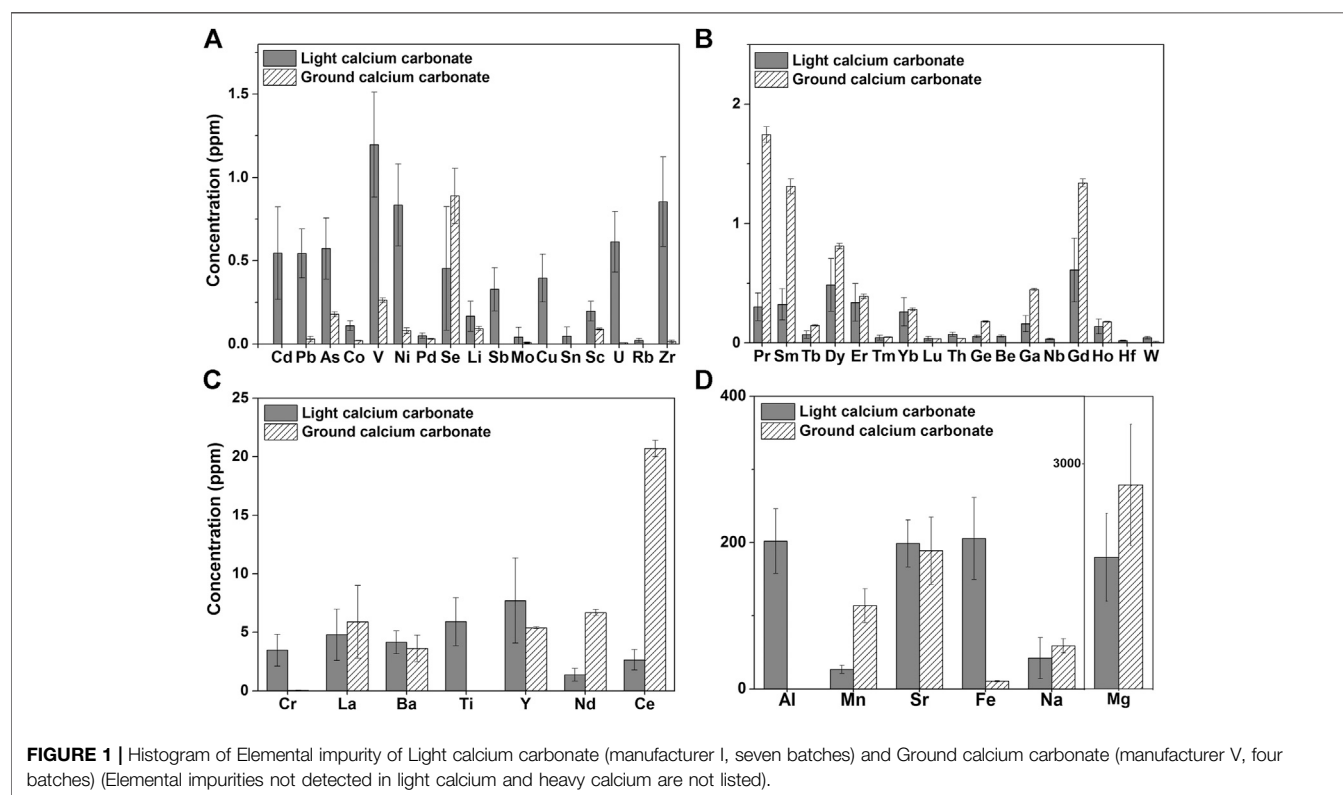
Element	Isotope	Mode	LOD	LOQ	Recovery (%, *n* = 3)			Repeatability (RSD%, *n* = 6)	Intermediate precision (RSD%, *n* = 12)	J (ppb)
					0.5J	1.0J	1.5J			
Cd	111	He	0.0009	0.003	86.8	101.2	98.8	9.7	9.6	2
Pb	208	He	0.006	0.02	78.4	86.4	88.4	11.0	10.1	2
As	75	He	0.005	0.02	86.4	99.9	99.0	9.9	9.5	4
Hg	201	He	0.02	0.05	100.5	102.0	110.5	3.1	2.9	8
Co.	59	He	0.002	0.008	89.3	100.0	98.3	8.0	8.4	4
V	51	He	0.005	0.02	89.3	99.6	96.1	8.7	8.7	20
Ni	60	He	0.006	0.02	90.3	100.0	103.0	4.3	3.7	4
Tl	205	He	0.004	0.01	87.8	89.8	96.6	7.2	5.4	2
Au	197	He	0.2	0.5	104.4	103.0	106.6	4.3	4.0	20
Pd	105	He	0.003	0.01	93.6	96.1	102.1	7.1	5.1	5
Os	189	He	0.04	0.1	104.4	113.3	135.3	7.8	8.3	0.5
Rh	103	He	0.001	0.005	96.1	97.2	104.2	6.9	5.1	0.4
Se	82	He	0.4	1.3	96.3	107.3	112.4	8.9	8.2	40
Ag	107	He	0.002	0.006	87.4	96.8	95.7	8.5	8.1	2
Pt	195	He	0.002	0.005	93.1	94.0	103.5	7.0	5.7	0.8
Li	7	No gas	0.03	0.1	99.2	97.0	98.7	1.4	17.9	5.0
Sb	121	He	0.002	0.006	93.7	103.9	115.6	7.4	6.1	5
Ba	137	He	0.01	0.03	70.5	88.7	90.2	13.3	12.6	10
Mo	95	He	0.004	0.01	93.1	103.1	101.3	8.0	7.9	8
Cu	63	He	0.03	0.08	89.6	100.2	97.4	8.4	8.4	100
Sn	118	He	0.01	0.03	105.2	106.0	115.4	8.1	5.8	0.4
Cr	52	He	0.01	0.04	99.5	108.3	114.8	4.4	3.5	60
B	11	No gas	0.9	3	88.1	86.1	86.3	1.5	16.4	200
Na	23	He	6	21	72.1	86.8	92.6	13.5	13.2	200
Sc	45	He	0.02	0.1	85.1	94.2	92.1	8.4	8.3	50
Ti	47	He	0.06	0.2	77.6	91.8	90.6	10.0	10.2	50
Fe	56	He	0.6	2	75.8	90.1	88.1	10.1	10.5	800
Zn	66	He	1	4	86.8	95.6	93.1	8.4	8.0	200
Ge	72	He	0.008	0.03	81.1	97.3	95.7	8.6	9.0	4
Br	79	He	1.5	4.9	67.7	81.4	81.7	10.0	9.0	120
Rb	85	He	0.002	0.005	75.4	90.6	87.2	10.6	8.8	0.4
Zr	90	He	0.005	0.02	89.0	98.7	98.1	9.1	8.6	20
In	115	He	0.004	0.01	85.5	95.7	94.9	8.6	8.6	50
Te	125	He	0.01	0.04	83.7	94.7	97.4	10.5	10.6	4
Pr	141	He	0.0003	0.0008	78.2	91.9	93.2	11.0	11.5	0.4
Ce	142	He	0.002	0.008	91.9	103.5	100.7	8.3	8.8	100
Nd	146	He	0.001	0.005	90.2	100.3	97.2	8.6	8.4	20
Sm	147	He	0.0005	0.002	92.6	101.1	100.1	8.5	8.9	8
Tb	159	He	0.0004	0.001	84.8	91.5	91.5	7.8	7.2	2
Dy	163	He	0.0002	0.0008	84.6	92.0	91.8	7.9	7.2	5
Er	166	He	0.0003	0.001	87.7	94.4	93.6	7.8	7.0	8
Tm	169	He	0.00004	0.0001	87.1	94.6	93.6	7.7	6.9	2
Yb	172	He	0.0004	0.001	87.9	95.0	93.8	7.6	6.9	20
Lu	175	He	0.0004	0.001	83.5	90.7	91.1	7.6	6.8	16
Bi	209	He	0.02	0.06	96.8	99.4	91.2	7.0	7.6	0.4
Th	232	He	0.0004	0.001	80.0	91.8	92.9	10.8	10.6	0.24
U	238	He	0.0002	0.0006	68.2	82.0	85.9	20.3	19.9	0.2
Be	9	No gas	0.001	0.004	93.8	102.7	89.6	7.7	14.2	2
Ga	71	He	0.002	0.006	100.7	106.6	114.1	6.9	5.5	4
Y	89	He	0.001	0.004	103.8	107.7	116.9	7.3	5.3	20
Nb	93	He	0.0005	0.002	119.2	119.2	123.5	5.8	6.6	0.4
Cs	133	He	0.0005	0.002	99.9	104.0	113.4	6.7	4.8	0.8
Gd	160	He	0.0006	0.002	103.0	108.2	116.4	3.4	2.8	8
Ho	165	He	0.00008	0.0003	101.4	103.6	112.8	6.4	4.5	0.8
Hf	178	He	0.0009	0.003	110.0	106.9	112.6	6.8	5.1	0.4
Ta	181	He	0.0006	0.002	111.4	107.4	114.2	6.9	5.3	0.2
W	182	He	0.001	0.004	105.3	103.9	112.9	6.8	4.8	2

(Continued on following page)

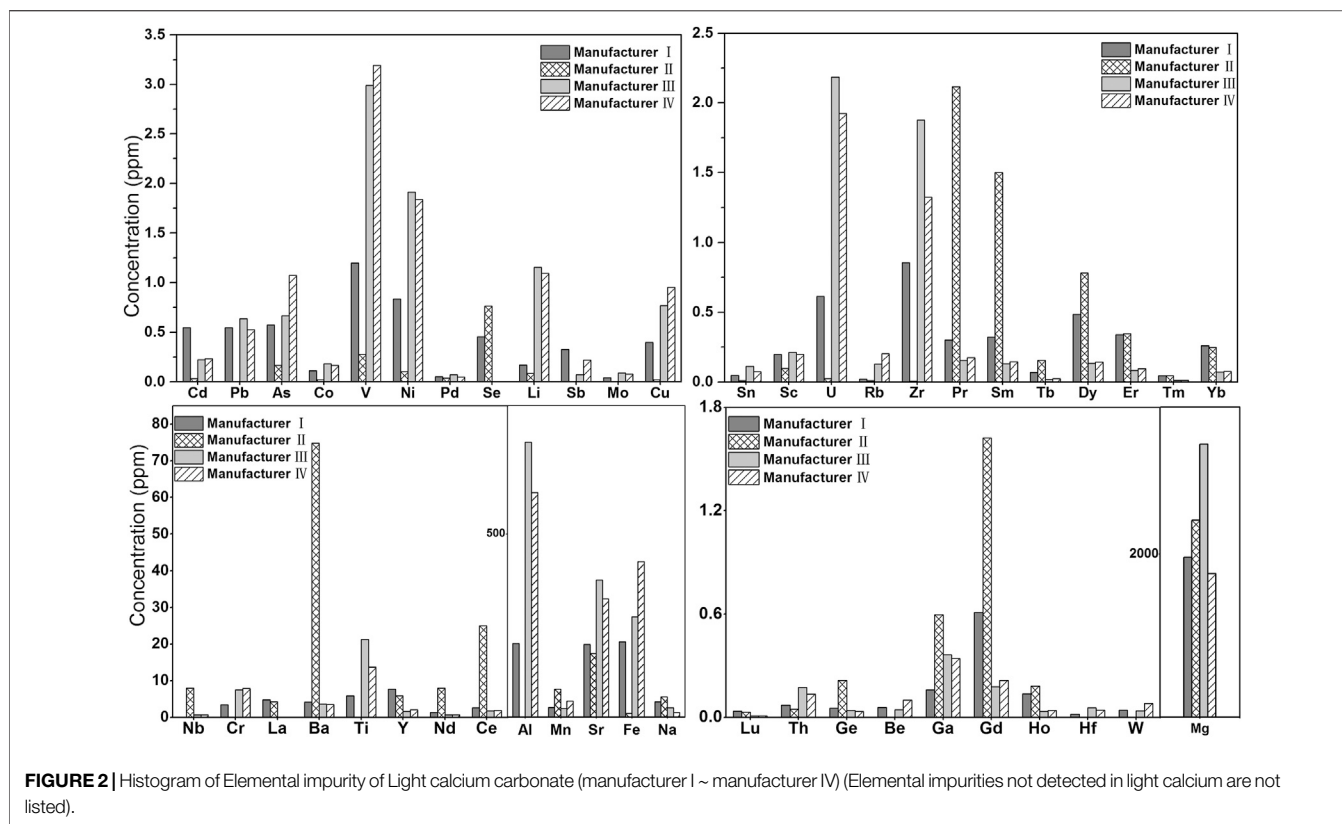TABLE 2 | (*Continued*) Accuracy (mean spike recovery%), repeatability, and intermediate precision (as RSD%).

Element	Isotope	Mode	LOD	LOQ	Recovery (%, n = 3)			Repeatability (RSD%, n = 6)	Intermediate precision (RSD%, n = 12)	J (ppb)
					0.5J	1.0J	1.5J			
Mg	24	He	0.6	2	87.7	112.6	98.8	8.4	5.9	1,000
Al	27	He	2	7	90.5	109.0	98.2	6.7	4.7	200
Mn	55	He	0.03	0.1	95.7	108.9	100.6	6.4	4.7	30
Sr	88	He	0.03	0.1	92.3	111.3	100.9	7.1	5.2	100
La	139	He	0.8	3	87.7	102.5	94.2	8.6	7.2	50

The J value was determined according to both the permitted daily exposure (PDA) value of the drug and the dilution multiple during sample preparation. Sample preparation: 100 mg to 25 ml, dilution multiple 4,000 (n), J = PDE/n.

FIGURE 1 | Histogram of Elemental impurity of Light calcium carbonate (manufacturer I, seven batches) and Ground calcium carbonate (manufacturer V, four batches) (Elemental impurities not detected in light calcium and heavy calcium are not listed).

three times the average value as the standard of no difference, we identified 15 elemental impurities with no difference between light and ground calcium carbonate, 22 elemental impurities with higher content in light calcium carbonate than in ground calcium carbonate, and only nine elemental impurities with higher content in ground calcium carbonate than in light calcium carbonate. Specifically, as shown in **Figure 1**, the contents of Cd, Pb, As, V, Ni, Cr, and Cu in light calcium carbonate were higher than those in ground calcium carbonate, and the values also showed a larger SD in light calcium carbonate (**Figure 1A**). By contrast, the contents of Ge, Ce, Nd, Sm, Ga, and other elements were higher in ground calcium carbonate than those in light calcium carbonate, but the SD was smaller than that in light calcium carbonate (**Figures 1B,C**). Among them, the content of

Ce in ground calcium carbonate was approximately 10 times higher than that in light calcium carbonate. In addition, the content of Mn in ground calcium carbonate was 114 ± 23 ppm, whereas that in light calcium carbonate was 28 ± 6 ppm, indicating both a higher mean and SD in ground calcium carbonate (**Figure 1D**). The differences between the two types of calcium carbonate were manifested in the quantity, content, and batch difference of their constituent elemental impurities. This overall comparison of the detection results of light calcium carbonate from manufacturer I and ground calcium carbonate from manufacturer V showed that ground calcium carbonate is slightly superior to light calcium carbonate in terms of the content, quantity, and variation degree of elemental impurities, whereas the content and variation of different elemental

FIGURE 2 | Histogram of Elemental impurity of Light calcium carbonate (manufacturer I ~ manufacturer IV) (Elemental impurities not detected in light calcium are not listed).

impurities had no absolute correlation with calcium carbonate type.

Among the 24 elements specified in the ICH Q3D, 12 impurities in light calcium carbonate from manufacturer I were detected at higher levels than those in ground calcium carbonate from manufacturer V. In particular, the levels of the primary elements Cd (0.6 ± 0.3 ppm) and Pb (0.5 ± 0.1 ppm) were higher than the limit requirements (0.5 ppm, based on a daily dose of 10 g), although the levels of other elements were lower than the control thresholds, with some notable variation. For elements not specified in the Q3D, we referred to the data on environmental exposure (Snyder, 1974) and set the limit far lower than the environmental exposure. Among these elements, La (~5 ppm), Sr (~200 ppm), Yb (~0.3 ppm), Dy (~0.7 ppm), and Er (~0.4ppm) were detected in both types of calcium carbonate with comparable content. The contents of Pr, Ce, and Nd in ground calcium carbonate were higher than the proposed limit value, and the contents of PR, Ce, and Nd differed substantially between light and ground calcium carbonate. For such elemental impurities without clearly defined limit requirements, in-depth toxicological studies should be conducted to establish reasonable limits.

At present, the Fe content in calcium carbonate raw materials is mainly controlled by comparison with a standard iron solution through a color reaction. The ChP specifies that the Fe content should not exceed 400 ppm, whereas the EP specifies a limit of 200 ppm. Using our ICP-MS method, the Fe content in light calcium carbonate products from manufacturer IV was 424 ppm,

which is close to or higher than the limit requirement, and it was difficult to distinguish accurately by visual colorimetry.

Importantly, the content of each elemental impurity detected in light calcium carbonate products from different manufacturers varied greatly (**Figure 2**). The Cd content in products from manufacturer I was 0.6 ppm, while that in products from manufacturer II was only 0.03 ppm. Other elemental impurities such as Pb (0–0.6 ppm), As (0.2–1.1 ppm), Fe (10–424 ppm), and La (0–5 ppm) also showed great content variations among products from different manufacturers. Among the ground calcium carbonate products from three manufacturers (**Supplementary Table S1**), the Ba (2,629 ppm) content of ground calcium carbonate from manufacturer VI did not meet the standard in the pharmacopoeia (ChP and USP), which is consistent with the detection results of this method. The La element in the ground calcium carbonate from manufacturer VIII was 26 ppm higher than that of other manufacturers (about 6 ppm), whereas the content of each elemental impurity in the ground calcium carbonate products from other manufacturers was consistent.

This observed difference in elemental impurities between light and ground calcium carbonate may be due to the fact that light calcium carbonate is generally produced by calcining natural limestone from broad sources, whereas ground calcium carbonate is generally produced by grinding natural calcite with high whiteness and purity. The sources of limestone as the raw material of calcium carbonate preparations may vary among manufacturers, resulting in large variations in the elemental

impurities in the light calcium carbonate produced by different manufacturers, whereas the elemental impurities in ground calcium carbonate prepared from calcite are relatively stable. Therefore, from the perspective of quality control, ground calcium carbonate is recommended as the raw material of calcium supplement preparations. In addition, considering the uncertainty about raw material sources, corresponding quality control methods should be established for both light and ground calcium carbonate, and only raw materials that meet the requirements for the production of preparations should be selected so as to ensure high quality.

Risk Assessment and Control of Impurity Elements in Calcium Carbonate Preparations

The elemental impurities of toxicological concern detected in multiple batches of calcium carbonate preparations from nine manufacturers all met the Q3D limit requirements. However, the limits of some elemental impurities differ from those of mineral indicators in infant formula food standards; therefore, these preparations may have certain risks when given to young children. The detailed test results are summarized in **Supplementary Table S2**. For example, the Se content in the products from manufacturers P1 (0.5 ± 0.06 ppm) and P9 (0.4 ± 0.03 ppm) exceeded the 0.06 ppm limit specified by infant formula food standards, but was far lower than the 15 ppm limit specified by the Q3D. In all products tested, the content of the heavy metal Cu did not exceed the limit of 0.9 ppm specified by infant formula food standards or the much higher limit requirement of the Q3D (300 ppm). In view of these mineral elements with different specified limits, it is suggested to attempt to meet the nutritional requirements only so as to avoid possible safety risks caused by an excessive dosage, especially for young children and infants.

The preparation from manufacturer P4 was a calcium supplement preparation specifically designed for children, and the Pb content was slightly higher than the control threshold, whereas the Pb content in preparation products from other manufacturers was 30% lower than the limit. The content of Pb in multiple batches of raw materials was above 0.5 ppm with a maximum of 0.2 ppm. These results demonstrated that the main source of Pb in the preparations was the raw materials, whereas the auxiliary materials had only a low or no contribution to the elemental impurities. The content of Pb in preparations from different manufacturers ranged from 0.01 to 0.2 ppm, indicating high variation among different manufacturers. Blood Pb levels above 10 μg/dl are known to affect various areas of the brain that influence behavior and cause many other health problems in children (Flannery et al., 2020). Therefore, an exclusive method should be adopted to ensure that the content of Pb meets the limit requirements. Hg, Os, and Pt were not detected in any of the preparations.

Although the contents of other elements varied among different products, they were all far lower than the Q3D limits. However, it is worth noting that the content of Na was 26,000 ppm in products from manufacturer P3 and was approximately 2,000 ppm in products from manufacturer P4. The content of Na in products from other manufacturers ranged between 25 ± 3 ppm and 258 ± 16 ppm, but was lower than 100 ppm in many batches of raw materials, and did not differ between the light and ground calcium carbonate. However, USP and ChP pharmacopoeia are no relevant inspection item for Na in the standards for calcium carbonate preparations, only alkali metal inspection items. According to the standards of the pharmacopoeia, calcium is precipitated from calcium carbonate raw materials by an ammonium oxalate test solution, sulfuric acid is added to the filtered solution for the reaction, and finally the levels of Mg and alkali metals (Li, Na, K, Rb, and Cs) in calcium carbonate raw materials are controlled based on an ignition residue not exceeding 1.0%. we know that the content of Na for meeting normal nutritional needs specified in the infant formula food standards for infants aged 0–12 months is 120–410 ppm (National Health Commission of the People's Republic of China, 2010; Standard for Infant Formula and Formulations for Special Medical Purposes Intended for Infants, 2007). The pharmacopoeia method obviously cannot meet the current testing requirements. Accordingly, the daily dosage for infants described in the instructions of preparations from manufacturers P3 and P4 are likely to cause Na to exceed the appropriate intake, imposing a great health risk. The variation in Na content among products is likely derived from its introduction in the preparation process. Sodium-containing excipients are commonly used in calcium carbonate preparations to avoid rapid precipitation of calcium carbonate. However, excessive Na causes hypertension and increases the excretion burden of the kidneys, which may lead to water and salt metabolic disorders in infants and toddlers, and may even cause organ injuries (Appel et al., 2015). Therefore, calcium carbonate preparations for children should avoid the use of sodium-containing excipients, and further research is needed to further evaluate Na as an introduced element in preparation products so as to avoid any risks of intake by young children.

The Fe content in calcium carbonate raw materials is controlled through specific inspection items, but no relevant control items are specified for preparation products. The content of Fe in preparations from manufacturer P4 and that in the light calcium carbonate raw material from manufacturer IV was 472 and 424 ppm, respectively, which were close to the limit requirements for raw materials, indicating that Fe might be introduced mainly from the raw materials or preparation processes. The content of Fe in the products from manufacturer P4 was far higher than the limit requirement of 11 ppm in infant formula food (National Health Commission of the People's Republic of China, 2010; Standard for Infant Formula and Formulations for Special Medical Purposes Intended for Infants, 2007), indicating certain risks for infants.

Overall, these results suggest that the elemental impurities in calcium carbonate preparations, such as Na and Fe, are mainly introduced in the preparation process as well as from the raw materials. However, there are no relevant inspection items in current drug standards or corresponding statements in the preparation instructions, which can impose an unknown

risk to young children. Therefore, inspection items for Na, Fe, and other elemental impurities should be added for calcium carbonate preparations, especially those labeled specifically as "for use in children." ICP-MS is a modern analytical method recommended by the USP 233. Therefore, ICP-MS should be selected as an alternative to traditional methods for evaluations and control of the elemental impurities in calcium carbonate from mineral sources and its preparation products.

CONCLUSION

The high-throughput ICP-MS method for the quantitative determination of 62 elemental impurities in high matric calcium carbonate samples were developed and used to evaluate calcium carbonate preparations used for child (including neonates, infants, toddlers, children, and adolescents) and two types of raw materials (light and ground calcium carbonate).

Results in raw materials indicated testing should be required for each batch because the levels of these impurities varied significantly from one batch to another due to variations in source. The elemental impurities which cause toxicological concerns in calcium carbonate products intended for children all met the current Q3D limit requirements, marked variations were found between different manufacturers and batches, especially for Pb, Na, and Fe. Specific inspection items should be set up, and modern

analysis methods such as ICP-MS should be adopted for accurate quality control so as to ensure the safety of long-term calcium supplementation in children.

Our results indicate the pediatric drugs should adhere to the concept of "tailor-made" and the quality standards for pediatric drugs should be formulated in addition to flavor and dosage forms to ensure the safety of pediatric medication, especially for calcium supplements which are commonly used.

DATA AVAILABILITY STATEMENT

The original contributions presented in the study are included in the article/**Supplementary Material**, further inquiries can be directed to the corresponding authors.

AUTHOR CONTRIBUTIONS

CX, RG, and XZ performed the experiment, CX, LZ, ZL, and CH conceived the project, CX and LZ analyzed the data, CX and LZ wrote the paper.

SUPPLEMENTARY MATERIAL

The Supplementary Material for this article can be found online at: https://www.frontiersin.org/articles/10.3389/fchem.2021.682798/full#supplementary-material

REFERENCES

Al Osman, M., Yang, F., and Massey, I. Y. (2019). Exposure Routes and Health Effects of Heavy Metals on Children. *Biometals* 32 (4), 563–573. doi:10.1007/s10534-019-00193-5

Appel, L. J., Lichtenstein, A. H., Callahan, E. A., Sinaiko, A., Van Horn, L., and Whitsel, L. (2015). Reducing Sodium Intake in Children: A Public Health Investment. *J. Clin. Hypertens.* 17 (9), 657–662. doi:10.1111/jch.12615

Avula, B., Wang, Y.-H., Smillie, T. J., Duzgoren-Aydin, N. S., and Khan, I. A. (2010). Quantitative Determination of Multiple Elements in Botanicals and Dietary Supplements Using ICP-MS. *J. Agric. Food Chem.* 58 (16), 8887–8894. doi:10.1021/jf101598g

Baker, S. S., Cochran, W. J., Flores, C. A., Georgieff, M. K., Jacobson, M. S., Jaksic, T., et al. (1999). American Academy of Pediatrics. Committee on Nutrition. Calcium Requirements of Infants, Children, and Adolescents. *Pediatrics* 104 (5 Pt 1), 1152–1157.

Barin, J. S., Mello, P. A., Mesko, M. F., Duarte, F. A., and Flores, E. M. M. (2016). Determination of Elemental Impurities in Pharmaceutical Products and Related Matrices by ICP-Based Methods: a Review. *Anal. Bioanal. Chem.* 408 (17), 4547–4566. doi:10.1007/s00216-016-9471-6

Brandão, M. H. T., and Gontijo, B. (2012). Contact Sensitivity to Metals (Chromium, Cobalt and Nickel) in Childhood. *Bras. Dermatol.* 87 (2), 269–276. doi:10.1590/s0365-05962012000200012

Chawla, R. K., Panda, S., Umasankar, K., Panda, S. P., and Damayanthi, D. (2020). Risk Assessment, Screening and Control of Elemental Impurities in Pharmaceutical Drug Products: A Review. *Cpa* 16 (7), 801–805. doi:10.2174/1573412915666190314144134

Chowdhury, A. R., Maheshwari, N., Soni, J., Kapil, M., Mehta, T., and Mukharya, A. (2020). Quantitative X-Ray Fluorescence Analysis: Trace Level Detection of

Toxic Elemental Impurities in Drug Product by ED-XRF Spectrometer. *J. Pharm. Biomed. Anal.* 189, 113292. doi:10.1016/j.jpba.2020.113292

Colognato, R., Bonelli, A., Ponti, J., Farina, M., Bergamaschi, E., Sabbioni, E., et al. (2008). Comparative Genotoxicity of Cobalt Nanoparticles and Ions on Human Peripheral Leukocytes In Vitro. *Mutagenesis* 23 (5), 377–382. doi:10.1093/mutage/gen024

Flannery, B. M., Dolan, L. C., Hoffman-Pennesi, D., Gavelek, A., Jones, O. E., Kanwal, R., et al. (2020). U.S. Food and Drug Administration's Interim Reference Levels for Dietary Lead Exposure in Children and Women of Childbearing Age. *Regul. Toxicol. Pharmacol.* 110, 104516. doi:10.1016/j.yrtph.2019.104516

International Council for Harmonization of Technical Requirements for Pharmaceuticals for Human Use(ICH) (2019). Guideline for Elemental Impurities. Q3D. Available at: http://www.ich.org/products/guidelines/quality/artical/quality-guidelines.html.

Janchevska, K., Stafilov, T., Memed-Sejfulah, S., Bogdanoska, M., Ugarkovic, S., and Petrushevski, G. (2020). ICH Q3D Based Elemental Impurities Study in Liquid Pharmaceutical Dosage Form with High Daily Intake - Comparative Analysis by ICP-OES and ICP-MS. *Drug Dev. Ind. Pharm.* 46 (3), 456–461. doi:10.1080/03639045.2020.1724136

Jurowski, K., Krośniak, M., Fołta, M., Tatar, B., Cole, M., and Piekoszewski, W. (2019). Safety Assessment of the Trace Element Impurities Ni and Cr in Pharmaceutical Herbal Products for Teething from Polish Pharmacies. *Biol. Trace Elem. Res.* 191 (2), 517–521. doi:10.1007/s12011-019-1643-8

Kamath, S. U., Pemiah, B., Rajan, K. S., Krishnaswamy, S., Sethuraman, S., and Krishnan, U. M. (2014). Variations in Physicochemical Properties of a Traditional Mercury-Based Nanopowder Formulation: Need for Standard Manufacturing Practices. *Indian J. Pharm. Sci.* 76 (6), 495–503.

Kutty, V. R., Abraham, S., and Kartha, C. C. (1996). Geographical Distribution of Endomyocardial Fibrosis in South Kerala. *Int. J. Epidemiol.* 25 (6), 1202–1207. doi:10.1093/ije/25.6.1202

Lee, W. T., and Jiang, J. (2008). Calcium Requirements for Asian Children and Adolescents. *Asia Pac. J. Clin. Nutr.* 17 (Suppl. 1), 33–36.

Levin, R., Brown, M. J., Kashtock, M. E., Jacobs, D. E., Whelan, E. A., Rodman, J., et al. (2008). Lead Exposures in U.S. Children, 2008: Implications for Prevention. *Environ. Health Perspect.* 116 (10), 1285–1293. doi:10.1289/ehp.11241

Linshaw, M., Aigbe, M., and Kaskel, F. (1998). The Mineral Disorders in Pediatrics. *Semin. Nephrol.* 18 (3), 280–294.

Merusomayajula, K. V., Tirukkovalluri, S. R., Kommula, R. S., Chakkirala, S. V., and Kottapalli, P. K. S. R. (2021). Development and Validation of a Simple and Rapid ICP-OES Method for Quantification of Elemental Impurities in Voriconazole Drug Substance. *Future J. Pharm. Sci.* 7 (1), 45. doi:10.1186/s43094-020-00159-2

National Health Commission of the People's Republic of China (2010). *National Food Safety Standard Infant Formula.*

National Research Council Committee on Measuring Lead in Critical P (1993). in *By the National Academy of Sciences* (Washington (DC): National Academies Press (US) CopyrightAll rights reserved).

Olympio, K. P. K., Gonçalves, C., Günther, W. M. R., and Bechara, E. J. H. (2009). Neurotoxicity and Aggressiveness Triggered by Low-Level Lead in Children: a Review. *Rev. Panam Salud Publica* 26 (3), 266–275. doi:10.1590/s1020-49892009000900011

Pu, F., Chen, N., and Xue, S. (2016). Calcium Intake, Calcium Homeostasis and Health. *Food Sci. Hum. Wellness* 5 (1), 8–16. doi:10.1016/j.fshw.2016.01.001

Sauer, B., Xiao, Y., Zoontjes, M., and Kroll, C. (2020). Application of X-Ray Fluorescence Spectrometry for Screening Pharmaceutical Products for Elemental Impurities According to ICH Guideline Q3D. *J. Pharm. Biomed. Anal.* 179, 113005. doi:10.1016/j.jpba.2019.113005

Sheth, A. C., and Patel, P. U. (2020). Review of Elemental Impurities in Pharmaceuticals Arena. *ijpqa* 11 (2), 214–218. doi:10.25258/ijpqa.11.2.3

Singh, R., Gautam, N., Mishra, A., and Gupta, R. (2011). Heavy Metals and Living Systems: An Overview. *Indian J. Pharmacol.* 43 (3), 246–253. doi:10.4103/0253-7613.81505

Snyder, W. S. (1974). Report of the Task Group on Reference Man. *Ann. ICRP* 3, 1–4. doi:10.1016/0146-6453(79)90123-4

Standard for Infant Formula and Formulas for Special Medical Purposes Intended for Infants (2007). CODEX STAN 72-1981. Available at: http://wwwcodexalimentariusnet/web/more_infojsp?id_sta=288.

US Food and Drug Administration (2020). Q3D Elemental Impurities- Guidance for Industry. Available at: https://www.fda.gov/downloads/drugs/guidances/ucm371025.pdf. (Accessed January 16, 2019).

U.S. EPA (2009). *IRIS Toxicological Review of Cerium Oxide and Cerium Compounds (Interagency Science Discussion Draft)*. Washington, D.C.: U.S. Environmental Protection Agency.

Wang, Q., Han, M. F., and Wang, J. W. (2007). Manufacture Process of Light Calcium Carbonate from Limestone. *Kem* 336–338, 1843–1845. doi:10.4028/www.scientific.net/KEM.336-338.1843

Conflict of Interest: The authors declare that the research was conducted in the absence of any commercial or financial relationships that could be construed as a potential conflict of interest.

Novel Pyran-Linked Phthalazinone-Pyrazole Hybrids: Synthesis, Cytotoxicity Evaluation, Molecular Modeling, and Descriptor Studies

M. Shaheer Malik[1]*, Basim H. Asghar[1]*, Riyaz Syed[2], Reem I. Alsantali[3], Moataz Morad[1], Hatem M. Altass[1,4], Ziad Moussa[5], Ismail I. Althagafi[1], Rabab S. Jassas[6] and Saleh A. Ahmed[1,7]*

[1]Department of Chemistry, Faculty of Applied Sciences, Umm Al-Qura University, Makkah, Saudi Arabia, [2]Department of Chemistry, Jawaharlal Nehru Technological University, Hyderabad, India, [3]Department of Pharmaceutical Chemistry, Pharmacy College, Taif University, Makkah, Saudi Arabia, [4]Research Laboratories Unit, Faculty of Applied Science, Umm Al-Qura University, Makkah, Saudi Arabia, [5]Department of Chemistry, College of Science, United Arab Emirates University, Al Ain, United Arab Emirates, [6]Department of Chemistry, Jamoum University College, Umm Al-Qura University, Makkah, Saudi Arabia, [7]Department of Chemistry, Faculty of Science, Assiut University, Assiut, Egypt

A series of novel pyran-linked phthalazinone-pyrazole hybrids were designed and synthesized by a facile one-pot three-component reaction employing substituted phthalazinone, 1H-pyrazole-5-carbaldehyde, and active methylene compounds. Optimization studies led to the identification of L-proline and ethanol as efficient catalyst and solvent, respectively. This was followed by evaluation of anticancer activity against solid tumor cell lines of lung and cervical carcinoma that displayed IC_{50} values in the range of 9.8–41.6 μM. Molecular modeling studies were performed, and crucial interactions with the target protein were identified. The drug likeliness nature of the compounds and molecular descriptors such as molecular flexibility, complexity, and shape index were also calculated to understand the potential of the synthesized molecules to act as lead-like molecule upon further detailed biological investigations as well as 3D-QSAR studies.

Keywords: phthalazinone, pyrazole hybrids, pyran, multicomponent, anticancer activity, molecular modelling, molecular descriptors

INTRODUCTION

Phthalazine and its derivative phthalazinone are heterocyclic scaffolds that are extensively explored for potential application in the treatment of a wide range of medical conditions (Vila et al., 2015). Given its significance as a pharmacophore, phthalazine is a key moiety in various new chemical entities that exhibit antidiabetic, anticonvulsant, anti-inflammatory, antihypertensive, and analgesic activities (Young Taek et al., 2017; Sangshetti et al., 2019; Mohd and Mohammad, 2020). Particularly, a wide array of phthalazine-derived compounds have been reported as anticancer agents for various molecular targets (Sung Kim et al., 2004; Loh et al., 2005; Wang et al., 2014). Further, the importance of phthalazine is highlighted by the presence of such pharmacophore as a part of several marketed drugs such as olaparib, azelastine, vatalanib, and zopolrestat (**Figure 1**; Inskeep et al., 1994; Joensuu
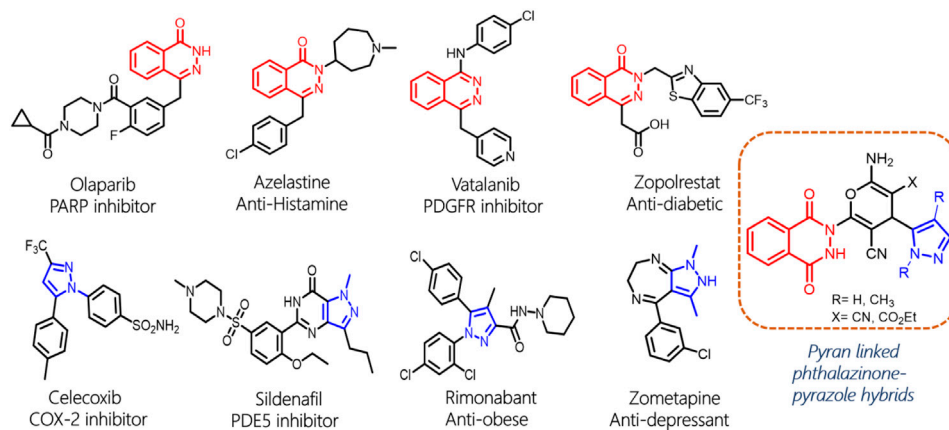
FIGURE 1 | Drugs with phthalazine or pyrazole moieties and design strategy of phthalazine pyrazoles.

et al., 2011; Gunderson and Moore, 2015; Cheng et al., 2019). Moreover, phthalazines also exhibit promising prospects as fluorescence probes and luminescence materials (Saha et al., 2013; Martins et al., 2019). Similarly, the pyrazole molecule, a five-membered heterocycle with two nitrogen atoms, has emerged as a powerful scaffold due to its therapeutic potential. Pyrazole scaffold–containing chemical agents have a broad spectrum of biological activity and are well documented to display a plethora of pharmacological properties, such as antiviral, antibacterial, anti-HIV, anti-fungicidal, antidepressant, antidiabetic, antitumor, anti-inflammatory, and antihelminthic activities (Khan et al., 2016; Karrouchi et al., 2018; Bennani et al., 2020). Additionally, the pyrazole scaffold is a cornerstone in various marketed drugs such as celecoxib, sildenafil, rimonabant, and zometapine that are widely used for different therapeutic indications (Boyd and Fremming, 2005; Krasselt and Baerwald, 2019; Krishnappa et al., 2019).

The advent of green and efficient multicomponent reactions (MCRs) offers immense opportunity to explore new chemical reactions, which could generate vital pharmacophores in a facile and eco-friendly way (Isambert and Lavilla, 2008; Dömling et al., 2012; Rotstein et al., 2014). In MCRs, multiple bonds are formed between three or more reactants in a single step with environmental benignity and greener aspects such as atom economy, less solvent consumption, and reduced waste generation. Some other added advantages are improved yields, higher selectivity, facile construction of complex molecules, and no need for isolation of intermediates (Cioc et al., 2014). In recent years, the research endeavors focused on developing new MCRs, and several synthetic protocols have been reported in this direction (Jethava et al., 2020; Wang et al., 2021). The amalgamation of MCRs with a naturally occurring catalyst renders a more environmental-friendly chemical methodology. The naturally occurring amino acid, L-proline, and its derivatives are prime organocatalysts with a

wide application profile in asymmetric organic synthesis (Sarita et al., 2016; Liu and Wang, 2017).

In continuation of our research endeavors in the development of novel anticancer agents (Malik et al., 2019; Malik et al., 2021) and considering the pharmaceutical significance of two heterocyclic scaffolds, phthalazine and pyrazole, we envisaged to tether these scaffolds in a single chemical entity with a pyran ring as the linker. Interestingly, the pyran moiety itself exhibits immense pharmaceutical potential such as anticancer, antiviral, diuretic, and other properties (Kumar et al., 2017). On the chemical synthesis front, the multicomponent reactions, catalyzed by environmental-friendly catalysts, need to be harnessed to access novel chemical compounds with improved sustainability and lowered environmental burden. Herein, we report the synthesis of novel pyran-linked phthalazinone-pyrazole hybrids by one-pot three-component reactions by using L-proline as a catalyst. The synthesized compounds were screened for their anticancer activity on selected cancer cell lines of lung and cervix cancers. The active hybrids were docked to understand their interaction with human serine hydroxymethyltransferase 2 (SHMT2), a protein that is upregulated in lung and other cancer cells. Finally, the drug likeliness properties and molecular descriptors are computationally calculated to identify molecules for further development.

MATERIALS AND METHODS

Reactions were monitored by thin-layer chromatography (silica gel glass plates containing 60 F-254), and TLC plates were visualized by UV light or iodine indicator. Infrared (IR) spectra were recorded on VERTEX 70 Brucker by using KBr. NMR spectra were recorded on a Bruker DRX-400 spectrometer, and chemical shifts were reported in ppm, downfield from internal TMS standard. Mass spectra were recorded on

Agilent-LCMS instrument. Starting materials and reagents were procured commercially or synthesized in the laboratory.

Chemical Synthesis

General procedure for the synthesis of pyran-linked phthalazinone-pyrazole hybrids **4a–h**:

3-(1,4-dioxo-3,4-dihydrophthalazin-2(1H)-yl)-3-oxopropanenitrile (**1**) (1 equiv, 2.29 g, 10 mmol), 1H-pyrazole-5-carbaldehyde (**2a–2d**) (1 equiv, 10 mmol), and malononitrile **3a** (1equiv, 0.66 g, 10 mmol) or ethyl 2-cyanoacetate **3b** (1eq, 1.13 g, 10 mmol) were added into ethanol (50 ml) in the presence of 20 mol% L-proline (0.23 g) as a catalyst and heated at 70–75°C for 50–60 min. The progress of the reaction was monitored by TLC. After completion of the reaction, the reaction mixture was cooled to 30–35°C, and cold water was added to the reaction mixture and stirred for 30 min. The resulting solid was separated through direct filtration to afford crude form of **4a–h**. Finally, the product was recrystallized from ethanol and dried at 60–65°C for 10–12 h to obtain pure form of **4a–h**.

2-Amino-6-(1,4-dioxo-3,4-dihydrophthalazin-2(1H)-yl)-4-(1H-pyrazol-5-yl)-4H-pyran-3,5-dicarbonitrile (**4a**): Mp 250–252°C; IR (KBr) cm^{-1}: 3,184–3,544 (-NH-), 2,191 (-CN-), 1,739 (-CO-); ^{1}H-NMR (DMSO-d$_6$, 400 MHz): δ 6.5 (s, 1H, -CH), 7.4 (d, 1H, J = 7.8 Hz, Ar-H), 7.9–8.1 (m, 4H, Ar-H), 8.2 (d, 1H, J = 7.5, Ar-H), 9.8 (s, 2H, -NH$_2$), 11.4 (s, 1H, -NH), 12.2 (s, 1H, -NH); ^{13}C NMR (DMSO-d$_6$, 100 MHz): δ 48.7, 75.1, 87.2, 113.9, 115.8, 124.2, 125.8, 128.6, 129.5, 131.7, 134.3, 137.1, 155.8, 157.1, 163.3, 163.5 [M + H$^+$]: 374 (see **Supplementary Material**).

2-Amino-6-(1,4-dioxo-3,4-dihydrophthalazin-2(1H)-yl)-4-(1-methyl-1H-pyrazol-5-yl)-4H-pyran-3,5-dicarbonitrile (**4b**): Mp: 242–244°C; IR (KBr) cm^{-1}: 3,093–3,519 (-NH-), 2,258 (-CN-), 1748 (-CO-); ^{1}H-NMR (DMSO-d$_6$, 400 MHz): δ 2.9 (s, 3H, -CH$_3$), 6.5 (s, 1H, -CH), 7.4 (d, 1H, J = 7.8 Hz, Ar-H), 7.9–8.1 (m, 4H, Ar-H), 8.1 (d, 1H, J = 7.5 Hz, Ar-H), 9.6 (s, 2H, -NH$_2$), 12.0 (s, 1H, -NH); ^{13}C NMR (DMSO-d$_6$, 100 MHz): δ 28.8, 48.5, 75.4, 86.7, 114.5, 115.0, 124.5, 127.9, 128.6, 129.7, 130.8, 134.1, 136.0, 155.7, 157.4, 163.0, 163.6 [M + H$^+$]: 388.

2-Amino-6-(1,4-dioxo-3,4-dihydrophthalazin-2(1H)-yl)-4-(4-methyl-1H-pyrazol-5-yl)-4H-pyran-3,5-dicarbonitrile (**4c**): Mp: 238–240°C; IR (KBr) cm^{-1}: 3,137–3,584 (-NH-), 2,252 (-CN-), 1742 (-CO-); ^{1}H-NMR (DMSO-d$_6$, 400 MHz): δ 3.4 (s, 3H, -CH$_3$), 6.4 (s, 1H, -CH), 7.9–8.1 (m, 4H, Ar-H), 8.2 (d, 1H, J = 7.5, Ar-H), 9.8 (s, 2H, -NH$_2$), 11.3 (s, 1H, -NH), 12.1 (s, 1H, -NH); ^{13}C NMR (DMSO-d$_6$, 100 MHz): δ 34.0, 49.4, 74.2, 84.5, 115.2, 116.5, 123.4, 126.8, 128.9, 129.9, 131.7, 133.9, 136.2, 154.8, 157.6, 162.1, 163.3 [M + H$^+$]: 388.

2-Amino-6-(1,4-dioxo-3,4-dihydrophthalazin-2(1H)-yl)-4-(1H-pyrazol-4-yl)-4H-pyran-3,5-dicarbonitrile (**4d**): Mp: 254–256°C IR (KBr) cm^{-1}: 3,038–3,586 (-NH-), 2,256 (-CN-), 1745 (-CO-); ^{1}H-NMR (DMSO-d$_6$, 400 MHz): δ 6.4 (s, 1H, -CH), 7.4–8.2 (m, 6H, Ar-H), 9.9 (s, 2H, -NH$_2$), 11.3 (s, 1H, -NH),12.2 (s, 1H, -NH); ^{13}C NMR (DMSO-d$_6$, 100 MHz): δ 46.6, 74.5, 86.3, 114.6, 115.9, 125.5, 127.7, 129.2, 129.9, 131.6, 134.4, 137.5, 155.2, 157.4, 163.5, 163.9 [M + H$^+$]: 374.

Ethyl 2-amino-5-cyano-6-(1,4-dioxo-3,4-dihydrophthalazin-2(1H)-yl)-4-(1H-pyrazol-5-yl)-4H-pyran-3-carboxylate (**4e**): Mp: 234–236°C; IR (KBr) cm^{-1}: 3,159–3,401 (-NH-), 2,218 (-CN-), 1724 (-CO-); ^{1}H-NMR (DMSO-d$_6$, 400 MHz): δ 1.2 (t, 3H, J = 6.8 Hz, -CH$_3$), 3.0 (q, 2H, J = 7.6 Hz, -CH$_2$), 6.6 (s, 1H, -CH), 7.4 (d, 1H, J = 7.4 Hz, Ar-H), 7.5 (t, 2H, J = 7.6 Hz, Ar-H), 7.6 (t, 2H, J = 7.5 Hz, Ar-H), 8.0 (d, 1H, J = 7.4 Hz, Ar-H), 9.6 (s, 2H, -NH$_2$), 11.5 (s, 1H, -NH), 13.0 (s, 1H, -NH); ^{13}C NMR (DMSO-d$_6$, 100 MHz): δ 14.0, 41.2, 58.1, 76.7, 88.1, 111.2, 113.6, 115.7, 117.9, 118.9, 122.2, 124.9, 126.0, 127.3, 128.8, 131.3, 137.1, 141.1, 158.7, 167.7, 167.7; [M + H$^+$]: 421.

Ethyl 2-amino-5-cyano-6-(1,4-dioxo-3,4-dihydrophthalazin-2(1H)-yl)-4-(1-methyl-1H-pyrazol-5-yl)-4H-pyran-3-carboxylate (**4f**): Mp: 243–245°C; IR (KBr) cm^{-1}: 3,037–3,581 (-NH-), 2,257 (-CN-), 1748 (-CO-); ^{1}H-NMR (DMSO-d$_6$, 400 MHz): δ 1.2 (t, 3H, J = 6.8 Hz, -CH$_3$), 2.8 (s, 3H, -CH$_3$), 3.0 (q, 2H, J = 7.6 Hz, -CH$_2$), 6.6 (s, 1H, -CH), 7.3 (d, 1H, J = 7.3 Hz, Ar-H), 7.5 (t, 2H, J = 7.6 Hz, Ar-H), 7.6 (t, 2H, J = 7.6 Hz, Ar-H), 8.0 (d, 1H, J = 7.5 Hz, Ar-H), 9.6 (s, 2H, -NH$_2$), 13.0 (s, 1H, -NH); ^{13}C NMR (DMSO-d$_6$, 100 MHz): δ 14.1, 19.9, 36.4, 42.4, 58.1, 76.7, 88.1, 112.4, 112.8, 115.7, 118.0, 118.8, 123.0, 125.2, 126.0, 128.1, 128.8, 131.3, 139.1, 141.8, 159.7, 167.1, 167.4 [M + H$^+$]: 435.

Ethyl 2-amino-5-cyano-6-(1,4-dioxo-3,4-dihydrophthalazin-2(1H)-yl)-4-(4-methyl-1H-pyrazol-5-yl)-4H-pyran-3-carboxylate (**4g**): Mp: 256–258°C; IR (KBr) cm^{-1}: 3,138–3,482 (-NH-), 2,156 (-CN-), 1732 (-CO-); ^{1}H-NMR (DMSO-d$_6$, 400 MHz): δ 1.1 (t, 3H, J = 6.8 Hz, -CH$_3$), 2.9 (s, 3H, -CH$_3$), 3.1 (q, 2H, J = 7.4 Hz, -CH$_2$), 6.5 (s, 1H, -CH), 7.5 (t, 2H, J = 7.4 Hz, Ar-H), 7.6 (t, 2H, J = 7.6 Hz, Ar-H), 8.1 (d, 1H, J = 7.4 Hz, Ar-H), 9.5 (s, 2H, -NH$_2$), 13.1 (s, 1H, -NH); ^{13}C NMR (DMSO-d$_6$, 100 MHz): δ 14.2, 18.9, 36.3, 41.5, 58.2, 76.6, 88.4, 111.3, 112.9, 114.8, 118.1, 118.9, 123.1, 124.1, 125.8, 128.2, 128.9, 131.5, 139.4, 141.9, 159.8, 167.5, 167.9 [M + H$^+$]: 435.

Ethyl 2-amino-5-cyano-6-(1,4-dioxo-3,4-dihydrophthalazin-2(1H)-yl)-4-(1H-pyrazol-4-yl)-4H-pyran-3-carboxylate (**4h**): Mp: 253–255°C; IR (KBr) cm^{-1}: 3,136–3,482 (-NH-), 2,256 (-CN-), 1743 (-CO-); ^{1}H-NMR (DMSO-d$_6$, 400 MHz): δ 1.1 (t, 3H, J = 6.8 Hz, -CH$_3$), 3.1 (q, 2H, J = 7.4 Hz, -CH$_2$), 6.5 (s, 1H, -CH), 7.2 (s, 1H, Ar-H), 7.4 (t, 2H, J = 7.5 Hz, Ar-H), 7.6 (t, 2H, J = 7.6 Hz, Ar-H), 8.1 (s, 1H, Ar-H), 9.5 (s, 2H, -NH$_2$), 11.4 (s, 1H, -NH), 13.1 (s, 1H, -NH); ^{13}C NMR (DMSO-d$_6$, 100 MHz): δ 14.1, 41.4, 57.3, 75.8, 89.3, 111.4, 113.7, 115.8, 117.8, 118.5, 121.4, 124.5, 126.2, 127.5, 128.8, 131.4, 137.2, 141.4, 158.6, 167.6, 167.9 [M + H$^+$]: 421.

Cytotoxicity Assay

The cell viability of A549 (human lung carcinoma) and Hela (human cervical carcinoma) cells was evaluated by using the MTT colorimetric assay (Sigma, United States) (Mosmann, 1983). The cancer cells were seeded at a density of 2×10^4 cells in 100 µL of cell culture medium (DMEM containing 10% fetal bovine serum, 100 µg/ml streptomycin, and 100 µg/ml penicillin) per well of 96-well plate and grown for a period of 24 h prior to the addition of the test compounds. Cells were incubated with different concentrations of test compounds for 48 h. After incubation, the wells were washed with 200 µL of PBS, and then 10% MTT solution was added to each well and incubated for 2 h at 37°C. The formazan crystals were solubilized by the addition of 100 µL of DMSO, and then

TABLE 1 | Optimization studies of the multicomponent reaction with the model substrate **2a**.

Entry	Solvent	20 mol % catalyst	Temperature (°C)	Time (h)	4a (%)
1	Ethanol	L-proline	rt	5	60
2	Ethanol	Pyridine	rt	5	45
3	Ethanol	Piperidine	rt	4.5	40
4	Methanol	L-proline	rt	5	60
5	Methanol	Pyridine	rt	5.5	45
6	Methanol	Piperidine	rt	5	42
7	DMF	L-proline	rt	7.5	45
8	DMF	Pyridine	rt	9	35
9	DMF	Piperidine	rt	8	34
10	Ethanol	L-proline	70–75	50 min	88
11	Methanol	L-proline	70–75	1.5	80
12	DMF	L-proline	70–75	1.5	70

the optical density was recorded at 570 nm using a multimode reader (Tecan Infinite 200 PRO, Switzerland). Each experiment was repeated three times ($n = 3$), and the results are specified as mean with standard deviation.

Computational Studies
Molecular Docking

In silico binding of synthesized compounds with respect to inhibition of human serine hydroxymethyltransferase 2 (SHMT2) protein was performed by molecular docking in the active site of the target protein using AutoDockTools 4.2.51 (Morris et al., 2009). The 3D crystal structure of human SHMT2 (PDB ID: 5V7I) was downloaded from the RCSB Protein Data Bank and used as the model for docking. The co-crystalized hetero molecules and water were removed from the target protein. The ligand structures (**4b** and **4c**) were constructed using ChemDraw ultra 19.0 software and subsequently converted to 3D structures and saved in .pdb format using Chem3D ultra 19.0 software. The ligand energies were minimized using MOPAC (semiempirical quantum mechanics) with AM1 MOZYME geometry acceleration with 100 iterations, and RMS gradient of 0.10. For each docked ligand, ten poses were generated. The structure with relative lower binding free energy (Kcal/mol) was selected as best conformation among all the poses. In order to validate the results, the co-crystal ligand 8Z1 ((4R)-6-amino-3-methyl-4-(propan-2-yl)-4-[3-(pyrrolidin-1-yl)-5-(trifluoromethyl)phenyl]-1,4-dihydropyrano[2,3-c]pyrazole-5-carbonitrile) was re-docked with the target protein. PyMol and LIGPLOT tools were used for 3D and 2D visualization of the docked complexes, respectively (Wallace et al., 1995).

Molecular Descriptors and Other Studies

Pharmacological and physiochemical properties of the synthesized molecules were evaluated by using Molinspiration and SwissADME online web tools (Daina et al., 2017). The lipophilicity (logP), topological polar surface area (TPSA), and drug likeliness were determined for all the synthesized compounds. To explore the properties of molecular flexibility, complexity, and shape index of the synthesized molecules, OSIRIS property explorer tool was used.

RESULTS AND DISCUSSIONS

Chemical Synthesis

The synthesis of the novel pyran-linked phthalazinone-pyrazole hybrids was accomplished by employing an atom economical multicomponent reaction strategy. A phthalazinone derivative, 3-(1,4-dioxo-3,4-dihydrophthalazin-2(1H)-yl)-3-oxopropanenitrile **1**, with an appropriately substituted oxopropanenitrile group that involves in the multicomponent reaction was synthesized from phthalic anhydride and 2-cyanoacetohydrazide (Kumar et al., 2014).

TABLE 2 | Effect of catalyst loading.

Entry	Amount of catalyst	Time (min)	4a (%)
1	10 mol % L-proline	90	82
2	20 mol % L-proline	50	88
3	30 mol % L-proline	45	81
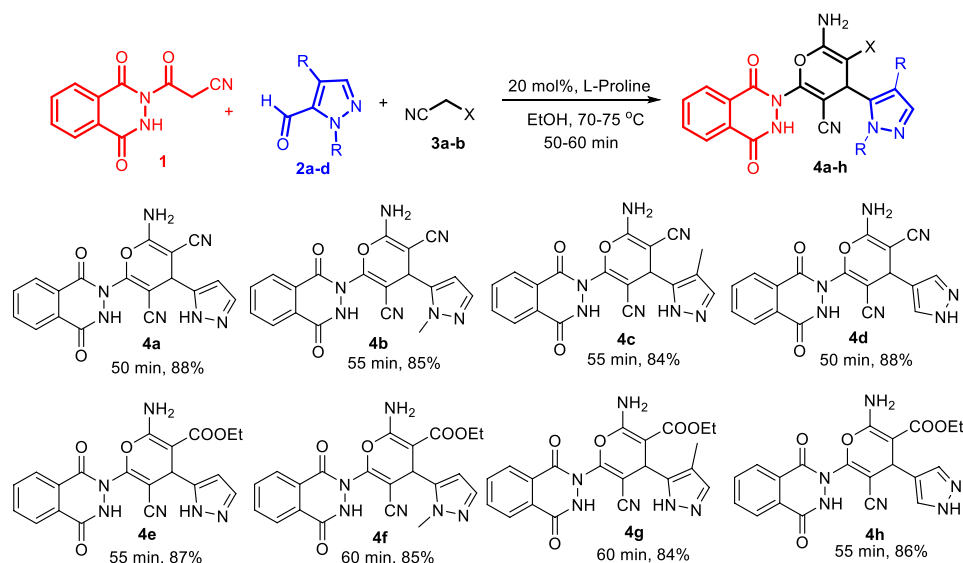
SCHEME 1 | One-pot synthesis of novel pyran-linked phthalazinone-pyrazole hybrids **4a–h**.

FIGURE 2 | Plausible mechanism of formation of pyran-linked phthalazinone-pyrazole hybrids.
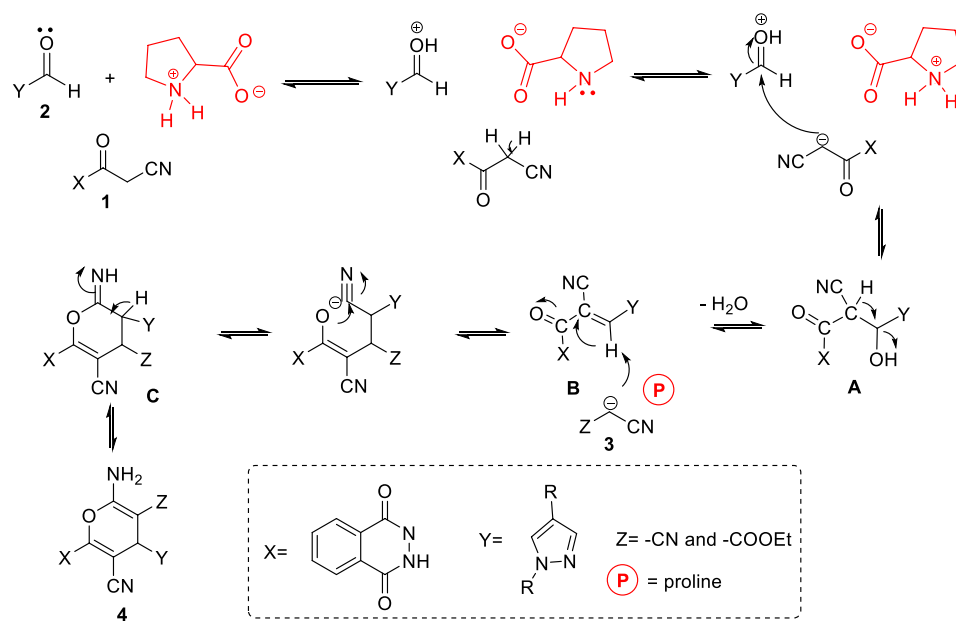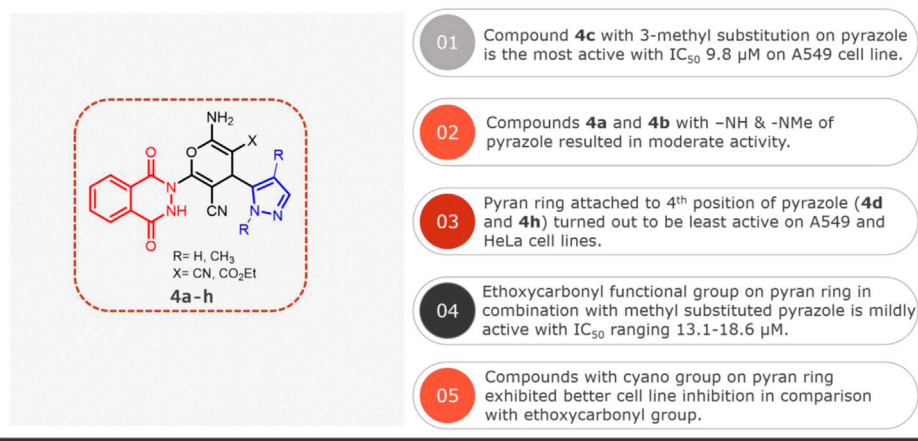
The other components employed in this MCR were substituted 1H-pyrazole-5-carbaldehyde **2a** and an active methylene–containing compounds. Initially, an optimization study for the one-pot reaction was undertaken with model substrate 1H-pyrazole-5-carbaldehyde **2a** along with other components such as phthalazinone **1** and malononitrile **3a** to identify the best reaction conditions (**Table 1**). In this study, different parameters such as base catalyst, solvents, reaction temperature, and catalyst loading were investigated. For this purpose, different organic bases such as L-proline, pyridine, and piperidine were screened as catalyst in solvents like methanol, ethanol,

and dimethylformamide (DMF) at varying temperature. The model MCR with the tested base catalysts proceeded with modest yields (34–45%) using DMF as solvent at room temperature in 7.5–9 h (entries 7–9). Interestingly, on using protic solvents like ethanol and methanol, the yields of the reaction were improved (40–60%), accompanied by reduction in reaction time (4.5–5.5 h, entries 1–6). The results showed that both the protic solvents were equally efficient; however, L-proline provided the best yields in all the cases. Temperature is a critical parameter in optimization studies; therefore, we

TABLE 3 | Cytotoxicity and structure activity relationship of novel pyran-linked phthalazinone-pyrazole hybrids **4a–h**.

Compound	IC_{50} ($\mu M \pm SD$)	
	A549	HeLa
4a	14.1 ± 0.9	17.9 ± 1.0
4b	10.6 ± 1.2	11.8 ± 1.2
4c	9.8 ± 0.9	10.1 ± 0.9
4d	28.9 ± 1.3	30.5 ± 1.4
4e	26.3 ± 1.2	20.9 ± 1.1
4f	16.4 ± 1.0	18.6 ± 0.9
4g	15.6 ± 1.1	13.1 ± 0.8
4h	41.6 ± 1.8	31.6 ± 1.3
Doxorubicin (positive control)	0.69 ± 0.1	0.81 ± 0.1

Structure Activity Relationship

01 Compound **4c** with 3-methyl substitution on pyrazole is the most active with IC_{50} 9.8 μM on A549 cell line.

02 Compounds **4a** and **4b** with –NH & -NMe of pyrazole resulted in moderate activity.

03 Pyran ring attached to 4th position of pyrazole (**4d** and **4h**) turned out to be least active on A549 and HeLa cell lines.

04 Ethoxycarbonyl functional group on pyran ring in combination with methyl substituted pyrazole is mildly active with IC_{50} ranging 13.1-18.6 μM.

05 Compounds with cyano group on pyran ring exhibited better cell line inhibition in comparison with ethoxycarbonyl group.

investigated the model reaction with L-proline at elevated temperature (70–75°C) with all the three base catalysts. It was observed that the reaction in DMF and methanol afforded 70 and 80% yield, respectively, in reaction time of 1.5 h (entries 11 and 12). However, the best results were obtained with ethanol and the reaction afforded the product **4a** in very good yield (88%) in a short reaction time of only 50 min (entry 10). To further improve the efficiency of the reaction, different catalyst loadings were also investigated; nonetheless, 20% catalyst loading showed the best results (**Table 2**).

Finally, the scope of the reaction was explored under the optimized conditions to afford a series of novel pyran-linked phthalazinone-pyrazole hybrids. The MCR was carried out with phthalazinone derivative **1**, various substituted 1H-pyrazole-5-carbaldehydes **2a-d** and active methylene–containing compounds (malononitrile **3a** and ethyl 2-cyanoacetate **3b**) with L-proline as a catalyst in ethanol at elevated temperature (**Scheme 1**). The multicomponent reaction proceeded with similar efficiency with different reactants, and the desired novel pyran-linked phthalazinone-pyrazole hybrids **4a–h** were obtained in high yield in the range of 84–88%. A plausible mechanism for the synthesis of hybrids **4a–h** in the presence of L-proline is proposed (**Figure 2**). L-proline exists in the form of zwitterion acting as a bifunctional catalyst. It protonates the aldehyde **2** and also abstracts the hydrogen of active methylene
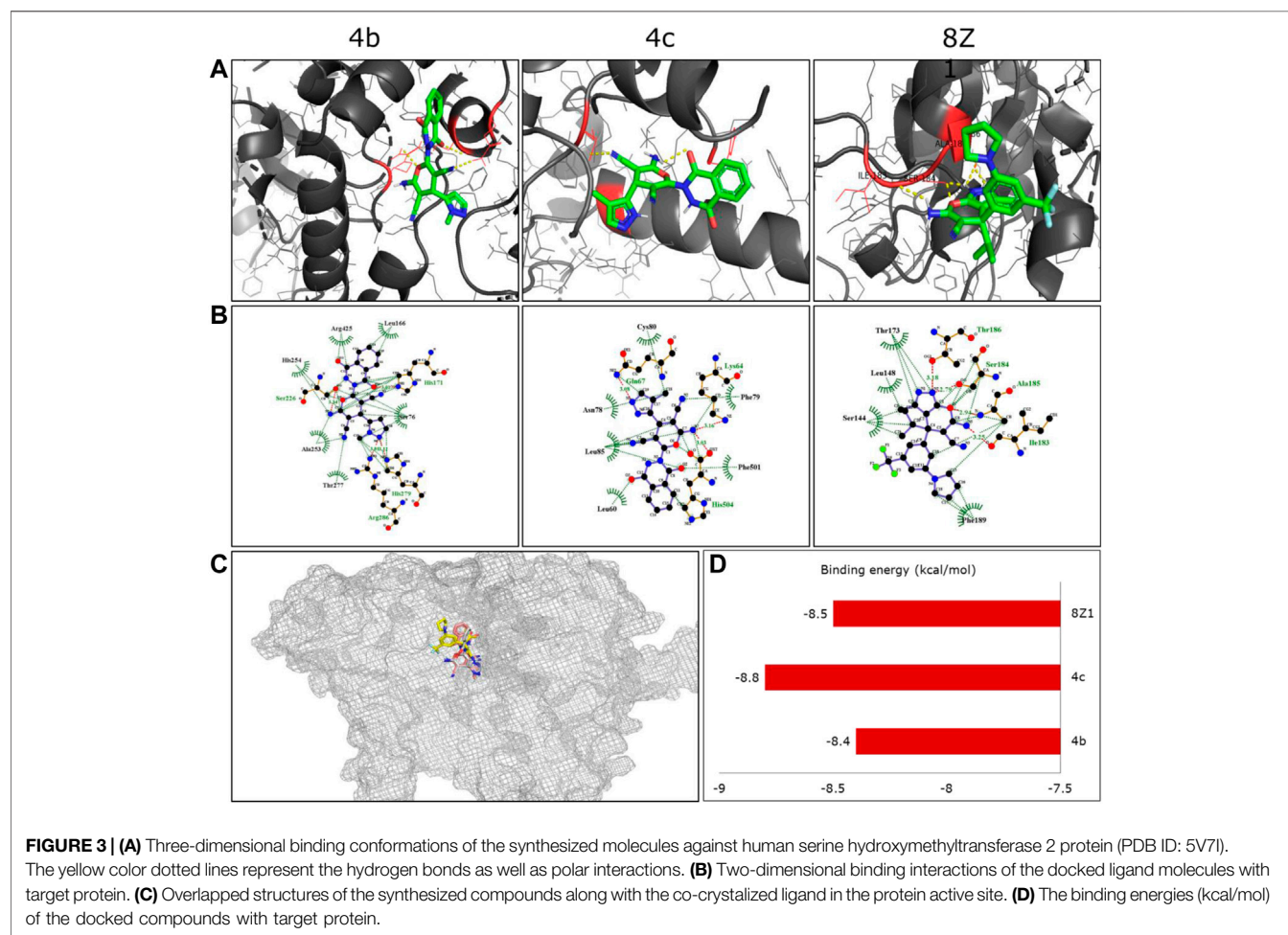
functionality of **3** to afford carbanion species, which further attacks the protonated aldehyde **2** forming intermediate **A**. This is followed by loss of water molecule from **A,** affording an α,β-unsaturated diketone intermediate **B**. The intermediate B undergoes Michael addition by carbanion **3** followed by nucleophilic addition to afford imine intermediate **C**. Finally, the tautomerization of intermediate **C** yields the final product **4**.

Anticancer Activity

The phthalazine and pyrazole moieties are known to exhibit anticancer activity; therefore, the cytotoxicity potential of the synthesized novel pyran-linked phthalazinone-pyrazole hybrids was investigated. Globally, lung cancer is a leading cause of cancer death, and on the other hand, cervical cancer is one of the major cancers in women with high incidence and mortality (Thakur et al., 2020; Ferlay et al., 2021). Therefore, we screened the synthesized novel hybrids (**4a–h**) against human lung carcinoma cells (A549) and human cervical carcinoma cells (HeLa) by employing the MTT assay. All the tested hybrids were active and displayed moderate-to-good activity with an IC_{50} ranging from 9.8 to 41.6 μM against A549 cells and 10.1 to 31.6 μM against HeLa cells (**Table 3**). Based on the results, compound **4c** was the most promising hybrid from the series that exhibited significant activity against A549 cells with an IC_{50} value of 9.8 μM. In case

TABLE 4 | Amino acid residues of the target protein that interacts with ligands **4a** and **4b**.

Ligand	Protein–ligand interactions	
	H-bond/s	Hydrophobic bonds
4b	His171, Ser226, His279, Arg286	Ser76, Leu166, Ala253, His254, Thr277, Arg425
4c	Lys64, Gln67, His504	Leu60, Asn78, Phe79, Cys80, Leu85, Phe501
8Z1 (co-crystal ligand)	Thr186, Ser184, Ala185, Ile183	Ser144, Leu148, Thr173, Phe189

FIGURE 3 | (A) Three-dimensional binding conformations of the synthesized molecules against human serine hydroxymethyltransferase 2 protein (PDB ID: 5V7I). The yellow color dotted lines represent the hydrogen bonds as well as polar interactions. **(B)** Two-dimensional binding interactions of the docked ligand molecules with target protein. **(C)** Overlapped structures of the synthesized compounds along with the co-crystalized ligand in the protein active site. **(D)** The binding energies (kcal/mol) of the docked compounds with target protein.

of HeLa cancer cell lines, it exhibited similar potency with IC$_{50}$ value of 10.1 μM. The other hybrids **4a**, **4b**, **4f**, and **4g** showed good activity against A549 cells with IC$_{50}$ values of 14.1, 10.6, 16.4, and 15.6 μM, respectively, and modest cytotoxicity against HeLa cells with IC$_{50}$ values of 17.9, 11.8, 18.6, and 13.1 μM, respectively. The hybrids **4d**, **4e**, and **4h** were the least active compounds in the series against the tested cells. The structure activity relationship (SAR) pattern of the novel pyran-linked phthalazinone-pyrazole hybrids is provided as an infographic in the table.

In Silico Binding Studies

The serine hydroxymethyltransferase (SHMT) catalyzed the conversion of serine to glycine, thereby releasing one carbon unit essential in cell regulation. One of the mitochondrial isoforms, SHMT2, is linked to cancer survival and is upregulated in the lung and other cancer cells (Tong et al., 2020). A pyrazolopyran scaffold (8Z1) is reported to inhibit this protein at the molecular level. The structural similarity of our novel pyran-linked phthalazinone-pyrazole hybrids to 8ZI prompted us to perform molecular docking studies to understand the binding affinity with SHMT2 protein. From the preliminary anticancer results, the active compounds **4b** and **4c** were examined for docking with hydroxymethyltransferase 2 protein co-crystalized with 8Z1. The ligands exhibited good binding affinities toward target protein as compared with 8Z1. The hydrogen and hydrophobic interactions played a major role in

FIGURE 4 | Predicted parameters of Lipinski's rule of five for the synthesized compounds were calculated using SwissADME and represented in the Doughnut graph. The compounds that violate the rule were represented in the filled pattern format. Each circle represents one parameter of Lipinski's rule. The parameters LogP, HBA, HBD, and MW showed from inner to outer circles, respectively.

the binding of ligands with target protein. Almost ten different conformations per each docked ligand were generated, and the best conformation was displayed in the **Figures 3A,B**. The docking results revealed that the hybrids **4b** and **4c** occupied the same binding site of the co-crystalized ligand binding site (**Figure 3C**) and exhibited excellent affinity with binding energy of −8.4 and −8.8 kcal/mol, respectively (**Figure 3D**). Interestingly, the binding affinity of hybrid **4c** was better than that of the co-crystal ligand 8Z1 (a pyrazolopyran inhibitor), which exhibited −8.5 kcal/mol of binding energy. The docking results influenced both hydrogen and hydrophobic interactions, and the amino acid residues of the target protein that interacted with the docked ligands are presented in **Table 4**.

Drug Likeliness Nature

The physiochemical properties of all the synthesized molecules toward drug likeliness were calculated, and the results revealed that all the compounds showed acceptable properties. Based on Lipinski's rule of five and its components, the endpoint values for all the four parameters that describe possible outcome of a drug candidate for good absorption are MW ≤ 500, LogP ≤ 5, HBD ≤ 10, and HBA ≤ 5 (Lipinski, 2004). It was observed that almost all the molecules occupied space within Lipinski's rule of five (**Figure 4**); besides, only four compounds exhibited only a single violation. Compounds **4e**, **4f, 4g,** and **4h** showed one violation with respect to the number of hydrogen bond donors (HBDs). The predicted LogP values for all the compounds indicate that compounds exhibit good
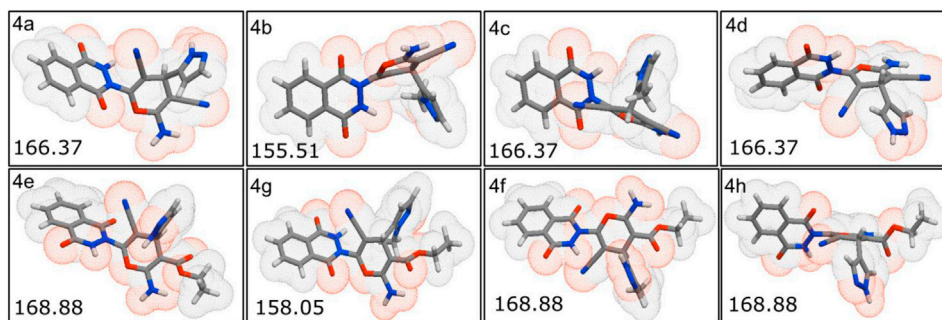

FIGURE 5 | Three-dimensional polar surface area visualization of all the synthesized molecules using Molinspiration tool.
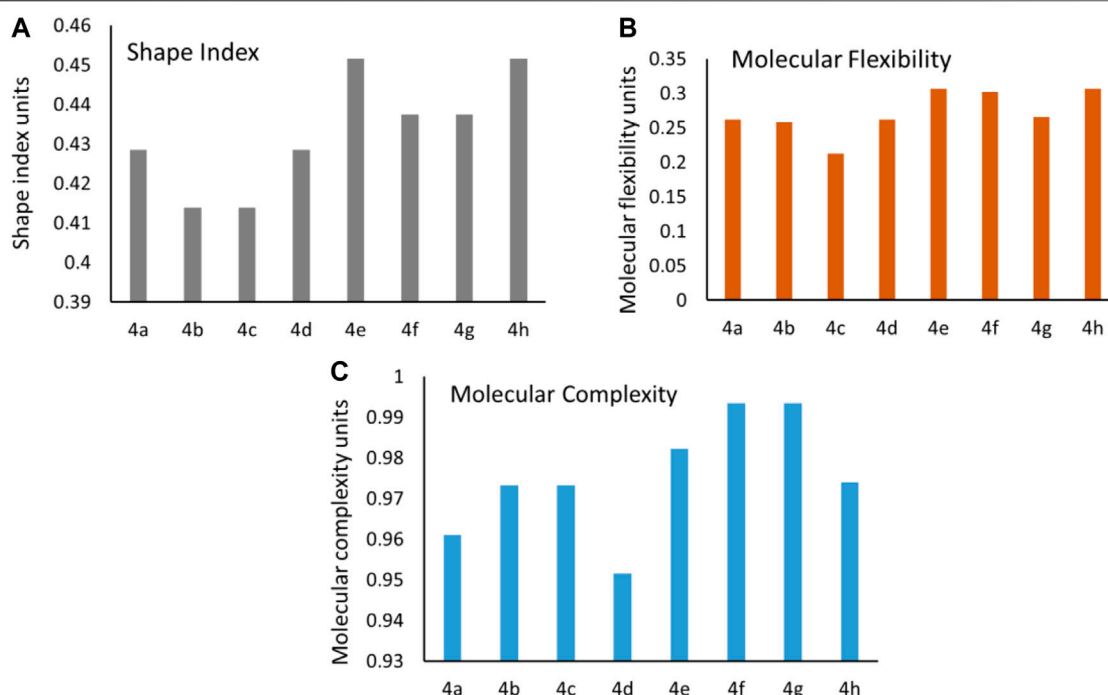
FIGURE 6 | Predicted values of the **(A)** shape index, **(B)** molecular flexibility, and **(C)** molecular complexity for the synthesized molecules.

permeability across cell membrane. The calculated LogP values for the test compounds are in the range of 1.03–2.38, which are in the accepted range. The 3D polar surface area visualizations were generated, and the calculated TPSA was >140 Å for all the compounds; this indicates the reduced oral bio-availability of the compounds (**Figure 5**; Prasanna and Doerksen (2009)).

Molecular Flexibility, Complexity, and Shape Index

The conformational flexibility, molecular complexity, and shape index of a molecule are important parameters influencing the ligand to target protein binding in drug design (Wicker and Cooper, 2016; Méndez-Lucio and Medina-Franco, 2017). Shape index of the synthesized molecules was calculated using DataWarrior, and it determines 3D shape of compounds. In general, shape index less than 0.5 in molecules suggests the presence of spherical or non-flat scaffolds, whereas shape index more than 0.5 is for flat scaffolds. The synthesized molecules exhibited an average shape index of 0.43, which is less than 0.5 [**Figure 6A**]. These results suggest that the compounds were spherical or non-flat scaffolds. Few reports proposed that a majority of non-flat or spherical compounds were observed in natural products (Lovering et al., 2009). This suggests that spherical scaffolds may be essential for anticancer activity. Further, the structural flexibility and complexity of the molecules were predicted using DataWarrior. Less than 0.5 value of flexibility and complexity in molecules suggests that the molecules are of

low complexity and flexibility. The synthesized molecules exhibited an average of 0.27; this indicates the molecules are low-to-intermediate flexible [**Figure 6B**]. Additionally, 0.97 average value for molecular complexity in molecules suggests the molecules are complex in nature [**Figure 6C**] (Méndez-Lucio and Medina-Franco, 2017).

CONCLUSION

In conclusion, a series of novel pyran-linked phthalazinone-pyrazole hybrids were designed and synthesized by a facile one-pot three-component reaction in the presence of L-proline, which acted as a catalyst. The assessment of cytotoxicity potency revealed that the methyl substitution on pyrazole and two cyano groups on pyran, as in **4b** and **4c**, were necessary to elicit a good inhibitory response toward the tested lung and cervix cancer cells. Interestingly, the molecular modeling studies with hydroxymethyltransferase 2 (SHMT2), a protein that is upregulated in lung and other cancers, revealed that the active hybrids **4b** and **4c** displayed comparable-to-superior binding affinity than ligand 8Z1, a pyrazolopyran inhibitor. The hybrids showed good drug likeliness properties as elucidated by Lipinski's rule, with four compounds exhibiting a single violation. Similarly, the results obtained through molecular descriptor predictions provided an understanding about the potential of the synthesized molecules to transform into lead-like molecules. It can be said that upon further structural optimizations (particularly **4b** and **4c**) and a thorough biological

mechanistic investigation, the synthesized scaffolds may likely turn into potential anticancer agents.

DATA AVAILABILITY STATEMENT

The original contributions presented in the study are included in the article/**Supplementary Material**; further inquiries can be directed to the corresponding authors.

AUTHOR CONTRIBUTIONS

MSM, SA, and BA: conceptualization, methodology, data curation, validation, investigation, visualization, project administration, supervision, funding acquisition, writing-reviewing, and editing the manuscript. RS and ZM: software, data curation, validation, investigation, visualization, and draft preparation. RA, MM, HA, IA, and RJ: validation, data curation, investigation, and writing the draft.

FUNDING

SUPPLEMENTARY MATERIAL

The Supplementary Material for this article can be found online at: https://www.frontiersin.org/articles/10.3389/fchem.2021.666573/full#supplementary-material

REFERENCES

Bennani, F. E., Doudach, L., Cherrah, Y., Ramli, Y., Karrouchi, K., Ansar, M. h., et al. (2020). Overview of Recent Developments of Pyrazole Derivatives as an Anticancer Agent in Different Cell Line. *Bioorg. Chem.* 97, 103470. doi:10.1016/j.bioorg.2019.103470

Boyd, S. T., and Fremming, B. A. (2005). Rimonabant-A Selective CB1 Antagonist. *Ann. Pharmacother.* 39 (4), 684–690. doi:10.1345/aph.1e499

Cheng, L. H., Lee, J. C., Wu, P. C., Lin, Y. Y., Chu, Y. H., and Wang, H. W. (2019). Azelastine Nasal Spray Inhibiting Sympathetic Function on Human Nasal Mucosa in Patients with Allergy Rhinitis. *Rhinology* 57 (4), 268–272. doi:10.4193/Rhin18.274

Cioc, R. C., Ruijter, E., and Orru, R. V. A. (2014). Multicomponent Reactions: Advanced Tools for Sustainable Organic Synthesis. *Green. Chem.* 16 (6), 2958–2975. doi:10.1039/c4gc00013g

Daina, A., Michielin, O., and Zoete, V. (2017). SwissADME: A Free Web Tool to Evaluate Pharmacokinetics, Drug-Likeness and Medicinal Chemistry Friendliness of Small Molecules. *Sci. Rep.* 7 (1), 42717. doi:10.1038/srep42717

Dömling, A., Wang, W., and Wang, K. (2012). Chemistry and Biology of Multicomponent Reactions. *Chem. Rev.* 112 (6), 3083–3135. doi:10.1021/cr100233r

Ferlay, J., Colombet, M., Soerjomataram, I., Parkin, D. M., Piñeros, M., Znaor, A., et al. (2021). Cancer Statistics for the Year 2020: an Overview. *Int. J. Cancer* [Epub ahead of print]. doi:10.1002/ijc.33588

Gunderson, C. C., and Moore, K. N. (2015). Olaparib: An Oral PARP-1 and PARP-2 Inhibitor with Promising Activity in Ovarian Cancer. *Future Oncol.* 11 (5), 747–757. doi:10.2217/fon.14.313

Inskeep, P. B., Ronfeld, R. A., Peterson, M. J., and Gerber, N. (1994). Pharmacokinetics of the Aldose Reductase Inhibitor, Zopolrestat, in Humans. *J. Clin. Pharmacol.* 34 (7), 760–766. doi:10.1002/j.1552-4604.1994.tb02037.x

Isambert, N., and Lavilla, R. (2008). Heterocycles as Key Substrates in Multicomponent Reactions: The Fast Lane towards Molecular Complexity. *Chem. Eur. J.* 14 (28), 8444–8454. doi:10.1002/chem.200800473

Jethava, K. P., Fine, J., Chen, Y., Hossain, A., and Chopra, G. (2020). Accelerated Reactivity Mechanism and Interpretable Machine Learning Model of N-Sulfonylimines toward Fast Multicomponent Reactions. *Org. Lett.* 22 (21), 8480–8486. doi:10.1021/acs.orglett.0c03083

Joensuu, H., De Braud, F., Grignagni, G., De Pas, T., Spitalieri, G., Coco, P., et al. (2011). Vatalanib for Metastatic Gastrointestinal Stromal Tumour (GIST) Resistant to Imatinib: Final Results of a Phase II Study. *Br. J. Cancer* 104 (11), 1686–1690. doi:10.1038/bjc.2011.151

Karrouchi, K., Radi, S., Ramli, Y., Taoufik, J., Mabkhot, Y. N., Al-Aizari, F. A., et al. (2018). Synthesis and Pharmacological Activities of Pyrazole Derivatives: A Review. *Molecules* 23 (1). doi:10.3390/molecules23010134

Khan, M. F., Alam, M. M., Verma, G., Akhtar, W., Akhter, M., and Shaquiquzzaman, M. (2016). The Therapeutic Voyage of Pyrazole and its

Analogs: A Review. *Eur. J. Med. Chem.* 120, 170–201. doi:10.1016/j.ejmech.2016.04.077

Krasselt, M., and Baerwald, C. (2019). Celecoxib for the Treatment of Musculoskeletal Arthritis. *Expert Opin. Pharmacother.* 20 (14), 1689–1702. doi:10.1080/14656566.2019.1645123

Krishnappa, P., Fernandez-Pascual, E., Carballido, J., and Martinez-Salamanca, J. I. (2019). Sildenafil/Viagra in the Treatment of Premature Ejaculation. *Int. J. Impot Res.* 31 (2), 65–70. doi:10.1038/s41443-018-0099-2

Kumar, D., Sharma, P., Singh, H., Nepali, K., Gupta, G. K., Jain, S. K., et al. (2017). The Value of Pyrans as Anticancer Scaffolds in Medicinal Chemistry. *RSC Adv.* 7 (59), 36977–36999. doi:10.1039/c7ra05441f

Kumar, P. P., Reddy, Y. D., Reddy, C. V. R., Devi, B. R., and Dubey, P. K. (2014). One Pot, Three-Component Synthesis of Novel 3,4-Dihydrophthalazin-2(1h)-Yl-4-Phenyl-4h-Pyrans. *Tetrahedron Lett.* 55 (14), 2177–2182. doi:10.1016/j.tetlet.2014.02.020

Lipinski, C. A. (2004). Lead- and Drug-like Compounds: the Rule-Of-Five Revolution. *Drug Discov. Today Tech.* 1 (4), 337–341. doi:10.1016/j.ddtec.2004.11.007

Liu, J., and Wang, L. (2017). Recent Advances in Asymmetric Reactions Catalyzed by Proline and its Derivatives. *Synthesis* 49 (05), 960–972. doi:10.1055/s-0036-1588901

Loh, V. M., Jr., Cockcroft, X.-l., Dillon, K. J., Dixon, L., Drzewiecki, J., Eversley, P. J., et al. (2005). Phthalazinones. Part 1: The Design and Synthesis of a Novel Series of Potent Inhibitors of poly(ADP-Ribose)polymerase. *Bioorg. Med. Chem. Lett.* 15 (9), 2235–2238. doi:10.1016/j.bmcl.2005.03.026

Lovering, F., Bikker, J., and Humblet, C. (2009). Escape from Flatland: Increasing Saturation as an Approach to Improving Clinical Success. *J. Med. Chem.* 52 (21), 6752–6756. doi:10.1021/jm901241e

Malik, M. S., Seddigi, Z. S., Bajee, S., Azeeza, S., Riyaz, S., Ahmed, S. A., et al. (2019). Multicomponent Access to Novel Proline/cyclized Cysteine Tethered Monastrol Conjugates as Potential Anticancer Agents. *J. Saudi Chem. Soc.* 23 (4), 503–513. doi:10.1016/j.jscs.2019.01.003

Malik, M. S., Adil, S. F., Altass, H. M., Moussa, Z., Althagafi, I. I., Morad, M., et al. (2021). Rational Design and Synthesis of Naphthalene Diimide Linked Bisnaphthalimides as DNA Interactive Agents. *Front. Chem.* 9, 630357. doi:10.3389/fchem.2021.630357

Martins, F. T., Maia, L. J. Q., Gasparotto, G., Valdo, A. K. S. M., Nascimento Neto, J. A., Ribeiro, L., et al. (2019). Phthalazine-trione as a Blue-Green Light-Emitting Moiety: Crystal Structures, Photoluminescence and Theoretical Calculations. *New J. Chem.* 43 (3), 1313–1321. doi:10.1039/c8nj02976h

Méndez-Lucio, O., and Medina-Franco, J. L. (2017). The Many Roles of Molecular Complexity in Drug Discovery. *Drug Discov. Today* 22 (1), 120–126. doi:10.1016/j.drudis.2016.08.009

Mohd, I., and Mohammad, A. (2020). Study of Various Pyridazine and Phthalazine Drugs with Diverse Therapeutical and Agrochemical Activities. *Russ. J. Bioorg. Chem.* 46 (5), 745–767. doi:10.1134/S1068162020050167

Morris, G. M., Huey, R., Lindstrom, W., Sanner, M. F., Belew, R. K., Goodsell, D. S., et al. (2009). AutoDock4 and AutoDockTools4: Automated Docking with Selective Receptor Flexibility. *J. Comput. Chem.* 30 (16), 2785–2791. doi:10.1002/jcc.21256

Mosmann, T. (1983). Rapid Colorimetric Assay for Cellular Growth and Survival: Application to Proliferation and Cytotoxicity Assays. *J. Immunol. Methods* 65 (1-2), 55–63. doi:10.1016/0022-1759(83)90303-4

Prasanna, S., and Doerksen, R. (2009). Topological Polar Surface Area: A Useful Descriptor in 2D-QSAR. *Cmc* 16 (1), 21–41. doi:10.2174/092986709787002817

Rotstein, B. H., Zaretsky, S., Rai, V., and Yudin, A. K. (2014). Small Heterocycles in Multicomponent Reactions. *Chem. Rev.* 114 (16), 8323–8359. doi:10.1021/cr400615v

Saha, M., Phukan, S., Jamatia, R., Mitra, S., and Pal, A. K. (2013). Solvent Free, Ni-Nanoparticle Catalyzed Greener Synthesis and Photophysical Studies of Novel 2H-Indazolo[2,1-B] Phthalazine-Trione Derivatives. *RSC Adv.* 3 (6), 1714–1721. doi:10.1039/c2ra22396a

Sangshetti, J., Pathan, S. K., Patil, R., Akber Ansari, S., Chhajed, S., Arote, R., et al. (2019). Synthesis and Biological Activity of Structurally Diverse Phthalazine Derivatives: A Systematic Review. *Bioorg. Med. Chem.* 27 (18), 3979–3997. doi:10.1016/j.bmc.2019.07.050

Sarita, K., Yogesh Kumar, T., and Mahendra, K. (2016). L-proline Catalyzed Multicomponent Reactions. *Curr. Organocatal.* 3 (2), 176–204. doi:10.2174/2213337202666150624172658

Sung Kim, J., Lee, H.-J., Suh, M.-E., Choo, H.-Y. P., Lee, S. K., Park, H. J., et al. (2004). Synthesis and Cytotoxicity of 1-substituted 2-Methyl-1h-Imidazo [4,5-G]phthalazine-4,9-Dione Derivatives. *Bioorg. Med. Chem.* 12 (13), 3683–3686. doi:10.1016/j.bmc.2004.04.014

Thakur, S. K., Singh, D. P., and Choudhary, J. (2020). Lung Cancer Identification: a Review on Detection and Classification. *Cancer Metastasis Rev.* 39 (3), 989–998. doi:10.1007/s10555-020-09901-x

Tong, J., Krieger, J. R., Taylor, P., Bagshaw, R., Kang, J., Jeedigunta, S., et al. (2020). Cancer Proteome and Metabolite Changes Linked to SHMT2. *PLoS One* 15 (9), e0237981. doi:10.1371/journal.pone.0237981

Vila, N., Besada, P., Costas, T., Costas-Lago, M. C., and Terán, C. (2015). Phthalazin-1(2H)-one as a Remarkable Scaffold in Drug Discovery. *Eur. J. Med. Chem.* 97, 462–482. doi:10.1016/j.ejmech.2014.11.043

Wallace, A. C., Laskowski, R. A., and Thornton, J. M. (1995). LIGPLOT: A Program to Generate Schematic Diagrams of Protein-Ligand Interactions. *Protein Eng. Des. Sel* 8 (2), 127–134. doi:10.1093/protein/8.2.127

Wang, C., Lai, Z., Xie, H., and Cui, S. (2021). Triazenyl Alkynes as Versatile Building Blocks in Multicomponent Reactions: Diastereoselective Synthesis of β-Amino Amides. *Angew. Chem. Int. Ed.* 60, 5147–5151. doi:10.1002/anie.202014686

Wang, L.-x., Zhou, X.-b., Xiao, M.-l., Jiang, N., Liu, F., Zhou, W.-x., et al. (2014). Synthesis and Biological Evaluation of Substituted 4-(thiophen-2-Ylmethyl)-2h-Phthalazin-1-Ones as Potent PARP-1 Inhibitors. *Bioorg. Med. Chem. Lett.* 24 (16), 3739–3743. doi:10.1016/j.bmcl.2014.07.001

Wicker, J. G. P., and Cooper, R. I. (2016). Beyond Rotatable Bond Counts: Capturing 3D Conformational Flexibility in a Single Descriptor. *J. Chem. Inf. Model.* 56 (12), 2347–2352. doi:10.1021/acs.jcim.6b00565

Young Taek, H., Jong-Wha, J., and Nam-Jung, K. (2017). Recent Advances in the Synthesis of Biologically Active Cinnoline, Phthalazine and Quinoxaline Derivatives. *Curr. Org. Chem.* 21 (14), 1265–1291. doi:10.2174/1385272821666170221150901

Practical and Computational Studies of Bivalence Metal Complexes of Sulfaclozine and Biological Studies

Abeer A Sharfalddin[1], Abdul-Hamid Emwas[2], Mariusz Jaremko[3] and Mostafa A. Hussien[1,4]*

[1]Department of Chemistry, Faculty of Science, King Abdulaziz University, Jeddah, Saudi Arabia, [2]King Abdullah University of Science and Technology (KAUST), Thuwal, Saudi Arabia, [3]King Abdullah University of Science and Technology (KAUST), Biological and Environmental Science and Engineering (BESE), Thuwal, Saudi Arabia, [4]Department of Chemistry, Faculty of Science, Port Said University, Port Said, Egypt

In the search for novel, metal-based drug complexes that may be of value as anticancer agents, five new transition metal complexes of sulfaclozine (SCZ) with Cu(II), Co(II), Ni(II), Zn(II), and Fe(II) were successfully synthesized. The chemical structure of each complex was characterized using elemental analysis (CHN), IR spectroscopy, UV–Vis spectroscopy, thermogravimetric analysis (TGA), and electronic paramagnetic resonance (EPR) spectroscopy. IR spectra indicated that the donor atoms were one sulfonyl oxygen atom and one pyrazine nitrogen atom, which associated with the metal ions to form a stable hexagonal coordination ring. The metal–ligand stability constant (K_f) revealed that Cu(II) and Ni(II) have good coordination stability among the metal compounds. Theoretical studies using DFT/B3LYP were performed to further validate the proposed structures. The obtained results indicated that Cu(II) has a trigonal bipyramidal geometry, whereas Fe(II), Co(II), and Ni(II) have an octahedral structure, while Zn(II) has a tetrahedral arrangement. The bio-activities of the characterized complexes were evaluated using DNA binding titration and molecular docking. The binding constant values for the metal complexes were promising, with a maximum value for the copper metal ion complex, which was 9×10^5 M^{-1}. Molecular docking simulations were also carried out to evaluate the interaction strength and properties of the synthesized metal complexes with both DNA and selected cancer-relevant proteins. These results were supported by *in vitro* cytotoxicity assays showing that the Cu(II) and Ni(II) complexes display promising antitumor activity against colon and breast cancer cell lines.

Keywords: electronic paramagnetic resonance analysis, DFT, sulfaclozine, molecular docking, anticancer

INTRODUCTION

Sulfonamide is a well-known antibacterial compound that has been in use for around 50 years (Stober and DeWitte, 1982). It came to prominence when Domagk et al. reported that Prontosil, a sulfamidochrysoidine azo dye, was reduced to the antibiotic sulfonamide and triamine benzene in living cells (Domagk, 1935), with sulfonamide being the affected part in this dye molecule. Metal ions have played key roles as components of pharmaceuticals in the field of anticancer therapy (Wong and Giandomenico, 1999), arthritis (Roberts et al., 1996), and cardiovascular medicine (Navarro et al., 2004). Thus, searching for novel metal-based drug complexes is a high priority for medicinal biochemists.

FIGURE 1 | Structures of sulfonamide and sulfaclozine.
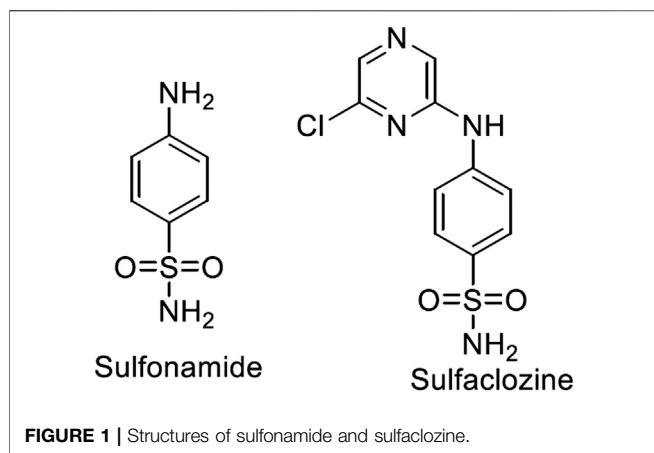
Metal complexes of sulfonamide drugs, **Figure 1**, have drawn attention from the scientific community because of their superior clinical applications compared to the free drugs. For instance, the zinc sulfadiazine complex has a 1:2 molar ratio and is used to promote wound healing and control infections (Fox, 1977). Additionally, the Ag(I) sulfadiazine complex is utilized as a topical antibacterial agent for treating first-, second-, and third-degree burns (Carr et al., 1973). Due to the effectiveness of sulfonamide metal complexes in the clinic, a diversity of metal complexes, metals based on sulfonamide or its derivative compounds, with transition metals, Cu(II), Co(II), and Ni(II) (Ajibade et al., 2006; Rocha et al., 2019), or with transition metals of platinum group, Pt(II), Pd(II) (Ajibade et al., 2013), and Ru(III) (Refat et al., 2016), or with heavy metals (Khedr and Saad, 2015), have been obtained to enhance their antimicrobial properties (Ajibade et al., 2006; Rocha et al., 2019).

Sulfaclozine (SCZ), **Figure 1**, is a derivative of the sulfonamide drug in which an amide group (NH) binds to a chloropyrazine aromatic ring. It is used as an oral antibiotic to treat various poultry diseases (Şentepe and Eraslan, 2010) and murine toxoplasmosis (Zeng et al., 2012; Ismail et al., 2016). Interestingly, it has several potential binding sites that could be coordinated with metal ions, namely, two pyrazine nitrogen atoms, sulfonyl oxygen atoms, and sulfonamide nitrogen atoms and an amino group at its tail. In addition, the chloropyrazine ring in SCZ could enhance its biological properties more than sulfonamide.

To the best of our knowledge, no published reports have described the complexation between divalent transition metals and SCZ. In this work, a new synthesis of metal complexes in ethanol solution was performed. The molecular structures of all the new complexes were characterized by analytical, spectroscopic, and thermal techniques. The structures of the prepared complexes were optimized by DFT with the exchange–correlation functional approach (B3LYP) to study the geometric arrangement around the metal ions. Moreover, the energy gap calculated from the HOMO and LUMO was used to predict the biological properties. Experimentally, various techniques were carried out to investigate the potential influence of the metal ion coordination on their potential as

therapeutics. One of the least expensive and simplest methods is spectroscopic titration experiments with CT-DNA to study binding affinity of the metal complexes with the pharmacological target. A molecular docking approach was also used to examine the molecular interaction of the newly synthesized compounds and the free ligand to test their inhibitory capacity toward different cancer proteins. A previous study tested the inhibitory effect of sulfonamide and its derivatives on a selected cancer cell line (Refat et al., 2016). Hence, in this work, *in vitro* cytotoxicity assays using two cell lines, a breast cancer cell line (MCF-7) and a colon cancer cell line (CaCo-2), were used to evaluate all compounds.

MATERIALS AND METHODS

Chemicals and Reagents

Sulfaclozine (SCZ) of 99% purity was purchased from Aldrich. The metal chlorides were obtained from Fisher Scientific. Solvents and analytical reagents were commercially obtained from the BDH chemical company and used as received.

Synthesis of Metal Complexes

The appropriate ratio of metal chlorides of Cu(II), Co(II), Zn(II), Fe(II), and Ni(II) of 1.0 mmol volume in 20 ml ethyl alcohol was added to the SCZ ligand (2.0 mmol in 30 ml ethyl alcohol). The mixed solution was placed on a hot plate at 80°C for 2–3 h with continuous stirring and refluxing until the color precipitates formed. The resulting solution was allowed to evaporate at room temperature, and the solids were washed with diethyl ether and dried under vacuum.

The Molar Ratio Method and the Metal Sulfaclozine Stability Constants Procedure

The stoichiometric composition of the complexes in ethanol was determined by the molar relation method (Davila et al., 2012). The concentration of the metal ion was kept constant (0.36×10^{-4} M), and the concentration of the SCZ ligand varied from [L] = 0.18 to 1.25×10^{-4} M. The solutions were stabilized at 25.0°C for 10 min to let the reaction reach equilibrium. Next, the spectra were recorded in the Shimadzu UV/Vis spectrometer with a cell width of 1 cm optical path length, in the 200–500 nm range.

The metal–ligand stability constant (K_f) of the complexes was calculated using the following equilibrium equation:

$$[M] + 2[SCZ] \leftrightarrow [ML_2],$$

$$K_f = \left(\frac{[ML_2]}{[M] \times [L]^2} \right) = \left(\frac{[ML_2]}{(C_M - [ML_2]) \times (C_L - 2[ML_2])^2} \right).$$

Using Beer's law (A = εbc), the equation can be rewritten for the stability constants of complexes (Panhwar and Memon, 2012; Samsonowicz and Regulska, 2017) as

$$K_f = \left(\frac{A/\varepsilon}{\left(C_M - A/\varepsilon \right) \times \left(C_L - 2 A/\varepsilon \right)^2} \right),$$

where A is the measured absorbance and ε is the molar absorption coefficient.

Structure Analysis

The micro-analytical ratio analyses (C, H, and N) were carried out in a PerkinElmer CHN 2400 elemental analyzer. The molar conductance of the metal complexes in the DMF solvent (10^{-3} M) was measured on a Hach conductivity meter model. A Bruker infrared spectrophotometer was utilized to record the infrared spectra of the ligand and its complex in the range of 400–4000 cm^{-1}. An electronic spectroscopic study of SCZ and the metal compounds in DMSO solution with a concentration of 10^{-3} M was obtained by the Shimadzu UV/Vis spectrometer in the range of 200–1100 nm. The electron paramagnetic resonance study for the solid sample was recorded on a Bruker EMX PLUS spectrometer using the X band frequency (9.5 GHz) using reported experimental details (Alahmari et al., 2019; Alghrably et al., 2019). The content of metal ions was calculated gravimetrically as metal oxides. The TG–DTG experiment was conducted using the Mettler Toledo STARe software. All experiments were under air at a flow rate of 30 ml/min and a heating rate of 10°C/min starting from 25°C and ending at 800°C using a single loose top loop. The percentage of metal ions was calculated gravimetrically as metal oxides. Magnetic measurements of metal complexes were measured at room temperature using Gouy's method by a magnetic susceptibility balance from the Johnson Matthey and Sherwood model.

Computational Details

The initial molecular geometries of SCZ and the metal complexes were optimized in the gas phase using the Gaussian 09W (Frisch et al., 2009) program package employing hybrid DFT/B3LYP at 6-31G (d,p) level for the free ligand and LAND for the metal complexes. The frequencies calculated were followed by optimization to ensure that the obtained structures were in the minima energy state. The GaussView molecular visualization program (Dennington et al., 2016) was used to visualize the input files and extract the HOMO–LUMO energies. The reactivity descriptors: chemical potential (μ), global hardness (η), chemical softness (S), and electrophilicity (ω), were calculated using the following formulas (Sharfalddina et al., 2020a):

$$\mu = -\left(E_{LUMO} - E_{HOMO}/2\right),$$
$$\eta = -\left(E_{LUMO} - E_{HOMO}/2\right),$$
$$S = 1/2\,\eta,$$
$$\omega = \pi2/2\,\eta\,R.$$

Bio-Activity Analysis
DNA Binding Methodology

The DNA binding protocol is reported in our previous work (Alsaeedi et al., 2020; Sharfalddina et al., 2020b). Compounds were dissolved in DMSO at room temperature with a fixed concentration that had absorbances between 1 and 1.2. The CT-DNA stock solution was prepared in a buffer solution (pH = 7.4) and kept at 5°C for 1 week. The ratio absorbance

for the stock at 280–290 nm was 1.8 (nucleotide to protein) indicating DNA is free of protein (Arjmand and Jamsheera, 2011). The molar absorption coefficient of 6600 M^{-1} cm^{-1} and the absorbance at 260 nm for CT-DNA were used to determine the DNA concentration (Tabassum et al., 2014; Mashat et al., 2019), which was 1.21×10^{-4} M. The experiments were performed by keeping the compound concentration constant and varying the DNA concentration from 1.69×10^{-6} to 5.55×10^{-6} M. The mixture solutions were allowed to incubate for 30 min at RT before recording the absorption. The binding constant was computed by the Wolfe–Shimer equation (Zehra et al., 2019) given as follows:

$$[DNA]\big/\left(\varepsilon_a - \varepsilon_f\right) = [DNA]\big/\left(\varepsilon_b - \varepsilon_f\right) + 1\big/K_b\left(\varepsilon_a - \varepsilon_f\right),$$

where [DNA] = concentration of CT-DNA in base pairs.
ε_a = extinction coefficient observed for $A_{obs}/$[compound] at the given DNA concentration.
ε_f = extinction coefficient of the free compound in solution.
ε_b = extinction coefficient of the compound when binding to DNA.
K_b = ratio of the slope to the intercept of the plot [DNA]/(ε_a–ε_f) versus [DNA].
K_b values were obtained by plotting the left side of the equation vs. DNA concentration and then calculating the ratio of the slope and intercept. The following equation was used to calculate Gibb's free energy values:
$\Delta G = -RT \ln K_b$, where R = 8.314 JK^{-1} mol^{-1} and T = 298K.

Molecular Docking

High-resolution crystallographic structures of proteins included in this study, breast cancer (PDB code = 1hK7) and colon cancer (PDB code = 4FM9) receptors, were downloaded from the Protein Data Bank into MOE software 2015 (MOE (The Molecular Operating Environment), 2015). The docking protocol is reported in our previous work (Abdel-Rhman et al., 2019). Protein preparation started with removing water molecules and co-ligand. The site finder was used to find the possible binding sites in the protein, and then the 3D protonation process was carried out to correct and fix the protein. The 3D structures of the compounds were minimized through the MMFF94X Force Field and optimized to obtain the lowest energy conformation with the best geometry using a gradient of 0.001. The docking parameters were the triangle matcher method for placing the compound and London dG for scoring and GBVI/WSA dG for rescoring. The ranking affinity of the ligand and metal compounds toward the amide protein was calculated using binding free energy and hydrogen bonds between the ligand and the amino acid. The measured hydrogen bond did not exceed the length of 3.1–3.7 A°.

Antitumor Assay

A human colon cancer cell line (CaCo-2) and human breast cancer cell line (MCF-7) were obtained from the VACSERA Tissue Culture Collection Unit. The propagation was done in Dulbecco's modified Eagle's medium (DMEM) completed with heat-inactivated fetal bovine serum (10%), 1% HEPES buffer,

Metal complex	M.Wt.	Color	Elemental analysis, % found (calc.)				Λ_m (Ωcm^2 mol^{-1})	Melting point
			C%	N%	S%	M%		
SCZ	250.05	White	47.99	22.39	12.31	-	1.3	130
			48	22.40	12.30			
[Cu(SCZ)$_2$Cl]Cl	635	Yellow ochre	34.13	15.92	9.10	9.09	94	170
			34.10	15.95	9.12	9.03		
[Co(SCZ)$_2$ClOH$_2$]Cl	628.39	Blue	34.35	15.89	10.17	9.35	70	205
			34.32	15.89	10.20	8.50		
[Ni(SCZ)$_2$Cl$_2$]	630.15	Light green	34.36	15.99	9.17	8.40	5.56	200
			34.40	16.05	9.19	8.41		
[Fe(SCZ)$_2$Cl$_2$]	627.30	Dark brown	34.52	16.10	9.21	8.02	1.56	158
			34.51	15.92	9.25	8.00		
[Zn(SCZ)$_2$]Cl$_2$	636.83	Sandy	34.04	15.60	9.09	9.26	152	214
			34.02	15.55	9.10	9.30		

L-glutamine, and gentamicin (50 µg/ml). Next, in a humidified atmosphere with 5% carbon dioxide, the cells were kept at 37°C and were sub-cultured two times a week. The determination of sample cytotoxicity on cells (MTT protocol) was performed as reported (Alley et al., 1988; Van de Loosdrecht et al., 1994). 1×10^5 cells/ml (100 µl/well) were incubated in a 96-well tissue culture plate at 37°C for 24 h to create a complete monolayer sheet. After an aggregate sheet of cells was formed, the monolayer cells were separated from the growth medium and washed twice with wash media. 2% of serum as a maintenance medium was used to dilute the tested sample twofold in the RPMI medium. A constant volume (0.1 ml) of each diluted sample was added simultaneously in various wells in the maintenance medium at 37°C, with three wells without treatment used as control cells. The samples were checked for any physical signs of toxicity such as partial or complete loss of the monolayer every 24 h. The MTT protocol depends on tetrazolium salt reduction from yellow to purple by metabolically viable cells. Therefore, 20 µl of the solution (5 mg/ml in PBS) was added to each well and maintained (37°C, 5% CO_2) for 1–5 h until the cell metabolization process was completed. After drying the wells by dumping the media, 200 µl DMSO was added to re-suspend the MTT metabolic product and was mixed thoroughly. The spectrophotometric absorbance at OD = 560 nm was measured and then subtracted from the background sample (50 µL MTT + 50 µL of media) at 620 nm.

The percentage of cell survival was calculated as follows:

$$Survival\ fraction = \frac{O.D.\ (treated\ cells)}{O.D.\ (controlled\ cells)} \times 100.$$

Each experiment was repeated three times to obtain a linear relationship between optical density and cell quantity.

RESULTS AND DISCUSSION

Analytical Data of the Metal Complexes

The analytical data and physical properties of the ligand and its metal complexes are summarized in **Table 1**. The isolated colored solid complexes are stable at room temperature, except for the Zn(II) complex, which turned light brown due to the absorption of water molecules over time. Moreover, they are soluble in DMF and DMSO. The molar conductance of Cu(II) and Co(II) at 10^{-3} M in DMF had values fall in the 66–95 Ω cm^2 mol^{-1} range, indicating the presence of two ion types in the solution, which are 1:1 of cationic and anionic species (Ali et al., 2013). The zinc complex showed a higher value, 152 Ω cm^2 mol^{-1}, suggesting two Cl^- ions out of the coordination sphere. In contrast, for Ni(II) and Fe(II), the molecular conductance was too low to account for any dissociation to Cl^- ions; thus, they are non-electrolytes.

Stoichiometry and Metal–Ligand Stability Constant

The collected absorption is plotted toward the ratio of [M]/[M]+[L] and presented in **Supplementary Figure S1** for the metallic complexes. The reflection line upon increasing the ligand concentration was around 0.33 and revealed that one mole of the metal reacted with two moles of the ligand.

The obtained values of K_f by the previous equations were in the order Zn–SCZ (1.74×10^{-5}) >Cu–SCZ (1.47×10^{-5}) > Ni–SCZ (0.48×10^{-5}) > Fe–SCZ (0.25×10^{-5}) > Co–SCZ (0.17×10^{-5}) and showed good interaction of Zn(II) and Cu(II) ions forming a stable coordination complex.

Infrared Spectroscopy

The comparison spectra of the free ligand and the five metal complexes are illustrated in **Supplementary Figure S2**, and the essential bands are given in **Supplementary Table S1**. The divalent metal complexes had similar infrared spectra to their SCZ drug, and thus, careful observation of peak shift was performed. The NH_2 stretching appeared at 3295–2966 cm^{-1} for asymmetric and symmetric modes, respectively, maintained in the same range for all complexes. As a consequence of the hydrogen bonding interaction between the NH_2 and SO_2 groups, a significant shift to higher frequencies (Rocha et al., 2019) was observed for those bands. Moreover, the NH_2 binding at 1682 cm^{-1} was
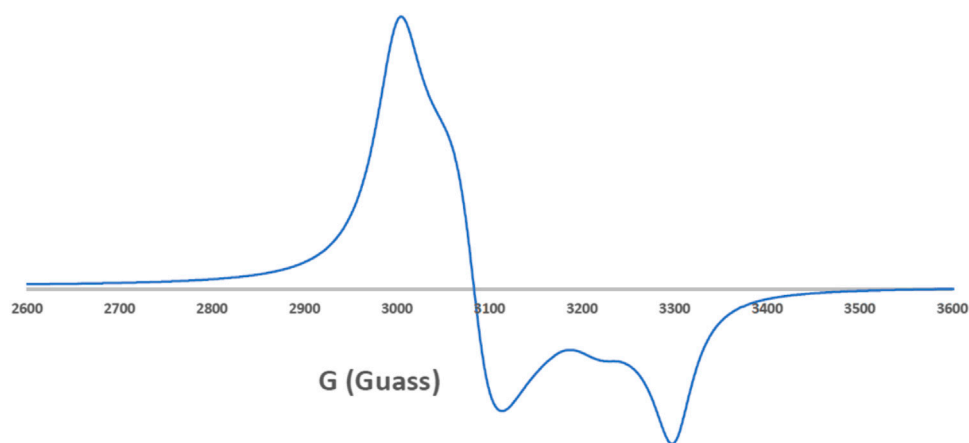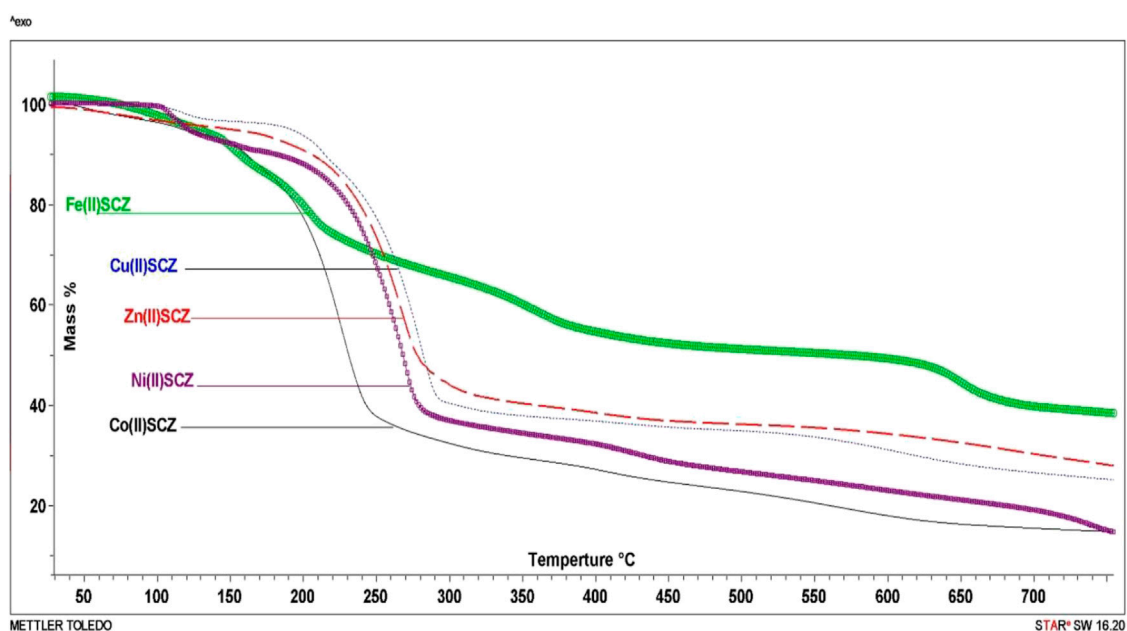
FIGURE 2 | EPR spectrum of the Cu–SCZ complex.

FIGURE 3 | TG curves of [Cu(SCZ)$_2$Cl]Cl.2H$_2$O, [Co(SCZ)$_2$ClOH$_2$]Cl.2H$_2$O, [Ni(SCZ)$_2$Cl$_2$].2H$_2$O, [Zn(SCZ)$_2$]Cl$_2$.2H$_2$O, and [Fe(SCZ)$_2$Cl$_2$].2H$_2$O complexes.

preserved in the metal spectra, which revealed this assignment is not coordinated to the metal. Another donating atom group is the oxygen atoms of the SO$_2$ group, which could be associated with the metal center. There is noticeable disappearing for the symmetric SO$_2$ at 1149 cm^{-1} or red-shift for asymmetric stretching modes at 1344 cm^{-1} indicating the coordination of the sulfonamide oxygen to the metal ion. The intensity bands corresponding to the C = N group in the pyrazine ring at 1580,1512, and 1433 cm^{-1}(Stober and DeWitte, 1982) shifted slightly after coordination to the metal concerning those of the free ligand, thus proving that N$_4$ pyridine associated with the complexation to form a hexagon ring. The assignment of the M–O and M–N stretching

modes in the metal complex spectra was indicated by the low-intensity band in the ranges 742–600 cm^{-1} and 420–400 cm^{-1}, respectively.

Electronic Paramagnetic Resonance Analysis for the Cu(II) Complex

EPR spectroscopy is a selective method where only unpaired electron species can be detected, while all other parts of the studied molecules are EPR silent. Thus, EPR spectroscopy is a powerful approach to study the formation of organic radicals (Mattar et al., 2002) and monitor the coordination of paramagnetic transition metals such as the Cu(II) and

TABLE 2 | Electronic parameters of the metal complexes.

Compound	$V_{ligand\ band\ shift}$		V3	V2	10Dq	B	β
SCZ	274(36500)	313(31500)		-	-		
[Cu(SCZ)$_2$Cl]Cl	275(36400)	321(31200)		810(12346)	12350	-	-
[Co(SCZ)$_2$ClOH$_2$]Cl	278(36000)	315(31500)	589(16977)	685(14600)	7770	708	0.730
[Ni(SCZ)$_2$Cl$_2$]	297(25189)	405(24700)	680(14700)	760(12900)	5400	760	0.738
[Fe(SCZ)$_2$Cl$_2$]	276	335(29900)	-	-	-	-	-

Mn(II) complexes (Emwas et al., 2013; Haque et al., 2019). In this study, we employed EPR spectroscopy to study the ligand coordination of the [Cu(SCZ)$_2$Cl]Cl complex. The solid EPR presented in **Figure 2** shows two peaks with different g-values: the one with parallel orientation with term g‖ and the other with perpendicular orientation with term g⊥, which was higher than the last one (g⊥ = 2.189 > g‖ = 2.044). This value suggested a compression on the Z axial and a pentacoordinate arrangement strongly shifted toward the trigonal bipyramid (Kozlevčar, 2008), with a Cl$^-$ atom and two oxygen atoms from two different ligand molecules in the equatorial plane and two nitrogen atoms in the axial position. The ground state will be ^{2}A$_{1g}$, which is a combination of dz^2 and dx^2–y^2 orbitals (Garribba and Micera, 2006; Lakshmi et al., 2012). Moreover, the nature of binding to the SCZ ligand was calculated by g$_{av}$ = (g‖ + 2 g⊥)/3 (Ibrahim et al., 2015) and was 2.14< 2.3, which indicated a highly covalent character of the metal–ligand bond.

Electronic Spectroscopic and Magnetic Susceptibility

The UV–Vis spectroscopic analysis was performed for the ligand and the metal complexes in DMSO in the range of 200–900 nm, **Supplementary Figure S3**. The bands at 276 nm of both ligand and complex spectra can be assigned to an n→π transition. Moreover, a band between 300 and 400 nm was observed in the free ligand for the π→π* transition of the aromatic ring (Zhao et al., 1992) and shifted to a higher frequency in all metal complexes, confirming the coordination to the aromatic pyrazine ring (Yang et al., 2005). There is a peak at low energy in the range 10, 500–14, 600 cm^{-1} in the Cu(II) spectrum, suggesting the symmetry of D$_{3h}$ for the five coordination Cu(II) complexes (Slade et al., 1968). The observed absorption at 790 nm was assigned to the allowed transition state ^{2}A$_1$→ ^{2}E (Slade et al., 1968; Sabolová et al., 2011). The complex [Ni(SCZ)$_2$]Cl$_2$ showed an octahedral structure, indicated by the magnetic moment of 2.63 BM. Furthermore, two bands at 673 and 755 nm were assigned to the transition states ^{3}T$_1$ → ^{3}A$_2$ and ^{3}T$_1$ (F) → ^{3}T$_1$ (P) (Ramírez-Delgado et al., 2015), respectively. The spectrum of the cobalt compound has essential transitions bands for the octahedral structure that were from ^{4}T$_{1g}$ → ^{4}T$_{2g}$ and from ^{4}A$_{2g}$ → ^{4}T$_{1g}$ located at 605 and 685 nm, respectively. As reported, the octahedral structure of Fe(II) can be confirmed by the absence of the band around 1100 nm (Goodwin, 1976; Gütlich et al., 1996), **Supplementary**

Figure S3. The brown color is due to charge transfer transitions from the metal to the ligand orbitals (Gütlich et al., 1996). Moreover, the magnetic moment for Fe(II) confirmed the low spin d^6 configuration (0.952 BM). The nephelauxetic parameters such as the interelectronic repulsion parameter (B), covalency factor (β), and ligand-field splitting energy (10Dq) are listed in **Table 2**, calculated by the following equations (James E. House, 2013; König, 1971) for Co(II):

$$Dq = [(85V32 − 4(V3 − 2V2)2)^§ − 9(V3 − 2V2)]/340,$$
$$B = (V3 − 2V2 + 30Dq)/15,$$
$$β = B/B0 (B0 = 971),$$

while for Ni(II),

$$Dq = [(9V2 + V3) − (85(V2 − V3)2 − 4(V2 + V3)2)^§]/340,$$
$$B = (V2 + V3 − 30Dq)/15,$$
$$β = B/B0 (B0 = 1030).$$

Thermal Gravimetric Analysis and Kinetic Thermodynamics

The isolated solid metal complexes were analyzed by TGA to characterize the thermal stability within the temperature range of 25–800°C. The decomposed stages and their assignments are listed in **Table 3**. **Figure 3** shows the TG curve for the metal complexes. The Cu(II) complex presented two stages starting from 150°C with the loss of two water molecules, losing weight of 4.5%. The second step was at 205–240°C with the loss of all the organic molecules (75.3 %) and leaving CuO as a final metallic residue. In addition, Co(II) and Ni(II) had the same number of water molecules in the first stage in the range 100–170°C, followed by decomposing at 250°C for anhydrase [Co(SCZ)$_2$ClOH$_2$]Cl and 230°C for [Ni(SCZ)$_2$Cl$_2$] leaving a metallic residue percentage of 17.4% and 23.2%, respectively. On the contrary, [Fe(SCZ)$_2$Cl$_2$].3H$_2$O had four steps, which were assigned to slow degradation beginning with evaporating three outside lattice water molecules. The second step had the highest weight loss (22.5%) of the complex at 160–170°C. The last two steps were similar by losing sulfonamide and coupling amine groups at each step until 230°C to complete decomposition. The one-step Zn(II) complex was thermally stable until 200°C and began a full fragmentation that was finished at 260°C. The final resultant residues were metal oxides and counted carbon atoms.

TABLE 3 | Thermogravimetric data of the five metal complexes.

Complex	Step	Temp. range	Weight loss % found (calc.)	Assignments	Total mass loss/% found (calc.)	Final solid state residue found (calc.)
$[Cu(SCZ)_2Cl]Cl.2H_2O$	1st	150–160	4.5 (5)	$2H_2O$	79.8 (79.9)	CuO 11.3 (11.3)
	2nd	205–240	75.3 (74.7)	$2HCl+2SO_2+4N_2+7C_2H_4$		
$[Co(SCZ)_2ClOH_2]Cl.2H_2O$	1st	164–172	10.1 (10.5)	$2H_2O+C_2H_2+2NH_3$	75.3 (76.1)	$CoO+10C$ 17.4 (18.5)
	2nd	215–246	65.2 (65.6)	$2HCl+2SO_2+3N_2+4C_2H_2$		
$[Zn(SCZ)_2]Cl_2$	One step	217–260	72.7 (71.9)	$2HCl+2HSO_2+4N_2+4C_2H_4$	72.7 (71.9)	$ZnO+7C$ 20.7 (20.1)
$[Fe(SCZ)_2Cl_2].3H_2O$	1st	115–131	8.9 (7.8)	$3 H_2O$	59.39 (58.9)	Fe_2O_3+8C 26.49 (27.83)
	2nd	157–177	22.5 (23)	$2CN+5C_2H_2$		
	3rd	302.33–340	13.4 (13.1)	$2N_2+SO_2$		
	4th	625–660	14.59 (15)	$2N_2+SO_2$		
$[Ni(SCZ)_2Cl_2].2H_2O$	1st	80–94	10.8 (10.5)	$2H_2O+C_2H_2$	73.7 (74.4)	$NiO+8C$ 23.2 (23.5)
	2nd	199–234	62.9 (63.9)	$2HCl+2SO_2+4N_2+4C_2H_2$		
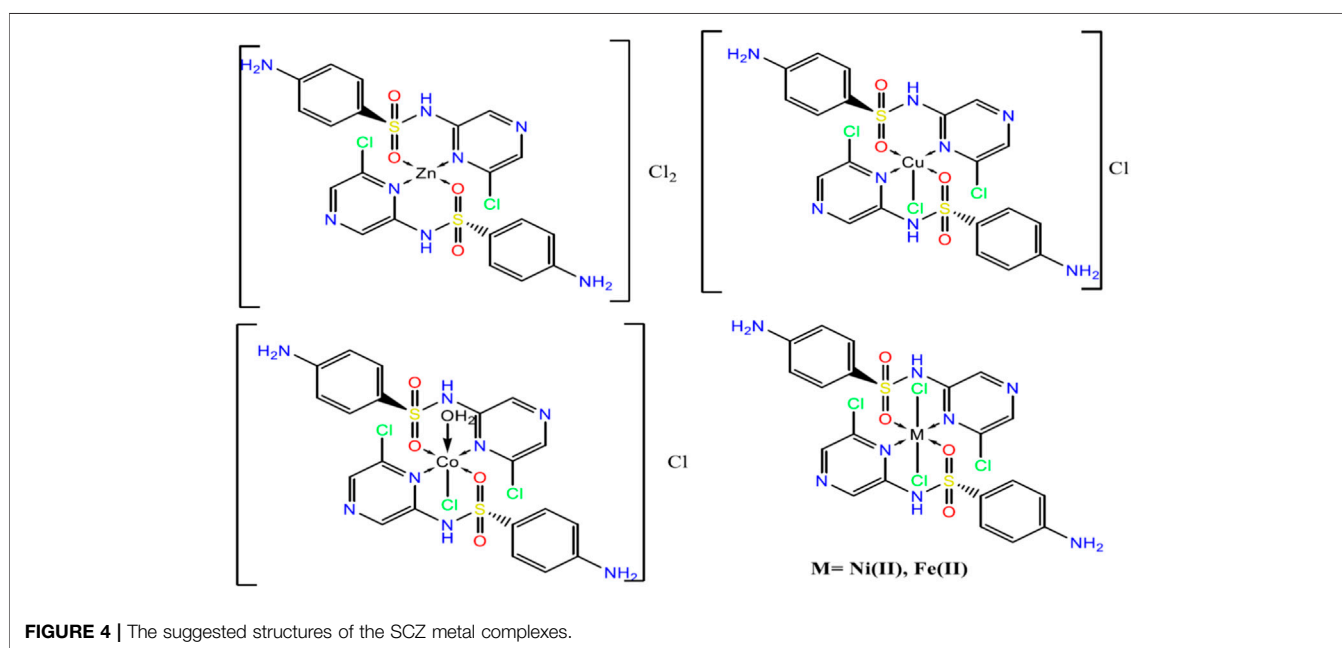
FIGURE 4 | The suggested structures of the SCZ metal complexes.

Thermodynamic data, activation energy (Ea, kJmol^{-1}), and Arrhenius factor (A, S^{-1}) for the metal complexes were obtained by plotting the relationship of the Coats–Redfern (CR) equation (Coats and Redfern, 1964) or Horowitz–Metzger (HM) equation (Horowitz and Metzger, 1963), as recorded in **Supplementary Table S2**. The following equations were employed to calculate enthalpy activation $\Delta H = Ea-RT$, activation entropy $\Delta S = R[In(Ah/kT)]$, and Gibbs free energy $\Delta G = \Delta H - T\Delta S$ for each decomposition step. From the results in **Supplementary Table S3**, it can be seen that the activation energy E_a values were high and varied between 10^5 and 10^4 kJ mol^{-1}, which translate to good stability for SCZ metal complexes. Moreover, the negative entropy values indicated the activated metal complexes need a higher-order system than the reactants. Enthalpy results support the endothermic DTG curve reactions ($\Delta H > 0$).

Structural Interpretation

From the above observations, the suggested coordination mode of the SCZ drug toward M(II) metal ions conformed with the structure and formulas designed as shown in **Figure 4**. The coordination sites with SO_2 and/or pyrazine were reported in the literature (Khedr and Saad, 2015; Radha et al., 2016; Abdel-Kader et al., 2019). Moreover, the Cu(II) complex has a trigonal bipyramidal structure containing the bidentate ligand and one Cl ion. The octahedral arrangements were observed in three metal ions, Ni(II), Fe(II), and Co(II), binding to Cl ions, compatible with the conductance results. The Zn(II) complex showed a tetrahedral geometry, which is one of the passable possible structures for an ion metal (Dudev and Lim, 2000; Jana et al., 2017). There were many attempts to get single crystals from the metal complexes using the diffusion method with DMS and chloroform or ethanol and benzene but all
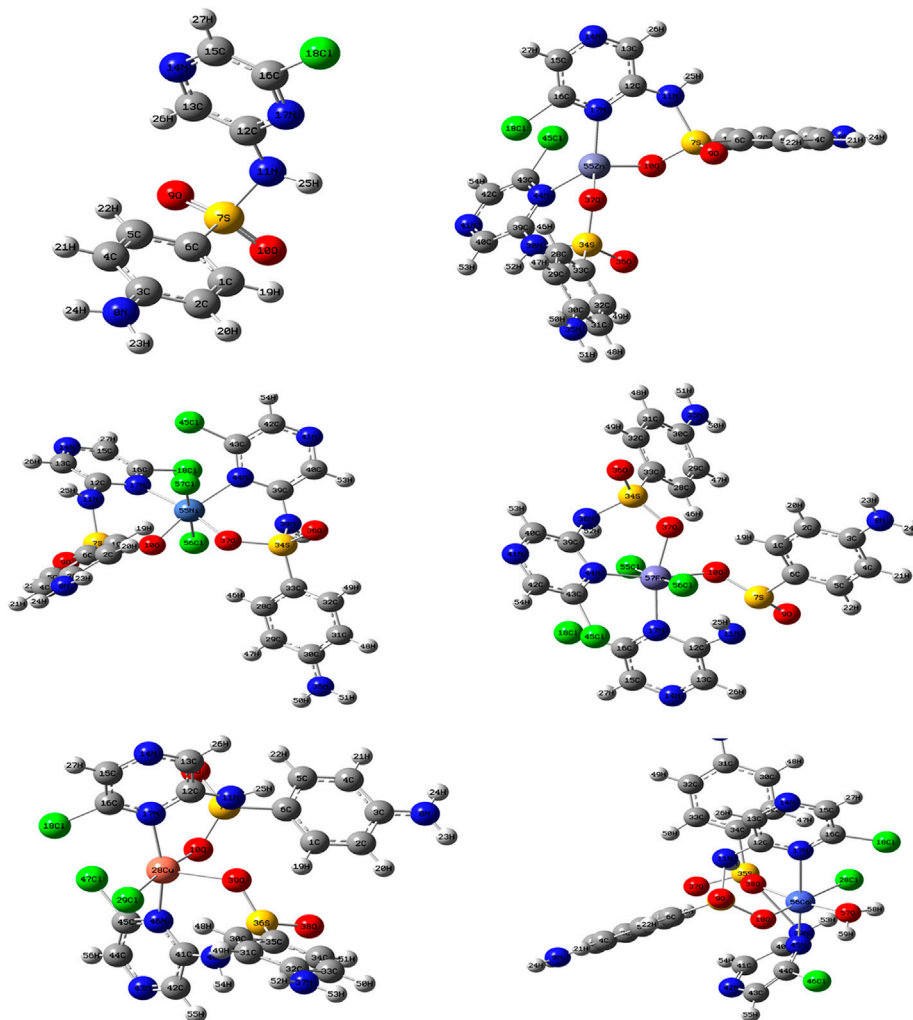
FIGURE 5 | The optimized geometry with the numbering system of the free SCZ ligand and the five metal complexes.

failed. Therefore, a theoretical calculation was carried out to verify the structural and biological features.

Molecular Orbital Calculations
Geometry of the Ligand and Metal Complex

The comparison between the optimized geometry parameters such as the bond length and the angles of the free ligand and the complexes, Cu–SCZ, Co–SCZ, Ni–SCZ, Zn–SCZ, and Fe–SCZ, is illustrated in **Supplementary Table S4**. The optimized geometry and numbering system of all studied metal complexes are presented in **Figure 5**. In general, the bond lengths around the metal ion in the complexes are longer than those of the free ligand due to the influence of the coordination process. In the Co–SCZ complex, the coordination sphere was completed with one Cl ion and one water molecule forming an octahedral arrangement. In contrast, Ni(II) and Fe(II) bonded to two Cl ions. The bond lengths of the Ni(II), Co(II), and Fe(II) ions with the donating sites of the ligand (**Supplementary Table S4**) suggest a minor

distorted octahedral geometry around the central metal (El-Sonbati et al., 2016; Abdel-Kader et al., 2019). The new bond length of M–N and M–O bonds showed varied elongation upon complexation. Those bonds were in the range 1.94–2.4 Å, which indicates small ionic properties of the covalent bonds (Abdel-Kader et al., 2019). For the trigonal bipyramid, Cu(II) complex, the angles of O10–M–N17 and O38–M–Cl28 were 92.6 and 91.9o, respectively, which showed a small deviation from the regular penta-coordination geometry angle between the two nearest neighbor atoms (Gillespie, 1961). The average of the angles of the Zn(II) complex is 112.3o, indicating that this complex adopts a square planar with distortion by 0.03°.

The Frontier Molecular Orbital and Reactivity Properties

Frontier molecular orbital, FMO, studies provide the electronic characteristics of molecular systems and the reactivity of the compounds (Abdel-Kader et al., 2019; Sharfalddina al., 2020a). Thus, the map of HOMO and LUMO energies of the studied
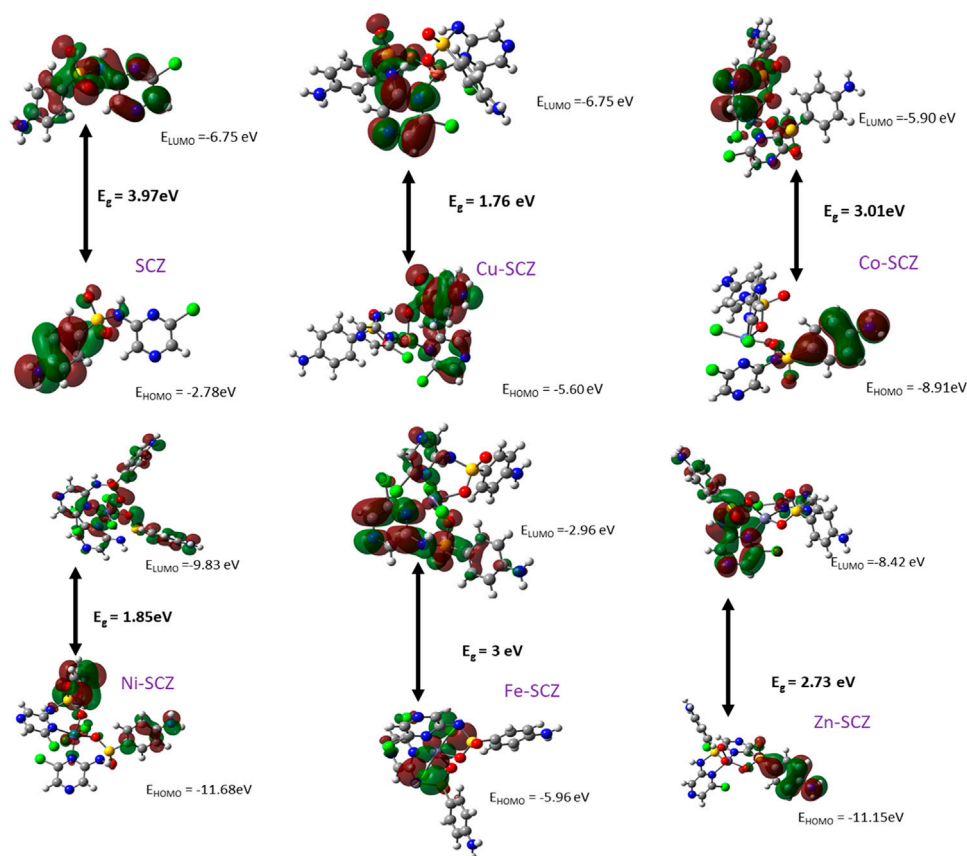
FIGURE 6 | HOMO and LUMO plots of the SCZ and the metal complexes using DFT/B3LYP.
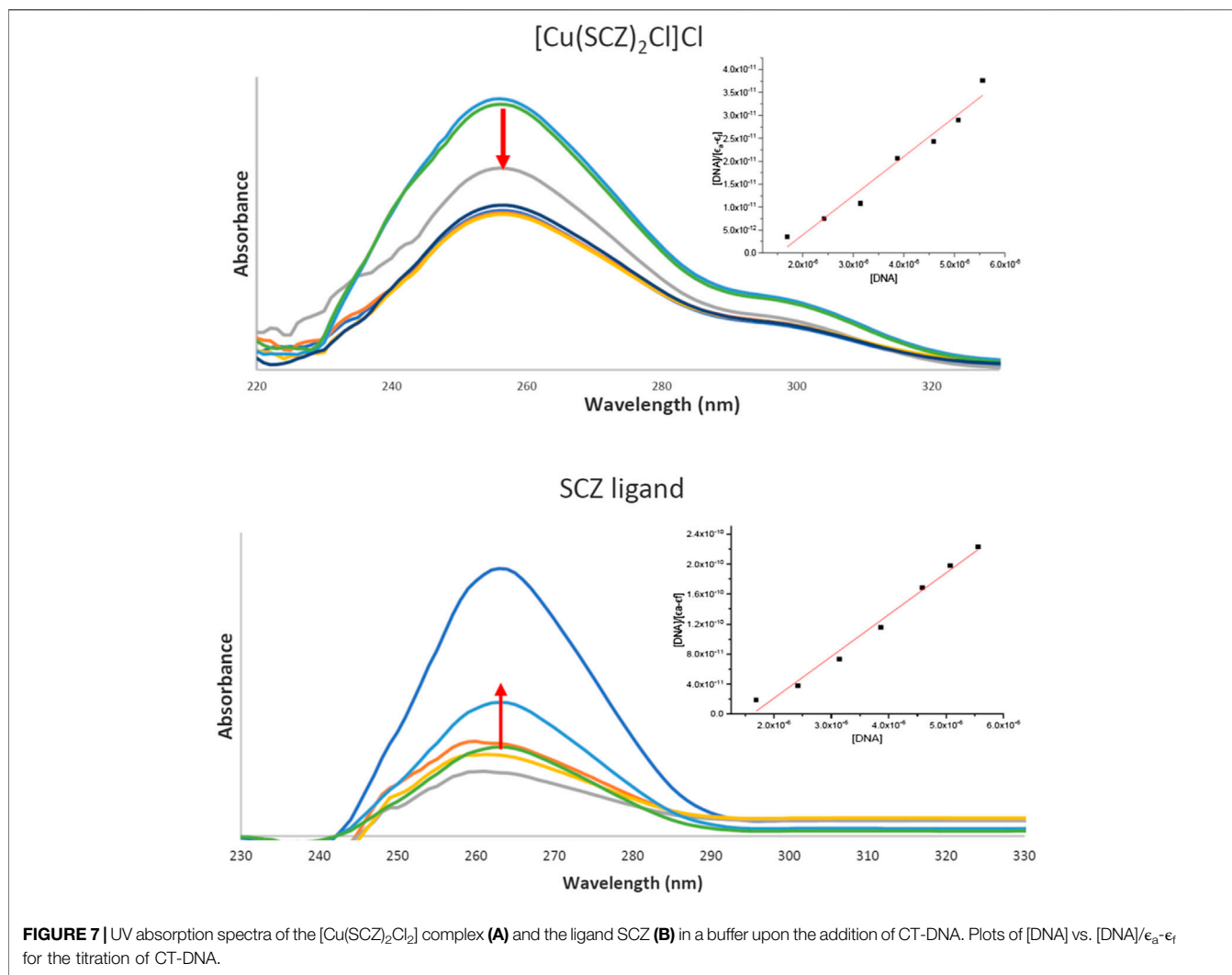
ligand and its complexes in the ground state was extracted and is presented in **Figure 6**. Moreover, the calculation of the gap energy (E_g) with the difference between the E_{HOMO} and the E_{LUMO} gives a good indicator of the molecular stability and can be used to describe the compound hardness or softness. Large E_g values indicate a hard molecule and low reactivity, while soft molecules have a small E_g value and more polarizable ability. The E_{HOMO} for the free SCZ was –3.97 eV and located on the sulfonylaniline moiety, and the E_{LUMO} = –6.75 eV was distributed over the molecule. **Supplementary Table S5** presents the E_g and the global reactivity descriptors. The Cu(II) complex had practical reactivity among the synthesized metal complexes. Ni(II) followed this compound with low E_g = 1.85 eV. The chemical hardness values showed that Co(II) and Fe(II) are the most stable complexes with less reactivity. In contrast, Cu(II) and Ni(II) had the lowest values reflecting the softness and the inhibition ability of the molecules. The negative values of the chemical potential of all complexes indicated that all coordination processes are spontaneous (Rahmouni et al., 2019).

Biological Studies
DNA Binding Study and Cleavage Experiments
Drugs work largely by binding to a biological target such as DNA or specific protein and modifying its structure or inhibiting its activity. DNA in the biomolecules represents a major target in the development strategies of the drugs designed. Thus, a spectroscopic technique was used to study the binding ability of the free ligand and the five metal complexes simultaneously with varying concentrations of CT-DNA. In **Supplementary Table S6**, the maxima absorption band for the fixed concentration solution in DMSO/buffer and the binding parameter for SCZ and metal compounds are presented. Although all compounds had a blue shift, the SCZ ligand was hyperchromic in the molar absorptivity, while the SCZ metal complexes had a hypochromic effect (**Figure 7A,B**) due to a strong change in DNA conformation in its structure after interacting with the ligand or the metal complex (Sirajuddin et al., 2013). The hyperchromic effect is a result of DNA helix denaturation due to the resulting binding to the compound. This resulted in a limitation of the hydrogen bond between the complementary bases in the DNA double helix and the formation of a single-stranded DNA. The presence of numerous bases in free form in the solution increased the absorbance of the single-stranded DNA (Sirajuddin et al., 2013; Alsaeedi et al., 2020). Hypochromic type is due to the strong damage of the double-helical structure (Sirajuddin et al., 2012), which leads the π^* orbital of the ligand in the synthesized metal complexes to couple with the π orbitals in the DNA base

FIGURE 7 | UV absorption spectra of the [Cu(SCZ)$_2$Cl$_2$] complex **(A)** and the ligand SCZ **(B)** in a buffer upon the addition of CT-DNA. Plots of [DNA] vs. [DNA]/ϵ_a-ϵ_f for the titration of CT-DNA.

pairs after binding. The resulting coupled $\pi^\star$ will be partially filled, thus decreasing the possibility of electron transition, causing hypochromicity (Ju et al., 2011; Sirajuddin et al., 2012).

The binding constant, K$_b$, was between the value of the DNA minor groove binding Ru(II) complexes and classical intercalator (10^4–10^7 M^{-1}) (Vahdati et al., 2014), thus indicating an intercalation interaction mode with the DNA biomolecule. The K$_b$ value of the Cu(II) complex was higher than that of the free ligand and the other complexes, which suggested a good impact and proved the role of the cation Cu(II) in the binding process (Al-Amiery et al., 2012; Emwas et al., 2013). In sum, metal complexes could be ordered according to the decreasing Ka value: Cu(II) > Ni(II) = Fe(II) > Zn(II) > Co(II). Moreover, the negative value of ΔG showed the spontaneous interaction of the compound with DNA, **Supplementary Table S6**.

Molecular Docking

Molecular docking is a theoretical calculation approach in drug design and discovery that can also be used to help scientists

propose a drug interaction model and to understand the behavior of the new drug toward a biological target (Gupta et al., 2018; Márquez et al., 2020). Moreover, this method can be used to predict the binding affinity between a selected biological target and drug compounds. We performed a molecular docking study of the five metal complexes first with DNA. This revealed a strong DNA binding constant for only the Cu(II) compound. Thus, docking with a DNA helix was conducted to obtain more details of this interaction. **Figure 8** shows that the Cu–SCZ complex fits well between base pairs of B-DNA, forming intercalation interactions using hydrogen bonds with amino bases leading to uncoiling of the base pairs. It has been reported that this stacking model leads to inhibition of DNA replication in rapidly growing cancer cells (Shahabadi et al., 2017).

We also performed molecular docking of the free ligand and the five metal complexes with colon and breast cancer–related proteins. For colon cancer, we selected TNIK (PDB = 2X7F) and topoisomerase II enzyme (PDB = 4F9M), which are candidate therapeutic targets for colorectal cancer (Sapna
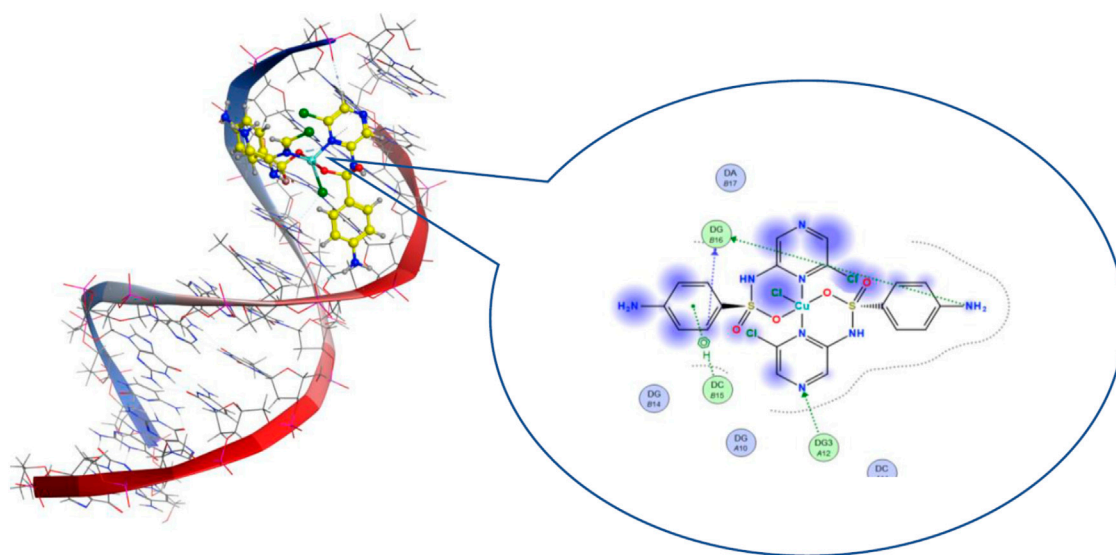
FIGURE 8 | 3D and 2D views of interactions of 8 with B-DNA.

Rani and Kumar, 2014; Lee et al., 2017; Rosita and Begum, 2020). Moreover, the breast cancer–associated estrogen receptor (ID: 3ERT) and Hsp90 protein receptor (ID: 1H7K) were chosen based on previous research suggesting their value as targets for potential breast cancer therapy (Zagouri et al., 2013; Acharya et al., 2019). **Table 4** presents the binding scores for the ligand and metal complexes against the selected proteins. The strongly negative values of free binding energy (S) suggest a good binding to both proteins. Generally, Cu–SCZ showed a stronger interaction pattern toward the investigated proteins than the free SCZ ligand and the other complexes. Comparing the interaction of the free ligand to the colon cancer–associated protein 2X7F with that of the Cu(II) compound, the interaction for the SCZ molecule was established by donating a hydrogen atom to the oxygen atom in glutamic acid and accepting an H bond from cysteine to one of the sulfonyl oxygen atoms. Moreover, the chloropyrazine ring interacted with both valine 39 and valine 170 to increase the free energy binding. Although the Cu(II) complex had the same binding constant with the investigated protein as the free ligand, the former had two ionic interactions with the glutamic residue with the binding energy of -6.5 kcal mol^{-1} that could enhance the interaction. In contrast, the breast cancer–associated protein

receptor 3ERT displayed different binding characteristics with the free ligand and the Cu(II) complex. The amino group (NH$_2$) in the SCZ molecule formed a hydrogen bond by donating this hydrogen to the glutamic and leucine oxygen atoms. The presence of two amino groups in the Cu(II) molecules elevated the interaction energies to 4.5 kcal mol^{-1} which bonded to methionine 538, methionine 343, and cysteine. Additionally, it formed an ionic interaction with the asparagine amino residue, which stabilizes this interaction more than the SCZ ligand. The different interaction models of the SCZ ligand and Cu(II) complex are presented in **Table 5**.

The surface maps were built over the dummy atoms as receptors to provide a better view of the molecular surface that was expressed in purple color for H-bonding, green for hydrophobic sites, and blue for polarity. The ligand and metal complex exhibited high occupancy inside the groove surface for both investigated proteins. Thus, good inhibitory activity is predicted for those compounds.
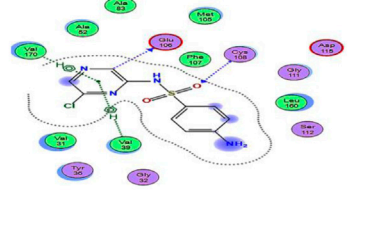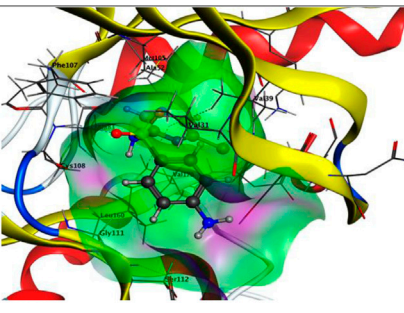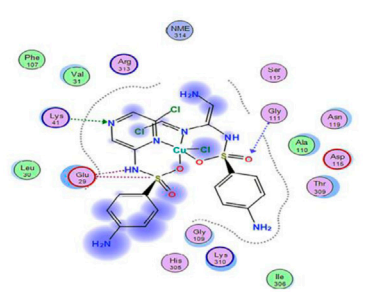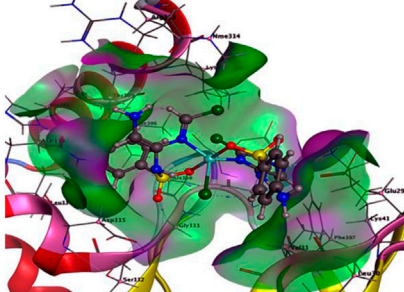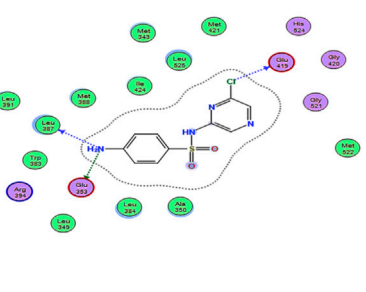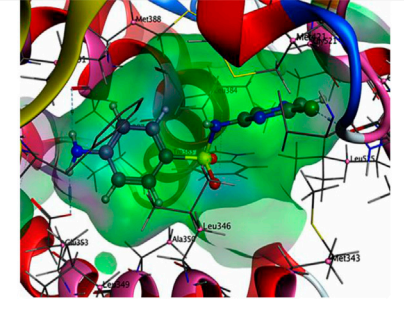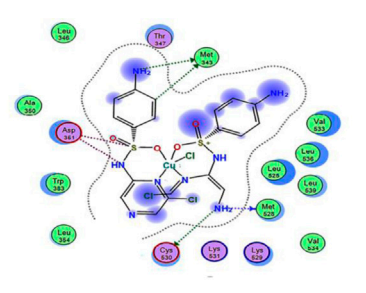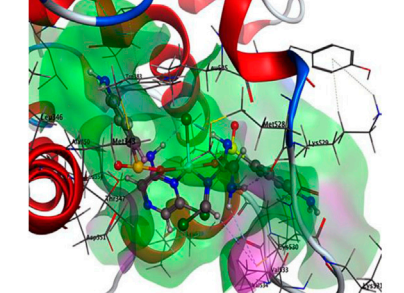
Cytotoxicity Results
There are several human cancer cell lines derived from different cancer types that have been commonly used to evaluate the anticancer properties of potential drugs. Among those types,

TABLE 4 | Energy score (kcal mol^{-1}) calculation for SCZ and its metal complexes toward four protein receptors.

Protein/complex		SCZ	Cu–SCZ	Co–SCZ	Ni–SCZ	Fe–SCZ	Zn–SCZ
Colon cancer protein	2X7F	−5.67657	−6.67613	−6.39108	−5.68732	−6.39108	−6.36569
	4F9M	−6.55138	−7.24939	−6.71789	−6.88243	−6.80609	−7.2411
Breast cancer protein	3ERT	−6.02021	−6.5352	−6.18126	−6.0157	−6.24734	−6.01604
	1H7K	−5.49007	−7.73247	−6.22617	−6.80484	−6.55553	−7.10101

TABLE 5 | 2D and 3D molecular docking mode and interaction between SCZ and the Cu(II) complex with the colon protein receptor (2X7F) and the breast protein receptor (3ERT).

compound	protein	2D	3D
SCZ	colon protein receptor (2X7F)		
Cu-SCZ			
SCZ	breast protein receptor (3ERT)		
Cu-SCZ			

Legend:
- polar
- acidic
- basic
- greasy
- proximity contour
- sidechain acceptor
- sidechain donor
- backbone acceptor
- backbone donor
- ligand exposure
- solvent residue
- metal complex
- solvent contact
- metal/ion contact
- receptor exposure
- arene-arene
- arene-H
- arene-cation

TABLE 6 | Cytotoxic activity of SCZ and its metal complexes against human tumor cells and SD values.

Compound	In vitro cytotoxicity IC$_{50}$ (µg/ml)[1]/SD			
	Breast cell line (MCF-7)	SD	Colon cell line (CaCo-2)	SD
SCZ ligand	215.24	±0.67	97.6	±0.45
[Cu(SCZ)$_2$Cl]Cl	86.2	±0.64	23.84	±0.33
[Zn(SCZ)$_2$]Cl$_2$	111.91	±0.36	198.44	±0.25
[Ni(SCZ)$_2$Cl$_2$]	45.62	±0.28	106.87	±0.34
[Co(SCZ)$_2$ClOH$_2$]Cl	54.23	±0.52	190.1	±0.30
[Fe(SCZ)$_2$Cl$_2$]	284.25	±0.31	362.9	±0.41

[1]IC$_{50}$ (mg/ml): 1–10 (very strong), 11–20 (strong), 21–50 (moderate), 51–100 (weak), and above 100 (non-cytotoxic).

we selected the breast cancer cell line (MCF-7), which is a good candidate particularly for estrogen receptor (ER)–positive breast cancer cell experiments (Sweeney et al., 2012; Comşa et al., 2015), and CaCo-2, which expresses normal enterocytic phenotypes (Hirata et al., 1993).

In vitro cytotoxicity of SCZ and the metal complexes was examined with the two cancer cell lines, human breast cancer (MCF-7) and human colon cancer (CaCo-2). The obtained results for the free drug and metal complexes are listed in **Table 6** as the inhibitory concentration (IC$_{50}$) for each cell line and SD values. Initially, the results matched the docking prediction, revealing that the Cu–SCZ complex has the highest activity against the human colon cancer cell line (CaCo-2) with IC$_{50}$ = 23.84 µg/ml. This is more effective than that reported for Ru(III) complexes of sulfadimidine against colon cell lines (Refat et al., 2016). There are some features of copper complexes that can contribute to them forming more functional metal drugs for cancer treatments (Martin et al., 2018). For example, the associated compounds can modulate the properties of the metal ions and enhance solubility in extracellular fluids (Jungwirth et al., 2011). Moreover, they can also balance their lipophilic–hydrophilic properties to traverse the two layers' lipid membrane (Santini et al., 2013).

In the breast cell line (MCF-7), the Ni(II) complex could also inhibit the growth of breast cancer lines (MCF-7) from 45.62 µg/ml to 50%. This effectiveness likely derives from the practical roles of nickel ions in cellular functions and their abundance in the human body (Deo et al., 2016).

Other tested compounds showed varied results, and those with values between 51 and 100 µg/ml were weakly cytotoxic, while those above 100 µg/ml were non-cytotoxic.

CONCLUSION

The new metal-based drugs, Cu(II), Co(II), Zn(II), Ni(II), and Fe(II), of sulfaclozine complexes were synthesized, and their structures were affirmed by various analytical approaches. The molar ratio method indicated that the ratio of the metal to the ligand was 1:2. Moreover, spectroscopic data from IR spectroscopy showed that SCZ is a bidentate ligand coordinated by one oxygen atom of the SO$_2$ group and the pyrazine nitrogen atom. Moreover, the absorption results revealed that the Fe(II), Co(II), and Ni(II) metal complexes have an octahedral structure. The solid EPR spectrum showed a trigonal bipyramidal geometry for the Cu(II) complex. The thermal decomposition assignments agreed with the suggested structure of the obtained complexes. The optimized geometries were match the experimental-suggested structures. The energy gap, E$_g$, values for the complexes were lower than that of the ligand, meaning that the complexes are more reactive. The low computed hardness parameter of Cu(II) revealed strong bio-reactivity. The DNA K$_b$ values were presented in descending order, Cu(II) > N(II) = Fe(II) > Co(II) > Zn(II), and were greater than the binding constant for the free ligand (6.67 × 10^5 M^{-1}). The computed free binding energy for the two proteins, breast cancer receptor protein and colon cancer receptor protein, illustrated the lowest negative score for the Cu(II) and Ni(II) complexes. The experimental cytotoxicity results presented a moderated anticancer strength of the Cu–SCZ compound. Finally, we suggest as a future perspective to study the activity of these complexes or other metal complexes by external inducements such as light or oxidizing materials.

DATA AVAILABILITY STATEMENT

The original contributions presented in the study are included in the article/**Supplementary Material**, and further inquiries can be directed to the corresponding author.

AUTHOR CONTRIBUTIONS

AAS synthesized and characterized the metal complexes. MAA supervised the project and wrote the original draft. AE performed EPR analysis. AE and MJ wrote, reviewed, and edited the paper. All authors read and agreed to the published version of the manuscript.

ACKNOWLEDGMENTS

SUPPLEMENTARY MATERIAL

The Supplementary Material for this article can be found online at: https://www.frontiersin.org/articles/10.3389/fchem.2021.644691/full#supplementary-material

REFERENCES

Abdel-Kader, N. S., Abdel-Latif, S. A., El-Ansary, A. L., and Sayed, A. G. (2019). Combined Experimental, DFT Theoretical Calculations and Biological Activity of Sulfaclozine Azo Dye with 1-Hydroxy-2-Naphthoic Acid and its Complexes with Some Metal Ions. *New J. Chem.* 43, 17466–17485. doi:10.1039/c9nj04594e

Abdel-Rhman, M. H., Hussien, M. A., Mahmoud, H. M., and Hosny, N. M. (2019). Synthesis, Characterization, Molecular Docking and Cytotoxicity Studies on N-Benzyl-2-Isonicotinoylhydrazine-1-Carbothioamide and its Metal Complexes. *J. Mol. Struct.* 1196, 417–428. doi:10.1016/j.molstruc.2019.06.092

Acharya, R., Chacko, S., Bose, P., Lapenna, A., and Pattanayak, S. P. (2019). Structure Based Multitargeted Molecular Docking Analysis of Selected Furanocoumarins against Breast Cancer. *Sci. Rep.* 9, 1–13. doi:10.1038/s41598-019-52162-0

Ajibade, P. A., Idemudia, O. G., and Okoh, A. I. (2013). Synthesis, Characterization and Antibacterial Studies of Metal Complexes of Sulfadiazine with N-Alkyl-N-Phenyldithiocarbamate. *Bull. Chem. Soc. Ethiopia* 27, 77–84. doi:10.4314/bcse.v27i1.8

Ajibade, P. A., Kolawole, G. A., O'Brien, P., Helliwell, M., and Raftery, J. (2006). Cobalt(II) Complexes of the Antibiotic Sulfadiazine, the X-ray Single crystal Structure of [Co(C10H9N4O2S)2(CH3OH)2]. *Inorg. Chim. Acta* 359, 3111–3116. doi:10.1016/j.ica.2006.03.030

Al-Amiery, A. A., Kadhum, A. A. H., and Mohamad, A. B. (2012). Antifungal and Antioxidant Activities of Pyrrolidone Thiosemicarbazone Complexes. *Bioinorganic Chem. Appl.* 2012, 795812. doi:10.1155/2012/795812

Alahmari, F., Davaasuren, B., Emwas, A.-H., M.F.J. Costa, P., and Rothenberger, A. (2019). Tris(ethylenediamine)Nickel(II) Thio-Hydroxogermanate Monohydrate: Synthesis, crystal Structure, 1H NMR, EPR, Optical and Magnetic Properties. *Inorg. Chim. Acta* 488, 145–151. doi:10.1016/j.ica.2019.01.019

Alghrably, M., Dudek, D., Emwas, A-H., Jaremko, Ł., Jaremko, M., and Rowińska-Żyrek, M.(2019). MCopper (II) and Amylin Analogues: A Complicated Relationship. *Inorg. Chem.* 59 (4), 2527–2535. doi:10.1021/acs.inorgchem.9b03498

Ali, I., Wani, W. A., and Saleem, K. (2013). Empirical Formulae to Molecular Structures of Metal Complexes by Molar Conductance. *Synth. Reactivity Inorg. Metal-Organic, Nano-Metal Chem.* 43, 1162–1170. doi:10.1080/15533174.2012.756898

Alley, M. C., Scudiero, D. A., Monks, A., Hursey, M. L., Czerwinski, M. J., Fine, D. L., et al. (1988). Feasibility of Drug Screening with Panels of Human Tumor Cell Lines Using a Microculture Tetrazolium Assay. *Cancer Res.* 48, 589–601.

Alsaeedi, M. S., Babgi, B. A., Hussien, M. A., Abdellattif, M. H., and Humphrey, M. G. (2020). DNA-binding and Anticancer Activity of Binuclear Gold(I) Alkynyl Complexes with a Phenanthrenyl Bridging Ligand. *Molecules* 25, 1033. doi:10.3390/molecules25051033

Arjmand, F., and Jamsheera, A. (2011). DNA Binding Studies of New Valine Derived Chiral Complexes of Tin(IV) and Zirconium(IV). *Spectrochimica Acta A: Mol. Biomol. Spectrosc.* 78, 45–51. doi:10.1016/j.saa.2010.06.009

Carr, H. S., Wlodkowski, T. J., and Rosenkranz, H. S. (1973). Silver Sulfadiazine: In Vitro Antibacterial Activity. *Antimicrob. Agents Chemother.* 4, 585–587. doi:10.1128/aac.4.5.585

Coats, A. W., and Redfern, J. P. (1964). Kinetic Parameters from Thermogravimetric Data. *Nature* 201, 68–69. doi:10.1038/201068a0

Comşa, Ş., Cimpean, A. M., and Raica, M. (2015). The story of MCF-7 Breast Cancer Cell Line: 40 Years of Experience in Research. *Anticancer Res.* 35, 3147–3154.

Davila, Y. A., Sancho, M. I., Almandoz, M. C., and Blanco, S. E. (2012). Structural and Spectroscopic Study of Al(III)-3-hydroxyflavone Complex: Determination of the Stability Constants in Water-Methanol Mixtures. *Spectrochim. Acta Part A: Mol. Biomol. Spectrosc.* 95, 1–7. doi:10.1016/j.saa.2012.04.034

Dennington, R., Keith, T., and Millam, J. (2016). *GaussView, Version 6*. Shawnee Mission, KS: Semichem Inc.

Deo, K., Pages, B., Ang, D., Gordon, C., and Aldrich-Wright, J. (2016). Transition Metal Intercalators as Anticancer Agents-Recent Advances. *Int. J. Mol. Sci.* 17, 1818. doi:10.3390/ijms17111818

Domagk, G. (1935). Ein beitrag zur chemotherapie der bakteriellen infektionen. *Dtsch Med. Wochenschr* 61, 250–253. doi:10.1055/s-0028-1129486

Dudev, T., and Lim, C. (2000). Tetrahedral vs Octahedral Zinc Complexes with Ligands of Biological Interest: a DFT/CDM Study. *J. Am. Chem. Soc.* 122, 11146–11153. doi:10.1021/ja0010296

El-Sonbati, A. Z., Diab, M. A., El-Bindary, A. A., Abou-Dobara, M. I., and Seyam, H. A. (2016). Molecular Docking, DNA Binding, thermal Studies and Antimicrobial Activities of Schiff Base Complexes. *J. Mol. Liquids* 218, 434–456. doi:10.1016/j.molliq.2016.02.072

Emwas, A.-H. M., Al-Talla, Z. A., Guo, X., Al-Ghamdi, S., and Al-Masri, H. T. (2013). Utilizing NMR and EPR Spectroscopy to Probe the Role of Copper in Prion Diseases. *Magn. Reson. Chem.* 51, 255–268. doi:10.1002/mrc.3936

Fox, C. L., Jr (1977). Zinc Sulfadiazine and its Use in the Treatment of burns. U.S. Patent No. 4,049,802, September 20, 1977.

Frisch, M., Trucks, G., Schlegel, H. B., Scuseria, G. E., Robb, M. A., Cheeseman, J. R., et al. (2009). *Gaussian 09, Revision D.01*. Wallingford CT: Gaussian. Inc, 201.

Garribba, E., and Micera, G. (2006). The Determination of the Geometry of Cu(II) Complexes: An EPR Spectroscopy Experiment. *J. Chem. Educ.* 83, 1229. doi:10.1021/ed083p1229

Gillespie, R. J. (1961). Bond Lengths and Bond Angles in Octahedral, Trigonal-Bipyramidal, and Related Molecules of the Non-transition Elements. *Can. J. Chem.* 39, 318–323. doi:10.1139/v61-037

Goodwin, H. A. (1976). Spin Transitions in Six-Coordinate Iron(II) Complexes. *Coord. Chem. Rev.* 18, 293–325. doi:10.1016/s0010-8545(00)80430-0

Gupta, M., Sharma, R., and Kumar, A. (2018). Docking Techniques in Pharmacology: How Much Promising? *Comput. Biol. Chem.* 76, 210–217. doi:10.1016/j.compbiolchem.2018.06.005

Gütlich, P., Jung, J., and Goodwin, H. A. (1996). "Spin Transitions in Iron(II) Complexes," in *Molecular Magnetism: From Molecular Assemblies to the Devices. NATO ASI Series (Series E: Applied Sciences)*. Editors E. Coronado, P. Delhaes, D. Gatteschi and J. S. Miller (Dordrecht: Springer), Vol. 321, 327–378. doi:10.1007/978-94-017-2319-0_13

Haque, M. A., Gandi, A. N., Mohanraman, R., Weng, Y., Davaasuren, B., Emwas, A. H., et al. (2019). A 0D Lead-Free Hybrid Crystal with Ultralow Thermal Conductivity. *Adv. Funct. Mater.* 29, 1809166. doi:10.1002/adfm.201809166

Hirata, M., Bamba, T., and Hosoda, S. (1993). The Human colon Cancer Cell Line CaCo-2 Produces Secretory Components during Enterocytic Differentiation. *Gastroenterol. Jpn.* 28, 528–534. doi:10.1007/bf02776951

Horowitz, H. H., and Metzger, G. (1963). A New Analysis of Thermogravimetric Traces. *Anal. Chem.* 35, 1464–1468. doi:10.1021/ac60203a013

House, J. E. (2013). *Inorganic Chemistry*. Amsterdam: Elsevier Inc.

Ibrahim, M. M., Ramadan, A.-M. M., El-Sheshtawy, H. S., Mohamed, M. A., Soliman, M., and I.M. Zayed, S. S. (2015). Synthesis, Characterization and Medical Efficacy (Hepatoprotective and Antioxidative) of Albendazole-Based Copper(II) Complexes - an Experimental and Theoretical Approach. *J. Coord. Chem.* 68, 4296–4313. doi:10.1080/00958972.2015.1093124

Ismail, L., Rifai, A., Ferronato, C., Fine, L., Jaber, F., and Chovelon, J.-M. (2016). Towards a Better Understanding of the Reactive Species Involved in the Photocatalytic Degradation of Sulfaclozine. *Appl. Catal. B: Environ.* 185, 88–99. doi:10.1016/j.apcatb.2015.12.008

Jana, K., Maity, T., Mahapatra, T. S., Das Mohapatra, P. K., Debnath, S. C., Das, S., et al. (2017). A Square Pyramidal Copper(II) Complex of a Schiff Base Ligand: Synthesis, crystal Structure, Antibacterial and DNA Interaction Studies. *Transit. Met. Chem.* 42, 69–78. doi:10.1007/s11243-016-0108-6

Ju, C.-C., Zhang, A.-G., Yuan, C.-L., Zhao, X.-L., and Wang, K.-Z. (2011). The Interesting DNA-Binding Properties of Three Novel Dinuclear Ru(II) Complexes with Varied Lengths of Flexible Bridges. *J. Inorg. Biochem.* 105, 435–443. doi:10.1016/j.jinorgbio.2010.12.004

Jungwirth, U., Kowol, C. R., Keppler, B. K., Hartinger, C. G., Berger, W., and Heffeter, P. (2011). Anticancer Activity of Metal Complexes: Involvement of Redox Processes. *Antioxid. Redox Signaling* 15, 1085–1127. doi:10.1089/ars.2010.3663

Khedr, A. M., and Saad, F. A. (2015). Synthesis, Structural Characterization, and Antimicrobial Efficiency of Sulfadiazine Azo-Azomethine Dyes and Their Bi-homonuclear Uranyl Complexes for Chemotherapeutic Use. *Turk J. Chem.* 39, 267–280. doi:10.3906/kim-1409-21

König, E. (1971). "The Nephelauxetic Effect Calculation and Accuracy of the Interelectronic Repulsion Parameters I. Cubic high-spin d2, d3, d7, and d8 systems," in *Structutal and Bonding*. Berlin: Springer, vol 9, 175–212.

Kozlevčar, B. (2008). Structural Analysis of a Series of Copper (II) Coordination Compounds and Correlation with Their Magnetic Properties. *Croatica Chem. Acta* 81, 369–379.

Lakshmi, S., Endo, T., and Siva, G. (2012). Electronic (Absorption) Spectra of 3d Transition Metal Complexes, in *Advanced Aspects of Spectroscopy*, 1–41. doi:10.5772/48089

Lee, Y., Jung, J.-I., Park, K.-Y., Kim, S. A., and Kim, J. (2017). Synergistic Inhibition Effect of TNIK Inhibitor KY-05009 and Receptor Tyrosine Kinase Inhibitor Dovitinib on IL-6-induced Proliferation and Wnt Signaling Pathway in Human Multiple Myeloma Cells. *Oncotarget* 8, 41091–41101. doi:10.18632/oncotarget.17056

Márquez, E., Mora, J. R., Flores-Morales, V., Insuasty, D., and Calle, L. (2020). Modeling the Antileukemia Activity of Ellipticine-Related Compounds: QSAR and Molecular Docking Study. *Molecules* 25, 24. doi:10.3390/molecules25010024

Martin, J., Alés, M., and Asuero, A. (2018). An Overview on Ligands of Therapeutically Interest. *Pharm. Pharmacol. Int. J.* 6, 198–214. doi:10.15406/ppij.2018.06.00177

Mashat, K. H., Babgi, B. A., Hussien, M. A., Nadeem Arshad, M., and Abdellattif, M. H. (2019). Synthesis, Structures, DNA-Binding and Anticancer Activities of Some Copper(I)-phosphine Complexes. *Polyhedron* 158, 164–172. doi:10.1016/j.poly.2018.10.062

Mattar, S. M., Stephens, A. D., and Emwas, A. H. (2002). Generation and Spectroscopic Characterization of the 2,3,5,6-Tetramethoxy-1,4-Benzosemiquinone Reactive Intermediate. *Chem. Phys. Lett.* 352, 39–47. doi:10.1016/s0009-2614(01)01415-4

MOE (The Molecular Operating Environment) (2015). Software Available from Chemical Computing Group Inc. Montreal: 1010 Sherbrooke Street West, Suite 910.Canada H3A 2R7. Available at: https://www.chemcomp.com/Products.htm (Accessed May 1, 2020).

Navarro, M., Vásquez, F., Sánchez-Delgado, R. A., Pérez, H., Sinou, V., and Schrével, J. (2004). Toward a Novel Metal-Based Chemotherapy against Tropical Diseases. 7. Synthesis and In Vitro Antimalarial Activity of New Gold−Chloroquine Complexes. *J. Med. Chem.* 47, 5204–5209. doi:10.1021/jm049792o

Panhwar, Q. K., and Memon, S. (2012). Synthesis and Properties of Zirconium(IV) and Molybdate(II) Morin Complexes. *J. Coord. Chem.* 65, 1130–1143. doi:10.1080/00958972.2012.668617

Radha, S., KKl, M., and Thamaraichelvan, A. (2016). Elangovana. Synthesis, Characterization and Biological Studies of Sulfadiazine Drug Based Transition Metal Complexes. *J. Chem. Pharm. Res.* 8, 202–211.

Rahmouni, N. T., Houda Bensiradj, N. E., Megatli, S. A., Djebbar, S., and Baitich, O. B. (2019). New Mixed Amino Acids Complexes of Iron (III) and Zinc (II) with Isonitrosoacetophenone: Synthesis, Spectral Characterization, DFT Study and Anticancer Activity. *Spectrochim. Acta Part A: Mol. Biomol. Spectrosc.* 213, 235–248. doi:10.1016/j.saa.2019.01.042

Ramírez-Delgado, V., Osorio-Monreal, G., Hernández-Ayala, L. F., Reyes-Vidal, Y., García-Ramos, J. C., Ruiz-Azuara, L., et al. (2015). Electrochemical Behavior of Ni (II) Complexes with N2S2 and N6 Ligands as Potential Catalysts in Hydrogen Evolution Reaction. *J. Mexican Chem. Soc.* 59, 294–301.

Rani, S., Ajeet, A., and Kumar, A. (2014). Designing of Sulfanilamide/sulfacetamide Derivatives as Human Topoisomerase II Inhibitor: a Docking Approach. *Ajps* 2, 42–46. doi:10.12691/ajps-2-2-3

Refat, M. S., Sharshar, T., Elsabawy, K. M., El-Sayed, M. Y., and Adam, A. M. A. (2016). Synthesis, Physicochemical Characterization and Anticancer Screening of Sulfa Drug Ruthenium Complexes as Anticancer Agent. *J. Mol. Liquids* 222, 334–349. doi:10.1016/j.molliq.2016.07.006

Roberts, J. R., Xiao, J., Schliesman, B., Parsons, D. J., and Shaw, C. F. (1996). Kinetics and Mechanism of the Reaction between Serum Albumin and Auranofin (And its Isopropyl Analogue)In Vitro. *Inorg. Chem.* 35, 424–433. doi:10.1021/ic9414280

Rocha, M., Piro, O. E., Echeverría, G. A., Pastoriza, A. C., Sgariglia, M. A., Soberón, J. R., et al. (2019). Co(II), Ni(II) and Cu(II) Ternary Complexes with Sulfadiazine and Dimethylformamide: Synthesis, Spectroscopic Characterization, Crystallographic Study and Antibacterial Activity. *J. Mol. Struct.* 1176, 605–613. doi:10.1016/j.molstruc.2018.09.008

Rosita, A. S., and Begum, T. N. (2020). Molecular Docking Analysis of the TNIK Receptor Protein with a Potential Inhibitor from the NPACT Database. *Bioinformation* 16, 387–392. doi:10.6026/97320630016387

Sabolová, D., Kožurková, M., Plichta, T., Ondrušová, Z., Hudecová, D., Šimkovič, M., et al. (2011). Interaction of a Copper(II)-Schiff Base Complexes with Calf Thymus DNA and Their Antimicrobial Activity. *Int. J. Biol. Macromol.* 48, 319–325. doi:10.1016/j.ijbiomac.2010.12.001

Samsonowicz, M., and Regulska, E. (2017). Spectroscopic Study of Molecular Structure, Antioxidant Activity and Biological Effects of Metal Hydroxyflavonol Complexes. *Spectrochim. Acta Part A: Mol. Biomol. Spectrosc.* 173, 757–771. doi:10.1016/j.saa.2016.10.031

Santini, C., Pellei, M., Gandin, V., Porchia, M., Tisato, F., and Marzano, C. (2013). Advances in Copper Complexes as Anticancer Agents. *Chem. Rev.* 114, 815–862. doi:10.1021/cr400135x

Şentepe, I., and Eraslan, G. (2010). Pharmacokinetic of Sulfaclozine in Broiler Chickens. *Food Chem. Toxicol.* 48, 448–451. doi:10.1016/j.fct.2009.10.044

Shahabadi, N., Hakimi, M., Morovati, T., and Fatahi, N. (2017). DNA Binding Affinity of a Macrocyclic Copper(II) Complex: Spectroscopic and Molecular Docking Studies. *Nucleosides, Nucleotides and Nucleic Acids* 36, 497–510. doi:10.1080/15257770.2017.1332370

Sharfalddina, A. A., Davaasurenb, B., Emwasb, A-H., Jaremkoc, M., Jaremko, Ł., and Hussien, M. A. (2020a). Single crystal, Hirshfeld Surface and Theoretical Analysis of Methyl 4-Hydroxybenzoate, a Common Cosmetics, Drugs and Foods Preservative – Experiment versus Theory. *PLoS One* 15, e0239200. doi:10.1371/journal.pone.0239200

Sharfalddina, A. A., Emwasb, A-H., Jaremkoc, M., and Hussien, M. A. (2020b). Transition Metal Complexes of 6-Mercaptopurine; Characterization, DFT Calculation, DNA Binding, Molecular Docking, and Anticancer Activity. *Appl. Organomet. Chem.* 35 (1), e6041. doi:10.1002/aoc.6041

Sirajuddin, M., Ali, S., and Badshah, A. (2013). Drug-DNA Interactions and Their Study by UV-Visible, Fluorescence Spectroscopies and Cyclic Voltametry. *J. Photochem. Photobiol. B: Biol.* 124, 1–19. doi:10.1016/j.jphotobiol.2013.03.013

Sirajuddin, M., Ali, S., Haider, A., Shah, N. A., Shah, A., and Khan, M. R. (2012). Synthesis, Characterization, Biological Screenings and Interaction with Calf Thymus DNA as Well as Electrochemical Studies of Adducts Formed by Azomethine [2-((3,5-dimethylphenylimino)methyl)phenol] and Organotin(IV) Chlorides. *Polyhedron* 40, 19–31. doi:10.1016/j.poly.2012.03.048

Slade, R., Tomlinson, A., Hathaway, B., and Billing, D. (1968). The Electronic Properties of Trigonal Bipyramidal Complexes of the Copper (II) Ion. *J. Chem. Soc. A: Inorg., Phys., Theor.* 61–63.

Stober, H., and DeWitte, W. (1982). Sulfadiazine. *Anal. Profiles Drug Subst.*, 523–551. doi:10.1016/s0099-5428(08)60274-9

Sweeney, E. E., McDaniel, R. E., Maximov, P. Y., Fan, P., and Jordan, V. C. (2012). Models and Mechanisms of Acquired Antihormone Resistance in Breast Cancer: Significant Clinical Progress Despite Limitations. *Horm. Mol. Biol. Clin. Invest.* 9, 143–163. doi:10.1515/hmbci-2011-0004

Tabassum, S., Zaki, M., Ahmad, M., Afzal, M., Srivastav, S., Srikrishna, S., et al. (2014). Synthesis and crystal Structure Determination of Copper(II)-complex: In Vitro DNA and HSA Binding, pBR322 Plasmid Cleavage, Cell Imaging and Cytotoxic Studies. *Eur. J. Med. Chem.* 83, 141–154. doi:10.1016/j.ejmech.2014.06.018

Vahdati, R. F., Housaindokht, M. R., Jalal, R., Eshtiagh, H. H., Verdian, D. A., and Sadeghi, G. S. (2014). Spectroscopic and Molecular Modeling Based Approaches to Study on the Binding Behavior of DNA with a Copper (II) Complex. *J. Fluoresc* 24, 1225–1234. doi:10.1007/s10895-014-1405-0

Van de Loosdrecht, A. A., Beelen, R. H. J., Ossenkoppele, G. J., Broekhoven, M. G., and Langenhuijsen, M. M. A. C. (1994). Ossenkoppele G, Broekhoven M and Langenhuijsen MA Tetrazolium-Based Colorimetric MTT Assay to Quantitate Human Monocyte Mediated Cytotoxicity against Leukemic Cells from Cell Lines and Patients with Acute Myeloid Leukemia. *J. Immunol. Methods* 174, 311–320. doi:10.1016/0022-1759(94)90034-5

Wong, E., and Giandomenico, C. M. (1999). Current Status of Platinum-Based Antitumor Drugs. *Chem. Rev.* 99, 2451–2466. doi:10.1021/cr980420v

Yang, X.-L., Liu, J., Yang, L., and Zhang, X.-Y. (2005). Synthesis, Characterization, and Susceptibility of Bacteria of Selenium Dioxide Complexes with Sulfadrugs. *Synth. Reactivity Inorg. Metal-Organic, Nano-Metal Chem.* 35, 761–766. doi:10.1080/15533170500359620

Zagouri, F., Sergentanis, T. N., Chrysikos, D., Papadimitriou, C. A., Dimopoulos, M.-A., and Psaltopoulou, T. (2013). Hsp90 Inhibitors in Breast Cancer: a Systematic Review. *The Breast* 22, 569–578. doi:10.1016/j.breast.2013.06.003

Zehra, S., Roisnel, T., and Arjmand, F. (2019). Enantiomeric Amino Acid Schiff Base Copper(II) Complexes as a New Class of RNA-Targeted Metallo-Intercalators: Single X-ray Crystal Structural Details, Comparative In Vitro DNA/RNA Binding Profile, Cleavage, and Cytotoxicity. *ACS Omega* 4, 7691–7705. doi:10.1021/acsomega.9b00131

Zeng, Y.-B., Zhu, S.-H., Dong, H., Han, H.-Y., Jiang, L.-L., Wang, Q., et al. (2012). Great Efficacy of Sulfachloropyrazine-Sodium against Acute Murine Toxoplasmosis. *Asian Pac. J. Trop. Biomed.* 2, 70–75. doi:10.1016/s2221-1691(11)60193-7

Zhao, Z., Zhou, X., Zhang, W., and Zhao, W. (1992). *Textbook of Instrument Analyses.* Beijing: Higher Education Press.

Factorial Investigation of Cobalt Retention by Ti and Fe Oxides-Modified Carbon Nanotubes: Multivariate Against Univariate Analysis

Ismail Fasfous[1]*, Amjad El-Sheikh[1], Anas Awwad[1], Yahya Al-Degs[1], Ebaa Fayyoumi[2] and Jamal Dawoud[1]

[1]Department of Chemistry, Faculty of Science, The Hashemite University, Zarqa, Jordan, [2]Department of Computer Science, Faculty of Prince Al-Hussein Bin Abdullah II for Information Technology, The Hashemite University, Zarqa, Jordan

Fe/Ti-oxides-modified-carbon nanotubes CNTs nanocomposites were prepared and tested toward Co removal from solution under different operational conditions. The final performance of the nanocomposites for Co was highly dependent on the type and loaded amount of the oxides. The nanocomposites were characterized by standard methods and the results evidenced that the presence of CNTs hampers the growth of Fe_3O_4 and TiO_2 particles and forming smaller nano-particles leading to better Co removal from solution. Analysis of isotherms at different temperatures indicated that Co retention was two-fold increased upon adding Ti-oxides up to 90.2%. All isotherms were fairly presented using Langmuir-Freundlich isotherm and most surfaces have high heterogeneity particularly after deposition of oxides. The combined influence of the factors was investigated by running a multivariate analysis. An empirical equation was generated by principal component analysis (PCA) for predicting Co retention assuming different relationships and the binary-interaction behavior between factors was the most dominant: Co retention (mg/g) = 5.12 + 1.25Conc + 1.47Temp – 1.38CNT% – 6.03Ti% – 5.03Fe% – 0.01Conc^2 + 0.12Temp^2 – 0.55CNT%^{2} – 1.53Ti%^{2} – 3.44Fe%^{2} + 0.17Conc × Temp + 0.07Conc × CNT% + 0.07Conc × Ti% + 0.10Conc × Fe% + 0.21Temp × CNT% + 0.10Temp × Ti% + 0.17Temp × Fe% – 1.67CNT% × Ti% – 1.45CNT% × Fe% – 4.11Ti% × Fe%. The most dominant factors on Co retention were temperature and concentration (positive linear correlation) and the positive interaction between temperature/concentration and temperature/CNTs mass. PCA indicated that the coefficient Temp × CNTs (+0.21) was higher than Temp × Ti% (+0.10). The negative coefficients of Ti/Fe with CNTs (1.45–4.11) indicated better Co retention at higher Ti/Fe loads and lower mass of CNTs. The results support that fact that incorporation of CNTs with Ti/Fe oxides may have a positive synergic impact on Co retention.

Keywords: multivariate calibration, carbon nanotubes, adsorption, iron oxide, titanium oxide, cobalt

INTRODUCTION

Pollution of water resources with heavy metals is of high environmental concern due to their acute and chronic toxicity (Ikehata et al., 2015). Cobalt is an essential micronutrient, constituent of vitamin B_{12}, and is also needed for the production of red blood cells (Steven et al., 2000; Simonsen et al., 2012). However, excess intake of cobalt can lead to unwanted health consequences (Simonsen et al., 2012). Therefore, it is necessary to remove Co(II) from ground and surface waters for public health and a clean environment.

Due to their unique properties and applications, carbon nanotubes CNTs and metal oxides modified forms have gained considerable attention (Iijima, 1991; Gao et al., 2009; Gupta and Saleh, 2011; Al-Degs et al., 2012; Li et al., 2013; Mallakpour and Khadem 2016). Much attention is given to CNTs coupled with magnetic iron oxide (i.e., Fe_3O_4) nanoparticles to tackle environmental problems due to direct separation and recyclability (Mallakpour and Khadem, 2016), easiness of preparation, and minimal environmental impact and specific affinity (Sadegh et al., 2017). Hu et al. (Hu et al., 2010) have prepared ß-cyclodextrin-modified-CNTs and Fe-oxides-CNTs and the surfaces were tested toward Pb (II) and 1-naphthol. Better retention for pollutants was reported upon adding cyclodextrin to Fe-oxides/CNTs, which attributed to the favorable interaction between hydroxyl groups and hydrophobic cavity of ß-cyclodextrin with Pb (II) and 1-naphthol. In the same line, Hamza et al. (Asmaly et al., 2015) have loaded Fe_2O_3 on CNTs fibers following simple impregnation methodology and the final surface was tested toward phenol. The better uptake upon loading Fe-oxides was attributed to nanoparticles of the oxide.

There are two strategies for handling multifactor processes like Co retention, univariate and multivariate analyses (Brereton, 2004). Univariate analysis is often adopted where retention of the solute is monitored as a function of a certain factor (pH for example) while controlling other factors. Following univariate analysis, adsorption isotherms (concentration variations) and thermodynamics (temperature variations) were well reported for many systems. However, multivariate analysis is less tedious as the influence of all factors on the target response is manipulated in little but organized experimental design. Compared with univariate analysis, the interaction between factors and nonlinear behavior of factors on solute retention (response) would be uncovered by the application of multivariate analysis (Brereton, 2004; Al-Degs et al., 2012).

The literature encompasses many studies on CNTs/TiO_2 composites focused on characterization and other chemical properties (Gao et al., 2009; Zhao et al., 2013) and only a few studies on metals uptake. Although CNTs and Fe-oxides-CNTs have been studied for many metals retention, an in-depth study of Co(II) retention by CNTs and oxides-modified-CNTs is still not available. Herein, synthesis of different nanocomposites of CNTs and Fe_3O_4 or TiO_2 and testing their affinity for Co is the principal goal of this research work. Emphasis will be placed on the potential influence of deposited oxides on Co retention. Co adsorption by modified adsorbents and at different operational conditions will be investigated to pick up the best composite for further testing. The combined influence of some significant factors, including Co content, temperature, and amount of loaded Fe and Ti oxides on Co retention from solution, will be modeled using multivariate analysis to uncover the interaction between factors.

MATERIALS AND METHODS

Materials

Carbon nanotubes were purchased from Shenzhen Nanotech port Co. Ltd, Shenzhen, China. They are in the form of multiwalled carbon nanotubes CNTs with dimensions of 5–15 µm length and 10–30 nm external diameter. Cobalt (II) chloride hexahydrate (GCC, United Kingdom), Iron (II) chloride tetrahydrate (BDH, England), Iron (III) chloride hexahydrate (Scharlau, Spain), Titanium (IV) isopropoxide (Sigma Aldrich, United States) were used. All chemicals used were analytical grade unless stated otherwise. Triply distilled water was used to prepare all solutions.

## Synthesis of Fe/Ti-Oxides-CNTs Nanocomposites

In brief, as-received CNTs were refluxed in a 12.0 M HNO_3 solution for 6.0 h. After cooling, the oxidized CNTs were recovered by filtration, rinsed with enough distilled water to have a neutral filtrate pH, and then dried overnight at 110°C. the acid-treated substrate was abbreviated as O-CNTs. Chemical co-precipitation (Lee et al., 2010) and sol-gel (Gao, Chen et al., 2009) methods were used to prepare CNTs/Fe_3O_4 and CNTs/TiO_2 nanocomposites, respectively. In all preparations, O-CNTs was used due to its better reactivity. For Fe-CNTs, 0.90 g of $FeCl_3.6H_2O$/$FeCl_2.4H_2O$ (1:3.5, w/w) mixture was added to 0.50 g of O-CNTs in 800 ml distilled water with sonication for 2.0 h. The suspension solution was transferred into a three-neck round-bottom flask and stirred under the purge of nitrogen gas. 10 ml of 7.0 M NH_4OH solution was added to the suspension and kept stirring for 30 min to yield a black colloidal solution. The colloidal solution was then filtered through 0.45 µm micropore membranes, washed with water several times, dried at 100°C for 2.0 h, and labeled as Fe-CNTs (31.8% Fe-oxide). The same procedure was repeated to prepare Fe-CNTs (48.2% Fe-oxide) and Fe-CNTs (18.9% Fe-oxide) composites. All samples were then calcined at 440°C for 4.0 h to get crystalline iron oxide in the nanocomposites as confirmed by XRD. All samples were ground into a powder and stored in a desiccator until used. A control sample was prepared as outlined earlier but in the absence of the substrate and labeled as Fe_3O_4. For Ti-CNTs nanocomposites, 0.10 g of O-CNTs was dispersed into a 30 ml of isopropanol/water (1:10, v/v) solution under sonication for 2.0 h. A 21.4 ml of titanium isopropoxide/isopropanol (1:5.27, v/v) was added dropwise into the suspension under stirring. After 2 h, the solid precipitate was then filtered, washed with ethanol/water (2:1, v/v) solution several times, dried at 100°C for 1.5 h, and labeled as Ti-CNTs (90.2% Ti-oxides). The same procedure was repeated using different levels of Ti concentration to prepare the following composites Ti-CNTs (87.4% Ti-oxides), Ti-TiO_2 (82.1% Ti-oxides), Ti-CNTs (69.6% Ti-oxides), respectively. The samples were then calcined, ground, and stored as

described earlier. A control sample was also prepared but in the absence of O-CNTs and labeled as TiO_2. In summary, eleven solid adsorbents were prepared to test Co removal from solution under different operational conditions.

The mass ratio Fe-CNTs was calculated based on the measured mass of O-CNTs and the theoretical yield of Fe_3O_4 upon mixing $FeCl_3.6H_2O$ with $FeCl_2.4H_2O$ in the basic medium (ammonium hydroxide) as shown in chemical equation. The stoichiometric ratio is 2:1 (Fe^{3+}/Fe^{2+}).

$$2Fe^{3+} + Fe^{2+} + 8OH^- \rightarrow Fe_3O_4 + 4H_2O \quad (1)$$
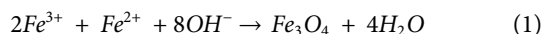
While the mass ratio Ti-CNTs was calculated based on the theoretical yield of TiO_2 upon reaction titanium isopropoxide with water to deposit TiO_2 as shown in reaction below

$$Ti(OCH(CH_3)_2)_4 + 2\,H_2O \rightarrow TiO_2 + 4(CH_3)_2CHOH \quad (2)$$
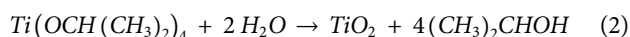
Characterization of Nanocomposites and Determination of Cobalt

Specific surface area (SSA) and surface functional groups were measured following standard procedures as described elsewhere (El-Sheikh, 2008). Fourier transform infrared spectra (FTIR) of samples in a range of 4,000–400 cm^{-1} were recorded using a Bruker vertex-70 spectrometer (Ettlingen, Germany). The quantitative determination of Co was performed by using flame atomic absorption spectrometer (iCE 3000 series, Thermo Scientific, United States) under the following instrumental conditions: λ = 240.7 nm, Lamp current = 75 mA, Slit width = 0.2 nm, Burner height = 7 mm, Acetylene flow = 1 L min^{-1}, Airflow = 10 L min^{-1}. Identification of deposited oxides was carried out using powder X-ray diffraction [X-ray diffractometer (XRD-6000), Shimadzu, Japan] XRD-6000. BARNSTEAD/Thermolyne furnace (Barnstead International, United States) operated up to 1,200°C was used to anneal the composites under inert atmosphere.

Adsorption Isotherms

In the current study, effects of concentration, temperature, and amount of loaded oxides on Co retention were investigated while keeping pH, mass of adsorbent, and contact time at specified levels. Concentration-variation isotherms were carried out as described elsewhere (Al-Degs et al., 2012). Briefly, A 5.0 mg (±0.0001 g) of dried nano-adsorbent was contacted with 10.0 ml solution containing various concentrations of cobalt (1, 2, 3, 4, 5, 7.5, 10, 15, 20, 25, 30, 35 and 40 mg/L) in 30 ml screw caps vials to prevent solvent vaporization. The vials were agitated in a water bath shaker for 24.0 h. The equilibrium time (24.0 h) was measured from separate kinetic runs, which was found reasonable for all adsorbents. After completion of thermostat shaking (±1°C), mixtures were left to settle for another 1 h at the selected temperature to get a clean suspension solution. Then, a 3.0 ml of clean supernatant was withdrawn for Co quantification bythe flame atomic absorption spectrometer. Co removal by all adsorbents was carried out at pH 6.4 (±0.2) to avoid serious precipitation with OH^- ions and prevent possible leaching of Fe or Ti ions from the modified

surface in the solution which would limit the practical application the surfaces (Oliveira et al., 2002). Adsorption isotherm was measured at three temperatures (30.0, 40.0, and 50.0°C) to study the thermodynamic of the process. To ensure the reliability of the data, blank samples were prepared (without adding nano-adsorbent) and handled in parallel for each test. The pH experiments were performed in the same procedure described above at a cobalt concentration of 20 mg/L and temperature of 30 ± 1°C. In summary, 33 isotherms were measured to study the effect of concentration, temperature, and loaded oxides on Co removal.

Modeling Co Retention from Solution: Isothermal and Thermodynamic Behaviors

The amount of Co adsorbed q_e (mg/g) was estimated from equilibrium concentration in solution C_e (mg/L) as following:

$$q_e = \frac{(C_o - C_e)V}{m} \quad (3)$$

Where C_o, V, and m stand for initial concentration of C_o (mg/L), volume of solution (ml), and m is the mass of adsorbent (g). For more validation of the proposed procedure, certain isotherms were repeated and a relative error of 2–5% was reported indicating the acceptable repeatability of the procedure. Five isotherms were used to represent equilibrium data points including Langmuir (Allen et al., 2004), Freundlich (Freundlich, 1906), Langmuir-Freundlich (Jeppu and Clement, 2012), Temkin (Temkin and Pyzhev, 1940), and Dubinin-Radushkevich (El-Sheikh et al., 2011). The parameters of the models were estimated following nonlinear regression analysis using Origin lab 8$^®$ computer program. Modeling of isotherms and estimation of thermodynamic parameters are outlined in **Supplementary Material**.

Multivariate Analysis of Co Retention From Solution: Combined Influence of Factors

Unlike univariate analysis (Section *Modeling Co Retention From Solution: Isothermal and Thermodynamic Behaviors*), multivariate analysis can handle large size of adsorption data to uncover the interaction between factors. Adsorption of Co was tested using 11 adsorbents while changing five factors with a total of 429 tests.

As a multifactor process, Co retention by all tested adsorbents and at different factors would be presented by the empirical equation:

$$\begin{aligned} Co\ retention\ (mg/g) = {} & b_0 + b_1 Conc + b_2 Temp + b_3 CNT\% \\ & + b_4 Ti\% + b_5 Fe\% + b_{11} Conc^2 \\ & + b_{22} Temp^2 + b_{33} CNT\%^2 + b_{44} Ti\%^2 \\ & + b_{55} Fe\%^2 + b_{12} Conc \times Temp + b_{13} Conc \\ & \times CNT\% + b_{14} Conc \times Ti\% + b_{15} Conc \\ & \times Fe\% + b_{23} Temp \times CNT\% + b_{24} Temp \\ & \times Ti\% + b_{25} Temp \times Fe\% + b_{34} CNT\% \\ & \times Ti\% + b_{35} CNT\% \times Fe\% + b_{45} Ti\% \\ & \times Fe\% \end{aligned}$$

$$(4)$$

Where b_0, (b_1–b_5), (b_{11}–b_{55}), and (b_{12}–b_{45}) represented the intercept, coefficients of linear terms, coefficients of quadratic (non-linear) terms, and interaction terms, respectively. As indicated in **Eq. 4**, modeling Co retention while changing other factors is a complex process as linear, quadratic, and interaction terms are included to handle the process. Linear terms assign the factor(s) that are linearly dependent on Co retention regardless of the variations in the levels of other factors. The quadratic terms are also necessary to account for nonlinear behavior that may involve in the process, for example, retention of Co by Ti-CNTs may not be linearly correlated with loaded amounts (i.e, non-linear correlation). Interaction terms are also necessary to account for any synergetic influence among factors, for example, better Co removal would achieve when the surface is highly loaded with Ti-oxides but at high temperature. The experimental design was placed in matrix **C** while the dependent factor (Co retention values) was placed in vector q to build the following equation (Brereton, 2004):

$$q = Cb \qquad (5)$$

The dimensions of q, C, and b were 429 × 1, 429 × 22, and 22 × 1, respectively (429 tests and 22 coefficients related to the significance of factors on the process). Using PCA, matrix C was decomposed into smaller matrices which were then used to find b and build the model the complex of the relationship between C and q and finally to find the coefficients of **Eq. 4** (Brereton, 2004). Initially, **Eq. 4** was solved by including linear terms only (b_1-b_5 besides intercept b_0). In the next step, the model was created by adding quadratic terms and finally by adding interaction terms. The best model was the one that accurately predicts Co-retention from the experimental design. PCA was carried out using home-made codes based on the algorithm outlined in the literature (Brereton, 2004). The quality of fit for models was estimated by finding relative error of prediction (Brereton, 2004):

$$REP\% = 100 \times \left(\frac{\sum_{i=1}^{m} \left(q_{i,pred} - q_{i,measur} \right)^2}{\sum_{i=1}^{m} \left(q_{i,measur} \right)^2} \right)^{1/2} \qquad (6)$$

Where q_{measur}, q_{prd}, and m, are the measured Co retention value (mg/g), the predicted Co retention value (mg/g) by PCA, and the number of tests, respectively. Before running PCA, the levels of factors were properly coded to get a uniform significance of all factors on Co retention and to end up with an accurate estimation of the coefficients (Brereton, 2004). Retention values were (429 data) were also mean-centered prior to PCA.

RESULTS AND DISCUSSION

Physicochemical Properties of CNTs and Modified Forms

For a better assessment of the surfaces, detailed characterization tests were carried out which was necessary to evaluate the nature of interaction with cobalt in solution. **Table 1** summarizes the main physicochemical parameters along with Co retention for each adsorbent.

Upon oxidation, the contents of acidic groups were increased, and the maximum increase was seen in phenolic content. For O-CNTs, the role of acidic groups for Co retention was not significant as only 5% of the carboxylic groups would involve in the process assuming 1:1 complexation with Co^{2+} ions. In fact adding Fe and Ti to CNTs has ended up with selective surfaces able to attract more Co ions. The involvement of functional groups for attracting the particles Ti and Fe oxides was highly possible as supported by the lower contents of functional groups with loaded oxides (Chiang et al., 2011; Martínez et al., 2011). For Fe-CNTs, the load of Fe% was increased up to 48.2% leading to a reduction of 50% in original acidity while the content of basic groups was increased from 1.88 to 2.82 mmol/g. In fact, the large reduction in acidity upon Fe deposition may support the selective interaction between ionisable carboxylic groups with the particles of Fe_3O_4. The same behavior seems to be repeated with TiO_2 particles where a mix of 90.2% Ti resulting in a 70% reduction in the acidity while total basicity was unchanged.

All surfaces exhibited a lower surface area against O-CNTs due to the accumulation of oxides and blocking the micropores, filling up the gaps between CNTs and clogging nanotube openings, thereby reducing the nanocomposite surface area as theorized elsewhere (Gao et al., 2009; Lio et al., 2011). Interestingly, pure Fe and Ti oxides have a modest affinity which supported the fact that spreading both oxides particles (especially TiO_2) over CNTs has improved Co. Heterogeneity index (**Table 1**), indicated a better homogeneity of modified surfaces. Ti-oxide has generated better surfaces for Co with maximum retention of 29.80 mg/g at loadings of 90.2%. On the other hand, more Fe-oxide was loaded (48.2%) to reach Co retention of 20.32 mg/g.

The adsorption capacity of Ti-CNTs (90.2%) was notably higher than other adsorbents reported in the literature. Retention values of 8.84, 8.78, 16.26, 72.43 mg/g were reported for iron oxide-MWCNTs (Wang et al., 2011), polyacrylic-MWCNTs (Chen et al., 2012), hydroxyapatite-MWCNTs (Liu et al., 2013), and β-cyclodextrin-graphene oxide (Song et al., 2013), respectively.

IR Measurement and XRD Pattern of the Active Composites

IR analysis was made to most effective surfaces as shown in **Figure 1**.

Two IR bands appeared in CNTs which positioned at 3,420 and 1,624 cm^{-1} and mainly attributed to aromatic phenolic and carboxylic surface groups. Upon oxidation, the earlier bands were increased indicating a more acidic surface. The short band that appeared at 2,921 cm^{-1} was attributed to vibrations of -OH in a carboxylic acid. In general, the spectra of oxides-modified-CNTs exhibited a decrease in the intensity of absorption peaks over 1,630–1,780 cm^{-1} and 3,200–3,550 cm^{-1} against the original substrate which obviously reflected the special linkage between particles of oxides with carboxylic/phenolic surface groups. The IR spectra of Ti-CNTs showed a low intensity of 1,113 cm^{-1}, which was assigned to the Ti-O-C bond (Wang et al., 2011). For

TABLE 1 | Physicochemical parameters of tested absorbents along with maximum affinities toward Co retention from solution.

| Nanocomposites[a]	CNTs%[b]	Fe%[b]	Ti%[b]	SSA[c] m²/g	Saturation value (mg/g)[d]	Heterogeneity index[e]	Functionality[e] (mmol/g)		
							a	b	c
CNTs	100	—	—	193.19	13.86	1.13	4.70	3.92	1.96
O-CNTs	100	—	—	207.28	15.27	0.75	1.88	9.80	4.90
TiO₂	—	—	100%	122.12	10.42	0.66			
Ti-CNTs (69.6%)	30.4	—	69.6	189.13	16.56	2.14	3.76	5.88	3.92
Ti-CNTs (82.1%)	17.9	—	82.1	179.31	21.43	1.02	2.82	4.90	1.96
Ti-CNTs (87.4%)	12.6	—	87.4	171.16	24.63	1.18	2.82	3.92	1.96
Ti-CNTs (90.2%)	9.8	—	90.2	168.61	29.80	1.71	1.88	2.94	0.98
Fe₃O₄	—	100	—	129.10	7.68	0.88			
Fe-CNTs (18.9%)	81.1	18.9	—	185.19	13.30	1.10	3.76	6.86	3.92
Fe-CNTs (31.8%)	68.2	31.8	—	179.31	21.16	1.88	3.76	5.88	2.94
Fe-CNTs (48.2%)	51.8	48.2	—	176.51	20.32	1.62	2.82	4.90	1.96

[a]Values between brackets indicated the ratios the nano-materials in the final mix.

[b]Percentages were calculated based on limiting reactant of the reagents involved in synthesis of Fe₃O₄ and TiO₂.

[c]SSA is determined using methylene adsorption method.

[d]Both saturation values and heterogeneity indices were estimated from Langmuir-Freundlich isotherm equation measured at 50°C, 5 mg adsorbent, Co range 1–40 mg/L, pH 6.4, and shaking time 24 h.

[e]Based on Bohem's method, a total basic group (mainly ketonics and amines), b total acidic groups (mainly alcoholic, phenolic and carboxylic acid groups) and c carboxylic acid group.
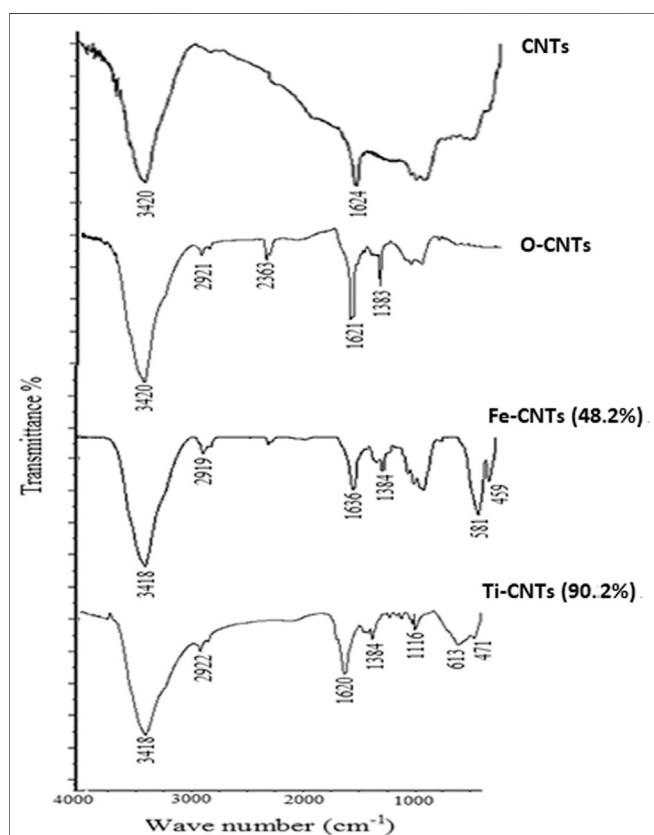
FIGURE 1 | IR spectra of oxides-loaded-CNTs beside original substrates.

Fe-CNTs, the sharp two peaks that appeared at 581 and 459 cm^{-1} were evidenced by the vibrations of the Fe-O bond [26]. On other hand, the intensity of absorption peaks at 400–700 cm^{-1} were increased upon adding more oxides.

Identification of both oxides was further studied by XRD. **Figure 2** shows XRD patterns of main samples.

As indicated in **Figure 2**, the characteristic peaks of O-CNTs were seen at 2θ 26.04 and 42.80° which are assigned to (002) (100) planes of reflection, respectively (Chen et al., 2011). Upon loading Fe-oxides, the following peaks of variable intensities were observed: 26.12, 30.20, 35.64, 42.96, 53.96, 57.20, and 62.84°. The intrinsic XRD peaks of O-CNTs still detected even after loading large amounts of the oxide. The other diffraction peaks are consistent with the JCPD standard XRD patterns for magnetite Fe₃O₄ with cubic crystal system (Wang et al., 2011) (89–3,854, 2θ = 30.088, 35.439, 43.07, 53.432, 56.958, 62.546°), and gamma hematite (γ-Fe₂O₃) (89–5,892, 2θ = 30.266, 35.651, 43.332, 53.766, 57.319, 62.949°). However, the XRD pattern of iron oxide (not provided) alone cannot distinguish between hematite and magnetite phases where both have practically indistinguishable patterns (Sun et al., 2005; Wang et al., 2011). It should realize that the peak intensities of O-CNTs decrease after combining with Fe₃O₄ nanoparticles. For TiO₂, many sharp peaks were centered at: 25.46, 37.88, 48.16, 53.96, 55.06, 62.8, 68.8, 70.34, and 75.08°. The strong peaks were seen at 25.46 and 48.16° supporting the formation of anatasephase (Lu et al., 2013; Zhang et al., 2015). The XRD pattern of CNTs loaded with TiO₂ indicating the following peaks at 2θ: 26.14, 37.62, 42.66, 48.00, 53.92, 62.58, and 69.86°. As was the case in CNTs-Fe, the characteristic peaks of the substrate are still seen, however, the main anatase peak (25.46°) may overlap with the intense peak of O-CNTs (26.04o). The average crystallite size was estimated from the corresponding intensive diffraction peak using Scherrer's equation (Scherrer, 1918): $d = \frac{K.\lambda}{\beta \cos \theta}$, where ß is the full width at half maximum intensity in radians, θ is the diffraction angle of the XRD peak in degrees, and K is the Scherrer's constant (0.91) (Liu et al., 2013). The results indicated that all adsorbents were in nano-size with diameter of 5.64, 6.33, and 7.32 nm for O-CNTs, Fe-CNTs, and Ti-CNTs, respectively. As indicated from the diameters, deposition of oxides has increased the diameter of
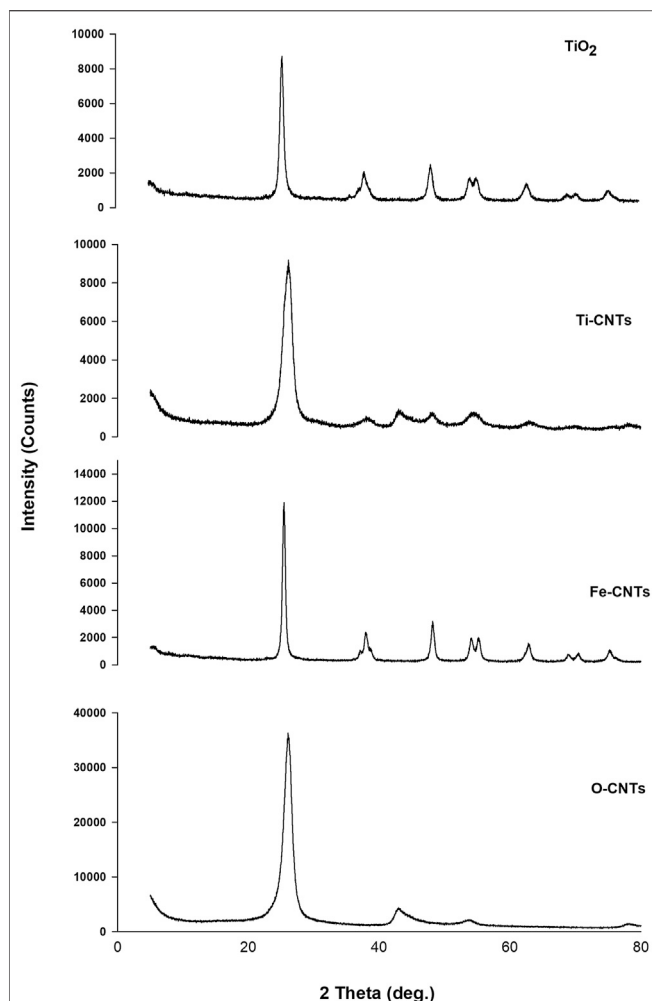
FIGURE 2 | XRD of some main oxides-modified-CNTs surfaces and O-CNTs.

the original substrate, however, it remains in the nano-range (1–100 nm). Due to the intense overlap between the O-CNTs (26.04°) and TiO_2 (25.46°), the average crystallite size of the Ti-CNTs was then calculated based on the peak at position 48.16°, which has negligible interference the substrate. The results showed that the average crystallite size of the composites was less than that of pure TiO_2 (average diameter 16.5 nm) indicating that the presence of CNTs in the nanocomposites hinders the particle growth and leads to a smaller TiO_2 nanocrystallite size (Gao et al., 2009; Li et al., 2011; Wang et al., 2011).

Adsorption Isotherms: Isothermal and Thermodynamic Behavior
pH and Optimum Co Retention
Initial studies indicated that pH has a significant influence on Co removal and this was noticed for all surfaces. For better comparison, all isotherms were carried out at certain pH.

Figure 3 shows the removal behavior of Co over the pH range (2.0–12.0).

The removal of cobalt (%) increases slowly at pH ≤ 4.0, then quickly at pH 6.0–10.0, sustains a steady or slight increase at pH ≥ 10.0. At low pH (<4.0), both cobalt species and the surface of the nanocomposite are positively charged, which explains the low removal efficiency of the nanocomposite. Over the range of 4.0–9.0, the surface of the nanocomposite becomes more negatively charged depending on the functional groups being ionized, and the electrostatic interaction between cobalt ions and nanocomposite surface increases, leading to more adsorption. At pH > 9, retention is mainly governed by precipitation in the form of cobalt hydroxide as theorized elsewhere (Wang et al., 2011; Hongqin et al., 2012; Li et al., 2013; Chen et al., 2015; Wang et al., 2015).

Co Retention and Loadings of Oxides: Univariate Analysis
As indicated in **Figure 4**, retention of Co ions from solution was significantly improved upon adding Ti and Fe oxides to CNTs. Retention of Co as a function of loaded oxides was studied at different temperatures, and the main results are depicted in **Figure 4**.

As indicated in **Figure 4A**, retention of Co by loaded surfaces is influenced by the loaded amount. In general, to get better Co uptake, the surface should be loaded with amounts higher than 30%. The interesting point in **Figure 4A** was the reduction in Co uptake by Fe-CNTs (18.9%) and at 50.0°C. For all tested surfaces, uptake of Co improved at higher temperature and best efficiency was observed at surface oxide loading of 48.2%. In fact, the relationship between Co uptake and loaded oxides is not purely linear and this would be attributed to the involvement of other factors like nature of interaction with composites, the extent of pore-filling, and mode of distribution of nanoparticles by the surface. For Ti-CNTs, better linearity between Co retention with loaded amounts was observed. In all cases, Co retention was
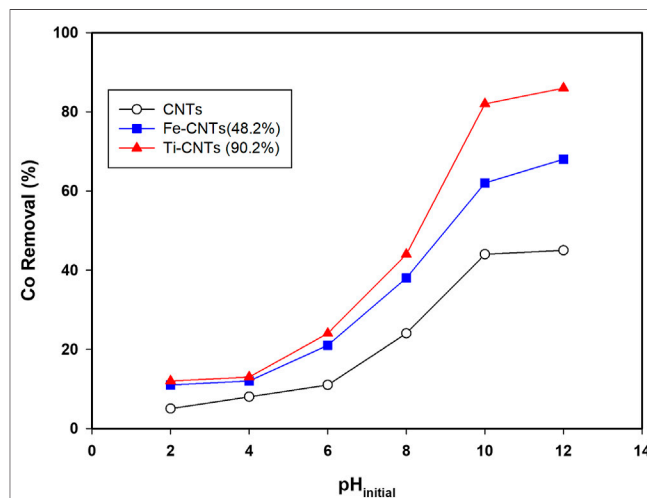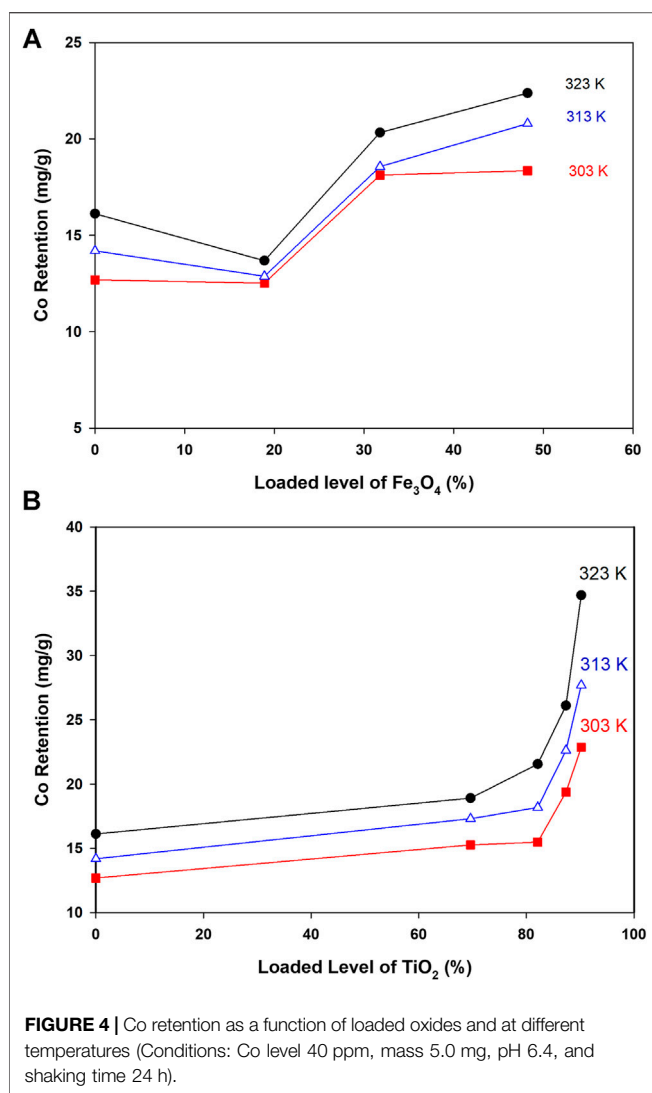

FIGURE 3 | Influence of solution pH on Co removal (Conditions: mass 5.0 mg, Co level 20 mg/L, temp = 30°C, and shaking time 24 h).

FIGURE 4 | Co retention as a function of loaded oxides and at different temperatures (Conditions: Co level 40 ppm, mass 5.0 mg, pH 6.4, and shaking time 24 h).

the penetration of different amounts of Co ions from the surface into aggregates of the nanoparticles (Tamura et al., 1997). had reported that the adsorption ability of a series metal oxides for cobalt ions in solution increases in this order $Al_2O_3 < Fe_2O_3 < TiO_2 < Fe_3O_4 < MnO_2$. They reported a positive correlation between cobalt adsorption capacities and increasing the electronegativity of the metal cation in the oxide lattice structure, which enhances the acid surface hydroxyl group deportation before bonding with Co^{2+}.

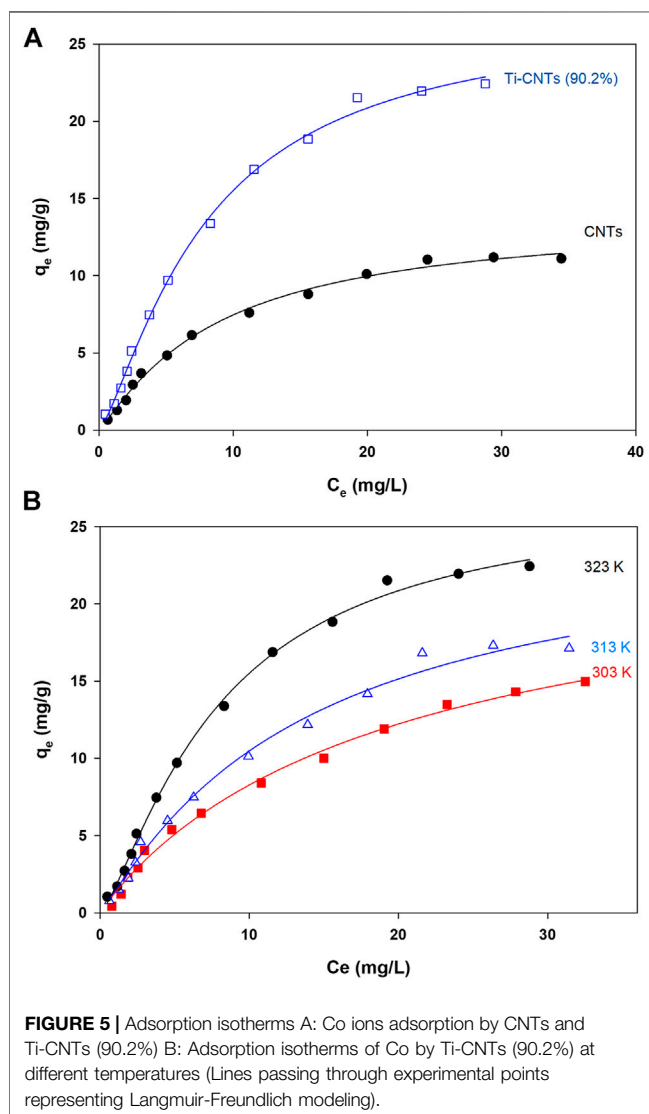## Isotherms and Thermodynamic Parameters

Measurement of Co isotherms at different temperatures provides crucial information about the physiochemical properties of nanocomposites and instant insights on the sorption process. The experimental data (C_e and q_e) were analyzed by different isotherms and at three temperatures to find thermodynamic parameters. The number of measured isotherms was high (33 isotherms), however, the analysis was limited to Ti-CNTs (90.2%) as the best efficiency was reported for this material. For comparison purposes, adsorption isotherms of Co by CNTs were also included. Typical isotherms are depicted in **Figure 5** while isotherms and other thermodynamic parameters are presented in **Table 3**.

As shown in **Figure 4**, the typical L2-shape of isotherms was obtained based on Giles and Smith classification of isotherms (Giles et al., 1974). In L2 isotherm, surface concentration is steeply raised at low Co content in solution and then increased at the higher concentrations (Giles et al., 1974). This may indicate the high affinity between Co ions and the surface. Indicial L2-shapes were reported for Co and other heavy metals retention by natural silicate minerals (Giles et al., 1974). In general, L2-type isotherms are often reported for ionic solutes adsorption with weak-solvent-competition (Giles et al., 1974). The parameters of isotherms and quality of fit X^2 are provided in **Table 3**. In general, Langmuir and Langmuir-Freundlich isotherms were workable for presenting retention behavior of Co by CNTs and Ti-CNTs with X^2 values 0.2–1.0. The maximum retention values (q_m) of Co that predicted by the Langmuir model were slightly higher for CNTs and notably higher for Ti-CNTs when compared to those depicted in **Figure 5A**. However, Langmuir-Freundlich isotherm was reasonably predicted maximum retention values indicating the workability of the model which can account for the presence of homogeneous and heterogeneous surfaces (Jeppu and Clement, 2012).

The magnitudes of q_m also confirmed the enhancement of Co retention upon modification, 13.86 and 29.83 mgCo/g CNTs and Ti-CNTs, respectively. In the same line, both K_L and K_{LM} reflected the higher affinity of Co to the surface after deposition of Ti-oxides. Although Langmuir and Langmuir-Freundlich isotherms were workable for presenting Co retention from solution, checking the workability of other isotherms is still necessary. As indicated in **Table 3**, Freundlich isotherm was not effective as observed for the earlier isotherms for presenting Co retention. X^2 values were 1.7 and 4.0 for CNTs and Ti-CNTs, respectively. The limited application of Freundlich isotherm was expected as this model works well for highly heterogeneous surfaces. Although the model was not highly applicable in this case, K_F indicated a

increased with loaded TiO_2 and the maximum uptake was 34.7 mg/g at surface loading of 90.2%. The main conclusion that drawn from **Figure 4** is that Ti-CNTs outperformed Fe-CNTs for Co uptake and more Fe-oxide was needed to get better Co retention. Comparable behavior was in the literature on the synergistic influence of metal oxides-CNTs toward adsorption from solution (Oliveira et al., 2002; Wang et al., 2007; Hu et al., 2010; Li et al., 2011; Wang et al., 2011). For example, Li et al. (Li et al., 2011) reported that the presence of CNTs in the composites enhanced the textural properties of the CNTs/TiO_2 composites compared to pure TiO_2 aggregated particles, and by providing an open structure and high surface area support for the formation of metal oxide films. **Table 2** shows a comparison of the maximum cobalt retention of the prepared nanocomposites with other adsorbents in the literature.

The remarkable affinity of Ti-CNTs over the Fe-CNTs toward cobalt species can be explained by the difference in the surface properties of the metal oxides such as crystal lattice structure, particle size, morphology, the quantity of the oxide, and functional groups (mainly hydroxyl), which probably results in

TABLE 2 | Comparison of Co retention of prepared nanocomposites and the previous studies in the literature.

Sorbent	Retention capacity, (mg/g)	Condition				Ref
		pH	Temp K	Ionic strength	m/v g/L	
Iron oxide/CNTs	2.88	6.4	293	0.01 M	0.50	Wang et al. (2011)
CNTs	2.60	9	293	—	5.00	Stafiej and Pyrzynska (2007)
Activated carbon	1.2	6	303	—	180.0	Sulaymon et al. (2009)
Magnetite/graphene oxide	12.98	6.8	303	0.01 M	0.40	Liu et al. (2011)
β–Cyclodextrin/graphene oxide	72.43	6	303	0.01 M	0.10	Song et al. (2013)
Titanate/graphene oxide	81.3	6	293	0.01 M	0.17	Wang et al. (2015)
Fe_3O_4/bentonite	18.76	8	293	—	0.10	Hashemian et al. (2014)
O-CNTs	15.27	6.4	323	—	0.50	This work
Fe-CNTs (48.2%)	20.32	6.4	323	—	0.50	This work
Ti-CNTs (90.2%)	29.80	6.4	323	—	0.50	This work

FIGURE 5 | Adsorption isotherms A: Co ions adsorption by CNTs and Ti-CNTs (90.2%) B: Adsorption isotherms of Co by Ti-CNTs (90.2%) at different temperatures (Lines passing through experimental points representing Langmuir-Freundlich modeling).

favorable Co retention by both surfaces ($K_F > 1$). Temkin isotherm, in fact, was found acceptable for presenting Co retention by both surfaces as indicated from X^2 values (2.2–3.5). Moreover, the variation in adsorption energy in the

model (i.e., b parameter) was positive for both systems which indicated that Co retention from solution was an endothermic process. The three-parameter isotherm (Dubinin-Radushkevich) was also workable for presenting Co retention by both surfaces with acceptable X^2 values, however, q_m values were not in agreement with experimental ones. For example, the predicted q_m of Co retention by CNTs was 10.2 mg/g and this value is lower than the experimental value 13.0 mg/g (**Figure 5**). In fact, Langmuir-Freundlich isotherm was more accurate in predicting q_m Co retention in both systems. The energy parameter of Dubinin-Radushkevich isotherm (B) also confirmed the better affinity of Co toward Ti-CNTs. In fact, binding energies of Co with surfaces were 4.8 and 4.3 kJ/mol for CNTs and Ti-CNTs, respectively. Thermodynamic parameters provide valuable information about the spontaneity, randomness and heat change in the sorption process (Liu, 2009; Anastopoulos and Kyzas, 2016). By plotting a graph of lnK vs. (1/T) (K may be taken as Langmuir or Langmuir-Freundlich constants), thermodynamic parameters were estimated and presented in **Table 3**. The positive enthalpy change (10.56–33.37 kJ/mol) suggests that Co retention was endothermic, and this was reported for all surfaces. The values of ΔG° are negative (about −23 kJ/mol), which reveal a spontaneous and thermodynamically favorable process. The positive ΔS (102.1–174.3 J/k.mol) revealed high randomness at the solid-liquid interface. Similar results were also reported for Co removal by other adsorbents (Wang et al., 2011; Hongqin et al., 2012; Song et al., 2013; Wang et al., 2015). Thermodynamic and isotherms parameters would be used to elucidate the nature of the interaction of Co with nanocomposite. The heat of Co adsorption is taken as the sum of three energies: the energy needed to break the intermolecular forces between Co and solvent molecules, the energy needed to break the intermolecular forces between Co ions, and the released energy due to bond formation between Co ions and the composite. Accordingly, the following equation would be provided: $\Delta H_{process} = \Delta H_{Co-H2O} + \Delta H_{Co-Co} + \Delta H_{Co-composite}$. The first two terms are positives (endothermic processes) while the last one is negative (exothermic process). From **Table 3**, $\Delta H_{process}$ and $\Delta H_{Co-composite}$ were (33.37 and 4.8 kJ/mol) for Co retention by CNTs and (10.56 and 4.3 kJ/mol) for Co retention by Ti-CNTs. Accordingly, the sums of $\Delta H_{Co-H2O} + \Delta H_{Co-Co}$ were 28.57 and for 6.26 kJ/mol, respectively. Simply, 85 and 60% of total energy were used to break

TABLE 3 | Parameters of the tested isotherms and thermodynamic values of Co retention by CNTs and Ti-CNTs.

Model[a]	CNTs	Ti-CNTs (90.2%)
Langmuir	K_L = 0.09	K_L = 0.074
	q_m = 15.3	q_m = 34.7
	X^2 = 0.3	X^2 = 1.0
Freundlich	K_F = 1.98	K_F = 3.39
	n_F = 0.52	n_F = 0.59
	X^2 = 1.7	X^2 = 4.0
Langmuir-Freundlich	K_{LF} = 0.11	K_{LF} = 0.21
	q_m = 13.86	q_m = 29.83
	n = 1.13	n= 1.72
	X^2 = 0.2	X^2 = 0.7
Temkin	K_T = 1.17	K_T = 1.18
	b = 1.1×10^{-3}	b = 2.3×10^{-3}
	X^2 = 2.2	X^2 = 3.5
Dubinin–Radushkevich	q_m = 10.2	q_m = 29.9
	B = 2.2	B = 2.6
	E(kJ/mol) = 4.8	E(kJ/mol) = 4.3
	X^2 = 3.7	X^2 = 4.9
Thermodynamics[b]	ΔH° = 33.37 kJ/mol	ΔH° = 10.56 kJ/mol
	ΔS° = 174.3 J/k.mol	ΔS° = 102.1 J/k.mol
	ΔG° = −22.96 (kJ/mol at 50°C)	ΔG° = −22.44 (kJ/mol at 50°C)

[a]The collected parameters were obtained by fitting adoption data (C_e and q_e) by the models following non-linear regression procedures. Conditions: 50°C, 5.0 mg adsorbent, Co range 1–40 mg/L, pH 6.4, and shaking time 24 h.
[b]Thermodynamic parameters were estimated as outlined earlier.

down the forces between Co-H_2O and Co-Co interactions. In fact, interactions between Co ions are not high compared with Co-H_2O due to the low content of the ion. Both Harkin-Jura and Halsey isotherms were also found of limited application for presenting Co retention by both surfaces and this was excluded the formation of multilayer of Co by the surface.

Multivariate Analysis of Co Retention

The combined influence of all factors on Co retention will be analyzed by PCA to uncover the interaction between factors or to exclude unnecessary factors from the process. The combined influence of factors on Co removal would be anticipated from the final outputs of PCA analysis. Co retention by different adsorbents and conditions is presented using **Eq. 7**:

$$
\begin{aligned}
\text{Co retention} \, (mg/g) =\ & 5.12 + 1.25\text{Conc} + 1.47\text{Temp} \\
& - 1.38\text{CNT}\% - 6.03\text{Ti}\% - 5.03\text{Fe}\% \\
& - 0.01\text{Conc}^2 + 0.12\text{Temp}^2 \\
& - 0.55\text{CNT}\%^2 - 1.53\text{Ti}\%^2 - 3.44\text{Fe}\%^2 \\
& + 0.17\text{Conc} \times \text{Temp} + 0.07\text{Conc} \\
& \times \text{CNT}\% + 0.07\text{Conc} \times \text{Ti}\% + 0.10\text{Conc} \\
& \times \text{Fe}\% + 0.21\text{Temp} \times \text{CNT}\% \\
& + 0.10\text{Temp} \times \text{Ti}\% + 0.17\text{Temp} \times \text{Fe}\% \\
& - 1.67\text{CNT}\% \times \text{Ti}\% - 1.45\text{CNT}\% \\
& \times \text{Fe}\% - 4.11\text{Ti}\% \times \text{Fe}\%
\end{aligned}
$$

(7)

The value of intercept (b_o) gives an average value of all terms, linear, quadratic, and interaction terms. The coefficients of linear terms (1.25, 1.47, −1.38, −6.03, −5.03) allow for a direct relationship between uptake and a given factor. Quadratic terms (−0.01, 0.12, −0.55, −1.53, −3.44) allow to balance out linear terms and this is necessary for certain systems when the optimum uptake is achieved at a specific level (i.e, nonlinear behavior). Interaction terms (0.17, 0.07, 0.07, 0.10, 0.21, 0.10, 0.17, −1.67, −1.45, −4.11) allow to assess the influence of two factors on uptake and this influence is rarely independent. Value of coefficient, in fact, can tell how significant the factor (or combination of factors) is. For linear terms, the high coefficient of a certain factor indicated its linear influence on Co uptake. If the interaction coefficient of two factors is high, then a higher response would be achieved when these factors are maintained at their higher limits and vice versa. Once the coefficients of **Eq. 7** were estimated, then the exact influence of factors on Co retention would be ascertained.

As indicated in **Eq. 7**, the coefficient of concentration and temperature factors were high and positive (1.25 and 1.47) indicating their positive and linear effect on Co uptake under the tested operational factors. The high and positive values of the earlier factors reflected the high correlation between Co retention and concentration/temperature regardless of the variations in the levels of other factors. Simply, an intense increase in Co retention at higher concentrations is expected whether the temperature is high (323 K) or low (303 K).

For the rest of the factors (CNTs%, Ti%, and Fe%), the high and negative coefficients (−1.38, −6.03, and −5.03) indicating anti-correlation with Co. uptake from solution. Regarding the effect of Ti% and Fe% on Co retention, the high and negative coefficients (−6.03 and −5.03) excluding any positive linearity in the process. In fact, including other terms (quadratic and interaction terms) was necessary at this stage to build the model. Among quadratic terms, the high coefficients of Ti% and Fe% indicated a strong nonlinear correlation between

FIGURE 6 | Prediction of Co retention by PCA. A: Linear terms, B: Quadratic terms, C: Interaction terms.
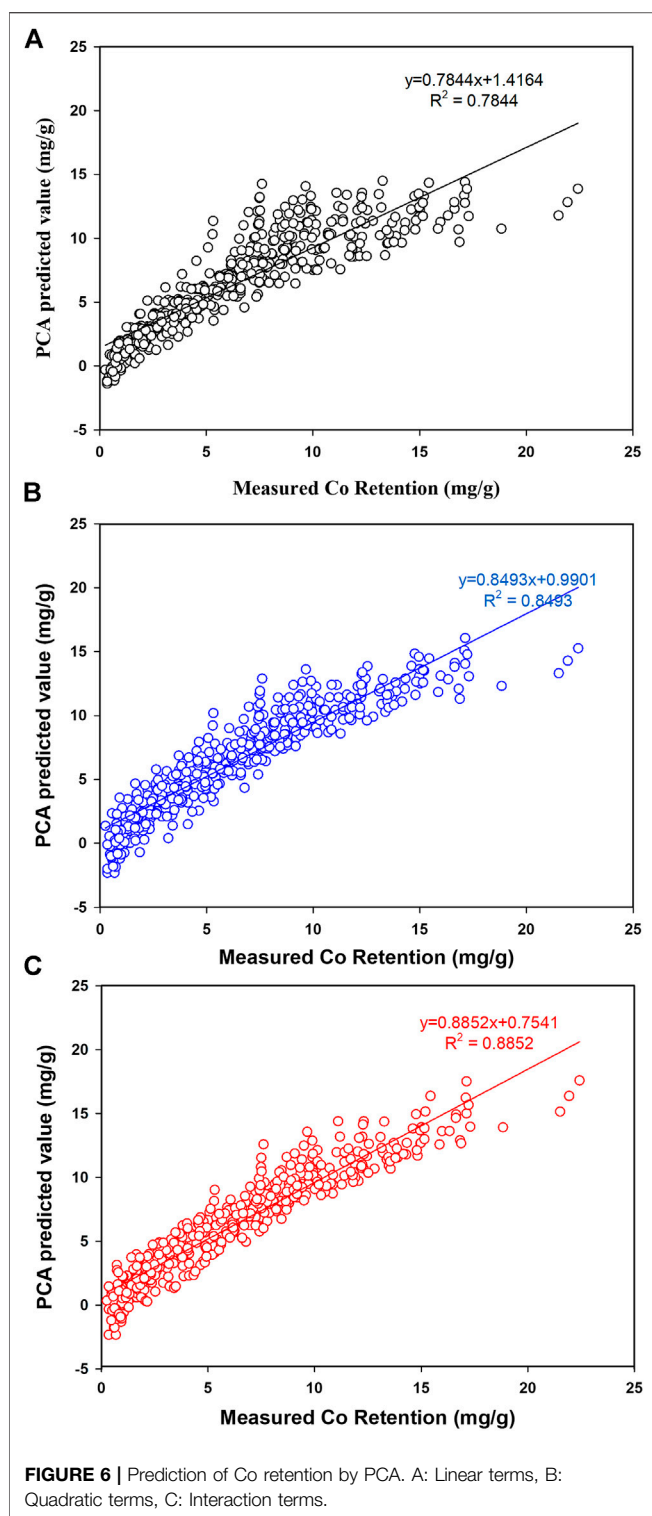
these significant factors and Co retention from solution while changing other factors. The interesting point was the modest linear and quadratic relationship between Co retention and CNT% and this may be attributed to the inner-dependency between CNTs% and amount of loaded oxides.

The interaction among factors has a higher influence on Co retention and this was obvious from the high and negative coefficients of interaction terms, −4.11, −1.67, and −1.45 for Ti % × Fe%, CNT% × Ti%, and CNT% × Fe%, respectively. Moreover, positive coefficients (0.07–0.17) between concentration and other factors were found indicating a high Co retention would be obtained by keeping concentration and other factors at their higher limits. The positive interaction of concentration with other factors was expected due to the strong linear correlation with Co retention. As predicted by PCA, the maximum interaction was between Ti% and Fe% (−4.11) indicating that the best Co retention should be achieved when both factors at their opposite limits (i.e., either at high Ti and low Fe or vice versa). The same behavior is true between CNTs-TI and CNTs-Fe. With high coefficients (0.17–0.21), PCA analysis of the 429 tests predicted favourable Co retention when temperature, concentration, and CNTs maintained at their upper limits. The interaction between CNTs/concentration, Ti/concentration seems to be not promising as indicated by their corresponding coefficients (0.07).

The higher coefficient of Fe/concentration (0.10) compared to Ti/concentration (0.07) would reflect the importance of Fe compared to Ti for better Co retention. In general, the coefficient of Conc × Temp was not high (0.17) which makes the increasing temperature (from 303 to 323) may be unnecessary. The best effect of temperature was noticed at higher CNTs with a positive coefficient of +0.21. Moreover, better Co uptake is expected at high temperature and Fe (+0.17) compared to Ti (+0.10).

Figure 6 depicts the influence of adding linear, quadratic, and interaction terms on modeling Co retention in all tests and the final REP% are presented in **Table 4**.

As indicated in **Figure 6A**, modeling Co retention using linear terms has ended up with a high REP% value of 26% reflecting the complex process and possible interaction between factors. As viewed in **Figure 6A**, a poor prediction of Co retention particularly at lower retention values (<5.0 mg/g) and negative values were also observed. This observation would be attributed to the significant interaction between factors making linear terms not workable to model the process. A small improvement (**Figure 6B**) was observed upon including quadratic coefficient (which would help to account for nonlinear correlations) but the overall fitness was modest with $R^2 = 0.8493$ and REP% of 22%. Again, the PCA model was not workable for predicting Co retention at lower retentions and this was attributed to the intense interaction between factors. The optimum prediction of Co retention was accomplished when interaction terms were included in the model. **Figure 6C** confirmed the workability of PCA for simulating Co retention even at low retentions with $R^2 = 0.8852$ and REP% of 19%.

Experimentally, the maximum Co retention was 22.4 mg/g and accomplished at the following operational conditions (40.0 ppm, 323 K, CNT 9.8%, and Ti 90.2%). In fact, the high Co affinity at aforementioned conditions agrees with PCA as the levels of Co, Ti, and temperature were at their upper limits and assured the importance of the positive interaction between factors. Although Co retention was relatively high, results indicated that 29% of the ultimate capacity (80 mg/g) was utilized. Accordingly, other experimental factors like pH and ionic strength should be tested for better Co retention from the solution.

TABLE 4 | Prediction of Co retention (%REP) by principal component regression while including all possible interactions.

Factors	Linear terms (%)	Quadratic terms (%)	Interaction terms (%)
Conc-Temp-CNT%-Ti%-Fe%	26	22	19

CONCLUSION

The potential application of many modified nano-adsorbents to remove Co ions from solution was demonstrated. The large size of adsorption tests was analyzed using both univariate and multivariate procedures to model Co retention from the solution. Univariate analysis indicated that Co retention increased with initial concentration, loaded oxides, pH, and temperature. All isotherms were fairly presented using Langmuir-Freundlich isotherm as the model predicted the maximum retention of Co. Thermodynamic studies indicated that Co interaction by all surfaces was a spontaneous and endothermic process. Incorporation of CNTs with TiO_2 and Fe_3O_4 has a synergic impact on Co removal as confirmed by multivariate analysis.

PCA analysis uncovers the interaction among factors that can improve Co retention from solution. The negative coefficients of Ti/Fe with CNTs (1.45–4.11) indicated better Co retention at higher Ti/Fe loads and lower mass of adsorbent. Moreover, the analysis indicated that Ti and Fe should be at their opposite limit to get high Co uptake from solution.

DATA AVAILABILITY STATEMENT

The original contributions presented in the study are included in the article/**Supplementary Material**; further inquiries can be directed to the corresponding author.

REFERENCES

Al-Degs, Y. S., Abu-El-Halawa, R., and Abu-Alrub, S. S. (2012). Analyzing Adsorption Data of Erythrosine Dye Using Principal Component Analysis. *Chem. Eng. J.* 191, 185–194. doi:10.1016/j.cej.2012.03.002

Allen, S. J., McKay, G., and Porter, J. F. (2004). Adsorption Isotherm Models for Basic Dye Adsorption by Peat in Single and Binary Component Systems. *J. Colloid Interf. Sci.* 280 (2), 322–333. doi:10.1016/j.jcis.2004.08.078

Anastopoulos, I., and Kyzas, G. Z. (2016). Are the Thermodynamic Parameters Correctly Estimated in Liquid-phase Adsorption Phenomena? *J. Mol. Liquids* 218, 174–185. doi:10.1016/j.molliq.2016.02.059

Asmaly, H. A., Abussaud, B., Ihsanullah, F., Saleh, T. A., Gupta, V. K., and Atieh, M. A. (2015). Ferric Oxide Nanoparticles Decorated Carbon Nanotubes and Carbon Nanofibers: From Synthesis to Enhanced Removal of Phenol. *J. Saudi Chem. Soc.* 19 (5), 511–520. doi:10.1016/j.jscs.2015.06.002

Brereton, R. G. (2003). *Chemometrics: Data Analysis for the Laboratory and Chemical Plant*. Chichester, United Kingdom: John Wiley & Sons Ltd.

Chen, H., Li, J., Shao, D., Ren, X., and Wang, X. (2012). Poly(acrylic Acid) Grafted Multiwall Carbon Nanotubes by Plasma Techniques for Co(II) Removal from Aqueous Solution. *Chem. Eng. J.* 210, 475–481. doi:10.1016/j.cej.2012.08.082

Chen, L., Lu, S., Wu, S., Zhou, J., and Wang, X. (2015). Removal of Radiocobalt from Aqueous Solutions Using Titanate/graphene Oxide Composites. *J. Mol. Liquids* 209, 397–403. doi:10.1016/j.molliq.2015.06.012

AUTHOR CONTRIBUTIONS

IF initiated the research project, supervised the work, and interpreted the results, AE-S co-supervised the work. AA prepared materials and carried out experiments. YE-D and EF helped to run the multivariate analysis with interpretation. JD helped in the discussion of various isotherms outcomes. All authors contributed to submitted the manuscript and approved it.

FUNDING

ACKNOWLEDGMENTS

SUPPLEMENTARY MATERIAL

The Supplementary Material for this article can be found online at: https://www.frontiersin.org/articles/10.3389/fchem.2021.690420/full#supplementary-material

Chen, M., Zhang, F., and Oh, W. (2011). Fabrication and Performances of MWCNT/TiO2 Composites Derived from MWCNTs and Titanium (IV) Alkoxide Precursors. *Bull. Mater. Sci.* 34 (4), 835–841. doi:10.1007/s12034-011-0203-4

Chiang, Y.-C., Lin, W.-H., and Chang, Y.-C. (2011). The Influence of Treatment Duration on Multi-Walled Carbon Nanotubes Functionalized by H2SO4/HNO3 Oxidation. *Appl. Surf. Sci.* 257 (6), 2401–2410. doi:10.1016/j.apsusc.2010.09.110

El-Sheikh, A. H., Al-Degs, Y. S., Al-As'ad, R. M., and Sweileh, J. A. (2011). Effect of Oxidation and Geometrical Dimensions of Carbon Nanotubes on Hg(II) Sorption and Preconcentration from Real Waters. *Desalination* 270 (1), 214–220. doi:10.1016/j.desal.2010.11.048

El-Sheikh, A. H. (2008). Effect of Chemical Treatment of Multi-Walled Carbon Nanotubes with Various Oxidizing Agents on its Preconcentration Performance of Some Metals. *Jordan J. Chem.* 3 (3), 293–304.

Freundlich, H. (1906). über die adsorption in lö sungen (Adsorption in solution). *Z. für Physikalische Chem.* 75, 87. doi:10.1515/zpch-1907-5723

Gao, B., Chen, G. Z., and Li Puma, G. (2009). Carbon Nanotubes/titanium Dioxide (CNTs/TiO2) Nanocomposites Prepared by Conventional and Novel Surfactant Wrapping Sol-Gel Methods Exhibiting Enhanced Photocatalytic Activity. *Appl. Catal. B: Environ.* 89 (3–4), 503–509. doi:10.1016/j.apcatb.2009.01.009

Giles, C. H., Smith, D., and Huitson, A. (1974). A General Treatment and Classification of the Solute Adsorption Isotherm. I. Theoretical.

J. Colloid Interf. Sci. 47 (3), 755–765. doi:10.1016/0021-9797(74)90252-5

Gupta, V., and Saleh, T. (2011). *Syntheses of Carbon Nanotube-Metal Oxides Composites; Adsorption and Photo-Degradation.* doi:10.5772/18009

Hashemian, S., Saffari, H., and Ragabion, S. (2014). Adsorption of Cobalt(II) from Aqueous Solutions by Fe3O4/Bentonite Nanocomposite. *Water Air Soil Pollut.* 226, 2212. doi:10.1007/s11270-014-2212-6

Hongqin, X., Duilin, W., Zhe, J., Xiaowei, L., Shouwei, Z., Yan, L., et al. (2012). Kinetic and Thermodynamic Sorption Study of Radiocobalt by Magnetic Hydroxyapatite Nanoparticles. *J. Radioanal. Nucl. Chem.* 292 (2), 637–647. doi:10.1007/s10967-011-1458-3

Hu, J., Shao, D., Chen, C., Sheng, G., Li, J., Wang, X., et al. (2010). Plasma-Induced Grafting of Cyclodextrin onto Multiwall Carbon Nanotube/Iron Oxides for Adsorbent Application. *J. Phys. Chem. B.* 114 (20), 6779–6785. doi:10.1021/jp911424k

Iijima, S. (1991). Helical Microtubules of Graphitic Carbon. *Nature* 354 (6348), 56–58. doi:10.1038/354056a0

Ikehata, K., Jin, Y., Maleky, N., and Lin, A. (2015). "Heavy Metal Pollution in Water Resources in China—Occurrences and Public Health Implications," in *Heavy Metals in Water: Presence, Removal and Safety* (The Royal Society of Chemistry), 141–167.

Jeppu, G. P., and Clement, T. P. (2012). A Modified Langmuir-Freundlich Isotherm Model for Simulating pH-dependent Adsorption Effects. *J. Contaminant Hydrol.* 129-130, 46–53. doi:10.1016/j.jconhyd.2011.12.001

Lee, P.-L., Chiu, Y.-K., Sun, Y.-C., and Ling, Y.-C. (2010). Synthesis of a Hybrid Material Consisting of Magnetic Iron-Oxide Nanoparticles and Carbon Nanotubes as a Gas Adsorbent. *Carbon* 48 (5), 1397–1404. doi:10.1016/j.carbon.2009.12.030

Li, J., Wen, F., Pan, L., Liu, Z., and Dong, Y. (2013a). Removal of Radiocobalt Ions from Aqueous Solutions by Natural Halloysite Nanotubes. *J. Radioanal. Nucl. Chem.* 295 (1), 431–438. doi:10.1007/s10967-012-1823-x

Li, K., Hu, J., Liu, Z., Chen, L., and Dong, Y. (2013b). Sorption of Radiocobalt(II) onto MWCNTs: Effects of Solid Content, Contact Time, pH, Ionic Strength, Humic Acid and Temperature. *J. Radioanal. Nucl. Chem.* 295 (3), 2125–2133. doi:10.1007/s10967-012-2222-z

Li, Z., Gao, B., Chen, G. Z., Mokaya, R., Sotiropoulos, S., and Li Puma, G. (2011). Carbon Nanotube/titanium Dioxide (CNT/TiO2) Core-Shell Nanocomposites with Tailored Shell Thickness, CNT Content and Photocatalytic/photoelectrocatalytic Properties. *Appl. Catal. B: Environ.* 110, 50–57. doi:10.1016/j.apcatb.2011.08.023

Liu, M., Chen, C., Hu, J., Wu, X., and Wang, X. (2011). Synthesis of Magnetite/Graphene Oxide Composite and Application for Cobalt(II) Removal. *J. Phys. Chem. C* 115, 25234–25240. doi:10.1021/jp208575m

Liu, Y. (2009). Is the Free Energy Change of Adsorption Correctly Calculated?. *J. Chem. Eng. Data* 54 (7), 1981–1985. doi:10.1021/je800661q

Liu, Z., Chen, L., Zhang, Z., Li, Y., Dong, Y., and Sun, Y. (2013). Synthesis of Multi-Walled Carbon Nanotube-Hydroxyapatite Composites and its Application in the Sorption of Co(II) from Aqueous Solutions. *J. Mol. Liquids* 179, 46–53. doi:10.1016/j.molliq.2012.12.011

Lu, J., Wang, M., Deng, C., and Zhang, X. (2013). Facile Synthesis of Fe3O4@mesoporous TiO2 Microspheres for Selective Enrichment of Phosphopeptides for Phosphoproteomics Analysis. *Talanta* 105, 20–27. doi:10.1016/j.talanta.2012.11.030

Mallakpour, S., and Khadem, E. (2016). Carbon Nanotube-Metal Oxide Nanocomposites: Fabrication, Properties and Applications. *Chem. Eng. J.* 302, 344–367. doi:10.1016/j.cej.2016.05.038

Martínez, C., Canle, L., Fernández, M. I., Santaballa, J. A., and Faria, J. (2011). Kinetics and Mechanism of Aqueous Degradation of Carbamazepine by Heterogeneous Photocatalysis Using Nanocrystalline TiO2, ZnO and Multi-Walled Carbon Nanotubes-Anatase Composites. *Appl. Catal. B: Environ.* 102 (3–4), 563–571. doi:10.1016/j.apcatb.2010.12.039

Oliveira, L. C. A., Rios, R. V. R. A., Fabris, J. D., Garg, V., Sapag, K., and Lago, R. M. (2002). Activated Carbon/iron Oxide Magnetic Composites for the Adsorption

of Contaminants in Water. *Carbon* 40 (12), 2177–2183. doi:10.1016/s0008-6223(02)00076-3

Sadegh, H., Ali, G. A. M., Gupta, V. K., Makhlouf, A. S. H., Shahryari-ghoshekandi, R., Nadagouda, M. N., et al. (2017). The Role of Nanomaterials as Effective Adsorbents and Their Applications in Wastewater Treatment. *J. Nanostruct Chem.* 7 (1), 1–14. doi:10.1007/s40097-017-0219-4

Scherrer, P. (1918). *Bestimmung der Grosse und der Inneren Struktur von Kolloidteilchen Mittels Rontgenstrahlen, Nachrichten von der Gesellschaft der Wissenschaften.* Gottingen: Mathematisch-Physikalische Klasse, 3.

Simonsen, L. O., Harbak, H., and Bennekou, P. (2012). Cobalt Metabolism and Toxicology-A Brief Update. *Sci. Total Environ.* 432, 210–215. doi:10.1016/j.scitotenv.2012.06.009

Song, W., Hu, J., Zhao, Y., Shao, D., and Li, J. (2013). Efficient Removal of Cobalt from Aqueous Solution Using β-cyclodextrin Modified Graphene Oxide. *RSC Adv.* 3 (24), 9514–9521. doi:10.1039/c3ra41434e

Stafiej, A., and Pyrzynska, K. (2007). Adsorption of heavy metal ions with carbon nanotubes. *Sep. Purif. Technol.* 58, 49–52. doi:10.1016/j.seppur.2007.07.008

Steven, G., Donkin, D. L. O., and Teaf, C. M. (2000). "Properties and Effects of Metals," in *Principles of Toxicology: Environmental and Industrial Applications.* Editors R. C. J. Phillip, L. Williams, and M. Stephen (Roberts USA: John Wiley & Sons), 325–344.

Sulaymon, A. H., Abid, B. A., and Al-Najar, J. (2009). Removal of lead copper chromium and cobalt ions onto granular activated carbon in batch and fixed-bed adsorbers. *Chem. Eng. J.* 155, 647–653. doi:10.1016/j.cej.2009.08.021

Sun, Z., Liu, Z., Wang, Y., Han, B., Du, J., and Zhang, J. (2005). Fabrication and Characterization of Magnetic Carbon Nanotube Composites. *J. Mater. Chem.* 15 (42), 4497–4501. doi:10.1039/b509968d

Tamura, H., Katayama, N., and Furuichi, R. (1997). The Co2+Adsorption Properties of Al2O3, Fe2O3, Fe3O4, TiO2, and MnO2Evaluated by Modeling with the Frumkin Isotherm. *J. Colloid Interf. Sci.* 195 (1), 192–202. doi:10.1006/jcis.1997.5148

Temkin, M., and Pyzhev, V. (1940). Kinetics of Ammonia Synthesis on Promoted Iron Catalysts. *Acta Physicochimica URSS* 12, 327–356.

Wang, Q., Li, J., Chen, C., Ren, X., Hu, J., and Wang, X. (2011). Removal of Cobalt from Aqueous Solution by Magnetic Multiwalled Carbon Nanotube/iron Oxide Composites. *Chem. Eng. J.* 174 (1), 126–133. doi:10.1016/j.cej.2011.08.059

Wang, S., Gong, W., Liu, X., Yao, Y., Gao, B., and Yue, Q. (2007). Removal of Lead(II) from Aqueous Solution by Adsorption onto Manganese Oxide-Coated Carbon Nanotubes. *Sep. Purif. Tech.* 58 (1), 17–23. doi:10.1016/j.seppur.2007.07.006

Wang, X., Lu, S., and Liu, M. (2015). Effect of environmental conditions on the sorption of radiocobalt on titanate/graphene oxide composites. *J. Radioanal. Nucl. Chem.* 303 (3), 2391–2398. doi:10.1007/s10967-014-3717-6

Zhang, P., Mo, Z., Han, L., Wang, Y., Zhao, G., Zhang, C., et al. (2015). Magnetic Recyclable TiO2/multi-Walled Carbon Nanotube Nanocomposite: Synthesis, Characterization and Enhanced Photocatalytic Activity. *J. Mol. Catal. A: Chem.* 402, 17–22. doi:10.1016/j.molcata.2015.03.005

Zhao, D., Yang, X., Chen, C., and Wang, X. (2013). Enhanced Photocatalytic Degradation of Methylene Blue on Multiwalled Carbon Nanotubes-TiO2. *J. Colloid Interf. Sci.* 398, 234–239. doi:10.1016/j.jcis.2013.02.017

Check for updates

Edge Mostar Indices of Cacti Graph With Fixed Cycles

Farhana Yasmeen[1]*, Shehnaz Akhter[2], Kashif Ali[1] and Syed Tahir Raza Rizvi[1]

[1]Department of Mathematics, COMSATS University Islamabad, Lahore, Pakistan, [2]School of Natural Science, National University of Science and Technology, Islamabad, Pakistan

Topological invariants are the significant invariants that are used to study the physicochemical and thermodynamic characteristics of chemical compounds. Recently, a new bond additive invariant named the Mostar invariant has been introduced. For any connected graph $\mathcal{H}$, the edge Mostar invariant is described as $Mo_e(\mathcal{H}) = \sum_{gx \in E(\mathcal{H})} |m_{\mathcal{H}}(g) - m_{\mathcal{H}}(x)|$, where $m_{\mathcal{H}}(g)$ (or $m_{\mathcal{H}}(x)$) is the number of edges of $\mathcal{H}$ lying closer to vertex g (or x) than to vertex x (or g). A graph having at most one common vertex between any two cycles is called a cactus graph. In this study, we compute the greatest edge Mostar invariant for cacti graphs with a fixed number of cycles and n vertices. Moreover, we calculate the sharp upper bound of the edge Mostar invariant for cacti graphs in $\mathfrak{C}(n, s)$, where s is the number of cycles.

Keywords: topological invariants, Mostar invariant, edge Mostar invariant, cacti graphs, graph theory

1 INTRODUCTION

Let $\mathcal{H} = (V(\mathcal{H}), E(\mathcal{H}))$ be a simple, undirected, and connected graph with the vertex set $V(\mathcal{H})$ and the edge set $E(\mathcal{H})$. The degree of $g \in V(\mathcal{H})$, represented as $deg_{\mathcal{H}}(g)$, is described as the number of edges directly linked with g. The neighbors of a vertex g in $\mathcal{H}$ is the set of all of its adjacent vertices in $\mathcal{H}$. For $g, x \in V(\mathcal{H})$, the number of edges in the shortest path between two vertices g and x is called the distance between them and is expressed as $\mathsf{d}_{\mathcal{H}}(g, x)$. A pendent vertex p in $\mathcal{H}$ is a vertex with degree one, and an edge having one pendent vertex as one of its end vertices is called a pendent edge. The set of all pendent vertices of $\mathcal{H}$ is represented as $P_{\mathcal{H}}$, and the set of all pendent vertices adjacent to a fix vertex g is represented as $P_{\mathcal{H}}(g)$. An edge in $\mathcal{H}$ is presented as a cut edge if, by deleting that edge, the graph is converted into exactly two components. Let P_n, C_n, and S_n be used for the representation of the path, the cycle, and the star with order n.

In the fields of chemical sciences, mathematical chemistry, chemical graph theory, and pharmaceutical science, topological invariants are of significant importance because of their definitional use. The physicochemical properties of chemical structures can be forecasted by using topological invariants. A numerical value related to biological activity, chemical reactivity, and physical properties of chemical structures is known as a topological invariant. Topological invariants are mainly separated into different manners like degree, distance, eccentricity, and spectrum. A distance-based invariant is a topological invariant based on the distance between the vertices or edges of a given graph. The Wiener invariant (Wiener, 1947) is the most significant oldest topological invariant that belongs to distance-based invariants, and the Harary invariant (Mihalić and Trinajstić, 1992) and the Balaban invariant (Zhou and Trinajstić, 2008) also belong to distance-based invariants. Degree-based invariants are another well-studied group of invariants. The first degree-based invariant was introduced as the Randić invariant (Randic, 1975). A rich theory of distance- and degree-based invariants is mentioned in (Li and Shi, 2008; Gutman, 2013; Knor et al.,

The recently introduced Mostar invariant (Došlić et al., 2018) belongs to bound additive invariants as they capture the relevant properties of a graph by summing up the contributions of individual edges (Vukičević and Gašperov, 2010; Vukičević, 2011). Peripherality is one such property that could be of interest. An edge is a peripheral edge if there are many more vertices closer to one of its end vertices than to the other one. In short, for an edge gx in $\mathcal{H}$, the greatest value of absolute difference of the cardinality of vertices closer to g than to x, presented by $n_{\mathcal{H}}(g)$, and the cardinality of vertices closer to x than to g, denoted by $n_{\mathcal{H}}(x)$, indicates a peripheral position of gx in $\mathcal{H}$. The Mostar invariant of a graph $\mathcal{H}$ is defined as follows:

$$Mo_v(\mathcal{H}) = \sum_{e=gx \in E(\mathcal{H})} |n_{\mathcal{H}}(g) - n_{\mathcal{H}}(x)|, \qquad (1)$$

and this represents a global measure of peripherality of a graph $\mathcal{H}$. Došlić et al. (2018) determined the Mostar invariant of the benzenoid system. Tratnik proved that the Mostar invariant of the weighted graph can be deduced in the form of the Mostar invariant of quotient graphs (Tratnik, 2019). Arockiaraj et al. (2019) introduced the edge Mostar invariant as follows:

$$Mo_e(\mathcal{H}) = \sum_{e=gx \in E(\mathcal{H})} |m_{\mathcal{H}}(g) - m_{\mathcal{H}}(x)|, \qquad (2)$$

where $m_{\mathcal{H}}(g)$ (or $m_{\mathcal{H}}(x)$) is the cardinality of edges closer to g (or x) than to x (or g). Akhter et al. (2021) computed the Mostar indices for the molecular graphs of SiO_2 layer structures and the melem chain with the help of the cut method. Liu et al. (2020) found the extremal values of the edge Mostar invariant of cacti graphs. Imran et al. (2020) found the edge Mostar invariant of chemical structures and nanostructures using graph operations. Arockiaraj et al. (2020) calculated the weighted Mostar indices of molecular peripheral shapes with applications in graphene, graphyne, and graphdiyne nanoribbons. Liu et al. (2020) determined the maximum edge Mostar index of cacti graphs with the following given conditions.

Theorem 1.1. *Let $\mathcal{G} \in \mathfrak{C}(n,s)$ be a connected graph:*

- *if $n \geq 10$ and $n < 4s$, then $Mo_e(\mathcal{G}) \leq 2n^2 - 8n + (24 - 4n)s$ with equality if and only if $\mathcal{G} \cong \mathcal{G}^n\left(\underbrace{3,3,3,\ldots 3}_{4s-n}, \underbrace{4,4,4\ldots 4}_{n-3s}\right)$,*
- *if $n \geq 10$ and $n \geq 4s$, then $Mo_e(\mathcal{G}) \leq n^2 - n - 12s$ with equality if and only if $\mathcal{G} \cong \mathcal{G}^n(4,4,\ldots 4)$,*
- *if $n = 9$, then $Mo_e(\mathcal{G})7 = 72 - 12s$ with equality if and only if $\mathcal{G} \cong \mathcal{G}_9$, and*
- *if $n < 9$, then $Mo_e(\mathcal{G}) \leq n^2 - n - (n+3)s$ with equality if and only if $\mathcal{G} \cong \mathcal{G}^n(3,3,3,\ldots 3)$.*

Liu et al. (2020) determined the second maximum edge Mostar index of cacti graphs with the following given conditions.

Theorem 1.2. *Let $\mathcal{G} \in \mathfrak{C}(n,s) \backslash \mathfrak{C}_0(n,s)$ with $n \geq 10$ and $n \geq 4s > 0$:*

- *$Mo_e(\mathcal{G}) \leq 89 - 12s$ forn $= 10$ with equality if and only if $\mathcal{G} \cong \mathcal{G}\left(3, \underbrace{4,4,4\ldots 4}_{s-1}\right)$,*
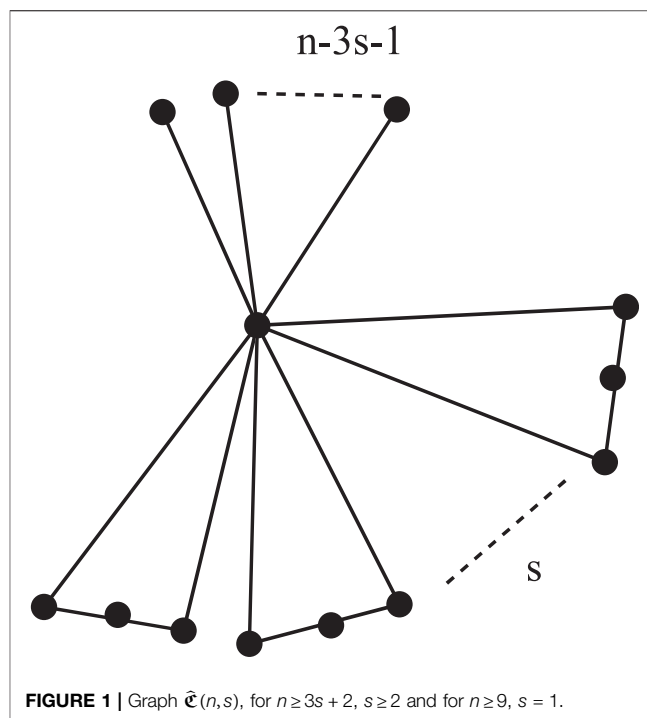

FIGURE 1 | Graph $\hat{\mathfrak{C}}(n,s)$, for $n \geq 3s + 2$, $s \geq 2$ and for $n \geq 9$, $s = 1$.

- *$Mo_e(\mathcal{G}) \leq 108 - 12s$ for $n = 11$ with equality if and only if $\mathcal{G} \cong \mathcal{G}\left(3, \underbrace{4,4,4\ldots 4}_{s-1}\right)$, and*
- *$Mo_e(\mathcal{G}) \leq n^2 - n - 12s - 2$ with equality if and only if $\mathcal{G} \cong \mathcal{G}_1(n,s)$.*

For more results related to Mostar and edge Mostar invariants, see (Hayat and Zhou, 2019a; Akhter, 2019; Tepeh, 2019; Akhter et al., 2020; Dehgardi and Azari, 2020; Deng and Li, 2020; Ghorbani et al., 2020; Huang et al., 2020; Deng and Li, 2021a; Deng and Li, 2021b).

A connected graph is a cactus if all its blocks are either edges or cycles, that is, any two of its cycles have at most one common vertex. Until now, many results in chemistry and graph theory related to the cacti have been acquired. The first three smallest Gutman invariants among the cacti have been determined by Chen (2016). Using the Zagreb invariants, Li et al. (2012) found the upper and lower bounds of the cacti. The bounds of the Harary invariant related to cacti have been found by Wang and Kang (2013). The extremal cacti having the greatest hyper-Wiener invariant have been characterized by Wang and Tan (2015). The extremal graphs with the greatest and smallest vertex PI invariants among all cacti with a fixed number of vertices have been determined by Wang et al. (2016). The sharp upper bound of the Mostar invariant for cacti of order n with s cycles has been given by Hayat and Zhou (2019b), and they also found the greatest Mostar invariant for all n-vertex cacti. For more results related to cacti graphs, see (Liu et al., 2016; Wang and Wei, 2016; Wang, 2017).

Motivated by the results of chemical invariants and their applications, it may be interesting to characterize the cacti
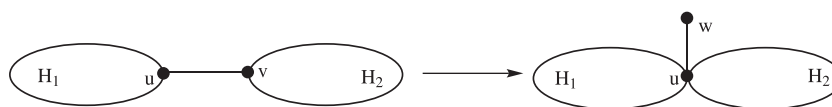
FIGURE 2 | Graphs $\mathcal{G}_1$ and $\mathcal{G}_2$ of Lemma 2.1.

with the greatest and smallest edge Mostar invariants for some fixed parameters. In this study, we consider the cacti with a fixed number of cycles and find the greatest edge Mostar invariant for all the n-vertex cacti. In the end, we give a sharp upper bound of the edge Mostar invariant for these cacti.

2 MAIN RESULTS

Let $\mathfrak{C}(n)$ be the set of all cacti graphs of order $n \geq 2$ and $\mathfrak{C}(n, s)$ be the set of all cacti graphs of order $n \geq 2$ with the number of cycles s. Let $\widehat{\mathfrak{C}}(n, s) \in \mathfrak{C}(n, s)$ be the n-vertex cactus, for $n \geq 3s + 2$, $s \geq 2$ and for $n \geq 9$, $s = 1$, consisting of s number of C_4 and $n - 3s - 1$ pendent edges such that every c_4 and pendent edge has exactly one vertex in common (see **Figure 1**).

In this section, we derive the greatest value of cacti graphs for the edge Mostar invariant. First of all, some basic lemmas are proved so that the main result can be proved easily.

Proposition 2.1. (Imran et al., 2020) *The edge Mostar invariant of a path P_n and a cycle C_n with n vertices is $Mo_e(P_n) = \left\lceil \frac{(n-1)^2}{2} \right\rceil$ and $Mo_e(C_n) = 0$, respectively.*

In Lemma 2.1, we establish a graph $\mathcal{G}_2$ by converting a cut edge uv into a pendent edge uw in $\mathcal{G}_1$, such that the new graph $\mathcal{G}_2$ has a greater edge Mostar invariant.

Lemma 2.1: *Consider two connected graphs H_1 and H_2 such that they are connected to each other by an edge uv, where $u \in V(H_1)$ and $v \in V(H_2)$, and acquired the graph $\mathcal{G}_1$. Now, we construct the graph $\mathcal{G}_2$ by deleting the cut edge uv and attaching a pendent edge uw at vertex u in $\mathcal{G}_1$ (see **Figure 2**). Then $Mo_e(\mathcal{G}_1) < Mo_e(\mathcal{G}_2)$.*

Proof: Let H_1 and H_2 be the subgraphs of $\mathcal{G}_1$, as shown in **Figure 2**. By the construction of $\mathcal{G}_2$, the number of closer edges of the end vertices of a fixed edge of H_1 and H_2 in $\mathcal{G}_1$ remains the same in $\mathcal{G}_2$, respectively. Therefore, for an edge $gx \in E(H_l)$, where $l \in \{1, 2\}$, we have the following:

$$m_{\mathcal{G}_1}(g) = m_{\mathcal{G}_2}(g), \qquad m_{\mathcal{G}_1}(x) = m_{\mathcal{G}_2}(x) \qquad (3)$$

For the cut edge uv in $\mathcal{G}_1$ and the pendent edge uw in $\mathcal{G}_2$, we have the following:

$$m_{\mathcal{G}_1}(u) = |E(H_1)|, \quad m_{\mathcal{G}_1}(v) = |E(H_2)|,$$
$$m_{\mathcal{G}_2}(u) = |E(H_1)| + |E(H_2)|, \quad m_{\mathcal{G}_2}(w) = 0. \qquad (4)$$

Using the definition of the edge Mostar invariant and substituting the values from **Eqs 3**, **4** , we acquire the following:

$$Mo_e(\mathcal{G}_1) - Mo_e(\mathcal{G}_2) = |m_{\mathcal{G}_1}(u) - m_{\mathcal{G}_1}(v)| + \sum_{l=1}^{2} \sum_{gx \in E(H_l)} |m_{\mathcal{G}_1}(g) - m_{\mathcal{G}_1}(x)| - |m_{\mathcal{G}_2}(u) - m_{\mathcal{G}_2}(w)|$$
$$- \sum_{l=1}^{2} \sum_{gx \in E(H_l)} |m_{\mathcal{G}_2}(g) - m_{\mathcal{G}_2}(x)|$$
$$= ||E(H_1)| + |E(H_2)|| + \sum_{l=1}^{2} \sum_{gx \in E(H_l)} |m_{\mathcal{G}_1}(g) - m_{\mathcal{G}_1}(x)| - ||E(H_2)| - |E(H_1)||$$
$$- \sum_{l=1}^{2} \sum_{gx \in E(H_l)} |m_{\mathcal{G}_1}(g) - m_{\mathcal{G}_1}(x)|$$
$$= ||E(H_1)| - |E(H_2)|| - ||E(H_1)| + |E(H_2)||.$$

There are two cases:

1. if $|E(H_1)| > |E(H_2)|$, then we get $|E(H_1)| - |E(H_2)| - |E(H_1)| - |E(H_2)| = -2|E(H_2)| < 0$, and

2. if $|E(H_1)| < |E(H_2)|$, then we get $-|E(H_1)| + |E(H_2)| - |E(H_1)| - |E(H_2)| = -2|E(H_1)| < 0$.
   In either case, we acquire $Mo_e(\mathcal{G}_1) - Mo_e(\mathcal{G}_2) < 0$.
   This completes the proof. ■
   Next, we establish a new $\mathcal{G}_2$ graph from $\mathcal{G}_1$ by moving all pendent edges, all C_4 cycles, and all C_3 cycles from different vertices of a fixed cycle C_s to a unique vertex, such that the new graph has a larger edge Mostar invariant.

Lemma 2.2: *Let $\mathcal{G}$ be a cyclic graph constructed by attaching r_i, for $r_i \geq 0$, number of pendent vertices, t_i, for $t_i \geq 0$, number of C_4 cycles and m_i, for $m_i \geq 0$, number of C_3 cycles, at the vertices v_i, for $1 \leq i \leq s - 1$, of C_s, where $s \geq 3$. Consider a graph H having a common vertex $v \in V(H)$ with $\mathcal{G}$ and present it by $\mathcal{G}_1$. We construct $\mathcal{G}_2$ from $\mathcal{G}_1$ by removing all the pendent vertices, C_4's, and C_3's of $\mathcal{G}$ and attaching them at v (see **Figure 3**). Then, we have $Mo_e(\mathcal{G}_1) < Mo_e(\mathcal{G}_2)$.*

Proof: Suppose that the vertices of C_s are $v_0(= v), v_1, v_2, \ldots, v_{s-1}$ and there are r_i number of pendent edges, t_i number of C_4 cycles, and m_i number of C_3 cycles rooted at v_i, for $1 \leq i \leq s - 1$, in $\mathcal{G}_1$. By the construction of $\mathcal{G}_2$, the number of closer edges of the end vertices of a fixed edge of H in $\mathcal{G}_1$ remains the same in $\mathcal{G}_2$. Therefore, for any edge $u_1 u_2 \in E(H)$, we have the following:

$$m_{\mathcal{G}_1}(u_1) = m_{\mathcal{G}_2}(u_1), \qquad m_{\mathcal{G}_1}(u_2) = m_{\mathcal{G}_2}(u_2). \qquad (5)$$

For the pendent edges $v_i u$ rooted on v_i, for $1 \leq i \leq s - 1$ and $u \in P(\mathcal{G})$, in $\mathcal{G}_1$, we have the following:

$$m_{\mathcal{G}_1}(v_i) = |E(H)| + |E(\mathcal{G})| - 1, m_{\mathcal{G}_1}(u) = 0 = m_{\mathcal{G}_2}(u) \, m_{\mathcal{G}_2}(v = v_0)$$
$$= |E(H)| + |E(\mathcal{G})| - 1.$$
$$(6)$$

For every C_4 cycle rooted on a fixed vertex v_i, for $1 \leq i \leq s - 1$, the edge set is $\{w_0 w_1, w_1 w_2, w_2 w_3, w_3 w_0\}$, and then, there are the following cases:
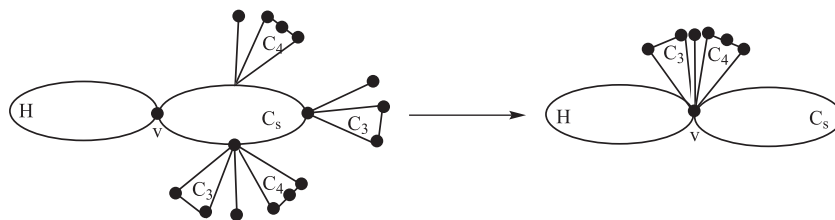
FIGURE 3 | Graphs $\mathcal{G}_1$ and $\mathcal{G}_2$ of Lemma 2.2.

1. For $w_i w_{i+1}$, $i = 0, 1$, we have $m_{\mathcal{G}_1}(w_i) = |E(H)| + |E(\mathcal{G})| - 3 = m_{\mathcal{G}_2}(w_i)$ and $m_{\mathcal{G}_1}(w_{i+1}) = 1 = m_{\mathcal{G}_2}(w_{i+1})$.

2. For $w_2 w_3$, we have $m_{\mathcal{G}_1}(w_3) = |E(H)| + |E(\mathcal{G})| - 3 = m_{\mathcal{G}_2}(w_3)$ and $m_{\mathcal{G}_1}(w_2) = 1 = m_{\mathcal{G}_2}(w_2)$.

3. For $w_0 w_3$, we have $m_{\mathcal{G}_1}(w_0) = |E(H)| + |E(\mathcal{G})| - 3 = m_{\mathcal{G}_2}(w_0)$ and $m_{\mathcal{G}_1}(w_3) = 1 = m_{\mathcal{G}_2}(w_3)$.

For every C_3 cycle rooted on a fixed vertex v_i, for $1 \le i \le s - 1$, the edge set is $\{g_0 g_1, g_1 g_2, g_2 g_3, g_3 g_0\}$, and then, there are the following cases:

1. For $g_0 g_1$, we have $m_{\mathcal{G}_1}(g_0) = |E(H)| + |E(\mathcal{G})| - 2 = m_{\mathcal{G}_2}(g_0)$ and $m_{\mathcal{G}_1}(g_1) = 1 = m_{\mathcal{G}_2}(g_1)$.

2. For $g_1 g_2$, we have $m_{\mathcal{G}_1}(g_3) = m_{\mathcal{G}_1}(g_2)$ and $m_{\mathcal{G}_2}(g_3) = m_{\mathcal{G}_2}(g_2)$.

3. For $g_0 g_2$, we have $m_{\mathcal{G}_1}(g_0) = |E(H)| + |E(\mathcal{G})| - 2 = m_{\mathcal{G}_2}(g_0)$ and $m_{\mathcal{G}_1}(g_2) = 1 = m_{\mathcal{G}_2}(g_2)$.

Suppose C_s is an even cycle; then there are the following cases:

1. For $v_0 v_1$, we have $m_{\mathcal{G}_1}(v_0) = |E(H)| + \frac{s}{2} - 1 + \sum_{p=\frac{s}{2}+1}^{\frac{s}{2}} (r_p + t_p + m_p)$ and $m_{\mathcal{G}_1}(v_1) = \frac{s}{2} - 1 + \sum_{p=1}^{\frac{s}{2}} (r_p + t_p + m_p)$.

2. For $v_i v_{i+1}$, where $1 \le i \le \frac{s}{2} - 1$, we have $m_{\mathcal{G}_1}(v_i) = |E(H)| + \frac{s}{2} - 1 + \sum_{p=\frac{s}{2}+i+1}^{s-1} (r_p + t_p + m_p) + \sum_{p=1}^{i} (r_p + t_p + m_p)$ and $m_{\mathcal{G}_1}(v_{i+1}) = \frac{s}{2} - 1 + \sum_{p=i+1}^{\frac{s}{2}+i} (r_p + t_p + m_p)$.

3. For $v_i v_{i+1}$, where $\frac{s}{2} \le i \le s - 2$, we have $m_{\mathcal{G}_1}(v_i) = \frac{s}{2} - 1 + \sum_{p=i-\left(\frac{s}{2}-1\right)}^{i} (r_p + t_p + m_p)$ and $m_{\mathcal{G}_1}(v_{i+1}) = |E(H)| + \frac{s}{2} - 1 + \sum_{p=i+1}^{s-1} (r_p + t_p + m_p) + \sum_{p=1}^{i-s} (r_p + t_p + m_p)$.

4. For $v_0 v_{s-1}$, we have $m_{\mathcal{G}_1}(v_0) = |E(H)| + \frac{s}{2} - 1 + \sum_{p=1}^{\frac{s}{2}-1} (r_p + t_p + m_p)$ and $m_{\mathcal{G}_1}(v_{s-1}) = \frac{s}{2} - 1 + \sum_{p=\frac{s}{2}}^{s-1} (r_p + t_p + m_p)$.

5. For $v_i v_{i+1}$, where $0 \le i \le \frac{s}{2} - 1$, we have $m_{\mathcal{G}_2}(v_i) = |E(H)| + \frac{s}{2} - 1 + \sum_{p=1}^{s-1} (r_p + t_p + m_p)$ and $m_{\mathcal{G}_2}(v_{i+1}) = \frac{s}{2} - 1$.

6. For $v_i v_{i+1}$, where $\frac{s}{2} \le i \le s - 2$, we have $m_{\mathcal{G}_2}(v_i) = \frac{s}{2} - 1$ and $m_{\mathcal{G}_2}(v_{i+1}) = |E(H)| + \frac{s}{2} - 1 + \sum_{p=1}^{s-1} (r_p + t_p + m_p)$.

7. For $v_0 v_{s-1}$, we have $m_{\mathcal{G}_2}(v_0) = |E(H)| + \frac{s}{2} - 1 + \sum_{p=1}^{s-1} (r_p + t_p + m_p)$ and $m_{\mathcal{G}_2}(v_{s-1}) = \frac{s}{2} - 1$.

Substituting the values from **Eqs 5**, **6** and the information from all the cases above in the definition of the edge Mostar invariant, we acquire the following:

$$
\begin{aligned}
Mo_e(\mathcal{G}_1) - Mo_e(\mathcal{G}_2) &= \sum_{u_1 u_2 \in E(H)} \left| m_{\mathcal{G}_1}(u_1) - m_{\mathcal{G}_1}(u_2) \right| + \sum_{v_i u \in E(\mathcal{G}), u \in P_{\mathcal{G}}(v_i)} \left| m_{\mathcal{G}_1}(v_i) - m_{\mathcal{G}_1}(u) \right| \\
&+ \sum_{i=0}^{3} \sum_{w_i w_{i+1} \in E(C_4)} \left| m_{\mathcal{G}_1}(w_i) - m_{\mathcal{G}_1}(w_{i+1}) \right| + \left| m_{\mathcal{G}_1}(w_0) - m_{\mathcal{G}_1}(w_3) \right| \\
&+ \sum_{i=0}^{2} \sum_{g_i g_{i+1} \in E(C_3)} \left| m_{\mathcal{G}_1}(g_i) - m_{\mathcal{G}_1}(g_{i+1}) \right| + \left| m_{\mathcal{G}_1}(g_0) - m_{\mathcal{G}_1}(g_2) \right| + \sum_{i=0}^{s-2} \left| m_{\mathcal{G}_1}(v_i) \right. \\
&- \left. m_{\mathcal{G}_1}(v_{i+1}) \right| + \left| m_{\mathcal{G}_1}(v_0) - m_{\mathcal{G}_1}(v_{s-1}) \right| - \sum_{u_1 u_2 \in E(H)} \left| m_{\mathcal{G}_2}(u_1) - m_{\mathcal{G}_2}(u_2) \right| \\
&- \sum_{vu \in E(\mathcal{G}), u \in P_{\mathcal{G}}(v_i)} \left| m_{\mathcal{G}_2}(u) - m_{\mathcal{G}_2}(v) \right| - \sum_{i=0}^{3} \sum_{w_i w_{i+1} \in E(C_4)} \left| m_{\mathcal{G}_2}(w_i) - m_{\mathcal{G}_2}(w_{i+1}) \right| \\
&- \left| m_{\mathcal{G}_2}(w_0) - m_{\mathcal{G}_2}(w_3) \right| - \sum_{i=0}^{2} \sum_{g_i g_{i+1} \in E(C_3)} \left| m_{\mathcal{G}_2}(g_i) - m_{\mathcal{G}_2}(g_{i+1}) \right| - \left| m_{\mathcal{G}_2}(g_0) \right. \\
&- \left. m_{\mathcal{G}_2}(g_2) \right| - \sum_{i=0}^{s-2} \left| m_{\mathcal{G}_2}(v_i) - m_{\mathcal{G}_2}(v_{i+1}) \right| - \left| m_{\mathcal{G}_2}(v_0) - m_{\mathcal{G}_2}(v_{s-1}) \right| \\
&= \sum_{u_1 u_2 \in E(H)} \left| m_{\mathcal{H}_1}(u_1) - m_{\mathcal{H}_1}(u_2) \right| + r ||E(H)| + |E(\mathcal{G})| - 1| + 4t ||E(H)| + |E(\mathcal{G})| - 4| + 2m ||E(H)| + |E(\mathcal{G})| - 3| \\
&+ \left| |E(H)| + \frac{s}{2} - 1 \right. \\
&+ \left. \sum_{p=\frac{s}{2}+i+1}^{s-1} (r_p + t_p + m_p) + \frac{s}{2} - 1 - \frac{s}{2} + 1 - \sum_{p=i+1}^{\frac{s}{2}+i} (r_p + t_p + m_p) \right| + \sum_{i=\frac{s}{2}}^{s-2} \left| \sum_{p=i-\left(\frac{s}{2}-1\right)}^{i} (r_p + t_p + m_p) \right. \\
&+ \left. \frac{s}{2} - 1 - \frac{s}{2} + 1 - \sum_{p=i+1}^{s-1} (r_p + t_p + m_p) - |E(H)| - \sum_{p=1}^{i} (r_p + t_p + m_p) \right| + \left| |E(H)| + \frac{s}{2} - 1 \right. \\
&+ \left. \sum_{p=\frac{s}{2}+1}^{s-1} (r_p + t_p + m_p) - \frac{s}{2} + 1 - \sum_{p=1}^{\frac{s}{2}} (r_p + t_p + m_p) \right| - \sum_{u_1 u_2 \in E(H)} \left| m_{\mathcal{H}_1}(u_1) - m_{\mathcal{H}_1}(u_2) \right| - r ||E(H)| \\
&+ |E(\mathcal{G})| - 1| - 4t ||E(H)| + |E(\mathcal{G})| - 4| - 2m ||E(H)| + |E(\mathcal{G})| - 3| - \sum_{i=0}^{\frac{s}{2}-1} \left| |E(H)| + \frac{s}{2} - 1 + \sum_{p=1}^{s-1} \right. \\
&\left. (r_p + t_p + m_p) - \frac{s}{2} + 1 \right| - \sum_{i=\frac{s}{2}}^{s-2} \left| \frac{s}{2} - 1 - |E(H)| - \frac{s}{2} + 1 - \sum_{p=1}^{s-1} (r_p + t_p + m_p) \right| - \left| |E(H)| + \frac{s}{2} - 1 + \sum_{p=1}^{s-1} (r_p + t_p + m_p) \right. \\
&\left. - \frac{s}{2} + 1 \right| \le |E(H)| + \sum_{p=1}^{s-1} (r_p + t_p + m_p) + \sum_{i=1}^{\frac{s}{2}-1} \left(|E(H)| + \sum_{p=1}^{s-1} (r_p + t_p + m_p) \right) + \sum_{i=\frac{s}{2}}^{s-2} \left(|E(H)| + \sum_{p=1}^{s-1} (r_p + t_p + m_p) \right) \\
&+ |E(H)| + \sum_{p=1}^{s-1} (r_p + t_p + m_p) - \sum_{i=0}^{\frac{s}{2}-1} \left(|E(H)| + \sum_{p=1}^{s-1} (r_p + t_p + m_p) \right) - \sum_{i=\frac{s}{2}}^{s-2} \left(|E(H)| + \sum_{p=1}^{s-1} (r_p + t_p + m_p) \right) \\
&- \left(|E(H)| + \sum_{p=1}^{s-1} (r_p + t_p + m_p) \right) \le |E(H)| + r + t + m + \sum_{i=1}^{s-2} (|E(H)| + r + t + m) - \sum_{i=0}^{s-2} (|E(H)| + r + t + m) \\
&\le |E(H)| + r + t + m + (s-2)(|E(H)| + r + t + m) - (s-1)(|E(H)| + r + t + m) \le 0.
\end{aligned}
$$

The proof for an odd cycle C_s is similar to that above; therefore, we omit it here. This completes the proof. ∎
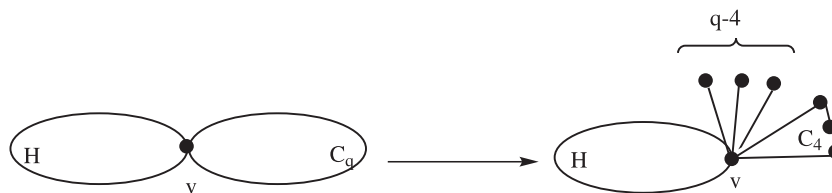
FIGURE 4 | Graphs $\mathcal{G}_1$ and $\mathcal{G}_2$ of Lemma 2.3.

In Lemma 2.3, we establish a new graph $\mathcal{G}_2$ from a given graph $\mathcal{G}_1$ by replacing C_q with C_4 and attaching $q-4$ pendent edges in $\mathcal{G}_1$ such that the new graph has a greater edge Mostar invariant.

Lemma 2.3: *Consider a graph H having a common vertex* $v \in V(H)$ *with* C_q *such that* $\deg_H(v) \geq 3$ *and* $q \geq 5$, *and denote it as* $\mathcal{G}_1$. *Let* $\mathcal{G}_2$ *be the graph acquired from* G_1 *by replacing* C_q *with* C_4 *and attaching* $q-4$ *pendent edges at* $v \in V(H)$ *(see* **Figure 4**). *Then, we have* $Mo_e(\mathcal{G}_1) \leq Mo_e(\mathcal{G}_2)$.

Proof: Let H be a subgraph of $\mathcal{G}_1$ and the vertices of C_q be $v_0(=v), v_1, v_2, \ldots, v_{q-1}$, as shown in **Figure 4**. By the construction of $\mathcal{G}_2$, the number of closer edges of the end vertices of a fixed edge of H in $\mathcal{G}_1$ remains the same in $\mathcal{G}_2$. Therefore, for any edge $u_1u_2 \in E(H)$, we have the following:

$$m_{\mathcal{G}_1}(u_1) = m_{\mathcal{G}_2}(u_1), \quad m_{\mathcal{G}_1}(u_2) = m_{\mathcal{G}_2}(u_2). \tag{7}$$

Suppose q is even; then there are three cases:

1. For v_iv_{i+1}, where $0 \leq i \leq \frac{q}{2}-1$, we have $m_{\mathcal{G}_1}(v_i) = |E(H)| + \frac{q}{2} - 1$ and $m_{\mathcal{G}_1}(v_{i+1}) = \frac{q}{2} - 1$.
2. For v_iv_{i+1}, where $\frac{q}{2} \leq i \leq q-2$, we have $m_{\mathcal{G}_1}(v_i) = \frac{q}{2} - 1$ and $m_{\mathcal{G}_1}(v_{i+1}) = |E(H)| + \frac{q}{2} - 1$.
3. For v_0v_{q-1}, we have $m_{\mathcal{G}_1}(v_0) = |E(H)| + \frac{q}{2} - 1$ and $m_{\mathcal{G}_1}(v_{q-1}) = \frac{q}{2} - 1$.

Suppose q is odd; then there are three cases:

1. For v_iv_{i+1}, where $0 \leq i \leq \frac{q}{2}-1$, we have $m_{\mathcal{G}_1}(v_i) = |E(H)| + \frac{q-1}{2}$ and $m_{\mathcal{G}_1}(v_{i+1}) = \frac{q-1}{2}$.
2. For v_iv_{i+1}, where $\frac{q}{2} \leq i \leq q-2$, we have $m_{\mathcal{G}_1}(v_i) = \frac{q-1}{2}$ and $m_{\mathcal{G}_1}(v_{i+1}) = |E(H)| + \frac{q-1}{2}$.
3. For v_0v_{q-1}, we have $m_{\mathcal{G}_1}(v_0) = |E(H)| + \frac{q-1}{2}$ and $m_{\mathcal{G}_1}(v_{q-1}) = \frac{q-1}{2}$.

   In $\mathcal{G}_2$, for any pendent edge vv_i, where $4 \leq i \leq q-1$, rooted at v, we have the following:

$$m_{\mathcal{G}_2}(v) = |E(H)| + q - 1, \qquad m_{\mathcal{G}_2}(v_i) = 0. \tag{8}$$

For $v_0v_1, v_1v_2, v_2v_3, v_3v_0$ in $\mathcal{G}_2$, there are the following cases:

1. For v_iv_{i+1}, $i = 0, 1$, we have $m_{\mathcal{G}_2}(v_i) = |E(H)| + q - 3$ and $m_{\mathcal{G}_2}(v_{i+1}) = 1$.
2. For v_2v_3, we have $m_{\mathcal{G}_2}(v_3) = |E(H)| + q - 3$ and $m_{\mathcal{G}_2}(v_2) = 1$.
3. For v_0v_3, we have $m_{\mathcal{G}_2}(v_0) = |E(H)| + q - 3$ and $m_{\mathcal{G}_2}(v_3) = 1$.

Case 1: When q is even, using the definition of the edge Mostar invariant and substituting the values from **Eqs 7**, **8** and the cases above, we get the following:

$$Mo_e(\mathcal{G}_1) - Mo_e(\mathcal{G}_2) = \sum_{u_1u_2 \in E(H)} |m_{\mathcal{G}_1}(u_1) - m_{\mathcal{G}_1}(u_2)| + \sum_{i=0}^{q-2} |m_{\mathcal{G}_1}(v_i) - m_{\mathcal{G}_1}(v_{i+1})| + |m_{\mathcal{G}_1}(v_0)|$$

$$- m_{\mathcal{G}_1}(v_{q-1})| - \sum_{u_1u_2 \in E(H)} |m_{\mathcal{G}_2}(u_1) - m_{\mathcal{G}_2}(u_2)| - \sum_{i=4}^{q-1} |m_{\mathcal{G}_2}(v) - m_{\mathcal{G}_2}(v_i)|$$

$$- |m_{\mathcal{G}_2}(v_0) - m_{\mathcal{G}_2}(v_1)| - |m_{\mathcal{G}_2}(v_1) - m_{\mathcal{G}_2}(v_2)| - |m_{\mathcal{G}_2}(v_2) - m_{\mathcal{G}_2}(v_3)| - |m_{\mathcal{G}_2}(v_3) - m_{\mathcal{G}_2}(v_0)|$$

$$= \sum_{u_1u_2 \in E(H)} |m_{\mathcal{G}_1}(u_1) - m_{\mathcal{G}_1}(u_2)| + \sum_{i=0}^{\frac{q}{2}-1} \left| |E(H)| + \frac{q}{2} - 1 - \left(\frac{q}{2} - 1\right) \right|$$

$$+ \sum_{i=\frac{q}{2}}^{q-2} \left| \frac{q}{2} - 1 - \left(|E(H)| + \frac{q}{2} - 1\right) \right| + \left| |E(H)| + \frac{q}{2} - 1 - \left(\frac{q}{2} - 1\right) \right|$$

$$- \sum_{u_1u_2 \in E(H)} |m_{\mathcal{G}_2}(u_1) - m_{\mathcal{G}_2}(u_2)| - \sum_{i=4}^{q-1} ||E(H)| + q - 1 - 0| - 4||E(H)| + q - 3 - 1|$$

$$= \sum_{u_1u_2 \in E(H)} |m_{\mathcal{G}_1}(u_1) - m_{\mathcal{G}_1}(u_2)| + \sum_{i=0}^{\frac{q}{2}-1} |E(H)| + \sum_{i=\frac{q}{2}}^{q-2} |E(H)| + |E(H)|$$

$$- \sum_{u_1u_2 \in E(H)} |m_{\mathcal{G}_1}(u_1) - m_{\mathcal{G}_1}(u_2)| - \sum_{i=4}^{q-1} ||E(H)| + q - 1| - 4||E(H)| + q - 4| \leq q|E(H)|$$

$$- (q-4)|E(H)| - (q-4)q + (q-4) - 4|E(H)| - 4q + 16 \leq -q^2 + q + 12 < 0.$$

Case 2: When q is odd, using the definition of the edge Mostar invariant and substituting the values from **Eqs 7**, **8** and the cases above, we get the following:

$$Mo_e(\mathcal{G}_1) - Mo_e(\mathcal{G}_2) = \sum_{u_1u_2 \in E(H)} |m_{\mathcal{G}_1}(u_1) - m_{\mathcal{G}_1}(u_2)| + \sum_{i=0}^{q-2} |m_{\mathcal{G}_1}(v_i) - m_{\mathcal{G}_1}(v_{i+1})| + |m_{\mathcal{G}_1}(v_0)|$$

$$- m_{\mathcal{G}_1}(v_{q-1})| - \sum_{u_1u_2 \in E(H)} |m_{\mathcal{G}_2}(u_1) - m_{\mathcal{G}_2}(u_2)| - \sum_{i=4}^{q-1} |m_{\mathcal{G}_2}(v) - m_{\mathcal{G}_2}(v_i)| - |m_{\mathcal{G}_2}(v_0) - m_{\mathcal{G}_2}(v_1)|$$

$$- |m_{\mathcal{G}_2}(v_1) - m_{\mathcal{G}_2}(v_2)| - |m_{\mathcal{G}_2}(v_2) - m_{\mathcal{G}_2}(v_3)| - |m_{\mathcal{G}_2}(v_3) - m_{\mathcal{G}_2}(v_0)|,$$

$$Mo_e(\mathcal{G}_1) - Mo_e(\mathcal{G}_2) = \sum_{u_1u_2 \in E(H)} |m_{\mathcal{G}_1}(u_1) - m_{\mathcal{G}_1}(u_2)| + \sum_{i=0}^{\frac{q-1}{2}} \left| |E(H)| + \frac{q-1}{2} - \left(\frac{q-1}{2}\right) \right|$$

$$+ \sum_{i=\frac{q}{2}}^{q-2} \left| \frac{q-1}{2} - \left(|E(H)| + \frac{q-1}{2}\right) \right| + \left| |E(H)| + \frac{q-1}{2} - \left(\frac{q-1}{2}\right) \right|$$

$$- \sum_{u_1u_2 \in E(H)} |m_{\mathcal{G}_2}(u_1) - m_{\mathcal{G}_2}(u_2)| - \sum_{i=4}^{q-1} ||E(H)| + q - 1 - 0| - 4||E(H)| + q - 3 - 1|$$

$$= \sum_{u_1u_2 \in E(H)} |m_{\mathcal{G}_1}(u_1) - m_{\mathcal{G}_1}(u_2)| + \sum_{i=0}^{\frac{q-1}{2}} |E(H)| + \sum_{i=\frac{q}{2}}^{q-2} |E(H)| + |E(H)|$$

$$- \sum_{u_1u_2 \in E(H)} |m_{\mathcal{G}_1}(u_1) - m_{\mathcal{G}_1}(u_2)| - \sum_{i=4}^{q-1} ||E(H)| + q - 1| - 4||E(H)| + q - 4| \leq q|E(H)|$$

$$- (q-4)|E(H)| - (q-4)q + (q-4) - 4|E(H)| - 4q + 16 \leq -q^2 + q + 12 < 0.$$

This completes the proof. ∎

Lemma 2.4: *Consider a graph H having a common vertex* $v \in V(H)$ *with* C_3 *and at least one pendent edge* vu, *and this graph is presented as* $\mathcal{G}_1$. *Let* $\mathcal{G}_2$ *be the graph obtained from* $\mathcal{G}_1$ *by replacing* C_3 *and* vu *with* C_4 *(see* **Figure 5**). *Then, we have* $Mo_e(\mathcal{G}_1) < Mo_e(\mathcal{G}_2)$.

Proof: By the construction of $\mathcal{G}_2$, the number of closer edges of the end vertices of a fixed edge of H in $\mathcal{G}_1$ remains the same in $\mathcal{G}_2$. Therefore, for any edge $u_1u_2 \in E(H)$, we have the following:
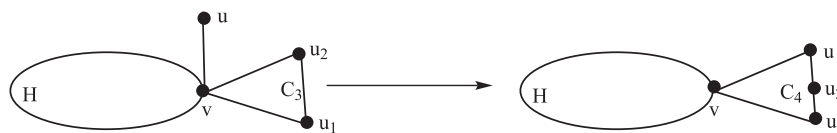
FIGURE 5 | Graphs $\mathcal{G}_1$. and $\mathcal{G}_2$ of Lemma 2.4.

$$m_{\mathcal{G}_1}(u_1) = m_{\mathcal{G}_2}(u_1), \qquad m_{\mathcal{G}_1}(u_2) = m_{\mathcal{G}_2}(u_2). \qquad (9)$$

There are the following cases in $\mathcal{G}_1$:

1. For pendent edge $uv \in E(\mathcal{G}_1)$, we have $m_{\mathcal{G}_1}(v) = |E(H)| + 3$ and $m_{\mathcal{G}_1}(u) = 0$.
2. For $vu_1 \in E(C_3)$, we have $m_{\mathcal{G}_1}(v) = |E(H)| + 2$ and $m_{\mathcal{G}_1}(u_1) = 1$.
3. For $vu_2 \in E(C_3)$, we have $m_{\mathcal{G}_1}(v) = |E(H)| + 2$ and $m_{\mathcal{G}_1}(u_2) = 1$.
4. For $u_1 u_2 \in E(C_3)$, we have $m_{\mathcal{G}_1}(u_1) = m_{\mathcal{G}_1}(u_2)$.
   By the construction of G_2, we have the following:

1. For $uv \in E(C_4)$, we have $m_{\mathcal{G}_2}(u) = 1$ and $m_{\mathcal{G}_1}(v) = |E(H)| + 1$.
2. For $vu_1 \in E(C_4)$, we have $m_{\mathcal{G}_2}(v) = |E(H)| + 1$ and $m_{\mathcal{G}_2}(u_1) = 1$.
3. For $u_1 u_2 \in E(C_4)$, we have $m_{\mathcal{G}_2}(u_1) = |E(H)| + 1$ and $m_{\mathcal{G}_2}(u_2) = 1$.
4. For $u_2 u \in E(C_4)$, we have $m_{\mathcal{G}_2}(u_2) = 1$ and $m_{\mathcal{G}_2}(u) = |E(H)| + 1$.
   Using the definition of the edge Mostar invariant and substituting the values from cases, we get the following:

$$
\begin{aligned}
Mo_e(\mathcal{G}_1) - Mo_e(\mathcal{G}_2) = & \sum_{u_1 u_2 \in E(H)} |m_{\mathcal{G}_1}(u_1) - m_{\mathcal{G}_1}(u_2)| + \sum_{i=0}^{q-2} |m_{\mathcal{G}_1}(v_i) - m_{\mathcal{G}_1}(v_{i+1})| \\
& + |m_{\mathcal{G}_1}(v_0) - m_{\mathcal{G}_1}(v_{q-1})| - \sum_{u_1 u_2 \in E(H)} |m_{\mathcal{G}_2}(u_1) - m_{\mathcal{G}_2}(u_2)| \\
& - \sum_{i=4}^{q-1} |m_{\mathcal{G}_2}(v) - m_{\mathcal{G}_2}(v_i)| - |m_{\mathcal{G}_2}(v_0) - m_{\mathcal{G}_2}(v_1)| \\
& - |m_{\mathcal{G}_2}(v_1) - m_{\mathcal{G}_2}(v_2)| - |m_{\mathcal{G}_2}(v_2) - m_{\mathcal{G}_2}(v_3)| - |m_{\mathcal{G}_2}(v_3) - m_{\mathcal{G}_2}(v_0)|,
\end{aligned}
$$

$$
\begin{aligned}
Mo_e(\mathcal{G}_1) - Mo_e(\mathcal{G}_2) = & \sum_{u_1 u_2 \in E(H)} |m_{\mathcal{G}_1}(u_1) - m_{\mathcal{G}_1}(u_2)| + \sum_{i=0}^{\frac{q}{2}-1} \left| |E(H)| + \frac{q-1}{2} - \left(\frac{q-1}{2} \right) \right| \\
& + \sum_{i=\frac{q}{2}}^{q-2} \left| \frac{q-1}{2} - \left(|E(H)| + \frac{q-1}{2} \right) \right| + \left| |E(H)| + \frac{q-1}{2} - \left(\frac{q-1}{2} \right) \right| \\
& - \sum_{u_1 u_2 \in E(H)} |m_{\mathcal{G}_2}(u_1) - m_{\mathcal{G}_2}(u_2)| - \sum_{i=4}^{q-1} ||E(H)| + q - 1 - 0| \\
& - 4||E(H)| + q - 3 - 1| = \sum_{u_1 u_2 \in E(H)} |m_{\mathcal{G}_1}(u_1) - m_{\mathcal{G}_1}(u_2)| \\
& + \sum_{i=0}^{\frac{q}{2}-1} |E(H)| + \sum_{i=\frac{q}{2}}^{q-2} |E(H)| + |E(H)| - \sum_{u_1 u_2 \in E(H)} |m_{\mathcal{G}_1}(u_1) - m_{\mathcal{G}_1}(u_2)| \\
& - \sum_{i=4}^{q-1} ||E(H)| + q - 1| - 4||E(H)| + q - 4| \leq q|E(H)| \\
& - (q-4)|E(H)| - (q-4)q + (q-4) - 4|E(H)| \\
& - 4q + 16 \leq -q^2 + q + 12 < 0.
\end{aligned}
$$

This completes the proof. ■

Theorem 2.1: *Among all the cacti graphs in* $\mathfrak{C}(n,s)$, *the cactus* $\widehat{\mathfrak{C}}(n,s)$, *for* $n \geq 3s + 2$, $s \geq 2$ *and for* $n \geq 9$, $s = 1$, *shown in* **Figure 1** *has the largest edge Mostar invariant. Thus, for any cactus* $G \in \mathfrak{C}(n,s)$, *we have* $Mo_e(\mathcal{G}) \leq Mo_e(\tilde{\mathfrak{C}}(n,s))$.

Proof: Let $\mathcal{G} \in \mathfrak{C}(n,s)$ be a cactus graph where $s \geq 0$ and $n \geq 2$. If $\mathcal{G} \not\cong \tilde{\mathfrak{C}}(n,s)$ and $\mathcal{G}$ has a cut edge, then repeatedly applying Lemma 2.1, we get a sequence of new cacti graphs $\mathcal{G}_1, \mathcal{G}_2, \ldots, \mathcal{G}_b$, where $\mathcal{G}_b$ is a cactus without any cut edge, such that $Mo_e(\mathcal{G}) < Mo_e(\mathcal{G}_1) < Mo_e(\mathcal{G}_2) < \cdots < Mo_e(\mathcal{G}_b)$. Now, if $\mathcal{G}_b \not\cong \tilde{\mathfrak{C}}(n,s)$ and $\mathcal{G}_b$ have a cyclic subgraph $\mathcal{G}'$ that is constructed by attaching r_i, for $r_i \geq 0$, number of pendent vertices, t_i, for $t_i \geq 0$, number of C_4 cycles and m_i, for $m_i \geq 0$, number of C_3 cycles, at the vertices v_i, for $1 \leq i \leq s - 1$, of C_s, where $s \geq 3$, then by applying Lemma 2.2 repeatedly, we acquire a sequence of cacti graphs $\mathcal{G}_b, \mathcal{G}_{b_1}, \mathcal{G}_{b_2}, \ldots, \mathcal{G}_{b_k}$ satisfying $Mo_e(\mathcal{G}_b) < Mo_e(\mathcal{G}_{b_1}) < Mo_e(\mathcal{G}_{b_2}) < \cdots < Mo_e(\mathcal{G}_{b_k})$, where $\mathcal{G}_{b_k}$ is a cactus graph such that every vertex of cycles of $\mathcal{G}_{b_k}$ has degree 2 except common vertices. If $\mathcal{G}_{b_k} \not\cong \tilde{\mathfrak{C}}(n,s)$ and $\mathcal{G}_{b_k}$ have a cycle C_q, for $q \geq 5$, then by applying Lemma 2.3 repeatedly, we acquire a sequence of cacti graphs $\mathcal{G}_{b_k}, \mathcal{G}_{b_{k_1}}, \mathcal{G}_{b_{k_2}}, \ldots, \mathcal{G}_{b_{k_c}}$ satisfying $Mo_e(\mathcal{G}_{b_k}) < Mo_e(\mathcal{G}_{b_{k_1}}) < Mo_e(\mathcal{G}_{b_{k_2}}) < \ldots < Mo_e(\mathcal{G}_{b_{k_c}})$, where $\mathcal{G}_{b_{k_c}} \cong \tilde{\mathfrak{C}}(n,s)$. If $\mathcal{G}_{b_{k_c}}$ has a triangle C_3 and at least one pendent edge vw, then by using Lemma 2.4, we construct a cactus graph $\mathcal{G}'_{b_{k_c}}$ with a cycle C_4 and get the greatest Mostar invariant and then $Mo_e(\mathcal{G}_{b_{k_c}})$.

This completes the proof. ■

By Theorem 2.1 and simple calculation, we have the following results:

Corollary 2.1. *Let* $\mathcal{G} \in \mathfrak{C}(n,s)$ *be a cactus graph with* $n \geq 2$ *and number of cycles s; then we have the following:*

$$
Mo_e(\mathcal{G}) \leq
\begin{cases}
n^2 - 3n + 2, & \text{if } s = 0 \text{ and } n \geq 2, \\
n^2 - n - 12, & \text{if } s = 1 \text{ and } n \geq 9, \\
n^2 + (2s - 3)n + s^2 - 15s + 2, & \text{if } s \geq 2 \text{ and } n \geq 3s + 2,
\end{cases}
$$

equality holds if $\mathcal{G} \cong \tilde{\mathfrak{C}}(n,s)$.

3 CONCLUSION

The ongoing direction of numerical coding of the fundamental chemical structures with topological descriptors has been substantiated as completely victorious. This approach substantiates the contrast, quarry, renewal, interpretation, and swift troupe of chemical structures within enormous particularities. Eventually, topological descriptors can lead to productive measures for quantitative structure–activity relationships (QSARs) and quantitative structure–property relationships (QSPRs), which are imitations that identify chemical structures with chemical reactivity, physical properties, or biological activity. The edge Mostar index is a newly proposed quantity; it has not been used in physicochemical or biological research.

Recently, a work (Imran et al., 2020) has been completed in this direction for chemical structures and nanostructures using graph operations. The authors have found the edge Mostar indices of nanostructures. Motivated by these results, we have studied the maximum edge Mostar invariant of the n-vertex cacti graphs with a fixed number of cycles in this study. For this, we have proved some lemmas in which we use the transformation of graphs and some calculations. In future, we want to find the largest and smallest edge Mostar invariants of the n-vertex cacti graphs with some fixed parameters other than the number of cycles.

REFERENCES

Akhter, S., Imran, M., and Iqbal, Z. (2021). Mostar Indices of Nanostructures and Melem Chain Nanostructures. *Int. J. Quan. Chem.* 121, e26520. doi:10.1002/qua.26520

Akhter, S., Iqbal, Z., Aslam, A., and Gao, W. (2020). *Mostar index of Graph Operations*, 09416. arXiv:2005.

Akhter, S. (2019). Two Degree Distance Based Topological Indices of Chemical Trees. *IEEE Access* 7, 95653–95658. doi:10.1109/access.2019.2927091

Arockiaraj, M., Clement, J., and Tratnik, N. (2019). Mostar Indices of Carbon Nanostructures and Circumscribed Donut Benzenoid Systems. *Int. J. Quan. Chem.* 119 (24), e26043. doi:10.1002/qua.26043

Arockiaraj, M., Clement, J., Tratnik, N., Mushtaq, S., and Balasubramanian, K. (2020). Weighted Mostar Indices as Measures of Molecular Peripheral Shapes with Applications to Graphene, Graphyne and Graphdiyne Nanoribbons. *SAR QSAR Environ. Res.* 31 (3), 187–208. doi:10.1080/1062936x.2019.1708459

Chen, S. (2016). Cacti with the Smallest, Second Smallest, and Third Smallest Gutman index. *J. Comb. Optim.* 31 (1), 327–332. doi:10.1007/s10878-014-9743-z

Dehgardi, N., and Azari, M. (2020). More on Mostar index. *Appl. Math. E-notes* 20, 316–322. doi:10.24869/psyd.2017.39

Deng, K. C., and Li, S. (2021). Chemical Trees with Extremal Mostar index. *MATCH Commun. Math. Comput. Chem.* 85, 161–180. doi:10.2298/fil1919453h

Deng, K., and Li, S. (2020). Extremal Catacondensed Benzenoids with Respect to the Mostar index. *J. Math. Chem.* 58, 1437–1465. doi:10.1007/s10910-020-01135-0

Deng, K., and Li, S. (2021). On the Extremal Values for the Mostar index of Trees with Given Degree Sequence. *Appl. Math. Comput.* 390, 125598. doi:10.1016/j.amc.2020.125598

Došlić, T., Martinjak, I., Škrekovski, R., Spužević, S. T., and Zubac, I. (2018). Mostar index. *J. Math. Chem.* 56 (10), 2995–3013. doi:10.1007/s10910-018-0928-z

Ghorbani, M., Rahmani, S., and Eslampoor, M. J. (2020). Some New Results on Mostar index of Graphs. *Iranian J. Math. Chem.* 11 (1), 33–42. doi:10.21136/cpm.1987.118302

Gutman, I. (2013). Degree-based Topological Indices. *Croat. Chem. Acta* 86 (4), 351–361. doi:10.5562/cca2294

Hayat, F., and Zhou, B. (2019). On Cacti with Large Mostar index. *Filomat* 33 (15), 4865–4873. doi:10.2298/fil1915865h

Hayat, F., and Zhou, B. (2019). On Mostar index of Trees with Parameters. *Filomat* 33 (19), 6453–6458. doi:10.2298/fil1919453h

Huang, S., Li, S., and Zhang, M. (2020). On the Extremal Mostar Indices of Hexagonal Chains. *MATCH Commun. Math. Comput. Chem.* 84, 249–271. doi:10.22541/au.161825077.77699117/v1

Imran, M., Akhter, S., and Iqbal, Z. (2020). Edge Mostar index of Chemical Structures and Nanostructures Using Graph Operations. *Int. J. Quan. Chem.* 120 (15), e26259. doi:10.1002/qua.26259

Knor, M., Škrekovski, R., and Tepeh, A. (2015). *Mathematical Aspects of Wiener index*. arXiv preprint arXiv:1510.00800.

Knor, M., and Škrekovski, R. (2014). "Wiener index of Line Graphs," in *Quantitative Graph Theory: Mathematical Foundations and Applications*. Editors M. Dehmer and F. Emmert-Streib (Upper Saddle River: CRC Press), 279–301.

Li, S., Yang, H., and Zhao, Q. (2012). Sharp Bounds on Zagreb Indices of Cacti with K Pendant Vertices. *Filomat* 26 (6), 1189–1200. doi:10.2298/fil1206189l

Li, X., and Shi, Y. (2008). A Survey on the Randić index. *MATCH Commun. Math. Comput. Chem.* 59 (1), 127–156. doi:10.1063/1.5020470

Liu, H., Song, L., Xiao, Q., and Tang, Z. (2020). On Edge Mostar index of Graphs, Iran. *J. Math. Chem.* 11 (2), 95–106. doi:10.1155/2021/6651220

Liu, J.-B., Wang, W.-R., Zhang, Y.-M., and Pan, X.-F. (2016). On Degree Resistance Distance of Cacti. *Discrete Appl. Math.* 203, 217–225. doi:10.1016/j.dam.2015.09.006

Mihalić, Z., and Trinajstić, N. (1992). A Graph-Theoretical Approach to Structure-Property Relationships. *J. Chem. Educ.* 69, 701–712.

Randic, M. (1975). Characterization of Molecular Branching. *J. Am. Chem. Soc.* 97, 6609–6615. doi:10.1021/ja00856a001

Tepeh, A. (2019). Extremal Bicyclic Graphs with Respect to Mostar index. *Appl. Math. Comput.* 355, 319–324. doi:10.1016/j.amc.2019.03.014

Tratnik, N. (2019). *Computing the Mostar index in Networks with Applications to Molecular Graphs*. arxiv.org/abs/1904.04131.

Vukičević, D. (2011). Bond Additive Modeling 4. QSPR and QSAR Studies of the Variable Adriatic Indices. *Croat. Chem. Acta* 84 (1), 87–91. doi:10.5562/cca1666

Vukičević, D., and Gašperov, M. (2010). Bond Additive Modeling 1. Adriatic Indices. *Croat. Chem. Acta* 83 (3), 243–260. doi:10.5562/cca1666

Wang, C., Wang, S., and Wei, B. (2016). Cacti with Extremal PI index. *Trans. Comb.* 5, 1–8. doi:10.3390/math7010083

Wang, D. F., and Tan, S. W. (2015). The Maximum Hyper-Wiener index of Cacti. *J. Appl. Math. Comput.* 47 (1-2), 91–102. doi:10.1007/s12190-014-0763-8

Wang, H., and Kang, L. (2013). On the Harary index of Cacti. *J. Appl. Math. Comput.* 43 (1-2), 369–386. doi:10.1007/s12190-013-0668-y

Wang, S. (2017). On Extremal Cacti with Respect to the Szeged index. *Appl. Math. Comput.* 309, 85–92. doi:10.1016/j.amc.2017.03.036

Wang, S., and Wei, B. (2016). Multiplicative Zagreb Indices of Cacti. *Discrete Math. Algorithm. Appl.* 08, 1650040. doi:10.1142/s1793830916500403

Wiener, H. (1947). Structural Determination of Paraffin Boiling Points. *J. Am. Chem. Soc.* 69 (1), 17–20. doi:10.1021/ja01193a005

Zhou, B., and Trinajstić, N. (2008). Bounds on the Balaban index. *Croat. Chem. Acta* 81 (2), 319–323. doi:10.1016/j.amc.2015.07.021

DATA AVAILABILITY STATEMENT

The original contributions presented in the study are included in the article/Supplementary Material; further inquiries can be directed to the corresponding author.

AUTHOR CONTRIBUTIONS

FY: Data curation; investigation; methodology; project administration; software; validation. SA: Conceptualization; formal analysis; methodology; visualization. KA: Methodology; resources; visualization; writing-review and editing. SR: Visualization.

Synthesis and Antifungal Activity of Pyrimidine Derivatives Containing an Amide Moiety

Wenneng Wu *, Wenjun Lan, Chenyan Wu and Qiang Fei *

Food and Pharmaceutical Engineering Institute, Guiyang University, Guiyang, China

In this study, 17 novel pyrimidine derivatives containing an amide moiety were synthesized. Then their *in vitro* antifungal activities against *Botryosphaeria dothidea* (*B. dothidea*), *Phomopsis* sp., and *Botrytis cinereal* (*B. cinereal*) were determined. A preliminary biological test showed that compounds 5-bromo-2-fluoro-*N*-(2-((2-methyl-6-(trifluoromethyl) pyrimidin-4-yl)oxy)phenyl)benzamide (**5f**) and 5-bromo-2-fluoro-*N*-(3-((2-methyl-6-(trifluoromethyl)pyrimidin-4-yl)oxy)phenyl)benzamide (**5o**) exhibited higher antifungal activity against *Phomopsis* sp., with an inhibition rate of 100% compared to that of Pyrimethanil at 85.1%. In particular, compound **5o** exhibited excellent antifungal activity against *Phompsis* sp., with the EC_{50} value of 10.5 μg/ml, which was even better than that of Pyrimethanil (32.1 μg/ml). As far as we know, this is the first report on the antifungal activities against *B. dothidea*, *Phomopsis* sp., and *B. cinereal* of this series of pyrimidine derivatives containing an amide moiety.

Keywords: pyrimidine, amide, synthesize, antifungal activity, kiwifruit soft rot disease

INTRODUCTION

Plant fungal diseases pose serious threats to crop production and caused huge economic losses throughout the world (Strange and Scott, 2005). In recent years, crop cultivators continually battle with plant fungal diseases affecting crops. The available traditional fungicides used for plant fungal diseases control represent a danger to the living system by killing not only the target fungi but also affecting beneficial living systems (Patel et al., 2014). To protect crops from fungal diseases, commercial agriculture relies heavily on the inputs of chemical pesticides. The resistance of plant fungal diseases against fungicides is rapidly becoming a serious problem. Therefore, the development of novel and promising fungicides is urgently required.

Pyrimidines are important substances in the synthesis of various active molecules that are extensively used in the intermediate skeleton of agrochemicals (Chen et al., 2015; Wu et al., 2015) and have attracted more and more attention due to their extensive biological activities (Sun et al., 2006), including antiviral (Wu et al., 2016a), antibacterial (Wu et al., 2016b), antifungal (Wu et al., 2019, 2020), and insecticidal (Liu et al., 2017; Wu et al., 2020) activities. For example, Zan et al. reported pyrimidine derivatives bearing a dithioacetal moiety as effective antiviral agents for controlling the tomato chlorosis virus (ToCV) (Zan et al., 2021). Zhang et al. found a series of arylpyrazole pyrimidine ether derivatives with promising bioactivity for combating cucumber downy mildew (Zhang et al., 2019). Li and coworkers showed that pyrimidine thiourea derivatives had good herbicidal activities against *Digitaria adscendens* and *Amaranthus retroflexus* (Li et al., 2021a). In the past few years, several pyrimidine compounds have been commercialized as fungicides (such as Pyrimethanil, Fenarimol, Diflumetorim, and Mepanioyrim) for controlling plant fungal diseases,
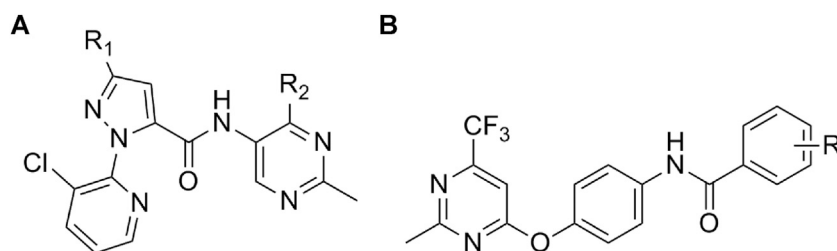
FIGURE 1 | Structures of pyrimidine derivatives containing an amide moiety reported in our previous works.

FIGURE 2 | EC$_{50}$ values of the target compounds **5f**, **5o,** and **5p** against *Phomopsis* sp.

such as cucumber gray mold (Wang et al., 2021), grape downy mildew (Huang et al., 2018), kiwifruit leaf spot (Shi et al., 2021), and so on. Due to the excellent features of low toxicity, the fact that it is easily synthetized and derived, and considering pyrimidine as a parent compound, the development of promising agrochemical candidates will soon become a reality. Meanwhile, amine, a key moiety in heterocyclic chemistry, play a leading role in pesticide chemistry due to their potent bioactivities including antifungal (Cheng et al., 2020; Chen et al., 2021a), antibacterial (Chen et al., 2021a), antiviral (Tang et al., 2020), herbicidal (Sun et al., 2020), and insecticidal (Chen et al., 2021b; Li et al., 2021b) activities. In our previous work, we reported a series of novel pyrimidine derivatives containing an amine moiety (**Figure 1**) and found that the target compounds revealed certain antifungal, insecticidal, and antiviral activities (Wu et al., 2016a; Wu et al., 2020).

This study aimed to design and synthesize a series of novel pyrimidine derivatives containing an amide moiety, and investigate their *in vitro* antifungal activities against *Botryosphaeria dothidea* (*B. dothidea*), *Phomopsis* sp., and *Botrytis cinereal* (*B. cinereal*). A biological test showed that compound 5-bromo-2-fluoro-*N*-(3-((2-methyl-6-(trifluoromethyl)pyrimidin-4-yl)oxy) phenyl)benzamide (**5o**) exhibited excellent antifungal activity against *Phompsis* sp., with an EC$_{50}$ value of 10.5 μg/ml, which is even better than Pyrimethanil (32.1 μg/ml).

MATERIALS AND METHODS

General Information
The melting points of the products were determined on an XT-4 binocular microscope (Beijing Tech Instrument Co., China) and were not corrected. ^{1}H and ^{13}C NMR (solvent DMSO-d_6) spectra were recorded on a Bruker AVANCE HD 600 MHz Digital NMR Spectrometer (Bruker Company, Billerica, MA, United States) at room temperature using TMS as an internal standard. High-resolution mass spectrometry (HRMS) was carried out on an Agilent Technologies 6540 UHD Accurate-Mass Q-TOF LC/MS (Agilent Technologies, Palo Alto, CA, United States). All anhydrous solvents were dried and purified according to standard techniques before use. Unless otherwise noted, all common reagents and solvents were used as obtained from commercial supplies without further purifications.

Synthesis
General Procedure for the Preparation of the Intermediates 2–4
As shown in **Scheme 1**, to a 250 ml round bottom flask, trifluoroacetoacetate (**1**, 0.05 mol), acetamidine hydrochloride (0.05 mol), sodium methoxide (0.075 mol), and ethanol (100 ml) were added and refluxed for 10 h. After that, the mixture was acidified with dilute HCl to pH 7. The crude products were extracted using ethyl acetate to produce intermediate **2**. Then, intermediate **2** (0.05 mol), POCl$_3$ (0.1 mol), and CH$_3$CN (120 ml) were added to a 250 ml round bottom flask to react for 0.5 h at a reflux temperature and then diisopropylethylamine (0.06 mol) was added dropwise. After continuously refluxing for 8 h, excess POCl$_3$ and CH$_3$CN were distilled and then ice water (60 ml) was added. Finally, the mixture was alkalified with dilute NaOH to pH 9 and extracted using CH$_2$Cl$_2$ to give intermediate **3**.
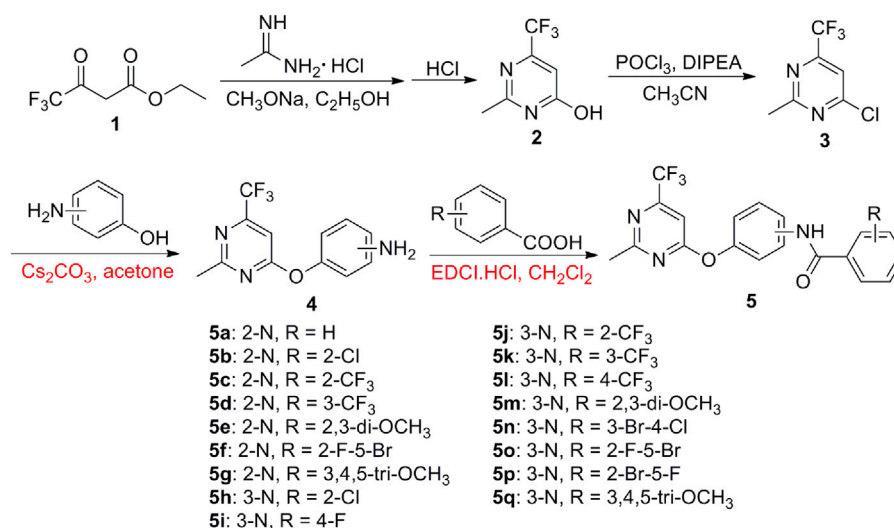
SCHEME 1 | Synthetic routes of the target compounds 5a–5q.

To a 50 ml three-necked round-bottomed flask equipped with a magnetic stirrer, the key intermediate **3** (0.01 mol) was dissolved in acetone (50 ml), Cs$_2$CO$_3$ (0.012 mol), and 3-aminophenol or 2-aminophenol (0.01 mol) were added. The reactions reacted for 5–6 h at room temperature, and the solvent was removed. The residue was added with water, the precipitate formed was filtered off and recrystallized from ethanol to give the intermediate **4**.

General Procedure for the Preparation of the Target Compounds 5a-5q

To a 50 ml three-necked round-bottomed flask equipped with a magnetic stirrer, the key intermediate **4** (0.02 mol), aromatic acid (0.02 mol), and dimethylaminopyridine (0.0002 mol) dissolved in dichloromethane (10 ml), and 1-(3-dimethylaminopropyl)-3-ethylcarbodiimide hydrochloride (0.03 mol) were added. The reactions were reacted for 8–10 h at room temperature. The solvent was then dried under vacuum and recrystallized from ethanol to give the pure target compounds **5a–5q**.

The structures were confirmed by ^{1}H NMR, ^{13}C NMR, and HRMS. ^{1}H NMR, ^{13}C NMR, and HRMS spectral data for the target compounds **5a–5q** are reported in the **Supplementary Material**. In the ^{1}H NMR spectra of **5a–5q**, one singlet at δ 9.70–10.74 ppm were attributed to the -CONH-. A singlet at δ 6.90–7.54 ppm demonstrated the presence of the proton of the pyrimidine fragment. A singlet at δ 2.31–2.54 ppm integrating for three protons was assigned to Pyrimidine-CH$_3$ protons. The structure of **5a–5q** was also confirmed by its HRMS spectral data. In all HRMS spectrum, the molecular ion peak was noticed m/z for ([M + H]$^+$) corresponding to all of the target molecular weight.

N-(2-((2-methyl-6-(trifluoromethyl)pyrimidin-4-yl)oxy) phenyl)benzamide (**5a**). White solid; yield 75%; m.p. 173–175°C; ^{1}H NMR (DMSO-d_6, 600 MHz, ppm) δ: 9.72 (s, 1H), 7.96 (d, 2H, *J* = 7.8 Hz), 7.76 (d, 1H, *J* = 7.2 Hz), 7.71 (t, 1H, *J* = 8.4 Hz), 7.53 (t,

2H, *J* = 9.0 Hz), 7.41–7.31 (m, 3H, Ph-H), 6.90 (s, 1H), 2.32 (s, 3H); ^{13}C NMR (DMSO-d_6, 150 MHz, ppm) δ: 168.66, 164.39, 162.11, 152.99 (q, *J* = 33.6 Hz), 144.29, 134.43, 130.75, 130.08, 129.35, 129.22, 126.84, 126.40, 125.99, 124.06, 122.24 (q, *J* = 272.85 Hz), 100.17, 25.75; HRMS (calcd.) for C$_{19}$H$_{14}$F$_3$N$_3$O$_2$ (M + H)$^+$ 374.1107, found 374.1107.

2-Chloro-*N*-(2-((2-methyl-6-(trifluoromethyl)pyrimidin-4-yl)oxy)phenyl)benzamide (5b). White solid; yield 49%; m.p. 157–158°C; ^{1}H NMR (DMSO-d_6, 600 MHz, ppm) δ: 9.73 (s, 1H), 7.93 (d, 1H, *J* = 7.8 Hz), 7.82 (d, 1H, *J* = 6.0 Hz), 7.66–7.63 (m, 2H), 7.49–7.46 (m, 1H), 7.43 (d, 1H, *J* = 7.8 Hz), 7.40–7.33 (m, 2H), 6.91 (s, 1H), 2.38 (s, 3H); ^{13}C NMR (DMSO-d_6, 150 MHz, ppm) δ: 168.75, 162.96, 162.24, 153.25 (q, *J* = 33.6 Hz), 144.14, 134.62, 133.51, 132.34, 131.70, 130.75, 128.70, 127.80, 127.14, 126.60, 123.97, 122.28 (q, *J* = 272.55 Hz), 120.46, 100.24, 25.86; HRMS (calcd.) for C$_{19}$H$_{13}$ClF$_3$N$_3$O$_2$ (M + H)$^+$ 408.0721, found 408.0720.

N-(2-((2-methyl-6-(trifluoromethyl)pyrimidin-4-yl)oxy) phenyl)-2-(trifluoromethyl)benzamide (**5c**). White solid; yield 46%; m.p. 148–150°C; ^{1}H NMR (DMSO-d_6, 600 MHz, ppm) δ: 9.77 (s, 1H), 7.94 (t, 2H, *J* = 6.0 Hz), 7.86–7.81 (m, 3H), 7.41–7.36 (m, 3H), 6.92 (s, 1H), 2.39 (s, 3H); ^{13}C NMR (DMSO-d_6, 150 MHz, ppm) δ: 168.75, 163.97, 162.25, 153.52 (q, *J* = 33.6 Hz), 144.03, 133.33, 133.21, 131.22, 130.77, 129.50, 128.33, 128.11 (q, *J* = 31.95 Hz), 127.52, 127.36, 126.57, 124.65 (q, *J* = 272.1 Hz), 123.45, 122.25 (q, *J* = 272.7 Hz), 120.45, 100.23, 25.85; HRMS (calcd.) for C$_{20}$H$_{13}$F$_6$N$_3$O$_2$ (M + H)$^+$ 442.0985, found 442.0979.

N-(2-((2-methyl-6-(trifluoromethyl)pyrimidin-4-yl)oxy) phenyl)-3-(trifluoromethyl)benzamide (**5d**). White solid; yield 68%; m.p. 138–140°C; $_1$H NMR (DMSO-d_6, 600 MHz, ppm) δ: 9.81 (s, 1H), 8.30 (d, 1H, *J* = 7.8 Hz), 8.14 (s, 1H), 8.09 (d, 1H, *J* = 7.8 Hz), 7.82 (t, 1H, *J* = 7.8 Hz), 7.78 (d, 1H, *J* = 7.2 Hz), 7.48 (d, 1H, *J* = 8.4 Hz), 7.41–7.35 (m, 2H), 6.91 (s, 1H), 2.30 (s, 3H); ^{13}C NMR (DMSO-d_6, 150 MHz, ppm) δ: 168.66, 163.13, 162.04,

153.33 (q, J = 34.2 Hz), 144.11, 134.06, 130.82, 130.77, 130.60, 130.55, 130.16 (q, J = 31.65 Hz), 127.09, 126.44, 126.08, 126.00, 124.92 (q, J = 270.9 Hz), 124.18, 123.10 (q, J = 270.6 Hz), 100.10, 25.60; HRMS (calcd.) for $C_{20}H_{13}F_6N_3O_2$ (M + H)$^+$ 442.0985, found 442.0979.

2,3-Dimethoxy-*N*-(2-((2-methyl-6-(trifluoromethyl) pyrimidin-4-yl)oxy)phenyl)benzamide (5e). White solid; yield 50%; m.p. 130–131°C; ^{1}H NMR (DMSO-d_6, 600 MHz, ppm) δ: 7.63 (s, 1H), 7.54 (d, 1H, J = 7.6 Hz), 7.46 (t, 1H, J = 7.4 Hz), 7.41 (d, 1H, J = 8.1 Hz), 7.35–7.33 (m, 2H), 7.06 (d, 1H, J = 8.1 Hz), 6.97 (t, 1H, J = 7.9 Hz), 6.92 (d, 1H, J = 7.6 Hz), 3.76 (s, 3H), 3.69 (s, 3H), 2.40 (s, 3H); ^{13}C NMR (DMSO-d_6, 150 MHz, ppm) δ: 169.52, 168.91, 162.84, 156.21 (q, J = 35.25 Hz), 152.54, 147.60, 145.80, 132.19, 131.54, 130.54, 127.24, 124.32, 124.10, 121.66 (q, J = 273.45 Hz), 115.48, 108.51, 103.05, 61.44, 56.28, 25.56; HRMS (calcd.) for $C_{21}H_{18}F_3N_3O_4$ (M + H)$^+$ 434.1322, found 434.1318.

3,4,5-trimethoxy-*N*-(2-((2-methyl-6-(trifluoromethyl) pyrimidin-4-yl)oxy)phenyl)benzamide (5g). White solid; yield 58%; m.p. 127–128°C; ^{1}H NMR (DMSO-d_6, 600 MHz, ppm) δ: 9.74 (s, 1H), 7.72 (d, 1H, J = 7.8 Hz), 7.40–7.35 (m, 3H), 7.21 (s, 2H, Ph-H), 6.89 (s, 1H), 3.78 (s, 6H), 3.75 (s, 3H) 2.33 (s, 3H); ^{13}C NMR (DMSO-d_6, 150 MHz, ppm) δ: 168.77, 163.92, 153.21 (q, J = 34.6 Hz), 153.18, 142.77, 130.66, 126.93, 124.22, 120.40 (q, J = 272.3 Hz), 107.36, 60.67, 56.37, 25.76; HRMS (calcd.) for $C_{22}H_{20}F_3N_3O_5$ (M + H)$^+$ 464.1428, found 464.1420.

2-Chloro-*N*-(3-((2-methyl-6-(trifluoromethyl)pyrimidin-4-yl)oxy)phenyl)benzamide (5h). White solid; yield 62%; m.p.136–139°C; 1H NMR (DMSO-d_6, 600 MHz, ppm) δ: 10.74 (s, 1H), 7.75 (s, 1H), 7.62–7.58 (m, 3H), 7.54–7.52 (m, 2H), 7.49–7.45 (m, 2H), 7.04 (dd, 1H, J_1 = 1.3 Hz, J_2 = 8.0 Hz), 2.54 (s, 3H); ^{13}C NMR (DMSO-d_6, 150 MHz, ppm) δ: 170.52, 169.76, 165.62, 156.54 (q, J = 34.65 Hz), 155.83, 152.36, 140.85, 137.16, 131.74, 130.56, 130.40, 130.18, 129.43, 127.78, 123.67 (q, J = 273.45 Hz), 117.52, 117.46, 112.91, 103.46, 25.94; HRMS (calcd.) for $C_{19}H_{13}ClF_3N_3O_2$ (M + H)$^+$ 408.0721, found 408.0716.

4-Fluoro-*N*-(3-((2-methyl-6-(trifluoromethyl)pyrimidin-4-yl)oxy)phenyl)benzamide (5i). White solid; yield 85%; m.p. 136–139°C; ^{1}H NMR (DMSO-d_6, 600 MHz, ppm) δ: 9.72 (s, 1H), 8.06–8.04 (dd, 2H, J_1 = 5.4 Hz, J_2 = 8.4 Hz), 7.79 (d, 1H, J = 7.2 Hz), 7.41–7.35 (m, 5H), 7.31 (t, 1H, J = 7.8 Hz), 6.91 (s, 1H), 2.37 (s, 3H); ^{13}C NMR (DMSO-d_6, 150 MHz, ppm) δ: 168.67, 167.65, 165.07, 163.46, 162.07, 153.20 (q, J = 33.75 Hz), 144.08, 133.11, 130.74, 126.87, 126.30, 125.99, 125.89, 124.18, 122.23 (q, J = 272.85 Hz), 116.48, 100.25, 25.75; HRMS (calcd.) for $C_{19}H_{13}F_4N_3O_2$ (M + H)$^+$ 392.1017, found 392.1013.

***N*-(3-((2-methyl-6-(trifluoromethyl)pyrimidin-4-yl)oxy)phenyl)-2-(trifluoromethyl)benzamide (5j).** White solid; yield 73%; m.p. 140–142°C; ^{1}H NMR (DMSO-d_6, 600 MHz, ppm) δ: 10.80 (s, 1H), 7.87 (d, 1H, J = 7.7 Hz), 7.82 (t, 1H, J = 7.3 Hz), 7.75–7.72 (m, 3H), 7.58 (d, 1H, J = 7.9 Hz), 7.52 (s, 1H), 7.47 (t, 1H, J = 8.2 Hz), 7.05 (d, 1H, J = 7.7 Hz), 2.54 (s, 3H); ^{13}C NMR (DMSO-d_6, 150 MHz, ppm) δ: 170.48, 169.75, 166.26, 156.33 (q, J = 33.6 Hz), 152.36, 140.81, 136.36, 133.14, 130.55, 129.02, 126.84, 126.46 (q, J = 31.05 Hz), 123.32 (q, J = 271.8 Hz), 121.84 (q, J = 272.85 Hz), 117.50, 112.97, 103.46, 25.91; HRMS (calcd.) for $C_{20}H_{13}F_6N_3O_2$ (M + H)$^+$ 442.0985, found 442.0982.

N-(3-((2-methyl-6-(trifluoromethyl)pyrimidin-4-yl)oxy)phenyl)-3-(trifluoromethyl)benzamide (5k). White solid; yield 73%; m.p. 101–103°C; ^{1}H NMR (DMSO-d_6, 600 MHz, ppm) δ: 10.65 (s, 1H), 8.30 (s, 1H), 8.27 (d, 1H, J = 7.8 Hz), 7.97 (d, 1H, J = 7.7 Hz), 7.81–7.79 (m, 2H), 7.71 (d, 1H, J = 8.1 Hz), 7.50 (s, 1H), 7.48 (d, 1H, J = 8.2 Hz), 7.05 (d, 1H, J = 8.0 Hz), 2.53 (s, 3H); ^{13}C NMR (DMSO-d_6, 150 MHz, ppm) δ: 170.56, 169.79, 164.71, 156.34 (q, J = 33.6 Hz), 152.29, 140.81, 136.01, 132.35, 130.22, 130.02, 129.81 (q, J = 31.8 Hz), 128.74, 125.31 (q, J = 271.8 Hz), 124.75, 123.52, 121.82 (q, J = 273.0 Hz), 118.39, 117.52, 113.84, 103.36, 25.91; HRMS (calcd.) for $C_{20}H_{13}F_6N_3O_2$ (M + H)$^+$ 442.0985, found 442.0983.

***N*-(3-((2-methyl-6-(trifluoromethyl)pyrimidin-4-yl)oxy)phenyl)-4-(trifluoromethyl)benzamide (5l).** White solid; yield 80%; m.p. 94–96°C; ^{1}H NMR (DMSO-d_6, 600 MHz, ppm) δ: 10.66 (s, 1H), 8.15 (d, 2H, J = 8.4 Hz), 7.94 (d, 2H, J = 7.8 Hz), 7.79 (t, 1H, J = 1.8 Hz), 7.69 (d, 1H, J = 9.6 Hz), 7.52 (s, 1H), 7.49 (t, 1H, J = 8.4 Hz), 7.06 (d, 2H, J = 7.8 Hz), 2.53 (s, 3H); ^{13}C NMR (DMSO-d_6, 150 MHz, ppm) δ: 170.59, 169.80, 165.13, 156.34 (q, J = 34.6 Hz), 152.31, 140.83, 138.99, 132.11 (q, J = 31.62 Hz), 130.52, 129.16, 125.98, 125.31 (q, J = 273.25 Hz), 120.05 (q, J = 272.51 Hz), 118.35, 117.61 103.48, 25.98; HRMS (calcd.) for $C_{20}H_{13}F_6N_3O_2$ (M + H)$^+$ 442.0985, found 442.0978.

2,3-Dimethoxy-*N*-(3-((2-methyl-6-(trifluoromethyl)pyrimidin-4-yl)oxy)phenyl)benzamide (5m). White solid; yield 52%; m.p. 108–109°C; ^{1}H NMR (DMSO-d_6, 600 MHz, ppm) δ: 10. 47 (s, 1H), 7.78 (s, 1H), 7.62 (d, 1H, J = 7.9 Hz), 7.51 (s, 1H), 7.45 (t, 1H, J = 8.2 Hz), 7.22–7.17 (m, 2H), 7.13 (dd, 1H, J_1 = 1.4 Hz, J_2 = 7.3 Hz), 7.02 (dd, 1H, J_1 = 1.3 Hz, J_2 = 8.0 Hz), 3.87 (s, 3H), 3.82 (s, 3H), 2.54 (s, 3H); ^{13}C NMR (DMSO-d_6, 150 MHz, ppm) δ: 170.55, 169.79, 165.59, 156.31 (q, J = 34.8 Hz), 153.05, 152.35, 146.32, 141.05, 131.70, 130.46, 124.72, 121.85 (q, J = 273.45 Hz), 120.45, 117.54, 117.10, 115.23, 112.91, 103.40, 61.57, 56.42, 25.92; HRMS (calcd.) for $C_{21}H_{18}F_3N_3O_4$ (M + H)$^+$ 434.1322, found 434.1318.

3-Bromo-4-chloro-*N*-(3-((2-methyl-6-(trifluoromethyl)pyrimidin-4-yl)oxy)phenyl)benzamide (5n). White solid; yield 68%; m.p. 143–145°C; 1H NMR (DMSO-d_6, 600 MHz, ppm) δ: 10.56 (s, 1H), 8.35 (d, 1H, J = 1.9 Hz), 7.97 (dd, 1H, J_1 = 2.1 Hz, J_2 = 8.3 Hz), 7.80 (d, 1H, J = 8.4 Hz), 7.76 (s, 1H), 7.68 (d, 1H, J = 8.1 Hz), 7.54–7.52 (m, 2H, Ph-H), 7.49–7.46 (m, 2H), 7.04 (dd, 1H, J_1 = 1.4 Hz, J_2 = 8.0 Hz), 2.53 (s, 3H); ^{13}C NMR (DMSO-d_6, 150 MHz, ppm) δ: 170.54, 169.79, 163.71, 156.33 (q, J = 34.8 Hz), 152.27, 140.74, 137.07, 135.34, 133.25, 131.05, 130.42, 129.12, 122.11, 121.81 (q, J = 273.3 Hz), 118.31, 117.51, 113.76, 103.37, 25.92; HRMS (calcd.) for $C_{19}H_{12}BrClF_3N_3O_2$ (M + H)$^+$ 485.9826, found 485.9822.

5-Bromo-2-fluoro-*N*-(3-((2-methyl-6-(trifluoromethyl)pyrimidin-4-yl)oxy)phenyl)benzamide (5o). White solid; yield 52%; m.p.147–149 °C; ^{1}H NMR (DMSO-d_6, 600 MHz, ppm) δ: 10.74 (s, 1H), 7.89–7.87 (m, 1H), 7.79–7.77 (m, 1H, Ph-H), 7.73 (s, 1H), 7.60 (d, 1H, J = 7.9 Hz), 7.50 (s, 1H), 7.47 (t, 1H, J = 8.2 Hz), 7.38 (t, 1H, J = 9.3 Hz), 7.05 (dd, 1H, J_1 = 1.4 Hz, J_2 = 8.0 Hz), 2.53 (s, 3H); ^{13}C NMR (DMSO-d_6, 150 MHz, ppm) δ: 170.52, 169.76, 161.91, 159.46, 157.80, 156.32 (q, J = 34.65 Hz), 152.34, 140.55, 135.67, 132.64, 130.58, 127.15, 121.83 (q, J = 273.15 Hz), 119.24, 117.66, 116.63, 113.19, 103.42, 25.92;

TABLE 1 | The antifungal activities of the title compounds against *B. dothidea*, *Phomopsis* sp., and *B. cinereal* at 50 μg/ml.

Compounds	Inhibition rate (%)		
	B. dothidea	*Phomopsis* sp	*B. cinerea*
5a	75.6 ± 2.1	73.6 ± 2.2	60.3 ± 1.8
5b	76.2 ± 1.3	81.0 ± 1.3	73.1 ± 1.3
5c	62.5 ± 1.1	75.5 ± 1.8	80.0 ± 2.5
5d	70.5 ± 1.6	80.2 ± 2.2	70.6 ± 1.2
5e	54.6 ± 1.5	76.0 ± 1.4	73.3 ± 1.9
5f	72.3 ± 1.9	100.0 ± 2.1	59.7 ± 2.4
5g	46.8 ± 1.0	60.1 ± 2.0	73.8 ± 2.0
5h	78.5 ± 2.6	86.1 ± 1.9	75.8 ± 2.6
5i	82.1 ± 3.0	84.4 ± 2.1	79.6 ± 1.4
5g	72.4 ± 1.9	78.0 ± 2.2	72.1 ± 3.2
5k	76.9 ± 1.0	81.2 ± 1.8	77.5 ± 1.8
5l	81.1 ± 1.2	84.5 ± 1.7	80.4 ± 1.2
5m	48.9 ± 1.7	57.8 ± 1.3	83.6 ± 1.2
5n	84.1 ± 2.3	91.8 ± 1.4	79.7 ± 2.4
5o	88.5 ± 3.3	100.0 ± 1.0	84.7 ± 2.6
5p	79.9 ± 1.8	93.4 ± 1.5	75.2 ± 1.2
5q	54.5 ± 1.6	62.1 ± 1.4	80.5 ± 0.9
Pyrimethanil	84.4 ± 2.1	85.1 ± 1.4	82.8 ± 1.4

TABLE 2 | The EC50 values of the target compounds against *Phompsis* sp.

Compounds	Toxic regression equation	r	EC$_{50}$ (μg/mL)
5f	y = 2.42x + 3.62	0.99	15.1 ± 2.0
5o	y = 2.38x + 4.20	0.99	10.5 ± 1.4
5p	y = 3.45x + 2.65	0.99	19.6 ± 2.5
Pyrimethanil	y = 2.18x + 8.25	0.99	32.1 ± 2.0

HRMS(calcd.) for $C_{19}H_{12}BrF_4N_3O_2$ (M + H)$^+$ 470.0122, found 470.0117.

2-Bromo-5-fluoro-*N*-(3-((2-methyl-6-(trifluoromethyl) pyrimidin-4-yl)oxy)phenyl)benzamide (5p). White solid; yield 60%; m.p.152–153 °C; 1H NMR (DMSO-d_6, 600 MHz, ppm) δ: 10.78 (s, 1H), 7.78 (q, 1H, *J* = 5.0 Hz), 7.72 (s, 1H), 7.59–7.58 (m, 2H), 7.52 (s, 1H), 7.48 (t, 1H, *J* = 8.2 Hz), 7.34 (dd, 1H, J_1 = 3.0 Hz, J_2 = 8.6 Hz, Ph-H), 7.06 (dd, 1H, J_1 = 1.4 Hz, J_2 = 8.0 Hz), 2.54 (s, 3H); ^{13}C NMR (DMSO-d_6, 150 MHz, ppm) δ: 170.49, 169.75, 165.15, 162.38, 160.74, 156.31 (q, *J* = 34.65 Hz), 152.36, 140.82, 140.64, 135.16, 130.60, 121.84 (q, *J* = 273.15 Hz), 118.87, 117.59, 116.63, 114.21, 112.98, 103.49, 25.94; HRMS(calcd.) for $C_{19}H_{12}BrF_4N_3O_2$ (M + H)$^+$ 470.0122, found 470.0118.

3,4,5-trimethoxy-*N*-(3-((2-methyl-6-(trifluoromethyl) pyrimidin-4-yl)oxy)phenyl)benzamide (5q). White solid; yield 78%; m.p.116–117 °C; ^{1}H NMR (DMSO-d_6, 600 MHz, ppm) δ: 10.31 (s, 1H), 7.73 (s, 1H), 7.69 (d, 1H, *J* = 7.8 Hz), 7.51 (s, 1H), 7.48 (t, 1H, *J* = 7.8 Hz), 7.28 (s, 2H), 7.03 (d, 1H, *J* = 7.8 Hz), 3.87 (s, 3H), 3.74 (s, 3H), 2.51 (s, 3H); ^{13}C NMR (DMSO-d_6, 150 MHz, ppm) δ: 170.59, 169.79, 165.58, 156.31 (q, *J* = 34.65 Hz), 153.11, 152.27, 141.07, 140.90, 130.37, 130.23, 120.02 (q, *J* = 272.85 Hz), 118.41, 117.19, 113.82, 105.78, 103.35, 60.58, 56.55, 25.92; HRMS(calcd.) for $C_{22}H_{20}F_3N_3O_2$ (M + H)$^+$ 464.1428, found 464.1425.

In Vitro Antifungal Activity Test

The antifungal activities of all synthesized compounds at the concentration of 50 μg/ml were evaluated for their *in vitro* antifungal activities against the pathogenic fungi, including *B. dothidea*, *Phompsis* sp., and *B. cinerea* by the poison plate technique (Min et al., 2016). All the compounds were dissolved in 1 ml dimethyl sulfoxide (DMSO) before mixing with 90 ml potato dextrose agar (PDA). Mycelia dishes of approximately 5 mm diameter were cut from the culture medium and then picked up with a germfree inoculation needle and inoculated in the middle of the PDA plate aseptically. The inoculated plates were fostered at 27 ± 1 C for 3–4 days. DMSO in sterile distilled water served as a negative control, while Pyrimethanil acted as a positive control. For each treatment, three replicates were conducted. The inhibition rate *I* (%) was calculated by the following formula, where C (cm) represents the diameter of fungi growth on untreated PDA, and T (cm) represents the diameter of fungi on treated PDA.

$$I(\%) = [(C - T)/(C - 0.4)] \times 100$$

RESULTS AND DISCUSSION

Antifungal Activity Test *in vitro*

The *in vitro* antifungal activities of the title compounds against the pathogenic fungi, including *B. dothidea*, *Phomopsis* sp., and *B. cinereal* at 50 μg/ml were tested and the results are shown in **Table 1**. Bioassay results showed that compounds **5i**, **5l**, **5n**, and **5o** had good inhibition rates on *B. dothidea*, with the inhibition rates of 82.1, 81.1, 84.1, and 88.5%, respectively, which were similar to Pyrimethanil (84.4%). Meanwhile, the inhibition rates of compounds **5f**, **5n**, **5o**, and **5p** against *Phomopsis* sp. were 100.0, 91.8, 100.0, and 93.4%, which were even better than Pyrimethanil (85.1%). In addition, some of the target compounds, for example compounds **5c** (80.0%), **5i** (79.6%), **5l** (80.4%), **5m** (83.6%), **5n** (79.7%), **5o** (84.7%), and **5q** (80.5%), showed equally antifungal activity against *B. cinerea* to Pyrimethanil (82.8%).

The EC$_{50}$ values and antifungal diagram of the target compounds **5f**, **5o**, and **5p** were also tested and are presented in **Table 2** and **Figure 2** respectively. **Table 2** shows that compounds **5f**, **5o**, and **5p** exhibited excellent antifungal activity against *Phomopsis* sp., with the EC$_{50}$ values of 15.1, 10.5, and 19.6 μg/ml, which were superior to that of Pyrimethanil (32.1 μg/ml).

Structure-Function Relationship Analysis

In order to design novel and more promising active small molecules of pyrimidine derivatives, SAR analysis was also performed. The chemical structure of the target compounds indicated that the position of the amine group and the position and size of the substituent group R of the target compounds significantly influence the antifungal activities against. *B. dothidea*, *Phomopsis* sp. and *B. cinereal*. With the amine group at 3-position of the benzene ring and F and Br atoms at 2- and 5-position, respectively, compound **5o** exhibited excellent antifungal activities against. *B. dothidea*, *Phomopsis* sp. and *B. cinereal*, which were even better than those of Pyrimethanil. Meanwhile, in general terms, the

antifungal activities of the target compounds with the amine group at 3-position of benzene ring were better than those of the corresponding target compounds with the amine group at 2-position of the benzene ring, for example, **5h > 5b** and **5k > 5d**.

CONCLUSION

In conclusion, a total of 17 pyrimidine derivatives containing an amide moiety were synthesized and evaluated for their *in vitro* fungicidal activities against *B. dothidea*, *Phompsis* sp., and *B. cinerea* by the poison plate technique. Bioassay results demonstrated that compound 5-bromo-2-fluoro-*N*-(3-((2-methyl-6-(trifluoromethyl)pyrimidin-4-yl)oxy)phenyl)benzamide (**5o**) exhibited excellent antifungal activity against *Phompsis* sp., with the EC_{50} value of 10.5 μg/ml, which were even better than that of Pyrimethanil. This study provided a practical tool for guiding the design and synthesis of novel and more promising active small molecules of pyrimidine derivatives for controlling *Phompsis* sp., This study also demonstrated that this series of pyrimidine derivatives containing an amide moiety can be used to develop potential agrochemicals. In accordance with the pesticide registration requirements in China, further field and toxicity studies of compound **5o** will be undertaken in a future study.

DATA AVAILABILITY STATEMENT

The original contributions presented in the study are included in the article/**Supplementary Material**, further inquiries can be directed to the corresponding authors.

AUTHOR CONTRIBUTIONS

WW and QF contributed to the synthesis, purification, characterization of all compounds, and prepared the original manuscript. LW and CW performed the activity research. QF and LW perfected the language and assisted with the structure elucidation and manuscript revision. WW designed and supervised the research and revised the manuscript. All authors discussed, edited, and approved the final version.

FUNDING

SUPPLEMENTARY MATERIAL

The Supplementary Material for this article can be found online at: https://www.frontiersin.org/articles/10.3389/fchem.2021.695628/full#supplementary-material.

REFERENCES

Chen, M., Lu, D., Zhang, X., Chen, M., Dong, C., Wang, X., et al. (2021a). Synthesis and Biological Activities of Novel S-β-D-Glucopyranoside Derivatives of 1,2,4-triazole. *Phosphorus, Sulfur, Silicon Relat. Elem.*, 1–6. doi:10.1080/10426507.2021.1901704

Chen, S., Zhang, Y., Liu, Y., and Wang, Q. (2021b). Highly Efficient Synthesis and Acaricidal and Insecticidal Activities of Novel Oxazolines with *N*-Heterocyclic Substituents. *J. Agric. Food Chem.* 69, 3601–3606. doi:10.1021/acs.jafc.0c05558

Chen, X. M., Wang, S. H., Cui, D. L., and Li, B. (2015). The Synthesis and Herbicidal Activity of 5-(substituted-Phenyl)-4,6-Dioxo-4,5,6,7-Tetrahydropyrazolo[3,4-D]pyrimidines. *J. Heterocyclic Chem.* 52, 607–610. doi:10.1002/jhet.2047

Cheng, Y.-N., Jiang, Z.-H., Sun, L.-S., Su, Z.-Y., Zhang, M.-M., and Li, H.-L. (2020). Synthesis of 1, 2, 4-triazole Benzoyl Arylamine Derivatives and Their High Antifungal Activities. *Eur. J. Med. Chem.* 200, 112463. doi:10.1016/j.ejmech.2020.112463

Huang, Y. X., Li, M., Pan, X. J., Wu, X. M., Xiang, X. L., Li, W. Z., et al. (2018). Control Effect of Several Fungicides on Grape Downy Mildew. *Agrochemicals* 57, 836–839. doi:10.16820/j.cnki.1006-0413.2018.11.017

Li, H., Zhao, Y., Sun, P., Gao, L., Li, Y., Xiong, L., et al. (2021a). Synthesis and Insecticidal Evaluation of Novel Anthranilic Diamides Derivatives Containing 4-Chlorine Substituted N -Pyridylpyrazole. *Chin. J. Chem.* 39, 75–80. doi:10.1002/cjoc.202000013

Li, J.-h., Wang, Y., Wu, Y.-p., Li, R.-h., Liang, S., Zhang, J., et al. (2021b). Synthesis, Herbicidal Activity Study and Molecular Docking of Novel Pyrimidine Thiourea. *Pestic. Biochem. Physiol.* 172, 104766. doi:10.1016/j.pestbp.2020.104766

Liu, X.-H., Wang, Q., Sun, Z.-H., Wedge, D. E., Becnel, J. J., Estep, A. S., et al. (2017). Synthesis and Insecticidal Activity of Novel Pyrimidine Derivatives Containing Urea Pharmacophore againstAedes Aegypti. *Pest Manag. Sci.* 73, 953–959. doi:10.1002/ps.4370

Min, L.-J., Shi, Y.-X., Wu, H.-K., Sun, Z.-H., Liu, X.-H., Li, B.-J., et al. (2016). Microwave-assisted Synthesis and Antifungal Activity of Some Novel Thioethers Containing 1,2,4-triazole Moiety. *Appl. Sci.* 5, 1211–1220. doi:10.3390/app5041211

Patel, N., Desai, P., Patel, N., Jha, A., and Gautam, H. K. (2014). Agronanotechnology for Plant Fungal Disease Management: A Review. *Int. J. Curr. Microbiol. App. Sci.* 3, 71–84. doi:10.5455/ijmsph.2014.110320141

Shi, J. Q., Zhang, R. Q., He, L. N., Chen, J., Hu, A. L., Yin, X. H., et al. (2021). Screening of Fungicide for Controlling Kiwifruit Leaf Spot. *Agrochemicals* 60, 294–296. doi:10.16820/j.cnki.1006-0413.2021.04.016

Strange, R. N., and Scott, P. R. (2005). Plant Disease: a Threat to Global Food Security. *Annu. Rev. Phytopathol.* 43, 83–116. doi:10.1146/annurev.phyto.43.113004.133839

Sun, F. F., Ma, N., and Li, Z. M. (2006). 2-Amino-4-(2,2,2-trifluoroethoxy) Pyrimidine. *Acta Cryst.* 62, 3864–3865. doi:10.1107/s1600536806029564

Sun, X., Ji, Z., Wei, S., and Ji, Z. (2020). Design, Synthesis and Herbicidal Activity of 5-Cyclopropyl-*N*-Phenylisoxazole-4-Carboxamides. *J. Mol. Struct.* 1220, 128628. doi:10.1016/j.molstruc.2020.128628

Tang, X., Zhang, C., Chen, M., Xue, Y., Liu, T., and Xue, W. (2020). Synthesis and Antiviral Activity of Novel Myricetin Derivatives Containing Ferulic Acid Amide Scaffolds. *New J. Chem.* 44, 2374–2379. doi:10.1039/C9NJ05867B

Wang, Y., Li, J., Zhang, X. Y., Li, Y. L., Hu, B., Sun, H., et al. (2021). Controlling Test of High Efficiency and Low Toxicity Fungicides to *Botrytis Cinerea* on Cucumber. *Vegetables* 1, 38–41.

Wu, W.-N., Gao, M.-N., Tu, H., and Ouyang, G.-P. (2016a). Synthesis and Antibacterial Activity of Novel Substituted Purine Derivatives. *J. Heterocyclic Chem.* 53, 2042–2048. doi:10.1002/jhet.2527

Wu, W.-N., Jiang, Y.-M., Fei, Q., and Du, H.-T. (2019). Synthesis and Fungicidal Activity of Novel 1,2,4-triazole Derivatives Containing a Pyrimidine Moiety. *Phosphorus, Sulfur, Silicon Relat. Elem.* 194, 1171–1175. doi:10.1080/10426507.2019.1633321

Wu, W.-N., Tai, A.-Q., Chen, Q., and Ouyang, G.-P. (2016b). Synthesis and Antiviral Bioactivity of Novel 2-substituted Methlthio-5-(4-Amino-2-Methylpyrimidin-5-Yl)-1,3,4-Thiadiazole Derivatives. *J. Heterocyclic Chem.* 53, 626–632. doi:10.1002/jhet.2435

Wu, W., Chen, M., Fei, Q., Ge, Y., Zhu, Y., Chen, H., et al. (2020). Synthesis and Bioactivities Study of Novel Pyridylpyrazol Amide Derivatives Containing Pyrimidine Motifs. *Front. Chem.* 8, 522. doi:10.3389/fchem.2020.00522

Wu, W., Chen, Q., Tai, A., Jiang, G., and Ouyang, G. (2015). Synthesis and Antiviral Activity of 2-substituted Methylthio-5-(4-Amino-2-Methylpyrimidin-5-Yl)-1,3,4-Oxadiazole Derivatives. *Bioorg. Med. Chem. Lett.* 25, 2243–2246. doi:10.1016/j.bmcl.2015.02.069

Zan, N., Xie, D., Li, M., Jiang, D., and Song, B. (2020). Design, Synthesis, and Anti-ToCV Activity of Novel Pyrimidine Derivatives Bearing a Dithioacetal Moiety that Targets ToCV Coat Protein. *J. Agric. Food Chem.* 68, 6280–6285. doi:10.1021/acs.jafc.0c00987

Zhang, P., Guan, A., Xia, X., Sun, X., Wei, S., Yang, J., et al. (2019). Design, Synthesis, and Structure-Activity Relationship of New Arylpyrazole Pyrimidine Ether Derivatives as Fungicides. *J. Agric. Food Chem.* 67, 11893–11900. doi:10.1021/acs.jafc.9b05185

Advantages of publishing in Frontiers

OPEN ACCESS
Articles are free to read
for greatest visibility
and readership

FAST PUBLICATION
Around 90 days
from submission
to decision

HIGH QUALITY PEER-REVIEW
Rigorous, collaborative,
and constructive
peer-review

TRANSPARENT PEER-REVIEW
Editors and reviewers
acknowledged by name
on published articles

Frontiers
Avenue du Tribunal-Fédéral 34
1005 Lausanne | Switzerland

Visit us: www.frontiersin.org
Contact us: frontiersin.org/about/contact

REPRODUCIBILITY OF RESEARCH
Support open data
and methods to enhance
research reproducibility

DIGITAL PUBLISHING
Articles designed
for optimal readership
across devices

FOLLOW US
@frontiersin

IMPACT METRICS
Advanced article metrics
track visibility across
digital media

EXTENSIVE PROMOTION
Marketing
and promotion
of impactful research

LOOP RESEARCH NETWORK
Our network
increases your
article's readership